



*materials*

# Recent Advances in Corrosion Science

---

Edited by  
Jacek Ryl

Printed Edition of the Special Issue Published in *Materials*

# **Recent Advances in Corrosion Science**



# Recent Advances in Corrosion Science

Special Issue Editor

**Jacek Ryl**

MDPI • Basel • Beijing • Wuhan • Barcelona • Belgrade • Manchester • Tokyo • Cluj • Tianjin



*Special Issue Editor*

Jacek Ryl

Gdansk University of Technology

Poland

*Editorial Office*

MDPI

St. Alban-Anlage 66

4052 Basel, Switzerland

This is a reprint of articles from the Special Issue published online in the open access journal *Materials* (ISSN 1996-1944) (available at: [https://www.mdpi.com/journal/materials/special\\_issues/Corrosion\\_Science](https://www.mdpi.com/journal/materials/special_issues/Corrosion_Science)).

For citation purposes, cite each article independently as indicated on the article page online and as indicated below:

LastName, A.A.; LastName, B.B.; LastName, C.C. Article Title. <i>Journal Name</i> <b>Year</b> , Article Number, Page Range.
---

**ISBN 978-3-03936-176-2 (Hbk)**

**ISBN 978-3-03936-177-9 (PDF)**

© 2020 by the authors. Articles in this book are Open Access and distributed under the Creative Commons Attribution (CC BY) license, which allows users to download, copy and build upon published articles, as long as the author and publisher are properly credited, which ensures maximum dissemination and a wider impact of our publications.

The book as a whole is distributed by MDPI under the terms and conditions of the Creative Commons license CC BY-NC-ND.

# Contents

<b>About the Special Issue Editor</b> . . . . .	vii	
<b>Jacek Ryl</b> Special Issue: Recent Advances in Corrosion Science Reprinted from: <i>Materials</i> <b>2020</b> , <i>13</i> , 1927, doi:10.3390/ma13081927 . . . . .		1
<b>Hanbin Chen, Zhenbo Qin, Meifeng He, Yichun Liu and Zhong Wu</b> Application of Electrochemical Atomic Force Microscopy (EC-AFM) in the Corrosion Study of Metallic Materials Reprinted from: <i>Materials</i> <b>2020</b> , <i>13</i> , 668, doi:10.3390/ma13030668 . . . . .		3
<b>Dezheng Liu, Yan Li, Xiangdong Xie and Jing Zhao</b> Effect of Pre-Corrosion Pits on Residual Fatigue Life for 42CrMo Steel Reprinted from: <i>Materials</i> <b>2019</b> , <i>12</i> , 2130, doi:10.3390/ma12132130 . . . . .		51
<b>Qiumei Yang, Yajun Zhou, Zheng Li and Daheng Mao</b> Effect of Hot Deformation Process Parameters on Microstructure and Corrosion Behavior of 35CrMoV Steel Reprinted from: <i>Materials</i> <b>2019</b> , <i>12</i> , 1455, doi:10.3390/ma12091455 . . . . .		65
<b>Asiful H. Seikh, Amit Sarkar, Jitendra Kumar Singh, Sohail M. A. Khan Mohammed, Nabeel Alharthi and Manojit Ghosh</b> Corrosion Characteristics of Copper-Added Austempered Gray Cast Iron (AGCI) Reprinted from: <i>Materials</i> <b>2019</b> , <i>12</i> , 503, doi:10.3390/ma12030503 . . . . .		85
<b>Peixuan Ouyang, Guangbao Mi, Peijie Li, Liangju He, Jingxia Cao and Xu Huang</b> Non-Isothermal Oxidation Behaviors and Mechanisms of Ti-Al Intermetallic Compounds Reprinted from: <i>Materials</i> <b>2019</b> , <i>12</i> , 2114, doi:10.3390/ma12132114 . . . . .		103
<b>Nader El-Bagoury, Sameh I. Ahmed, Ola Ahmed Abu Ali, Shimaa El-Hadad, Ahmed M. Fallatah, G.A.M. Mersal, Mohamed M. Ibrahim, Joanna Wysocka, Jacek Ryl, Rabah Boukherroub and Mohammed A. Amin</b> The Influence of Microstructure on the Passive Layer Chemistry and Corrosion Resistance for Some Titanium-Based Alloys Reprinted from: <i>Materials</i> <b>2019</b> , <i>12</i> , 1233, doi:10.3390/ma12081233 . . . . .		125
<b>Marián Palcut, Libor Ďuriška, Ivona Černíčková, Sandra Brunovská, Žaneta Gerhátová, Martin Sahul, Ľubomír Čaplovič and Jozef Janovec</b> Relationship between Phase Occurrence, Chemical Composition, and Corrosion Behavior of as-Solidified Al-Pd-Co Alloys Reprinted from: <i>Materials</i> <b>2019</b> , <i>12</i> , 1661, doi:10.3390/ma12101661 . . . . .		145
<b>Jing Ren, Enyu Guo, Xuejian Wang, Huijun Kang, Zongning Chen and Tongmin Wang</b> Influence of Alloyed Ga on the Microstructure and Corrosion Properties of As-Cast Mg-5Sn Alloys Reprinted from: <i>Materials</i> <b>2019</b> , <i>12</i> , 3686, doi:10.3390/ma12223686 . . . . .		163
<b>Shenyang Xu, Shengtao Zhang, Lei Guo, Li Feng and Bochuan Tan</b> Experimental and Theoretical Studies on the Corrosion Inhibition of Carbon Steel by Two Indazole Derivatives in HCl Medium Reprinted from: <i>Materials</i> <b>2019</b> , <i>12</i> , 1339, doi:10.3390/ma12081339 . . . . .		179

<b>Mingjin Tang, Jianbo Li, Zhida Li, Luoping Fu, Bo Zeng and Jie Lv</b> Mannich Base as Corrosion Inhibitors for N80 Steel in a CO <sub>2</sub> Saturated Solution Containing 3 wt % NaCl Reprinted from: <i>Materials</i> <b>2019</b> , <i>12</i> , 449, doi:10.3390/ma12030449 . . . . .	<b>191</b>
<b>Jacek Ryl, Mateusz Brodowski, Marcin Kowalski, Wiktoria Lipinska, Pawel Niedzialkowski and Joanna Wysocka</b> Corrosion Inhibition Mechanism and Efficiency Differentiation of Dihydroxybenzene Isomers Towards Aluminum Alloy 5754 in Alkaline Media Reprinted from: <i>Materials</i> <b>2019</b> , <i>12</i> , 3067, doi:10.3390/ma12193067 . . . . .	<b>207</b>
<b>Milan Parchovianský, Ivana Parchovianská, Peter Švančárek, Günter Motz and Dušan Galusek</b> PDC Glass/Ceramic Coatings Applied to Differently Pretreated AISI441 Stainless Steel Substrates Reprinted from: <i>Materials</i> <b>2020</b> , <i>13</i> , 629, doi:10.3390/ma13030629 . . . . .	<b>227</b>
<b>Juliusz Winiarski, Anna Niciejewska, Jacek Ryl, Kazimierz Darowicki, Sylwia Baśladyńska, Katarzyna Winiarska and Bogdan Szczygieł</b> Ni/cerium Molybdenum Oxide Hydrate Microflakes Composite Coatings Electrodeposited from Choline Chloride: Ethylene Glycol Deep Eutectic Solvent Reprinted from: <i>Materials</i> <b>2020</b> , <i>13</i> , 924, doi:10.3390/ma13040924 . . . . .	<b>243</b>
<b>Henryk Kania and Jacek Sipa</b> Microstructure Characterization and Corrosion Resistance of Zinc Coating Obtained on High-Strength Grade 10.9 Bolts Using a New Thermal Diffusion Process Reprinted from: <i>Materials</i> <b>2019</b> , <i>12</i> , 1400, doi:10.3390/ma12091400 . . . . .	<b>261</b>
<b>Jacek Ryl, Mateusz Cieslik, Artur Zielinski, Mateusz Ficek, Bartłomiej Dec, Kazimierz Darowicki and Robert Bogdanowicz</b> High-Temperature Oxidation of Heavy Boron-Doped Diamond Electrodes: Microstructural and Electrochemical Performance Modification Reprinted from: <i>Materials</i> <b>2020</b> , <i>13</i> , 964, doi:10.3390/ma13040964 . . . . .	<b>273</b>

## About the Special Issue Editor

**Jacek Ryl** is an Associate Professor in the Faculty of Chemistry, Gdansk University of Technology. He has received a Ph.D. (2010) and habilitation (2018) in Chemical Technology at GUT. His principal area of scientific activity lies in applied electrochemistry and surface physic-chemistry, in particular corrosion science, electrochemical sensors, and materials for energy storage and conversion. He is involved in the development of instantaneous impedance techniques with multisine perturbation, dedicated to the assessment of nonstationary processes. Jacek Ryl is coauthor of over 90 peer-reviewed papers (h-index=21). In 2015–2020, he was the principal investigator of programs Sonata NCN and Iuventus Plus. His most notable awards include a scientific scholarship by the Minister of Science and Higher Education of Poland (2017) and the IV Division (Engineering Sciences) of the Polish Academy of Sciences award for scientific achievements (2019). Currently, he serves on the Editorial Board for *Molecules*, MDPI.





Editorial

## Special Issue: Recent Advances in Corrosion Science

Jacek Ryl

Department of Electrochemistry, Corrosion and Materials Engineering, Gdansk University of Technology, Narutowicza 11/12, 80-233 Gdansk, Poland; jacek.ryl@pg.edu.pl

Received: 13 April 2020; Accepted: 17 April 2020; Published: 19 April 2020

---

The International Union of Pure and Applied Chemistry (IUPAC) and European Federation of Corrosion (EFC) define corrosion as an irreversible interfacial reaction of a material with its environment which results in its consumption or dissolution, often resulting in effects detrimental to the usage of the material considered. Corrosion failure is a significant problem in any given type of industry, leading to substantial economic consequences, but also often influencing human health and the environment negatively, among other unmeasurable factors. The industry estimates indicate that the total direct cost of corrosion ranges between 3% and 5% of GDP [1], while the indirect costs (outages, delays, revenue losses, etc.) which much harder to evaluate, are estimated to be equal to this. These numbers point out that investments in corrosion protection are, by all means, economically justified.

The dynamic development of the global industry and growing demand for new material technologies generates constantly increasing problems regarding premature material degradation and the requirement to determine corrosion mechanisms and to develop new protection/evaluation approaches. This Special Issue, “Recent Advances in Corrosion Science”, brings together fourteen articles and one review, providing a snapshot of the recent activity and development in this field.

The corrosion properties of ferrous metals remain the most popular subject of investigation, which naturally found coverage in numerous research articles present within this Special Issue. The primary source of this versatility is achieved by a proper selection of alloying additives and metalworking, which guarantee the demanded mechanical and physicochemical properties. On the other hand, the alteration of metal structure leads to the formation of galvanic microcells, often translating into various forms of local corrosion. The search for alloying additives enhancing the corrosion resistance without sacrificing the desired characteristics continues, intending to reduce alloy corrosion rate and bring measurable economic profits. Within this Special Issue, you will find multiple original research papers strictly devoted to this issue for both ferrous [2–4] and non-ferrous metals [5–8]. The influence of novel microscopy tools, which enable the direct observation of local corrosion processes, cannot be overestimated. For this reason, I would like to recommend a very interesting and important review prepared by Chen et al. [9], referring to the advances in electrochemical atomic force microscopy (EC-AFM), an outstanding tool to perform real-time in situ corrosion studies of galvanic microcells.

Affecting the corrosion process by electrochemical protection (cathodic or anodic), barrier properties obtained with the use of paints or coatings as well as environment modification with dedicated corrosion inhibitors, are the three primary ways to reduce the corrosion rate found in both principle and industrial studies regarding anti-corrosion technologies. All of these research areas are represented within this Special Issue. The works of Xu et al. [10], Tang, et al. [11] and Ryl et al. [12] reveal various aspects concerning the search for efficient organic corrosion inhibitors and the tools used to evaluate protection mechanisms. The studies of Parchoviansky et al. [13] and Winiarski et al. [14] provide an insight on the development of anti-corrosion composite coatings, while an interesting report from Kania and Sipa [15] shows the improved corrosion resistance of anodic zinc coatings, obtained using a new thermal diffusion process.

It is important to emphasize that, nowadays, corrosion issues are not solely connected with the degradation of metals. Modern composite or semiconductor electrode materials are constantly

developed to be used in numerous branches of applied electrochemistry, such as energy storage and conversion, electrochemical sensors and electrocatalytic processes. Their stable performance under aggressive environmental factors is often questionable. Thus, the final manuscript of this Special Issue presents work in this new field, which was devoted to high-temperature oxidation and the degradation of boron-doped diamond nanostructures [16].

**Conflicts of Interest:** The authors declare no conflict of interest.

## References

- Koch, G.H.; Brongers, M.P.H.; Thompson, N.G.; Virmani, Y.P.; Payer, J.H. *Corrosion Cost and Preventive Strategies in the United States*; FHWA-RD-01-156, R315-01; United States, Federal Highway Administration: Washington, DC, USA, 2001.
- Liu, D.; Li, Y.; Xie, X.; Zhao, J. Effect of Pre-Corrosion Pits on Residual Fatigue Life for 42CrMo Steel. *Materials* **2019**, *12*, 2130. [[CrossRef](#)] [[PubMed](#)]
- Yang, Q.; Zhou, Y.; Li, Z.; Mao, D. Effect of Hot Deformation Process Parameters on Microstructure and Corrosion Behavior of 35CrMoV Steel. *Materials* **2019**, *12*, 1455. [[CrossRef](#)] [[PubMed](#)]
- Seikh, A.H.; Sarkar, A.; Singh, J.K.; Mohammed, S.M.A.K.; Alharthi, N.; Ghosh, M. Corrosion Characteristics of Copper-Added Austempered Gray Cast Iron (AGCI). *Materials* **2019**, *12*, 503. [[CrossRef](#)] [[PubMed](#)]
- Ren, J.; Guo, E.; Wang, X.; Kang, H.; Chen, Z.; Wang, T. Influence of Alloyed Ga on the Microstructure and Corrosion Properties of As-Cast Mg–5Sn Alloys. *Materials* **2019**, *12*, 3686. [[CrossRef](#)] [[PubMed](#)]
- Ouyang, P.; Mi, G.; Li, P.; He, L.; Cao, J.; Huang, X. Non-Isothermal Oxidation Behaviors and Mechanisms of Ti–Al Intermetallic Compounds. *Materials* **2019**, *12*, 2114. [[CrossRef](#)] [[PubMed](#)]
- Palcut, M.; Đuriška, L.; Černičková, I.; Brunovská, S.; Gerhátová, Ž.; Sahul, M.; Čaplovič, L.; Janovec, J. Relationship between Phase Occurrence, Chemical Composition, and Corrosion Behavior of as-Solidified Al–Pd–Co Alloys. *Materials* **2019**, *12*, 1661. [[CrossRef](#)] [[PubMed](#)]
- El-Bagoury, N.; Ahmed, S.I.; Ahmed Abu Ali, O.; El-Hadad, S.; Fallatah, A.M.; Mersal, G.A.M.; Ibrahim, M.M.; Wysocka, J.; Ryl, J.; Boukherroub, R.; et al. The Influence of Microstructure on the Passive Layer Chemistry and Corrosion Resistance for Some Titanium-Based Alloys. *Materials* **2019**, *12*, 1233. [[CrossRef](#)] [[PubMed](#)]
- Chen, H.; Qin, Z.; He, M.; Liu, Y.; Wu, Z. Application of Electrochemical Atomic Force Microscopy (EC-AFM) in the Corrosion Study of Metallic Materials. *Materials* **2020**, *13*, 668. [[CrossRef](#)] [[PubMed](#)]
- Xu, S.; Zhang, S.; Guo, L.; Feng, L.; Tan, B. Experimental and Theoretical Studies on the Corrosion Inhibition of Carbon Steel by Two Indazole Derivatives in HCl Medium. *Materials* **2019**, *12*, 1339. [[CrossRef](#)] [[PubMed](#)]
- Tang, M.; Li, J.; Li, Z.; Fu, L.; Zeng, B.; Lv, J. Mannich Base as Corrosion Inhibitors for N80 Steel in a CO<sub>2</sub> Saturated Solution Containing 3 wt % NaCl. *Materials* **2019**, *12*, 449. [[CrossRef](#)] [[PubMed](#)]
- Ryl, J.; Brodowski, M.; Kowalski, M.; Lipinska, W.; Niedzialkowski, P.; Wysocka, J. Corrosion Inhibition Mechanism and Efficiency Differentiation of Dihydroxybenzene Isomers Towards Aluminum Alloy 5754 in Alkaline Media. *Materials* **2019**, *12*, 3067. [[CrossRef](#)] [[PubMed](#)]
- Parchovianský, M.; Parchovianská, I.; Švančárek, P.; Motz, G.; Galusek, D. PDC Glass/Ceramic Coatings Applied to Differently Pretreated AISI441 Stainless Steel Substrates. *Materials* **2020**, *13*, 629. [[CrossRef](#)] [[PubMed](#)]
- Winiarski, J.; Niciejewska, A.; Ryl, J.; Darowicki, K.; Baśladyńska, S.; Winiarska, K.; Szczygieł, B. Ni/cerium Molybdenum Oxide Hydrate Microflakes Composite Coatings Electrodeposited from Choline Chloride: Ethylene Glycol Deep Eutectic Solvent. *Materials* **2020**, *13*, 924. [[CrossRef](#)] [[PubMed](#)]
- Kania, H.; Sipa. Microstructure Characterization and Corrosion Resistance of Zinc Coating Obtained on High-Strength Grade 10.9 Bolts Using a New Thermal Diffusion Process. *Materials* **2019**, *12*, 1400.
- Ryl, J.; Cieslik, M.; Zielinski, A.; Ficek, M.; Dec, B.; Darowicki, K.; Bogdanowicz, R. High-Temperature Oxidation of Heavy Boron-Doped Diamond Electrodes: Microstructural and Electrochemical Performance Modification. *Materials* **2020**, *13*, 964. [[CrossRef](#)] [[PubMed](#)]



© 2020 by the author. Licensee MDPI, Basel, Switzerland. This article is an open access article distributed under the terms and conditions of the Creative Commons Attribution (CC BY) license (<http://creativecommons.org/licenses/by/4.0/>).

Review

# Application of Electrochemical Atomic Force Microscopy (EC-AFM) in the Corrosion Study of Metallic Materials

Hanbing Chen <sup>1</sup>, Zhenbo Qin <sup>2</sup>, Meifeng He <sup>1,\*</sup>, Yichun Liu <sup>3</sup> and Zhong Wu <sup>2,\*</sup>

<sup>1</sup> School of Materials Science and Engineering, University of Shanghai for Science and Technology, Shanghai 200093, China; chb19940420@163.com

<sup>2</sup> Key Laboratory of Advanced Ceramics and Machining Technology (Ministry of Education), Tianjin University, Tianjin 300072, China; qinzhb@tju.edu.cn

<sup>3</sup> School of Materials Science and Engineering, Kunming University of Science and Technology, Kunming 650093, China; spsjtu@163.com

\* Correspondence: hmf752@usst.edu.cn (M.H.); zhong.wu@tju.edu.cn (Z.W.)

Received: 27 December 2019; Accepted: 26 January 2020; Published: 3 February 2020

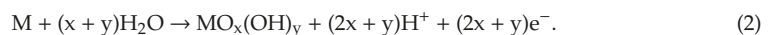
**Abstract:** Electrochemical atomic force microscopy (EC-AFM), a branch of a scanning probe microscopy (SPM), can image substrate topography with high resolution. Since its inception, it was extended to a wide range of research areas through continuous improvement. The presence of an electrolytic cell and a potentiostat makes it possible to observe the topographical changes of the sample surface in real time. EC-AFM is used in in situ corrosion research because the samples are not required to be electrically conductive. It is widely used in passive film properties, surface dissolution, early-stage corrosion initiation, inhibitor efficiency, and many other branches of corrosion science. This review provides the research progress of EC-AFM and summarizes the extensive applications and investigations using EC-AFM in corrosion science.

**Keywords:** EC-AFM; corrosion; metallic materials

## 1. Introduction

As is known, all materials have a certain service life and will suffer various forms of direct or indirect damage during use. Although the material will be damaged in a variety of forms, corrosion is the most important and common form, which is a gradual process and cannot be restored. The problem of material corrosion occurs in various fields of the national economy, from daily life to industrial and agricultural production, as well as from advanced science and technology to the development of the national defense industry. Corrosion can lead to huge economic losses and even catastrophic accidents, which not only consume a large amount of resources and energy but also pollute the environment, resulting in a huge loss in the gross domestic product (GDP) [1]. Therefore, it is necessary to clarify the failure mechanism of materials in corrosive environments and take reasonable protective measures to achieve the purpose of preventing or controlling corrosion, to improve the life cycle of materials.

Corrosion is the irreparable damage or deterioration of materials caused by chemical, electrochemical, and physical effects of environmental media. In processes of metallic material corrosion, a chemical or electrochemical multiphase reaction occurs on the surface or interface of the metal, resulting in the conversion of the metal to an oxidized (ionic) state. Corrosion of metallic substance is started via the oxidation of metals.



In order to maintain the neutral condition, a counter cathodic reaction of the electrolyte occurs [2].



The basic process of metallic corrosion in an aqueous solution consists of the anodic dissolution of metals and the cathodic reduction of oxidants. The redox reactions (Equations (1)–(7)) involve the transfer of electrons and ions between the metal and the solution. According to the corrosion kinetics, the anodic oxidation current of the metal degradation is equal to the cathodic reduction current of the oxidant at the corrosion potential. When the metal electrode potential is more positive, the rates of cathodic reactions increase and the rates of anodic reactions decrease accordingly. Conversely, as the metal electrode potential becomes more negative, the effect on the reactions is opposite.

The development of corrosion science is inseparable from the advancement of research methods and instruments. Conventional electrochemical measurements can only obtain macroscopic electrochemical information on the surface of the material. In situ electrochemical scanning probe technology with high spatial resolution facilitated the development of corrosion science, elucidating the microstructure and dynamic properties of materials and interfaces at the molecular/atomic level.

The electrochemical atomic force microscope (EC-AFM) was developed in 1991 on the basis of the atomic force microscope (AFM) [3]. It is well known that AFM is a kind of scanning probe microscope (SPM) and an extension of the scanning tunneling microscope (STM) [4]. The STM was invented by Gerd Binnig and Heinrich Rohrer in the 1980s, and it was able to image individual atoms for the first time. In 1982, Binnig and co-workers indicated that vacuum tunneling with an externally controllable tunnel distance is feasible, even under the conditions of room temperature and non-ultra-high vacuum, which was the first step in the development of scanning tunneling microscopy [5]. The  $7 \times 7$  reconstruction on Si(111) observed in real space with STM was considered the first scientific success [6]. G. Binnig and H. Rohrer went into detail about STM, and they were rewarded with the Nobel Prize in Physics for their work in the field of STM in 1986 [7,8]. At present, STM is still an important method in surface science. However, due to the operation principle of STM being based on the quantum tunneling effect, STM has a severe restriction that requires the samples to be conductive. STM can only directly observe the surface structure of conducting and semiconducting materials. In order to overcome the shortcomings of STM, the AFM was invented by Binnig, Quate, and Gerber in 1986 [4]. The AFM can image the surfaces of a flat sample through the weak interaction force (atomic force) between the probe (mounted to a cantilever) and the sample, which is measured by monitoring the deflection of the microcantilever. Therefore, the AFM is suitable for both conductive and non-conductive samples, and its application field is more extensive. In addition, the AFM is a high-resolution microscope with atomic-scale resolution, which developed into a powerful micro/nanometer-scale surface analysis technique [9,10]. On the basis of different capabilities, a large number of techniques were developed after the invention of AFM, such as Kelvin probe force microscopy (KPFM), magnetic force microscopy (MFM), scanning electrochemical microscopy/atomic force microscopy (SECM-AFM), electrostatic force microscopy (EFM), and EC-AFM. These technologies are not only imaging tools; they can also accurately and quantitatively measure local physical and chemical phenomena.

EC-AFM extends AFM technology to the field of electrochemistry for in situ studying of the solid–liquid interface. The main difference between EC-AFM and AFM in liquids is that the applied potential of the sample with respect to the reference electrode is controlled by a potentiostat [11]. Topographic changes of the sample are achieved by measuring the force between the tip and the substrate in a three-electrode electrochemical cell composed of the counter electrode, reference electrode,

and working electrode (substrate). EC-AFM is applied to in situ electrodeposition [12,13], biological science [14], supercapacitors [15], batteries and electrodes [16], corrosion and protection, and so on. After the invention of EC-AFM, its electrolytic cell, imaging mode, and probe performance were continuously improved, which opens a new prospect for the understanding of the corrosion mechanism [17,18].

In this review, we illustrate the application of EC-AFM to metal corrosion with specific examples, including understanding the properties of passive films, surface dissolution, pitting corrosion, selective corrosion, intergranular corrosion, inhibitor efficiency, coating protection, and other branches of corrosion science. The main purpose of this review is to provide the present situation and trend of corrosion research on various metal materials by EC-AFM and outline future prospects for the technique.

## 2. Principle and Operation Modes of EC-AFM

The basic working principle of EC-AFM is similar to that of AFM, and it shares its key components. Primarily, a nanoscale sharp tip located at the end of the cantilever of the probe is used to feel the interaction force between the tip and the sample, a piezo scanner is used for controlling the movement of the tip or sample in the  $x$ -,  $y$ -, and  $z$ -directions, a feedback control system and feedback circuit are used to control the deflection of the cantilever, and a computer system is used to display the results and control the operational parameters [19,20]. In addition, EC-AFM requires an electrochemical cell that can accommodate the working electrode (WE), counter electrode (CE), and reference electrode (RE), as well as a potentiostat for normal potentiostat control in a three-electrode system. Generally, the electrochemical cell is made from chemical-resistant polycarbonate, which can be used with a wide variety of liquids. Eight-degree nose assemblies are recommended for imaging in liquid because the smaller angle considers the different angles at which the laser goes in and out of the fluid, compared to operation in air. The electrochemical cell typically contains retaining clips, an O-ring gasket, and a liquid cell plate. When assembled, the sample itself comprises the bottom of the liquid container. Therefore, the sample must be large enough for the O-ring to seat. The WE should be relatively small, and each point on the WE should be geometrically equivalent to the counter electrode CE, which ensures that the current and potential across the electrode are evenly distributed. Others are based on conventional electrochemical testing requirements. Figure 1 shows the diagram of a typical electrochemical AFM cell with a potentiostat. During the scanning, the sample to which the potential is applied is placed in the electrolytic cell as the working electrode and scanned with the tip mounted on the cantilever. The force between the tip and the sample is measured by monitoring the deflection of the cantilever. By plotting the deflection of the cantilever versus its position on the sample, a topographic image of the sample is obtained [21].

The operation mode of EC-AFM is also similar to that of AFM, and the instrument can be operated either in constant height mode or constant force mode. Based on the interaction force between the tip and the sample, it is generally divided into different operation modes in the imaging process, such as contact mode, non-contact mode, intermittent tapping (tapping mode), torsional resonance mode, and peak force tapping mode. The first is the contact mode, in which the tip of the probe is always in contact with the surface of the sample, and the force between the tip and the sample is a repulsive force. Since the silicon nitride cantilever is soft enough to be deflected and has a high resonance frequency to avoid vibration instability, a silicon nitride probe is often used in contact mode. The contact mode has the advantage of high resolution and high scan speed, but it may cause damage to the surface of the sample. Both the transverse shear force and the capillary force on the surface may have adverse effects [22]. The second type is the non-contact mode, in which the cantilever vibrates above the sample surface, and the distance between the tip and the sample is usually several nanometers [23]. The force between the tip and the sample is van der Waals attraction. In the non-contact mode, there is no damage to the surface of the sample and the lateral force is the smallest, but the resolution is low and the scanning speed is slow. In order to avoid being stuck to the water film on the sample surface, it is often used to scan hydrophobic surfaces and soft samples. However, the development

and improvement of this device in recent years enabled non-contact mode to detect repulsion and obtain atomic resolution images. Miyata used a non-contact-mode AFM to observe the dissolution of calcite in water at high speed [24]. This may well be applicable to the observation of corrosion processes on metal surfaces. The third type is the intermittent tapping (tapping mode), in which the cantilever oscillates at a frequency close to its resonance frequency and the oscillation amplitude is monitored [25]. The cantilever oscillates near its resonant frequency above the surface of the sample, and the probe contacts the sample surface once at the bottom of the oscillation during each vibration period. The difference with the non-contact mode is that the amplitude (amplitude > 20 nm) of the cantilever is larger than that of the non-contact mode (amplitude < 10 nm). It not only reduces damage to the sample and reduces the effects of transverse force, but it also has a higher lateral resolution on most samples. The disadvantage is that the scanning speed is limited.

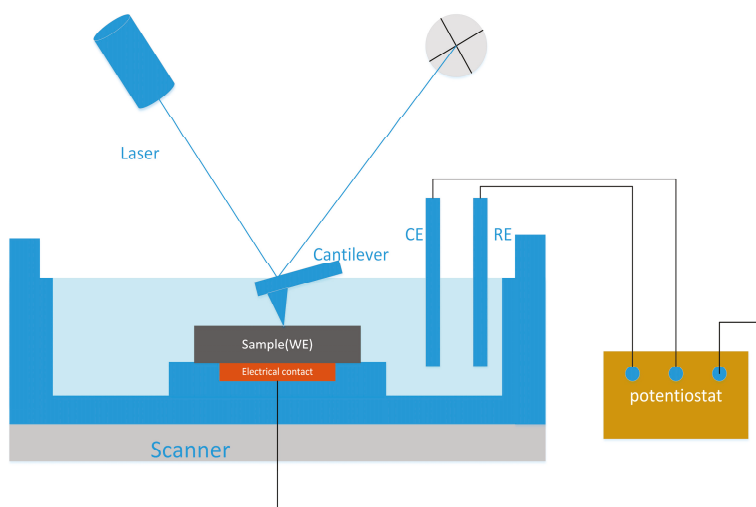


**Figure 1.** The schematic diagram of electrochemical atomic force microscopy (EC-AFM) electrolytic cell.

In addition, in order to further understand the properties of nanomaterials, a torsional resonance mode (TRmode) AFM was developed, which can measure both vertical and lateral force concurrently [26]. In the torsional resonance mode, the cantilever conducts torsional vibration with the long axis as the center and causes the tip to be in the vibration state. When the probe encounters transverse force on the surface, the system can detect the change in the cantilever torsion vibration and detect the fluctuation in the surface topography of sample [27]. It should be noted that the tapping mode applies a compressive force and the TR mode applies a torsional force; thus, the normal and shear performance is measured in the tapping mode and the TR mode, respectively [28]. Another newly developed operation mode is the peak force tapping mode, in which the tip is oscillated periodically in the vertical direction at a frequency well below cantilever resonance, tapping the sample until the maximum repulsion force reaches the setpoint in each tap [29]. The z piezo is driven with sinusoids rather than a triangular waveform in conventional force–distance (F–D) curves [30]. This mode directly controls the interaction between the tip and the sample, reducing the depth of deformation and the corresponding contact area, minimizing damage to the probe or sample [31,32]. Moreover, the force–distance interactions can be measured directly through peak force tapping mode.

Table 1 summarizes the operation mode of EC-AFM with the necessary parameters added. In the field of corrosion, contact mode and intermittent tapping (tapping mode) are mainly used.

**Table 1.** Comparison of common operation modes of EC-AFM.

Mode	Probes (Nominal Spring Constants)	Cantilever	Tip-Sample Distance	Force	Scan Rate
Contact mode	Silicon nitride probes (less than tapping and non-contact mode)	The cantilever is deflected: constant force or constant height	<0.5 nm	Repulsive $10^{-9}$ – $10^{-6}$ N	High scan speeds
Non-contact mode	Silicon probes (20–100 N/m)	The cantilever is oscillated (amplitude < 10 nm)	1–10 nm	Attractive $10^{-12}$ N	Slower scan speed than tapping and contact mode
Intermittent tapping (tapping mode)	Silicon probes (2–50 N/m)	The cantilever is oscillated (amplitude > 20 nm)	0.5–2 nm (intermittent contact)	Both repulsive and attractive forces	slower scan speed

### 3. Application of EC-AFM in Metal Corrosion and Corrosion Protection

#### 3.1. The Micro-Area Corrosion

##### 3.1.1. The Corrosion Product Film

EC-AFM can characterize the real-time nanoscale topographic changes of a corrosion product film on a metal surface under different potentials in aqueous environments, which avoids the potential contamination and degradation of the corrosion product film during conventional ex situ characterization and analysis techniques.

A typical example of studying corrosion product films with EC-AFM was presented by Li and co-workers, who studied the surface passivation film and its substructure of carbon steel in a carbonate/bicarbonate solution by EC-AFM in contact mode [33]. They designed a solution container for the EC-AFM, which was large enough to accommodate the three-electrode system and avoid evaporation during testing. The topographic characterization of the sample surface was performed at the passivation potentials of  $-0.1 V_{(SCE)}$  (saturated calomel electrode),  $0.5 V_{(SCE)}$  and  $0.7 V_{(SCE)}$ . The results showed that, at  $-0.1 V_{(SCE)}$  and  $0.5 V_{(SCE)}$ , as the passivation time increased, the nanoscale features, i.e., the scale-like spots on the surface of the sample, increased in diameter, indicating the growth of the passive film. When the grooves caused by the surface treatment were not observed, a thick passivation film was formed on the surface of the sample. The surface roughness calculated from the topographic profile was small and changed little, indicating that the passive film was relatively uniform. When the potential reached  $0.7 V_{(SCE)}$ , the roughness increased and the passive film became non-uniform, as shown in Figure 2.

In addition, based on the morphology, they found that the passive films contained a mixture of  $Fe_3O_4$ ,  $Fe_2O_3$ , and  $FeOOH$  when passivated at the active-passive transition potential. The inner layer of the passive film was  $Fe_3O_4$  and the outer layer was  $Fe_2O_3/FeOOH$ . When the film-forming potential changed from  $-0.1 V_{(SCE)}$  to  $0.5 V_{(SCE)}$ , the chemical composition did not change, but the thickness of the inner layer became thicker, leading to an increase in the thickness of the oxide film from about 4.5 nm to 5.8 nm, and the compactness improved, which made the film more protective. On the contrary, when the potential was at  $0.7 V_{(SCE)}$ , although the thickness of the film increased, its chemical composition changed greatly and an amorphous structure appeared, which reduced the corrosion resistance of the film.

Padhy et al. [34] investigated the passive film properties of 304L stainless steel in the nitric acid medium in both ex situ and in situ conditions. The ex situ study on the surface morphology of the passive film showed that the surface morphology of 304L stainless steel depended on the stability of the passive film in nitric acid. The morphology features of the passive film in nitric acid medium increased with time and solution concentration. The passive film in 1 M and 4 M nitric acid solution was stable. However, in 8 M and 11.5 M nitric acid, breakdown of the passive film was observed. In situ surface morphology changes of the passive film were monitored by EC-AFM in 0.1 M, 0.5 M, 0.6 M, and 1 M nitric acid. It was found that, at lower concentrations of 0.1 M and 0.5 M nitric acid, the passive film grew in a platelet-like structure. At nitric acid concentrations of 0.6 M and 1 M, platelet-like structures aggregated, homogenized,



and began to deplete from the surface, causing selective dissolution. The results of X-ray photoelectron spectroscopy (XPS) analysis showed that the passive film at lower concentration was composed of a hydroxide and oxide layer. However, at high concentrations, the passive film consisted only of an oxide layer. The passivity of 304L stainless steel under the action of low-concentration nitric acid started from the formation of chromium hydroxide, and the surface was in the form of platelet-like structures. As the concentration increased, the hydroxide layer changed to a homogenous oxide layer. As the concentration continued to increase, the protective oxide film was depleted from the structural heterogeneous zone, leading to the opening of the oxidation boundary. The depletion of the oxide layer caused selective dissolution and local corrosion of 304L stainless steel.

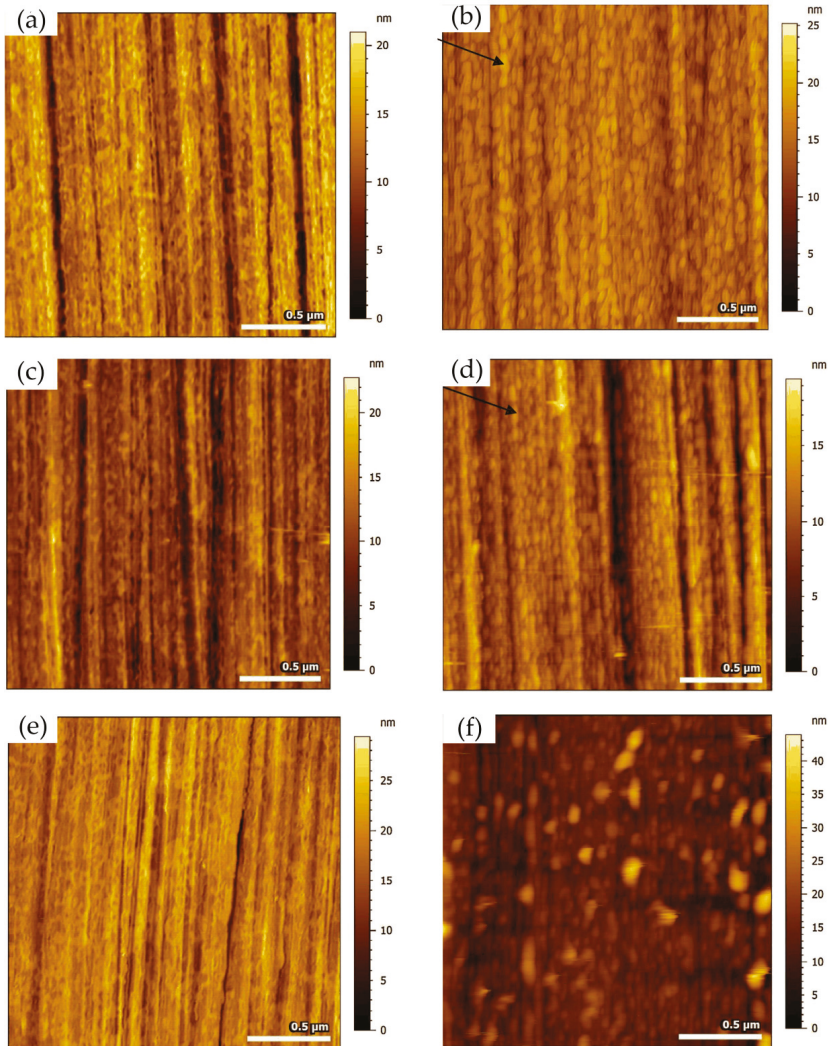


**Figure 2.** The AFM images of the steel specimen polarized at  $-0.1 V_{(SCE)}$  (saturated calomel electrode) for (a) 0.5 min and (b) 60 min, at  $0.5 V_{(SCE)}$  for (c) 0.5 min and (d) 60 min, and at  $0.7 V_{(SCE)}$  for (e) 0.5 min and (f) 60 min. The black arrow points to scale-like spots. Adapted with permission from Reference [33]; copyright 2017 Elsevier Ltd.

Many researchers reported the corrosion process and mechanism of AA 2024 and identified the corrosion products. Kreta et al. [35] explored the changes on the surface during exposure to the sodium chloride environment. In their experiment, the development of the passive film of AA 2024-T3 was analyzed with different analytical tools during exposure to 0.5 M NaCl. In order to track the morphology changes of the protective hydroxide/oxide film, the in situ EC-AFM measurements were carried out on the site without inclusions in a tapping mode. In situ EC-AFM images were taken from samples exposed to different potentials in various time steps. The parameters such as roughness are not only a function of potential, but also a time-dependent function. It can be observed that the surface roughness gradually increased during immersion in sodium chloride solution, and there was a similar increase in surface roughness after the application of external potential, which was mainly due to the formation of an oxyhydroxide layer. In addition, the deposition of the corrosion products led to the formation of a spiky surface, as shown in Figure 3. The profile lines measured over the corroding intermetallic particle are shown in Figure 3e, which allows observing the formation and roughness changes of the corrosion product film. The further increase in potential was most probably responsible for the significant increase in the thickness of the passivation layer. Under a certain potential, the corrosion potential spikes formed but disappeared after the thicker passivating oxyhydroxide layer was formed.

In terms of biomaterials, the inflammatory state of local body fluids in the body may affect the corrosion of implanted metallic biomaterials such as CoCrMo alloys. In the study of Liu and Gilbert, the surface of CoCrMo alloy was imaged by in situ EC-AFM to evaluate the morphology of the oxide film and surface dissolution under different physiologically possible potentials in phosphate buffer saline (PBS) solution and simulated inflammation (SI) solution (PBS solution with 30 mM H<sub>2</sub>O<sub>2</sub>), respectively [36]. EC-AFM images in SI solution showed different topographic changes compared with PBS solution alone, in which the alloy matrix was corroded and the carbide protruded. In contrast, a less compact oxide layer appeared and gradually covered the outermost surface in the case of PBS solution. The authors speculated that the addition of H<sub>2</sub>O<sub>2</sub> changed or removed the passive oxide films and greatly affected anodic dissolution on CoCrMo alloy. In addition, the grain boundaries and carbide boundaries were preferential parts for the dissolution of oxides, which was mainly due to effects of Cr depletion, a heterogeneous structure, and Cr distribution along grain boundaries and carbide boundaries.

In the work of Bearinger and co-workers, the effects of different potentials and hydration on the properties and structure of passive oxide films on the surface of titanium, 6-aluminum, 4-vanadium (Ti-6Al-4V) were investigated by in situ EC-AFM [37]. The AFM imaging of the different surfaces showed that all samples were covered with a protective titanium oxide dome. Due to hydration, the dome area gradually increased, and coalescence occurred with the increase in applied voltage and time. In addition, Bearinger et al. [38] characterized hydration of titanium/titanium oxide surfaces under freely corroding and potentiostatically held conditions using EC-AFM. In contrast to conventional high-vacuum techniques, EC-AFM enables the measurement of morphological surface structures in the in situ hydrated state. The results showed that the titanium surface covered the oxidized dome and grew laterally during hydration. The applied potential altered the growth rate. Under open-circuit potential, growth proceeded approximately six times faster than under  $-1$  V applied voltage. The oxide growth was partly due to the lateral expansion and overgrowth of the dome at the oxide–solution interface. The method was successfully used to study dynamic changes in the surface morphology.

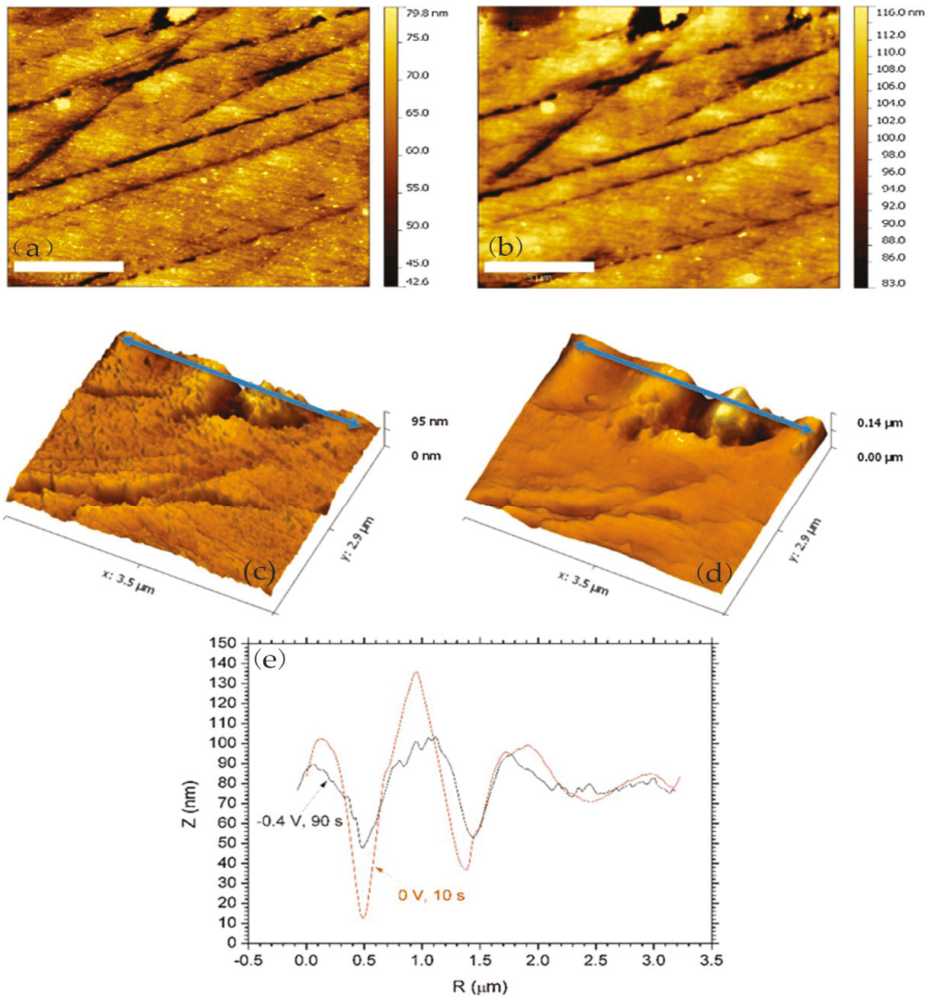


**Figure 3.** The in situ AFM images of AA 224: (a) 226 min,  $-0.4\text{ V}/\text{Ag}/\text{AgCl}/\text{KCl}_{\text{sat}}$ , 90 s; (b) 328 min,  $0\text{ V}/\text{Ag}/\text{AgCl}/\text{KCl}_{\text{sat}}$ , 10 s. (c,d) The corroding sites on top of the images (a,b) as three-dimensional (3D) images. (e) The profile lines measured over the corroding intermetallic particle. Reprinted with permission from Reference [35]; copyright 2016 Elsevier Ltd.

Metallic glass has excellent mechanical, magnetic, and chemical properties due to its unique structure. It is noted that the corrosion resistance of metallic glass is not only sensitive to its chemical composition but also inseparable from the structure. The influence of the structure on the corrosion of metallic glass is closely related to the dissolution, passivation, and durability of the passive film. Wang et al. [39] selected  $\text{Ni}_{50}\text{Nb}_{50}$  metallic glass with polymorphic transition during devitrification to clarify the relationship between the amorphous structure and corrosion, especially the stability of the passive film. By comparing amorphous alloys with its crystalline alloys, the breakdown behavior of passive films and characteristics of the surface film were studied in detail. The surface topography of the samples was characterized by in situ EC-AFM in tapping mode. The results confirmed that the surface of both amorphous and crystalline samples could form metastable pits at nanoscale, but the number of nanometer pits on amorphous samples was much smaller than that on crystalline samples.

Moreover, amorphous alloys only had a few deep pits and no shallow pits, as shown in Figure 4a,c, while crystalline alloys had many deep pits and shallow pits, as shown in Figure 4b,d. Although the composition of the passive film on the surface of the two alloys was similar, the amorphous structure could significantly inhibit the formation of pits in corrosive environment. Therefore, amorphous alloys had stronger resistance to pit formation than crystalline alloys.

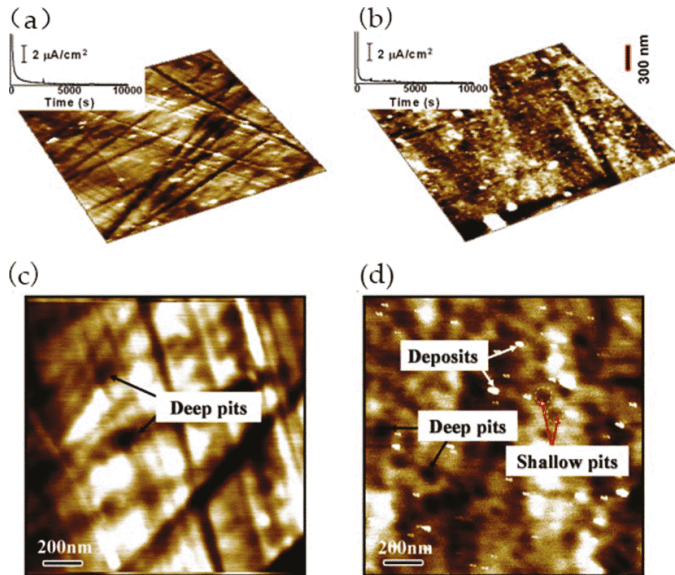


**Figure 4.** AFM images of the surfaces of amorphous and crystallized Ni<sub>50</sub>Nb<sub>50</sub> alloys after polarization at 1.0 V in 1 mol/L HCl solution. (a,b) Surface morphologies of the amorphous and crystallized samples. Inserts are the corresponding I-t curves during potentiostatic treatments. (c,d) High-magnification images of selective areas in amorphous and crystallized samples. Adapted with permission from Reference [39]; copyright 2010 Elsevier Ltd.

Phase imaging is an extension of the conventional tapping mode AFM (TM-AFM), through which topographic images and phase images can be obtained simultaneously. The phase images can reflect local nanoscale mechanical properties such as friction, hardness, and viscoelasticity. During the AFM scanning process, different nanometer-scale crystalline phases and their size, shape, and distribution can be identified in the matrix according to the phase change. Zhang et al. [40] studied the formation of the passive film in the Al–Ni–Ce metallic glass by in situ EC-AFM. In situ EC-AFM measurements were performed in open-circuit potential (OCP) conditions and stepped the potential into pitting potential ( $E_{\text{pit}}$ ). They identified  $\alpha$ -Al nanophase from the amorphous matrix by TM-AFM. It can be clearly seen from the phase image that the small  $\alpha$ -Al islands were randomly distributed on the surface, which had a negative phase shift with respect to the matrix. In the partially magnified phase image, the  $\alpha$ -Al island is surrounded by bright ringed patches, as shown in Figure 5.

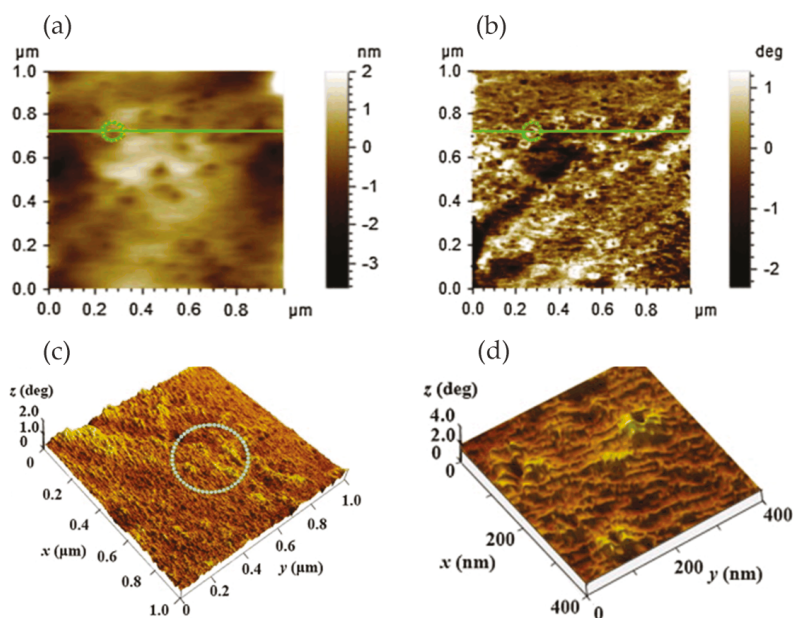


**Figure 5.** In situ tapping mode (TM) AFM images of the annealed  $\text{Al}_{88}\text{Ni}_8\text{Ce}_4$  amorphous nanocrystalline sample at open-circuit potential (OCP) held for 3 min in 0.01 mol/L NaCl solution. Topography image (a) and phase image (b). Three-dimensional (3D) images of phase (c) and the (d) local enlarged phase image of the marked circle in (c). Reprinted with permission from Reference [40]; copyright 2014 Elsevier Ltd.

In addition, the nucleation and growth process of the passive film was observed in real time by in-situ EC-AFM, and it was found that the presence of nanocrystalline  $\alpha$ -Al precipitates changed the nucleation mechanism of the passive film in the amorphous matrix from instantaneous nucleation to progressive nucleation. Due to the galvanic coupling between the  $\alpha$ -Al nanophase (anodic position) and surrounding amorphous matrix (cathodic position), the formation of the corrosion product  $\text{Al}(\text{OH})_3$  was in the early stage of formation of the passivation film, which was mixed into the passive film, changing the local structure and composition of the passive film. The density of hydroxide in the passive film was lower than that of the oxidation film formed on the amorphous matrix, which reduced the compactness of the passive film and its stability. Therefore, compared with fully metallic glass, metallic glass containing nanometer  $\alpha$ -Al precipitation had lower corrosion resistance.

Most previous research focused on steady-state corrosion reactions of steel, such as the study of pipeline corrosion in bicarbonate solutions or carbonate bicarbonate electrolytes. However, some researchers also studied the early stage of steel corrosion. Li et al. discussed the influence of bicarbonate concentration on the topographic evolution and corrosion mechanism [41]. In their work, the early stage of X100 pipeline steel corrosion in bicarbonate solution with different concentrations was characterized by in situ EC-AFM in the contact mode. The relationship between surface roughness and the corrosion process of pipeline steel was established. The pipeline steel was fixed to the bottom of the homemade solution container as the working electrode, which prevented evaporation of the test solution during testing. The authors found that the early stage of the steel corrosion in 0.01 M  $\text{NaHCO}_3$  solution could be divided into three stages. When the steel was immersed in the solution, the oxides on the surface of the steel began to dissolve, the OCP dropped, and the surface roughness increased rapidly, representing stage I. When the steel was corroded, the OCP further dropped, and the surface roughness increased gradually, representing stage II. In stage III, as the corrosion of steel reached a steady state, the surface roughness and OCP maintained a stable value, and the formation of corrosion products

reached a dynamic equilibrium state. However, in solutions with increased bicarbonate concentration, such as 0.1 M and 0.5 M  $\text{NaHCO}_3$ , steel could be passivated. In addition, as the passive capacity of bicarbonate solution increased with the increase in concentration, the morphology of the steel surface in 0.5 M  $\text{NaHCO}_3$  solution was smoother than that in the 0.1 M solution, consistent with the results of power spectral density (PSD) analysis. Compared with the passive film formed at a low concentration (0.1 M), the passive film formed in a solution with a high concentration (0.5 M) could eliminate the large-scale morphological features.

In addition, AFM–SECM is considered to be a particularly attractive research tool in corrosion science [42]. The clear topographical information obtained by EC–AFM and the electrochemical information provided by SECM can be obtained in a single experiment, which makes up for the deficiencies of the two instruments. Izquierdo et al. [43] modified AFM tips to achieve a bifunctional AFM–SECM tip. Conductive microelectrodes were integrated into an AFM probe to obtain an SCEM signal, through which the changes in surface morphology and current density were achieved to observe the progress of corrosion. Local release of  $\text{Cu}^{2+}$  ions was monitored by electrochemical reduction and deposition of metal ions on the AFM–SECM probe. The formation and breakdown of passive layers were characterized from the perspective of surface roughness and current density, reflecting the initial growth of the passive layer, subsequent breakdown, and formation of the pit.

In the research on microzone corrosion carried out by our research group, Ding studied the corrosion behavior and the formation of a corrosion product film on nickel–aluminum bronze (NAB) in 3.5 wt% NaCl solution. The in situ AFM in contact mode at open-circuit potential was used to observe the formation of the corrosion product film on different phases [44]. Figure 6 shows the in situ AFM topography of the specimen surface.

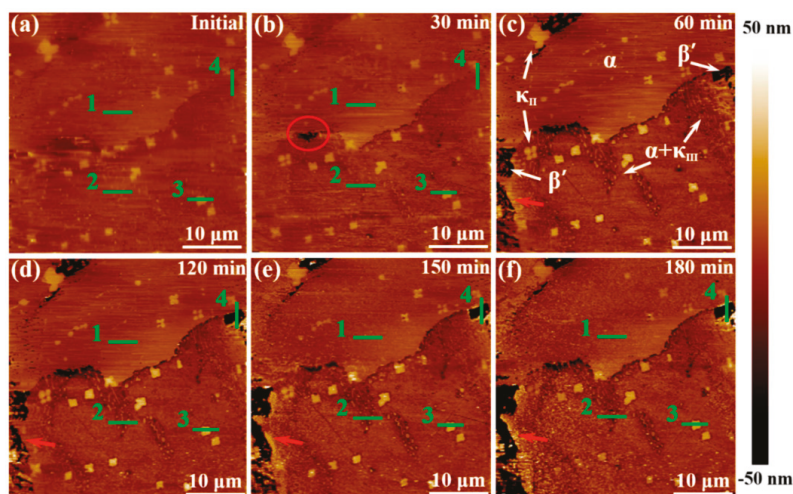


**Figure 6.** In situ topography images of nickel–aluminum bronze (NAB) specimen surface after exposure to 3.5 wt% NaCl solution at different times: (a) initial; (b) 30 min; (c) 60 min; (d) 120 min; (e) 150 min; (f) 180 min. Site 1 corresponds to the  $\alpha$  phase, site 2 corresponds to the  $\alpha + \kappa_{\text{III}}$  eutectoid structure, and site 3 corresponds to the  $\kappa_{\text{II}}$  phase, while site 4 corresponds to the  $\beta'$  phase. Reprinted with permission from Reference [44]; copyright 2019 MDPI.

The  $\alpha$  phase exhibited different corrosion behavior at different locations. Serious corrosion occurred at the lamellar  $\alpha$  phase within the  $\alpha + \kappa_{\text{III}}$  eutectoid structure, while the  $\alpha$  phase far away from the  $\kappa$  phase was not eroded, mainly due to the formation of many micro galvanic cells in the eutectoid. The  $\kappa_{\text{II}}$  and  $\kappa_{\text{III}}$  phases exhibited significant corrosion resistance due to the formation of a stable, dense protective film in a short period of time. It is worth noting that the film on the  $\kappa_{\text{II}}$  phase

was thicker, related to the  $\kappa_{II}$  phase based on  $Fe_3Al$  intermetallic compounds and containing more iron. Compared with nickel oxide, iron oxide is fluffier and more unstable; thus, the film on the  $\kappa_{II}$  phase was thicker. Since the metastable martensite structure struggled to form a protective film, the  $\beta'$  phase suffered the most severe corrosion. When the immersion time reached 150 min, the corrosion product deposition was almost dispersed on the entire surface, and the corrosion depth of each phase was suppressed, as shown in Figure 7. The formation of the corrosion product film tended to be uniform, which prevented the NAB alloy matrix from contacting the corrosive medium and hindered the transport of ions and charges, as well as improved the corrosion resistance of the NAB alloy.

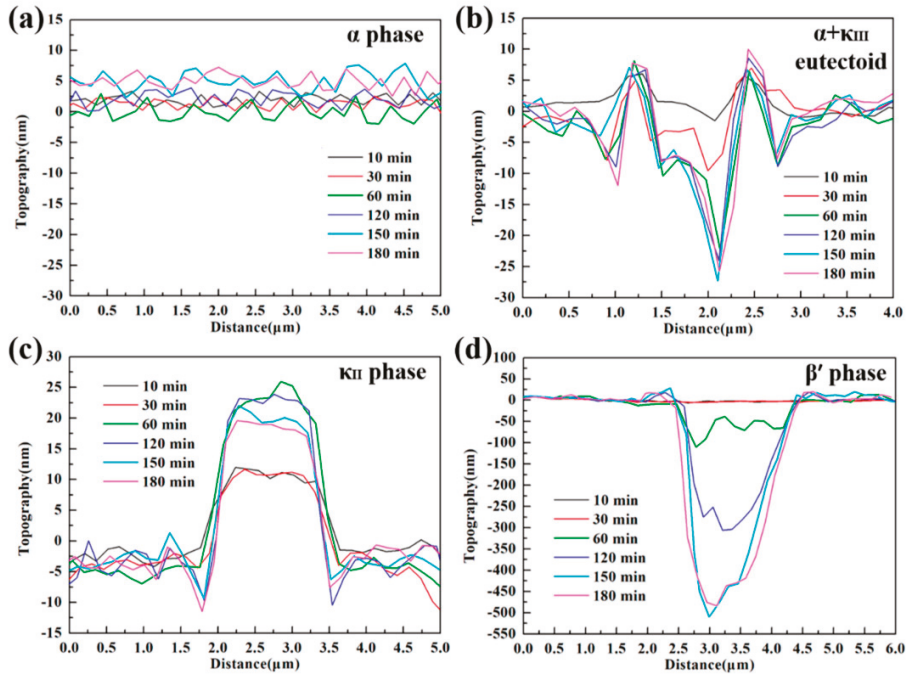


**Figure 7.** In situ line profiles corresponding to sites 1, 2, 3, and 4 marked in Figure 6, respectively: (a)  $\alpha$  phase; (b)  $\alpha + \kappa_{III}$  eutectoid structure; (c)  $\kappa_{II}$  phase; (d)  $\beta'$  phase. Reprinted with permission from Reference [44]; copyright 2019 MDPI.

EC-AFM has great advantages in studying the formation process and microstructure of corrosion product films on a metal surface, especially in characterizing the evolution of early corrosion product films, which is conducive to analyzing the corrosion behavior of metals and promoting the research on the corrosion resistance of metal. The application of EC-AFM in corrosion product films is summarized in Table 2.

**Table 2.** Summary of the application of EC-AFM in corrosion product films.

	Materials	Solution	Mode	Reference
Corrosion product film	carbon steel	Carbonate/bicarbonate solution	Contact mode	[33]
	304L stainless steel	Nitric acid		[34]
	AA 2024-T3	0.5 M NaCl solution	Tapping mode	[35]
	CoCrMo alloy	Phosphate buffer saline (PBS) and simulated inflammation (SI) solution	Contact mode	[36]
	Ti-6Al-4V	PBS	Contact mode	[37]
	Ni50Nb50 metallic glass	1 mol/L HCl solution	Tapping mode	[39]
	Al-Ni-Ce metallic glass	0.01 mol/L NaCl solution	Tapping mode	[40]
	X100 pipeline steel	0.01 M NaHCO <sub>3</sub> solution	Contact mode	[41]
	NAB	3.5 wt% NaCl solution	Contact mode	[44]

### 3.1.2. Pitting Corrosion

Pitting corrosion was extensively studied in the past few decades, as it has greater destructive and hidden dangers. Generally, the pitting mechanism is related to the properties of impurities on the surface or matrix. Pitting corrosion near inclusions, precipitates, or matrix/impurity interfaces is often caused by the inherent potential difference between the matrix and the inclusions or precipitates. Due to the small anode area, the corrosion rate is very fast, which can lead to sudden accidents. When trying to limit or avoid pitting corrosion, EC-AFM is helpful for improving the understanding of random pitting distribution, including nucleation and growth of pitting.

Pitting corrosion of various stainless steels was the focus of research for many years. As the most used material in the orthopedic and orthodontic bracket, AISI 316 L austenitic stainless steel has good mechanical properties. However, because it is susceptible to localized corrosion in chlorine-containing environments, it is often challenged by corrosive environments in the body. Conradi et al. [45] studied localized corrosion of austenitic stainless steel of the type AISI 316 L and duplex 2205 stainless steel (DSS 2205) using in situ EC-AFM in two different solutions, including simulated physiological solution known as Hank's solution (PS) and artificial saliva (AS). The topography and surface roughness of DSS 2205 and AISI 316 L changed with the increase in chloride ion concentration. EC-AFM topographic images showed that the surface of DSS 2205 had prominent square-like corrosion products in both solutions. Compared with AS, the erosion of PS was manifested by the decrease in the time scale of DSS 2205 surface change due to the increase in chloride ion concentration, as shown in Figure 8. Even though the DSS 2205 steel was exposed to anodic potentials in the region of transpassive oxidation, the samples had high pitting corrosion resistance in both solutions. On the contrary, AISI 316 L steel had stable corrosion resistance to AS. However, when AISI 316 L steel was exposed to PS solution, the sample was easily corroded and showed obvious pitting corrosion with the increase in Cl<sup>-</sup> ion concentration, as shown in Figure 9. The surface of AISI 316 L included ellipse-like deposits. This was due to the change in the chemical composition of the matrix material, which formed different growth patterns on the surface of the sample with the growth of chromium, iron, and nickel oxides. Therefore, DSS 2205 had high corrosion resistance compared to AISI 316 L stainless steel. In medical applications, DSS 2205 will be a promising medical material if the nickel hypersensitivity effect can be reduced in patients receiving treatment.



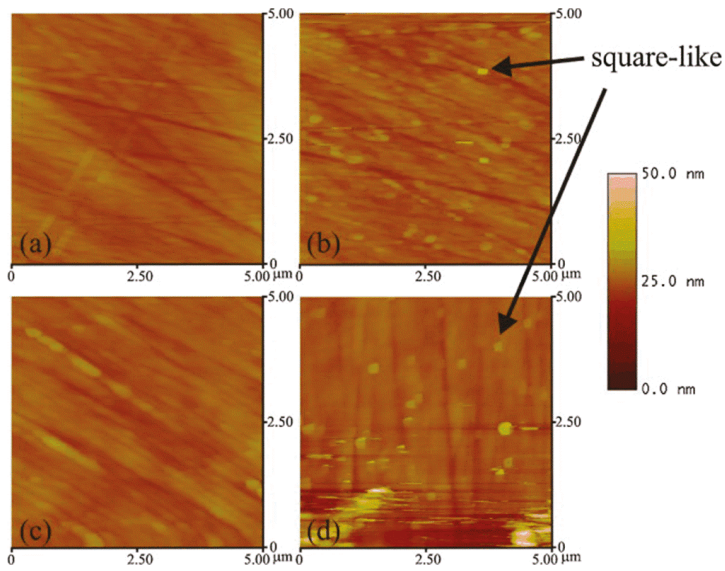


**Figure 8.** AFM images of DSS 2205 sample: (a) in artificial saliva (AS) after being exposed to the potential of 0.8 V for 45 min, (b) in AS after additional exposure to the potential of 1 V for 11.6 min, (c) in physiological solution (PS) after being exposed to a potential of 0.8 V for 17.2 min, and (d) in PS after additional exposure to 1 V for 7.5 min. Adapted with permission from Reference [45]; copyright 2011 Elsevier Ltd.

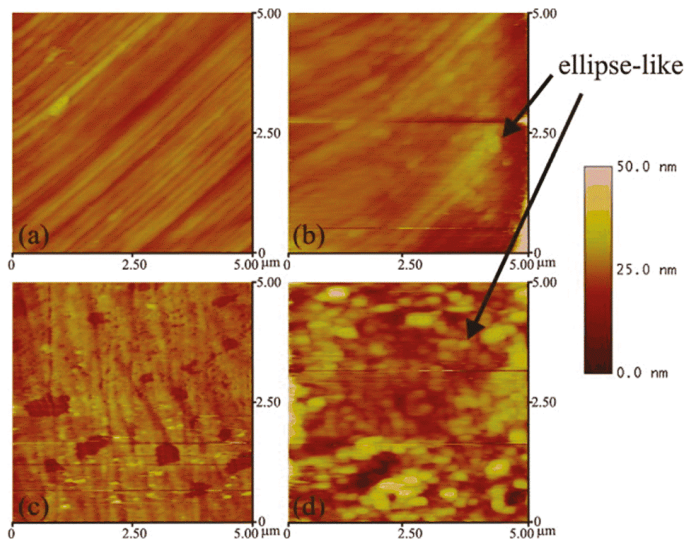


**Figure 9.** AFM image of AISI 316L sample: (a) in AS after exposing the sample to anodic potential of 0.5 V for 10 min, (b) in AS after additional exposure of the sample to 0.5 V for 6.6 min, (c) in PS immediately after the test cyclic voltammogram in the range of potentials from  $-0.5$  V to 0.8 V, and (d) in PS after additional exposure to 0.5 V for 30 s. Adapted with permission from Reference [45]; copyright 2011 Elsevier Ltd.

Martin et al. [46] studied the pitting corrosion of austenitic 304L stainless steel in chloride borate buffer solution using in situ EC-AFM in contact mode. In order to determine whether the pits were randomly distributed at the nanometer scale, the study focused on the location where pits were initiated under controlled potential. In the AFM image, it is clear that the chain of pits (black, right image) was related to the chain of relief islands (white, left image), as shown in Figure 10. However, we can see an intermediate state rather than a typical direct transition, which indicates that the pitting process was a gradual process, as shown in Figure 11. In the final step of surface preparation, the local chemical reactivity of the surface may have led to the formation of a passive film and small oxidized hydroxide aggregate defects. The authors believed that the local chemical defects in the sample preparation process could affect the formation of the passive film, which would eventually cause local differences compared to the rest of the film. These local chemicals or structural defects would reduce the local pitting resistance of the film. In addition, based on the reasonable model that the surface potential under tensile stress would be higher than that under compressive stress, when the strain hardening zone (caused by mechanical polishing) appeared on the surface of the sample, pitting corrosion preferentially initiated in this area.

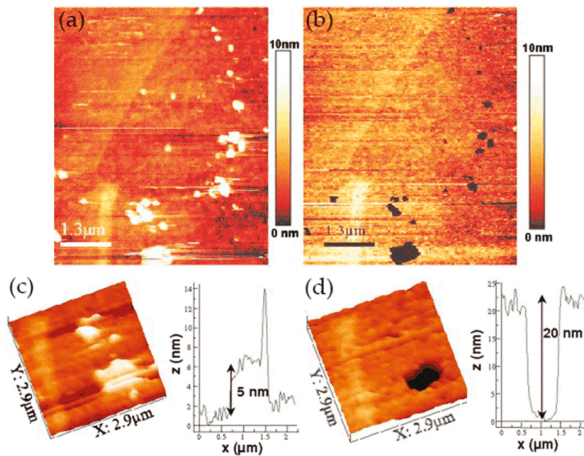


**Figure 10.** AFM images of the surface at open-circuit potential (a) and at pitting potential (b). (c,d) The pit chain (in black, right image) profiles made on images at higher magnification (bottom insets) show that the average relief of the islands was about 5 nm, whereas the average depth of the pits was about 20 nm. Reprinted with permission from Reference [46]; copyright 2008 Elsevier Ltd.

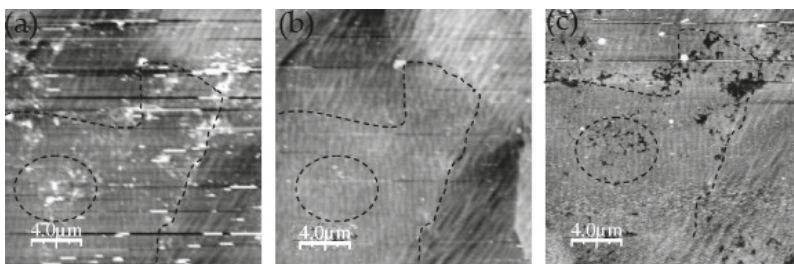


**Figure 11.** AFM images of the surface, taken at (a) open-circuit potential, (b) corrosion potential after cathodic scan, and (c) pitting potential. Reprinted with permission from Reference [46]; copyright 2008 Elsevier Ltd.

It is generally believed that sulfide inclusions (MnS and mixed oxide/sulfide) in a stainless-steel matrix are most likely to cause pitting corrosion. The products produced by the dissolution of sulfide inclusions form a local corrosive environment, which in turn causes more severe pitting corrosion. Wijesinghe et al. [47] discussed the adverse effect of sulfide inclusion on pitting resistance of stainless steel. The results showed that the sulfide inclusions were clustered on the surface of the stainless steel. As the volume composition of the stainless-steel sulfide increased, the number of inclusions per cluster increased. The pitting corrosion was imaged in real time using in situ EC-AFM, and it was found that pits were formed near the sulfide inclusions, consistent with the three main mechanisms proposed previously, i.e., aggressive local chemical reactions based on inclusion dissolution, stressed oxide, and chromium depletion.

In the work of Zhang and co-workers, the pitting corrosion of the solution- and sensitization-treated austenitic stainless steel SUS304 was studied using in situ AFM in 3.5 wt% sodium chloride solution [48]. This study adopted two observation methods. One was in situ continuous observation, in which the corrosion current was continuously applied to the surface of the sample. Another method was in situ interrupted observation, i.e., the observation was carried out at intervals to minimize the impact of probe scanning on corrosion reactions. In situ observation of the corrosion pit of the solution-treated sample showed that the pit became larger as the corrosion time increased from  $t = 2.46$  to  $2.70$  ks, but no corrosion products were found, as shown in Figure 12. A series of in situ intermittent observations of the sample after solution treatment revealed two large pits (D and E), but the size of the pits did not change with time. In addition, no corrosion products were found on the two large pits, as shown in Figure 13.

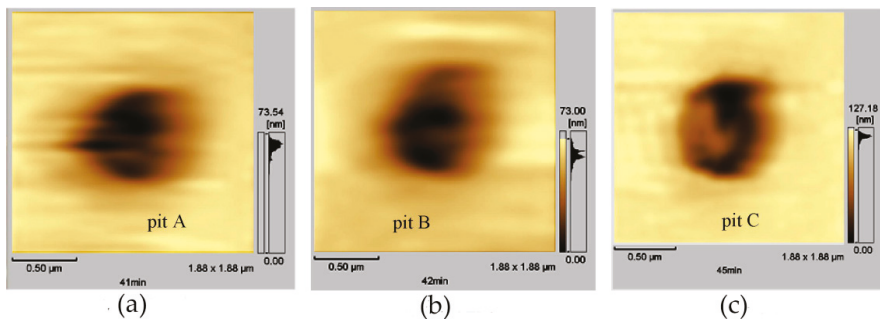


**Figure 12.** AFM images of solution-treated SUS304 stainless steel during corrosion in 3.5 wt% sodium chloride solution at 298 K ( $I = 10$  A/m<sup>2</sup>): (a)  $t = 2.46$  ks; (b)  $t = 2.52$  ks; (c)  $t = 2.7$  ks. Reprinted with permission from Reference [48]; copyright 2005 Elsevier Ltd.

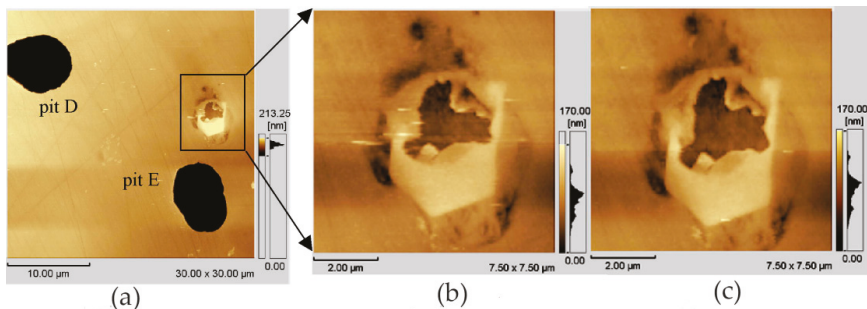


**Figure 13.** AFM images of solution-treated SUS304 stainless steel after corrosion in sodium chloride solution at 298 K ( $I = 5$  A/m<sup>2</sup>): (a)  $t = 1.5$  ks; (b)  $t = 1.5$  ks and (c)  $t = 7.2$  ks are the magnified images of the framed area of (a), showing the presence of the corrosion product. Reprinted with permission from Reference [48]; copyright 2005 Elsevier Ltd.

The authors believed that the corrosion product may have been moved to other locations by the probe or dissolved with the rapid dissolution of the matrix. After the corrosion product was removed, the concentration of local chloride ions and hydrogen ions decreased, and the growth rate of the pits decreased. This means that the corrosion products played an important role in the growth of corrosion pits. When the corrosion product covers the pit, it can lead to an acidic environment and accelerate pitting. On the sensitization-treated sample, the irregular pits were distributed near the grain boundaries. Chromium carbide deposits and pitting occurred in the chromium-depleted area around the carbide, as shown in Figure 14. Cross-sectional profiles of pits along a–b lines in Figure 14a and c–f lines in Figure 14c are shown in Figure 14d. Since no carbide particles were found in the pit according to the cross-sectional profiles, they might have dissolved with pit growth. The dissolution of carbides in pits caused the pit to grow further.

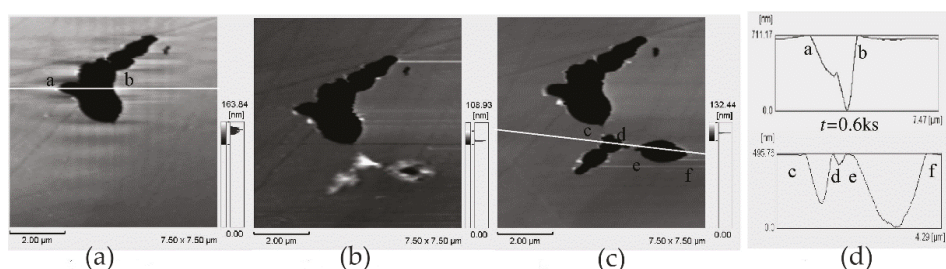


**Figure 14.** AFM images of sensitization-treated SUS304 stainless steel after corrosion in sodium chloride solution ( $I = 1 \text{ A/m}^2$ ): (a)  $t = 0.6 \text{ ks}$ ; (b)  $t = 0.9 \text{ ks}$ ; (c)  $t = 1.2 \text{ ks}$ . (d) Cross-sectional profiles of pits along a–b and c–f lines. Reprinted with permission from Reference [48]; copyright 2005 Elsevier Ltd.

When we study the corrosion of self-passivation metals covered with a semiconductor protective film, there is no doubt that EC-AFM, which does not need the conductivity of the matrix, is more suitable. Qu et al. [49] investigated the corrosion behavior of pure aluminum using in situ AFM in 0.01 mol/L  $\text{FeCl}_3$  solution. The pitting corrosion process of pure aluminum induced by the potentiodynamic sweep and the repassivation process of active pits were studied. In addition, the effect of mechanical damage on the metal surface caused by AFM tip scratching on the pitting behavior of the sample was emphasized. The topographical images of the sample surface at different immersion times were traced under open-circuit conditions using AFM in contact mode, and the AFM tip scratching process was carried out with a loading force of 800 nN. The results showed that different pitting regions exhibited different pitting activities under the same polarization conditions due to the diversity of physical and electrochemical characterization. The corrosion products contained abundant impure elements such as Fe and Cu. In situ AFM observation of pitting corrosion originated from artificial defects on the aluminum surface showed that physical defects had higher pitting activity and may have been attacked preferentially to pitting corrosion.

In the study of Davoodi and co-workers, the application of the EC-AFM and SECM integrated system for in situ studies of the influence of intermetallic particles on local corrosion of aluminum alloys was introduced [50]. The key to this method is fabricating a dual-mode cantilever/tip that can be used not only as a cantilever for the EC-AFM but also as a microelectrode or nano-electrode tip for the SECM. It can obtain the in situ AFM topographic images and SECM electrochemical current maps simultaneously with micrometer lateral resolution and provide detailed information of localized corrosion related to different kinds of intermetallic particles and the deposition of corrosion products. In their work, when the AA1050 sample was anodically polarized at 300 mV (close to the breakdown potential), the morphology observed using EC-AFM showed many small pits. However, this may have been because many of the active points were close to each other; thus, the local current could not be resolved in the SECM electrochemical current map. During the post-scan, some high-current

sites appeared in the lower part of the SECM image, which may have been related to the presence of pits or trenches on the surface, as shown in Figure 15. Preliminary results indicated that the localized dissolution of aluminum alloy may have occurred below the breakdown potential, but only involved a small number of particles.

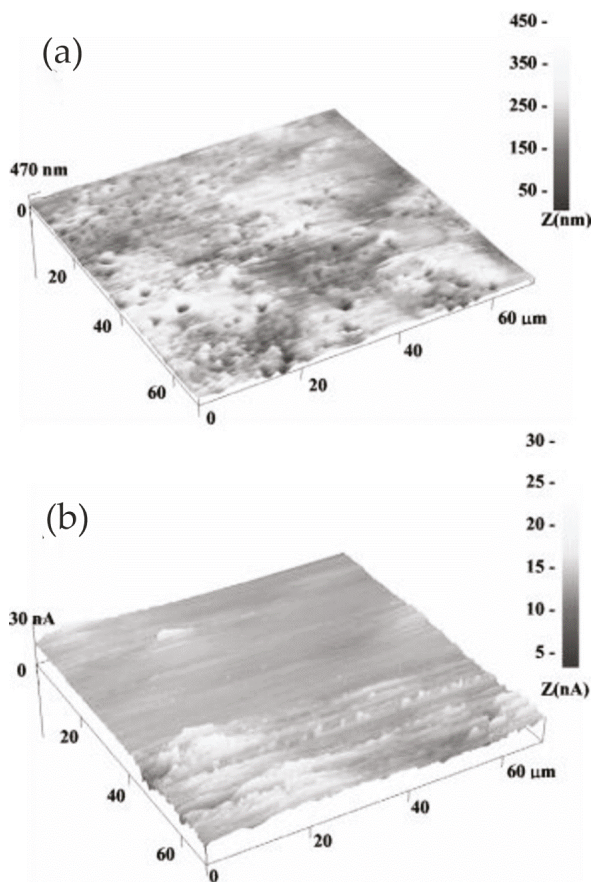


**Figure 15.** EC-AFM/scanning electrochemical microscopy (SECM) images of AA1050 in 10 mM NaCl+ 5 mM KI at 300 mV anodic polarization, and tip at +750 mV vs. Ag/AgCl: (a) topography; (b) electrochemical activity map. Adapted with permission from Reference [50]; copyright 2005 Electrochemical Society.

Metallic zinc is used not only for galvanizing steel but also for various applications such as batteries, die casting, and brass metallurgy. It is necessary to study the local corrosion of pure zinc and zinc alloys. Amin et al. [51] studied the passivation breakdown and pitting corrosion of zinc in 0.5 M sodium hydroxide solution containing different concentrations of  $\text{ClO}_3^-$  or  $\text{ClO}_4^-$  anions. The passivation breakdown and pitting sensitivity of the  $\text{Zn}/\text{OH}^-/\text{ClO}_3^-$  and  $\text{Zn}/\text{OH}^-/\text{ClO}_4^-$  interfaces were studied by potentiodynamic anodic polarization measurements, and the topography of pitted Zn surfaces was observed by AFM. The experimental results showed that metastable pitting corrosion was mainly caused by  $\text{Cl}^-$  ions (generated by reducing  $\text{ClO}_3^-$  and  $\text{ClO}_4^-$ ). According to the point defect model (PDM), this may have been due to the small size of  $\text{Cl}^-$  ion, which could occupy anion vacancies and cause pitting corrosion. Therefore,  $\text{Cl}^-$  was the invasive ion that caused metastable

pitting, rather than  $\text{ClO}_3^-$  and  $\text{ClO}_4^-$ . However, even in the absence of  $\text{Cl}^-$ ,  $\text{ClO}_3^-$  and  $\text{ClO}_4^-$  could induce stable pitting, in which  $\text{ClO}_3^-$  was more aggressive than  $\text{ClO}_4^-$ , which could be proven by the roughness calculated according to the AFM topography map. Compared with  $\text{ClO}_4^-$ , the Ra value was always higher in the presence of  $\text{ClO}_3^-$ , as shown in Figure 16.

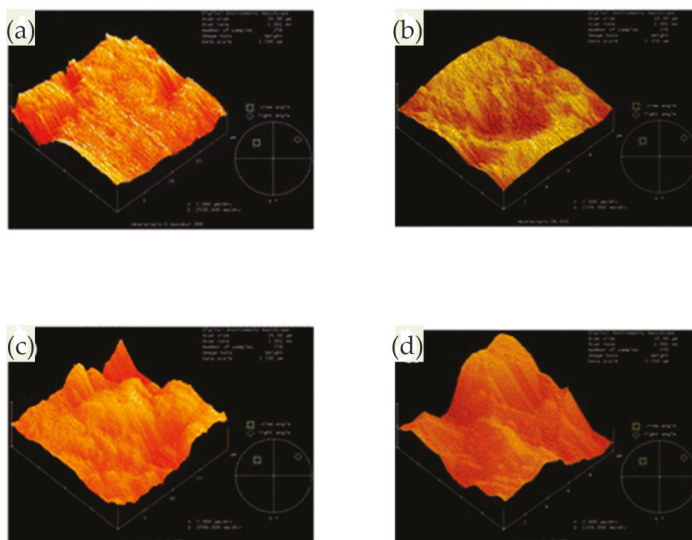


**Figure 16.** AFM images recorded for Zn in 0.5 M NaOH solution containing 0.05 M (a,b)  $\text{ClO}_4^-$  or (c,d)  $\text{ClO}_3^-$ . Adapted with permission from Reference [51]; copyright 2013 Springer.

Yong Hwan Kim et al. [52] studied the initial corrosion mechanism of a hot-dip-galvanized surface. The formation of corrosion products, the initiation and growth of pits, and the breakdown of the film were observed using in situ EC-AFM. At the initial stage of passivation, the corrosion product film of  $\text{ZnO}/\text{Zn}(\text{OH})_2$  formed in the dull sector was more unstable than that formed in the bright zone. The authors believed that the relative instability of the passive film in the initial stage was affected by the high-density lath-like structure. The uneven surface structure at the micro-scale, i.e., the lath-like structure, provided a favorable place for the  $\text{ZnO}/\text{Zn}(\text{OH})_2$  formation and pitting.

EC-AFM can provide detailed information of the localized dissolution associated with different kinds of intermetallic particles, as well as the deposition of corrosion products surrounding large particles or covering small pits, including the location of pitting initiation at controlled potentials, and whether pits are randomly distributed at the nanoscale. The application of EC-AFM in pitting corrosion is summarized in Table 3.

### 3.1.3. Selective Corrosion

Selective corrosion refers to the preferential dissolution of active components in the multicomponent alloy. The relative Volta potential difference is used as the index of selective corrosion caused by microelectronic coupling. Compared with the substrate, the intermetallic phase with positive potential is the cathodic phase. On the contrary, some intermetallics with more negative potential than the matrix show stronger activity during the corrosion process and act as micro-anodes.

Jia et al. [53] investigated the effects of intermetallics on the local corrosion behavior of AZ91 alloy added (La,Ce) mischmetal (MM), including corrosion initiation and propagation. The corrosion morphologies of different intermetallics were imaged using in situ EC-AFM in 0.1 mol/L NaCl solution, and Scanning Kelvin probe force microscopy (SKPFM) was performed to measure the local difference

of the relative Volta potential between the intermetallic phases and the  $\alpha$ -Mg matrix. In the experiment, the approximate compositions of several intermetallic phases were identified as  $Al_4(La,Ce)$ ,  $Al_8Mn_4Ce$ , and decreased  $b-Mg_{17}Al_{12}$  phases. SKPFM analysis showed that all intermetallics were noble compared with the  $\alpha$ -Mg matrix. The observation of in situ EC-AFM on the initial stages of corrosion indicated that the  $\alpha$ -Mg matrix surrounded by  $b-Mg_{17}Al_{12}$  or  $Al_8Mn_4Ce$  was prone to pitting corrosion. In detail, the  $b-Mg_{17}Al_{12}$  phase existed in both AZ91 and AZ91 alloys with (La,Ce) MM. Both elongated and dispersed granular  $b-Mg_{17}Al_{12}$  served as effective micro-cathodes, as shown in Figure 17.

**Table 3.** Summary of the application of EC-AFM in pitting corrosion.

	Materials	Solution	Mode	Reference
Pitting corrosion	AISI 316L and DSS 2205	Physiological solution and artificial saliva	Contact mode	[45]
	304L stainless steel	Chloride borate buffer solution	Contact mode	[46]
	SUS304	3.5 wt% NaCl solution		[48]
	pure aluminum	0.01 mol/L $FeCl_3$ solution	Contact mode	[49]
	AA1050	10 mM NaCl + 5 mM KI	Contact mode	[50]
	Metallic zinc	0.5 M NaOH solution containing different concentrations of $ClO_3^-$ or $ClO_4^-$ anions		[51]
	Hot-dip-galvanized surface	0.01 M NaOH	Contact mode	[52]

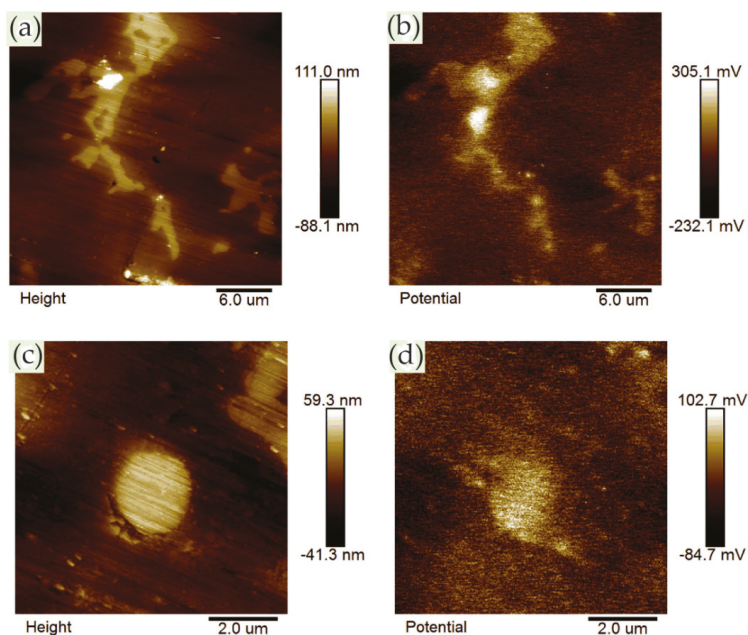


**Figure 17.** The polished AZ91 alloy (a) surface topography and (b) relative Volta potential map of elongated  $b-Mg_{17}Al_{12}$ ; (c) surface topography and (d) relative Volta potential map of granular-like  $b-Mg_{17}Al_{12}$ . Reprinted with permission from Reference [53]; copyright 2019 Elsevier Ltd.

$\text{Al}_4(\text{La,Ce})$  intermetallics, whether featuring an acicular shape or rod shape, were believed to produce significant galvanic coupling. However, the  $\alpha\text{-Mg}$  matrix near the  $\text{Al}_4(\text{La,Ce})$  phase did not have obvious corrosion. Moreover, although the  $\text{Al}_{18}\text{Mn}_4\text{Ce}$  phase showed a positive potential difference with respect to the matrix, the corrosion resistance of the alloy was not affected by its galvanic coupling, probably due to its lower amount, as shown in Figure 18.

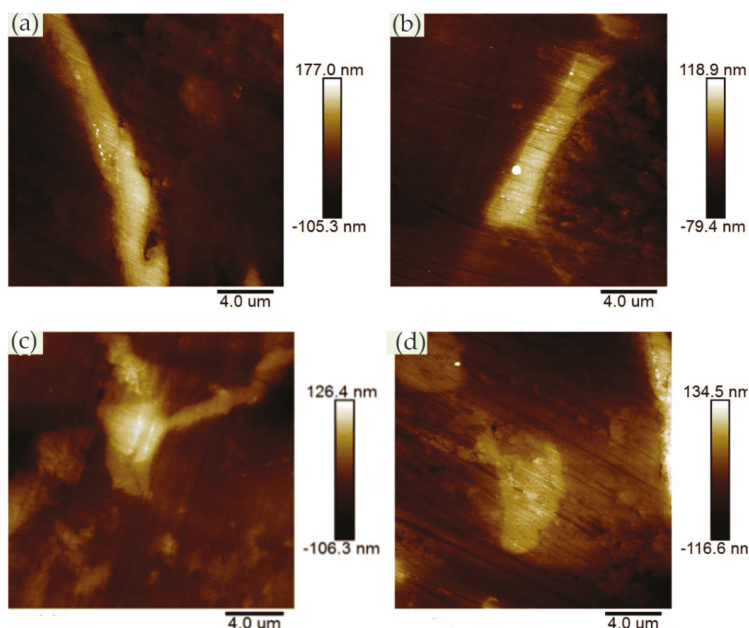


**Figure 18.** Typical in situ surface images for different intermetallics after immersion in 0.1 mol/L NaCl solution for 60 min: (a) acicular-like RE phase, (b) rod-like RE phase, (c) granular RE phase, and (d) dispersed granular b-Mg<sub>17</sub>Al<sub>12</sub> in AZ91 alloy with 1.0% (La,Ce) mischmetal (MM) addition. Reprinted with permission from Reference [52]; copyright 2019 Elsevier Ltd.

It can be seen that the intermetallics with the highest Volta potential differences relative to the matrix did not play the role of effective cathodes, just like the  $\text{Al}_4(\text{La,Ce})$  phase, which means that the localization of the cathode reaction was not only dependent on the Volta potential differences between the intermetallics and the matrix. The authors believed that the shape of the coupled anode and cathode had an important effect on the current density, i.e., the geometry of the intermetallic compound had an important influence on the micro-galvanic corrosion.

Zhang et al. [54] studied the anodization process of aluminum 6060 alloy under operating conditions and illustrated the effects of intermetallic particles (IMPs) and anodic Al oxide (AAO) film properties. The in situ EC-AFM measurement was performed continuously to monitor the surface topography changes under anodizing potentials in contact mode, revealing the details of localized dissolution and AAO film formation in Al 6060 samples in 0.2 M  $\text{Na}_2\text{SO}_4$  solution. The extruded Al 6060 alloy mainly contained two types of IMPs: AlFeSi primary particles and  $\text{Mg}_2\text{Si}$  particles. The Volta potential differences obtained by SKPFM showed that, relative to the aluminum matrix, AlFeSi was cathodic, but  $\text{Mg}_2\text{Si}$  was anodic. The in situ EC-AFM measurements showed that AlFeSi particles remained stable, but the local anodic dissolution of  $\text{Mg}_2\text{Si}$  particles occurred during anodization, which was consistent with the SKPFM results. As shown in Figure 19, the large particle in region I was likely an  $\alpha\text{-AlFeSi}$  particle. The particles in regions II, III, and IV were likely anodic  $\text{Mg}_2\text{Si}$  particles. The protruded large particle in region I remained stable during anodization, whereas the



small particles in region II in Figure 19a were dissolved upon the anodization. Moreover, upon the anodization at 1 V, some active dissolution started at certain sites (e.g., III), forming small holes, as shown in Figure 19b. During the anodization at 2, 4, and 8 V (Figure 19c–e), the small hole in area III became deeper, as displayed by the profile lines in Figure 19f, and pronounced localized dissolution occurred in area IV. Two small particles remained stable in the dissolved area (area IV in Figure 19d,e). Furthermore, in the area marked as V, localized dissolution at one site resulted in a small hole, and a deposited particle of a few  $\mu\text{m}$  in size formed (Figure 19c), but it disappeared at 4 V, exposing a much deeper pit (Figure 19d). In addition, the growth of AAO films occurred with partial anodic dissolution. The thickness of the anodic barrier film increased linearly with the anode potential, but the growth rate decreased due to local anodic dissolution associated with IMPs in the alloy.

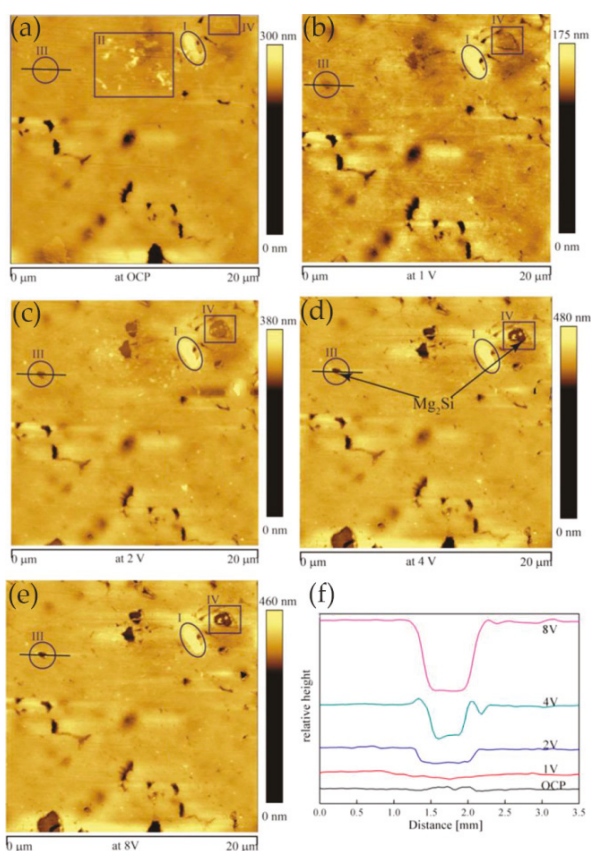


**Figure 19.** In situ EC-AFM topography images of the Al 6060 alloy in 0.2 M  $\text{Na}_2\text{SO}_4$  solution at (a) OCP, (b) 1 V, (c) 2 V, (d) 4 V, and (e) 8 V vs. Ag/AgCl. (f) Line profiles across the feature III in (a–d). Adapted with permission from Reference [54]; copyright 2016 Electrochemical Society.

In some cases, the presence of nitrides can adversely affect the corrosion resistance of the material. Bettini et al. [55] studied the effect of nano-sized quenched-in chromium nitride particles on the corrosion behavior of heat-treated 2205 duplex stainless steel (DSS) in a NaCl solution at room temperature and 50 °C (slightly higher than the critical pitting corrosion temperature). The relative nobility difference between the precipitated nitrides, austenite, and ferrite in the tested materials was evaluated at room temperature by atomic force microscopy-based Kelvin force microscopy (AFM/KFM).

The volt potential mapping at room temperature indicated that the ferritic had a lower relative nobility compared with austenite, and quenched-in Cr<sub>2</sub>N particles had a higher relative nobility to the surrounding ferritic matrix. The observation results of EC-AFM in 1 M NaCl solution at room temperature showed that the samples after heat treatment showed a wide range of passivation and a very stable surface up to 1.2 V<sub>Ag/AgCl</sub>, where the selective dissolution of ferrite phase occurred but the quenched-in Cr<sub>2</sub>N particles remained stable, as shown in Figure 20. Figure 20d shows the depth line profile from the image obtained after the polarization at 1.2 V<sub>Ag/AgCl</sub>, presenting a depth of ca. 200 nm between the dissolved ferrite phase and the remaining austenite phase. In addition, the very small nitride particles formed during the fast cooling process did not have enough time for the diffusion of elements and were unlikely to form a considerable composition gradient in the surrounding boundary region, which was one of the reasons for its stability. At temperatures above the critical pitting temperature (CPT = 50 °C), rapidly selective dissolution of the austenite phase occurred upon slight anodic polarization, which may have been related to the low content of chromium and molybdenum in the austenite phase. The authors believed that the finely dispersed quenched-in nitrides in the DSS did not cause local corrosion in 1 M NaCl solution. However, the exposure temperature had a great influence on the corrosion resistance of DSS, which changed the selective dissolution behavior of DSS.

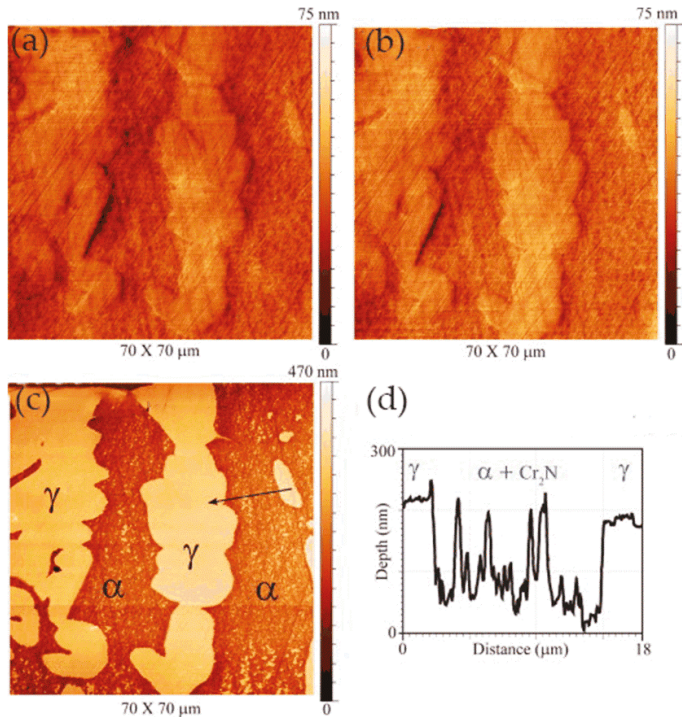


**Figure 20.** In situ EC-AFM images of the same area of the 2205 HT in 1 M NaCl at room temperature under electrochemical control at different applied potentials: (a) OCP, (b) 1.1 V<sub>Ag/AgCl</sub>, and (c) 1.2 V<sub>Ag/AgCl</sub>. (d) Depth line profile from the arrow in image (c) showing particles or particle clusters remaining in the dissolved ferrite area. Reprinted with permission from Reference [55]; copyright 2013 Elsevier Ltd.

Yasakau et al. [56] investigated the mechanism of initial steps of localized corrosion at the cutting edges of adhesively bonded Zn (Z) and Zn–Al–Mg (ZM) galvanized steel substrates. The topography of the initially localized corrosion of Z and ZM samples was measured using in situ AFM equipment under anodic polarization in the corrosive solution. The first corrosion pits at the Z cutting edge

were mainly formed on the zinc layer, and there was no preferential erosion on the adhesive/zinc or zinc/steel, as shown in Figure 21.

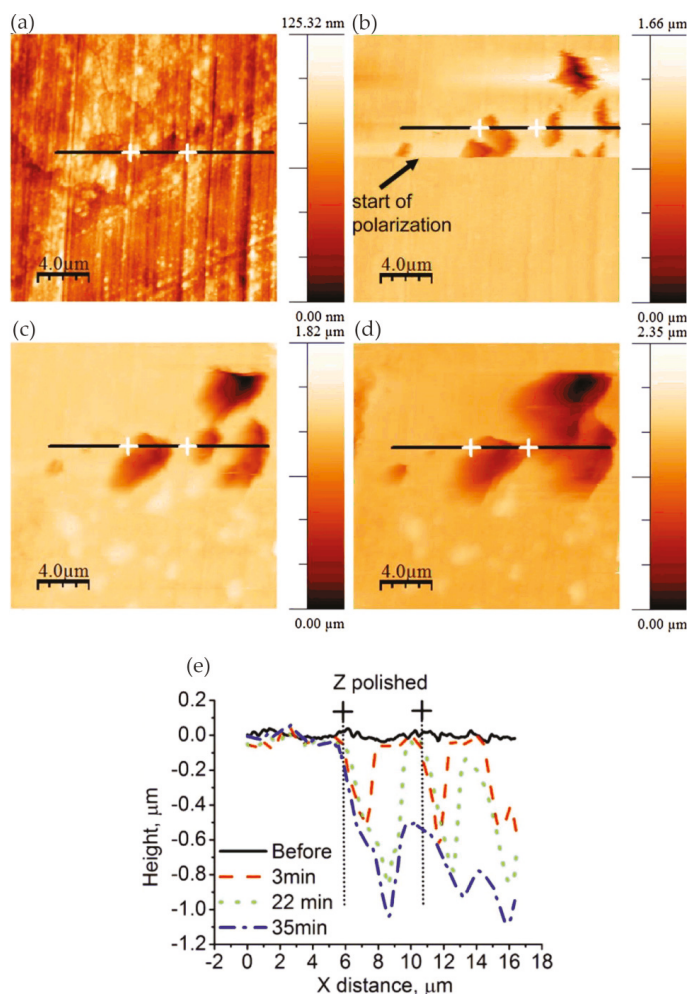


**Figure 21.** AFM topography maps made on cutting edge of adhesively bonded Zn (Z) substrate before immersion (a) and during 24 min (b), 1 h 5 min (c), and 2 h (d) of immersion in 0.001 M NaCl. (e) Evolution of topography across the black line profiles drawn in the same zones on AFM maps. Black arrows indicate local pits on the zinc layer. Reprinted with permission from Reference [56]; copyright 2016 Elsevier Ltd.

However, the types of attacks were different at the ZM cut edge, namely, pitting corrosion of the solid solution and selective dissolution at the eutectic zone. For the local corrosion at the adhesive/zinc interface, the first adhesive disbonding area was located near the cutting edge. The second adhesive disbonding zone was located at the buried deep zinc/adhesive interface, where local corrosion occurred in the solid solution phase and eutectic phase of the sample ZM. Under anodic polarization, the corrosion site was located in the eutectic phase at the interface between the eutectic zone and the solid solution zone, similar to the corrosion at the ZM cutting edge, as shown in Figure 22. In addition,

scanning vibrating electrode technology (SVET) and electrochemical impedance spectroscopy (EIS) electrochemical tests showed a decrease in corrosion kinetics at the Z and ZM cutting edges, which was due to the blocking effect of the dense film of corrosion products formed on the zinc and steel surfaces.

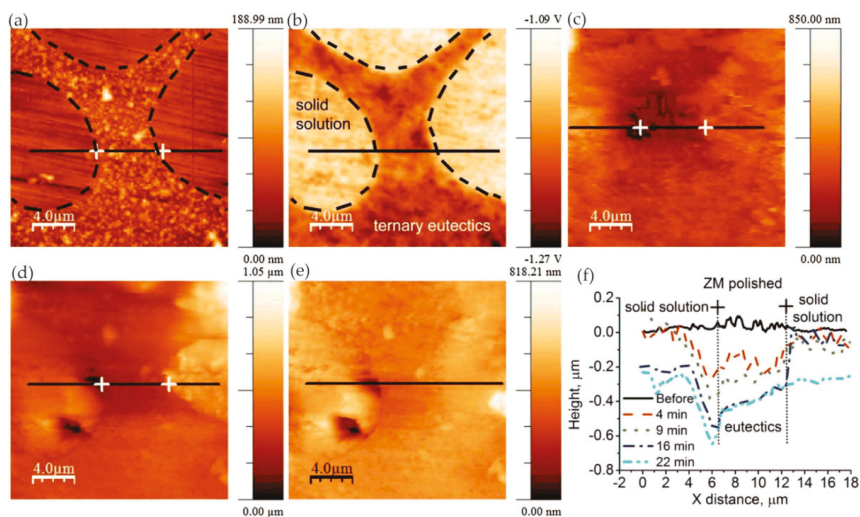


**Figure 22.** AFM topography (a) and SKPFM (b) maps of Zn–Al–Mg (ZM) galvanized coating before immersion and during immersion in 0.005 M NaCl for 4 min (c), 9 min (d), and 22 min (e). (f) Evolution of topography across the black line profiles. Reprinted with permission from Reference [56]; copyright 2016 Elsevier Ltd.

Depentori et al. [57] studied the corrosion behavior of neodymium-modified titanium alloy  $\text{Ti}_6\text{Al}_4\text{V}_2\text{Nd}$  in 1.5 wt% NaCl and compared it with a  $\text{Ti}_6\text{Al}_4\text{V}_2$  matrix using SKPFM and EC-AFM. Neodymium containing intermetallic compounds was precipitated at  $\beta$ -phase boundaries and inside the grains. The Volta potential maps obtained using SKPFM showed that the Volta potential of intermetallic compounds was lower than that of the Ti matrix. Therefore, intermetallic compounds had strong anodic behavior relative to titanium matrix and were the preferred site for local attack in  $\text{Ti}_6\text{Al}_4\text{V}_2\text{Nd}$  alloy. When the sample was immersed in 1.5 wt% NaCl solution, EC-AFM observation showed that the volume of the local area on  $\text{Ti}_6\text{Al}_4\text{V}_2\text{Nd}$  increased significantly, which was due to the formation of hydroxide and oxide. In addition, large amounts of debris were observed. The authors suggested this as a sign that the surface was loosely bound to  $\text{Nd}(\text{OH})_3$ . Cyclic voltammetry showed a clear oxidation reaction without a reduction reaction, and the oxidation peak moved to the right as the exposure time increased, which was a clear sign that the electrochemical reaction was irreversible and that the diffusion barrier formed and increased over time. Corresponding to the results of EC-AFM, the diffusion barrier was the  $\text{Nd}(\text{OH})_3$  layer formed by the corrosion of a large number of precipitates on the surface, which prevented further oxidation.

Davoodi et al. [58] investigated the difference in corrosion behavior between EN AW-3003 (Rolled 3xxx series Al alloys) and a newly developed Al–Mn–Si–Zr fin alloy. The Volta potential of the two alloys determined using SKPFM showed that the intermetallic particles behaved as cathodes relative to the alloy matrix. Compared to EN AW-3003, the Al–Mn–Si–Zr alloy had fewer particles with larger Volta potential difference with respect to the matrix. In situ AFM measurements showed that ring-like corrosion products were deposited on the EN AW-3003 alloy, while only a few corrosion sites and tunnel-like pits were found on Al–Mn–Si–Zr, as shown in Figure 23.

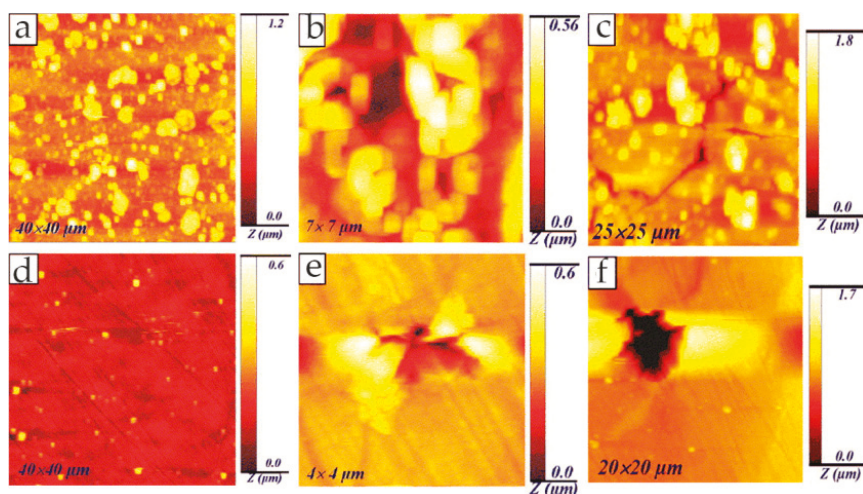


**Figure 23.** In situ AFM images of (a) EN AW-3003 and (b) Al-Mn-Si-Zr, after two days; (e) EN AW-3003 and (f) Al-Mn-Si-Zr, after 3.5 days in Sea Water Acetic Acid Test (SWAAT) solution of pH 4. (c,d) Magnified images of the framed areas of (a,b), respectively. Adapted with permission from Reference [58]; copyright 2007 Elsevier Ltd.

Topography and electrochemical currents obtained synchronously by the integrated SECM/AFM systems provided information on the pitting precursor and pitting process. Compared with Al-Mn-Si-Zr alloys, EN AW-3003 alloys had more active sites and extensive localized dissolution, resulting in higher material losses. Interestingly, some of the larger micron-sized intermetallic particles initiated localized dissolution at the boundary region of the particle-matrix, while the fine dispersions were not active. The intermetallic particles in the Al-Mn-Si-Zr alloy were few. Although they could induce selective dissolution and form small tunnel-like holes, because of their small weight loss, they were suitable for fin material in heat exchange applications.

The combination of EC-AFM and scanning Kelvin probe force microscopy (SKPFM) can simultaneously obtain topographical changes and Volta potential maps, which helps to better understand selective corrosion behavior and its mechanism. The application of EC-AFM in selective corrosion is summarized in Table 4.

**Table 4.** Summary of the application of EC-AFM in selective corrosion.

	Materials	Solution	Mode	Reference
	AZ91 alloy added (La,Ce) mischmetal	0.1 mol/L NaCl solution	Contact mode	[53]
	Al 6060 alloy	0.2 M Na <sub>2</sub> SO <sub>4</sub> solution	Contact mode	[54]
	2205 HT	1 M NaCl solution	Contact mode	[55]
Selective corrosion	Cutting edges of adhesively bonded Zn (Z) and Zn-Al-Mg (ZM) galvanized steel substrates	0.001 M NaCl solution	Tapping mode	[56]
	Ti <sub>6</sub> Al <sub>4</sub> V <sub>2</sub> Nd	1.5 wt% NaCl solution	Tapping mode	[57]
	EN AW-3003 and Al-Mn-Si-Zr fin alloy	SWAAT solution of pH 4	Contact mode	[58]

### 3.1.4. Intercrystalline Corrosion

Intercrystalline corrosion is a local corrosion phenomenon that occurs along the grain boundary of a metal material in a corrosive medium and causes the loss of bonding force between grains. When intercrystalline corrosion occurs in the material, there may be no macroscopic change, but the material's strength is almost completely lost, resulting in the sudden destruction of equipment. The main reason for intercrystalline corrosion is the difference in structure and chemical composition between the grains and grain boundaries of the material.

Based on EC-AFM, the contact mode high-speed AFM (HS-AFM) compensates for the shortcomings of AFM with short collection times. The long collection time is a limiting factor for AFM. Contact mode HS-AFM images multiple frames per second, making it orders of magnitude faster than traditional AFM. This enables real-time imaging processes with nano-scale lateral resolution and sub-nanometer-scale height resolution. The increase in speed can not only directly image dynamic nanoscale events, but also macroscopic regions of the sample surface without reducing resolution. It is a valuable imaging tool for in situ observation of nanoscale corrosion initiation events such as metastable pitting, grain boundary dissolution, and short crack formation during stress corrosion cracking.

In the work of Moore and co-workers, local corrosion phenomena such as pitting and intergranular attack (IGA) on thermally sensitized AISI 304 stainless steel were studied using HS-AFM in 1% NaCl [59]. Real-time in situ HS-AFM observations showed that an intergranular pit was formed within 0.5 s during a galvanostatic scan. Intergranular pits were distributed along the grain boundary (GB) in a chain shape, which was caused by the preferential corrosion of GB. Chromium carbide was precipitated along GBs, which resulted in the depletion of the local chromium elements in the area around GBs, greatly reducing the local corrosion resistance of GBs. By using HS-AFM and electrochemical data for the computational model, it was found that the radial diffusion state of the system was reached within 0.01 s, leading to rapid dissolution of materials.

Padhy et al. [60] used EC-AFM to study the surface morphology of austenitic stainless steel in nitric acid medium. In situ EC-AFM results showed that the surface presented a platelet-like structure in low-concentration nitric acid solution (0.1 M, 0.5 M), providing effective protection for the surface. When the concentration of HNO<sub>3</sub> was from 0.1 M to 0.6 M, the roughness decreased, which was related to the thinning of the passive film and marked the beginning of corrosion. From the morphology of 0.6 M HNO<sub>3</sub>, breakdown of the passive film and surface dissolution were observed. As the concentration continued to increase to 1 M, the roughness increased due to the intensification of the surface dissolution and selective dissolution of grain boundaries, as shown in Figure 24.

The early stages of localized corrosion are important as mentioned earlier, because they account for most of the lifetime of intergranular corrosion, stress corrosion cracking (SCC), or pitting, and they are more accessible to take remedial action. Williford et al. [61] used EC-AFM to obtain images of the early stages of intergranular corrosion (IGC) in 304L stainless steel. The observation of EC-AFM showed that IGC was present between the carbides, but not completely around the carbide in the early stage. Later, the grain boundaries became wider, the carbides were shortened, and the IGC completely surrounded the carbides. The matrix between carbides began to corrode, which was best explained by the fact that the carbides were cathodic with respect to the matrix; thus, when the matrix dissolved, they were protected by cathodic protection. In addition, the carbide was connected to adjacent grains through the ligaments of the matrix material, which may have meant that the SCC crack front was bridged by the carbide. The SCC crack front could move forward and surround the carbide, creating an area where the carbide bridged the crack.

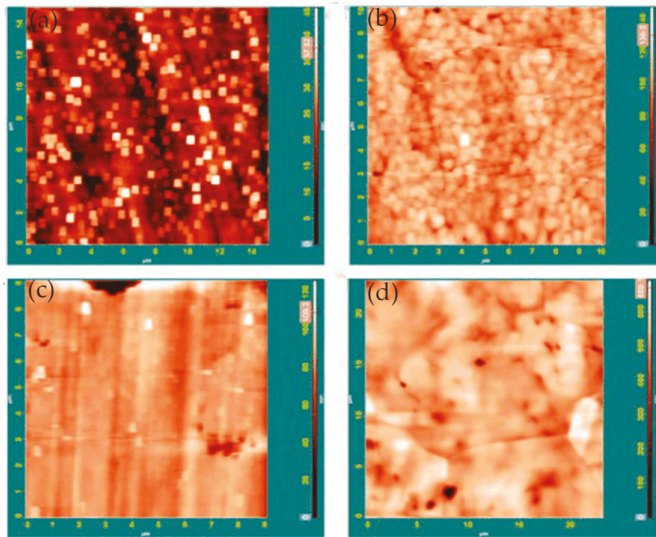


**Figure 24.** Surface morphology of 304L stainless steel at 1100 mV in (a) 0.1 M HNO<sub>3</sub>, (b) 0.5 M HNO<sub>3</sub>, (c) 0.6 M HNO<sub>3</sub>, and (d) 1 M HNO<sub>3</sub>. Reprinted with permission from Reference [60]; copyright 2010 Elsevier Ltd.

An AFM with a conductive probe can simultaneously obtain the surface topography and surface potential of the scanned surface. Fu et al. [62] studied the local corrosion of high-chromium cast iron in regions at different distances from interphase boundaries using EC-AFM in the contact mode. According to the measured local potential, a decrease in interface potential between carbide and matrix was observed. Moreover, the corrosion rate of the metal matrix near the primary carbide was significantly higher than that far away from the primary carbide. The morphology map obtained using EC-AFM showed that the area near the primary carbide/matrix interface corroded or dissolved more rapidly than the area away from the interface. Furthermore, the corrosion rate was found to be particularly rapid in areas with sharp edges. The authors suggested that, on the flat side, most of the electrons flowed into the half-space on one side of the matrix. However, at the sharp edge, electrons flowed into a larger space in the matrix, corresponding to a larger total electron flow, which greatly increased the corrosion rate of the sharp edge.

In high-entropy alloys (HEAs), the homogeneous elemental distribution is expected to improve corrosion resistance. In order to develop highly corrosion-resistant HEAs, it is necessary to study the relationship between chemical/microstructure segregation and localized corrosion. In the study of Shi and co-workers, localized corrosion of Al<sub>x</sub>CoCrFeNi HEAs was studied using in situ EC-AFM in 3.5 wt% NaCl solution. Surface topography changes at micron/submicron scales were monitored under different anodic potentials [63]. In the experiment, with the increase in aluminum content in HEAs, the microstructure changed from a single FCC (face-centered cubic) solid solution to the FCC phase and (ordered/disordered) BCC (face-centered cubic) phase. The EC-AFM image showed that the uniform single-phase Al<sub>0.3</sub>CoCrFeNi alloy had the best corrosion resistance, and the breakdown of its passive film was in the form of randomly distributed pits, as shown in Figure 25.

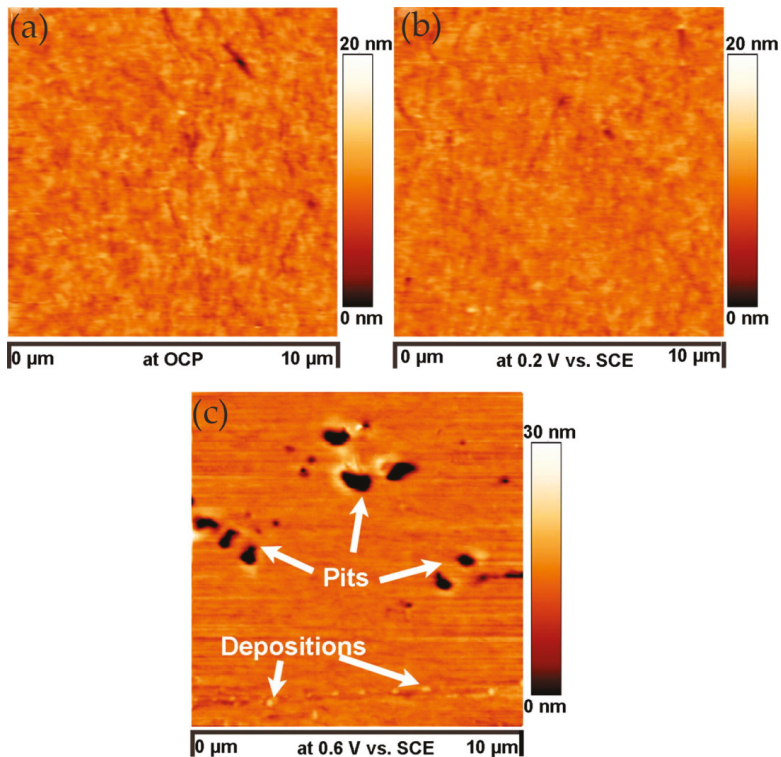


**Figure 25.** In situ EC-AFM topography images of the  $\text{Al}_{0.3}\text{CoCrFeNi}$  high-entropy alloy (HEA) in a 3.5 wt% NaCl solution after 10 min of exposure at (a) OCP, (b) 0.2 V, and (c) 0.6 V. Reprinted with permission from Reference [63]; copyright 2018 Elsevier Ltd.

With the increase in aluminum content, the BCC phase appeared in the  $\text{Al}_{0.5}\text{CoCrFeNi}$  alloy, resulting in a heterogeneous microstructure. Pits were formed preferentially along the FCC/BCC phase boundary, leading to the initial breakdown of the passive film, which was manifested as the decline in critical pitting potential value in the potentiodynamic polarization curve, as shown in Figure 26.

Pitting corrosion was not observed in the  $\text{Al}_{0.7}\text{CoCrFeNi}$  alloy with the increase in aluminum content and volume fraction of the BCC phase. In contrast, local corrosion along the dendritic/interdendritic boundaries and selective dissolution of the (Al, Ni)-rich ordered BCC phase occurred, as shown in Figure 27. Therefore, the author believed that, as the microstructure changed from single solid solution to multiphase, the breakdown of the passivation film changed from pitting to phase boundary dissolution, which led to a decrease in corrosion resistance.

Bettini et al. [64] studied the effects of carbides on the corrosion/dissolution behavior of biomedical CoCrMo alloys in PBS solution using EC-AFM at different applied potentials. SKPFM results showed that, compared with the matrix, the Volta potential of carbides was higher. In addition, the Volta potential decreased in the boundary region, which may have been related to local depletion of the main alloy elements. This indicated that the carbide boundary had a greater corrosion tendency and was the preferred site for corrosion/dissolution. In situ EC-AFM measurements of the CoCrMo alloys exposed to PBS showed that, at high anodic potential, a dissolution process at carbide boundaries was observed, and an increase in boundary depth was seen in line profiles across these boundaries, as shown in Figure 28. This was consistent with the SKPFM Volta potential mapping, which showed that



some of the boundary areas were weak sites for corrosion/dissolution due to lower relative nobility compared to the matrix.

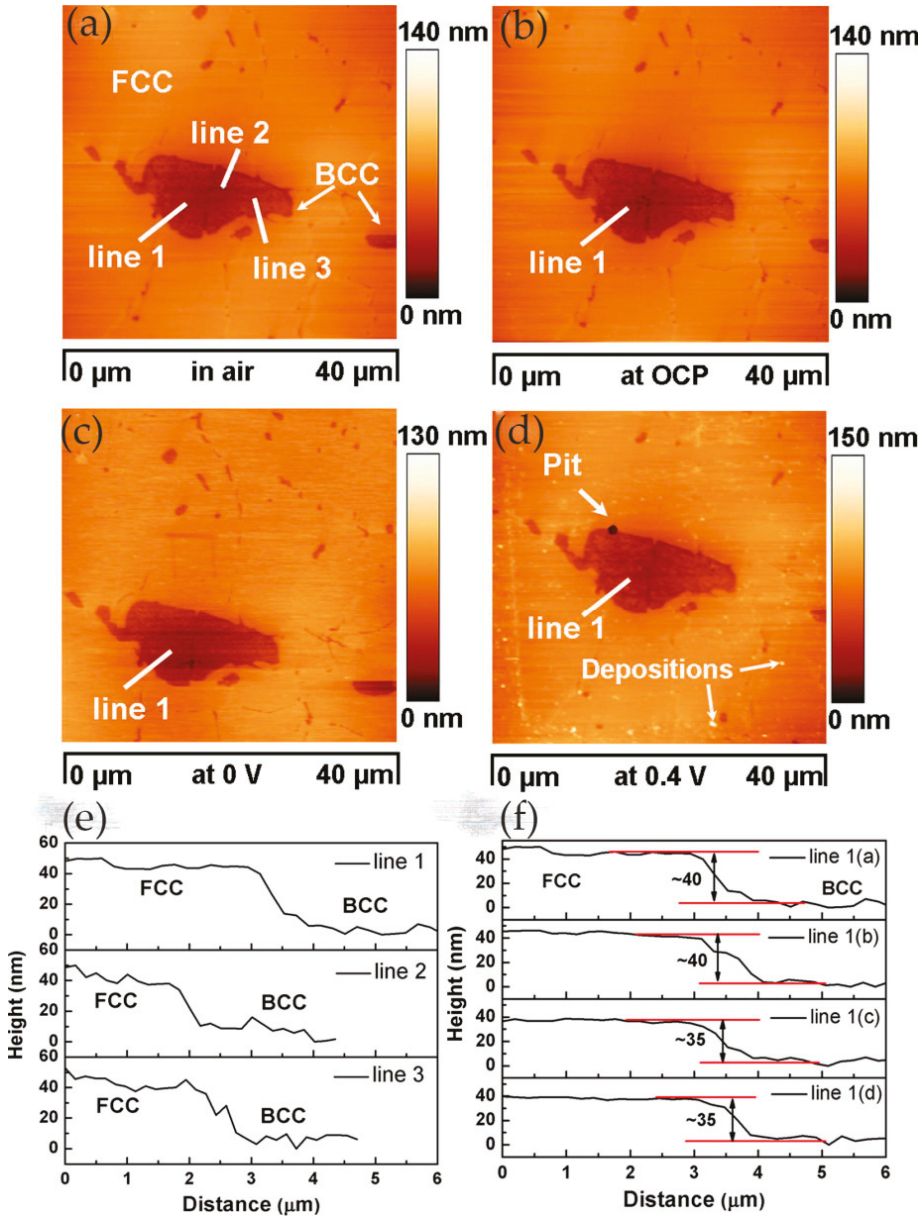


**Figure 26.** The AFM topography image in air (a), and in situ EC-AFM topography images of the Al<sub>0.5</sub>CoCrFeNi HEA after 10 min of exposure in a 3.5 wt. % NaCl solution at (b) OCP, (c) 0 V, and (d) 0.4 V. (e) Three-line profiles across the phase boundaries illustrated in (a). (f) Vertical profiles along line 1 of the surface in (a–d). Reprinted with permission from Reference [63]; copyright 2018 Elsevier Ltd.

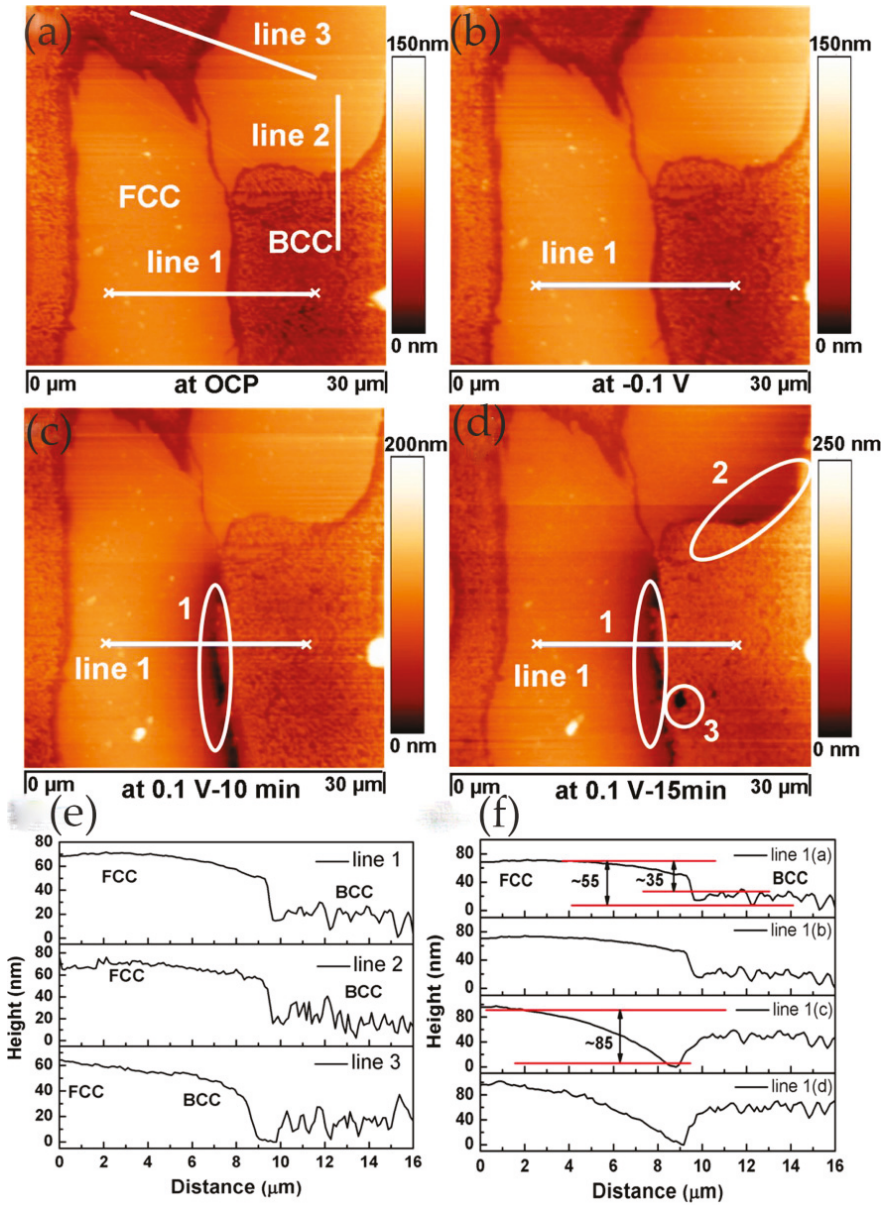


**Figure 27.** In situ EC-AFM topography images of the  $Al_{0.7}CoCrFeNi$  HEA after 10 min of exposure in a 3.5 wt% NaCl solution at (a) OCP, (b) 0.1 V, and (c) 0.1 V, and (d) after 15 min of exposure at 0.1 V vs. SCE. (e) Three-line profiles across the phase boundaries illustrated in (a). (f) Vertical profiles along line 1 of the surface in (a–d). Reprinted with permission from Reference [63]; copyright 2018 Elsevier Ltd.

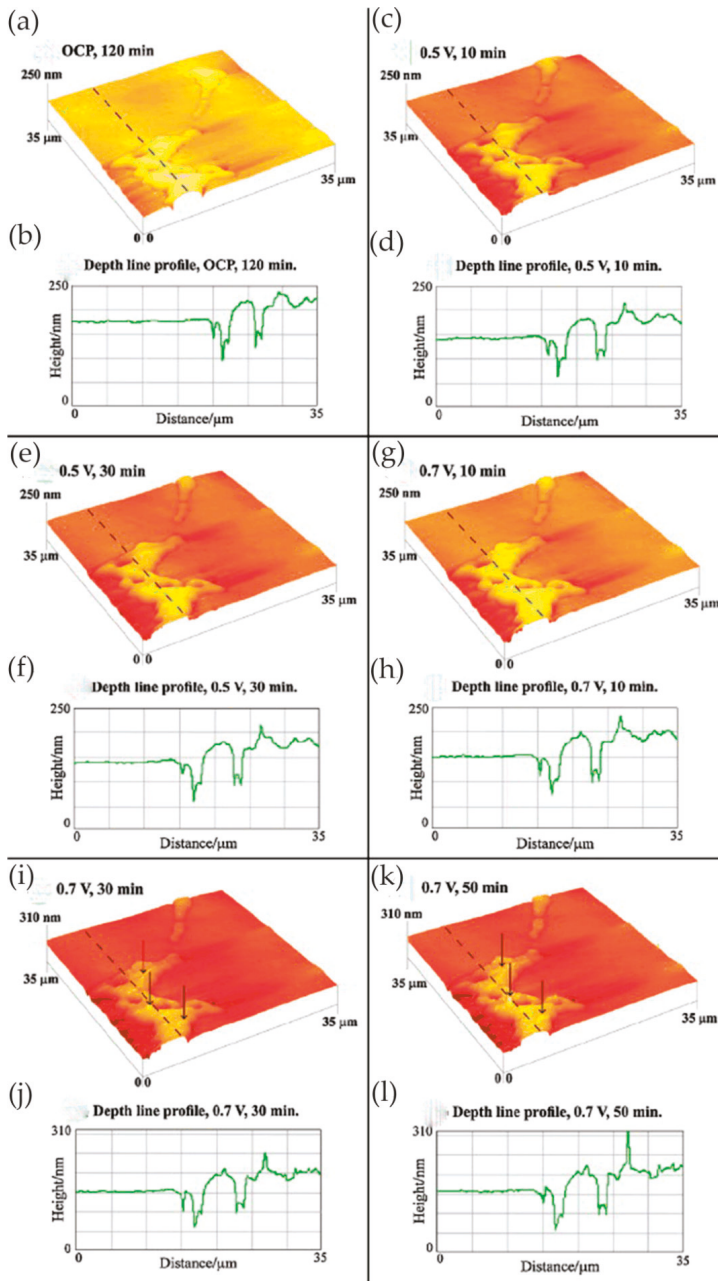


**Figure 28.** In situ AFM images of the same area of CoCrMo alloy under electrochemical control in PBS solution with pH 7.4, (a) after 120 min at OCP, (c,e) after 10 and 30 min at 0.5 Vsat Ag/AgCl, and (g,i,k) after 10, 30, and 50 min at 0.7 Vsat Ag/AgCl, with marked etching-like dissolution sites on the carbide (where visible). (b,d,f,h,j,l) Depth line profiles at the applied potential and time. Adapted with permission from Reference [64]; copyright 2011 Elsevier Ltd.

Davoodi et al. [65] studied the localized corrosion and preferential dissolution of Al alloys in chlorine solution using an integrated EC-AFM/SECM system. The integrated EC-AFM/SECM could simultaneously detect topographic changes and electrochemical active sites in the same region and reveals local corrosion processes related to IMPs. The results showed that preferential dissolution occurred in the interfacial region between the alloy matrix and IMPs. The formation of grooves around the larger IMPs indicated that different types of IMPs had different dissolution behaviors. In addition, they found that only a small number of IMPs were involved in the localized dissolution at any given time.

EC-AFM can clearly reveal the formation of trenches and the local dissolution of the grain/phase interface, and it can explore the causes and mechanisms of intercrystalline corrosion in combination with other test tools. Table 5 summarizes the application of EC-AFM in intercrystalline corrosion.

**Table 5.** Summary of the application of EC-AFM in intercrystalline corrosion.

	Materials	Solution	Mode	Reference
Intercrystalline corrosion	AISI 304 stainless steel	1.0 wt% NaCl solution		[59]
	304L stainless steel	0.6 M and 1 M HNO <sub>3</sub>		[60]
	High-chromium cast iron	3.0 wt% NaCl solution	Contact mode	[61]
	Al <sub>x</sub> CoCrFeNi HEAs	3.5 wt% NaCl solution	Tapping mode	[63]
	CoCrMo alloys	Phosphate-buffered saline solution	Contact mode	[64]

### 3.2. Metal Protection

#### 3.2.1. Coating Protection

One of the primary protection techniques for metallic materials is the use of a cover layer on the metal surface to avoid direct contact between the metal and the corrosive medium as much as possible. The coating provides an effective barrier to the substrate, slowing the corrosion of the metal. In general, the metal surface coating can be divided into the metal coating and non-metallic coating. The coating not only slows electron transfer between the anode and cathode; it can also act as a barrier to prevent oxygen from penetrating the cathode reaction. Microcrystalline coating, nanocrystalline coating, gradient coating, composite coating, etc. can effectively improve the overall performance of the material, including corrosion resistance.

Li and co-workers studied the electrochemical mechanism and corrosion protection properties of solvent-borne alkyd composite coating containing 1.0 wt% CeO<sub>2</sub> nanoparticles (CeNPs) and 1.0 wt% polyaniline (PANI) for carbon steel in NaCl solution [66]. In their work, the morphology changes of the coatings and redox reactions of PANI at the nanoscale were accurately monitored by linking the volume changes observed using in situ EC-AFM imaging with redox peaks measured using in situ cyclic voltammetry (CV). The results of EC-AFM showed that PANI nanoparticles in the alkyd matrix exhibited contracted morphology in the reduced state, leucoemeraldine base (LB), and expanded morphology in the oxidized state, emeraldine salt (ES). The surface did not change significantly, which indicated that the composite coating was stable in corrosive solutions even under very harsh potential conditions, as shown in Figure 29. OCP and EIS results indicated that the redox reaction of PANI ES/LB forms caused metal passivation, which was an active corrosion protection mechanism.

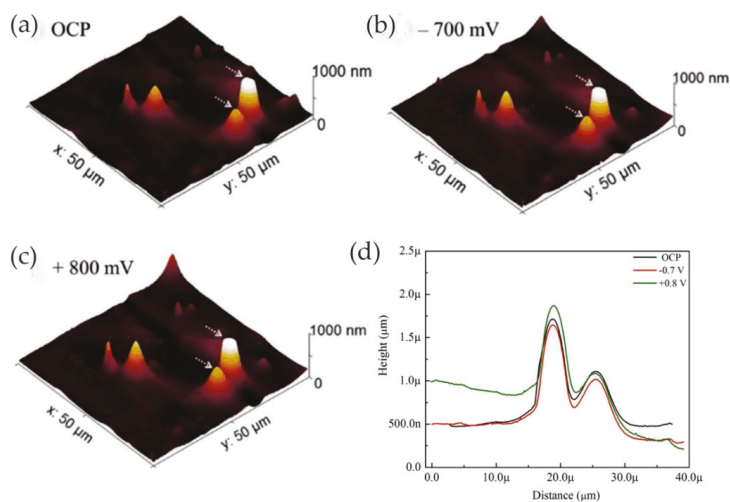


**Figure 29.** EC-AFM images (3D) of the same scan area of the composite coating in 3.0 wt% NaCl solution obtained after 60 min (a) at OCP, (b) at  $-700$  mV (vs. Ag/AgCl), and (c) at  $800$  mV (vs. Ag/AgCl). (d) Line profiles of CeO<sub>2</sub> nanoparticle (CeNP) aggregates when at the two applied potentials drawn by the crossing line. Reprinted with permission from Reference [66]; copyright 2019 Elsevier Ltd.

The evolution of OCP with exposure time under 3.0 wt% NaCl for composite coating and reference coating showed that the potential value of composite coating was higher than that of reference coating during the whole measurement process, indicating that the corrosion resistance of the composite coating was improved. The increase in OCP value was attributed to the fact that CeNPs significantly improved the barrier effect and slowed down the migration of corrosion ions. Therefore, the synergistic effect of PANI and CeNPs greatly improved the barrier performance and the corrosion resistance of alkyd composite coating.

In a series of studies by Li and his colleagues, they also studied the electrochemical activity of 1.0 wt% *p*-toluene sulfonic acid (PTSA)-doped PANI in solvent-borne alkyd composite coating, as well as its self-healing corrosion protection mechanism on carbon steel in 3.0 wt% NaCl solution [67]. Through the CV (cyclic voltammetry) curves and EC-AFM imaging, it was proven that doped PANI at low percentage had extremely high electrochemical activity, showing contraction at the reduction potential and expansion at the oxidation potential, which provided evidence for a reversible redox reaction between the ES and LB forms. The voltage potential diagram obtained using KFM under air conditions indicated that PTSA-doped PANI had sufficiently high electrochemical activity and stable reoxidation ability to keep the passivation region on the metal surface. The PTSA-doped PANI in alkyd composites caused structural mutations due to energy input, which increased the electrochemical activity and provided doped PANI with a good electrochemical connection to the metal surface. It played an important role in improving the self-healing corrosion protection of composite coatings. In addition, the EIS showed increased resistance of the composite coating, which may have been related to the interaction of PANI particles in the alkyd matrix forming a dense and more resistive network.

Moreover, they studied the corrosion protection properties of a waterborne acrylic composite coating with 1.0 wt% acetic acid-stabilized CeNPs on carbon steel in 3.0 wt% NaCl solution [68]. The results of in situ AFM showed that the CeNPs embedded in the composite coating could greatly reduce the nano-pinholes in the waterborne acrylic coating, as well as significantly improve the stability of the coating, which played an important role in improving the barrier property of the coating. In situ EC-AFM indicated that some CeNPs and aggregates were released from the coating surface during exposure, and then some particles and cerium compounds were precipitated, as shown in Figure 30.

The presence of CeNPs or aggregates acted as nucleation sites to promote precipitation on the coating surface and inside the coating pinholes, thereby preventing the entry of corrosive ions and the corrosion of the metal matrix.

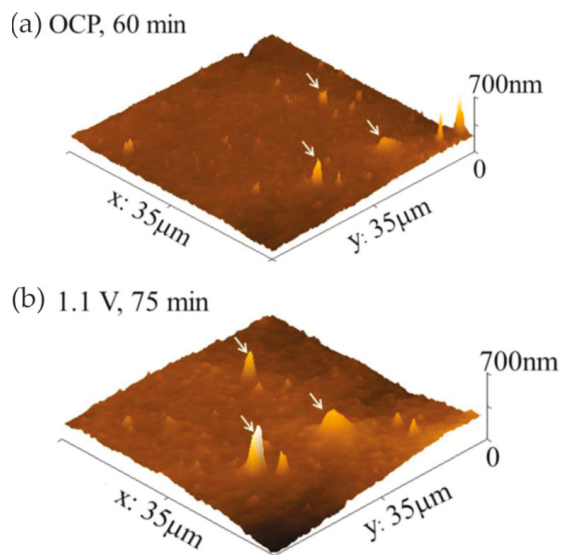


**Figure 30.** EC-AFM images (3D) of the same area of the composite coating obtained after 14 h of exposure in 3.0 wt% NaCl solution: (a) after 60 min at OCP; (b) after 75 min at 1.1 V vs. Ag/AgCl. Adapted with permission from Reference [68]; copyright 2015 Electrochemical Society.

Liu et al. [69] studied the pitting behavior of austenitic stainless steel with nanocrystalline (NC) and polycrystalline (PC) microstructures in 3.5 wt% NaCl solution. In situ AFM was used to study the process of passive film formation on the PC alloy and NC alloy under anodic potential. AFM observations showed that the passive film formed rapidly on the PC alloy, and pitting occurred after continuous film formation, which was a slow process of metastable pitting formation and repairation. However, the formation of a passive film on the NC alloy indicated that, due to the accumulation of many small particles on the surface, the oxide particles grew in the original position and eventually became a passive film. The voids and the boundaries of oxide particles may have been inoculation points for metastable pits. Although metastable pits were easy to initiate on the NC coating, the small grain size promoted the diffusion of elements, such that pits could be quickly repaired or healed. Therefore, the pitting mechanism of the NC coating was mainly characterized by rapid metastable pitting initiation and death, and its pitting resistance was higher than that of the PC alloy. In addition, in their other study, the characteristics of both pit initiation and pit growth processes on an austenitic stainless-steel NC coating were monitored using in situ AFM [70]. Pit initiation included the formation of metastable pits and repassivation process. Pitting growth included stable pit growth and material dissolution. The fine grain size promoted the formation and growth of nano-scale oxide particles, which significantly improved the repassivation ability and reduced the probability of stable pit formation. Compared with PC austenitic stainless steel, nanocrystals promoted the formation of metastable pits but reduced the rate of stable nucleation and growth of pits.

In the study of Pan and co-workers, the pitting corrosion of coarse crystal (CC) 304 stainless steel and its NC thin film was studied in 3.5 wt% NaCl solution, especially the influence of nanocrystalline on the pitting process [71]. The whole pit growth process was recorded using in situ AFM and the growth mechanism of stable pits on NC film was understood. The results showed that the initiation site

of the pit on the NC film was at the boundary of the oxide particles. As there were lots of boundaries on the surface, metastable pit events on NC films were more likely to occur than those on CC 304 stainless steel, which indicated that nanocrystallization promoted metastable pit processes, as shown in Figure 31.

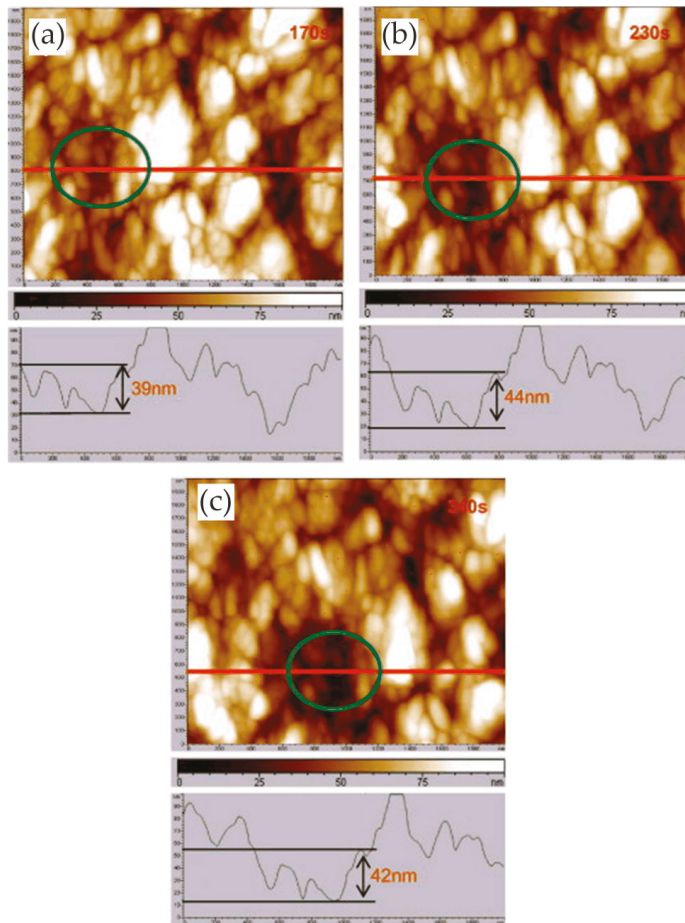


**Figure 31.** In situ AFM images of nanocrystalline (NC) thin film in the initial pitting stage under anodic polarization in 3.5 wt% NaCl solution: (a) 170 s; (b) 230 s; (c) 340 s. Reprinted with permission from Reference [71]; copyright 2013 Elsevier Ltd.

In addition, the transition from metastable pitting to stable pitting was inhibited due to the excellent repassivation ability of NC films. In the process of NC film deposition, the internal residual stress may have inhibited the formation of lace cover in the process of stable pit growth, and then changed the growth mechanism of the NC film surface stable pit. Therefore, the probability of developing from metastable pitting to stable pitting on NC films was much lower than that on CC 304L stainless steel. Nanocrystallization changed the geometry and growth mechanism of stable pits, slowing down the nucleation and growth process, which improved the pitting corrosion resistance of CC 304L stainless steel. Moreover, they also studied the corrosion behavior of a magnetron-sputtered NC 304L stainless steel coating in 0.05 M  $H_2SO_4$  + 0.2 M NaCl solution, which was compared with

conventional rolled CC 304L stainless steel [72]. The nanocrystalline structure reduced the adsorption capacity of  $\text{Cl}^-$  on the surface and inhibited the incorporation of  $\text{Cl}^-$  in the passive film. In situ AFM observation showed that the growth rate of the passive film on the NC film was greatly higher than that on the CC 304L stainless steel, as shown in Figure 32. In other words, the nanocrystalline structure improved the growth rate of the passive film and facilitated the healing of the passive film rupture. The composition of the passive film on the NC film determined by XPS had a higher ratio of chromium oxide to iron oxide. The higher content of chromium oxide improved the corrosion resistance of nanocrystalline samples. Since the structure of the passive film was more compact, the ratio of chromium oxide to iron oxide was higher, and the incorporation of  $\text{Cl}^-$  was less, the corrosion resistance of the NC film was greatly improved.

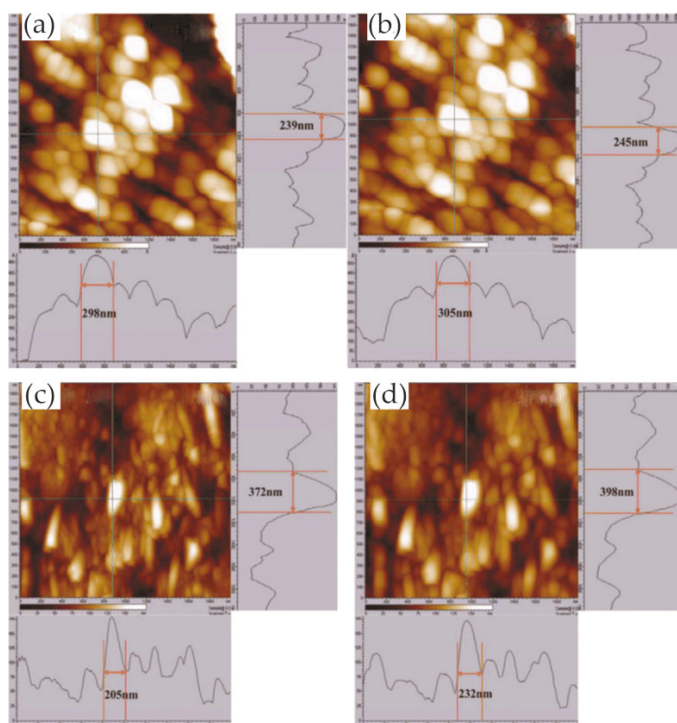


**Figure 32.** In situ AFM images of coarse crystal (CC) 304L stainless steel (a,b) and a NC thin film (c,d) (scale  $2\ \mu\text{m} \times 2\ \mu\text{m}$ ) in the growth stage of a passive film under anodic polarization in  $0.05\ \text{M}\ \text{H}_2\text{SO}_4 + 0.2\ \text{M}\ \text{NaCl}$  solution after passivation of 6 min (a,c) and 12 min (b,d). Reprinted with permission from Reference [72]; copyright 2012 Electrochemical Society.

In addition, the passive film growth mechanisms of the NC 304L stainless-steel thin film, deep-rolled bulk nanocrystalline (BN) 304 stainless steel, and CC 304 stainless steel in  $0.05\ \text{M}\ \text{H}_2\text{SO}_4 + 0.2\ \text{M}\ \text{NaCl}$  solution were studied using electrochemical measurements and in situ AFM [73]. The growth rate of the passive film on the three materials was in the following order: NC thin film > BN304 stainless steel > CC 304L stainless steel. Nanocrystallization changed the nucleation mechanism of passive films from gradual to instantaneous. The passive film on the CC 304L stainless steel and BN 304L stainless steel had a single-layer structure, while the passive film on the NC film had a multi-layer structure.



EC-AFM can not only detect the state of the coating surface through high-resolution imaging, but also produce coating defects by means of probe scraping to obtain direct information on the coating corrosion resistance. The application of EC-AFM in coating protection is summarized in Table 6.

**Table 6.** Summary of the application of EC-AFM in coating protection.

	Materials	Coating	Solution	Mode	Reference
Coating protection	Carbon steel	Solvent-borne alkyd composite coating containing 1.0 wt% CeO <sub>2</sub> nanoparticles (NPs) and 1.0 wt% polyaniline (PANI)	3.0 wt% NaCl solution	Contact mode	[66]
	Carbon steel	1.0 wt% <i>p</i> -toluene sulfonic acid (PTSA)-doped PANI in solvent-borne alkyd composite coating	3.0 wt% NaCl solution	Contact mode	[67]
	Carbon steel	Waterborne acrylic composite coating with 1 wt% acetic acid-stabilized CeO <sub>2</sub> nanoparticles	3.0 wt% NaCl solution	Contact mode	[68]
	Austenitic stainless steel	Nanocrystalline (NC) and polycrystalline (PC) microstructure coatings	3.5 wt% NaCl solution	Tapping mode	[69]
	304L stainless steel	Magnetron-sputtered NC	0.05 M H <sub>2</sub> SO <sub>4</sub> + 0.2 M NaCl solution	Tapping mode	[72]

### 3.2.2. Corrosion Inhibitor Protection

A corrosion inhibitor is a chemical or a mixture of several chemicals that prevents or slows corrosion when present in a corrosive environment (medium) in the proper concentration and form. The addition of corrosion inhibitors can significantly reduce the corrosion rate of metal materials. At the same time, the original physical and mechanical properties of the metal material can be maintained. The advantages of using corrosion inhibitors to protect metal lie in their low dosage, quick effect, low cost, and convenient use. At present, corrosion inhibitors are widely used in machinery, petrochemical, metallurgy, energy and other industries. In some studies, the authors used in situ EC-AFM under real-time operating conditions to detect changes in the corrosion morphology of the sample after the addition of the corrosion inhibitor, and then investigated the properties of the corrosion inhibitor and speculated on the corrosion inhibition mechanism.

The study of non-toxic corrosion inhibitors is important for replacing classical molecules with sulfur, nitrogen, or aromatic functions. Rocca et al. [74] reported the inhibition conditions and mechanisms of linear sodium heptanoate on copper corrosion. In situ EC-AFM under applied potential allowed observing the morphology of the passive film without damaging the layer. The result showed that, when pH = 5.7 and 11, for 0.08 M NaC<sub>7</sub>, large non-covering copper heptanoate crystals or non-covering copper oxide were formed on the surface, and the corrosion inhibitor efficiency was low in acidic medium. However, when the pH value was 8, for 0.08 M NaC<sub>7</sub>, a thin layer of heptanoic was formed, which acted as a barrier and effectively protected the metal matrix. The inhibition of sodium heptanoate was related to the formation of a protective layer consisting mainly of copper heptanoate on copper, and the optimum corrosion inhibition conditions were 0.08 M NaC<sub>7</sub>, pH 8 for copper corrosion.

Bertrand et al. [75] used in situ EC-AFM to study the corrosion behavior of a copper surface immersed in various electrolytes under dynamic potential conditions at room temperature. In sodium sulfate and sulfuric acid solutions, dissolution precipitation occurred on the surface, which changed the topographic characteristics of the metallic surface. On the contrary, when copper was immersed in borate or heptanoate solutions, passivation could be clearly observed. Regardless of the oxidation mode (constant potential or open-circuit condition), a thin passive layer was grown on the surface and was stable over time. In the borate medium, the sediments were composed of Cu<sub>2</sub>O and CuO oxides, while, in the heptanoate electrolyte, a metal soap composed of copper(II) heptanoate was detected. In addition, the inhibition mechanism of sodium heptanoate was identified, whereby a thin passive layer of copper metal soap was formed on the surface via dissolution precipitation.

The use of polymer corrosion inhibitors attracted attention. On the one hand, they have low cost and good stability. On the other hand, they have multiple adsorption sites that form complexes with metal ions covering the surface and protecting the metal from corrosion. Umoren et al. [76] studied the mechanism of polyacrylic acid (PAA) inhibiting the corrosion of pure cast aluminum in acidic medium and the synergistic effect with iodide ion addition. The in situ AFM morphology of the surface showed that PAA was adsorbed onto the surface of the aluminum and its arrangement was more orderly in the presence of iodide ions, as shown in Figure 33, resulting in higher inhibition efficiency. The authors believed that the alumina film was replaced by the adsorption of KI on aluminum, and then the PAA was adsorbed onto the KI such that the PAA molecules were arranged on the aluminum surface in an orderly manner, which enhanced the inhibition process.

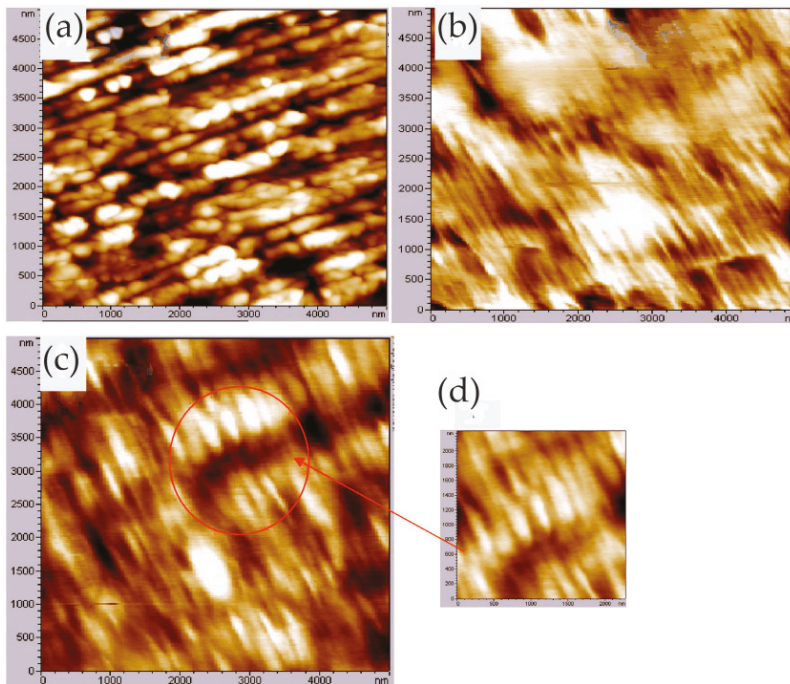


**Figure 33.** In situ AFM image of Al in 0.5 M H<sub>2</sub>SO<sub>4</sub> in the presence of polyacrylic acid (PAA) + KI at different potentials: (a)  $-1.0$  V, (b)  $-0.70$  V, and (c)  $-0.50$  V. (d) Magnified images of the framed area of (c). Adapted with permission from Reference [76]; copyright 2013 Taylor & Francis.

Zhang et al. [77] investigated the electrochemical corrosion behavior of AISI321 stainless steel in 36% ethylene glycol–water solution. It can be seen from the results of EC-AFM that the passive film became more complete and the number of defects decreased with the increase in polarization time. Moreover, as the passive potential increased, the particle diameter increased and surface defects decreased. When the potential ranged from  $-0.15$  to  $0.45$  V, an N-type oxide film adhered to the surface of the sample. However, when the potential was between  $0.45$  and  $0.75$  V, a P-type oxide film was formed on the surface. The passive film formed at high potential had fewer defects and excellent protective performance. Therefore, AISI321 stainless steel could be passivated in ethylene glycol solution and the passive potential ranged from  $-0.15$  V to  $0.75$  V. With the increase in passive potential, the protective performance of the passive film was significantly improved.

In the study of Nikhil and co-workers, ethyl-2-cyano-3-(4-(dimethylamino) phenyl) acrylate (ECDPA) and ZnO nanosheet composites were synthesized and used as corrosion inhibitors for copper in 1 M HCl. ECDPA acted as a barrier to acid molecules after adsorbing copper, delaying the corrosion of copper in hydrochloric acid [78]. EC-AFM analysis confirmed that ZnO nanoparticles promoted the adsorption of ECDPA. Adsorption/deposition of a small number of inhibitor molecules was found when ZnO was not added. After the addition of ZnO, the number of inhibitor molecules on the surface was significantly increased, and the size of the inhibitor molecule became larger as the ZnO calcination temperature increased, as shown in Figure 34.

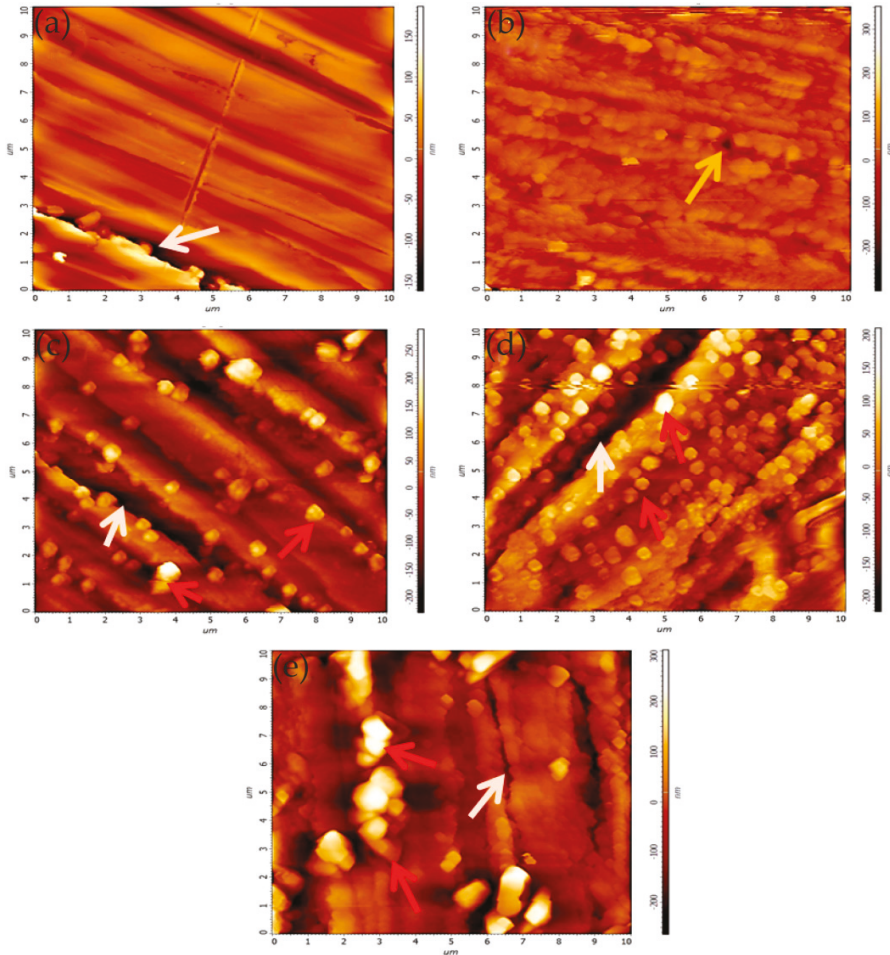


**Figure 34.** EC-AFM two-dimensional (2D) images of (a) polished copper, and copper (b) corroded, as well as inhibited by (c) ethyl-2-cyano-3-(4-(dimethylamino) phenyl) acrylate (ECDPA), (d) EZ3 (ECDPA–ZnO at 300 °C), and (e) EZ5 (ECDPA–ZnO at 500 °C) in 10 min of immersion in 1 M HCl at –0.005 V. Reprinted with permission from Reference [78]; copyright 2019 Elsevier Ltd.

The corrosion resistance tests of ECDPA, EZ3 (ECDPA–ZnO at 300 °C), and EZ5 (ECDPA–ZnO at 500 °C) showed that the composite had better protection performance than ECDPA alone. The maximum inhibition efficiency of ECDPA was approximately 75%, while the composite could be further improved

to 78% (EZ3) and 81% (EZ5). The improved corrosion inhibition performance of ECDPA–ZnO may have been related to the inclusion of ZnO nanoparticles, which promoted the adsorption of ECDPA over Cu.

Shaban et al. [79] studied the inhibition of dibenzylsulfoxide (DBSO) and *p*-chlorobenzohydroxamic acid (*p*-Cl-BHA) on copper corrosion in 0.5 M NaCl and 0.1 M Na<sub>2</sub>SO<sub>4</sub>, respectively. In situ AFM was used to observe the corrosion and inhibition process of the electrode surface. When DBSO was not added, the surface became rougher due to the dissolution of copper. In the presence of DBSO, the surface was not subject to severe corrosion and a relatively smooth surface was formed, as shown in Figure 35. Therefore, the authors thought that DBSO inhibited the corrosion of copper in sulfate solutions by converting it to a more stable, less soluble sulfide compound.

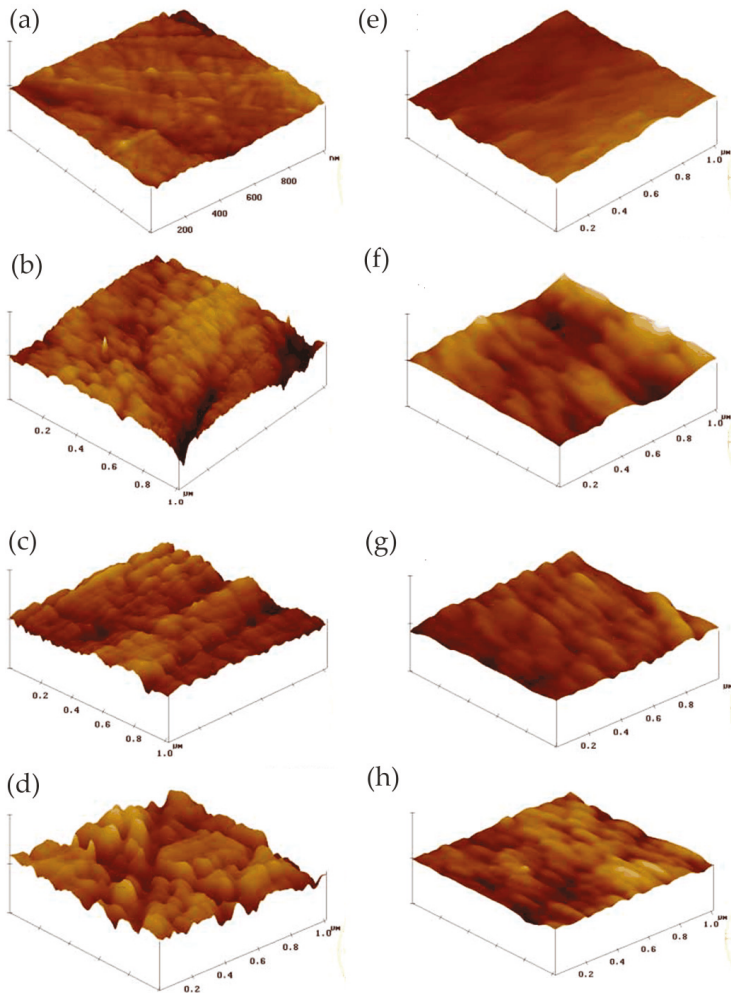


**Figure 35.** Morphological changes of copper in solution of 0.1 M Na<sub>2</sub>SO<sub>4</sub> (a–d) and 0.1 M Na<sub>2</sub>SO<sub>4</sub> + 0.5 mM dibenzylsulfoxide (DBSO) (e–h), at different times: (a,e) 0 min; (b,f) 15 min; (c,g) 30 min; (d,h) 45 min. Reprinted with permission from Reference [79]; copyright 1998 Springer.

In the absence of *p*-Cl-BHA, the formation and growth of pitting corrosion were detected. The addition of *p*-Cl-BHA significantly impeded the localized corrosion of copper and inhibited the

production of corrosion products that occurred when *p*-Cl-BHA was not added, as shown in Figure 36. Thus, the formation of a stable complex by adsorbing a corrosion inhibitor on a corroded surface effectively hindered further dissolution of the metal.

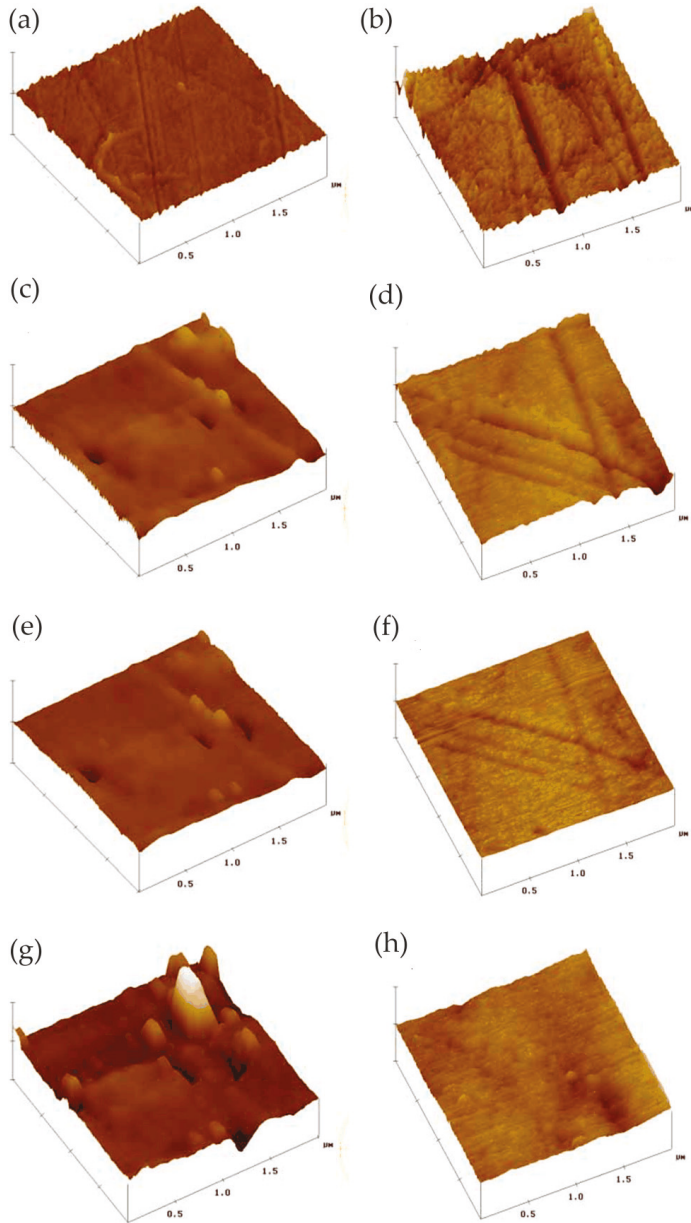


**Figure 36.** Morphological changes of copper in solution of 0.1 M NaCl (a–d) and 0.1 M NaCl + *p*-chlorobenzohydroxamic acid (*p*-Cl-BHA) (e–h), at different times: (a,e) 0 min; (b,f) 15 min; (c,g) 30 min; (d,h) 45 min. Reprinted with permission from Reference [79]; copyright 1998 Springer.

Cruickshank et al. [80] studied the anodic dissolution of polycrystalline copper in acid medium with or without corrosion inhibitor using EC-AFM. In 0.5 M H<sub>2</sub>SO<sub>4</sub>, the preferential corrosion of some grain surfaces occurred and then dissolved along grain boundaries. The addition of benzotriazole (BTA) formed a protective film that effectively inhibited the dissolution of copper. When the anode potential reached 200 mV, the protective film was stable. However, when the potential was as high as 300 mV, the film underwent local breakdown. In addition, Li et al. [81] investigated the effect of BTA on corrosion inhibition of copper using in situ EC-AFM in 0.01 M NaHCO<sub>3</sub>. The addition of BTA caused the copper surface to form a BTA film, effectively protecting the copper from erosion. The pitting potential of the copper surface covered by the BTA film could be significantly increased by more than 700 mV. Therefore, the author believed that, in fact, pitting was not a concern in the presence of BAT.

Through the morphology testing of EC-AFM, the adsorption–desorption states of corrosion inhibitors on an electrode surface can be intuitively understood, which is very beneficial for the exploration of electrochemical mechanisms of corrosion inhibitors. The application of EC-AFM in corrosion inhibitor protection is summarized in Table 7.

**Table 7.** Summary of the application of EC-AFM in corrosion inhibitor protection.

	Materials	Corrosion Inhibitor	Solution	Mode	Reference
Corrosion inhibitor protection	Copper	Linear sodium heptanoate	0.1 M Na <sub>2</sub> SO <sub>4</sub> solution	Contact Mode	[74]
	Pure cast aluminum	Polyacrylic acid (PAA) + KI	0.5 M H <sub>2</sub> SO <sub>4</sub>	Tapping Mode	[76]
	AISI321 stainless steel	36% ethylene glycol–water solution	Ethylene glycol–water solution	Tapping Mode	[77]
	Copper	Ethyl-2-cyano-3-(4-(dimethylamino) phenyl) acrylate (ECDPA) and ZnO nanosheet composites	1 M HCl		[78]
	Copper	Dibenzylsulfoxide (DBSO) and <i>p</i> -chlorobenzohydroxamic acid ( <i>p</i> -Cl-BHA)	0.5 M NaCl and 0.1 M Na <sub>2</sub> SO <sub>4</sub>	Contact Mode	[79]
	Polycrystalline copper	Benzotriazole (BTA)	0.5 M H <sub>2</sub> SO <sub>4</sub>	Contact Mode	[80]
	Copper	Benzotriazole (BTA)	0.01 M NaHCO <sub>3</sub>	Contact Mode	[81]

#### 4. Conclusions and Perspectives

This review introduced the evolution, principles, and operation modes of EC-AFM, as well as illustrated its application in corrosion science through specific examples.

In summary, EC-AFM can not only perform real-time in situ research on micro-area corrosion (passivation) in the field of corrosion electrochemistry; it also has higher resolution, which provides detailed information on corrosion phenomena, such as activation and passivation at submicroscopic scales, especially in the early stages of corrosion. The surface topography changes of the target sample can be quantitatively analyzed with the information of surface height changes with applied voltage or time, helping us better study the corrosion process and mechanism. In recent years, EC-AFM was continuously improved in electrolytic cells, imaging modes, and probes. Moreover, EC-AFM was combined with SKPFM, SVET, and SECM to study the surface state of metals, greatly expanding the scope of application.

However, EC-AFM also has some problems that affect research, which brings about difficulties obtaining reliable surface topography features, such as drift during the scanning process, alignment of the laser, changes in the refractive index of the electrochemical medium as the process of corrosion goes on, finding accurate resonant frequencies, etc. In addition, the EC-AFM scanning rate is limited, and some rapid interface reactions cannot be monitored in real time.

In the future, the development of EC-AFM will be toward multi-functionality, high sensitivity, high speed, and high efficiency. The continuous improvement of EC-AFM will help carrying out more in-depth research on the in situ dynamic corrosion process, as well as promoting the study of corrosion science.

**Author Contributions:** Conceptualization, Z.W., M.H., and Y.L.; formal analysis, H.C., Z.Q., and Z.W.; writing—original draft, H.C.; writing—review and editing, H.C. and Z.W. All authors have read and agreed to the published version of the manuscript.

**Funding:** This research was financed by the National Key Research and Development Program of China (2018YFB0703500) and the National Natural Science Foundation of China (No. 51971155, No. 51771120, and No. 51304136).

**Conflicts of Interest:** The authors declare no conflicts of interest.

## References

1. Kamachi Mudali, U.; Padhy, N. Electrochemical scanning probe microscope (EC-SPM) for the in situ corrosion study of materials: An overview with examples. *Corros. Rev.* **2011**, *29*, 1–2. [[CrossRef](#)]
2. Pondichery, S. A Study on the Effect of Magnetic Field on the Corrosion Behavior of Materials. Ph.D. Thesis, The University of Texas, Arlington, TX, USA, 2014.
3. Manne, S. Electrochemistry on a gold surface observed with the atomic force microscope. *J. Vac. Sci. Technol. B Microelectron. Nanometer Struct.* **1991**, *9*, 2. [[CrossRef](#)]
4. Binnig, G.; Quate, C.F.; Gerber, C. Atomic force microscope. *Phys. Rev. Lett.* **1986**, *56*, 930–933. [[CrossRef](#)] [[PubMed](#)]
5. Binnig, G.; Rohrer, H.; Gerber, C.; Weibel, E. Tunneling through a controllable vacuum gap. *Appl. Phys. Lett.* **1982**, *40*, 178–180. [[CrossRef](#)]
6. Binnig, G.; Rohrer, H.; Gerber, C.; Weibel, E.  $7 \times 7$  reconstruction on Si (111) resolved in real space. *Phys. Rev. Lett.* **1983**, *50*, 120. [[CrossRef](#)]
7. Binnig, G.; Rohrer, H.J. Surface imaging by scanning tunneling microscopy. *Ultramicroscopy* **1983**, *11*, 157–160. [[CrossRef](#)]
8. Binnig, G.; Rohrer, H.J.S. Scanning tunneling microscopy. *Surf. Sci.* **1983**, *126*, 236–244. [[CrossRef](#)]
9. Manne, S.; Hansma, P.K.; Massie, J.; Elings, V.B.; Gewirth, A.A. Atomic-resolution electrochemistry with the atomic force microscope: Copper deposition on gold. *Science* **1991**, *251*, 183–186. [[CrossRef](#)]
10. Ohnesorge, F.; Binnig, G. True atomic resolution by atomic force microscopy through repulsive and attractive forces. *Science* **1993**, *260*, 1451–1456. [[CrossRef](#)]
11. Utsunomiya, T.; Yokota, Y.; Fukui, K.-I. Electrochemical Atomic Force Microscopy. In *Compendium of Surface and Interface Analysis*; The Surface Science Society of Japan, Ed.; Springer: Singapore, 2018.
12. Reggente, M.; Passeri, D.; Rossi, M.; Tamburri, E.; Terranova, M.L. Electrochemical Atomic Force Microscopy: In Situ Monitoring of Electrochemical Processes. In *Nanoinnovation 2016*; Rossi, M., Dini, L., Passeri, D., Antisari, M.V., Eds.; AIP Publishing: Melville, NY, USA, 2017.
13. Xu, Z.; Qi, D.M.; Jiang, L.; Chen, Y.; Zhang, Z.; Zhang, J.Q. Progress of Research on Underpotential Deposition-II. Research Techniques and Application of Underpotential Deposition. *Acta Phys. Chim. Sin.* **2015**, *31*, 1231–1250.
14. Nault, L.; Taoufenua, C.; Anne, A.; Chovin, A.; Demaille, C.; Besong-Ndika, J.; Cardinale, D.; Carette, N.; Michon, T.; Walter, J. Electrochemical Atomic Force Microscopy Imaging of Redox-Immunomarked Proteins on Native Potyvirus: From Subparticle to Single-Protein Resolution. *ACS Nano* **2015**, *9*, 4911–4924. [[CrossRef](#)] [[PubMed](#)]
15. Deng, J.; Nellist, M.R.; Stevens, M.B.; Dette, C.; Wang, Y.; Boettcher, S.W. Morphology Dynamics of Single-Layered Ni(OH)<sub>2</sub>/NiOOH Nanosheets and Subsequent Fe Incorporation Studied by &ITin Situ&IT Electrochemical Atomic Force Microscopy. *Nano Lett.* **2017**, *17*, 6922–6926. [[PubMed](#)]
16. Wang, S.W.; Zhang, W.C.; Chen, Y.N.; Dai, Z.W.; Zhao, C.C.; Wang, D.Y.; Shen, C. Operando study of Fe<sub>3</sub>O<sub>4</sub> anodes by electrochemical atomic force microscopy. *Appl. Surf. Sci.* **2017**, *426*, 217–223. [[CrossRef](#)]
17. Valtiner, M.; Ankah, G.N.; Bashir, A.; Renner, F.U. Atomic force microscope imaging and force measurements at electrified and actively corroding interfaces: Challenges and novel cell design. *Rev. Sci. Instrum.* **2011**, *82*, 023703. [[CrossRef](#)]

18. Martin-Olmos, C.; Rasool, H.M.; Weiller, B.H.; Gimzewski, J.K. Graphene MEMS: AFM Probe Performance Improvement. *ACS Nano* **2013**, *7*, 4164–4170. [[CrossRef](#)]
19. Zhang, D.X.; Zhang, H.J.; Lin, X.F. In-situ study of corrosion with an atomic force microscope scanning in liquids. In *Nanophotonics, Nanostructure, and Nanometrology*; Zhu, X., Chow, S.Y., Arakawa, Y., Eds.; SPIE: Bellingham, DC, USA, 2005.
20. Zhong, J. From simple to complex: Investigating the effects of lipid composition and phase on the membrane interactions of biomolecules using in situ atomic force microscopy. *Integr. Biol.* **2011**, *3*, 632–644. [[CrossRef](#)]
21. Butt, H.J.; Cappella, B.; Kappell, M.J. Force measurements with the atomic force microscope: Technique, interpretation and applications. *Surf. Sci. Rep.* **2005**, *59*, 1–152. [[CrossRef](#)]
22. Marti, O.; Drake, B.; Hansma, P.K. Atomic force microscopy of liquid-covered surfaces: Atomic resolution images. *Appl. Phys. Lett.* **1987**, *51*, 484–486. [[CrossRef](#)]
23. Martin, Y.; Williams, C.C.; Wickramasinghe, H.K. Atomic force microscope–force mapping and profiling on a sub 100-Å scale. *J. Appl. Phys.* **1987**, *61*, 4723–4729. [[CrossRef](#)]
24. Miyata, K.; Tracey, J.; Miyazawa, K.; Haapasilta, V.; Spijker, P.; Kawagoe, Y.; Foster, A.S.; Tsukamoto, K.; Fukuma, T.J. Dissolution processes at step edges of calcite in water investigated by high-speed frequency modulation atomic force microscopy and simulation. *Nano Lett.* **2017**, *17*, 4083–4089. [[CrossRef](#)]
25. Alessandrini, A.; Facci, P. AFM: A versatile tool in biophysics. *Meas. Sci. Technol.* **2005**, *16*, R65–R92. [[CrossRef](#)]
26. Huang, L.; Su, C. A torsional resonance mode AFM for in-plane tip surface interactions. *Ultramicroscopy* **2004**, *100*, 277–285. [[CrossRef](#)] [[PubMed](#)]
27. Bhushan, B.; Kasai, T. A surface topography-independent friction measurement technique using torsional resonance mode in an AFM. *Nanotechnology* **2004**, *15*, 923–935. [[CrossRef](#)]
28. Kasai, T.; Bhushan, B.; Huang, L.; Su, C. Topography and phase imaging using the torsional resonance mode. *Nanotechnology* **2004**, *15*, 731–742. [[CrossRef](#)]
29. Hu, S.; Mininni, L.; Hu, Y.; Erina, N.; Kindt, J.; Su, C. *High-Speed Atomic Force Microscopy and Peak Force Tapping Control*; SPIE: Bellingham, DC, USA, 2012.
30. Alsteens, D.; Dupres, V.; Yunus, S.; Latge, J.P.; Heinisch, J.J.; Dufrene, Y.F. High-resolution imaging of chemical and biological sites on living cells using peak force tapping atomic force microscopy. *Langmuir* **2012**, *28*, 16738–16744. [[CrossRef](#)] [[PubMed](#)]
31. Liu, G.; Liu, J.; Sun, H.; Zheng, X.; Liu, Y.; Li, X.; Qi, H.; Bai, X.; Jackson, K.A.; Tao, X. In situ imaging of on-surface, solvent-free molecular single-crystal growth. *J. Am. Chem. Soc.* **2015**, *137*, 4972–4975. [[CrossRef](#)] [[PubMed](#)]
32. Luo, D.; Yang, F.; Wang, X.; Sun, H.; Gao, D.; Li, R.; Yang, J.; Li, Y. Anisotropic etching of graphite flakes with water vapor to produce armchair-edged graphene. *Small* **2014**, *10*, 2809–2814. [[CrossRef](#)]
33. Li, Y.; Cheng, Y.F. Passive film growth on carbon steel and its nanoscale features at various passivating potentials. *Appl. Surf. Sci.* **2017**, *396*, 144–153. [[CrossRef](#)]
34. Padhy, N.; Paul, R.; Kamachi Mudali, U.; Raj, B. Morphological and compositional analysis of passive film on austenitic stainless steel in nitric acid medium. *Appl. Surf. Sci.* **2011**, *257*, 5088–5097. [[CrossRef](#)]
35. Kreta, A.; Rodošek, M.; Slemenik Perše, L.; Orel, B.; Gaberšček, M.; Šurca Vuk, A. In situ electrochemical AFM, ex situ IR reflection–absorption and confocal Raman studies of corrosion processes of AA 2024-T3. *Corros. Sci.* **2016**, *104*, 290–309. [[CrossRef](#)]
36. Liu, Y.; Gilbert, J.L. Effect of simulated inflammatory conditions and potential on dissolution and surface oxide of CoCrMo alloy: In situ electrochemical atomic force microscopy study. *Electrochim. Acta* **2018**, *262*, 252–263. [[CrossRef](#)]
37. Bearer, J.P.; Orme, C.A.; Gilbert, J.L. In situ imaging and impedance measurements of titanium surfaces using AFM and SPIS. *Biomaterials* **2003**, *24*, 1837–1852. [[CrossRef](#)]
38. Bearer, J.P.; Orme, C.A.; Gilbert, J.L. Direct observation of hydration of TiO<sub>2</sub> on Ti using electrochemical AFM: Freely corroding versus potentiostatically held conditions. *Surf. Sci.* **2001**, *491*, 370–387. [[CrossRef](#)]
39. Wang, Z.M.; Zhang, J.; Chang, X.C.; Hou, W.L.; Wang, J.Q. Structure inhibited pit initiation in a Ni–Nb metallic glass. *Corros. Sci.* **2010**, *52*, 1342–1350. [[CrossRef](#)]
40. Zhang, S.D.; Liu, Z.W.; Wang, Z.M.; Wang, J.Q. In situ EC-AFM study of the effect of nanocrystals on the passivation and pit initiation in an Al-based metallic glass. *Corros. Sci.* **2014**, *83*, 111–123. [[CrossRef](#)]



41. Li, Y.; Cheng, Y.F. In-situ characterization of the early stage of pipeline steel corrosion in bicarbonate solutions by electrochemical atomic force microscopy. *Surf. Interface Anal.* **2017**, *49*, 133–139. [[CrossRef](#)]
42. Izquierdo, J.; Fernández-Pérez, B.M.; Eifert, A.; Souto, R.M.; Kranz, C. Simultaneous Atomic Force—Scanning Electrochemical Microscopy (Afm-SECM) Imaging of Copper Dissolution. *Electrochim. Acta* **2016**, *201*, 320–332. [[CrossRef](#)]
43. Izquierdo, J.; Eifert, A.; Kranz, C.; Souto, R.M. In situ investigation of copper corrosion in acidic chloride solution using atomic force—Scanning electrochemical microscopy. *Electrochim. Acta* **2017**, *247*, 588–599. [[CrossRef](#)]
44. Ding, Y.; Zhao, R.; Qin, Z.; Wu, Z.; Wang, L.; Liu, L.; Lu, W. Evolution of the Corrosion Product Film on Nickel-Aluminum Bronze and Its Corrosion Behavior in 3.5 wt % NaCl Solution. *Materials* **2019**, *12*, 209. [[CrossRef](#)]
45. Conradi, M.; Schön, P.M.; Kocijan, A.; Jenko, M.; Vancso, G.J. Surface analysis of localized corrosion of austenitic 316L and duplex 2205 stainless steels in simulated body solutions. *Mater. Chem. Phys.* **2011**, *130*, 708–713. [[CrossRef](#)]
46. Martin, F.A.; Bataillon, C.; Cousty, J. In situ AFM detection of pit onset location on a 304L stainless steel. *Corros. Sci.* **2008**, *50*, 84–92. [[CrossRef](#)]
47. Wijesinghe, T.L.S.L.; Blackwood, D.J. Real time pit initiation studies on stainless steels: The effect of sulphide inclusions. *Corros. Sci.* **2007**, *49*, 1755–1764. [[CrossRef](#)]
48. Zhang, Q.; Wang, R.; Kato, M.; Nakasa, K. Observation by atomic force microscope of corrosion product during pitting corrosion on SUS304 stainless steel. *Scr. Mater.* **2005**, *52*, 227–230. [[CrossRef](#)]
49. Qu, J.E.; Guo, X.P.; Wang, H.R.; Huang, J.Y. Corrosion behavior of pure aluminum in FeCl<sub>3</sub> solution. *Trans. Nonferrous Met. Soc. China* **2006**, *16*, 1460–1466. [[CrossRef](#)]
50. Davoodi, A.; Pan, J.; Leygraf, C.; Norgren, S. In situ investigation of localized corrosion of aluminum alloys in chloride solution using integrated EC-AFM/SECM techniques. *Electrochem. Solid-State Lett.* **2005**, *8*, B21–B24. [[CrossRef](#)]
51. Amin, M.A.; Abd El-Rehim, S.S.; Aarão Reis, F.D.A.; Cole, I.S. Metastable and stable pitting events at zinc passive layer in alkaline solutions. *Ionics* **2013**, *20*, 127–136. [[CrossRef](#)]
52. Kim, Y.H.; Rae, C.Y.; Kim, K.H.; Chung, W.S. Study of initial stage corrosion of hot-dip-coated zinc surface using in situ AFM. *J. Electrochem. Soc.* **2004**, *151*, B319–B324. [[CrossRef](#)]
53. Jia, R.; Yu, S.; Li, D.; Zhang, T.; Wang, F.; Zhong, C. Study on the effect of mischmetal (La,Ce) on the micro-galvanic corrosion of AZ91 alloy using multiscale methods. *J. Alloys Compd.* **2019**, *778*, 427–438. [[CrossRef](#)]
54. Zhang, F.; Nilsson, J.-O.; Pan, J. In Situ and Operando AFM and EIS Studies of Anodization of Al 6060: Influence of Intermetallic Particles. *J. Electrochem. Soc.* **2016**, *163*, C609–C618. [[CrossRef](#)]
55. Bettini, E.; Kivisäkk, U.; Leygraf, C.; Pan, J. Study of corrosion behavior of a 22% Cr duplex stainless steel: Influence of nano-sized chromium nitrides and exposure temperature. *Electrochim. Acta* **2013**, *113*, 280–289. [[CrossRef](#)]
56. Yasakau, K.A.; Kallip, S.; Lisenkov, A.; Ferreira, M.G.S.; Zheludkevich, M.L. Initial stages of localized corrosion at cut-edges of adhesively bonded Zn and Zn-Al-Mg galvanized steel. *Electrochim. Acta* **2016**, *211*, 126–141. [[CrossRef](#)]
57. Depentori, F.; Forcellini, C.; Andreatta, F.; Marin, E.; Maschio, S.; Brunke, F.; Benfer, S.; Siemers, C.; Fedrizzi, L.; Fürbeth, W. Oxidation of neodymium precipitates in a Ti<sub>6</sub>Al<sub>4</sub>V<sub>2</sub>Nd alloy in sodium chloride solution. *Mater. Corros.* **2016**, *67*, 277–285. [[CrossRef](#)]
58. Davoodi, A.; Pan, J.; Leygraf, C.; Norgren, S. Integrated AFM and SECM for in situ studies of localized corrosion of Al alloys. *Electrochim. Acta* **2007**, *52*, 7697–7705. [[CrossRef](#)]
59. Moore, S.; Burrows, R.; Picco, L.; Martin, T.L.; Greenwell, S.J.; Scott, T.B.; Payton, O.D. A study of dynamic nanoscale corrosion initiation events using HS-AFM. *Faraday Discuss.* **2018**, *210*, 409–428. [[CrossRef](#)] [[PubMed](#)]
60. Padhy, N.; Ningshen, S.; Kamachi Mudali, U.; Raj, B. In situ surface investigation of austenitic stainless steel in nitric acid medium using electrochemical atomic force microscopy. *Scr. Mater.* **2010**, *62*, 45–48. [[CrossRef](#)]
61. Williford, R.E.; Windisch, C.F., Jr.; Jones, R.H. In situ observations of the early stages of localized corrosion in Type 304 SS using the electrochemical atomic force microscope. *Mater. Sci. Eng. A* **2000**, *288*, 54–60. [[CrossRef](#)]

62. Fu, N.; Tang, X.; Li, D.Y.; Parent, L.; Tian, H. In situ investigation of local corrosion at interphase boundary under an electrochemical-atomic force microscope. *J. Solid State Electrochem.* **2014**, *19*, 337–344. [[CrossRef](#)]
63. Shi, Y.; Collins, L.; Balke, N.; Liaw, P.K.; Yang, B. In-situ electrochemical-AFM study of localized corrosion of Al CoCrFeNi high-entropy alloys in chloride solution. *Appl. Surf. Sci.* **2018**, *439*, 533–544. [[CrossRef](#)]
64. Bettini, E.; Eriksson, T.; Boström, M.; Leygraf, C.; Pan, J. Influence of metal carbides on dissolution behavior of biomedical CoCrMo alloy: SEM, TEM and AFM studies. *Electrochim. Acta* **2011**, *56*, 9413–9419. [[CrossRef](#)]
65. Davoodi, A.; Pan, J.; Leygraf, C.; Norgren, S. Probing of local dissolution of Al-alloys in chloride solutions by AFM and SEM. *Appl. Surf. Sci.* **2006**, *252*, 5499–5503. [[CrossRef](#)]
66. Li, J.; Ecco, L.; Ahniyaz, A.; Pan, J. Probing electrochemical mechanism of polyaniline and CeO<sub>2</sub> nanoparticles in alkyd coating with in-situ electrochemical-AFM and IRAS. *Prog. Org. Coat.* **2019**, *132*, 399–408. [[CrossRef](#)]
67. Li, J.; Huang, H.; Fielden, M.; Pan, J.; Ecco, L.; Schellbach, C.; Delmas, G.; Claesson, P.M. Towards the mechanism of electrochemical activity and self-healing of 1 wt% PTSA doped polyaniline in alkyd composite polymer coating: Combined AFM-based studies. *RSC Adv.* **2016**, *6*, 19111–19127. [[CrossRef](#)]
68. Li, J.; Ecco, L.; Ahniyaz, A.; Fedel, M.; Pan, J. In Situ AFM and Electrochemical Study of a Waterborne Acrylic Composite Coating with CeO<sub>2</sub>Nanoparticles for Corrosion Protection of Carbon Steel. *J. Electrochem. Soc.* **2015**, *162*, C610–C618. [[CrossRef](#)]
69. Liu, L.; Li, Y.; Wang, F. Pitting mechanism on an austenite stainless steel nanocrystalline coating investigated by electrochemical noise and in-situ AFM analysis. *Electrochim. Acta* **2008**, *54*, 768–780. [[CrossRef](#)]
70. Liu, L.; Li, Y.; Wang, F. Influence of nanocrystallization on pitting corrosion behavior of an austenitic stainless steel by stochastic approach and in situ AFM analysis. *Electrochim. Acta* **2010**, *55*, 2430–2436. [[CrossRef](#)]
71. Pan, C.; Liu, L.; Li, Y.; Wang, F. Pitting corrosion of 304ss nanocrystalline thin film. *Corros. Sci.* **2013**, *73*, 32–43. [[CrossRef](#)]
72. Pan, C.; Liu, L.; Li, Y.; Zhang, B.; Wang, F. The Electrochemical Corrosion Behavior of Nanocrystalline 304 Stainless Steel Prepared by Magnetron Sputtering. *J. Electrochem. Soc.* **2012**, *159*, C453–C460. [[CrossRef](#)]
73. Pan, C.; Liu, L.; Li, Y.; Wang, S.; Wang, F. Passive film growth mechanism of nanocrystalline 304 stainless steel prepared by magnetron sputtering and deep rolling techniques. *Electrochim. Acta* **2011**, *56*, 7740–7748. [[CrossRef](#)]
74. Rocca, E.; Bertrand, G.; Rapin, C.; Labrune, J.C. Inhibition of copper aqueous corrosion by non-toxic linear sodium heptanoate: Mechanism and ECAFM study. *J. Electroanal. Chem.* **2001**, *503*, 133–140. [[CrossRef](#)]
75. Bertrand, G.; Rocca, E.; Savall, C.; Rapin, C.; Labrune, J.C.; Steinmetz, P.J. In-situ electrochemical atomic force microscopy studies of aqueous corrosion and inhibition of copper. *J. Electroanal. Chem.* **2000**, *489*, 38–45. [[CrossRef](#)]
76. Umoren, S.A.; Pan, C.; Li, Y.; Wang, F.H. Elucidation of mechanism of corrosion inhibition by polyacrylic acid and synergistic action with iodide ions by in-situ AFM. *J. Adhes. Sci. Technol.* **2013**, *28*, 31–37. [[CrossRef](#)]
77. Zhang, X. Corrosion behavior of AISI321 stainless steel in an ethylene glycol-water solution. *Int. J. Electrochem. Sci.* **2019**, *14*, 2683–2692. [[CrossRef](#)]
78. Ji, G.; Prakash, R. Composites of Donor- $\pi$ -Acceptor type configured organic compound and porous ZnO nano sheets as corrosion inhibitors of copper in chloride environment. *J. Mol. Liq.* **2019**, *280*, 160–172.
79. Shaban, A.; Kálmán, E.; Telegdi, J.; Pálincás, G.; Dóra, G.J. Corrosion and inhibition of copper in different electrolyte solutions. *Appl. Phys. A* **1998**, *66*, S545–S549. [[CrossRef](#)]
80. Cruickshank, B.J.; Gewirth, A.A.; Rynders, R.M.; Alkire, R.C. In situ observations of shape evolution during copper dissolution using atomic force microscopy. *J. Electrochem. Soc.* **1992**, *139*, 2829–2832. [[CrossRef](#)]
81. Li, J.; Lampner, D.J.C.; Physicochemical, S.A.; Aspects, E. In-situ AFM study of pitting corrosion of Cu thin films. *Colloids Surf. A* **1999**, *154*, 227–237. [[CrossRef](#)]



© 2020 by the authors. Licensee MDPI, Basel, Switzerland. This article is an open access article distributed under the terms and conditions of the Creative Commons Attribution (CC BY) license (<http://creativecommons.org/licenses/by/4.0/>).



Article

# Effect of Pre-Corrosion Pits on Residual Fatigue Life for 42CrMo Steel

Dezheng Liu <sup>1,\*</sup>, Yan Li <sup>1</sup>, Xiangdong Xie <sup>2,\*</sup> and Jing Zhao <sup>1</sup>

<sup>1</sup> Hubei Key Laboratory of Power System Design and Test for Electrical Vehicle, Hubei University of Arts and Science; Xiangyang 441053, China

<sup>2</sup> School of Urban Construction, Yangtze University, Jingzhou 201800, China

\* Correspondence: liudezheng@hbuas.edu.cn (D.L.); xdxie@yangtzeu.edu.cn (X.X.)

Received: 13 June 2019; Accepted: 1 July 2019; Published: 2 July 2019

**Abstract:** The effect of pre-corrosion pits on residual fatigue life for the 42CrMo steel (American grade: AISI 4140) is investigated using the accelerated pre-corrosion specimen in the saline environment. Different pre-corroded times are used for the specimens, and fatigue tests with different loads are then carried out on specimens. The pre-corrosion fatigue life is studied, and the fatigue fracture surfaces are examined by a surface profiler and a scanning electron microscope (SEM) to identify the crack nucleation sites and to determine the size and geometry of corrosion pits. Moreover, the stress intensity factor varying with corrosion pits in different size parameters is analyzed based on finite element (FE) software ABAQUS to derive the regression formula of the stress intensity factor. Subsequently, by integrating the regression formula with the Paris formula, the residual fatigue life is predicted and compared with experimental results, and the relationship of the stress intensity factor, pit depth, and residual fatigue life are given under different corrosion degrees. The fatigue life predicted by the coupled formula agrees well with experiment results. It is observed from the SEM images that higher stress amplitude and longer pre-corroded time can significantly decrease the residual fatigue life of the steel. Additionally, the research work has brought about the discovery that the rate of crack extension accelerates when the crack length increases. The research in this paper also demonstrates that the corrosion pit size can be used as a damage index to assess the residual fatigue life.

**Keywords:** pre-corrosion pits; residual fatigue life; 42CrMo steel; stress intensity factor

## 1. Introduction

Most engineering materials are subject to corrosion, and corrosion research has received much attention from different perspectives [1–7]. The 42CrMo (American grade: AISI 4140) is a commonly used ultrahigh-strength steel. Due to its high strength, toughness, and hardenability, 42CrMo steel is widely used in quenched and tempered heavy forgings to build components such as pressure vessels, gears, vehicle axles, and deep oil drilling rod subs [8,9]. However, their corrosion resistance is relatively poor and this material is prone to corrosion. Corrosion pits can weaken the strength of the structure and decrease its fatigue life [10,11], since the fatigue cracks are easy to nucleate at corrosion pits and propagate rapidly under dynamic loads [12]. Thus, to further understand corrosion effects on the strength and residual fatigue life of 42CrMo material, the stress state around corrosion pits should be reasonably estimated.

In recent years, fatigue performance of pre-corroded metallic alloys has been studied extensively. For example, recent works [13–18] have reported the description of the stress concentration arising from corrosion pits based on the finite element (FE) method. Sharland [13] developed a mechanistic model of the propagation stage of an established pit or crevice to simulate the evolution of pit geometry and to describe the corrosion process. However, Wang [14] indicated that a detailed description of both the chemical reactions and the ionic transport was not included in it [13]. Through the use of interaction function to simulate the effect of the corrosion potential and corrosion current density on the corrosion

process, Xu [15] developed an FE model for the simulation of the mechano-electrochemical effect of pipeline corrosion. Because the fatigue strength of the metallic alloys decreases differently under the different corrosion depths and stress amplitudes [16], Pidaparti [17] established a new FE model to investigate the stress state around corrosion pits. However, the proposed FE model in [17] cannot be used to depict the growth process of corrosion pits with time. Through the use of the damage tolerance method to predict the corrosion fatigue life for 7075-T6 stainless steel, Huang [18] indicated that the nucleation time of pits and the material constant of crack propagation can affect the residual fatigue life of stainless steel significantly. On the basis of [16–18], Zheng [19] proposed that the decrease of fatigue life depends on the pre-corroded time and the size of pre-corrosion pits. Most recent studies on the fatigue life of steel in corrosion environments only consider the factors such as mass loss rate and corrosion pit depth, and rarely involve the stress intensity factor varying with corrosion pits in different size parameters. The stress concentration caused by corrosion pits can dramatically influence the basic macroscopic mechanical properties of a steel [20]. Despite the extensive research on the corrosion of metallic alloys [21–24], there are few detailed studies of the effect of pre-corrosion pits on residual fatigue life for 42CrMo steel.

In this study, the effect of stress distribution around corrosion pits on the stress intensity factor is firstly investigated. The crack nucleation sites and the geometry of corrosion pits are examined by a surface profiler and a scanning electron microscope (SEM), and then the relationship between the fatigue life and the maximum applied stress is obtained by fatigue tests of different pre-corroded specimens. Based on experiment results, an FE model is conducted to investigate stress distribution around corrosion pits, and regression formula of the stress intensity factor varying with corrosion pits in different size parameters is then derived. Subsequently, by coupling the regression formula with the Paris formula [25], the fatigue performance is predicted by the FE method and then compared with experimental tests. Under the different stress amplitudes and pre-corroded times, the FE predictions are finally validated by comparison with the experiment results.

## 2. Materials and Methods

### 2.1. Material and Specimen Preparation

To better understand the stress intensity factor varying with corrosion pits in different size parameters and to accurately depict the residual fatigue life of 42CrMo steel subject to corrosion, it is necessary to quantitatively investigate the effects of pre-corrosion levels on the fatigue behavior of 42CrMo steel. Experimental specimens were fabricated using the 42CrMo steel (American grade: AISI 4140), which was provided by Baowu Steel Company (Wuhan, China). Specimens were manufactured in the form of flat bare sheets with a thickness of 6 mm by wire cutting machine, the sizes of specimens are provided in Figure 1. The chemical composition was measured using an FLS980-stm Edinburgh fluorescence spectrometer (Edinburgh Instruments Ltd., Livingston, UK). A comparison of the measured chemical composition of 42CrMo specimens and the standard of GB/T3077-2015 (the national standard of the People’s Republic of China for alloy structural steel) for 42CrMo steel is presented in Table 1. It can be seen from Table 1 that the chemical composition of the specimens used in this study meets the requirement of the national standard.

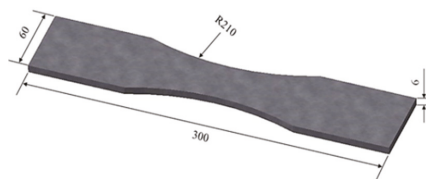
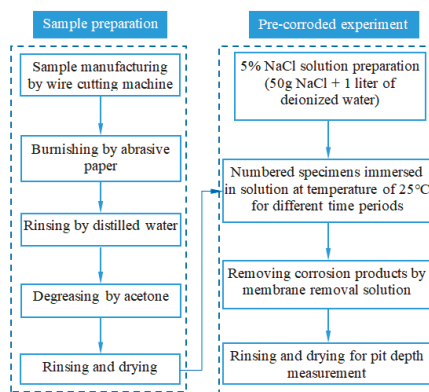


Figure 1. Schematic diagram of specimen sizes (mm).

**Table 1.** A comparison of the measured chemical composition of 42CrMo specimens and the standard of GB/T3077-2015 for 42CrMo steel (wt.%).

wt.%	C	S	P	Cr	Ni	Mn	Si	Cu	Mo
42CrMo	0.42	0.002	0.022	1.08	0.02	0.69	0.28	0.02	0.18
GB/T3077-2015	0.38–0.45	≤0.035		0.90–1.20	≤0.30	0.50–0.80	0.17–0.37	≤0.25	0.15–0.25

Twelve smooth samples were numbered and divided into four groups. The accelerated neutral salt spray corrosion experiment was established to achieve the pre-corroded steel plates based on the standard of JIS H 8502.5 [26]. A schematic drawing of the sample preparation and the pre-corroded experiment procedure is shown in Figure 2. The sample preparation was carried out in five steps: (1) samples were manufactured in the form of flat bare sheets with the dimensions in Figure 1 by wire cutting machine; (2) the surface of each sample was burnished by the 1000 grit abrasive paper to dispel burrs; (3) samples were rinsed in distilled water; (4) samples were degreased through the use of acetone solvent; (5) all surfaces of samples were rinsed with deionized water and dried by a blower for the pre-corroded experiment.

**Figure 2.** Schematic drawing of the sample preparation and the pre-corroded experiment procedure.

In this study, the pre-corroded experiment procedure can be devised as four main steps: (1) the pure NaCl crystals of 50 g were weighed by an electronic balance and poured into one liter of deionized water and stirred with glass rod at an ambient temperature of  $(25 \pm 1 \text{ }^\circ\text{C})$  for 5 min; (2) four groups of numbered samples were alternately immersed in 5% NaCl solution at an ambient temperature of  $(25 \pm 1 \text{ }^\circ\text{C})$  for 0 h, 24 h, 48 h, and 96 h, respectively; (3) the corrosion products were removed by membrane removal solution (prepared with 100 mL HCl, 100 mL deionized water and 0.6 g C6H12N4); (4) all surfaces of samples were rinsed with deionized water and dried by a blower for pit depth measurement.

## 2.2. Pre-Corrosion Pit Measurements and Fatigue Test

To achieve the morphology of the corrosion surface and to determine the size and geometry of pre-corrosion pits, a non-contact Dektak150 surface profiler (Veeco Instruments Shanghai Co., Ltd., Shanghai, China) and an S-4800 scanning electron microscope (Hitachi, Tokyo, Japan) were used in this study. A region of 30 mm  $\times$  20 mm (along the directions of longitude and transverse, respectively) for each specimen was approximately arranged at the area of pre-estimated fatigue fracture. It is noted that the rate of corrosion changes steadily with the increase of pre-corroded time [27], thus the relationship between the corrosion time and the depth of pre-corroded pits can be expressed by an exponential

function. Based on reference [28], the coefficient of exponential function can be determined by fitting the measured data, and exponential function expression can be described as:

$$\varphi = 1.235 t^{0.775} \quad (1)$$

where  $\varphi$  is the depth of a pre-corroded pit ( $\mu\text{m}$ ) and  $t$  is the pre-corroded time (h).

Based on the standard of ASTM E468-90 [29], the fatigue performance of corroded specimens (24 h, 48 h, and 96 h) were evaluated by a hydraulic universal testing machine (Instron-8803, Norwood, MA, USA) under a cyclic load amplitude with a frequency of 10 Hz. The loading operation was force controlled with a proportional error of  $\pm 1\%$ . A group of un-corroded specimens were also tested as a control for fatigue studies. The stress ratio was taken as 0.1, and the maximum applied stresses were 100 MPa, 200 MPa, and 300 MPa, respectively. After testing, the fractured specimens were processed by cutting machine and the morphology of the corrosion surface was observed by surface profiler and scanning electron microscope.

The pre-corrosion pit reduced the fatigue life substantially, particularly the interacting pits and sharp pits [30]. In this study, the Paris theory [25] was applied to analyze the relationship between the morphology of fatigue cracks and the stress state around corrosion pits. According to Paris theory [25], the stress intensity factor of cracks can be described as:

$$K_I = \sigma \sqrt{\pi a} f(\beta) \quad (2)$$

$$\beta = \frac{a}{b} \quad (3)$$

where  $K_I$  is the stress intensity factor of the crack,  $\sigma$  is the external stress under the plane stress state, and  $a$  is the crack length and  $b$  is the specimen width.

### 2.3. FE Model

The FE analysis model of the 42CrMo steel in the form of a corroded flat sheet with a thickness of 6 mm was created using the HyperWorks software (HyperWorks 11.0, Altair Corp., Troy, MI, USA). On the basis of the experiment test, a single semi-elliptical pit model was conducted, and the symmetry plane of the flat sheet and refined mesh around the pit are shown in Figure 3.

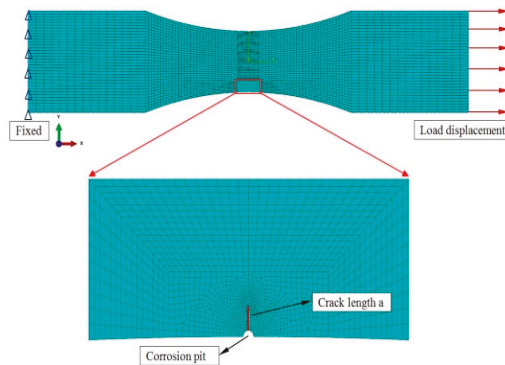


Figure 3. The FE analysis model.

The CPS8 quadrilateral element type was adopted in the FE model and cracks were prefabricated on the surface through the use of an assigned seam function that was provided by HyperWorks. The sweeping method [31] was used to generate the mesh in the integral region and the singularity of the mesh was controlled by the mesh regeneration technique [32]. The use of the above techniques [31,32] with local refinement and appropriate local mesh density can improve the precision of the calculation.

Subsequently, the FE analysis model with a preset corrosion pit was imported into the ABAQUS software (ABAQUS 6.10, Dassault Systemes Simulia Corp., Johnston, RI, USA) to analyze the stress and fatigue performance of the specimens.

### 3. Results and Discussion

#### 3.1. Corrosion Surface Characterization

When the 42CrMo specimens were immersed in NaCl solution, the Cl element in the solution adhered to the surface of specimens and reacted with the  $Fe^{2+}$  in the metal to form a soluble clathrate, which resulted in the anodic dissolution of the metal surface and the formation of corrosion pits. With the increase of pre-corroded time, more metal dissolved in the anode and the size of corrosion pit became larger and larger [33]. The specimens pre-corroded for 0 h, 24 h, 48 h, and 96 h were examined by an S-4800 scanning electron microscope and the morphologies of corrosion surface characterization are shown in Figure 4.

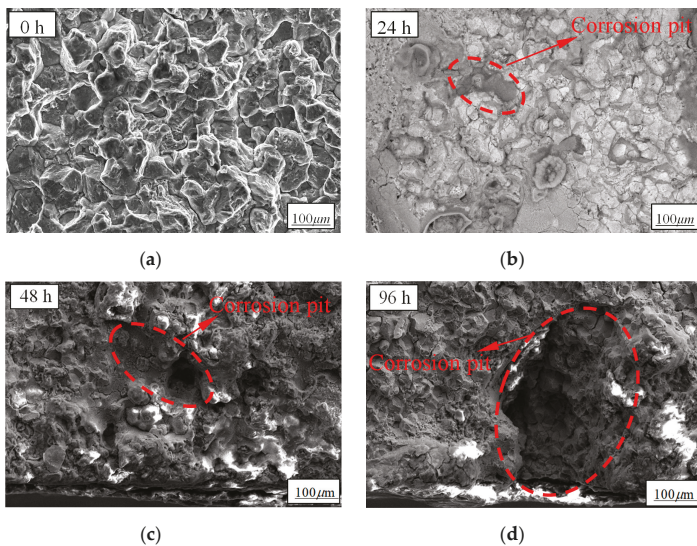


**Figure 4.** Corrosion surface characterization: (a) pre-corroded for 0 h; (b) pre-corroded for 24 h; (c) pre-corroded for 48 h; and (d) pre-corroded for 96 h.

According to Figure 4, corrosion surface characterization can be clearly observed and the obvious corrosion pits after pre-corrosion can be found within the crack source area in each diagram. As shown in Figure 4a, there was no corrosion pit on the surface of specimens without pre-corrosion. With the pre-corrosion treatment, Figure 4b shows that there were local micro-pits and pits distributed densely. With the increase of pre-corroded time, Figure 4c,d shows that corrosion pits became larger since the small pits were interconnected to form larger corrosion pits. A series of electrochemical corrosion processes occurred when the specimen was immersed in the NaCl solution. In this study, the corrosion process can be generally divided into two stages: 1) the initiation of the pits stage and 2) the pit development stage. In the first stage, adsorption and agglomeration of chloride ions took place at certain weak sites and the corrosion pits formed. In the second stage, the pits developed as a result of the anodic dissolution of the metal [34–36]. Thus, the small pits were interconnected to form larger corrosion pits.

To obtain the effect of the stress distribution around corrosion pits on the stress intensity factor and the residual fatigue life of corroded steel, the size of pre-corroded pits should be accurately assessed



and the depth of pre-corroded pits can be measured by a surface profiler. The schematic diagram of pre-corrosion pits under the pre-corroded times 24 h, 48 h, and 96 h is shown in Figure 5. From Figure 5, one can see that the depth of the maximum corrosion pit can be regarded as the radius of a semi-circular surface crack. The depth of the maximum corrosion pit was measured by a surface profiler and an SEM.

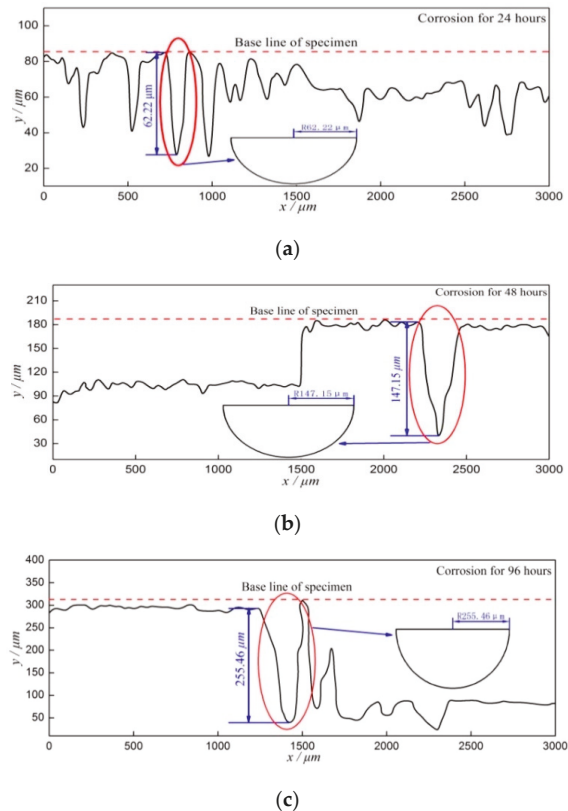


**Figure 5.** The schematic diagram of pre-corrosion pits under the different pre-corroded times: (a) pre-corroded for 24 h; (b) pre-corroded for 48 h; and (c) pre-corroded for 96 h.

### 3.2. Fatigue Test Results and Discussion

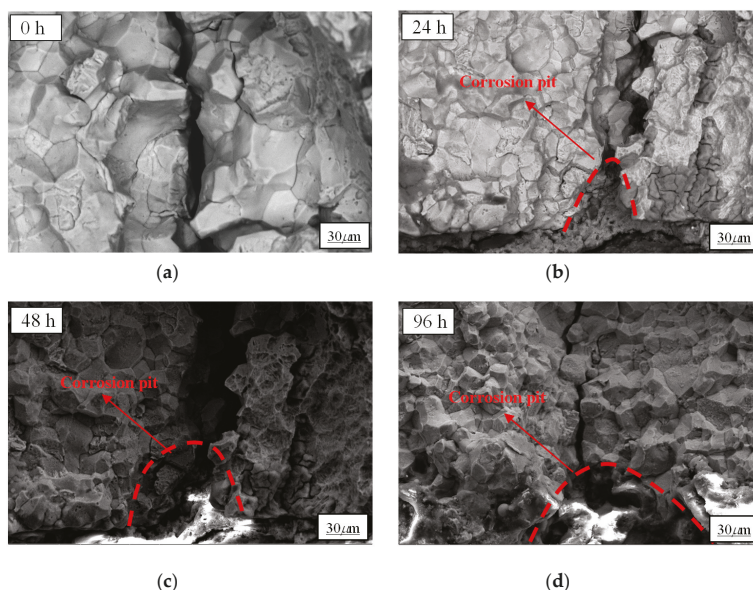
Pre-corrosion not only reduces residual fatigue life, but also leads to the change of the stress intensity factor. Under the cyclic load with a frequency of 10 Hz, the local stress concentration around the corrosion pits accelerated the process of fatigue damage and resulted in the reduced fatigue life of the specimen. Three constant stress levels (100 MPa, 200 MPa, and 300 MPa) were carried out to pre-corroded specimens for 0 h, 24 h, 48 h, and 96 h. The fatigue testing results of specimens with different exposure times are shown in Table 2.

Table 2 shows that the fatigue life decreased obviously with the increase of pre-corroded time under the same constant stress level. Furthermore, the fatigue life decreased approximately by more than 12% when the pre-corroded time was doubled, and the fatigue life decreased approximately by more than 11% when the applied stress level was doubled, indicating that both pre-corroded time and applied stress level can significantly affect the fatigue life of specimens, which shows a good agreement with the previous works [37,38]. Although the external load is normally invariant in practical engineering structures and residual fatigue life usually depends on corrosion surface condition and the nominal

stress level, the raised nominal stress caused by the reduction of the cross-sectional area of components due to corrosion still decreases the fatigue life of steel [39]. After fatigue testing, the fracture surface of the corroded specimens under 100 MPa was observed by SEM, and the results are shown in Figure 6.

**Table 2.** The fatigue testing results of specimens with different exposure times.

Pre-Corroded Time (h)	Fatigue Life ( $\times 10^5$ Cycles)		
	100 MPa	200 MPa	300 MPa
0	11.26	9.95	7.29
24	9.81	7.91	5.47
48	7.52	6.21	4.09
96	5.03	3.91	2.61



**Figure 6.** The fracture surface of the corroded specimens under 100 MPa: (a) pre-corroded for 0 h; (b) pre-corroded for 24 h; (c) pre-corroded for 48 h; and (d) pre-corroded for 96 h.

Figure 6a shows the fracture surface of the non-corroded specimen under the constant stress of 100 MPa, and it can be seen that the crack propagated along grain boundaries. Figure 6b–d reveal that the crack originated at the tip of the corrosion pit and propagated along the grain boundaries, and the white highlight area phenomena was caused by the deposition of corrosive elements. Due to the existence of corrosion defects, stress concentration occurred around the sharp intrusion at the pit bottom and accelerated the process of fatigue damage.

### 3.3. FE Investigations

Based on Equations (1)–(3), ABAQUS was applied to compute the stress intensity factor corresponding to different corrosion pit morphology characteristics, which were depicted in the previous section. The same material properties and loading conditions in Section 2.2 were applied to the FE models, and the computed stress distributions around the crack tip are shown in Figure 7.

The ashy area in Figure 7 represents the yielding zone in specimens. The numbers 1, 2, and 3 in Figure 7 denomination represent the constant stress level of 100 MPa, 200 MPa, and 300 MPa, respectively. From Figure 7, it can be seen that, under the same pre-corroded time, the yielding

zone increased with the increase of applied loads through the transverse comparison. Under the same applied loads, it can be seen that the yielding zone increased with the increase of the size of pre-corrosion pits. Moreover, the FEM investigations revealed that the rate of crack extension accelerated when the crack length increased.

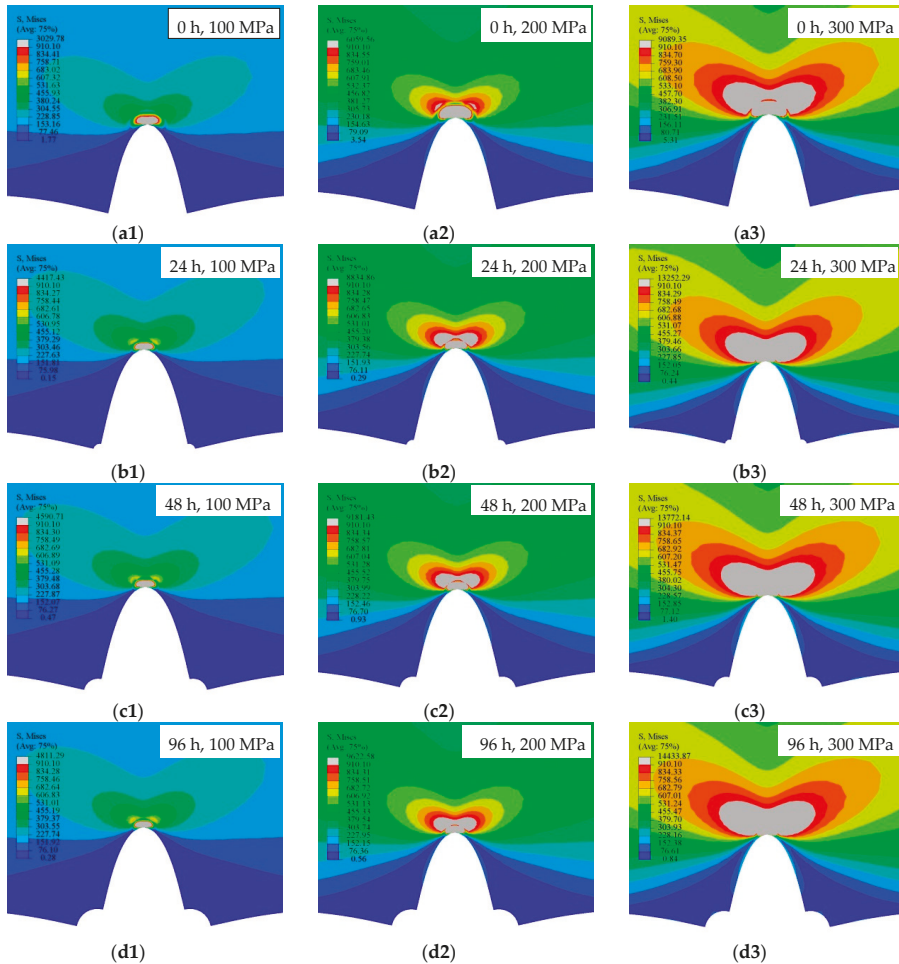


**Figure 7.** The stress distributions around the crack tip. (a1), (a2), and (a3): non-corroded specimen under the different constant stress levels; (b1), (b2), and (b3): 24 h pre-corroded specimen under the different constant stress levels; (c1), (c2), and (c3): 48 h pre-corroded specimen under the different constant stress levels; and (d1), (d2), and (d3): 96 h pre-corroded specimen under the different constant stress levels.

### 3.4. Regression Formula of the Stress Intensity Factor

By the adoption of Equations (2) and (3), the stress intensity factor around the crack tip in the process of crack propagation for non-corroded specimens can be calculated and compared with the stress intensity factor that was computed by ABAQUS software to validate the accuracy of the FE simulation results. A comparison of the stress intensity factor by theoretical Paris formula and FE simulation is shown in Figure 8.

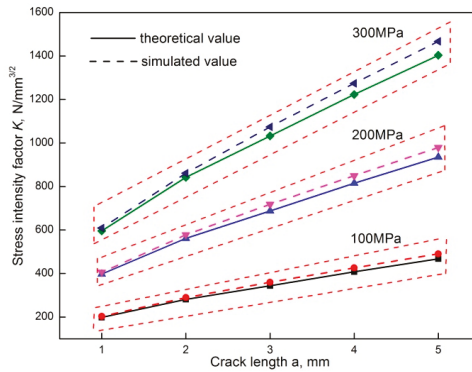


Figure 8. Comparison of the stress intensity factor by theoretical Paris formula and FE simulation.

The maximum percentage error of the calculated stress intensity factor between the theoretical Paris formula and the FEM is 4.7%, which indicates that the theoretical calculation agreed well with the simulated results. Through the integration of the ashy area around the crack tip in Figure 7, the stress intensity factor of the crack tip for pre-corroded specimens can be obtained and the relationship between the stress intensity factor at the crack tip and the depth of the pre-corrosion pits can be established.

Figure 9 shows the relationship between the stress intensity factor at the crack tip and the size of pre-corrosion pits. By using the numerical fitting method, the regression formula to represent the relationship between the stress intensity factor and the depth of the pre-corrosion pits is derived as:

$$\frac{K_{IS}}{K_{I0}} = 0.273e^{3.378\varphi} + 0.731 \tag{4}$$

where  $K_{IS}$  is the pre-corroded stress intensity factor,  $K_{I0}$  is the non-corroded stress intensity factor, and  $\varphi$  is the depth of corrosion pits. The fatigue life can be estimated according to the Paris formula [25]. The Paris formula is shown as follows:

$$\frac{da}{dN} = C\Delta K^m \tag{5}$$

where  $da/dN$  is the fatigue crack propagation,  $\Delta K$  is the stress intensity factor at the tip of cracks, and  $C$  and  $m$  are the equation coefficients, respectively. For the 42CrMo steel, the coefficients of  $C$  and  $m$  are taken as  $4.349 \times 10^{-12}$  and 3.07, respectively [40]. Through the integration of Equation (5), the fatigue life of 42CrMo steel can be estimated as:

$$N = \int \frac{da}{C(\Delta K)^{3.07}} \tag{6}$$

By combining Equations (4) and (6), the relationship between the fatigue life of pre-corroded and non-corroded specimens can be written as:

$$N_C = \left(0.273e^{3.378\varphi} + 0.731\right)^{-3.07} N_0 \tag{7}$$

where  $N_C$  is the fatigue life of pre-corroded specimens and  $N_0$  is the fatigue life of non-corroded specimens.

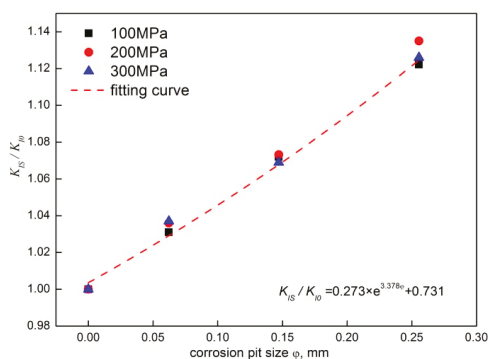


**Figure 9.** The relationship between the stress intensity factor and the depth of pre-corrosion pits.

Under different stress ranges and corrosion degrees, the residual fatigue life of pre-corrosion specimens is predicted through the use of Equation (7). The comparison of predicted fatigue life and experimental fatigue life is summarized in Table 3.

**Table 3.** Comparison of predicted fatigue life and experimental fatigue life.

Corrosion Pit Size ( $\mu\text{m}$ )	Load (Stress/MPa)	Experimental Values ( $\times 10^5$ Cycles)	Predicted Values ( $\times 10^5$ Cycles)	Errors (%)
62	100	9.82	10.13	3.15
	200	7.53	7.85	4.08
	300	5.02	5.31	5.46
147	100	8.24	8.73	5.61
	200	6.32	6.75	6.37
	300	4.21	4.53	7.06
255	100	5.62	6.61	8.17
	200	4.43	5.24	8.85
	300	2.95	3.25	9.23

Table 2 shows that the fatigue life predicted by the coupled formula agreed well with experiment results, and the percentage errors between predicted values and experimental values were less than 10%. In the case of low corrosion degrees and low stress levels, the percentage errors were less than 5%. With the increase of pre-corroded time and stress levels, the percentage error was increased to approximately 9.3%. The stress intensity factor at the tip of cracks was calculated on the basis of the linear elastic model and the morphology of the pre-corrosion pits simulated by FEM took pre-set defects in the middle of the specimen, while the practical corrosion pits had the characteristics of the uneven distribution and size of the specimen. Thus, the percentage errors between the predicted values and the experimental values were slightly increased with the increase of pre-corroded time and stress levels.

#### 4. Recommendation for Future Research

In this research, the effect of pre-corrosion pits on the residual fatigue life of the 42CrMo steel was experimentally and numerically studied. It was demonstrated in this paper that the corrosion pit size can be used as a damage index to assess the residual fatigue life. Therefore, the monitoring of corrosion pit size is important not only to know the corrosion status, but also to predict the residual fatigue life of the steel. With the recent development of structural health monitoring technology [41–44], especially the piezoceramic-based active sensing method [45–47], electromechanical impedance (EMI) approach [48–50], and imaging technology [51,52], it is now possible to monitor corrosion pit number

and size [10]. Future work should include the real-time monitoring of the onset and growth of the corrosion pit and the prediction of the residual fatigue life of the 42CrMo steel specimens. Future works should also focus on the quantitative analysis of corrosion pits to improve the predicted accuracy of the residual fatigue life for the corroded 42CrMo steel.

## 5. Conclusions

In summary, this study investigated the effect of pre-corrosion pits on the residual fatigue life of the 42CrMo steel. It was found that higher stress amplitude and longer pre-corroded time significantly decreased the residual fatigue life of the steel. The investigation of the residual fatigue life of pre-corrosion specimens was conducted through the use of the regression formula and experimental measures, and the fatigue life predicted by the regression formula agreed well with experiment results. Moreover, it was found that the rate of crack extension accelerated when the crack length increased. It is also demonstrated in this paper that the corrosion pit size can be used as a damage variable to assess the residual fatigue life. The recommendation for future research is to monitor corrosion pit characteristics and to predict the residual fatigue life of the 42CrMo steel.

**Author Contributions:** Conceptualization, D.L.; methodology, D.L. and J.Z.; software, D.L. and Y.L.; validation, Y.L.; formal analysis, X.X.; writing—original draft preparation, D.L.; writing—review and editing, X.X.; visualization, Y.L.; supervision, X.X.; project administration, D.L.

**Funding:** This research was funded by Hubei Superior and Distinctive Discipline Group of “Mechatronics and Automobiles” (No. XKQ2019009).

**Conflicts of Interest:** The authors declare no conflict of interest.

## References

1. El-Bagoury, N.; Ahmed, S.I.; Ahmed Abu Ali, O.; El-Hadad, S.; Fallatah, A.M.; Mersal, G.A.M.; Ibrahim, M.M.; Wysocka, J.; Ryl, J.; Boukherroub, R.; et al. The Influence of Microstructure on the Passive Layer Chemistry and Corrosion Resistance for Some Titanium-Based Alloys. *Materials* **2019**, *12*, 1233. [[CrossRef](#)]
2. Orlikowski, J.; Ryl, J.; Jarzynka, M.; Krakowiak, S.; Darowicki, K. Instantaneous Impedance Monitoring of Aluminum Alloy 7075 Corrosion in Borate Buffer with Admixed Chloride Ions. *Corrosion* **2015**, *71*, 828–838. [[CrossRef](#)]
3. Figueira, R. Electrochemical Sensors for Monitoring the Corrosion Conditions of Reinforced Concrete Structures: A Review. *Appl. Sci.* **2017**, *7*, 1157. [[CrossRef](#)]
4. Li, W.; Xu, C.; Ho, S.C.M.; Wang, B.; Song, G. Monitoring concrete deterioration due to reinforcement corrosion by integrating acoustic emission and FBG strain measurements. *Sensors* **2017**, *17*, 657. [[CrossRef](#)] [[PubMed](#)]
5. Ryl, J.; Arutunow, A.; Tobiszewski, M.T.; Wysocka, J. Aspects of intergranular corrosion of AISI 321 stainless steel in high-carbon-containing environments. *Anti-Corros. Method. Mater.* **2014**, *61*, 328–333. [[CrossRef](#)]
6. Huang, Y.; Gang, T.; Chen, L. Interacting effects induced by two neighboring pits considering relative position parameters and pit depth. *Materials* **2017**, *10*, 398. [[CrossRef](#)] [[PubMed](#)]
7. Zhao, W.; Zhang, T.; Wang, Y.; Qiao, J.; Wang, Z. Corrosion Failure Mechanism of Associated Gas Transmission Pipeline. *Materials* **2018**, *11*, 1935. [[CrossRef](#)] [[PubMed](#)]
8. Zhu, Z.; Lu, Y.; Xie, Q.; Li, D.; Gao, N. Mechanical properties and dynamic constitutive model of 42CrMo steel. *Mater. Des.* **2017**, *119*, 171–179. [[CrossRef](#)]
9. Sola, R.; Poli, G.; Veronesi, P.; Giovanardi, R. Effects of Surface Morphology on the Wear and Corrosion Resistance of Post-Treated Nitrided and Nitrocarburized 42CrMo4 Steel. *Metall. Mater. Trans. A* **2014**, *45*, 2827–2833. [[CrossRef](#)]
10. Du, G.; Kong, Q.; Wu, F.; Ruan, J.; Song, G. An experimental feasibility study of pipeline corrosion pit detection using a piezoceramic time reversal mirror. *Smart Mater. Struct.* **2016**, *25*, 037002. [[CrossRef](#)]
11. Ryl, J.; Wysocka, J.; Cieslik, M.; Gerengi, H.; Ossowski, T.; Krakowiak, S.; Niedzialkowski, P. Understanding the origin of high corrosion inhibition efficiency of bee products towards aluminium alloys in alkaline environments. *Electrochim. Acta* **2019**, *304*, 263–274. [[CrossRef](#)]

12. Fang, B.; Eadie, R.; Chen, W.; Elboujdaini, M. Passivation/immersion method to grow pits in pipeline steel and a study of pit nucleation and growth resulting from the method. *Brit. Corros. J.* **2013**, *44*, 32–42. [[CrossRef](#)]
13. Sharland, S.M.; Jackson, C.P.; Diver, A.J. A finite-element model of the propagation of corrosion crevices and pits. *Corros. Sci.* **1989**, *29*, 1149–1166. [[CrossRef](#)]
14. Wang, W.; Sun, H.; Sun, L.; Song, Z.; Zang, B. Numerical simulation for crevice corrosion of 304 stainless steel in sodium chloride solution. *Chem. Res. Chin. Univ.* **2010**, *26*, 822–828.
15. Xu, L.; Cheng, Y.; Xu, L. Development of a finite element model for simulation and prediction of mechano-electrochemical effect of pipeline corrosion. *Corros. Sci.* **2013**, *73*, 150–160. [[CrossRef](#)]
16. Ishihara, S.; Saka, S.; Nan, Z.Y.; Goshima, T.; Sunada, S. Prediction of corrosion fatigue lives of aluminium alloy on the basis of corrosion pit growth law. *Fatigue Fract. Eng. Mater.* **2006**, *29*, 472–480. [[CrossRef](#)]
17. Pidaparti, R.M.; Koombua, K.; Rao, A.S. Corrosion pit induced stresses prediction from SEM and finite element analysis. *Int. J. Comput. Meth. Eng. Sci. Mech.* **2009**, *10*, 117–123. [[CrossRef](#)]
18. Huang, Y.; Ye, X.; Hu, B.; Chen, L. Equivalent crack size model for pre-corrosion fatigue life prediction of aluminum alloy 7075-T6. *Int. J. Fatigue* **2016**, *88*, 217–226. [[CrossRef](#)]
19. Zheng, X.; Xie, X.; Li, X. Estimation model for steel wire crack propagation and its application in calculation of pre-corrosion fatigue life. *Chin. Civil. Eng. J.* **2017**, *50*, 101–107.
20. Apostolopoulos, C.A. The influence of corrosion and cross-section diameter on the mechanical properties of b500 c steel. *J. Mater. Eng. Perform* **2009**, *18*, 190–195. [[CrossRef](#)]
21. Li, W.; Ho, S.C.M.; Song, G. Corrosion detection of steel reinforced concrete using combined carbon fiber and fiber Bragg grating active thermal probe. *Smart Mater. Struct.* **2016**, *25*, 045017. [[CrossRef](#)]
22. Huo, L.; Li, C.; Jiang, T.; Li, H. Feasibility study of steel bar corrosion monitoring using a piezoceramic transducer enabled time reversal method. *Appl. Sci.* **2018**, *8*, 2304. [[CrossRef](#)]
23. Zhang, Y.; Tan, G.; Wang, S.; Cheng, Y.; Yang, S.; Sun, X. Flexural characteristics evaluation for reinforced concrete affected by steel corrosion based on an acoustic emission technique. *Appl. Sci.* **2019**, *9*, 1640. [[CrossRef](#)]
24. Tang, M.; Li, J.; Li, Z.; Fu, L.; Zeng, B.; Lv, J. Mannich Base as Corrosion Inhibitors for N80 Steel in a CO<sub>2</sub> Saturated Solution Containing 3 wt % NaCl. *Materials* **2019**, *12*, 449. [[CrossRef](#)]
25. Paris, P.C.; Gomez, M.P.; Anderson, W.P. A rational analytic theory of fatigue. *Trends Eng.* **1961**, *13*, 9–14.
26. Japanese Industrial Standard. Methods of corrosion resistance test for metallic coatings. In *JIS H 8502*; Japanese Standards Association: Tokyo, Japan, 1999.
27. Venkatraman, M.S.; Cole, I.S.; Emmanuel, B. Model for corrosion of metals covered with thin electrolyte layers: Pseudo-steady state diffusion of oxygen. *Electrochim. Acta* **2011**, *56*, 7171–7179. [[CrossRef](#)]
28. Nagarajan, S.; Karthega, M.; Rajendran, N. Pitting corrosion studies of super austenitic stainless steels in natural sea water using dynamic electrochemical impedance spectroscopy. *J. Appl. Electrochem.* **2007**, *37*, 195–201. [[CrossRef](#)]
29. ASTM E468–90. *Standard Practice for Presentation of Constant Amplitude Fatigue Tests Results for Metallic Materials*; American Society for Testing and Materials: West Conshohocken, PA, USA, 2004.
30. Xu, S.; Wang, Y. Estimating the effects of corrosion pits on the fatigue life of steel plate based on the 3D profile. *Int. J. Fatigue* **2015**, *72*, 27–41. [[CrossRef](#)]
31. Qian, J.; Zhang, Y.; Zhao, H. A fast sweeping method for static convex hamilton–jacobi equations. *J. Sci. Comput.* **2007**, *31*, 237–271. [[CrossRef](#)]
32. Min, C.K.; Kim, K.Y.; Lee, K.J. Electrical impedance imaging of phase boundary in two-phase systems with adaptive mesh regeneration technique. *Int. Commun. Heat. Mass.* **2005**, *32*, 954–963.
33. Wang, J.; Wang, J.; Shao, H. The corrosion and electrochemical behavior of pure aluminum in additive-containing alkaline methanol–water mixed solutions. *Mater. Corros.* **2015**, *60*, 269–273. [[CrossRef](#)]
34. Li, X.; Fan, C.; Wu, Q.; Dong, L.; Yin, Y.; Wang, C. Effect of solution pH, Cl<sup>−</sup> concentration and temperature on electrochemical behavior of ph13-8mo steel in acidic environments. *J. Iron. Steel. Res. Int.* **2017**, *24*, 1238–1247. [[CrossRef](#)]
35. Wen, Z.; Lan, W.; Zhao, S.; Cao, X.; Deng, H. Corrosion Behavior of 42CrMo Steel in Chloride Solution. *Surf. Technol.* **2017**, *42*, 216–220.
36. Duddu, R. Numerical modeling of corrosion pit propagation using the combined extended finite element and level set method. *Comput. Mech.* **2014**, *54*, 613–627. [[CrossRef](#)]

37. Lin, H.; Zhao, Y.; Ozbolt, J. The bond behavior between concrete and corroded steel bar under repeated loading. *Eng. Struct.* **2017**, *140*, 390–405. [[CrossRef](#)]
38. Perez, M.R.; Dominguez, A.G.; Palin, T.; Bathias, C. Very high cycle fatigue analysis of high strength steel with corrosion pitting. *Key Eng. Mat.* **2010**, *449*, 104–113. [[CrossRef](#)]
39. Gamboa, E.; Atrens, A. Material influence on the stress corrosion cracking of rock bolts. *Eng. Fail. Anal.* **2005**, *12*, 201–235. [[CrossRef](#)]
40. Jang, C. Approximation method for the calculation of stress intensity factors for the semi-elliptical surface flaws on thin-walled cylinder. *J. Mech. Sci. Technol.* **2006**, *20*, 319–328. [[CrossRef](#)]
41. Soh, C.K.; Annamdas, V.G.M.; Bhalla, S. Applications of structural health monitoring technology in Asia. *Struct. Health Monit.* **2015**, *16*, 324–346.
42. Song, G.; Li, W.; Wang, B.; Ho, S.C.M. A review of rock bolt monitoring using smart sensors. *Sensors* **2017**, *17*, 776. [[CrossRef](#)]
43. Annamdas, V.G.; Radhika, M.A. Electromechanical impedance of piezoelectric transducers for monitoring metallic and non-metallic structures: a review of wired, wireless and energy-harvesting methods. *J. Intel. Mater. Syst. Str.* **2013**, *24*, 1021–1042. [[CrossRef](#)]
44. Song, G.; Wang, C.; Wang, B. Structural health monitoring (SHM) of civil structures. *Appl. Sci.* **2017**, *7*, 789. [[CrossRef](#)]
45. Kong, Q.; Robert, R.H.; Silva, P.; Mo, Y.L. Cyclic crack monitoring of a reinforced concrete column under simulated pseudo-dynamic loading using piezoceramic-based smart aggregates. *Appl. Sci.* **2016**, *6*, 341. [[CrossRef](#)]
46. Jiang, T.; Zhang, Y.; Wang, L.; Zhang, L.; Song, G. Monitoring fatigue damage of modular bridge expansion joints using piezoceramic transducers. *Sensors* **2018**, *18*, 3973. [[CrossRef](#)] [[PubMed](#)]
47. Wang, F.; Huo, L.; Song, G. A piezoelectric active sensing method for quantitative monitoring of bolt loosening using energy dissipation caused by tangential damping based on the fractal contact theory. *Smart Mater. Struct.* **2017**, *27*, 015023. [[CrossRef](#)]
48. Zhang, J.; Zhang, C.; Xiao, J.; Jiang, J. A PZT-based electromechanical impedance method for monitoring the soil freeze–thaw process. *Sensors* **2019**, *19*, 1107. [[CrossRef](#)] [[PubMed](#)]
49. Wang, F.; Ho, S.C.M.; Huo, L.; Song, G. A novel fractal contact-electromechanical impedance model for quantitative monitoring of bolted joint looseness. *IEEE Access* **2018**, *6*, 40212–40220. [[CrossRef](#)]
50. Annamdas, V.G.M.; Yang, Y. Practical implementation of piezo-impedance sensors in monitoring of excavation support structures. *Struct. Control. Health Monit.* **2012**, *19*, 231–245. [[CrossRef](#)]
51. Lu, G.; Li, Y.; Song, G. A delay-and-Boolean-ADD imaging algorithm for damage detection with a small number of piezoceramic transducers. *Smart Mater. Struct.* **2016**, *25*, 095030. [[CrossRef](#)]
52. Lu, G.; Li, Y.; Zhou, M.; Feng, Q.; Song, G. Detecting damage size and shape in a plate structure using PZT transducer array. *J. Aerosp. Eng.* **2018**, *31*, 04018075. [[CrossRef](#)]



© 2019 by the authors. Licensee MDPI, Basel, Switzerland. This article is an open access article distributed under the terms and conditions of the Creative Commons Attribution (CC BY) license (<http://creativecommons.org/licenses/by/4.0/>).





Article

# Effect of Hot Deformation Process Parameters on Microstructure and Corrosion Behavior of 35CrMoV Steel

Qiumei Yang <sup>1</sup>, Yajun Zhou <sup>1,2,\*</sup>, Zheng Li <sup>1</sup> and Daheng Mao <sup>1</sup>

<sup>1</sup> School of Mechanical and Electrical Engineering, Central South University, Changsha 410083, China; YangQMei141@126.com (Q.Y.); lizheng2016@csu.edu.cn (Z.L.); mdh@csu.edu.cn (D.M.)

<sup>2</sup> National Key Laboratory of High-Performance Complex Manufacturing, Central South University, Changsha 410083, China

\* Correspondence: zhouyjun@csu.edu.cn; Tel.: +86-731-8887-7244

Received: 16 March 2019; Accepted: 1 May 2019; Published: 6 May 2019

**Abstract:** Hot deformation experiments of as-cast 35CrMoV steel, with strain rates of  $0.01\text{ s}^{-1}$  and  $10\text{ s}^{-1}$ , deformation temperatures of 850, 950, and 1050 °C, and an extreme deformation reaching 50%, were carried out using a Gleeble-3810 thermal simulator. Electrochemical corrosion experiments were conducted on the deformed specimens. The microstructure was observed by optical microscope (OM), and the corrosion morphology and corrosion products of the specimens were investigated by scanning electron microscopy (SEM), energy disperse spectroscopy (EDS), confocal laser scanning microscopy (CLSM), and X-ray diffraction (XRD) techniques. The results show that the grain size increased gradually with an increase in the deformation temperature at the same strain rate, whereas the corrosion resistance deteriorated. At the same deformation temperature, the grain size becomes smaller as the strain rate increases, which enhances the corrosion resistance. This is mainly attributed to the fine grains, which can form more grain boundaries, increase the grain boundary area, and accelerate the formation of the inner rust layer at the beginning of corrosion. Moreover, fine grains can also refine the rust particles and enhance the bonding strength between the inner rust layer and the matrix. The denseness and stability of the inner rust layer increases as the corrosion process progresses, thereby improving corrosion resistance.

**Keywords:** thermal deformation parameters; 35CrMoV steel; grain size; electrochemical corrosion

## 1. Introduction

It is well-known that 35CrMoV steel is a high-quality steel with good hardenability, creep properties, high strength, and a high fatigue limit. It is generally used to manufacture gear, marine power equipment, advanced turbine blowers and impellers, compressor engines, and other important parts which operate under high stress [1]. Under certain conditions, such as high stress and complex marine conditions (especially for complex marine conditions with strong corrosiveness),  $\text{Cl}^-$  has a strong penetrating power that can cause pitting corrosion of carbon steel and easy penetration of the surface defects. Furthermore, the invasion of  $\text{Cl}^-$  can force the surface of the passivation film to rupture, which will aggravate the stress corrosion cracking failure of the steel [2–4]. Therefore, in addition to the mechanical properties, its corrosion performance also seriously threatens the service life, safety, and efficiency of the marine components.

During thermal processing, different thermal deformation parameters have significant effects on the microstructure and properties of the material [5,6]. Numerous studies have been done into the evolution of the microstructure during thermal deformation in recent years [7–9]. Kingkam et al. [10] investigated the effects of the deformation temperature and strain rate on the dynamic recrystallization

behavior of high-strength low-alloy steel. It was observed that an increase of deformation temperature led to an increase of grain size and the effects of the microstructure on corrosion behavior were briefly discussed. Xiao et al. [11] observed that the smallest dynamic recrystallization grains were obtained at a higher strain rate and lower deformation temperature during hot deformation. Moreover, high temperatures and low strain rates are beneficial for grain growth. Lin et al. and Xu et al. established the constitutive equation and process diagram of 25Cr3Mo3Nb steel. It is reported that the change of grain size is closely related to the strain rate and, when the strain rate is  $1\text{ s}^{-1}$ , a uniform distribution and fine grains can be obtained [12]. Additionally, Huang [13] studied the dynamic recrystallization of 35CrMo steel and found that it was affected considerably by the deformation temperature and strain rate and was difficult to recrystallize at a lower temperature and higher strain rate. Lin et al. [14] studied the microstructure of a Ni-Fe-Cr-based superalloy by thermal compression experiments and the experimental results were consistent with the established dynamic recrystallization model. Quan et al. [15] obtained fine-grained, equiaxed-crystal re-crystallized structures of ASS alloys generated by the thermal deformation activation of dynamic recrystallization. These studies explored the evolution of the microstructure during the thermal deformation process, but rarely involved changes in microstructure that affected the corrosion resistance.

Some studies have exhibited that grain refinement can significantly improve the corrosion resistance of the material [16]. For instance, Argade and Alvarez-Lopez [17,18] showed that grain boundaries can serve as corrosion barriers and considered the role they play in delayed corrosion. Balyanov et al. believed that the rapid passivation of ultrafine Ti makes ultrafine crystals, which have a stronger corrosion resistance than coarse-grained industrial pure Ti [19]. Aung [20] discovered that small grains can reduce the corrosion rate of the AZ31B magnesium alloy. Zhao discussed the effect of the microstructure on the corrosion performance of the AZ91 alloy, and pointed out that the presence of a second phase and surface film can act as a corrosion barrier to prevent corrosion of the matrix [21–23]. Schino explored the inter-granular corrosion rate of AISI 304 austenitic stainless-steel and found that it decreases with a decrease of grain size in an  $\text{H}_2\text{SO}_4\text{-FeSO}_4$  solution. This is due to the increase of grain boundary per unit-volume and the decrease of Cr consumption caused by carbide precipitation, as the inter-granular corrosion rate goes down with the increase of the grain boundary area [24]. The results of Pradhan et al. showed that a fine-grained microstructure has similar or better corrosion resistance to a coarse-grained structure under the optimum distribution of grain boundary characteristics [25]. In addition, it was suggested that the grain boundary is favorable for passivation, high-density dislocations, and grain boundaries, and that grain refinements are propitious to form passivation film as grain refinement is helpful for the rapid formation of a passivation film on the surface, which can reduce the corrosion rate [26]. It was considered that coarse crystal samples are more susceptible to sensitization and inter-granular corrosion than fine-grained samples because their anode and cathode area are lower [27]. It was reported that the degree of sensitization decreases exponentially with the increase of the grain boundary surface-area [28–30], which means that Cr is diffused from the inside to the grain boundary, thereby reducing the growth of carbide precipitates, delaying the sensitization process, and improving corrosion resistance. The above studies show that the grain size, in both magnesium alloy and stainless-steel, affects the corrosion behavior of the material and that grain refinement can improve the corrosion resistance of the material. However, research on the influence of the microstructure evolution of 35CrMoV steel on the corrosion performance in the process of thermal deformation needs further study. Therefore, by adjusting the thermal processing parameters to study the changes of the microstructure in the thermal deformation process, and then analyzing the influence of grain size on corrosion behavior, more appropriate thermal deformation process parameters are obtained, which can provide technical guidance for obtaining large-size forgings with a fine grain size and good performance.

In this study, as-cast 35CrMoV is taken as the research object and thermal compression experiments are carried out at different strain rates and temperatures. The microstructure of 35CrMoV steel after thermal deformation is characterized by optical microscope (OM) and the grain sizes of specimens

with different thermal deformation parameters are obtained by a professional micro-image analysis system. The corrosion behaviors of different grain-size specimens obtained under different thermal deformation process parameters are studied in a 3.5 wt% NaCl solution through a three-electrode system. Furthermore, the corrosion performance of the samples is evaluated by electrochemical impedance spectroscopy (EIS) and TAFEL curves, and the corrosion morphology are observed by the energy disperse spectroscopy (EDS), confocal laser scanning microscopy (CLSM), and Hyperfield 3D microscopic systems. Therefore, we can determine the influence of grain size on corrosion resistance and reveal the influence mechanism of the microstructure, obtained under different parameters, on corrosion resistance.

**2. Materials and Methods**

*2.1. Materials*

Our research material, 35CrMoV steel, is a typical low-alloy steel for industrial use and its chemical composition is shown in Table 1. The as-cast 35CrMoV steel specimens of dimensions  $\Phi 400 \times 800$  mm and hot compression specimens with size  $\Phi 10 \times 15$  mm were cut at 1/2R (R is the radius of the as-cast, 200 mm) by a wire cutting machine. Then, the thermal compression test was carried out by using the Gleeble-3810 thermal simulator. The graphite sheet was placed between the two ends of the specimens, as well as the contact surface of the pressure head, before the beginning of the experiment, and lubricant was applied onto the two ends of the specimens so that the specimens could be subjected to uniform deformation during heating and compression. Before the beginning of the experiment, the graphite sheet was placed between the two ends of the specimens and the contact surface of the indenter, and lubricant was applied onto the two ends of the specimens to keep the temperature uniformly distributed during heating and compression. The process of thermal compression is shown in Figure 1. First, it was heated to 1200 °C, at a heating rate of 10 °C/s<sup>-1</sup>, for 5 min and then cooled to the deformation temperature (850 °C, 950 °C, 1150 °C), at a cooling rate of 10 °C/s<sup>-1</sup>, with heat preservation for 1 min to eliminate the temperature gradient of the specimens. Then, an extreme deformation, reaching 50%, was carried out at a strain rate of 0.01–10 s<sup>-1</sup>. Finally, the specimens were quenched in water immediately after compression and the same heat treatment was carried out, the specimens were heated to 850 °C for 30 min, then oil-cooled, re-heated to 620 °C for 30 min, and finally, were water-cooled.

**Table 1.** Composition of GB 35CrMoV steel (wt%).

Chemical Composition	C	Si	Mn	Mo	S	P	Cr	V	Fe
Measured	0.36	0.23	0.29	0.26	0.009	0.035	1.19	0.14	Bal

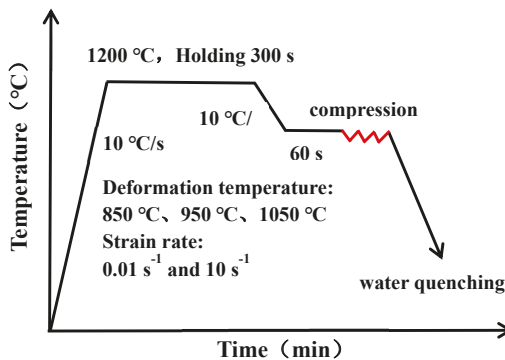


**Figure 1.** Schematic representation of hot compression test.

## 2.2. Microscopic Analysis

The microstructure of the specimens was observed by an Olympus DSX500 optical microscope, and the average grain size was calculated by an artificial cut-off method, according to the standard of GB/T6394-2002. Before the metallographic experiment, the specimens, with a diameter of  $10 \times 5 \text{ mm}^2$ , were taken along the axial direction of the compressed specimens by a wire cutter, and then they were ground, from coarse to fine sandpaper, on a grinding machine and polished with diamond spray until the surface of the specimens was bright. On this basis, the specimens were corroded in a self-made corrosion solution (2.5 g picric acid + 50 mL distilled water + 2 g dodecyl benzenesulfonic acid, sodium salt), heated, and kept at 60–80 °C for 4–8 min. After the corrosion was finished, the specimens were removed from the surface with cotton, washed with distilled water, and dried with hot air, so that the microstructure of the specimens could be observed under an optical microscope.

## 2.3. Electrochemical Measurements

Three dynamic potential polarization experiments were performed on the electrochemical workstation (Chi660e, CH Hua, Shanghai, China) using a three-electrode corrosion measurement system. Before the experiment, the specimens were ground to 1500# on the grinder and the polishing cloth was mechanically polished with diamond spray polish until the surface was smooth and free from scratches. Finally, it was washed with distilled water, ethanol, and then dried with hot air. The potentiodynamic polarization was measured by a three-electrode system in a 600 mL corrosion medium cell containing 3.5 wt% NaCl with a saturated calomel (Ag/AgCl) electrode as a reference electrode and platinum-plate as an auxiliary electrode. The surface area of the specimens exposed to the solution was  $10 \times 5 \text{ mm}^2$ . The specimens were immersed in the corrosive medium for 2400 s to obtain a stable open-circuit potential and, on this basis, electrochemical impedance spectroscopy (EIS) was carried out with a frequency range of 0.01– $10^5$  Hz and an AC excitation signal amplitude of 10 mV, which can obtain the phase angle diagram of Nyquist and Bode. Then, the appropriate equivalent circuit model was selected and the EIS results were found by equivalent-fitting with the ZSimpWin software. Ultimately, the potentiodynamic polarization curve was measured in the range of  $-1$  to 0 V vs. SCE, at a scanning rate of  $0.5 \text{ mV s}^{-1}$ , and the corrosion potential ( $E_{\text{corr}}$ ), corrosion current density ( $I_{\text{corr}}$ ), anode slope ( $B_a$ ), and cathodic slope ( $B_c$ ) were obtained by Tafel fitting.

## 2.4. Corrosion Surface Analysis

In order to better observe the corrosion morphology of the specimen surface and analyze the elements of the corrosion products, the surface of the specimens was first dried with a compressed air gun and then was observed by scanning electron microscope (SEM) (EvoMA 10C Zeiss Jena, Oberkochen, Germany). Moreover, the chemical elements of the surface corrosion products were analyzed by energy disperse spectroscopy (EDS) and the surface morphology of corrosion specimens is obtained by using Hyperfield 3D microscopic systems (Keyence VHX-5000, Osaka, Japan) and confocal laser scanning microscopy (CLSM) (Zeiss Axio LSM700, Oberkochen, Germany).

# 3. Results and Discussion

## 3.1. Microstructure

The microstructure, after hot deformation at different deformation temperatures and strain rates, is shown in Figure 2. The deformation temperatures and strain rates have a significant effect on the microstructure of the 35CrMoV steel. There is a dynamic recrystallization structure in all of the samples and the grain size distribution is not uniform, as displayed in Figure 2. A statistical analysis of the grain size in Figure 2 was carried out and the statistical results are shown in Figure 3. At the strain rate of  $0.01 \text{ s}^{-1}$ , the grain size increased gradually from 12.5 to 15.4  $\mu\text{m}$  when the deformation temperatures increased from 850 to 1050 °C (increasing by 20%), which is consistent with the law at the strain rates of 10 and  $0.01 \text{ s}^{-1}$ . The results show that, at the same strain rate, the grain growth

with the deformation temperature quickly increases, resulting in coarse grains. This can be attributed to higher deformation temperature making the dislocation motion more intense and more favorable to grain boundary migration, which enhances the diffusion and dislocation slip of vacancy atoms, increasing the nucleation of re-crystallization and the dynamic re-crystallization rate. As a result, small grains are continuously swallowed by large grains and the microstructure is coarsened. When the strain rates are increased from  $0.01$  to  $10\text{ s}^{-1}$  at the deformation temperature of  $850\text{ }^{\circ}\text{C}$ , the grain sizes decrease gradually from  $12.5$  to  $10.7\text{ }\mu\text{m}$ , decreasing by  $16\%$ . It can be noticed that, as the strain rates are increased from  $0.01$  to  $10\text{ s}^{-1}$  at the deformation temperatures of  $950$  and  $1050\text{ }^{\circ}\text{C}$ , the grain change is consistent with that at  $850\text{ }^{\circ}\text{C}$ , which indicates that an increase in strain rate is conducive to grain refinement and acquiring a fine-grained structure at the same deformation temperature. This is mainly due to larger strain rates accelerating the deformation of the samples, and so more strain storage-energy is generated, making the dynamic re-crystallization nucleation rate activate [31]. Thus, there are more phase deformation nuclei and a higher nucleation rate. Moreover, the re-crystallized grain does not have enough time to grow in this case, which reduces the dynamic recovery rate. In addition, the higher strain rate leads to enhanced accumulated strain energy and dislocation density in grains, which makes the dynamic re-crystallization easier to nucleate. It can also be seen from Figure 2 that the number of re-crystallized grains formed along the grain boundary at a strain rate of  $10\text{ s}^{-1}$  is higher than that at a strain rate of  $0.01\text{ s}^{-1}$ . Furthermore, the dynamic recrystallization rate is lower at lower-deformation temperatures, which can be attributed to the decrease of the grain boundary mobility at low deformation temperatures and high strain rates, as well as a tendency toward incomplete dynamic re-crystallization.

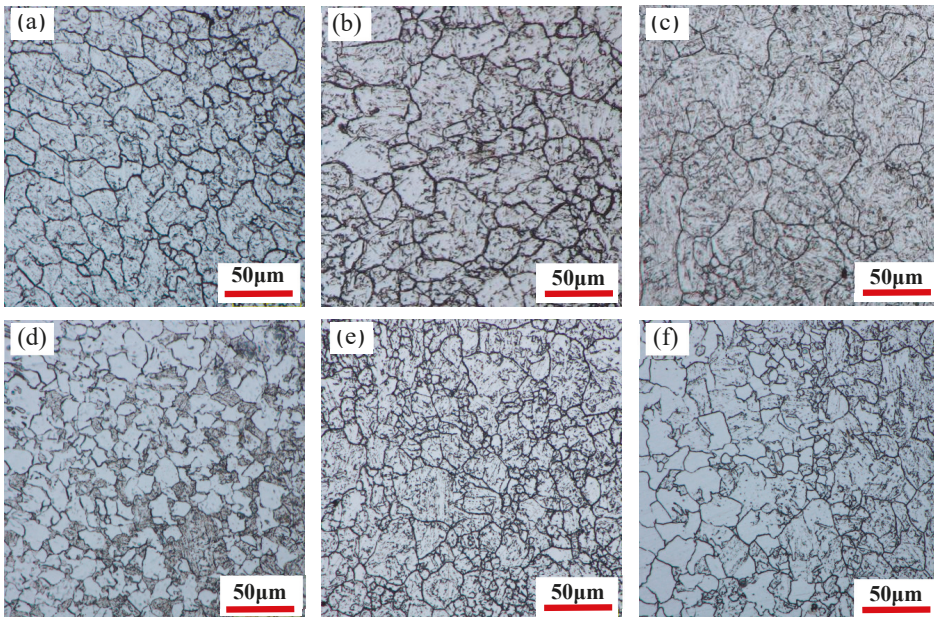


**Figure 2.** Microstructure of 35CrMoV steel at different deformation temperatures and strain rates: (a)  $0.01\text{ s}^{-1}$ ,  $850\text{ }^{\circ}\text{C}$ ; (b)  $0.01\text{ s}^{-1}$ ,  $950\text{ }^{\circ}\text{C}$ ; (c)  $0.01\text{ s}^{-1}$ ,  $1050\text{ }^{\circ}\text{C}$ ; (d)  $10\text{ s}^{-1}$ ,  $850\text{ }^{\circ}\text{C}$ ; (e)  $10\text{ s}^{-1}$ ,  $950\text{ }^{\circ}\text{C}$ ; (f)  $10\text{ s}^{-1}$ ,  $1050\text{ }^{\circ}\text{C}$ .

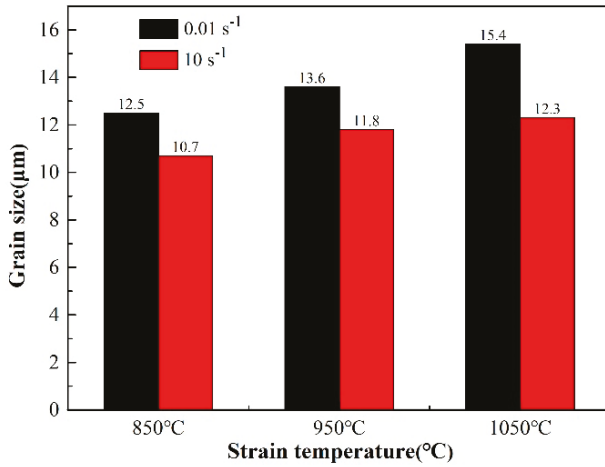


Figure 3. Grain size of 35CrMoV steel at different deformation temperatures and strain rates.

3.2. Electrochemical Analysis

3.2.1. Potentiodynamic Polarization Curve

In this section, the effects of grain sizes, obtained under different process parameters, on the corrosion resistance of 35CrMoV steel are discussed by potentiodynamic polarization experiments. Moreover, the electrochemical impedance spectroscopy and polarization curves are measured under the steady open-circuit potential (OCP). The change curve of an open-circuit potential, measured in 3.5 wt% NaCl solution, with respect to immersion time, is shown in Figure 4. It can be seen from Figure 4 that the change in the OCP of the studied samples follows a similar trend. At the beginning of the experiment, the potential decreases rapidly and all of the samples slowly reach the OCP when the immersion time is 2400 s. A steady OCP is observed at length.

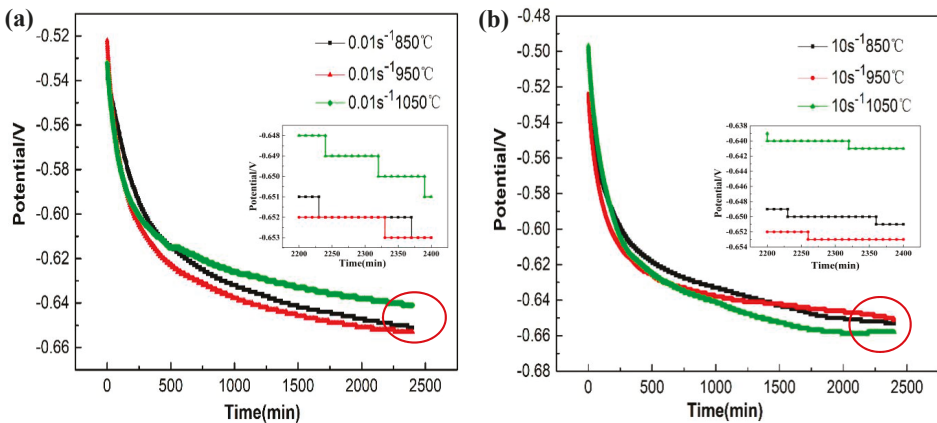
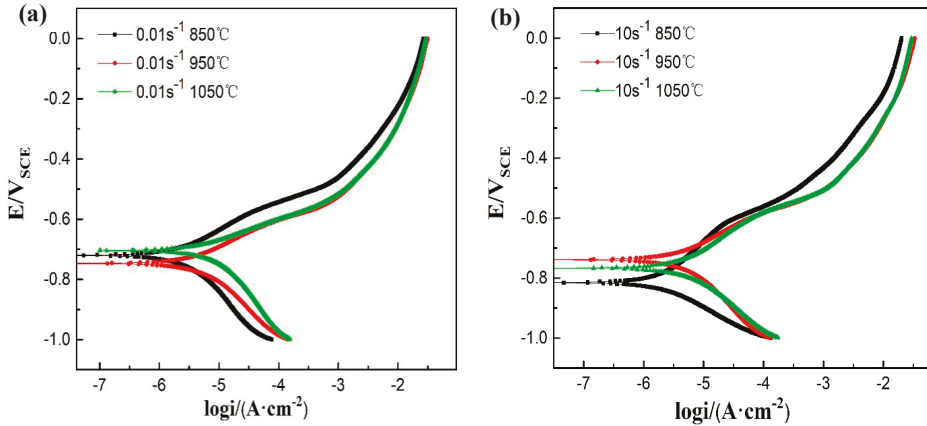


Figure 4. The open-circuit potential (OCP) curves of 35CrMoV steel in 3.5 wt% NaCl solution: (a) 0.01 s<sup>-1</sup>, 850–1050 °C; (b) 10 s<sup>-1</sup>, 850–1050 °C.

Figure 5 shows the potentiodynamic polarization curve of 35CrMoV steel immersed in 3.5 wt% NaCl solution after 40 min. It can be easily seen from Figure 5a,b, that the polarization curves obtained at different strain rates and deformation temperatures are similar in morphology and the

$I_{\text{corr}}$  displacement is obvious. There is no passivation and the anode region is an active dissolution of metal, which are the results of the characteristic adsorption of  $\text{Cl}^-$  onto the surface of the specimen, preventing the formation of the passivation film [1]. In addition, the  $E_{\text{corr}}$  shift of the polarization curve and obvious changes in the anode region can also be observed, where the anode region represents the dissolution of the matrix at high potential and the cathode region delegates the cathodic hydrogen evolution reaction associated with water reduction [12].



**Figure 5.** Polarization curves of 35CrMoV steel in 3.5 wt% NaCl solution: (a) 0.01 s<sup>-1</sup>, 850–1050 °C; and (b) 10 s<sup>-1</sup>, 850–1050 °C.

Tafel extrapolation is a rapid and effective method used to discuss the corrosion trend and behavior, and the corrosion rate obtained from it is mainly related to the initial surface corrosion [32]. The values of  $E_{\text{corr}}$ ,  $I_{\text{corr}}$ ,  $B_a$ , and  $B_c$  obtained from the polarization curves using Tafel extrapolation means (as shown in Figure 5) are listed in Table 2. It can be observed in Figure 5 and Table 2 that  $I_{\text{corr}}$  increases with an increase of deformation temperature at the same strain rate, and  $I_{\text{corr}}$  at the deformation temperature of 850 °C is 2.4  $\mu\text{A}/\text{cm}^2$ , whereas  $I_{\text{corr}}$  at the deformation temperature of 1050 °C is 5.4  $\mu\text{A}/\text{cm}^2$ . In comparison, the values  $I_{\text{corr}}$  obtained from 850 and 1050 °C increased by 2.2 times as much. Furthermore,  $I_{\text{corr}}$  increased from 2.3 to 5.3  $\mu\text{A}/\text{cm}^2$ , which is an increase of 2.3 times, at 10 s<sup>-1</sup>. Therefore, it can be concluded that the higher the deformation temperature of the hot working is, the more easily corrosion occurs. Besides, at the same deformation temperature,  $I_{\text{corr}}$  decreases with an increase in strain rate and the  $I_{\text{corr}}$  at 850 °C and 10 s<sup>-1</sup> is smaller than that at the strain rate of 0.01 s<sup>-1</sup>. It is well known that the smaller the value of  $I_{\text{corr}}$  is, the slower the corrosion reaction rate and the higher the corrosion resistance of the material. Accordingly, this shows that the corrosion resistance of 35CrMoV steel can be improved by obtaining smaller grains at high strain rates and low deformation temperatures.

**Table 2.** Electrochemical test results of 35CrMoV steel.

Sample	$E_{\text{corr}}/\text{V}_{\text{SCE}}$	$R_p/(\Omega\cdot\text{cm}^2)$	$I_{\text{corr}}/(\mu\text{A}/\text{cm}^2)$	$B_a/(\text{mV}/\text{dec})$	$B_c/(\text{mV}/\text{dec})$	
0.01 s <sup>-1</sup>	850 °C	-0.720	12,290.8	2.441	87.73	57.20
	950 °C	-0.747	6418.7	4.143	105.11	58.40
	1050 °C	-0.704	4083.5	5.393	145.06	52.38
10 s <sup>-1</sup>	850 °C	-0.815	12,927.8	2.332	55.69	88.50
	950 °C	-0.739	6795.4	4.354	90.24	56.71
	1050 °C	-0.767	6072.5	5.256	69.64	66.59



3.2.2. Electrochemical Impedance Spectroscopy characteristics

Generally, EIS is an effective technique for analyzing and studying the corrosion reaction between the structure of the alloy oxide film and the electrode interface, which can be used to evaluate the corrosion performance of an alloy. Figure 4 shows the curve of the OCP when measured by different specimens. For example, the stable OCP at 850 °C and 0.01 s<sup>-1</sup> is about 0.6509 V<sub>SCE</sub> and the EIS is recorded in the frequency range 0.1–100,000 Hz at the steady potential (0.6509 V<sub>SCE</sub>). The EIS of 35CrMoV steel is represented by the Nyquist plots and phase angle diagram displayed in Figures 6 and 7. It can be seen from Figure 6 that the EIS of the studied 35CrMoV steel can be greatly influenced by different deformation temperatures and strain rates. This is because the grain sizes of the specimens, acquired with the different thermal deformation parameters, showed in a comparison that the fine grains can make the grain-boundary area increase and the corrosion rate is accelerated at the early stage of corrosion, resulting in the formation of a dense oxide layer and a delaying and deepening of the corrosion. Consequently, the results show that the grain sizes obtained with the different thermal deformation parameters have a significant effect on corrosion resistance.

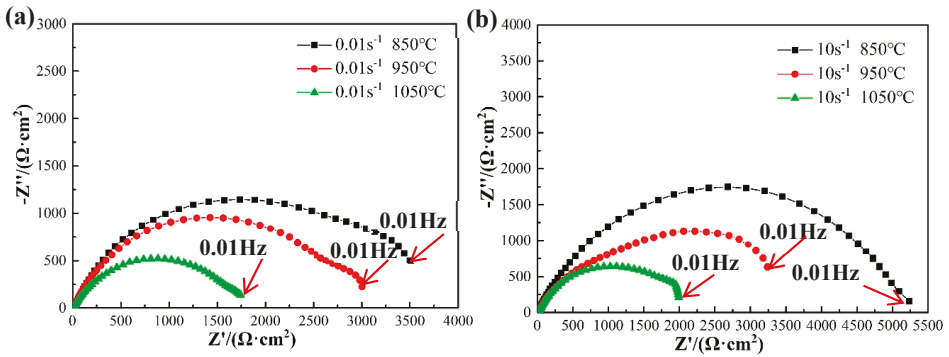


Figure 6. Nyquist plots of the 35CrMoV steel in 3.5 wt% NaCl solution: (a) 0.01 s<sup>-1</sup>, 850–1050 °C; (b) 10 s<sup>-1</sup>, 850–1050 °C.

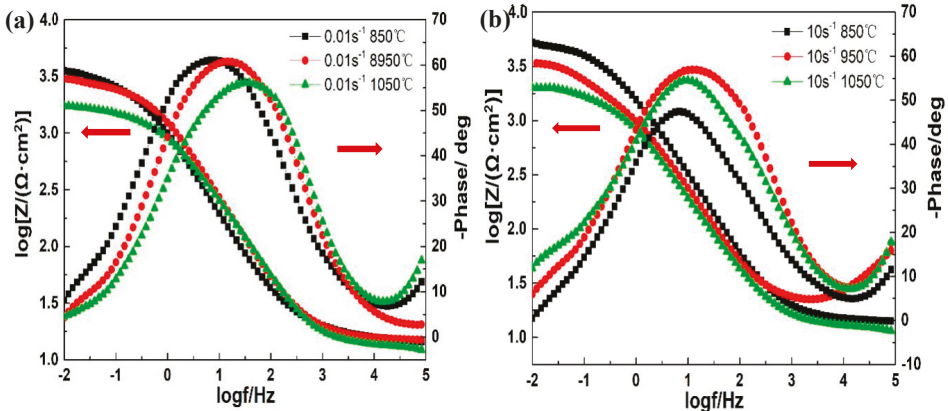


Figure 7. The Bode plots of 35CrMoV steel in 3.5 wt% NaCl solution: (a) 0.01 s<sup>-1</sup>, 850–1050 °C; (b) 10 s<sup>-1</sup>, 850–1050 °C.

The radius of the capacitive reactance arc is positively correlated with its corrosion resistance [21,33–35], the larger the arc radius, the lower the corrosion rate of the specimens in the corresponding solution [36–38]. It can be observed from Figure 6 that all samples have similar

semi-circular shapes, where the arc lines are similar and their diameters are different, indicating that the corrosion rate of the specimens is different but the corrosion mechanism is the same [20]. In addition, a larger arc radius can be seen at 850 °C, with strain rates of 0.01 and 10 s<sup>-1</sup>, which indicates that its corrosion resistance is better. At the same deformation temperature, the arc radius increases gradually with an increase of strain rate, which implies that the corrosion resistance is better (at the same strain rate), the arc radius decreases with an increase of deformation temperature, which indicates that the corrosion resistance is worse. Moreover, the arc-curve radius also reflects the impedance of the electron transfer process onto the electrode surface. It can be concluded that the hindrance can be enhanced and the corrosion rate can be decreased by a larger arc radius. As for metals, it can be noticed that the large resistance to electron transfer means that the gain and loss of electrons does not occur easily, indicating that the metals are difficult to corrode. Therefore, it is clear from Figure 6 that it is most difficult for corrosion to occur at 10 s<sup>-1</sup> and 850 °C, the result with the largest arc radius, which shows that a higher strain rate and lower deformation temperature can obtain smaller grains and better corrosion resistance.

Figure 7 shows the phase angle plots of the 35CrMoV steel with different strain rates and deformation temperatures. The phase angle plots can be divided into the high-, middle-, and low-frequency regions. From Figure 7 it can be seen that the phase angle in the high-frequency region (100–1000 KHz) is small (close to zero), indicating that the impedance of this frequency range is mainly a solution impedance, and that the resistance behavior is independent of the time constant. The phase angle of the intermediate-frequency region (1–1000 Hz) reaches the maximum value, which is a typical characteristic of solubilization. The maximum value of the phase angle of the samples at 0.01 s<sup>-1</sup>, 850 °C and 10 s<sup>-1</sup>, 850 °C moves slightly towards the low-frequency direction. It was found that the capacitance of the double layer is increased [39]. Meanwhile, the presence of a wide angular front in the intermediate- and low-frequency regions implies an interaction between the two relaxation processes, as shown in Figure 7. As per the above analysis, it can be concluded that the two time constants are the reflection of the charge transfer resistance and the corrosion product resistance [40]. In addition, the impedance value,  $|Z|$ , of the low-frequency region (0.01–1 Hz) shows the impedance of corrosion reaction, which is one of the parameters used to evaluate the corrosion performance. It indicates that the larger  $|Z|$  is, the better the corrosion resistance [41–43]. Additionally, it can be seen from Figure 7 that the impedance value of the specimens decreases with an increase in the deformation temperature, which indicates that the corrosion resistance of the sample surface decreases. Furthermore, at the same deformation temperature, the impedance value increases with the increase of the strain rate. This shows that the corrosion resistance of the sample is stronger. Consequently, the impedance value,  $|Z|$ , of the specimen, at 10 s<sup>-1</sup> and 850 °C, is observed in Figure 7, which is consistent with the results of the polarization curve, indicating the corrosion resistance is at its best and the corrosion product film on the surface is performing better.

In order to further quantitatively analyze the electrochemical corrosion behavior of the 35CrMoV steel in 3.5 wt%NaCl solution, an equivalent electrical circuit (R(Q (R (QR)) is established to fit the EIS spectra, which can well-express the corrosion mechanism of the metal interface or solution. The equivalent circuit consists of two time constants [44], as shown in Figure 8. The EIS, fitted by the ZsimpWin software (Buokamp, MA, USA), and the fitting results are shown in Table 3. The five different elements used in the equivalent circuit have different physical meanings and can be divided into three different categories. The first part,  $R_s$ , is the solution resistance of the electrolyte, which is used to characterize the kinematic velocity of the chloride produced on the surface of the specimens in the electrolyte. In the second part,  $Q_f$  and  $R_f$  are used to imply the capacitance and resistance of the corrosion product respectively, which can reflect the diffusion of ions in the corrosion product layer and the formation of the corrosion product on the substrate surface during electrochemical corrosion. Additionally,  $R_f$  is an important parameter used to characterize the protective effect of the oxide layer. It can be found that a larger corrosion product resistance means better protection of the oxide layer and a greater resistance to ion movement. In the third part,  $Q_{dl}$  and  $R_{ct}$  are used to characterize the

double-layer capacitance and charge transfer resistance of the reaction interface respectively, which are related to the electrochemical corrosion reaction between the sample matrix and the electrolytic solution. Furthermore,  $Q$  (in the second and third parts) is a constant phase angle element (CPE), which describes the physical quantity when the parameter of interface capacitance,  $C$ , deviates due to dispersion effects. In general, the reactions in the second and third parts occur in the middle- and low-frequency regions of EIS, which are related to the corrosion resistance of the specimens. The corrosion resistance of the samples is evaluated by combining the corrosion product resistance  $R_f$  with the charge transfer resistance  $R_{ct}$  ( $R_{corr} = R_f + R_{ct}$ ) [1,33,35,40]. Generally, the corrosion resistance enhances as  $R_{corr}$  increases. The polarization resistances ( $R_{corr}$ ) of the two groups of all of the samples studied are shown in Figure 9. It can be seen from Figure 9 that  $R_{corr}$  decreases with an increase of 35CrMoV steel thermal deformation temperature at the same strain rate, indicating that the corrosion rate is accelerated. This is because an increase in the 35CrMoV hot deformation temperature is conducive to grain growth, resulting in a coarse grain size and lower corrosion resistance. At the same temperature,  $R_{corr}$  increases with an increase in the strain rate and, more importantly, the highest  $R_{corr}$  appears at  $10\text{ s}^{-1}$  and  $850\text{ °C}$ , indicating that the fine grains obtained at high strain rates and low deformation temperatures can make the oxide layer denser and improve the corrosion resistance.

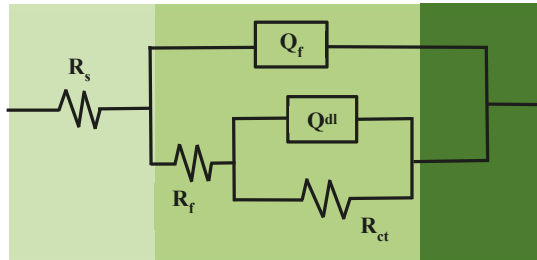


Figure 8. The equivalent electrical circuit of the 35CrMoV steel in 3.5 wt% NaCl solution.

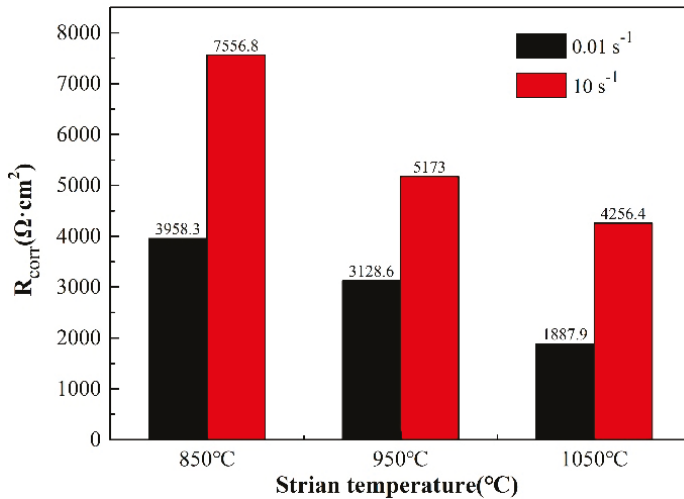


Figure 9. The corrosion rate of the 35CrMoV steel in 3.5 wt% NaCl solution.

**Table 3.** Spectra fitting results of experimental 35CrMoV steel in 3.5 wt% NaCl solution.

Sample		$R_s$ ( $\Omega \cdot \text{cm}^2$ )	$Y_f$ ( $\Omega^{-1} \cdot \text{cm}^{-2} \cdot \text{s}^n$ )	n	$R_f$ ( $\Omega \cdot \text{cm}^2$ )	$Y_{dl}$ ( $\Omega^{-1} \cdot \text{cm}^{-2} \cdot \text{s}^n$ )	n	$R_{ct}$ ( $\Omega \cdot \text{cm}^2$ )
0.01 s <sup>-1</sup>	850 °C	15.66	$2.316 \times 10^{-4}$	0.7438	3469.00	$2.081 \times 10^{-2}$	1.000	489.3
	950 °C	15.21	$1.544 \times 10^{-4}$	0.7619	2768.00	$1.585 \times 10^{-2}$	0.9732	360.6
	1050 °C	12.84	$1.637 \times 10^{-4}$	0.7451	961.30	$5.139 \times 10^{-4}$	0.3708	926.6
10 s <sup>-1</sup>	850 °C	17.85	$3.779 \times 10^{-4}$	0.6669	26.83	$1.88 \times 10^{-4}$	0.8759	7530.0
	950 °C	14.42	$1.236 \times 10^{-4}$	0.7733	3713.00	$3.016 \times 10^{-4}$	0.8368	1460.0
	1050 °C	36.56	$4.464 \times 10^{-5}$	1.0000	189.40	$3.157 \times 10^{-4}$	0.5485	4067.0

### 3.3. Corrosion Products and Corrosion Mechanism Analysis

In order to further discuss the effect of the grain sizes, obtained under different deformation conditions, on the corrosion resistance of the specimens, the two- and three-dimensional morphology of the specimens surface is observed, on the basis of the potentiodynamic polarization experiment. The two-dimensional corrosion morphology of four typical specimens with deformation temperatures of 850 °C and 1050 °C, at the strain rates of 0.01 s<sup>-1</sup> and 10 s<sup>-1</sup> respectively, immersed in 3.5 wt% NaCl solution for 1 h and placed for 3 days, is depicted in Figure 10. It can be observed from Figure 10 that the surface of the specimens display local corrosion, where the corrosion holes are in the direction of depth. The black and yellowish-brown areas are corrosion areas, and the bright white areas are un-corroded areas. The corrosion pits on the surface are covered with rust spots and corrosion products, as well as corrosion pits of different sizes. At the same strain rate, with an increase in the 35CrMoV hot deformation temperatures, the local corrosion gradually expands and connects to a larger area of corrosion. Furthermore, the corrosion area becomes smaller and the corrosion degree weakens with an increase of the strain rate at the same deformation temperature. The three-dimensional morphology of the a', b', c', and d' (see Figure 10) regions under the CLSM is shown in Figure 11. The size of the etch pits are measured, along the Y direction of the specimens, with the CLSM. The etch pit depths of (a'), (b'), (c'), and (d') in Figure 10 are 17.17, 49.55, 13.64, and 30.45  $\mu\text{m}$ , respectively. At the same strain rates (0.01 s<sup>-1</sup> and 10 s<sup>-1</sup>), the surface is locally corroded and there are corrosion pits at the deformation temperatures of 850 °C and 1050 °C, but the corrosion pit at the deformation temperature of 1050 °C is large and deep, which indicates that the corrosion resistance is poor at higher deformation temperatures. This is as the dynamic re-crystallization rate of the sample steel increases at high deformation temperatures, and the re-crystallized large grains continue to swallow small grains and grow. Additionally, at the same deformation temperature, the corrosion surface is smoother and the corrosion pit decreases with an increase of strain rate, which is consistent with the characterization in Figure 10. This is because the structure of the double layer at the interface between the matrix iron and the corrosion product film is prone to preferential adsorption of Cl<sup>-</sup>, which results in the surface deposition of Cl<sup>-</sup> fluids, which then combine with cations on the oxidation film to form soluble chloride and corrosion pits. However, the PH value of the corrosion pit decreases with the continuous hydrolysis of chloride, as well as the dissolution of the anode metal of the corrosion pit, and the external Cl<sup>-</sup> is invaded into the corrosion pit through the corrosion product film, which makes the corrosion proceed further. In this cycle, the deepening and expansion of the corrosion pit depth are the results of the corrosion catalysis of Cl<sup>-</sup>.

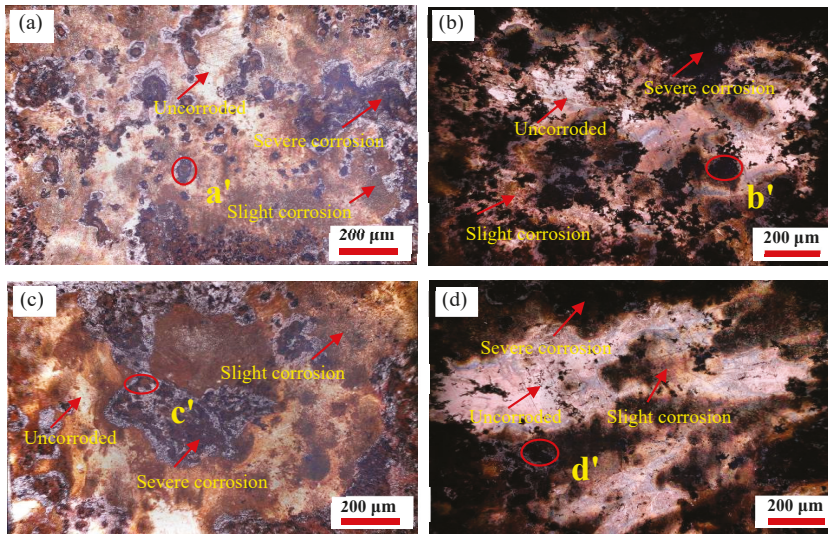


**Figure 10.** Corrosion morphology of the 35CrMoV steel: (a)  $0.01\text{ s}^{-1}$ ,  $850\text{ }^{\circ}\text{C}$ ; (b)  $0.01\text{ s}^{-1}$ ,  $1050\text{ }^{\circ}\text{C}$ ; (c)  $10\text{ s}^{-1}$ ,  $850\text{ }^{\circ}\text{C}$ ; (d)  $10\text{ s}^{-1}$ ,  $1050\text{ }^{\circ}\text{C}$ .

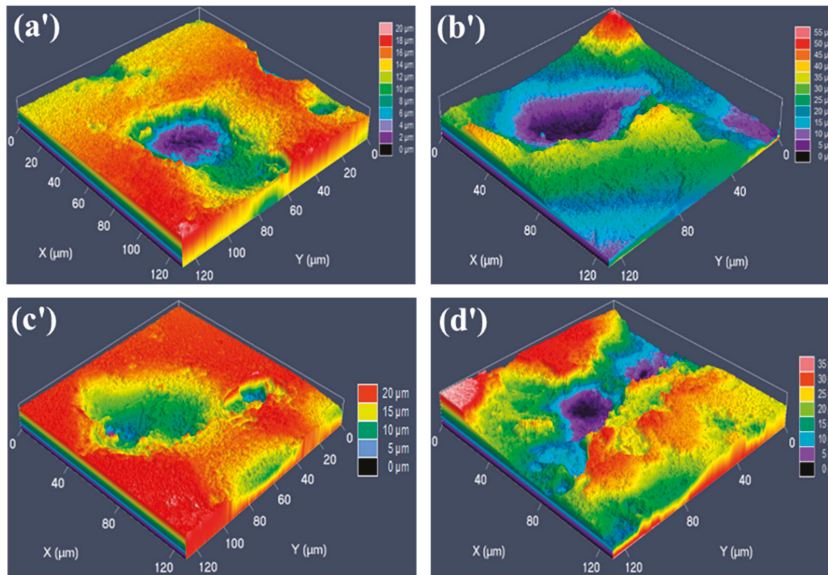


**Figure 11.** Three-dimensional corrosion morphology of the 35CrMoV steel: (a')  $0.01\text{ s}^{-1}$ ,  $850\text{ }^{\circ}\text{C}$ ; (b')  $0.01\text{ s}^{-1}$ ,  $1050\text{ }^{\circ}\text{C}$ ; (c')  $10\text{ s}^{-1}$ ,  $850\text{ }^{\circ}\text{C}$ ; (d')  $10\text{ s}^{-1}$ ,  $1050\text{ }^{\circ}\text{C}$ .

Figures 12 and 13 show the surface morphology of the specimens after polarization in 3.5 wt% NaCl solution. It can be observed from Figures (a), (b), and (c) in Figures 12 and 13 that there are cracks and platelet crystal-like corrosion product films on the surface of the specimens. At the same strain rate, the surface corrosion product-coverage area increases and the corrosion product accumulates with an increase of the deformation temperature. However, at the same deformation temperature, the accumulation of corrosion products decreases because of an increase in the strain rate, indicating

that the corrosion degree is weakened. The cracks on the corroded surface are displayed in Figure 12 and in Figure 13a'–c', and are due to dehydration after the sample immersion test [45]. The corrosion cracks are formed at the initial stage of corrosion which, with an increase of temperature, become wider, deeper, and looser at the same strain rate, and the corrosion products fall off slightly, indicating that corrosion is deepening. However, at the same deformation temperature, the corrosion cracks on the surface of the specimens become narrower, shallower, denser, and less detached as the strain rate increases, indicating that the corrosion rate is weakened. The platelet-like corrosion products (Figures 12 and 13d'–f') generated on the surface are due to the deepening of the surface corrosion, resulting in rust being generated and the corrosion products accumulating. In other words, with an increase of deformation temperature, the gap in platelet corrosion products becomes wider and looser at the same strain rate, which is more likely to cause oxidative corrosion on the surface, favorable to the further invasion of the corrosive medium which accelerates the corrosion. Furthermore, an increase of the deformation temperature is beneficial to grain growth, which then affects the corrosion rate at the same strain rate. Additionally, the cracks are narrower and the platelet-corrosion product film is densified and uniform at the same deformation temperature, due to strain rate increases. The deformation process becomes rapid, the dynamic recovery rate decreases, and the re-crystallized grains have not yet fully grown, resulting in smaller grains.

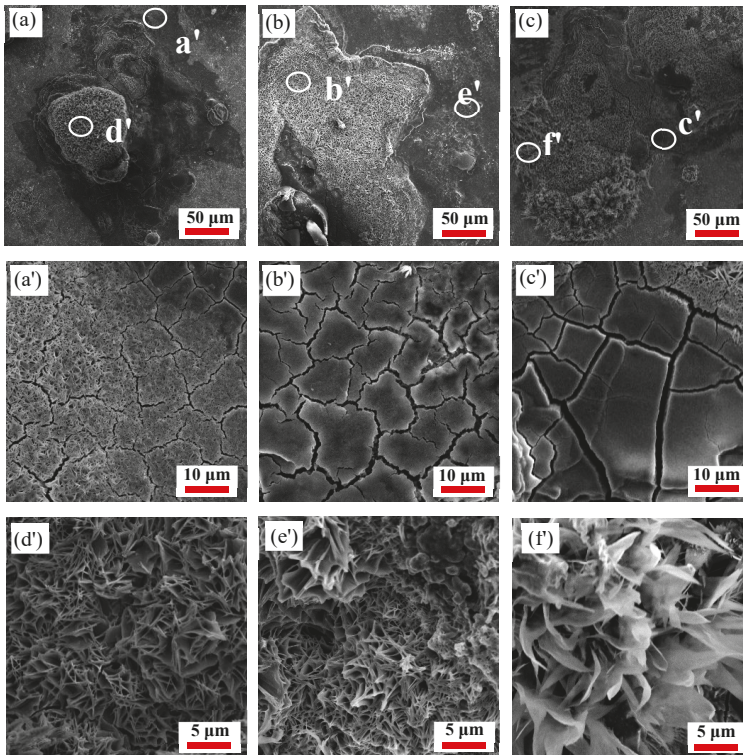


**Figure 12.** Scanning electron microscopy (SEM) corrosion morphology of the 35CrMoV steel: (a,a',d') 0.01 s<sup>-1</sup>, 850 °C; (b,b',e') 0.01 s<sup>-1</sup>, 950 °C; and (c,c',f') 0.01 s<sup>-1</sup>, 1050 °C.

The results show that the impedance modulus at the EIS (Figure 6) is the appropriate parameter to characterize the protective performance of the corrosion product film [46–48]. From Figure 6a, it can be seen that no scattering fluctuations were observed in all of specimens at 0.01 Hz, which indicates

that the corrosion product film has great stability and can effectively protect the matrix from  $\text{Cl}^-$  in 3.5 wt% NaCl solution, as well as preventing further corrosion [41].

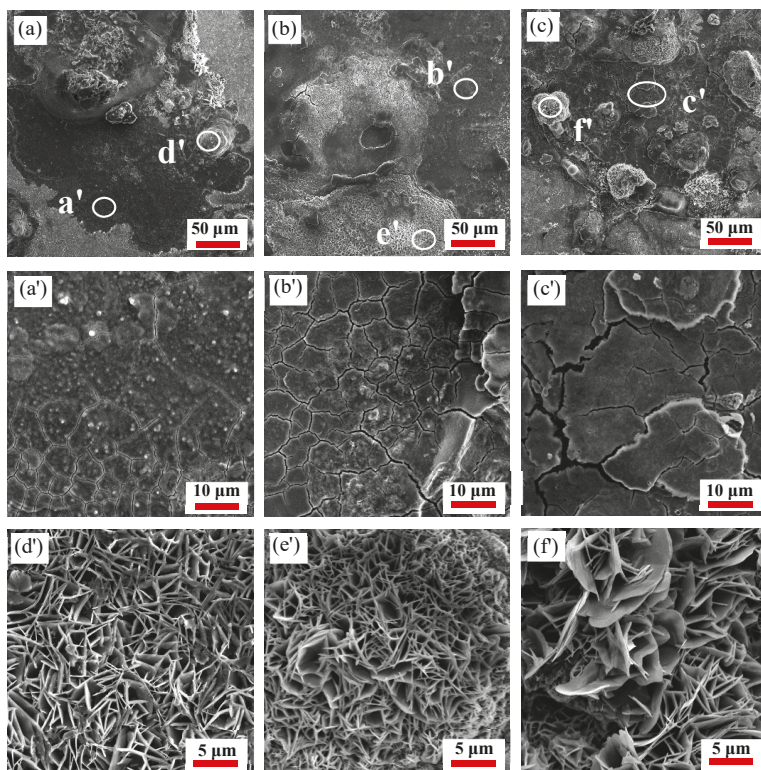


**Figure 13.** SEM corrosion morphology of the 35CrMoV steel: (a,a',d')  $10 \text{ s}^{-1}$ ,  $850 \text{ }^\circ\text{C}$ ; (b,b',e')  $10 \text{ s}^{-1}$ ,  $950 \text{ }^\circ\text{C}$ ; and (c,c',f')  $10 \text{ s}^{-1}$ ,  $1050 \text{ }^\circ\text{C}$ .

The surface of the specimens was scanned by EDS and two groups of specimens, with different strain rates at deformation temperature  $850 \text{ }^\circ\text{C}$ , were selected for analysis. Figure 14 shows the corrosion morphology and EDS analysis of the surface of the 35CrMoV steel at deformation temperature  $850 \text{ }^\circ\text{C}$  at  $0.01$  and  $10 \text{ s}^{-1}$ . Both of the specimens can be observed to have corrosion cracks (Figure 14(a1,b1)) and platelet-like products (Figure 14(a2,b2)) [20], produced on the surface of the 35CrMoV steel. Additionally, there is an obvious accumulation of massive corrosion products, and the thickness of the corrosion layer is uneven. The corrosion cracks (Figure 14(a1,b1)) of the specimens all contain O, Fe, C, and Cr, as revealed by EDS, and the oxygen content on the surface decreases obviously with the increase of the strain rate. Meanwhile, the surface of the platelet-like product (Figure 14(a2,b2)) is mainly composed of O, Fe, C, and Cr, and the oxygen content in  $0.01 \text{ s}^{-1}$  is obviously higher than that in  $10 \text{ s}^{-1}$ , indicating that the corrosion product is mainly oxide. Furthermore, the content of Cr in  $10 \text{ s}^{-1}$  obviously increased and the presence of Cr elements on the surface of the corrosion product film can effectively prevent the deep erosion of  $\text{Cl}^-$ , improve the chemical stability of the corrosion product film, and prevent further corrosion.

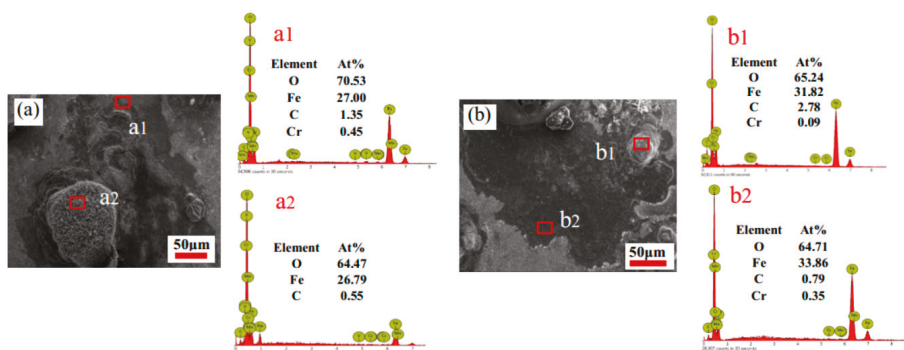


**Figure 14.** Corrosion morphology and energy disperse spectroscopy (EDS) analysis of the 35CrMoV steel at the same temperature (850 °C) and at different strain rates: (a) 0.01 s<sup>-1</sup>; and (b) 10 s<sup>-1</sup>.

X-ray diffraction analysis was conducted to determine the types of corrosion products (see Figure 15a) and the matrix (see Figure 15b) after corrosion on the surface of the samples. The energy spectrum analysis results of the 35CrMoV steel matrix and corrosion products after corrosion are displayed in Figure 15. It can be seen from Figure 15 that the surface of the matrix after heat treatment mainly contains Fe, and some studies have shown that its structure is tempered sorbite [49,50]. In summary, the corrosion products on the surface after corrosion are mainly FeOOH. Combined with the EDS analysis of Figure 14, it can be concluded that O, Fe, and C are the main components of the corrosion product. Therefore, it can be inferred that the cathode in the corrosion solution is depolarized by oxygen, due to adequate oxygen supply, and the surface is covered by a thin water film.

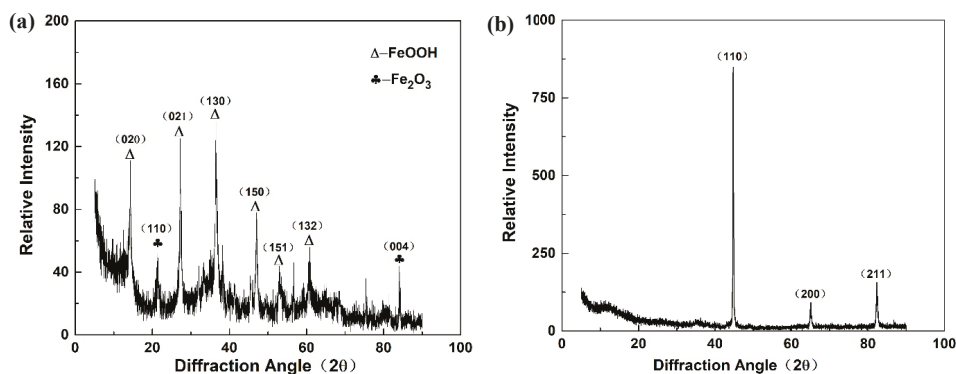
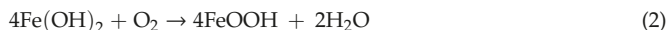


**Figure 15.** X-ray diffraction (XRD) analysis of the 35CrMoV steel: (a) corrosion products; and (b) matrix.

In the early stages of corrosion, Cl<sup>-</sup> adsorbed on the metal surface play an erosion role and Fe is dissolved from the anode to form Fe<sup>2+</sup>, combined with Cl<sup>-</sup> to form FeCl<sub>2</sub>·4H<sub>2</sub>O [51], and further decomposed to form Fe(OH)<sub>2</sub>. However, Fe(OH)<sub>2</sub> is unstable and decomposed into FeO or oxidized to FeOOH by the O<sub>2</sub> dissolved in the water film (see Equations (1) and (2)) [1,52–54]. In addition, some studies have shown that Fe(OH)<sub>2</sub> can continue to be oxidized and dehydrated to form Fe<sub>2</sub>O<sub>3</sub> and Fe<sub>3</sub>O<sub>4</sub>, which are both dense and difficult to decompose. Accordingly, the reduction in corrosion rate is the result of the Fe<sub>2</sub>O<sub>3</sub> and Fe<sub>3</sub>O<sub>4</sub> hindering the diffusion of oxygen and Cl<sup>-</sup>, which exist in the inner rust layer [55]. According to the Evans theory, the corrosion products will partially dissolve due to the



strong erosive  $\text{Cl}^-$  in the solution. Many cracks will occur in the rust layer, which can provide a gap between the corrosion media (such as  $\text{O}_2$ ) and spread, causing the corrosion to continue.



Grain refinement leads to an increase in grain boundary area per unit volume at lower deformation temperatures and higher strain rates. It is well known that the potential at grain boundaries is lower than inside the grain, which is as the crystal defect density at the grain boundary is large. In addition, the existence of a potential difference (PD) constitutes the grain–grain boundary corrosion micro-battery. As a result, the grain boundary (serving as an anode) has priority in corrosion. In the same corrosion environment, there is a certain potential difference between the grain and the grain boundary. The local anodic corrosion current density experienced by the grain boundary is relatively small when corroded, so it will not intrude very deep holes and cracks, and it will give the rust layer a good compactness. The grain size directly affects the corrosion rate at the beginning of corrosion. In contrast to the coarse-grain rate, the fine-grain corrosion rate is faster, which is mainly due to the fact that grain refinement increases the grain boundary area, and the grain boundary is increased in the microstructure. Besides this, the grain boundary is a high-active zone, which may make it vulnerable to pitting corrosion, leading to surface unevenness and increases in the anode surface area, and causing the electrochemical reaction to proceed rapidly [56]. This would result in a larger corrosion area, heavier corrosion, and faster anodic dissolution, which is conducive to the rapid formation of a protective inner rust layer. Thus, a finer-grain of the specimens is more favorable to the flatness of the rust layer/matrix interface in the specimens and a more-uniform dissolved matrix. At the same time, the rust particles are refined and there is a reduction of the cracks and pores in the rust layer, which can cause the matrix and rust layer to combine firmly. Furthermore, the rust layer becomes thicker, denser, and more stable and the alloying elements on the matrix surface play an important role in the development of corrosion [57,58], resulting in an increase in the self-corrosion potential of the sample while enhancing the corrosion resistance and reducing the dissolution rate of the anode. In addition, the current carrying density of the oxide film was reduced and the dissolution of the oxide film slowed down due to grain refinement [59,60], accordingly improving the corrosion resistance [61].

#### 4. Conclusions

The microstructure of 35 CrMoV steel under different hot deformation conditions and the short-term corrosion behavior in 3.5 wt% NaCl solution was discussed, and some important conclusions, as follows, were obtained:

(1) Deformation temperatures and strain rates have an important influence on the microscopic structure. At the same strain rate, the grain size increased with an increase in deformation temperature and decreased with an increase in strain rate at the same strain temperature. Amongst all of the hot deformation parameters studied, the grain size at a strain rate of  $10 \text{ s}^{-1}$  and a deformation temperature of  $850 \text{ }^\circ\text{C}$  was the smallest ( $10.7 \text{ }\mu\text{m}$ ), indicating that a finer-grain structure can be obtained at lower deformation temperatures and higher strain rates.

(2) The difference in grain sizes had a significant effect on the corrosion resistance of 35CrMoV steel. At the same strain rate, the grain size augmented with an increase in temperature and the corrosion resistance decreased with an increase in the grain size, within a certain corrosion time. Furthermore, the corrosion resistance was the worst when the grain size was the largest ( $15.4 \text{ }\mu\text{m}$ ). At the same deformation temperature, the higher the strain rate, the smaller the grain size, and therefore, the better the corrosion resistance of the specimens within a certain period of time. The smallest grain size ( $10.6 \text{ }\mu\text{m}$ ) was observed at a strain rate of  $10 \text{ s}^{-1}$  and a deformation temperature of  $850 \text{ }^\circ\text{C}$ , resulting in the lowest corrosion rate, which indicates low-deformation temperature and high-strain rate can

achieve the effect of refining grains and improving corrosion resistance. However, the long-term corrosion trends of these materials need to be studied further.

(3) The differences in the corrosion resistance of 35CrMoV steel were related to the grain boundary change after grain refinement. Grain refinement increased the grain boundary area and the grain boundary, which accelerated the formation of a protective oxide film at the initial stage of corrosion, improved the stability of the oxide film, and prevented the corrosion from proceeding deeply, thereby improving corrosion resistance.

**Author Contributions:** Conceptualization, Q.Y.; Data curation, Z.L.; Formal analysis, Z.L.; Funding acquisition, Y.Z. and D.M.; Methodology, Q.Y.; Project administration, Y.Z.; Resources, D.M.; Writing—original draft, Q.Y.; Writing—review & editing, Q.Y. and Y.Z.

**Funding:** This research was funded by the national 973 project of China, grant number No.2014CB046702 and the experimental cost were funded by the national 973 project of China.

**Acknowledgments:** The authors would like to acknowledge the financial assistance provided by the Major State Basic Research Development Program of China (No. 2014CB046702).

**Conflicts of Interest:** The authors declare no conflict of interest.

## References

- Jiang, X.; Zhou, Y.; Shi, C.; Mao, D. Effects of Ultrasonic-Aided Quenching on the Corrosion Resistance of GB 35CrMoV Steel in Seawater Environment. *Metals* **2018**, *8*, 104. [[CrossRef](#)]
- Niu, L.; Cheng, Y. Corrosion behavior of X-70 pipe steel in near-neutral pH solution. *Appl. Surf. Sci.* **2007**, *253*, 8626–8631. [[CrossRef](#)]
- Alizadeh, M.; Bordbar, S. The influence of microstructure on the protective properties of the corrosion product layer generated on the welded API X70 steel in chloride solution. *Corros. Sci.* **2013**, *70*, 170–179. [[CrossRef](#)]
- Shimura, T.; Aramaki, K. Prevention of passive film breakdown on iron by coverage with one-dimensional polymer films of a carboxylate ion self-assembled monolayer modified with alkyltriethoxysilanes. *Corros. Sci.* **2004**, *46*, 2563–2581.
- Zhang, B.; Zhang, B.; Ruan, X.; Zhang, Y. The Hot Deformation Behavior and Dynamic Recrystallization Model Of 35 crmo Steel. *Acta. Metall. Sin.* **2003**, *16*, 183–191.
- Wang, S.; Huang, Y.; Xiao, Z.; Liu, Y.; Liu, H. A Modified Johnson-Cook Model for Hot Deformation Behavior of 35CrMo Steel. *Metals* **2017**, *7*, 337. [[CrossRef](#)]
- Chen, X.-M.; Lin, Y.; Wen, D.-X.; Zhang, J.-L.; He, M. Dynamic recrystallization behavior of a typical nickel-based superalloy during hot deformation. *Mater. Des.* **2014**, *57*, 568–577. [[CrossRef](#)]
- He, D.-G.; Lin, Y.; Chen, J.; Chen, D.-D.; Huang, J.; Tang, Y.; Chen, M.-S. Microstructural evolution and support vector regression model for an aged Ni-based superalloy during two-stage hot forming with stepped strain rates. *Mater. Des.* **2018**, *154*, 51–62. [[CrossRef](#)]
- Ren, F.; Chen, F.; Chen, J.; Tang, X. Hot deformation behavior and processing maps of AISI 420 martensitic stainless steel. *J. Manuf. Process.* **2018**, *31*, 640–649. [[CrossRef](#)]
- Kingkam, W.; Zhao, C.-Z.; Li, H.; Zhang, H.-X.; Li, Z.-M. Hot Deformation and Corrosion Resistance of High-Strength Low-Alloy Steel. *Acta Met. Sin.* **2018**, *32*, 495–505. [[CrossRef](#)]
- Xiao, Z.-B.; Huang, Y.-C.; Liu, Y. Plastic Deformation Behavior and Processing Maps of 35CrMo Steel. *J. Mater. Eng. Perform.* **2016**, *25*, 1219–1227. [[CrossRef](#)]
- Xu, L.; Chen, L.; Chen, G.; Wang, M. Hot deformation behavior and microstructure analysis of 25Cr3Mo3NiNb steel during hot compression tests. *Vacuum* **2018**, *147*, 8–17. [[CrossRef](#)]
- Huang, Y.; Wang, S.; Xiao, Z.; Liu, H. Critical Condition of Dynamic Recrystallization in 35CrMo Steel. *Metals* **2017**, *7*, 161. [[CrossRef](#)]
- Wen, D.; Lin, Y.; Zhou, Y. A new dynamic recrystallization kinetics model for a Nb containing Ni-Fe-Cr-base superalloy considering influences of initial  $\delta$  phase. *Vacuum* **2017**, *141*, 316–327. [[CrossRef](#)]
- Quan, G.; Mao, A.; Zou, Z.; Luo, G.; Liang, J. Description of Grain Refinement by Dynamic Recrystallization Under Hot Compressions for As-Extruded 3Cr20Ni10W2 Heat-Resistant Alloy. *High Temp. Mater. Process.* **2015**, *34*, 697–713.

16. Song, D.; Ma, A.-B.; Jiang, J.-H.; Lin, P.-H.; Yang, D.-H. Corrosion behavior of ultra-fine grained industrial pure Al fabricated by ECAP. *Trans. Nonferrous Met. Soc.* **2009**, *19*, 1065–1070. [[CrossRef](#)]
17. Alvarez-Lopez, M.; Pereda, M.D.; Del Valle, J.; Fernandez-Lorenzo, M.; Garcia-Alonso, M.C.; Ruano, O.; Escudero, M.L.; Ruano, O. Corrosion behaviour of AZ31 magnesium alloy with different grain sizes in simulated biological fluids. *Biomaterials* **2010**, *6*, 1763–1771. [[CrossRef](#)]
18. Argade, G.; Panigrahi, S.; Mishra, R.; Mishra, R. Effects of grain size on the corrosion resistance of wrought magnesium alloys containing neodymium. *Corros. Sci.* **2012**, *58*, 145–151. [[CrossRef](#)]
19. Balyanov, A.; Kutnyakova, J.; Amirkhanova, N.; Stolyarov, V.; Valiev, R.; Liao, X.; Zhao, Y.; Jiang, Y.; Xu, H.; Lowe, T.; et al. Corrosion resistance of ultra fine-grained Ti. *Scr. Mater.* **2004**, *51*, 225–229. [[CrossRef](#)]
20. Aung, N.; Zhou, W. Effect of grain size and twins on corrosion behaviour of AZ31B magnesium alloy. *Corros. Sci.* **2010**, *52*, 589–594. [[CrossRef](#)]
21. Zhao, Y.; Wu, G.; Jiang, J.; Wong, H.M.; Yeung, K.W.; Chu, P.K. Improved corrosion resistance and cytocompatibility of magnesium alloy by two-stage cooling in thermal treatment. *Corros. Sci.* **2012**, *59*, 360–365. [[CrossRef](#)]
22. Song, G.-L.; Bowles, A.L.; StJohn, D.H. Corrosion resistance of aged die cast magnesium alloy AZ91D. *Mater. Sci. Eng. A* **2004**, *366*, 74–86. [[CrossRef](#)]
23. Hsiao, H.; Tsai, W. Effect of heat treatment on anodization and electrochemical behavior of AZ91D magnesium alloy. *J. Mater. Res.* **2005**, *20*, 2763–2771. [[CrossRef](#)]
24. Yu, X.; Chen, S.; Liu, Y.; Ren, F. A study of intergranular corrosion of austenitic stainless steel by electrochemical potentiodynamic reactivation, electron back-scattering diffraction and cellular automaton. *Corros. Sci.* **2010**, *52*, 1939–1947. [[CrossRef](#)]
25. Pradhan, S.; Bhuyan, P.; Mandal, S. Individual and synergistic influences of microstructural features on intergranular corrosion behavior in extra-low carbon type 304L austenitic stainless steel. *Corros. Sci.* **2018**, *139*, 319–332. [[CrossRef](#)]
26. Zhang, T.; Shao, Y.; Meng, G.; Cui, Z.; Wang, F. Corrosion of hot extrusion AZ91 magnesium alloy: I-relation between the microstructure and corrosion behavior. *Corros. Sci.* **2011**, *53*, 1960–1968. [[CrossRef](#)]
27. Qian, J.; Chen, C.; Yu, H.; Liu, F.; Yang, H.; Zhang, Z. The influence and the mechanism of the precipitate/austenite interfacial C-enrichment on the intergranular corrosion sensitivity in 310 S stainless steel. *Corros. Sci.* **2016**, *111*, 352–361. [[CrossRef](#)]
28. Singh, R.; Chowdhury, S.G.; Kumar, B.R.; Das, S.K.; De, P.; Chattoraj, I. The importance of grain size relative to grain boundary character on the sensitization of metastable austenitic stainless steel. *Scr. Mater.* **2007**, *57*, 185–188. [[CrossRef](#)]
29. Singh, R.; Chowdhury, S.; Chattoraj, I. Modification of Sensitization Resistance of AISI 304L Stainless Steel through Changes in Grain Size and Grain Boundary Character Distributions. *Metal. Mater. Tran. A.* **2008**, *39*, 2504–2512. [[CrossRef](#)]
30. Ahmedabadi, P.M.; Kain, V.; Muralidhar, K.V.; Samajdar, I. On the role of residual strain in controlling sensitisation of twin-boundary engineered type 304 stainless steel. *J. Mater.* **2013**, *432*, 243–251. [[CrossRef](#)]
31. Lin, Y.; Wu, X.-Y.; Chen, X.-M.; Chen, J.; Wen, D.-X.; Zhang, J.-L.; Li, L.-T. EBSD study of a hot deformed nickel-based superalloy. *J. Alloys Compd.* **2015**, *640*, 101–113. [[CrossRef](#)]
32. Zhao, M.-C.; Liu, M.; Song, G.-L.; Atrons, A. Influence of pH and chloride ion concentration on the corrosion of Mg alloy ZE41. *Corros. Sci.* **2008**, *50*, 3168–3178. [[CrossRef](#)]
33. Chen, J.; Zhou, Y.; Shi, C.; Mao, D. Microscopic Analysis and Electrochemical Behavior of Fe-Based Coating Produced by Laser Cladding. *Metals* **2017**, *7*, 435. [[CrossRef](#)]
34. Zhang, H.; Zou, Y.; Zou, Z.; Wu, D. Microstructure and properties of Fe-based composite coating by laser cladding Fe–Ti–V–Cr–C–CeO<sub>2</sub> powder. *Opt. Laser Technol.* **2015**, *65*, 119–125. [[CrossRef](#)]
35. Lin, Y.; Liu, G.; Chen, M.-S.; Zhang, J.-L.; Chen, Z.-G.; Jiang, Y.-Q.; Li, J. Corrosion resistance of a two-stage stress-aged Al–Cu–Mg alloy: Effects of external stress. *J. Alloys Compd.* **2016**, *661*, 221–230. [[CrossRef](#)]
36. Lv, J. Effect of grain size on mechanical property and corrosion resistance of the Ni-based alloy 690. *J. Mater. Sci. Technol.* **2018**, *34*, 1685–1691. [[CrossRef](#)]
37. Awasthi, S.; Pandey, S.K.; Juyal, A.; Pandey, C.P.; Balani, K. Synergistic effect of carbonaceous reinforcements on microstructural, electrochemical, magnetic and tribological properties of electrophoretically deposited nickel. *J. Alloys Compd.* **2017**, *711*, 424–433. [[CrossRef](#)]

38. Jiang, K.; Li, J.; Liu, J. Electrochemical codeposition of graphene platelets and nickel for improved corrosion resistant properties. *RSC Adv.* **2014**, *4*, 36245. [[CrossRef](#)]
39. Rai, P.K.; Shekhar, S.; Mondal, K. Development of gradient microstructure in mild steel and grain size dependence of its electrochemical response. *Corros. Sci.* **2018**, *138*, 85–95. [[CrossRef](#)]
40. Lin, Y.; Liu, G.; Chen, M.-S.; Huang, Y.-C.; Chen, Z.-G.; Ma, X.; Jiang, Y.-Q.; Li, J. Corrosion resistance of a two-stage stress-aged Al–Cu–Mg alloy: Effects of stress-aging temperature. *J. Alloys Compd.* **2016**, *657*, 855–865. [[CrossRef](#)]
41. Cai, C.; Song, R.; Wang, L.; Li, J. Surface corrosion behavior and reaction product film deposition mechanism of Mg–Zn–Zr–Nd alloys during degradation process in Hank’s solution. *Surf. Coatings Technol.* **2018**, *342*, 57–68. [[CrossRef](#)]
42. Jin, W.; Wu, G.; Feng, H.; Wang, W.; Zhang, X.; Chu, P.K. Improvement of corrosion resistance and biocompatibility of rare-earth WE43 magnesium alloy by neodymium self-ion implantation. *Corros. Sci.* **2015**, *94*, 142–155. [[CrossRef](#)]
43. Wu, P.-P.; Xu, F.-J.; Deng, K.-K.; Han, F.-Y.; Zhang, Z.-Z.; Gao, R. Effect of extrusion on corrosion properties of Mg–2Ca– $\chi$ Al ( $\chi = 0, 2, 3, 5$ ) alloys. *Corros. Sci.* **2017**, *127*, 280–290. [[CrossRef](#)]
44. Wu, G.; Feng, K.; Shanaghi, A.; Zhao, Y.; Xu, R.; Yuan, G.; Chu, P.K. Effects of surface alloying on electrochemical corrosion behavior of oxygen-plasma-modified biomedical magnesium alloy. *Surf. Coatings Technol.* **2012**, *206*, 3186–3195. [[CrossRef](#)]
45. Xu, R.; Shen, Y.; Zheng, J.; Wen, Q.; Li, Z.; Yang, X.; Chu, P. Effects of one-step hydrothermal treatment on the surface morphology and corrosion resistance of ZK60 magnesium alloy. *Surf. Coat. Technol.* **2016**, *206*, 3186–3195. [[CrossRef](#)]
46. Chen, Y.; Wang, X.; Li, J.; Lu, J.; Wang, F. Long-term anticorrosion behaviour of polyaniline on mild Steel. *Corros. Sci.* **2007**, *49*, 3052–3063. [[CrossRef](#)]
47. Jin, W.; Wang, G.; Lin, Z.; Feng, H.; Li, W.; Peng, X.; Qasim, A.M.; Chu, P.K. Corrosion resistance and cytocompatibility of tantalum-surface-functionalized biomedical ZK60 Mg alloy. *Corros. Sci.* **2017**, *114*, 45–56. [[CrossRef](#)]
48. Park, J.; Lee, G.; Nishikata, A.; Tsuru, T. Anticorrosive behavior of hydroxyapatite as an environmentally friendly pigment. *Corros. Sci.* **2002**, *44*, 1087–1095. [[CrossRef](#)]
49. Liu, L.; Li, Y.; Wang, F. Electrochemical Corrosion Behavior of Nanocrystalline Materials—A Review. *J. Mater. Sci. Technol.* **2010**, *26*, 1–14. [[CrossRef](#)]
50. Yao, Y.; Zhou, Y. Effects of deep cryogenic treatment on wear resistance and structure of GB 35CrMoV steel. *Metals* **2018**, *8*, 502. [[CrossRef](#)]
51. Zhang, H.; Li, X.; Du, C.; Qi, H.; Huang, Y. Raman and IR spectroscopy study of corrosion products on the surface of the hot-dip galvanized steel with alkaline mud adhesion. *J. Raman Spectrosc.* **2009**, *40*, 656–660. [[CrossRef](#)]
52. Eliyan, F.F.; Alfantazi, A. Corrosion of the Heat-Affected Zones (HAZs) of API-X100 pipeline steel in dilute bicarbonate solutions at 90 °C—An electrochemical evaluation. *Corros. Sci.* **2013**, *74*, 297–307. [[CrossRef](#)]
53. Kimura, M.; Kihira, H.; Ohta, N.; Hashimoto, M.; Senuma, T. Control of Fe (O,OH)<sub>6</sub> nano-network structures of rust for high atmospheric-corrosion resistance. *Corros. Sci.* **2005**, *47*, 2499–2509. [[CrossRef](#)]
54. Hao, X.; Su, P.; Xiao, K. Effect of different NaCl concentration on corrosion products of weathering steel. *Corros. Prot.* **2009**, *30*, 297–299.
55. Fu, A.; Cheng, Y. Characterization of corrosion of X65 pipeline steel under disbonded coating by scanning Kelvin probe. *Corros. Sci.* **2009**, *51*, 914–920. [[CrossRef](#)]
56. Li, Y.; Wang, F.; Liu, G. Grain Size Effect on the Electrochemical Corrosion Behavior of Surface Nanocrystallized Low-Carbon Steel. *Corrosion* **2004**, *60*, 891–896. [[CrossRef](#)]
57. Yamashita, M.; Miyukia, H.; Matsudaa, Y.; Naganoa, H.; Misawa, T. The long Term Growth of The Protective Rust Layer Formed on Weathering Steel by Atmospheric Corrosion during a Quarter of a Century. *Corros. Sci.* **1994**, *2*, 283. [[CrossRef](#)]
58. Misawa, T.; Asami, K.; Hashimoto, K.; Shimodaira, S. The mechanism of atmospheric rusting and the protective amorphous rust on low alloy steel. *Corros. Sci.* **1974**, *14*, 279–289. [[CrossRef](#)]
59. Wang, X. Effect of ultrafine grain boundary on corrosion resistance of metals. *Corros. Pro.* **2015**, *36*, 695–699.

60. Lin, Y.; Jiang, Y.-Q.; Zhang, X.-C.; Deng, J.; Chen, X.-M. Effect of creep-aging processing on corrosion resistance of an Al–Zn–Mg–Cu alloy. *Mater. Des.* **2014**, *61*, 228–238. [[CrossRef](#)]
61. Lin, Y.; Jiang, Y.; Xia, Y.; Zhang, X.; Zhou, H.; Deng, J. Effects of creep-aging processing on the corrosion resistance and mechanical properties of a typical Al-Cu-Mg alloy. *Mater. Sci. Eng. A* **2014**, *605*, 192–202. [[CrossRef](#)]



© 2019 by the authors. Licensee MDPI, Basel, Switzerland. This article is an open access article distributed under the terms and conditions of the Creative Commons Attribution (CC BY) license (<http://creativecommons.org/licenses/by/4.0/>).

Article

# Corrosion Characteristics of Copper-Added Austempered Gray Cast Iron (AGCI)

Asiful H. Sheikh <sup>1,\*</sup>, Amit Sarkar <sup>2</sup>, Jitendra Kumar Singh <sup>3,\*</sup>, Sohail M. A. Khan Mohammed <sup>4</sup>, Nabeel Alharthi <sup>1,5</sup> and Manojit Ghosh <sup>6</sup>

<sup>1</sup> Centre of Excellence for Research in Engineering Materials, King Saud University, Riyadh 11421, Saudi Arabia; alharthi@ksu.edu.sa

<sup>2</sup> Department of Metallurgical and Materials Engineering, Jadavpur University, Kolkata 700032, India; amitsarkar553@gmail.com

<sup>3</sup> Department of Architectural Engineering, Hanyang University, Ansan 15588, Korea

<sup>4</sup> Department of Mechanical and Industrial Engineering, Ryerson University, Toronto, ON M5B 2K3, Canada; sohailmazher5@gmail.com

<sup>5</sup> Mechanical Engineering Department, College of Engineering, King Saud University, Riyadh 11421, Saudi Arabia

<sup>6</sup> Department of Metallurgy and Materials Engineering, Indian Institute of Engineering Science and Technology, Shibpur 711103, India; manojit\_ghosh1@rediffmail.com

\* Correspondence: aseikh@ksu.edu.sa (A.H.S.); jk200386@hanyang.ac.kr (J.K.S.); Tel.: +96-61-467-0760 (A.H.S.); +82-31-436-8159 (J.K.S.)

Received: 16 January 2019; Accepted: 2 February 2019; Published: 6 February 2019

**Abstract:** The aim of this investigation was to assess the corrosion behavior of gray cast iron (GCI) alloyed with copper. Alloyed GCI specimens were austempered isothermally at varying temperatures. After austenitizing at 927 °C, the samples were austempered at different temperatures ranging from 260 to 385 °C with an interval of 25 °C for 60 min. As a result, these samples developed an ausferrite matrix with different percentages of austenite. The resulting microstructures were evaluated and characterized by optical microscope (OM), scanning electron microscope (SEM), and X-ray diffraction (XRD). The corrosion characteristics were determined using potentiodynamic polarization tests and electrochemical impedance spectroscopy (EIS) of these samples. These tests were carried out in a medium of 0.5 M H<sub>2</sub>SO<sub>4</sub> and 3.5% NaCl solution. It was observed from the potentiodynamic polarization results that with increasing austempering temperature, the corrosion rate decreased. All results of the EIS were in accordance with a constant phase element (CPE) model. It was found that with an increase in austempering temperature, the polarization resistance ( $R_p$ ) increased. The austenite content was also found to influence the corrosion behavior of the austempered gray cast iron (AGCI).

**Keywords:** austempered gray cast iron; austempering temperature; microstructure; potentiodynamic polarization; electrochemical impedance spectroscopy

## 1. Introduction

Gray cast iron (GCI) is a potential engineering material, which has a diverse range of applications including use in sophisticated automotive parts [1]. The wide applications of GCI are possible due to its unique properties such as good thermal conductivity, relatively low melting temperature, high damping capacity, and excellent castability [1,2]. The damage of the GCI components at the exterior parts through electrochemical corrosion has been the predominant restricting mechanism against enhancing its life span [3]. The presence of graphitization is a distinguishing feature of the deterioration properties of GCI [3,4]. Attempts have been made to combat the problem of corrosion

with the help of alloying additions with the aim of modifying the microstructure from ferrite to fine pearlite. It is also pertinent to mention that Si plays an important role in controlling the corrosion behavior of GCI: The higher the Si content, the higher the corrosion resistance [5]. Additionally, it is well known that single-phase microstructures like austenite, ferrite, and martensite perform better in corrosive media compared to two-phase mixtures like bainite, pearlite, and tempered martensite [6].

Several researchers [7–10] have tried to assess the effect of heat treatment and composition on the microstructure and corrosion behavior of austempered ductile iron (ADI). Prasanna et al. [7] and Banerjee et al. [8] studied the effect of the austempering treatment on the microstructure and corrosion properties of ductile iron. They found that both mechanical properties and corrosion resistance were enhanced due to the austempering of cast iron. Afolabi et al. [9] observed that the austempering temperature and time influenced the microstructure of the ductile iron, and thus its corrosion behavior was affected by the compositional structures. Hsu and Chen [10] concluded that the enhancement of corrosion resistance in ADI was due to the presence of retained austenite as a result of austempering. Similar studies with GCI are also common where the corrosion resistance and the mechanical properties were improved dramatically by tailoring the heat treatment pattern (tempering, austempering, and quenching [11–14]) and by alloy additions [8]. Further improvement of the mechanical properties, compared to those of conventional GCI, was observed in austempered gray cast iron (AGCI) due to the formation of a matrix of ausferritic structures (ferrite and stabilized austenite) or bainitic ferrite during austempering [12,15]. Thus, the domain of applicability of AGCI is even wider than that of GCI due to its favorable combination of enhanced mechanical properties [11–15] and improved wear characteristics [15–17]. The present literature, however, is lacking in reporting the corrosion behavior of AGCI, although a lot of work can be found on testing the corrosion behavior of ADI [7–10].

The above scientific observations indicated the necessity of the present investigation into the effect of austempering temperatures on the microstructure and corrosion behaviors of copper-alloyed AGCI, in order to establish a correlation between them.

## 2. Materials and Methods

### 2.1. Sample Preparation

Samples of GCI were prepared from cupola melts in a production foundry. The molten metal, at a temperature of 1420 °C was inoculated with 0.25 wt. % of FeSi-based inoculants in the cupola. During tapping, 0.5% Cu pieces of electrolyte grade were added to the metal stream for the sake of alloying. The specimens were cast in the form of standard 30-mm Y-shaped blocks in sand molds as shown in Figure 1a. Corrosion test coupons (Figure 1b) of suitable size ( $\Phi$  10 mm  $\times$  10 mm) were machined from the as-cast Y blocks. The uniform distribution of fine type-A graphite flakes is promoted by the inoculants during solidification [18]. Cu is soluble in austenite and increases the hardness, strength, corrosion resistance, and transformation time for the austempering process [19,20]. Cu has been accepted as an affordable alloying element for several engineering applications. As a result, the replacement of expensive Ni by Cu may become more prevalent. The final chemical composition (wt. %) of GCI was determined using a spectroscopy spark analyzer as shown in Table 1.

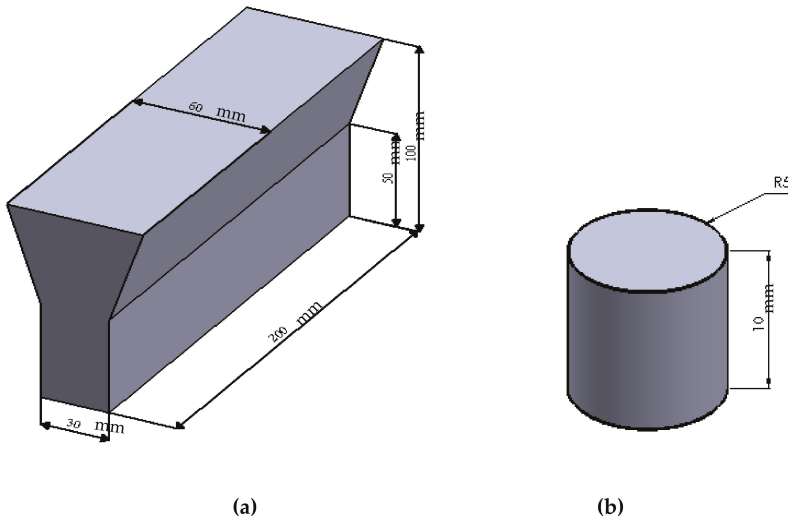


**Figure 1.** (a) Dimension (mm) of the Y-block casting and (b) schematic of the corrosion test piece ( $\Phi$  10 mm  $\times$  10 mm).

**Table 1.** Chemical composition of GCI (wt. %).

Element	C	Si	Mn	P	S	Cu	Fe
Composition	3.46	2.27	0.53	0.019	0.01	0.50	Bal.

2.2. Heat Treatment of Samples

The samples were initially heated to an austenitizing temperature ( $T_{\gamma} = 927\text{ }^{\circ}\text{C}$ ) and held for 60 min in order to develop a fully austenitic structure ( $\gamma$ ). The samples were then rapidly cooled in a molten salt bath comprising 53%  $\text{KNO}_3$ , 40%  $\text{NaNO}_2$ , and 7%  $\text{NaNO}_3$  at six different austempering temperatures ( $T_A$ ), 260, 285, 310, 335, 360, and 385  $^{\circ}\text{C}$ , for 60 min followed by air cooling to complete the phase transformation. Figure 2a schematically represents the entire heat treatment schedule for the austempering process and Figure 2b is the corresponding continuous cooling transformation (CCT) diagram.

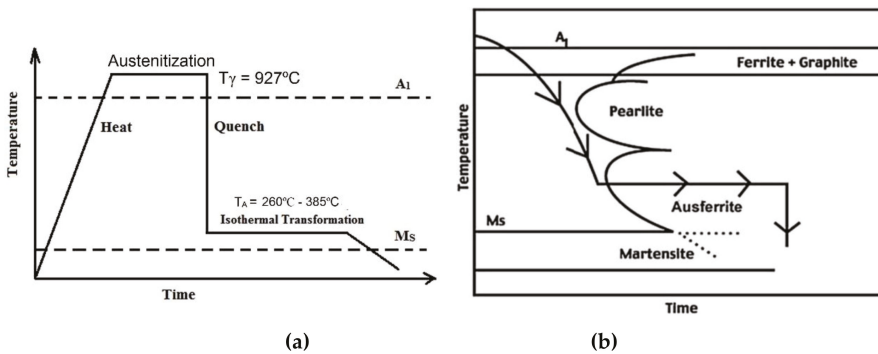


**Figure 2.** Schematic diagram of (a) heat treatment schedule for austempering and (b) CCT diagram for the proposed composition.



### 2.3. Metallography and X-ray Diffraction (XRD)

Samples were prepared for metallographic observation using standard polishing techniques. Moreover, the samples were etched using a 2% nital solution for observation under a scanning electron microscope (SEM, JSM 6360, Jeol techniques, Tokyo, Japan). The volume fractions of austenite were calculated by X-ray diffraction (XRD,) analysis as described by Dasgupta et al. [21]. The XRD data were collected using a Rigaku, Ultima III diffractometer (Japan) with a monochromatic copper Fe-K $\alpha$  radiation (1.54 Å) at 40 kV and 30 mA. Scanning was done at a rate of 1°/min from 30 to 90° to observe the peaks, which were later analyzed using Jade 7 software (7.1.08). The peak positions were analyzed for the (111), (220), and (311) planes of austenite (FCC) and the (110), (200), and (211) planes of ferrite (BCC). The carbon content in austenite ( $C_\gamma$ ) at various austempering temperatures was calculated using the following equation:

$$C_\gamma = \frac{a_\gamma - 3.548}{0.044}, \quad (1)$$

where  $a_\gamma$  is the lattice parameter calculated from the angular position of the austenite peak [22].

### 2.4. Electrochemical (Corrosion) Test

The heat-treated samples were subjected to electrochemical measurements in a 0.5 M H<sub>2</sub>SO<sub>4</sub> and 3.5% NaCl solution at 25 °C ( $\pm 2$  °C). The electrochemical studies were performed in a triplicate set of samples to obtain reproducible results. A cell composed of three electrodes was created, including a graphite one, which acts as a counter electrode; a saturated calomel electrode (SCE), which acts as a reference electrode; and the GCI sample which acts as the working electrode (WE), for potentiodynamic polarization and electrochemical impedance spectroscopy (EIS) measurements. The WE area was fixed at 1 cm<sup>2</sup>. Prior to the tests, the samples were ground and polished using SiC papers of 2500 grit size and rinsed in deionized water followed by immersion in the solution for 30 min in order to stabilize the open circuit potential value. The potentiodynamic polarization tests were carried out from  $-1.0$  to  $+1.0$  V at a scan rate of 1 mV/s, whereas, EIS tests were performed over a frequency ranging from 100 kHz to 0.01 Hz.

## 3. Results and Discussion

### 3.1. Microstructure and XRD Analysis

Figure 3a,b shows the optical and SEM microstructures of the as-cast gray iron sample, respectively. The matrix of as-cast gray iron is primarily composed of pearlite besides some randomly distributed ferrite. The as-cast specimens were austempered for 60 min and the resulting changes in the microstructure are presented in Figures 4a–f and 5a–f using an optical microscope (OM) and SEM, respectively. The dark, etched needle-like structures represent bainitic ferrite, while the brighter ones represent a mixture of austenite and bainitic ferrite. We can see that the effect of the austempering temperature on the microstructure of austempered irons was significant. It was observed that at lower temperatures (i.e., 260–285 °C), very fine needles of bainitic ferrite and austenite were formed and the volume fraction of ferrite was larger. As the austempering temperature increased, the needles of the bainitic ferrite were coarsened along with an increase in the austenite content. Similar observations in ADI were earlier reported by Patutunda et al. [23] and Yang et al. [24].

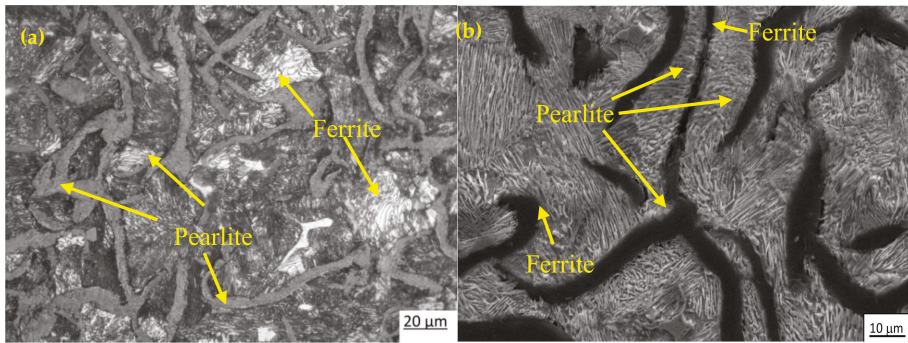


Figure 3. Micrographs of as-cast specimens: (a) optical micrograph and (b) SEM image.

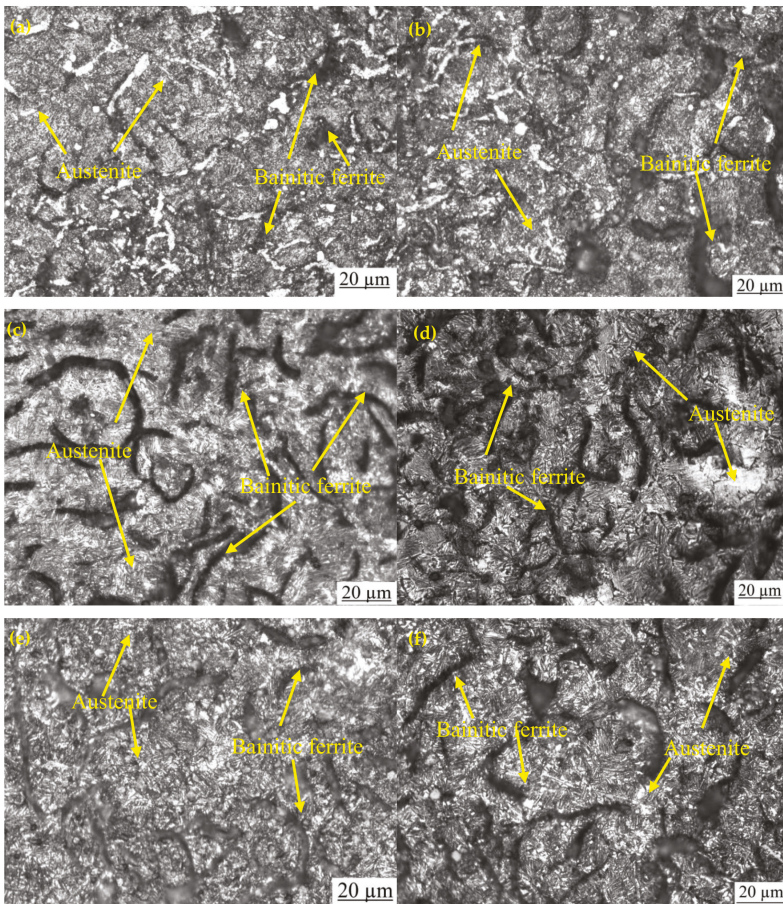
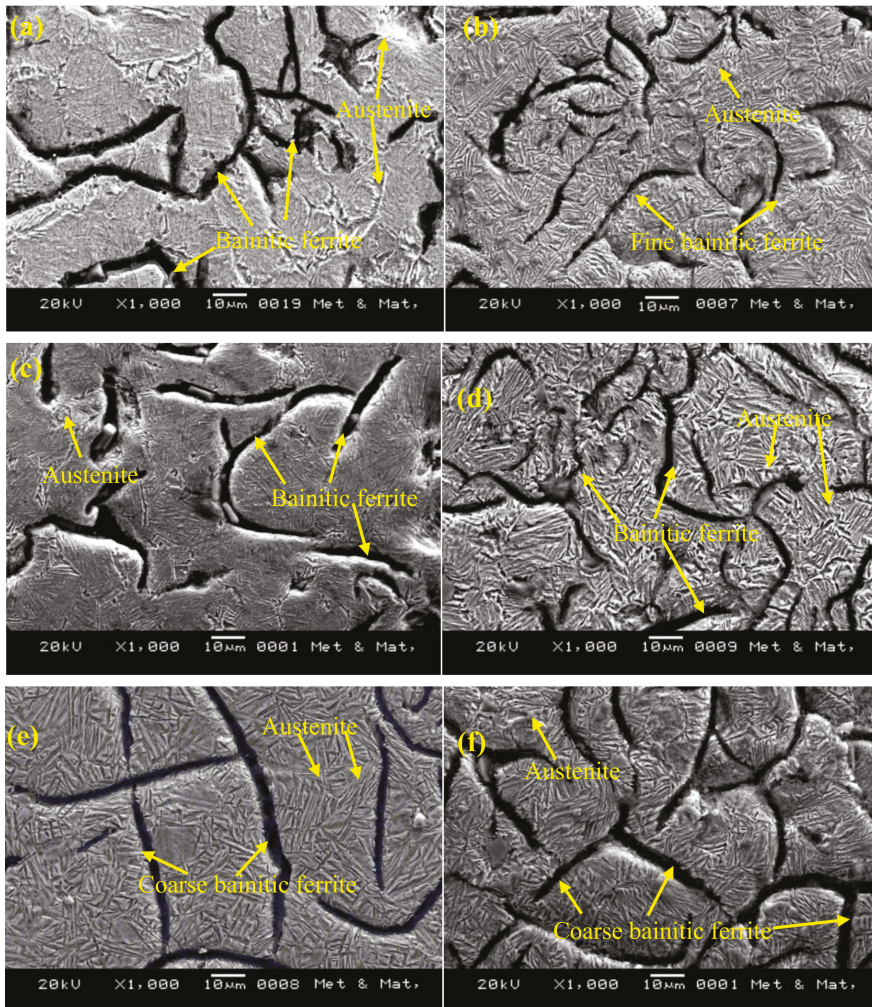


Figure 4. Optical micrographs of samples austempered for 60 min at (a) 260 °C, (b) 285 °C, (c) 310 °C, (d) 335 °C, (e) 360 °C, and (f) 385 °C.



**Figure 5.** SEM images of samples austempered for 60 min at (a) 260 °C, (b) 285 °C, (c) 310 °C, (d) 335 °C, (e) 360 °C, and (f) 385 °C.

Figure 6 presents the quantitative analysis of the XRD pattern. It is evident from the figure that the austempering temperature has a significant effect on the XRD patterns. It was seen that with changing heat treatment temperature, the amount of austenite was changed. The phases detected include ferrite and austenite. Figure 7 shows the volume fraction of austenite and the carbon content of austenite in the AGCI samples as a function of different austempering temperatures. The volume fraction of austenite was calculated by Jade7 software built in the XRD. It may be noted from Figure 7 that the austenite content increases with an increase in the austempering temperature. Greater supercooling at a lower austempering temperature resulted in finer ferrite and austenite as also reported by Patutunda et al. [23]. It is well known that the transformation reaction is more likely to be controlled by the nucleation process rather than growth [23,24]. During the process, it is necessary that the carbon must diffuse into austenite through the ferrite zone. At higher austempering temperatures a quite contrasting mechanism prevails due to lower supercooling which makes the nucleation of ferrite slower. This leads to the stabilization of more austenite in addition to incrementing the rate

of diffusion of carbon which leads to the formation of coarse ferrite. Thus, the volume fraction of austenite increases with the increase in austempering temperature.

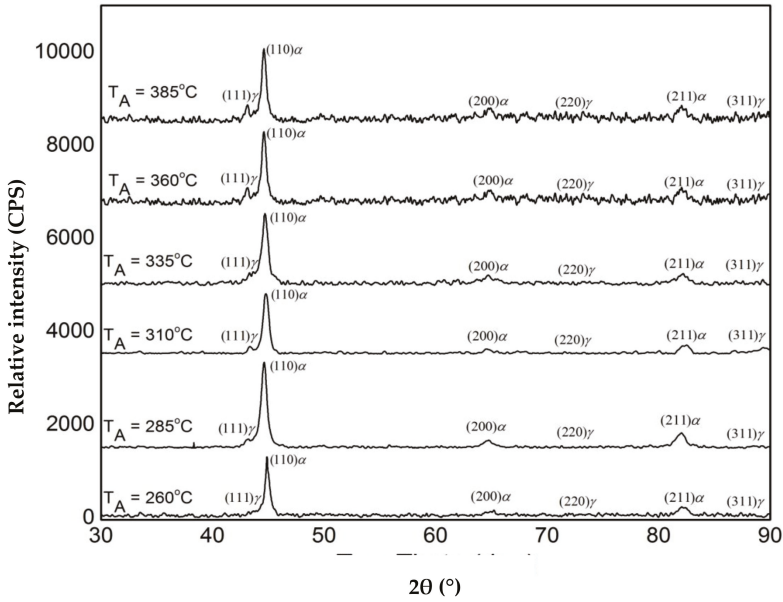


Figure 6. XRD phase analysis of austempered gray cast iron (AGCI) for different austempering temperatures held for 60 min (a) 260 °C, (b) 285 °C, (c) 310 °C, (d) 335 °C, (e) 360 °C, and (f) 385 °C.

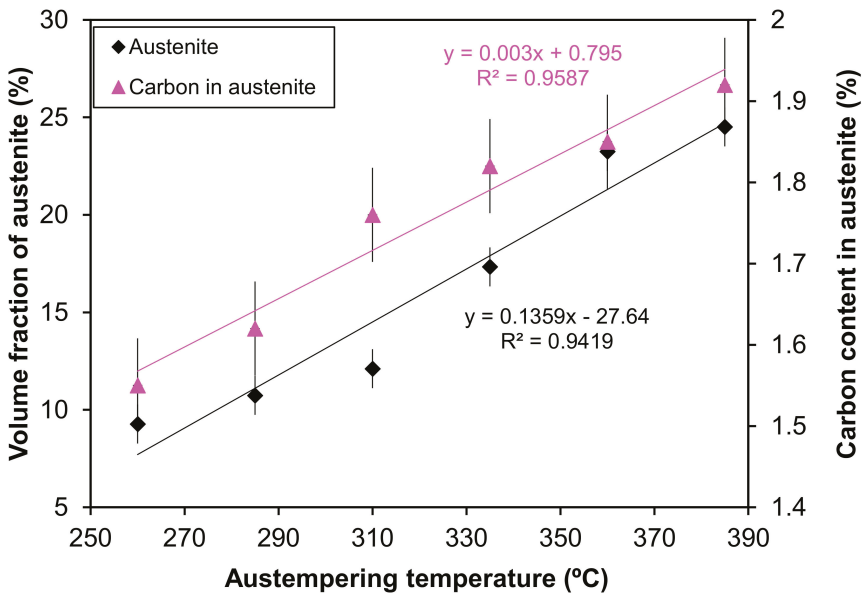


Figure 7. The influence of different austempering temperatures on the volume fraction of austenite and the carbon content of austenite.

3.2. Electrochemical Behavior of As-Cast Gray Iron and AGCI in Different Solutions

The results of potentiodynamic polarization studies of the as-cast gray iron and the AGCI are shown in Figures 8 and 9. The corrosion of iron in neutral 3.5% NaCl solution occurs according to the following equations,

Anodic reaction:

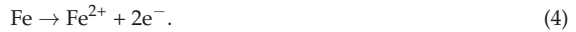


Cathodic reaction:



When iron is in contact with dilute sulfuric acid (0.5 M H<sub>2</sub>SO<sub>4</sub>), an immediate attack on the metal takes place with the formation of hydrogen gas and ferrous ions, as shown in Equations (4) and (5).

Anodic reaction:



Cathodic reaction:



The electrochemical parameters are extracted after the extrapolation of the potentiodynamic plots in a Tafel slope. From Figure 7 it is revealed that with increasing austempering temperature, the percentage of austenite increased while the corrosion current density ( $I_{\text{corr}}$ ) decreased and the corrosion potential ( $E_{\text{corr}}$ ) shifted to the cathodic side (Tables 2 and 3). Austenite acts as an anode and ferrite acts as a cathode. The galvanic corrosion is proportional to the cathodic/anodic area. Consequently, with increasing temperature, the austenite percentage increases with a simultaneous decrease in the ferrite percentage. Thus, due to the microstructural homogeneities, distinct localized anodic and cathodic microstructural areas develop, which act as micro-electrochemical cells in the presence of an electrolyte. Thus, the galvanic corrosion decreases in both solutions. From Tables 2 and 3, it can be seen that among the two corrosive mediums, 1 N H<sub>2</sub>SO<sub>4</sub> is more corrosive in all cases.

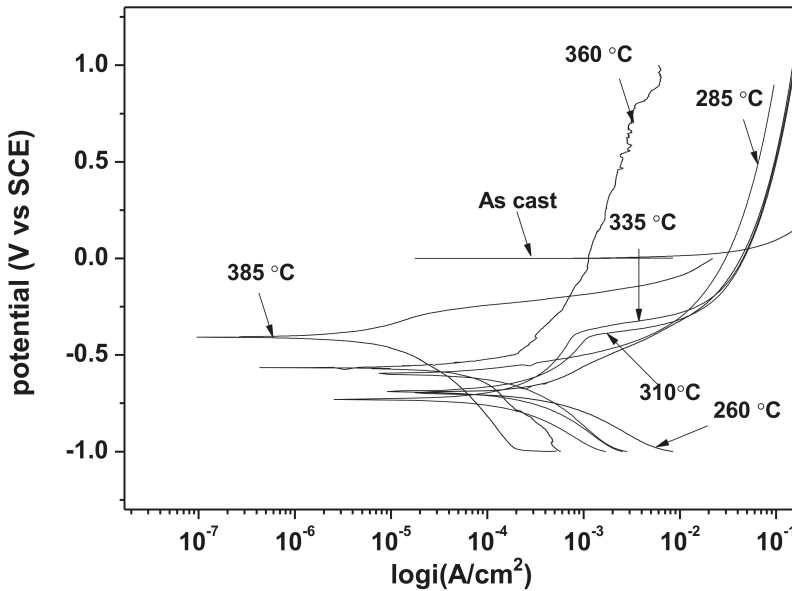


Figure 8. Potentiodynamic polarization curves in 3.5% NaCl solution.

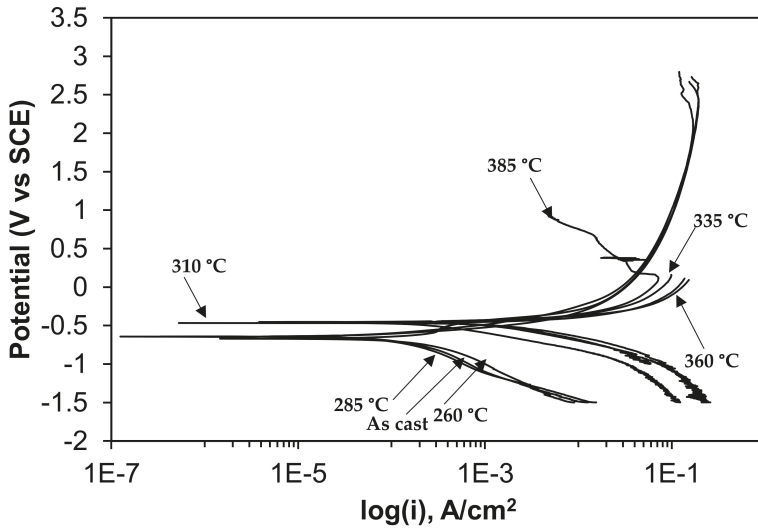


Figure 9. Potentiodynamic polarization curves in 0.5 M H<sub>2</sub>SO<sub>4</sub> solution.

Table 2. Potentiodynamic polarization results in 3.5% NaCl.

Sample Condition	I <sub>corr</sub> (μA/cm <sup>2</sup> )	E <sub>corr</sub> (V)
Austempering Temperature (°C)	-	-
As-cast gray iron	70	-0.80
927 °C–260 °C	62	-0.75
927 °C–285 °C	54	-0.70
927 °C–310 °C	42	-0.62
927 °C–335 °C	30	-0.50
927 °C–360 °C	16	-0.45
927 °C–385 °C	7	-0.40

Table 3. Potentiodynamic polarization results in 1 N H<sub>2</sub>SO<sub>4</sub>.

Sample Condition	I <sub>corr</sub> (μA/cm <sup>2</sup> )	E <sub>corr</sub> (V)
Austempering Temperature (°C)	-	-
As-cast gray iron	150	-0.60
927 °C–260 °C	130	-0.55
927 °C–285 °C	110	-0.50
927 °C–310 °C	98	-0.48
927 °C–335 °C	90	-0.42
927 °C–360 °C	82	-0.38
927 °C–385 °C	65	-0.36

Nyquist plots of samples exposed to 3.5% NaCl and 0.5 M H<sub>2</sub>SO<sub>4</sub> solutions are shown in the Figures 10 and 11, respectively. All plots show a depressed semicircle pattern in the whole frequency range, indicating that only one time constant exists between the interface of the solid electrode and the solution. Due to the low impedance value at the lower austempering temperature, the Nyquist plots become suppressed. The corresponding plots are shown in the insets of Figures 10 and 11 for exposure to 3.5% NaCl and 0.5 M H<sub>2</sub>SO<sub>4</sub> solutions, respectively. All the EIS data match well in a constant phase element (CPE) model. In a CPE model, R<sub>s</sub> is the solution resistance, R<sub>p</sub> is the polarization resistance, and Y<sub>0</sub> is the admittance. The inserted equivalent circuit shown in Figure 12 was used to fit the EIS

data, and the fitted polarization resistance ( $R_p$ ) data are shown in Tables 4 and 5 for 3.5% NaCl and 0.5 M  $H_2SO_4$  solution, respectively. It is known that the diameter of the Nyquist plot represents the  $R_p$ . It is also well known that the  $R_p$  is inversely proportional to the corrosion rate. With increasing austempering temperature, the diameter of the Nyquist plot increases with a consequent increase in the  $R_p$ . It is also seen from Tables 4 and 5 with the error bar (maximum  $\pm 7\%$ ) that the  $R_p$  is higher in 3.5% NaCl solution (Table 4) than it is in 0.5 M  $H_2SO_4$  solution (Table 5) for all cases.

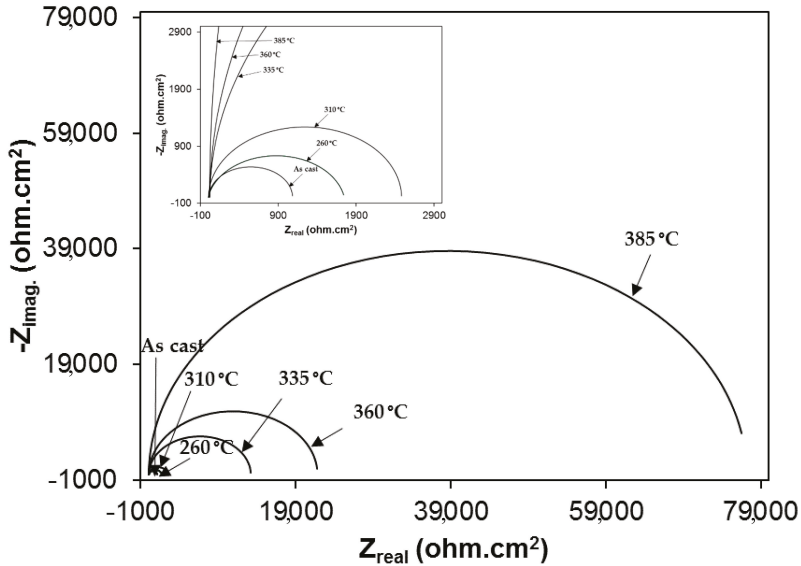


Figure 10. Electrochemical impedance spectroscopy (Nyquist plot) in 3.5% NaCl solution.

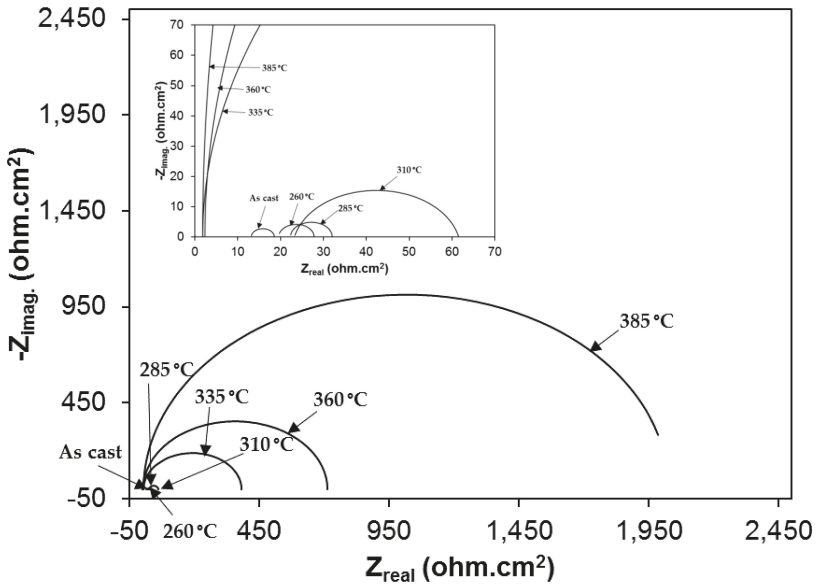


Figure 11. Cont.

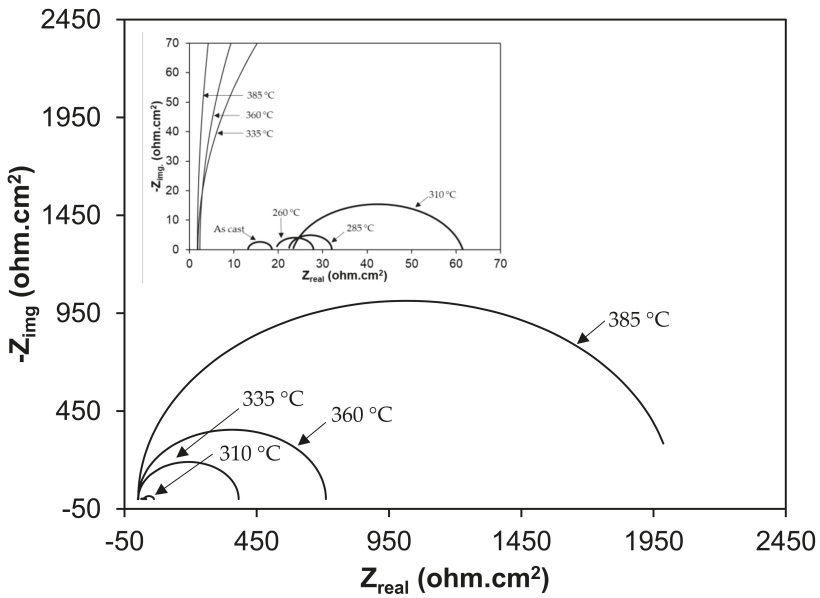


Figure 11. Electrochemical impedance spectroscopy (Nyquist plot) in 1 N H<sub>2</sub>SO<sub>4</sub> solution.

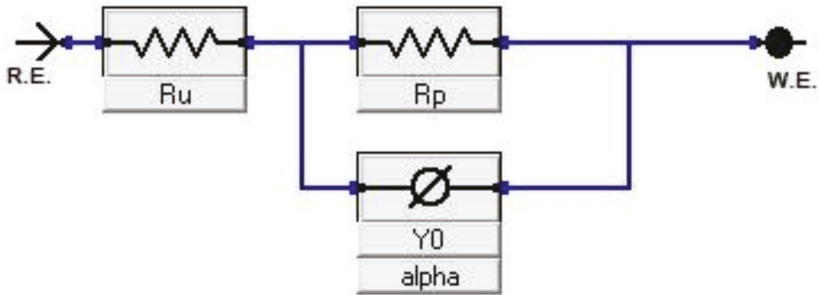


Figure 12. Equivalent circuit of electrochemical impedance spectroscopy (EIS).

Table 4. Electrochemical impedance spectroscopy results in 3.5% NaCl solution.

Sample Condition	R <sub>p</sub> (ohm.cm <sup>2</sup> )
Austempering Temperature (°C)	-
As-cast gray iron	930 (± 46)
927 °C–260 °C	1850 (± 91)
927 °C–310 °C	2550 (± 102)
927 °C–335 °C	15,000 (± 450)
927 °C–360 °C	20,000 (± 1100)
927 °C–385 °C	80,000 (± 1600)



**Table 5.** Electrochemical impedance spectroscopy results in 0.5 M H<sub>2</sub>SO<sub>4</sub> solution.

Sample Condition	R <sub>p</sub> (ohm.cm <sup>2</sup> )
<b>Austempering Temperature (°C)</b>	-
As-cast gray iron	20 (± 1)
927 °C–260 °C	28 (± 1)
927 °C–285 °C	32 (± 2)
927 °C–310 °C	62 (± 2)
927 °C–335 °C	450 (± 13)
927 °C–360 °C	700 (± 28)
927 °C–385 °C	2000 (± 85)

### 3.3. Effect of Austenite Content on Corrosion Behavior

Figures 13 and 14 show the plots of I<sub>corr</sub> obtained from the potentiodynamic polarization diagram against the volume fraction of the austenite for 3.5% NaCl and 1 N H<sub>2</sub>SO<sub>4</sub>, respectively. It was observed that with the increasing volume fraction of austenite, the corrosion rate decreased linearly to a sufficient extent in both cases. The linear fit regression value was 0.95 for 3.5% NaCl solution (Figure 13) and 0.84 for 1N H<sub>2</sub>SO<sub>4</sub> solution (Figure 14). A regression value close to 1 means the corrosion rate changes linearly with increasing austenite content.

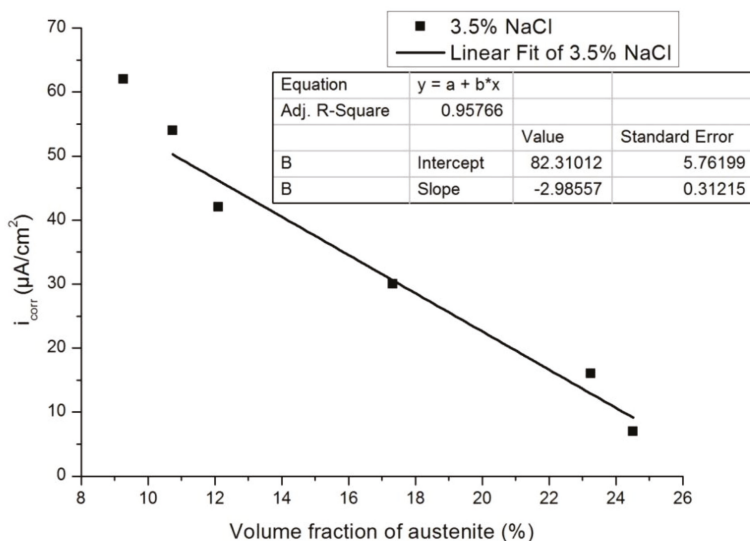


**Figure 13.** Influence of the volume fraction of the austenite on corrosion rate in 3.5% NaCl.

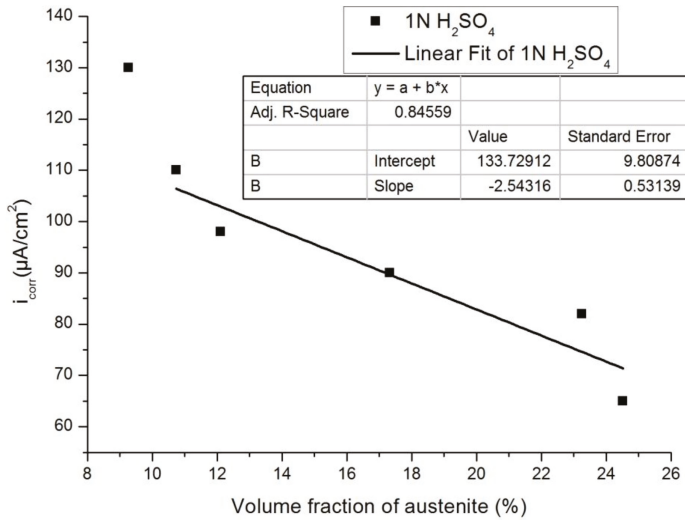


Figure 14. Influence of the volume fraction of the austenite on the corrosion rate in 0.5 M H<sub>2</sub>SO<sub>4</sub>.

### 3.4. Microstructure after Corrosion

#### 3.4.1. Optical Images after Corrosion in 3.5% NaCl Solution

Figure 15 shows the OM of as-cast gray iron and AGCI samples dipped in 3.5% NaCl solution. The corrosion products consist of compact structures. It is seen that compactness increases with increasing austempering temperature. It was also observed that in optical images of as-cast gray iron (Figure 15a) with a lower austempering temperature (260 °C and 285 °C), an exfoliation type pattern was present with smaller flake graphite. With increasing austempering temperature (310 °C and above), the exfoliation type pattern disappeared with bigger flake graphite. In addition, intergranular type corrosion was observed in the 3.5% NaCl solution. It is also seen that, in as-cast gray iron at a low austempering temperature, more pitting was seen. However, with increasing austempering temperature the pitting density decreased.

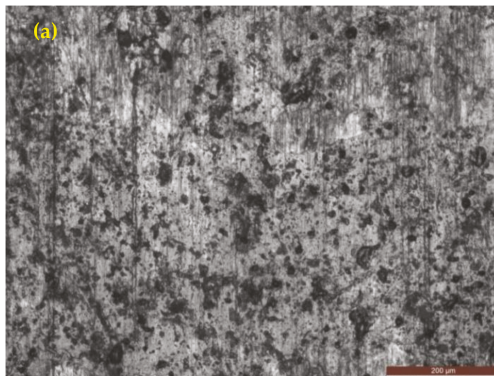
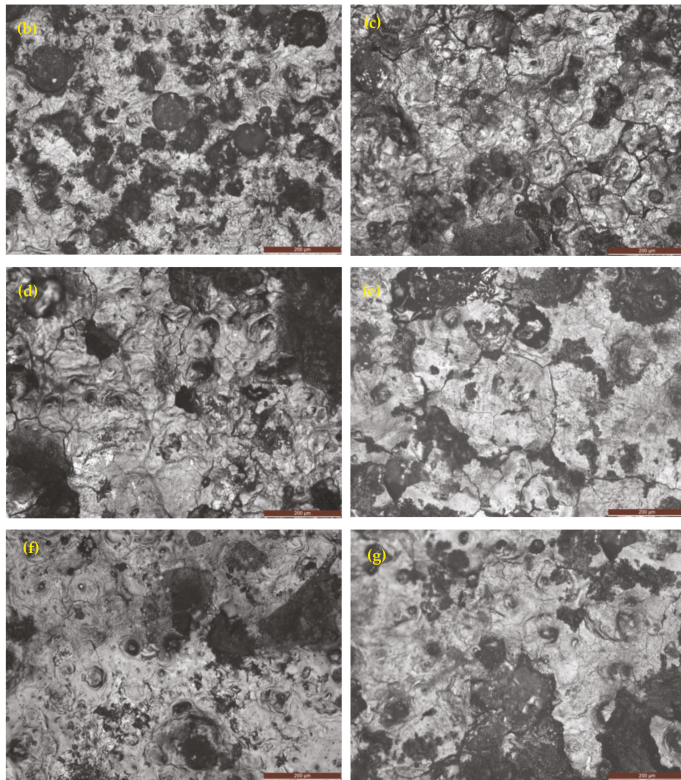


Figure 15. Cont.



**Figure 15.** Optical images of iron samples after a potentiodynamic polarization test in 3.5% NaCl solution. (a) As-cast gray iron; and AGCI at (b)  $T_{\gamma} = 927\text{ }^{\circ}\text{C}$ ,  $T_A = 260\text{ }^{\circ}\text{C}$ ; (c)  $T_{\gamma} = 927\text{ }^{\circ}\text{C}$ ,  $T_A = 285\text{ }^{\circ}\text{C}$ ; (d)  $T_{\gamma} = 927\text{ }^{\circ}\text{C}$ ,  $T_A = 310\text{ }^{\circ}\text{C}$ ; (e)  $T_{\gamma} = 927\text{ }^{\circ}\text{C}$ ,  $T_A = 335\text{ }^{\circ}\text{C}$ ; (f)  $T_{\gamma} = 927\text{ }^{\circ}\text{C}$ ,  $T_A = 360\text{ }^{\circ}\text{C}$ ; and (g)  $T_{\gamma} = 927\text{ }^{\circ}\text{C}$ ,  $T_A = 385\text{ }^{\circ}\text{C}$ .

### 3.4.2. Optical Images after Corrosion in 0.5 M $\text{H}_2\text{SO}_4$ Solution

Figure 16 shows the optical images (as-cast gray iron and AGCI) of corrosion products in 0.5 M  $\text{H}_2\text{SO}_4$  solution. It is seen that pitting formation decreased, with increasing austempering temperature. While with increasing austempering temperature, more metastable pits were formed. So it can be concluded that with increasing austempering temperature, pit formation gradually reduced. At the same temperature, compared to 3.5% NaCl solution, pitting density, radius of pits, and the flake graphite was larger in the case of 0.5 M  $\text{H}_2\text{SO}_4$  solution. It is also seen that more pits are formed in 1 N  $\text{H}_2\text{SO}_4$  than in 3.5% NaCl solution.

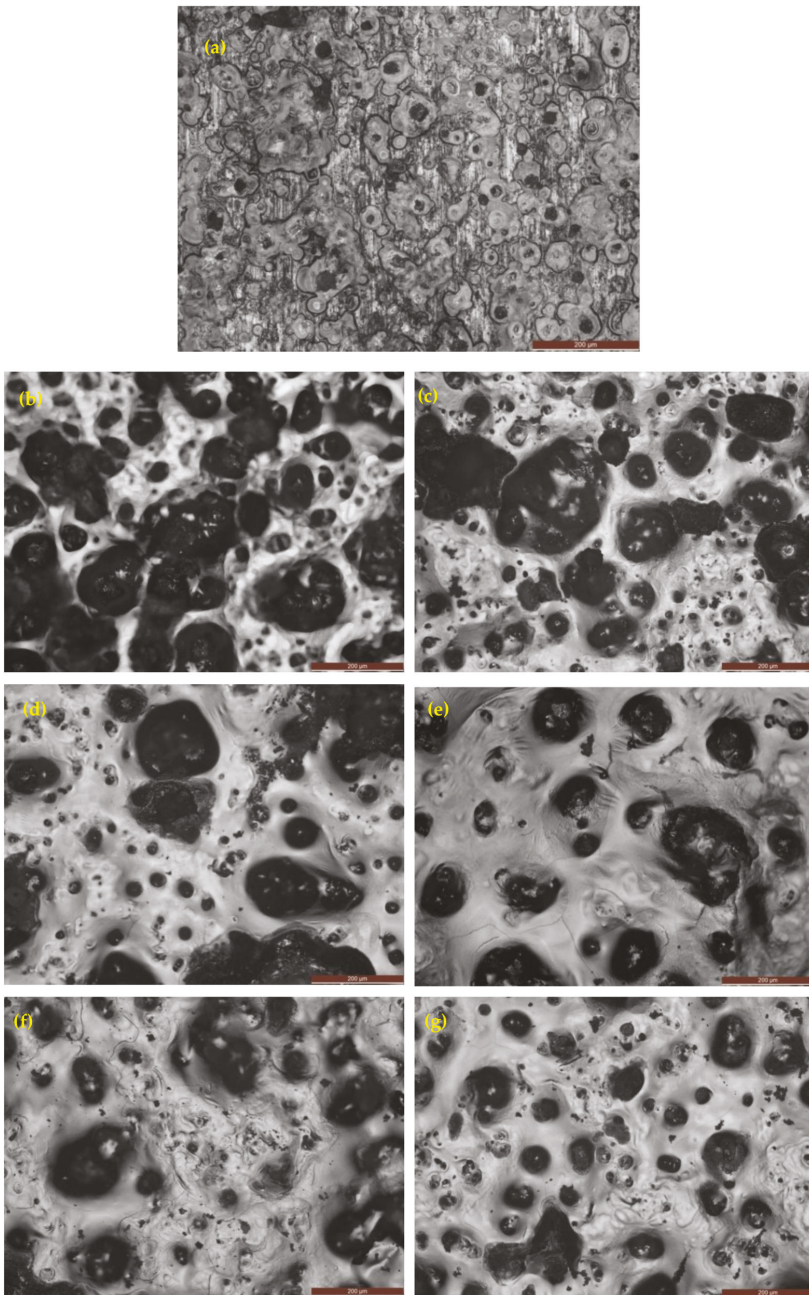


**Figure 16.** Optical images of iron samples after a potentiodynamic polarization test in 1 N H<sub>2</sub>SO<sub>4</sub> solution. (a) As-cast gray iron; and AGCI at (b) T<sub>γ</sub> = 927 °C, T<sub>A</sub> = 260 °C; (c) T<sub>γ</sub> = 927 °C, T<sub>A</sub> = 285 °C; (d) T<sub>γ</sub> = 927 °C, T<sub>A</sub> = 310 °C; (e) T<sub>γ</sub> = 927 °C, T<sub>A</sub> = 335 °C; (f) T<sub>γ</sub> = 927 °C, T<sub>A</sub> = 360 °C; and (g) T<sub>γ</sub> = 927 °C, T<sub>A</sub> = 385 °C.

#### 4. Conclusions

The following conclusions can be drawn from the present investigation:

(a) The microstructure of AGCI consists of special bainitic ferrite ( $\alpha$ ) and high-carbon austenite ( $\gamma$ ) which prevents corrosion. Thus, the corrosion-resistance susceptibility of AGCI is higher than that of as-cast gray iron.

(b) At higher austempering temperatures, the volume fraction of austenite increases with a consequent decrease in the corrosion rate.

(c) In the ausferrite matrix, the corrosion rate depends on the austenite content. An increase in the austenite content results in a decrease in the corrosion rate.

(d) Due to an increase in hydrogen generating reactions, 1 N H<sub>2</sub>SO<sub>4</sub> is more corrosive than 3.5% NaCl during exposure.

**Author Contributions:** Data curation: A.H.S. and M.G.; formal analysis: A.S., J.K.S., S.M.A.K.M. and M.G.; funding acquisition: A.H.S. and N.A.; methodology: A.H.S. and A.S.; project administration: A.H.S.; Supervision: A.H.S., S.M.A.K.M., and N.A.; validation: A.H.S., Amit Sarkar, and S.M.A.K.M.; writing—original draft: A.H.S., Amit Sarkar, J.K.S., S.M.A.K.M., N.A., and M.G.; Writing—review and editing: A.H.S., A.S., J.K.S., S.M.A.K.M., N.A. and M.G.

**Funding:** This research received no external funding.

**Acknowledgments:** The authors would like to extend their sincere appreciation to the Deanship of Scientific Research at King Saud University for its funding of this research through the Research Group Project No. RG-1439-029.

**Conflicts of Interest:** The authors declare no conflict of interest.

#### References

1. Khanna, O.P. *Foundry Technology*; Dhanpath Rai Publishers: New Delhi, India, 2011.
2. *ASM Hand Book, Properties and Selection: Irons, Steels, and High Performance Alloys*; ASM International: Geauga County, OH, USA, 1993.
3. Asadi, Z.S.; Melchers, R.E. Pitting corrosion of older underground cast iron pipes. *Corros. Eng. Sci. Technol.* **2017**, *52*, 459–469. [[CrossRef](#)]
4. Sami, A.A.; Saffa, M.H. Ductile and gray cast iron deterioration with time in various NaCl salt concentrations. *J. Eng. Technol.* **2008**, *26*, 1–15.
5. Rana, A.M.; Khan, A.; Amjad, S. Microstructure evaluation in heat treated cast irons. *J. Res. Sci.* **2001**, *12*, 65–71.
6. Muthukumarasamy, S.; Sadiq, B.A.; Sesham, S. High strength ductile irons-as cast bainitic ductile iron and austempered ductile iron. *Indian Foundry J.* **1992**, *8*, 23–29.
7. Prasanna, N.D.; Muralidhara, M.K.; Mohit, K.A. Mechanical properties and corrosion characteristics of IS400/12 grade ductile iron. In Proceedings of the Transactions of the 57th International Foundrymen Congress, Kolkata, India, 13–15 February 2009; pp. 89–95.
8. Banerjee, A.; Mitra, P.K.; Chattopadhyay, D.P. Effect of section thickness, 0.5% Cu addition and different austempering temperatures on the microstructure and corrosion properties of ADI. In Proceedings of the Transactions of 61st Indian Foundry Congress, Kolkata, India, 27–29 January 2013; pp. 1–3.
9. Afolabi, A.S. Effect of austempering temperature and time on corrosion behaviour of ductile iron in chloride and acidic media. *Anti-Corros. Methods Mater.* **2011**, *58*, 190–195. [[CrossRef](#)]
10. Hsu, C.-H.; Chen, M.-L. Corrosion behavior of nickel alloyed and austempered ductile irons in 3.5% sodium chloride. *Corros. Sci.* **2010**, *58*, 2945–2949. [[CrossRef](#)]
11. Kovacs, B.V.; Keough, J.R. Physical properties and application of austempered gray iron. *AFS Trans* **1993**, *93–141*, 283–291.
12. Hsu, C.H.; Shy, Y.H.; Yu, Y.H. Effect of austempering heat treatment on fracture toughness of copper alloyed gray iron. *Mater. Chem. Phys.* **2000**, *63*, 75–81. [[CrossRef](#)]
13. Rundman, K.B.; Parolini, J.R.; Moore, D.J. Relationship between tensile properties and matrix microstructure in austempered gray iron. *AFS Trans.* **2005**, *145*, 51–55.

14. Olawale, J.O.; Oluwaseguun, K.M.; Ezemenaka, D.I. Production of austempered gray iron (AGI) using forced air cooling. *Mater. Perform. Charact.* **2014**, *3*, 355–370. [[CrossRef](#)]
15. Sarkar, T.; Bose, P.K.; Sutradhar, G. Mechanical and Tribological Characteristics of Copper Alloyed Austempered Gray Cast Iron (AGI). *Mater. Today Proc.* **2018**, *5*, 3664–3673. [[CrossRef](#)]
16. Vadiraj, A.; Balachandran, G.; Kamaraj, M. Structure–property correlation in austempered alloyed hypereutectic gray cast irons. *Mater. Sci. Eng. A* **2010**, *527*, 782–788. [[CrossRef](#)]
17. Vadiraj, A.; Balachandran, G.; Kamaraj, M. Studies on mechanical and wear properties of alloyed hypereutectic gray cast irons in the as-cast pearlitic and austempered conditions. *Mater. Des.* **2010**, *31*, 951–955. [[CrossRef](#)]
18. Harvey, J.N.; Noble, G.A. Inoculation of cast irons—An overview. In Proceedings of the 55th Indian Foundry Congress, Agra, India, 2–4 February 2007; pp. 343–360.
19. Gorny, M.; Tyrala, E.; Lopez, H. Effect of copper and nickel on the transformation kinetics of austempered ductile iron. *J. Mater. Eng. Perform.* **2014**, *23*, 3505–3510. [[CrossRef](#)]
20. Bayati, H.; Elliott, R. The concept of an austempered heat treatment processing window. *Int. J. Cast Met. Res.* **1999**, *11*, 413–417. [[CrossRef](#)]
21. Dasgupta, R.K.; Mondal, D.K.; Chakrabarti, A.K. Evolution of microstructures during austempering of ductile irons alloyed with manganese and copper. *Metall. Mater. Trans. A* **2013**, *44*, 1376–1387. [[CrossRef](#)]
22. Bayati, H.; Elliott, R. Relationship between structure and mechanical properties in high manganese alloyed ductile iron. *Mater. Sci. Technol.* **1995**, *11*, 284–293. [[CrossRef](#)]
23. Patutunda, S.K. Development of austempered ductile iron (ADI) with simultaneous high yield strength and fracture toughness by a novel two-step austempering process. *Mater. Sci. Eng. A* **2001**, *315*, 70–80. [[CrossRef](#)]
24. Yang, J.; Putatunda, S.K. Improvement in strength and toughness of austempered ductile cast iron by novel two-step austempering process. *Mater. Des.* **2004**, *25*, 219–230. [[CrossRef](#)]



© 2019 by the authors. Licensee MDPI, Basel, Switzerland. This article is an open access article distributed under the terms and conditions of the Creative Commons Attribution (CC BY) license (<http://creativecommons.org/licenses/by/4.0/>).



Article

# Non-Isothermal Oxidation Behaviors and Mechanisms of Ti-Al Intermetallic Compounds

Peixuan Ouyang <sup>1,2,3</sup>, Guangbao Mi <sup>1,4,\*</sup>, Peijie Li <sup>2</sup>, Liangju He <sup>2</sup>, Jingxia Cao <sup>1</sup> and Xu Huang <sup>1</sup>

<sup>1</sup> Aviation Key Laboratory of Science and Technology on Advanced Titanium Alloys, AECC Beijing Institute of Aeronautical Materials, Beijing 100095, China

<sup>2</sup> National Center of Novel Materials for International Research, Tsinghua University, Beijing 100084, China

<sup>3</sup> School of Mechanical and Materials Engineering, North China University of Technology, Beijing 100144, China

<sup>4</sup> Beijing Engineering Research Center of Graphene and Application, Beijing 100095, China

\* Correspondence: miguangbao@163.com; Tel.: +86-10-62496627

Received: 25 May 2019; Accepted: 27 June 2019; Published: 30 June 2019

**Abstract:** Non-isothermal oxidation is one of the important issues for the safe application of Ti-Al alloys, so this study aimed to illustrate the non-isothermal oxidation behaviors and the corresponding mechanisms of a TiAl-based alloy in comparison with a Ti<sub>3</sub>Al-based alloy. The non-isothermal oxidation behaviors of Ti-46Al-2Cr-5Nb and Ti-24Al-15Nb-1.5Mo alloys in pure oxygen were comparatively investigated with a thermogravimetry-differential scanning calorimetry (TGA/DSC) simultaneous thermal analyzer heating from room temperature to 1450 °C with a heating rate of 40 °C/min. When the temperature rose above 1280 °C, the oxidation rate of the Ti-46Al-2Cr-5Nb alloy sharply increased and exceeded that of the Ti-24Al-15Nb-1.5Mo alloy owing to the occurrence of internal oxidation. When the temperature was higher than 1350 °C, the oxidation rate of the Ti-46Al-2Cr-5Nb alloy decreased obviously due to the generation of an oxygen-barrier β-Al<sub>2</sub>TiO<sub>5</sub>-rich layer by a chemical reaction between Al<sub>2</sub>O<sub>3</sub> and TiO<sub>2</sub> in the oxide scale. Based on Wagner's theory of internal oxidation, the reason for the occurrence of internal oxidation in the Ti-46Al-2Cr-5Nb alloy is the formation of the α phase in the subsurface, while no internal oxidation occurred in the Ti-24Al-15Nb-1.5Mo alloy due to the existence of the β phase in the subsurface with the enrichment of Nb and Mo.

**Keywords:** titanium aluminides; oxidation; non-isothermal; mechanism; internal oxidation

## 1. Introduction

TiAl-based alloys have received considerable attention as high-temperature structural materials for aerospace and automotive applications, since they maintain numerous outstanding properties, such as low density (3.9–4.2 g/cm<sup>3</sup>), high specific strength, good creep resistance and excellent fireproof performance [1–5]. Nevertheless, the insufficient high-temperature oxidation resistance of the TiAl-based alloys limits their wide application and development [6,7]. Numerous investigations have been carried out to study the high-temperature oxidation behaviors of the TiAl-based alloys, most of which were concerned about the long-term isothermal oxidation at normal service temperature (800–1000 °C) [8–10]. Few studies have been focused on the non-isothermal oxidation behaviors of the TiAl-based alloys, which is also deserving of attention since the alloys are often subject to non-isothermal oxidation in service. For example, aero-engine TiAl components are heated rapidly from room temperature to service temperature during the engine startup period. For another instance, aero-engine TiAl blades are likely to suffer from titanium fire, which consists of ignition and propagation combustion processes under the induction of external energies such as high-energy friction, fracture, melt droplets and so on [11], even though the fireproof performance of TiAl-based alloys is much better



than that of conventional titanium alloys. Ignition, which is the precursor process of titanium fire, is essentially a non-isothermal oxidation process [12,13] and the ignition points of titanium alloys are slightly lower than their melting points [11]. Hence, the non-isothermal oxidation of TiAl-based alloys with a rather wide temperature range has a major impact on their safe application in aeroengines.

In addition, the non-isothermal oxidation behaviors of the TiAl-based alloys should be more special than the isothermal oxidation behaviors, since the heating rate is so high that the oxidation may not reach dynamic equilibrium and the temperature range is so wide that phase transition may occur in the alloys. Many studies showed that oxidation temperature and time significantly affect isothermal oxidation behaviors of the TiAl-based alloys [14–17]. Moreover, Vaidya [18] found that during isothermal oxidation, the mass gain of Ti-48Al-2Nb-2Cr alloy exceeds that of Ti-25Al-10Nb-3V-1Mo alloy when the temperature is above 1200 °C, which breaks away from the general understanding that the oxidation resistance of the TiAl-based alloys is better than that of the Ti<sub>3</sub>Al-based alloys. This phenomenon is considered to be attributed to the doubly increased oxygen solubility of  $\gamma$  phase in the TiAl-based alloy at 1200 °C [18], while this explanation seems unreasonable since the maximum oxygen solubility of  $\gamma$  phase (~3 at.%) in the TiAl-based alloy is much lower than that of  $\alpha_2$  phase (~13 at.%) in the Ti<sub>3</sub>Al-based alloys [19]. Hence, in regards to non-isothermal oxidation, it should be of interest to people what behaviors the TiAl-based alloys would exhibit, whether there exists a similar phenomenon that the oxidation rate of the TiAl-based alloys exceeds that of the Ti<sub>3</sub>Al-based alloys at high temperature, as well as what is the reasonable explanation for this phenomenon. On the basis of the above questions, this paper examines the non-isothermal oxidation behaviors of a TiAl-based alloy in comparison with a Ti<sub>3</sub>Al-based alloy and illustrates the corresponding oxidation mechanisms. On one hand, this research helps to better understand the ignition mechanisms of TiAl alloys, on the other hand, it might promote the development of new-type TiAl alloys resistant to higher temperature and with less risk to titanium fire by ingredient optimum design.

TGA/DSC simultaneous thermal analysis is a common method to study the non-isothermal oxidation behaviors of metals and their alloys [20–23]. Adopting the TGA/DSC method, G.B. Mi et al. [22] studied the effect of Cr content on the non-isothermal oxidation behaviors of Ti-Cr fire-proof titanium alloys. The results showed that when the Cr content exceeds 10–15 wt.%, the oxidation resistance of Ti-Cr alloys increases with the Cr content due to the precipitation of Cr oxide [22]. Ouyang et al. [23] carried out a research on the non-isothermal oxidation behaviors of a high-temperature near- $\alpha$  titanium alloy (TA29 alloy), meanwhile discussed the effects of lattice transformation and alloying elements on the non-isothermal oxidation behaviors of the TA29 alloy.

In this paper, the non-isothermal oxidation behaviors of a TiAl-based alloy and a Ti<sub>3</sub>Al-based alloy in pure oxygen were studied with a TGA/DSC synchronous thermal analyzer heating from room temperature to 1450 °C with a heating rate of 40 °C/min. Combined with microstructural characterization and calculation of oxidation activation energy, the non-isothermal oxidation mechanisms of the TiAl-based alloy were elucidated. Furthermore, the reason for the poorer oxidation resistance of the TiAl-based alloy than that of the Ti<sub>3</sub>Al-based alloy at high temperature was revealed based on Wagner's theory of internal oxidation.

## 2. Experimental

### 2.1. Specimen Preparation

The nominal compositions of the TiAl-based and Ti<sub>3</sub>Al-based alloys studied in this paper are Ti-46Al-2Cr-5Nb (at.%) and Ti-24Al-15Nb-1.5Mo (at.%), respectively. Both the two alloys were prepared by melting, forging, heat treatment and mechanical processing. The microstructure of the as-received Ti-46Al-2Cr-5Nb alloy consists of coarse fully-lamellar  $\gamma + \alpha_2$  colonies, as shown in Figure 1a. The microstructure of the as-received Ti-24Al-15Nb-1.5Mo alloy is duplex, being composed of equiaxed primary  $\alpha_2$  and/or O phases, B2 transformed structure consisting of flaky secondary  $\alpha_2$  and O phases and residual B2 phase, as shown in Figure 1b. For non-isothermal oxidation experiments,

specimens with dimensions of  $3 \times 2 \times 2 \text{ mm}^3$  were cut from the two kinds of alloy sheets by a computerized numerical control (CNC) dicing saw (SYJ-400, Shenyang kejing instrument company, Shenyang, China). The specimens were ground with sandpapers up to 2000-grit to remove oxide scales and then ultrasonically cleaned with acetone and alcohol.

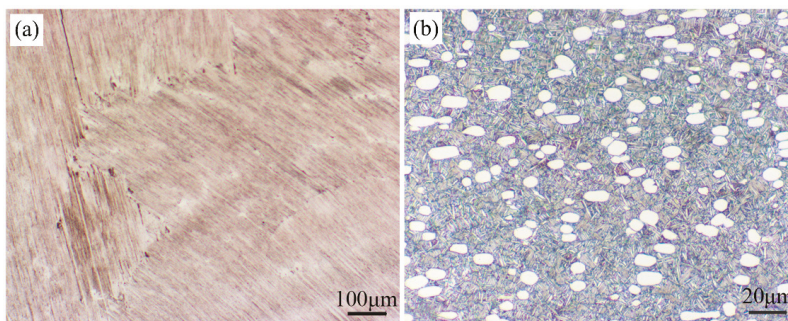


**Figure 1.** Optical micrographs showing the original microstructure of the (a) Ti-46Al-2Cr-5Nb and (b) Ti-24Al-15Nb-1.5Mo alloys.

## 2.2. Non-Isothermal Oxidation Experiment

Non-isothermal oxidation experiments were carried out in a TGA/DSC simultaneous thermal analyzer (TGA/DSC 1; Mettler Toledo, Zurich, Switzerland). The specimens of both the Ti-46Al-2Cr-5Nb and Ti-24Al-15Nb-1.5Mo alloys were heated from room temperature to 1450 °C at a heating rate of 40 °C/min under a pure oxygen flow of 50 mL/min. The oxygen flow was added to the system once the heating process was started and the flow was cut off when the heating process was completed. After furnace cooling the oxidized specimens were taken out. For each alloy, the mass-gain, mass-gain rate, and heat flux curves were obtained from three repeated experiments with the relative standard deviations less than 10%. Besides, in order to investigate the non-isothermal oxidation behaviors of the two alloys in detail, the specimens were heated to several interested temperatures below 1450 °C and then were furnace cooled to obtain the corresponding non-isothermal oxidation products.

## 2.3. Microstructural Characterization

Specimens were examined after non-isothermal oxidation using field emission scanning electron microscopy (FE-SEM; Hitachi SU8000, Tokyo, Japan) and X-ray diffraction (XRD; Bruker D8 Advance; Cu K $\alpha$ , Karlsruhe, Germany) to characterize surface morphologies of the oxide scales and identify oxide phases. For cross-sectional microstructure observation of the oxidized specimens, metallographic specimens were prepared by being placed in the transverse direction, being mounted with cold-setting resin, then being ground with 400–2000 grit SiC sandpapers, being polished with 1.0  $\mu\text{m}$  alumina suspension, being etched with Kroll reagent (92 mL H $_2$ O, 3 mL HF, 5 mL HNO $_3$ ) and finally being coated with a thin layer of carbon. The microstructures and elemental distributions on the cross-section of the oxide scales were characterized using an electron probe microanalyzer (EPMA; Shimadzu EPMA-1720H, Kyoto, Japan).

## 3. Calculation of Oxidation Activation Energy

Similar to traditional titanium alloys, the oxidation mass gains of the Ti-Al alloys also come from oxygen dissolution and growth of oxide scales. The two oxidation behaviors are competitive and one of them governs the mass gain at a certain temperature and time [24–26]. The rate-determining steps of the two oxidation behaviors are respectively the diffusion of O atom in the alloy and the diffusion of O $^{2-}$  in the oxide scale. Thus, it can be assumed that the mass-gain rate of the Ti-Al alloys during non-isothermal oxidation is limited by one-dimensional diffusion of one species A (A is O atom or

$O^{2-}$ ), so that the mass-gain rate per unit area of the Ti-Al alloys is proportional to the molar diffusion flux of specie A. Furthermore, based on the Fick's diffusion law and assuming that the diffusion of specie A satisfies Arrhenius kinetics, the relationship among the temperature, the mass gain and the oxidation activation energy of the Ti-Al alloys can be derived, as shown in Equation (1). Details for the derived process can be seen in our previous work [23].

$$-\ln \frac{d(\Delta m)}{dT} - \ln(\Delta m) = -\ln K^* + E/RT \quad (1)$$

where  $\Delta m$  is the mass gain per unit area,  $E$  is the oxidation activation energy,  $R$  is the molar gas constant and  $K^*$  is constant. Let the left side of Equation (1) be equal to  $Y(\Delta m)$ , thus  $Y(\Delta m)$  is linearly related to the reciprocal of temperature and the product of the corresponding positive slope and  $R$  is the oxidation activation energy.

## 4. Results and Discussion

### 4.1. Oxidation Mass Gain and Activation Energies

Figure 2 shows the mass-gain and mass-gain rate curves of the Ti-46Al-2Cr-5Nb and Ti-24Al-15Nb-1.5Mo alloys obtained during non-isothermal oxidation. The mass-gain rates of the two alloys were similar when the temperature was lower than 1280 °C. However, the mass-gain rate of the Ti-46Al-2Cr-5Nb alloy increased dramatically when the temperature was higher than 1280 °C, resulting that the mass gain of the Ti-46Al-2Cr-5Nb alloy significantly exceeded that of the Ti-24Al-15Nb-1.5Mo alloy. This phenomenon is not common but is similar to that reported by Vaidya [18]. Nevertheless, the mass-gain rate of the Ti-46Al-2Cr-5Nb alloy turned to decrease obviously when the temperature was above 1350 °C.

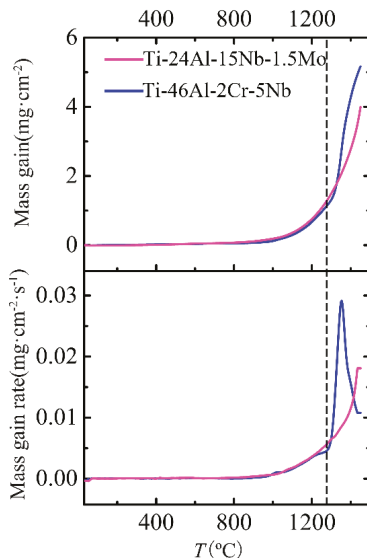


**Figure 2.** Comparisons of the mass-gain and mass-gain rate curves between the Ti-46Al-2Cr-5Nb and Ti-24Al-15Nb-1.5Mo alloys obtained during non-isothermal oxidation.

According to the evolution of the mass-gain rate, the non-isothermal oxidation process of the Ti-46Al-2Cr-5Nb alloy could be divided into five stages for further study, as shown in Figure 3a. When the temperature was below 870 °C (Stage I), the mass gain of the Ti-46Al-2Cr-5Nb alloy was few and

could be neglected. When the temperature rose to 870–980 °C (Stage II), the mass-gain rate increased slowly and the corresponding mass gain was 0.04 mg/cm<sup>2</sup>. When the temperature was increased to 980–1280 °C (Stage III), the mass-gain rate increased obviously and the corresponding mass gain was 1.05 mg/cm<sup>2</sup>. When the temperature was raised to 1280–1350 °C (Stage IV), the mass-gain rate increased sharply and the corresponding mass gain was 1.68 mg/cm<sup>2</sup>. Nevertheless, the mass-gain rate decreased significantly when the temperature was above 1350 °C (Stage V). It is concluded that the non-isothermal oxidation process of the Ti-46Al-2Cr-5Nb alloy consists of five stages, including nearly non-oxidation (Stage I, <870 °C), slow oxidation (Stage II, 870–980 °C), accelerated oxidation (Stage III, 980–1280 °C), severe oxidation (Stage IV, 1280–1350 °C) and decelerated oxidation (Stage V, 1350–1450 °C) stages. However, the non-isothermal oxidation process of the Ti-24Al-15Nb-1.5Mo alloy can be only divided into four stages according to the evolution of the mass-gain rate, as shown in Figure 3b, including nearly non-oxidation (Stage I, <800 °C), slow oxidation (Stage II, 800–1020 °C), accelerated oxidation (Stage III, 1020–1400 °C) and severe oxidation (Stage IV, 1400–1450 °C) stages. Table 1 gives a summary of the temperature ranges corresponding to the different stages of the non-isothermal oxidation process for the Ti-46Al-2Cr-5Nb and Ti-24Al-15Nb-1.5Mo alloys.

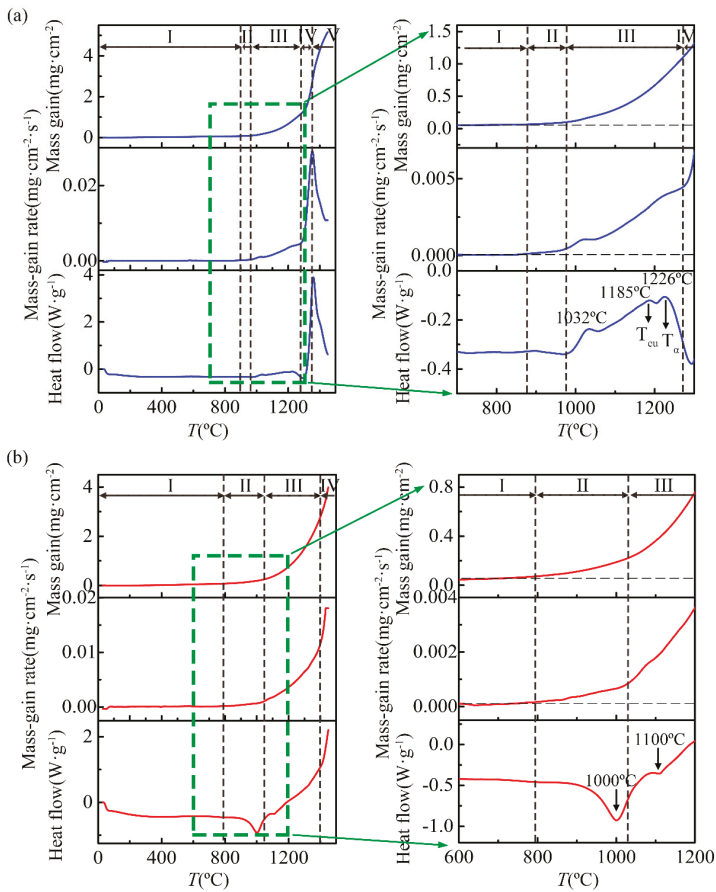


**Figure 3.** Stage divisions of the non-isothermal oxidation process for the (a) Ti-46Al-2Cr-5Nb and (b) Ti-24Al-15Nb-1.5Mo alloys according to the evolution of the mass-gain rates.

**Table 1.** Temperature ranges, oxidation activation energies and matrix phases corresponding to different stages of the non-isothermal oxidation for the Ti-46Al-2Cr-5Nb and Ti-24Al-15Nb-1.5Mo alloys.

Stage	Temperature Range (°C)		Activation Energy (kJ/mol)		Matrix Phases	
	TiAl <sup>1</sup>	Ti <sub>3</sub> Al <sup>2</sup>	TiAl <sup>1</sup>	Ti <sub>3</sub> Al <sup>2</sup>	TiAl <sup>1</sup>	Ti <sub>3</sub> Al <sup>2</sup>
I	<870	<800	-	-	$\gamma + \alpha_2$	$\alpha_2 + O + B2$
II	870–980	800–1020	217.8	143.2	$\gamma + \alpha_2$	$\alpha_2 + O + B2 \rightarrow \alpha_2 + B2$
III	980–1280	1020–1400	249.8	244.8	$\gamma + \alpha_2 \rightarrow \gamma + \alpha \rightarrow \alpha$	$\alpha_2 + B2 \rightarrow B2 \rightarrow \beta$
IV	1280–1350	1400–1450	985.0	608.6	$\alpha$	$\beta$
V	1350–1450	-	-	-	$\alpha$	-

<sup>1</sup> TiAl here refers to the Ti-46Al-2Cr-5Nb alloy. <sup>2</sup> Ti<sub>3</sub>Al here refers to the Ti-24Al-15Nb-1.5Mo alloy.

Figure 4 presents the  $Y(\Delta m) \sim 1/T$  curves and the corresponding linear fitting results of the two alloys. The evolutions of the slopes of the  $Y(\Delta m) \sim 1/T$  curves also clearly demonstrate that the non-isothermal oxidation processes of the Ti-46Al-2Cr-5Nb and Ti-24Al-15Nb-1.5Mo alloys are respectively composed of five stages and four stages. It should be noted that since the mass changes of the two alloys at Stage I were mainly induced by the small mass fluctuation of the thermogravimetric analysis equipment, the values of  $Y(\Delta m)$  at Stage I fluctuated around a certain value and are not shown in Figure 4. Besides, the  $Y(\Delta m) \sim 1/T$  curves of both the two alloys at Stages II, III and IV could be positive linearly fitted, so that the oxidation activation energies of the two alloys for the three stages were obtained, as presented in Table 1. It can be seen that the oxidation activation energies of the two alloys at Stage III are similar, while the oxidation activation energies of the two alloys both at Stage II and at Stage IV are quite different, which is related to their oxidation mechanisms and will be discussed in Section 4.3.

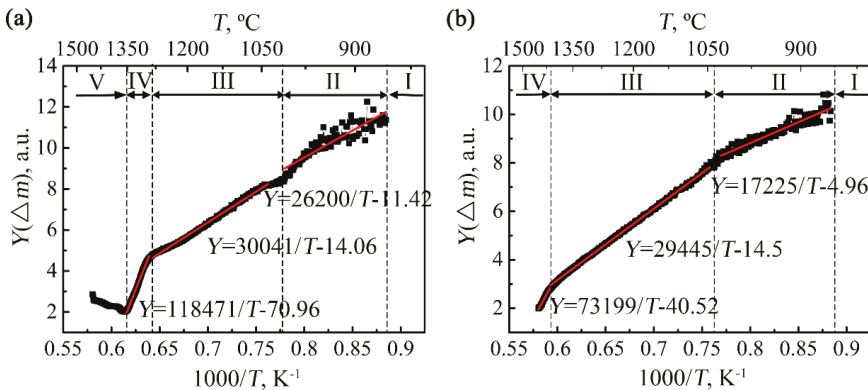


**Figure 4.** The  $Y(\Delta m) \sim 1/T$  curves and the corresponding linear fitting results of the (a) Ti-46Al-2Cr-5Nb and (b) Ti-24Al-15Nb-1.5Mo alloys.

#### 4.2. Matrix Phases

Since the non-isothermal oxidation experiments were carried out in a wide temperature range, the Ti-46Al-2Cr-5Nb and Ti-24Al-15Nb-1.5Mo alloys were likely to undergo phase transitions during non-isothermal oxidation.

Generally, the phase transition types and temperatures of the TiAl-based alloys are affected not only by the aluminum content (45–48 at.%), but also by kinds of other alloying elements (such as Cr, V, Mn, Nb, Ta, W, Si, C, P and B) and their contents (0.1–8 at.%) [27]. According to the Ti-Al phase diagram [28], the heat-flow and thermomechanical analysis (TMA) derivative curves of Ti-(46–47)Al-2Cr-(2–8)Nb alloy [29], the phase transitions of the Ti-46Al-2Cr-5Nb alloy heating from room temperature to 1450 °C are deduced to be  $\gamma + \alpha_2 \rightarrow \gamma + \alpha$  and  $\gamma + \alpha \rightarrow \alpha$  with the respective temperature range of

1175–1215 °C ( $T_{eu}$ ) and 1292–1295 °C ( $T_{\alpha}$ ). The deduced temperature ranges are in accordance with the two exothermic peaks with the respective temperatures of 1185 and 1226 °C in the heat-flow curve of the Ti-46Al-2Cr-5Nb alloy, as shown in Figure 3a. It confirms that the phase transitions of  $\gamma + \alpha_2 \rightarrow \gamma + \alpha$  and  $\gamma + \alpha \rightarrow \alpha$  occurred in the Ti-46Al-2Cr-5Nb alloy during the non-isothermal oxidation. Besides, it can be seen from Figure 3a that there exists another exothermic peak with a temperature of about 1032 °C in the heat-flow curve of the Ti-46Al-2Cr-5Nb alloy. It is not yet possible to explain the physical meaning of this peak based on the Ti-Al phase diagram. However, it has been reported that there exists a similar exothermic peak in the heat-flow curve of Ti-46Al-1.9Cr-3Nb alloy with typical duplex structure, which is ascribed to equilibrium transformation or uniformity when heating of the non-equilibrium structure generated by thermal mechanical processing [30]. Therefore, the matrix phases of the Ti-46Al-2Cr-5Nb alloy at different stages of the non-isothermal oxidation process could be concluded, as shown in Table 1.

As for the Ti-24Al-15Nb-1.5Mo alloy, the Nb equivalent is about 20 at.% since the beta phase stability of Mo is 3.6 times of that of Nb [31]. Thus, according to the Ti-25Al-Nb phase diagram [31], the phase transitions of the Ti-24Al-15Nb-1.5Mo alloy heating from room temperature to 1450 °C are deduced to be  $\alpha_2 + O + B2 \rightarrow \alpha_2 + B2$  (1010 °C),  $\alpha_2 + B2 \rightarrow B2$  (1100 °C) and  $B2 \rightarrow \beta$  (1220 °C). Since there exist two endothermic peaks with the respective temperatures of near 1000 and 1100 °C in the heat-flow curve of the Ti-24Al-15Nb-1.5Mo alloy during non-isothermal oxidation, as shown in Figure 3b, it demonstrates the occurrence of the former two phase transitions. Besides, no peak corresponding to the last phase transition could be found in the heat-flow curve of the Ti-24Al-15Nb-1.5Mo alloy, which is probably due to the small chemical heat for the disordering from B2 phase to  $\beta$  phase. As a result, the matrix phases of the Ti-24Al-15Nb-1.5Mo alloy at different stages of the non-isothermal oxidation process could be also concluded, as presented in Table 1.

#### 4.3. Non-Isothermal Oxidation Mechanisms

##### 4.3.1. Nearly Non-Oxidation Stage (Stage I)

Similar to the near- $\alpha$  titanium alloy TA29 [23], the oxidation mass gains of the Ti-46Al-2Cr-5Nb and Ti-24Al-15Nb-1.5Mo alloys at Stage I were very small and could be neglected (Figure 3), which is ascribed to the fact that a thin titanium oxide film (200 nm) rapidly forms on the alloys at room temperature and passivates the surface [14].

##### 4.3.2. Slow Oxidation Stage (Stage II)

When the temperature rose to Stage II (870–980 °C for the Ti-46Al-2Cr-5Nb alloy and 800–1020 °C for the Ti-24Al-15Nb-1.5Mo alloy), both the two alloys exhibited slow oxidation behaviors, which is also similar to the near- $\alpha$  titanium alloy TA29 at Stage II with the temperature range of 750–1000 °C [23]. As discussed in our previous work [23], the oxidation mechanism of the TA29 alloy at Stage II is oxygen dissolution with the rate-determining step of oxygen diffusion in the alloy. The oxidation activation energies of the TA29 alloy at Stage II (163.9 kJ/mol) [23] is about 20 kJ/mol higher than that of the Ti-24Al-15Nb-1.5Mo alloy (143.2 kJ/mol). The matrixes of the TA29 and Ti-24Al-15Nb-1.5Mo alloys at Stage II are respectively dominated by the  $\alpha$  and  $\alpha_2$  phases. Moreover, it has been reported that the activation energy for oxygen diffusion in the  $\alpha$  phase is 10–20 kJ/mol higher than that in the  $\alpha_2$  phase [32], which is equivalent to the difference of the oxidation activation energy between the TA29 and Ti-24Al-15Nb-1.5Mo alloys. Therefore, the oxidation mechanism of the Ti-24Al-15Nb-1.5Mo alloy at Stage II is also the oxygen dissolution in the alloy. It indicates that the thin titanium oxide film (200 nm) passivating the surface at Stage I could not prevent oxygen from diffusing into the alloys at Stage II, which might be due to the increase of the solubility of  $TiO_2$  in the alloys or the cracking of  $TiO_2$  film caused by phase transitions in the oxide film with the temperature increases.

The lower oxidation activation energy of the Ti-24Al-15Nb-1.5Mo alloy in comparison with the TA29 alloy indicates that oxygen atoms diffuse much easier in the former alloy. Since volume diffusion

is the main diffusion type in the alloys at such high temperature, the difference of oxygen diffusion ability can be explained by the difference of the lattice structure between the two alloys. The  $\alpha$  phase dominating in the TA29 alloy has the close-packed hexagonal structure (hcp, A3), where oxygen atoms tend to occupy the two  $Ti_6$  octahedral interstitial sites [33,34], as shown in Figure 5a. The  $\alpha_2$  phase dominating in the Ti-24Al-15Nb-1.5Mo alloy has the ordered close-packed hexagonal structure ( $DO_{19}$ ), where oxygen atoms prefer to occupy the  $Ti_6$  octahedral interstitial site instead of the  $Al_2Ti_4$  site [35,36], as shown in Figure 5b. Though the number of the  $Ti_6$  interstitial site in the lattice of the  $\alpha_2$  phase is lower than that in the lattice of the  $\alpha$  phase, which leads to the lower oxygen solubility in the  $\alpha_2$  phase than in the  $\alpha$  phase, the covalence of Ti-Al bond in the lattice of the  $\alpha_2$  phase makes electrons aggregate between Ti and Al atoms, resulting in the weaker Ti-O bond strength in the lattice of the  $\alpha_2$  phase compared with that in the lattice of the  $\alpha$  phase [32]. Therefore, the diffusion resistance of oxygen atoms in the lattice of the  $\alpha_2$  phase is smaller than that in the lattice of the  $\alpha$  phase. That is to say, the required activation energy for oxygen diffusion in the  $\alpha_2$  phase is smaller than in the  $\alpha$  phase.

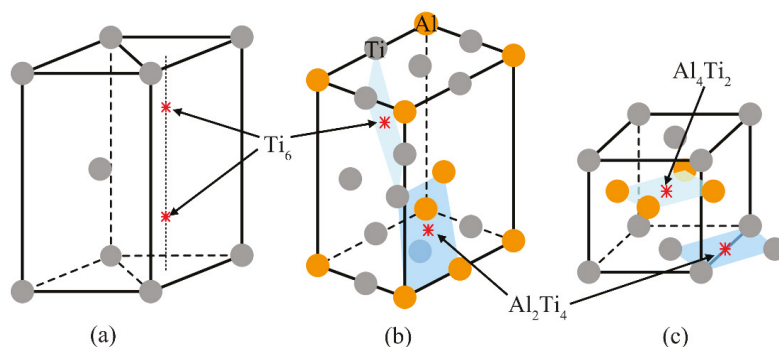


**Figure 5.** Octahedral interstitial sites for oxygen atoms in the lattices of the (a)  $\alpha$ , (b)  $\alpha_2$  and (c)  $\gamma$  phases.

As for the Ti-46Al-2Cr-5Nb alloy, the oxidation activation energy at Stage II (217.8 kJ/mol) is higher than that of the Ti-24Al-15Nb-1.5Mo alloy (143.2 kJ/mol). The  $\gamma$  phase dominating in the Ti-46Al-2Cr-5Nb alloy at Stage II has the ordered face-centered cubic structure ( $L_{10}$ ), where oxygen atoms can only occupy the interstitial octahedral sites surrounded by both titanium and aluminum atoms ( $Al_4Ti_2$  and  $Al_2Ti_4$ ), as shown in Figure 5c. Since the covalence of Ti-Al bond makes electrons aggregate between Ti and Al atoms, the Ti-O bond strength in the  $Al_4Ti_2$  and  $Al_2Ti_4$  octahedrons is higher than that in the  $Ti_6$  octahedron. Hence, the oxygen diffusion ability in the lattice of the  $\gamma$  phase is much weaker than that in the lattice of the  $\alpha_2$  phase, leading to the higher oxidation activation energy of the Ti-46Al-2Cr-5Nb alloy than that of the Ti-24Al-15Nb-1.5Mo alloy. The above analysis manifests that the oxidation mechanism of the Ti-46Al-2Cr-5Nb alloy at Stage II is the same with the Ti-24Al-15Nb-1.5Mo alloy, namely, oxygen dissolution in the alloy. Besides, since the oxygen solubility in the  $\gamma$  phase is much lower than that in the  $\alpha_2$  phase, the temperature range corresponding to Stage II for the Ti-46Al-2Cr-5Nb alloy (870–980 °C) is narrower than that for the Ti-24Al-15Nb-1.5Mo alloy (800–1020 °C).

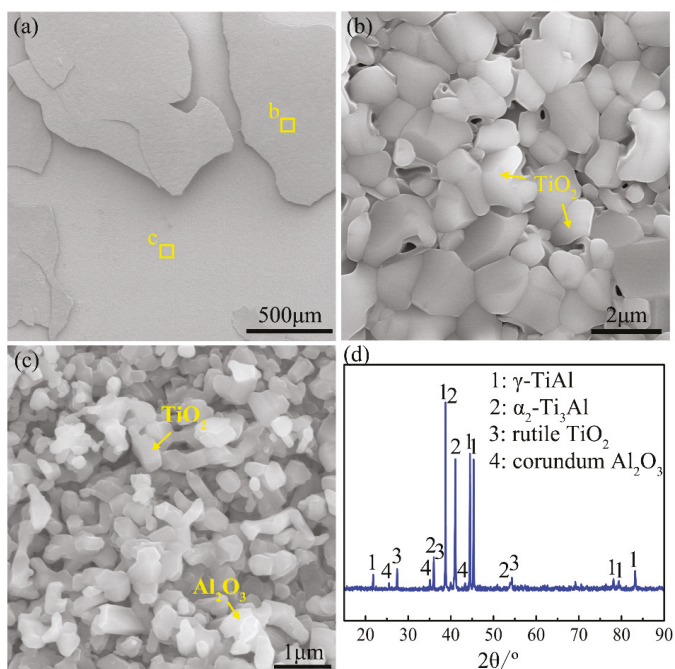
#### 4.3.3. Accelerated Oxidation Stage (Stage III)

When the temperature was raised to Stage III (980–1280 °C for the Ti-46Al-2Cr-5Nb alloy and 1020–1400 °C for the Ti-24Al-15Nb-1.5Mo alloy), the two alloys exhibited accelerated oxidation behaviors and the oxidation activation energies are respectively 249.8 and 244.8 kJ/mol, which is close to the diffusion activation energies of  $O^{2-}$  and  $Ti^{4+}$  in  $TiO_2$  (234 kJ/mol [37] and 257 kJ/mol [38], respectively). It indicates that the oxidation mechanisms of the two alloys at this stage are mainly the growth of oxide scales dominated by  $TiO_2$ . Since the diffusion rates of  $O^{2-}$  and  $Ti^{4+}$  in  $TiO_2$  are much

lower than that of oxygen atom in the alloy, the rate-determining step at this stage is the diffusion of  $O^{2-}$  and  $Ti^{4+}$  in the oxide scale so that the oxidation activation energy is independent with the matrix phases of the alloys.

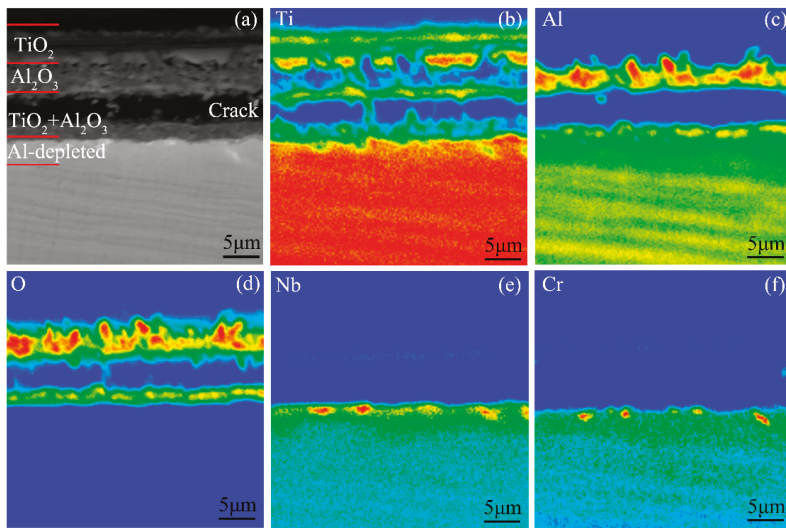
Figure 6 demonstrates the surface morphologies and XRD pattern of the oxide scale formed during heating the Ti-46Al-2Cr-5Nb alloy to the end of Stage III. As shown in the XRD pattern (Figure 6d), there are high contents of  $\gamma$  and  $\alpha_2$  phases besides rutile  $TiO_2$  and corundum  $\alpha-Al_2O_3$ . It manifests that the oxide is composed of rutile  $TiO_2$  and corundum  $\alpha-Al_2O_3$  (hereafter referred to as  $TiO_2$  and  $Al_2O_3$ ), and the thickness of the oxide scale is less than the detection depth of X-ray ( $\sim 20 \mu m$ ). The oxide scale is a multiple-layer structure (Figure 6a), the outer layer of which consists of coarse  $TiO_2$  crystals (Figure 6b) and is prone to peel off, exposing the inner layer of fine  $TiO_2$  and  $Al_2O_3$  crystals (Figure 6c).

Figure 7 presents the cross-sectional morphology and the corresponding elemental distribution maps of the oxide scale on the Ti-46Al-2Cr-5Nb alloy. The oxide scale is identified to be in the order of the  $TiO_2$  layer/ $Al_2O_3$ -rich layer/ $TiO_2 + Al_2O_3$  mixed layer from the outside to the inside. The total thickness of the oxide scale ( $\sim 13 \mu m$ ) is indeed less than the detection depth of X-ray, which is consistent with the result of the XRD pattern. An Al-depleted layer that deemed to be  $\alpha_2$  phase [16] is generated in the subsurface of the alloy. Besides, there is a transverse crack between the intermediate and inner layers (Figure 7a). However, the crack is considered to be produced during preparation of the metallographic specimen instead of during oxidation and during cooling, since no such crack is found in the oxide scale formed during heating the alloy to the end of Stage IV and the alloy exhibited much severer oxidation behavior at Stage IV than at Stage III. Thus, the crack is not taken into account when discussing the formation process of the oxide scale at Stage III.



**Figure 6.** (a–c) Surface morphologies and (d) X-ray diffraction (XRD) pattern of the oxide formed during heating the Ti-46Al-2Cr-5Nb alloy to the end of Stage III.





**Figure 7.** (a) Cross-sectional morphology and (b–f) the corresponding elemental distribution maps of the oxide scale formed during heating the Ti-46Al-2Cr-5Nb alloy to the end of Stage III.

The oxide scale formed during heating the Ti-46Al-2Cr-5Nb alloy from room temperature to the end of Stage III (Figures 6 and 7) is considered to be mainly generated at Stage III since the Ti-46Al-2Cr-5Nb alloy exhibits nearly non-oxidation behavior at Stage I and the oxidation mechanism at Stage II is oxygen dissolution in the alloy. The three-layer oxide scale structure formed at Stage III (980–1280 °C) is similar to the common oxide scale structure formed during isothermal oxidation at 800–1000 °C [14]. Hence, the growth mechanism of the oxide scale at Stage III could be deduced from the isothermal oxidation mechanism at 800–1000 °C. Firstly, an  $\text{Al}_2\text{O}_3$  film is rapidly generated on the oxygen-saturated Ti-46Al-2Cr-5Nb alloy [39]. Since the  $\text{Al}_2\text{O}_3$  film is grown by the inward diffusion of  $\text{O}^{2-}$  along the  $\text{Al}_2\text{O}_3$  grain boundaries and the outward diffusion of  $\text{Al}^{3+}$  along the  $\text{Al}_2\text{O}_3$  lattice, the  $\text{Al}_2\text{O}_3$  grain boundaries suffer compressive stress, resulting in curling deformation or even rupture of the  $\text{Al}_2\text{O}_3$  film [40]. Thus,  $\text{Ti}^{4+}$  and  $\text{O}^{2-}$  would diffuse in opposite directions along the cracks of the  $\text{Al}_2\text{O}_3$  film [40]. As a result, an outer  $\text{TiO}_2$  layer and an inner  $\text{TiO}_2 + \text{Al}_2\text{O}_3$  mixed layer are respectively formed on the outside and the inside of the ruptured  $\text{Al}_2\text{O}_3$  film, as shown in Figure 7. The growth process of the oxide scale at Stage III demonstrates that the growth rate of the oxide scale is mainly controlled by the diffusion of  $\text{Ti}^{4+}$  and  $\text{O}^{2-}$  in  $\text{TiO}_2$ , which is consistent with the result of the oxidation activation energy of the alloy at Stage III. Therefore, it is further confirmed that the oxidation mechanism of the Ti-46Al-2Cr-5Nb alloy at Stage III is the growth of the oxide scale dominated by  $\text{TiO}_2$ .

As for the Ti-24Al-15Nb-1.5Mo alloy, the oxide scale formed during heating the alloy to the end of Stage III has a three-layer structure, which is in the order of the  $\text{TiO}_2 + \text{Al}_2\text{O}_3$  mixed layer/ $\text{TiO}_2$ -rich layer/ $\text{TiO}_2(\text{Nb}, \text{Mo}) + \text{Al}_2\text{O}_3$  mixed layer from the outside to the inside, as shown in Figure 8. Consistent with the oxidation activation energy, the structure of the oxide scale also indicates that the oxidation mechanism of the Ti-24Al-15Nb-1.5Mo alloy is mainly the growth of the oxide scale dominated by  $\text{TiO}_2$ . Besides, a thin  $\beta$ -Ti layer enriched in Al, Nb and Mo elements was formed in the subsurface of the alloy. The microstructure between the  $\beta$ -Ti layer and the matrix is composed of  $\alpha$ -Ti(O) grains and a small amount of  $\beta$ -Ti phase enriched in Al, Nb, and Mo in the grain boundaries. As mentioned in Section 4.3, the matrix is dominated by  $\beta$  phase at the end of Stage III. Thus, it is referred that the microstructure between the subsurface of the alloy and the matrix is stabilized to  $\alpha$  phase by the inward-diffusing oxygen, while the microstructure of the subsurface still maintains  $\beta$  phase due to the enrichment of Nb and Mo.

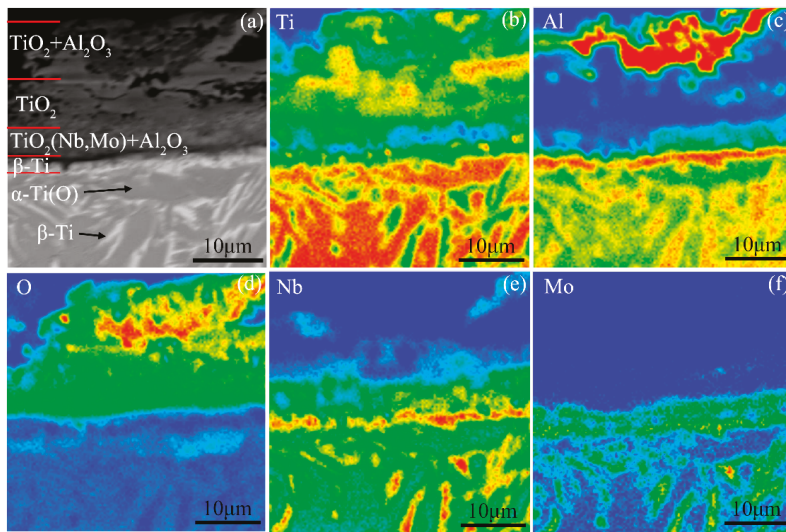


**Figure 8.** (a) Cross-sectional morphology and (b–f) the corresponding elemental distribution maps of the oxide scale formed during heating the Ti-24Al-15Nb-1.5Mo alloy to the end of Stage III.

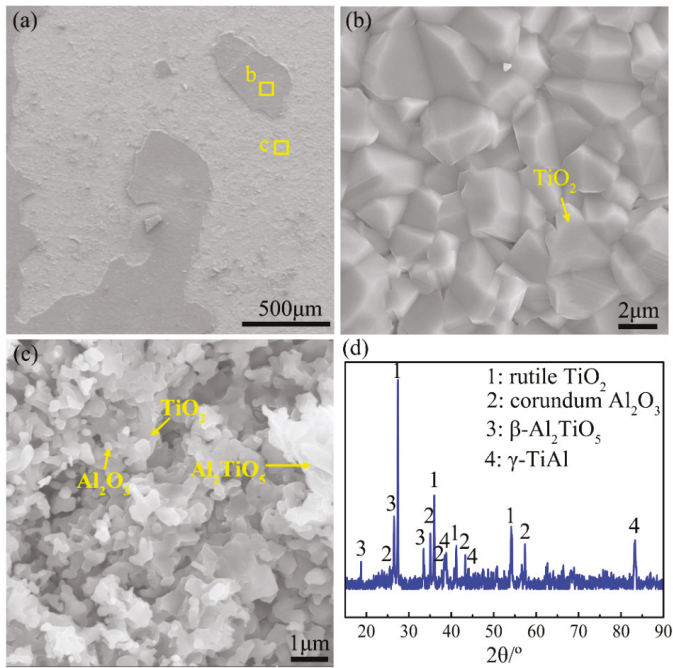
#### 4.3.4. Severe Oxidation Stage (Stage IV)

The two alloys exhibited severe oxidation behaviors when the temperature was raised to Stage IV, while the corresponding temperature range of the Ti-46Al-2Cr-5Nb alloy (1400–1450 °C) is much higher than that of the Ti-24Al-15Nb-1.5Mo alloy (1280–1350 °C). The oxidation activation energies of the Ti-46Al-2Cr-5Nb and Ti-24Al-15Nb-1.5Mo alloys are respectively 985.0 and 608.6 kJ/mol, which is significantly higher than those at Stage III (249.8 and 244.8 kJ/mol). Thus, the oxidation mechanisms at Stage IV should be somewhat different from that at Stage III.

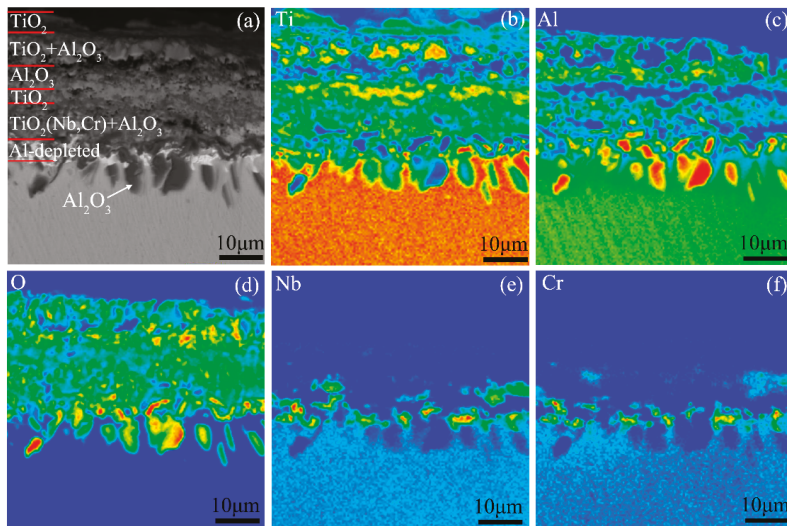
Figure 9 shows the surface morphologies and XRD pattern of the oxide scale formed during heating the Ti-46Al-2Cr-5Nb alloy to the end of Stage IV. As shown in the XRD pattern (Figure 9d), the oxide scale is mainly composed of a large amount of  $\text{TiO}_2$  as well as a small amount of  $\text{Al}_2\text{O}_3$  and  $\beta\text{-Al}_2\text{TiO}_5$ . Besides, the content of the  $\gamma$  phase is much lower than that detected after heating to the end of Stage III (Figure 6d). It manifests that the thickness of the oxide scale increased significantly at Stage IV compared with that at Stage III, which is consistent with the drastic increase of the oxidation rate at Stage IV (Figure 3). As shown in Figure 9a,b, the outer layer of the oxide scale is still a spalling-prone  $\text{TiO}_2$  layer, but it is relatively thin and dense compared with that formed at Stage III (Figure 6a,b). Below the outer layer, a few irregular sintering structures of  $\beta\text{-Al}_2\text{TiO}_5$  coexist with relatively regular crystals of  $\text{TiO}_2$  and  $\text{Al}_2\text{O}_3$ , as shown in Figure 9c. It can be seen from the  $\text{TiO}_2\text{-Al}_2\text{O}_3$  phase diagram [41] that the reaction of  $\text{TiO}_2 + \text{Al}_2\text{O}_3 \rightarrow \beta\text{-Al}_2\text{TiO}_5$  occurs when the temperature is higher than 1200 °C. Therefore, the irregular sintering structures of  $\beta\text{-Al}_2\text{TiO}_5$  was produced by the reaction between  $\text{TiO}_2$  and  $\text{Al}_2\text{O}_3$  in the oxide scale at Stage IV (1280–1350 °C).

Figure 10 presents the cross-sectional morphology and the corresponding elemental distribution maps of the oxide scale. The oxide scale is identified to be in the order of the  $\text{TiO}_2$  layer/ $\text{TiO}_2 + \text{Al}_2\text{O}_3$  mixed layer/ $\text{Al}_2\text{O}_3$ -rich layer/ $\text{TiO}_2$ -rich layer/ $\text{TiO}_2(\text{Nb, Cr}) + \text{Al}_2\text{O}_3$  mixed layer from the outside to the inside. In addition, an Al-depleted layer enriched in Nb and Cr elements is generated in the subsurface of the alloy. Moreover,  $\text{Al}_2\text{O}_3$  oxides are dispersed as islands in the subsurface, indicating the occurrence of internal oxidation at Stage IV. Since internal oxidation deteriorates the oxidation resistance of TiAl-based alloys [14], the severe oxidation behavior of the Ti-46Al-2Cr-5Nb alloy at this

stage resulted from the internal oxidation of Al, which is probably the cause for the much higher oxidation energy of the Ti-46Al-2Cr-5Nb alloy at Stage IV than that at Stage III.



**Figure 9.** (a–c) Surface morphologies and (d) XRD pattern of the oxide scale formed during heating the Ti-46Al-2Cr-5Nb alloy to the end of Stage IV.



**Figure 10.** (a) Cross-sectional morphology and (b–f) the corresponding elemental distribution maps of the oxide scale formed during heating the Ti-46Al-2Cr-5Nb alloy to the end of Stage IV.

As for the Ti-24Al-15Nb-1.5Mo alloy, the surface morphologies and XRD pattern of the oxide formed during heating the alloy to the end of Stage IV are shown in Figure 11. The XRD result shows that the oxide scale is mainly composed of  $\text{TiO}_2$  accompanied with a small amount of  $\beta\text{-Al}_2\text{TiO}_5$  (Figure 11d). The outer layer of the oxide scale is crimping (Figure 11a), consisting of coarse rod-like  $\text{TiO}_2$  particles and ridged structures composed of fine  $\beta\text{-Al}_2\text{TiO}_5$  particles (Figure 11c). The outer layer is prone to exfoliation (Figure 11a), revealing the layer of fine  $\text{TiO}_2$  particles (Figure 11b).

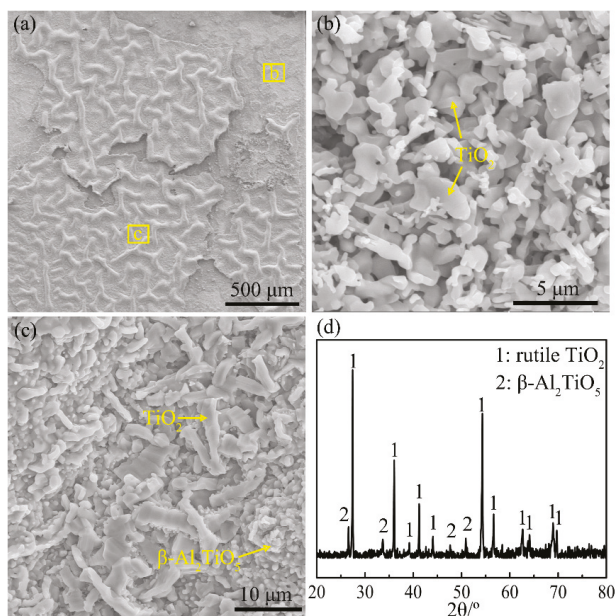


**Figure 11.** (a–c) Surface morphologies and (d) XRD pattern of the oxide formed during continuously heating the Ti-24Al-15Nb-1.5Mo alloy to the end of Stage IV.

Figure 12 presents the cross-sectional morphology and the corresponding elemental distribution maps of the oxide scale on the Ti-24Al-15Nb-1.5Mo alloy. The structure of the oxide scale is in the order of the  $\text{TiO}_2 + \text{Al}_2\text{TiO}_5$  layer/ $\text{TiO}_2$  layer/coarse  $\text{Al}_2\text{O}_3$  layer/porous  $\text{TiO}_2(\text{Nb, Mo})$  layer from the outside to the inside. The porous  $\text{TiO}_2(\text{Nb, Mo})$  inner layer and the coarse  $\text{Al}_2\text{O}_3$  immediate layer indicate that the  $\text{Al}_2\text{O}_3$  particles formed in the inner layer dissolved in the surrounding  $\text{TiO}_2(\text{Nb, Mo})$ , then migrated outward and re-precipitated in the immediate layer at Stage IV, the reason for which is that the decreasing oxygen pressure around the inner layer with the thickening of the oxide scale increases the solubility of  $\text{Al}_2\text{O}_3$  in  $\text{TiO}_2$  and reduces the stability of  $\text{Al}_2\text{O}_3$  [17]. It is reported that the dissolution, migration and re-precipitation of  $\text{Al}_2\text{O}_3$  destroys the oxygen-blocking ability of the original  $\text{Al}_2\text{O}_3$  barrier layer, leading to breakaway oxidation [17,42]. However, there is a transverse crack below the oxide scale and whether the crack contributed to the severe oxidation should be discussed. According to the crimping structure and the locally spalling morphology of the oxide scale (Figure 11a), the crack is considered to be induced during cooling after oxidation. The reason is that the oxide scale and the matrix were respectively subjected to compressive and tensile stresses during cooling since the thermal expansion coefficient of the oxide scale is generally smaller than that of the metal, and curling deformation was prone to occur in the oxide scale for stress release. Thus, the severe oxidation behavior of the Ti-24Al-15Nb-1.5Mo alloy at Stage IV is independent of the formation of the transverse crack. Consequently, the severe oxidation at this stage is due to the dissolution, migration and re-precipitation of  $\text{Al}_2\text{O}_3$ , which might lead to the higher oxidation energy at Stage IV than that at Stage III.

In addition, a thin  $\alpha$ -Ti(O) layer was formed at the interface between the oxide scale and the alloy, beneath which is a 10- $\mu$ m-thick layer composed of  $\beta$ -Ti rich in Nb, Mo, Al elements (referred to as *i* in Figure 12a) and several fine  $\alpha$ -Ti grains with an orientation nearly perpendicular to the matrix surface (referred to as *ii* in Figure 12a). The microstructure between the  $\beta$ -Ti layer and the matrix is still composed of  $\alpha$ -Ti(O) grains (referred to as *iii* in Figure 12a) and a small amount of  $\beta$ -Ti phase in the grain boundaries (referred to as *iv* in Figure 12a). The chemical compositions of these structures are shown in Table 2. The microstructures demonstrate that more oxygen diffused into the subsurface of the alloy at Stage IV in comparison with at Stage III, resulting in the transition from  $\beta$ -Ti to  $\alpha$ -Ti(O) in the near subsurface layer.

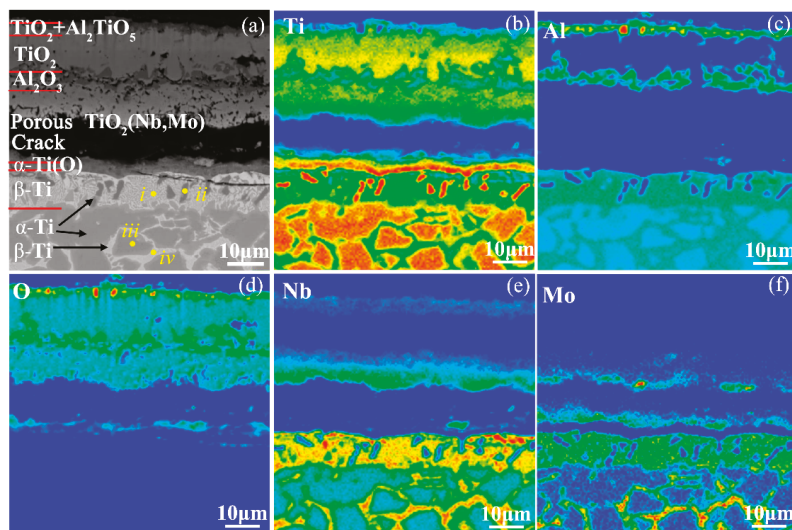


**Figure 12.** (a) Cross-sectional morphology and (b–f) the corresponding elemental distribution maps of the oxide scale formed during heating the Ti-24Al-15Nb-1.5Mo alloy to the end of Stage IV.

**Table 2.** Chemical compositions of the microstructures in the Ti-24Al-15Nb-1.5Mo alloy examined by an electron probe microanalyzer (EPMA) after heating the alloy to the end of Stage IV.

Microstructures in Figure 12a	Compositions (at.%)			
	Ti	Al	Nb	Mo
<i>i</i>	42.99	20.15	34.66	2.2
<i>ii</i>	87.35	4.95	7.7	-
<i>iii</i>	75.62	12.77	11.23	0.37
<i>iv</i>	42.67	19.57	34.77	2.99

#### 4.3.5. Decelerated Oxidation Stage (Stage V)

When the temperature increased to Stage V (1350–1450 °C), the oxidation rate of the Ti-46Al-2Cr-5Nb alloy decreased remarkably. Figure 13 presents the surface morphologies and XRD pattern of the oxide scale formed during heating the Ti-46Al-2Cr-5Nb alloy to the end of Stage V. There is no obvious exfoliation morphology on the surface of oxide scale (Figure 13a). Further, the scale becomes denser (Figure 13b) and the crystals in the surface of the scale become larger (Figure 13c) compared with those formed at Stage IV. As shown in the XRD pattern (Figure 13d), the oxide scale consists of a large quantity of  $\beta$ -Al<sub>2</sub>TiO<sub>5</sub> as well as some TiO<sub>2</sub> and Al<sub>2</sub>O<sub>3</sub>, indicating that the sintering reaction between TiO<sub>2</sub> and Al<sub>2</sub>O<sub>3</sub> in the oxide scale aggravated at Stage V.

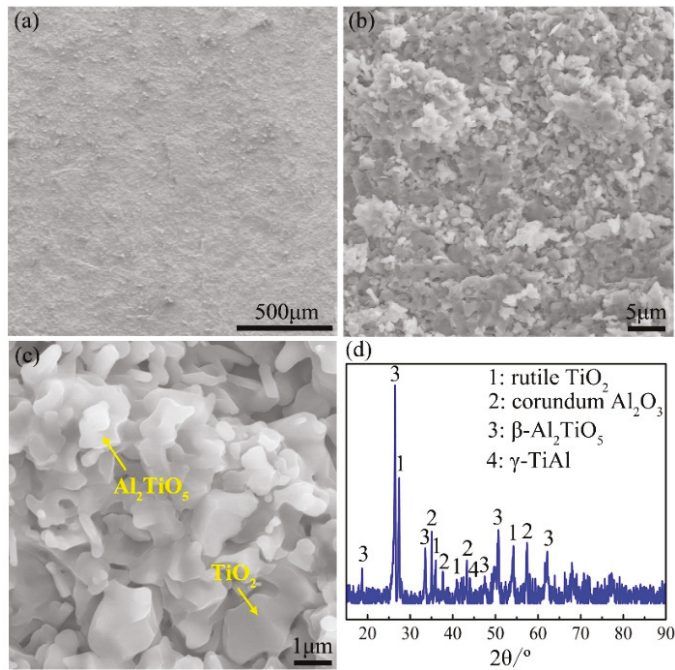


**Figure 13.** (a–c) Surface morphologies and (d) XRD pattern of the oxide scale formed during heating the Ti-46Al-2Cr-5Nb alloy to the end of Stage V.

Figure 14 shows the cross-sectional morphology and the corresponding elemental distribution maps of the oxide scale. The oxide scale from the outside to the inside is identified to be in the order of the  $\text{TiO}_2$  layer/ $\text{Al}_2\text{O}_3$ -rich layer/ $\text{TiO}_2$ -rich layer/ $\text{Al}_2\text{TiO}_5$  layer/mixed layer of  $\text{TiO}_2$  and fine  $\text{Al}_2\text{O}_3$  flakes. It is interesting that the  $\text{TiO}_2$  (referred to as *i* in Figure 14a) and the fine  $\text{Al}_2\text{O}_3$  flakes (referred to as *ii* in Figure 14a) distribute alternately in the inner layer, the compositions of which are presented in Table 3. White coarse particles (referred to as *iii* in Figure 14a) with an orientation perpendicular to the oxide/substrate interface were generated in the subsurface of the substrate. The detected composition as shown in Table 3 manifests that the white particles might be an alloy or an intermetallic of Nb. Moreover, there are a lot of fine  $\text{Al}_2\text{O}_3$  flakes distributing around the white coarse particles. Besides, it should be mentioned that there is a transverse crack in the oxide scale, which is not found in the oxide scale formed during heating the alloy to the end of Stage IV. This crack is considered to be produced during cooling after oxidation or during the preparation of metallographic specimens instead of during oxidation, since the oxidation rate at Stage V was significantly reduced in comparison with at Stage IV.

Through comparing the cross-sectional structures of the oxide scales respectively formed by heating the Ti-46Al-2Cr-5Nb alloy to the end of Stage IV and Stage V (Figures 10 and 14), the growth process of the oxide scale at Stage V can be inferred as follows: (1) oxygen from the atmosphere diffused into the alloy and the Al-depleted zones were preferentially oxidized nearby the  $\text{Al}_2\text{O}_3$  flakes which were generated due to the internal oxidation at Stage IV, thus forming the inner oxide layer structure where  $\text{TiO}_2$  and  $\text{Al}_2\text{O}_3$  flakes distributed alternately; (2) due to the limited solubility of the alloying elements (such as Nb, Cr and Al) in  $\text{TiO}_2$ , the alloying elements diffused towards the underlying substrate during the growth of the oxide scale, resulting in the formation of massive white coarse particles of Nb alloy or intermetallic in the newly-formed subsurface of the substrate; (3) the continuous inward diffusion of oxygen further induced the occurrence of internal oxidation in the subsurface, leading to the formation of fine  $\text{Al}_2\text{O}_3$  flakes around the white coarse particles and even

the underlying substrate. However, at the same time of the oxide growth, the sintering reaction between  $\text{TiO}_2$  and  $\text{Al}_2\text{O}_3$  in the oxide scale (mainly in the  $\text{TiO}_2 + \text{Al}_2\text{O}_3$  mixed layer) aggravated and an  $\beta\text{-Al}_2\text{TiO}_5$ -rich layer was formed in the oxide scale (Figure 14a). Since  $\beta\text{-Al}_2\text{TiO}_5$  has higher oxygen resistance than  $\text{TiO}_2$  [5,43], the formation of the  $\beta\text{-Al}_2\text{TiO}_5$ -rich layer could effectively slow down the inward diffusion of oxygen and the oxidation rate decreased. Hence, the decelerated oxidation behavior of the Ti-46Al-2Cr-5Nb alloy at Stage V is due to the generation of an oxygen-barrier  $\beta\text{-Al}_2\text{TiO}_5$ -rich layer in the oxide scale by the reaction between  $\text{TiO}_2$  and  $\text{Al}_2\text{O}_3$  in large scales.

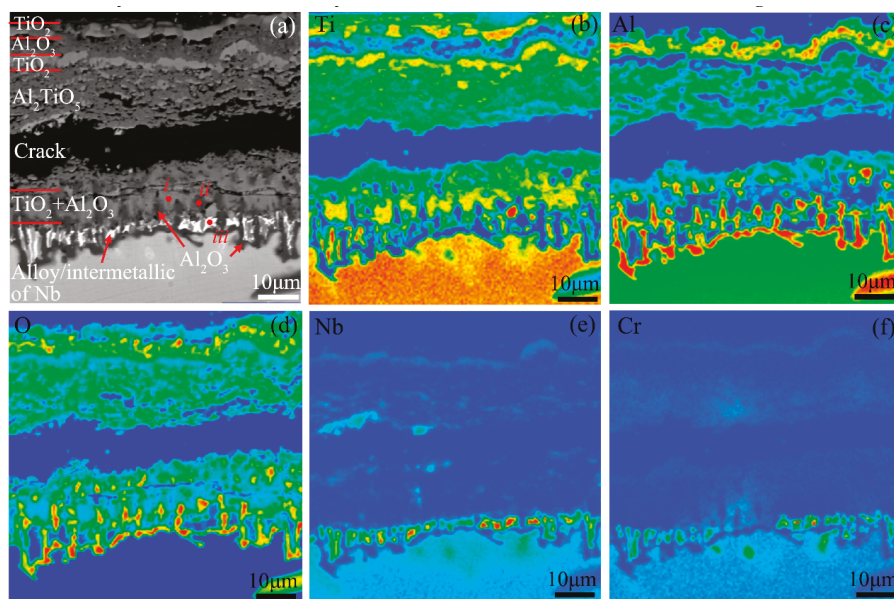


**Figure 14.** (a) Cross-sectional morphology and (b–f) the corresponding elemental distribution maps of the oxide scale formed during heating the Ti-46Al-2Cr-5Nb alloy to the end of Stage V.

**Table 3.** Chemical compositions of the microstructures in the inner layer of the oxide and in the subsurface of the Ti-46Al-2Cr-5Nb alloy examined by EPMA after heating the alloy to the end of Stage IV.

Microstructures in Figure 14a	Compositions (at.%)				
	Ti	Al	Nb	Cr	O
<i>i</i>	44.61	3.96	0.24	-	51.19
<i>ii</i>	5.66	26.09	-	-	68.25
<i>iii</i>	29.25	14.25	39.59	16.91	-

#### 4.4. Reasons for the Occurrence of Internal Oxidation in the Ti-46Al-2Cr-5Nb Alloy

In comparison with the Ti-24Al-15Nb-1.5Mo alloy, the Ti-46Al-2Cr-5Nb alloy suffered catastrophic oxidation at the temperature range of 1280–1350 °C due to the occurrence of internal oxidation. In order to improve the non-isothermal oxidation resistance of the Ti-46Al-2Cr-5Nb alloy, it is essential to shed light on the reasons for the occurrence of internal oxidation in the Ti-46Al-2Cr-5Nb alloy instead of in the Ti-24Al-15Nb-1.5Mo alloy. In accordance to the occurrence conditions of internal oxidation [44], it seems that the Ti-24Al-15Nb-1.5Mo alloy mainly dominated by  $\alpha_2$  phase should be more prone to suffer internal oxidation than the Ti-46Al-2Cr-5Nb alloy mainly dominated by  $\gamma$  phase, since both the oxygen solubility and the oxygen diffusion rate in  $\alpha_2$  phase are higher than those in the  $\gamma$  phase

and the Al content in the  $\alpha_2$  phase is lower than that in the  $\gamma$  phase. However, this is not the case. Therefore, the actual phases in the Ti-46Al-2Cr-5Nb and Ti-24Al-15Nb-1.5Mo alloys at the temperature range of 1280–1350 °C should be taken into account.

The initial temperature for the occurrence of internal oxidation in the Ti-46Al-2Cr-5Nb alloy (1280 °C) is close to the temperature of  $\gamma + \alpha \rightarrow \alpha$  phase transition (about 1226 °C, see Figure 3a). Hence, before the occurrence of internal oxidation ( $T < 1280$  °C), the substrate of the Ti-46Al-2Cr-5Nb alloy was mainly dominated by  $\gamma$  phase and the subsurface of the alloy was dominated by an Al-depleted layer of  $\alpha_2$  phase [16], as illustrated in Figure 15a. However, when the temperature rose above the initial temperature for the occurrence of internal oxidation ( $T > 1280$  °C), the main phases both in the substrate and the subsurface Al-depleted layer of the Ti-46Al-2Cr-5Nb alloy transformed to the  $\alpha$  phase, as illustrated in Figure 15b. As for the Ti-24Al-15Nb-1.5Mo alloy at the temperature range for the occurrence of internal oxidation in the Ti-46Al-2Cr-5Nb alloy (1280–1350 °C), the substrate was mainly dominated by  $\beta$  phase and the subsurface was also dominated by  $\beta$  phase due to the enrichment of Mo and Nb elements, even though the microstructure between the subsurface and the substrate was composed of  $\alpha$ -Ti(O) grains and a small amount of  $\beta$ -Ti phase, as illustrated in Figure 15c. It is obviously seen from Figure 15 that the phases in the subsurface where internal oxidation occurs are different. Hence, in order to reveal the effect of the phases in the subsurface on the internal oxidation tendency, the four phases involving in the Ti-Al alloys ( $\gamma$ ,  $\alpha_2$ ,  $\alpha$  and  $\beta$ ) were studied.

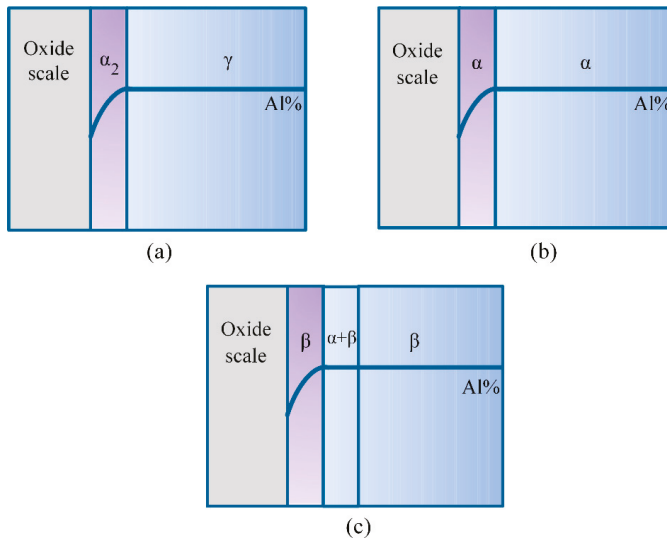


**Figure 15.** Schematic diagrams of the phase structures for (a) the Ti-46Al-2Cr-5Nb alloy when  $T < 1280$  °C, (b) the Ti-46Al-2Cr-5Nb alloy when  $T > 1280$  °C and (c) the Ti-24Al-15Nb-1.5Mo alloy at the temperature range of 1280–1350 °C.

The tendency of internal oxidation for the different phases in the Ti-46Al-2Cr-5Nb alloy at 1280 °C can be identified based on Wagner’s theory [44]. The critical criterion for the transition from internal oxidation to external oxidation is:

$$N_{Al} > N_{crit(Al)} = \left( \frac{\pi g^*}{2} \frac{V_m}{V_{ox}} \frac{D_O}{D_{Al}} N_O \right)^{0.5}, \quad (2)$$

where  $N_{crit(Al)}$  is the critical Al content required for the transition from internal oxidation to external oxidation,  $g^*$  is a constant factor in the case of an index of 0.3,  $V_m$  and  $V_{ox}$  are respectively the molar volumes of the Ti-46Al-2Cr-5Nb alloy and  $Al_2O_3$  oxide (in  $cm^3/mol$ ,  $V_{ox} = 25.5$   $cm^3/mol$ ),



$D_O$  and  $D_{Al}$  are respectively the diffusion coefficients of O and Al atoms in the lattice of the alloy,  $N_O$  and  $N_{Al}$  are respectively the oxygen content and Al content in the subsurface of the alloy. The composition in the subsurface of the Ti-46Al-2Cr-5Nb alloy after heating to 1280 °C was detected to be Ti-29.8Al-3.6O-3.0Cr-5.4Nb (in at.%) by EPMA, thus the values for  $N_O$  and  $N_{Al}$  are respectively 0.036 and 0.298. The values for the other parameters involved in Equation (2) are given in Table 4. It should be noted that the specific value for the oxygen diffusion coefficient in the  $\gamma$  phase has not been reported, but it is readily inferred that the oxygen diffusion coefficient in the  $\gamma$  phase is lower than that in the  $\alpha_2$  phase from their lattice structure differences, as mentioned in Section 4.3.2.

**Table 4.** Critical Al contents required for the transition from internal oxidation to external oxidation for the different phases in the subsurface of the Ti-46Al-2Cr-5Nb alloy at 1280 °C.

Phases	Parameters				Results
	$V_m$ /(cm <sup>3</sup> /mol)	$D_O$ /(m <sup>2</sup> /s)	$D_{Al}$ [45]/(m <sup>2</sup> /s)	$D_O/D_{Al}$	$N_{crit(Al)}$
$\gamma$	19.7	$<3.66 \times 10^{-15}$	$1.97 \times 10^{-14}$	$<0.186$	$<0.05$
$\alpha_2$	40.7	$3.66 \times 10^{-15}$ [32]	$1.37 \times 10^{-14}$	0.267	0.085
$\alpha$	10.6	$3.54 \times 10^{-11}$ [46]	$5.80 \times 10^{-14}$	610.3	2.08
$\beta$	11.0	$3.75 \times 10^{-10}$ [46]	$1.04 \times 10^{-12}$	360.6	1.62

Table 4 presents the calculation results of the critical Al contents required for the transition from internal oxidation to external oxidation for the different phases in the subsurface of the Ti-46Al-2Cr-5Nb alloy at 1280 °C. The critical Al contents required for the  $\alpha_2$  and  $\gamma$  phases are respectively 0.085 and less than 0.05, which is much lower than the actual Al content in the subsurface of the substrate ( $N_{Al} = 0.298$ ). It indicates that if the subsurface of the Ti-46Al-2Cr-5Nb alloy is dominated by  $\gamma$  phase and/or  $\alpha_2$  phase, an external oxide scale would form on the alloy and internal oxidation could not occur. However, the critical Al contents required for the  $\alpha$  and  $\beta$  phases are respectively 2.08 and 1.62, which is impractical since the contents are more than 1. This situation is caused by the fact that Wagner's theory of internal oxidation is based on a large number of idealized conditions that often could not be met in the actual system [44]. Nevertheless, Wagner's critical criterion can still reflect the tendency of internal oxidation for the different phases in the subsurface of the Ti-46Al-2Cr-5Nb alloy. The higher the required critical Al content, the more easily internal oxidation will occur. Therefore, the tendency of internal oxidation for the phases is in the order of  $\alpha > \beta > \alpha_2 > \gamma$ . Thus, it is easy to understand why internal oxidation occurred in the Ti-46Al-2Cr-5Nb alloy when the temperature exceeded 1280 °C, since the main phase in the subsurface of the Ti-46Al-2Cr-5Nb alloy changed from  $\alpha_2$  phase to  $\alpha$  phase when the temperature was higher than 1280 °C. In addition, the main phase in the substrate of the Ti-24Al-15Nb-1.5Mo alloy was  $\beta$  phase at the temperature range of 1280–1350 °C due to the enrichment of large amounts of  $\beta$ -stabilizing elements (Nb and Mo), so that no internal oxidation occurred in this alloy. Consequently, it is concluded that the formation of  $\alpha$  phase in the subsurface is the basic reason for the occurrence of internal oxidation in the Ti-46Al-2Cr-5Nb alloy. The tendency of internal oxidation in the TiAl-based alloys could be reduced through avoiding the formation of  $\alpha$  phase in the subsurface by optimizing alloy ingredients, such as increasing the Al content or adding  $\beta$ -stabilizing elements. However, it should be noted that the optimization of alloy ingredients is complicated and should be further investigated since not only the tendency of internal oxidation, but also other properties of the alloys such as the mechanical properties, should be taken into consideration in practical engineering.

## 5. Conclusions

1. The non-isothermal oxidation behaviors of the Ti-46Al-2Cr-5Nb and Ti-24Al-15Nb-1.5Mo alloys are similar when the temperature is below 1280 °C, while the Ti-46Al-2Cr-5Nb alloy exhibits poorer oxidation resistance than the Ti-24Al-15Nb-1.5Mo alloy when the temperature exceeds

1280 °C, even though the oxidation rate of the Ti-46Al-2Cr-5Nb alloy decreases significantly when the temperature is above 1350 °C.

- There are five stages in the non-isothermal oxidation process of the Ti-46Al-2Cr-5Nb alloy, including nearly non-oxidation (<870 °C), slow oxidation (870–980 °C), accelerated oxidation (980–1280 °C), severe oxidation (1280–1350 °C) and decelerated oxidation (1350–1450 °C) stages. The corresponding oxidation mechanisms are as follows: oxygen-barrier effect of the thin titanium oxide film; oxygen dissolution in the alloy; growth of the oxide scale dominated by TiO<sub>2</sub>; internal oxidation of Al; formation of an oxygen-barrier Al<sub>2</sub>TiO<sub>5</sub>-rich layer by reaction between TiO<sub>2</sub> and Al<sub>2</sub>O<sub>3</sub> in the oxide scale.
- There are four stages in the non-isothermal oxidation process of the Ti-24Al-15Nb-1.5Mo alloy, including nearly non-oxidation (<800 °C), slow oxidation (800–1020 °C), accelerated oxidation (1020–1400 °C) and severe oxidation (1400–1450 °C) stages. The oxidation mechanisms for the first three stages are the same with that of the Ti-46Al-2Cr-5Nb alloy, while the oxidation mechanism for the last stage is the dissolution, migration and re-precipitation of Al<sub>2</sub>O<sub>3</sub> in the oxide.
- The tendency of internal oxidation for the different phases in the subsurface of the Ti-46Al-2Cr-5Nb alloy is in the order of  $\alpha > \beta > \alpha_2 > \gamma$ . The formation of  $\alpha$  phase in the subsurface is the basic reason for the occurrence of internal oxidation in the Ti-46Al-2Cr-5Nb alloy. The tendency of internal oxidation in the TiAl-based alloys could be reduced through avoiding the formation of  $\alpha$  phase by optimizing alloy ingredients such as increasing Al content or adding  $\beta$ -stabilizing elements.

**Author Contributions:** Conceptualization, G.M. and P.L.; methodology, P.O.; investigation, P.O.; writing—original draft preparation, P.O.; writing—review and editing, G.M. and P.L.; supervision, X.H. and J.C.; project administration, L.H.; funding acquisition, G.M. and P.L.

**Funding:** This research was funded by the National Natural Science Foundation of China (Grant No. 51471155) and the Aviation Innovation Foundation of China (Grant No. 2014E62149R).

**Conflicts of Interest:** The authors declare no conflict of interest.

## References

- Wu, X. Review of alloy and process development of TiAl alloys. *Intermetallics* **2006**, *14*, 1114–1122. [[CrossRef](#)]
- Clemens, H.; Mayer, S. Design, processing, microstructure, properties, and applications of advanced intermetallic TiAl alloys. *Adv. Eng. Mater.* **2013**, *15*, 191–215. [[CrossRef](#)]
- Bewlay, B.; Weimer, M.; Kelly, T.; Suzuki, A.; Subramanian, P. The science, technology, and implementation of TiAl alloys in commercial aircraft engines. *MRS Online Proc. Lib. Arch.* **2013**, *1516*, 49–58. [[CrossRef](#)]
- Cai, J.; Mi, G.; Gao, F.; Huang, H.; Cao, J.; Huang, X.; Cao, C. Research and development of some advanced high temperature titanium alloys for aero-engine. *J. Mater. Eng.* **2016**, *44*, 1–10.
- Ouyang, P.; Mi, G.; Cao, J.; Huang, X.; He, L.; Li, P. Microstructure characteristics after combustion and fireproof mechanism of TiAl-based alloys. *Mater. Today Commun.* **2018**, *16*, 364–373. [[CrossRef](#)]
- Kim, D.; Seo, D.; Saari, H.; Sawatzky, T.; Kim, Y.W. Isothermal oxidation behavior of powder metallurgy beta gamma TiAl-2Nb-2Mo alloy. *Intermetallics* **2011**, *19*, 1509–1516. [[CrossRef](#)]
- Kim, S.W.; Hong, J.K.; Na, Y.S.; Yeom, J.T.; Kim, S.E. Development of TiAl alloys with excellent mechanical properties and oxidation resistance. *Mater. Design* **2014**, *54*, 814–819. [[CrossRef](#)]
- Legzdina, D.; Robertson, I.; Birnbaum, H. Oxidation behavior of a single phase  $\gamma$ -TiAl alloy in low-pressure oxygen and hydrogen. *Acta Mater.* **2005**, *53*, 601–608. [[CrossRef](#)]
- Lu, W.; Chen, C.; He, L.; Wang, F.; Lin, J.; Chen, G. (S)TEM study of different stages of Ti-45Al-8Nb-0.2W-0.2B-0.02Y alloy oxidation at 900 °C. *Corros. Sci.* **2008**, *50*, 978–988. [[CrossRef](#)]
- Qu, S.; Tang, S.; Feng, A.; Feng, C.; Shen, J.; Chen, D. Microstructural evolution and high-temperature oxidation mechanisms of a titanium aluminide based alloy. *Acta Mater.* **2018**, *148*, 300–310. [[CrossRef](#)]
- Strobridge, T.R.; Moulder, J.C.; Clark, A.F. *Titanium Combustion in Turbine Engines*; Report FAA-RD-79-51, NBSIR 79-1616; US National Bureau of Standards: Washington, DC, USA, 1979.
- Li, B.; Chen, G.; Zhang, H.; Sheng, C.D. Development of non-isothermal TGA–DSC for kinetics analysis of low temperature coal oxidation prior to ignition. *Fuel* **2014**, *118*, 385–391. [[CrossRef](#)]

13. Hosseini, S.G.; Sheikhpour, A.; Keshavarz, M.H.; Tavangar, S. The effect of metal oxide particle size on the thermal behavior and ignition kinetic of Mg-CuO thermite mixture. *Thermochim. Acta* **2016**, *626*, 1–8. [CrossRef]
14. Beye, R.; Verwerft, M.; Hosson, J.D.; Gronsky, R. Oxidation subscale of  $\gamma$ -titanium aluminide. *Acta Mater.* **1996**, *44*, 4225–4231. [CrossRef]
15. Beye, R.; Gronsky, R. Novel phases in the oxidation of  $\gamma$ -titanium aluminum. *Acta Metall. Mater.* **1994**, *42*, 1373–1381. [CrossRef]
16. Rahmel, A.; Schütze, M.; Quadackers, W. Fundamentals of TiAl oxidation—a critical review. *Mater. Corros.* **1995**, *46*, 271–285. [CrossRef]
17. Becker, S.; Rahmel, A.; Schorr, M.; Schütze, M. Mechanism of isothermal oxidation of the intermetallic TiAl and of TiAl alloys. *Oxid. Met.* **1992**, *38*, 425–464. [CrossRef]
18. Vaidya, R.U.; Park, Y.S.; Zhe, J.; Gray, G.T.; Butt, D.P. High-temperature oxidation of Ti-48Al-2Nb-2Cr and Ti-25Al-10Nb-3V-1Mo. *Oxid. Met.* **1998**, *50*, 215–240. [CrossRef]
19. Das, S. The Al-O-Ti (aluminum-oxygen-titanium) system. *J. Phase Equilib.* **2002**, *23*, 525–536. [CrossRef]
20. Chattopadhyay, K.; Mitra, R.; Ray, K. Nonisothermal and isothermal oxidation behavior of Nb-Si-Mo alloys. *Metall. Mater. Trans. A* **2008**, *39*, 577–592. [CrossRef]
21. Schulz, O.; Eisenreich, N.; Kelzenberg, S.; Schuppler, H.; Neutz, J.; Kondratenko, E. Non-isothermal and isothermal kinetics of high temperature oxidation of micrometer-sized titanium particles in air. *Thermochim. Acta* **2011**, *517*, 98–104. [CrossRef]
22. Mi, G.B.; Huang, X.S.; Li, P.J.; Cao, J.X.; Huang, X.; Cao, C.X. Non-isothermal oxidation and ignition prediction of Ti-Cr alloys. *Trans. Nonferr. Metal Soc.* **2012**, *22*, 2409–2415. [CrossRef]
23. Ouyang, P.; Mi, G.; Li, P.; He, L.; Cao, J.; Huang, X. Non-isothermal oxidation behavior and mechanism of a high temperature near- $\alpha$  titanium alloy. *Materials* **2018**, *11*, 2141. [CrossRef] [PubMed]
24. Kofstad, P. High-temperature oxidation of titanium. *J. Less-Common Metals* **1967**, *12*, 449–464. [CrossRef]
25. Kofstad, P.; Hauffe, K.; Kjollesdal, H. Investigation on the oxidation mechanism of titanium. *Acta Chem. Scand.* **1958**, *12*, 239–266. [CrossRef]
26. Kofstad, P.; Anderson, P.; Krudtaa, O. Oxidation of titanium in the temperature range 800–1200 °C. *J. Less-Common Metals* **1961**, *3*, 89–97. [CrossRef]
27. Overton, J.M. Thermophysical Property and Phase Transformation Determination of Gamma-TiAl Intermetallics. Master's Thesis, Carleton University, Ottawa, ON, Canada, May 2006.
28. Ishikawa, K.; Kazuhiro, R.; Ishida, K. The Ti-Al Binary System. Available online: [https://materials.springer.com/msi/phase-diagram/docs/sm\\_msi\\_r\\_10\\_010909\\_02\\_full\\_LnkDia0](https://materials.springer.com/msi/phase-diagram/docs/sm_msi_r_10_010909_02_full_LnkDia0) (accessed on 15 May 2019).
29. Terner, M.; Biamino, S.; Ugues, D.; Sabbadini, S.; Fino, P.; Pavese, M.; Badini, C. Phase transitions assessment on  $\gamma$ -TiAl by thermo mechanical analysis. *Intermetallics* **2013**, *37*, 7–10. [CrossRef]
30. Malinov, S.; Novoselova, T.; Sha, W. Experimental and modelling studies of the thermodynamics and kinetics of phase and structural transformations in a gamma TiAl-based alloy. *Mater. Sci. Eng. A* **2004**, *386*, 344–353. [CrossRef]
31. Huang, X. *Advanced Aeronautical Titanium Alloys and Applications*; National Defense Industry Press: Beijing, China, 2012.
32. Koizumi, Y.; Kishimoto, M.; Minamino, Y.; Nakajima, H. Oxygen diffusion in Ti<sub>3</sub>Al single crystals. *Philos. Mag.* **2008**, *88*, 2991–3010. [CrossRef]
33. Scotti, L.; Mottura, A. Interstitial diffusion of O, N, and C in  $\alpha$ -Ti from first-principles: Analytical model and kinetic Monte Carlo simulations. *J. Chem. Phys.* **2016**, *144*, 084701. [CrossRef] [PubMed]
34. Wu, H.H.; Trinkle, D.R. Direct diffusion through interpenetrating networks: Oxygen in titanium. *Phys. Rev. Lett.* **2011**, *107*, 045504. [CrossRef] [PubMed]
35. Bakulin, A.V.; Latyshev, A.M.; Kulkova, S.E. Absorption and diffusion of oxygen in the Ti<sub>3</sub>Al alloy. *J. Exp. Theor. Phys.* **2017**, *125*, 138–147. [CrossRef]
36. Jones, C.Y.; Luecke, W.E.; Copland, E. Neutron diffraction study of oxygen dissolution in  $\alpha_2$ -Ti<sub>3</sub>Al. *Intermetallics* **2006**, *14*, 54–60. [CrossRef]
37. Unnam, J.; Shenoy, R.; Clark, R. Oxidation of commercial purity titanium. *Oxid. Met.* **1986**, *26*, 231–252. [CrossRef]
38. Venkatu, D.; Poteat, L. Diffusion of titanium of single crystal rutile. *Mater. Sci. Eng.* **1970**, *5*, 258–262. [CrossRef]

39. Maurice, V.; Despert, G.; Zanna, S.; Josso, P.; Bacos, M.P.; Marcus, P. XPS study of the initial stages of oxidation of  $\alpha_2$ -Ti<sub>3</sub>Al and  $\gamma$ -TiAl intermetallic alloys. *Acta Mater.* **2007**, *55*, 3315–3325. [[CrossRef](#)]
40. Taniguchi, S.; Tachikawa, Y.; Shibata, T. Influence of oxygen partial pressure on the oxidation behaviour of TiAl at 1300 K. *Mater. Sci. Eng. A* **1997**, *232*, 47–54. [[CrossRef](#)]
41. Goldberg, D. Contribution to study of systems formed by alumina and some oxides of trivalent and tetravalent metals especially titanium oxide. *Rev. Int. Hautes Temp. Refract.* **1968**, *5*, 181.
42. Lang, C.; Schütze, M. TEM investigations of the early stages of TiAl oxidation. *Oxid. Met.* **1996**, *46*, 255–285. [[CrossRef](#)]
43. Swain, M.V. *Structure and Properties of Ceramics*; Wiley-VCH: Weinheim, Germany, 1994.
44. Leyens, C.; Peters, M. *Titanium and Titanium Alloys: Fundamentals and Applications*; Wiley: Hoboken, NJ, USA, 2006.
45. Mishin, Y.; Herzig, C. Diffusion in the Ti-Al system. *Acta Mater.* **2000**, *48*, 589–623. [[CrossRef](#)]
46. Liu, Z.; Welsch, G. Literature survey on diffusivities of oxygen, aluminum, and vanadium in alpha titanium, beta titanium, and in rutile. *Metall. Trans. A* **1988**, *19*, 1121–1125. [[CrossRef](#)]




© 2019 by the authors. Licensee MDPI, Basel, Switzerland. This article is an open access article distributed under the terms and conditions of the Creative Commons Attribution (CC BY) license (<http://creativecommons.org/licenses/by/4.0/>).



Article

# The Influence of Microstructure on the Passive Layer Chemistry and Corrosion Resistance for Some Titanium-Based Alloys

Nader El-Bagoury <sup>1,2</sup>, Sameh I. Ahmed <sup>2,3</sup>, Ola Ahmed Abu Ali <sup>1</sup>, Shima El-Hadad <sup>4</sup>, Ahmed M. Fallatah <sup>1</sup>, G. A. M. Mersal <sup>1,5</sup>, Mohamed M. Ibrahim <sup>1,6</sup>, Joanna Wysocka <sup>7</sup>, Jacek Ryl <sup>7,\*</sup>, Rabah Boukherroub <sup>8</sup> and Mohammed A. Amin <sup>1,9,\*</sup>

<sup>1</sup> Department of Chemistry, Faculty of Science, Taif University, P.O. Box 888, Taif 21974, Saudi Arabia; nader\_elbagoury@yahoo.com (N.E.-B.); o.abuali@tu.edu.sa (O.A.A.A.); a.fallatah.11@hotmail.com (A.M.F.); gamersal@yahoo.com (G.A.M.M.); ibrahim652001@yahoo.com (M.M.I.)

<sup>2</sup> Department of Physics, Faculty of Science, Taif University, Hawiya 888, Saudi Arabia; sameh@sci.asu.edu.eg

<sup>3</sup> Department of Physics, Faculty of Science, Ain Shams University, Abbassia 11566, Cairo, Egypt

<sup>4</sup> Central Metallurgical Research and Development Institute, P.O. Box 87, Helwan, Cairo, Egypt; shimaamohamad901@yahoo.com

<sup>5</sup> Chemistry Department, Faculty of Science, South Valley University, Qena 83523, Egypt

<sup>6</sup> Chemistry Department, Faculty of Science, Kafrelsheikh University, Kafr El-Sheikh 33516, Egypt

<sup>7</sup> Department of Electrochemistry, Corrosion and Materials Engineering, Chemical Faculty, Gdansk University of Technology, Narutowicza 11/12, 80-233 Gdansk, Poland; joanna.wer.wysocka@gmail.com

<sup>8</sup> Univ. Lille, CNRS, Centrale Lille, ISEN, Univ. Valenciennes, UMR 8520-IEMN, F-59000 Lille, France; rabah.boukherroub@univ-lille.fr

<sup>9</sup> Department of Chemistry, Faculty of Science, Ain Shams University, Abbassia 11566, Cairo, Egypt

\* Correspondence: jacek.ryl@pg.edu.pl (J.R.); maaismail@yahoo.com (M.A.A.); Tel.: +966-54-570-7507 (J.R.)

Received: 5 March 2019; Accepted: 9 April 2019; Published: 15 April 2019

**Abstract:** The effect of microstructure and chemistry on the kinetics of passive layer growth and passivity breakdown of some Ti-based alloys, namely Ti-6Al-4V, Ti-6Al-7Nb and TC21 alloys, was studied. The rate of pitting corrosion was evaluated using cyclic polarization measurements. Chronoamperometry was applied to assess the passive layer growth kinetics and breakdown. Microstructure influence on the uniform corrosion rate of these alloys was also investigated employing dynamic electrochemical impedance spectroscopy (DEIS). Corrosion studies were performed in 0.9% NaCl solution at 37 °C, and the obtained results were compared with ultrapure Ti (99.99%). The different phases of the microstructure were characterized by X-ray diffraction (XRD) and scanning electron microscopy (SEM). Chemical composition and chemistry of the corroded surfaces were studied using X-ray photoelectron spectroscopy (XPS) analysis. For all studied alloys, the microstructure consisted of  $\alpha$  matrix, which was strengthened by  $\beta$  phase. The highest and the lowest values of the  $\beta$  phase's volume fraction were recorded for TC21 and Ti-Al-Nb alloys, respectively. The susceptibility of the investigated alloys toward pitting corrosion was enhanced following the sequence: Ti-6Al-7Nb < Ti-6Al-4V << TC21. Ti-6Al-7Nb alloy recorded the lowest pitting corrosion resistance ( $R_{pit}$ ) among studied alloys, approaching that of pure Ti. The obvious changes in the microstructure of these alloys, together with XPS findings, were adopted to interpret the pronounced variation in the corrosion behavior of these materials.

**Keywords:** titanium-based alloys; microstructure; passivity breakdown; pitting corrosion

## 1. Introduction

Titanium and its alloys are widely used in many industrial applications, because of their highly desirable properties, including very good mechanical properties, excellent corrosion and erosion resistance, and favorable strength to weight ratio [1]. In fact, titanium and its alloys have experienced increased use in the past years as biomaterials, because of their superior biocompatibility, high resistance to localized and generalized corrosion, and their good mechanical properties (fatigue resistance) [2]. Among all titanium and its alloys, the commonly used materials in biomedical area are commercially pure titanium (cpTi) and its ( $\alpha + \beta$ ) Ti6-Al4-V alloy [3–5].

Next to biomedical applications, aerospace sector has dominated titanium use, instead of heavy steel components, in the fabrication of crucial and decisive systems such as airfoils and airframes [6–9]. About 50% of titanium used in the aerospace industry is the ( $\alpha + \beta$ ) Ti-6Al-4V alloy. This alloy possesses a perfect combination of operational and technological properties [10,11]. Titanium alloys have also found widespread applications in a variety of fields such as in chemical and petrochemical sectors due to their excellent corrosion resistance [12]. The outstanding characteristics (such as high specific strength, high fatigue strength, good corrosion resistance, etc.) of the titanium alloys (particularly Ti-6Al-4V) are attributed to a very stable native oxide film (1.5–10 nm) formed on the Ti and Ti-alloy surface upon exposure to atmosphere and/or aqueous environments [13,14]. However, this thin oxide layer can be damaged and thus strongly impacts the bioactivity and other characteristics of the material. To improve the performance of Ti and Ti-alloys for biomedical and aerospace applications, oxidation (anodization) has been applied as a successful approach to improve the material properties [15,16].

The microstructure, formed during various processing methods, is found to greatly influence the mechanical properties of titanium alloys [17]. The microstructure type (bimodal, lamellar and equiaxed) affects the mechanical properties of Ti based alloys [18]. Even though the corrosion of Ti-alloys in different environments has previously been studied [19–23], to the best of our knowledge, the literature contains no reports on the passive layer growth kinetics and breakdown, and subsequent initiation and propagation of pitting corrosion over the surfaces of Ti-6Al-7Nb, Ti-6Al-4V, and TC21 alloys. In this context, the main objective of our study was to assess the effect of microstructure changes of tested alloys on their surface morphology and chemistry using different techniques such as scanning electron microscopy with electron dispersive X-ray spectroscopy (SEM/EDX), X-ray diffraction (XRD), and X-ray Photoelectron Spectroscopy (XPS). The influence of microstructure changes on the anodic behavior and passive layer growth kinetics and breakdown was also investigated. The corrosion resistances were compared using potentiodynamic polarization and impedance spectroscopy tools. All measurements were conducted in 0.9% NaCl solution at 37 °C.

## 2. Materials and Methods

The working electrodes investigated in this study consisted of three Ti-based alloys, namely Ti-6Al-4V, Ti-6Al-7Nb and TC21; their chemical compositions are presented in Table 1. The as-received titanium alloy samples were prepared by melting in a 500 kg vacuum induction furnace to obtain billets. These billets were then forged and machined into 10 mm diameter bars. The microstructures of these alloys were studied by Meiji optical microscope (Meiji Techno Co., Ltd., Chikumazawa, Japan) fitted with a digital camera (Meiji Techno Co., Ltd., Chikumazawa, Japan). JEOL JSM5410 and Hitachi S-3400N scanning electron microscopes (LxRay Co., Ltd., Hyogo, Japan) (SEM) were also used for microstructure studies. For this purpose, the specimens were prepared following ASTM E3-11 standard metallographic procedures, and then etched in a mixture of 5 mL HNO<sub>3</sub>, 10 mL HF and 85 mL H<sub>2</sub>O. The alloys were machined in the form of rods to perform electrochemical measurements. These rods were mounted in a polyester resin offering an active cross-sectional area of ~0.2 cm<sup>2</sup>. Prior to conducting any electrochemical analysis, the surface of the working electrode was cleaned and polished using a silicon carbide paper (600-grit) installed on a polishing machine (Minitech 233). The surface was then washed copiously with distilled water and rinsed with absolute ethanol (SIGMA-ALDRICH, Steinheim, Germany).

**Table 1.** Chemical composition of investigated Ti alloys.

Alloy	Chemical Composition, wt %												
	Al	V	Nb	Sn	Zr	Mo	Cr	Si	Fe	C	N	O	Ti
Ti-6Al-4V	5.85	3.94	0.00	0.00	0.00	0.00	0.00	0.00	0.00	0.02	0.03	0.14	
Ti-6Al-7Nb	6.39	0.00	7.78	0.00	0.00	0.00	0.00	0.00	0.00	0.02	0.04	0.12	Bal.
TC21	5.89	0.00	2.41	2.51	1.59	2.27	1.58	0.067	0.05	0.01	0.01	0.13	

Electrochemical measurements were conducted in a standard, double-walled electrochemical cell (Princeton Applied Research, USA) with an inner volume capacity of 200 mL. Temperature of the test solution was maintained constant at the desired value by means of a temperature-controlled water bath (FP40-MA Refrigerated/Heating Circulator) (JULABO GmbH, Seelbach, Germany). The water, after being adjusted to  $37 \pm 0.1$  °C, was allowed to circulate through external jacket of the cell. The cover of the electrochemical cell had five openings with different sizes. Such openings were designed to be fitted to the working electrode, counter electrode (a long, coiled platinum wire), reference electrode (KCl-saturated calomel electrode (SCE)), a thermometer and a gas inlet/outlet for gas release. The reference electrode was placed in a Luggin capillary, the tip of which was adjusted to be close to the working electrode to minimize iR drop. The cell was connected to a Potentiostat (Autolab PGSTAT30) (Metrohm, Herisau, Switzerland). The test solution was a normal saline (0.9% NaCl). A Millipore Milli-Q water system (Merck Millipore, MA, USA) (18.2 MΩ cm) was used to freshly prepare the saline solution. The salt was of analytical grade and purchased from Sigma-Aldrich (Steinheim, Germany).

Linear sweep voltammetry (LSV), Tafel plots, and Electrochemical Impedance Spectroscopy (EIS) techniques were applied to investigate the uniform corrosion characteristics of the studied alloys. The susceptibility of these alloys to passivity breakdown was evaluated via conducting potentiodynamic polarization measurements. Uniform corrosion measurements were started by stabilizing the working electrode at the rest potential for 2 h, followed by conducting EIS measurements at the respective corrosion potential ( $E_{corr}$ ) every day for a week of exposure in 0.9% NaCl solution at 37 °C, covering a wide frequency range (100 kHz–10 mHz), with 15 mV perturbation amplitude. Uniform corrosion study was assessed by constructing Tafel plots via sweeping the electrode potential around the Tafel potential ( $E = E_{corr} \pm 250$  mV), applying a sweep rate of 1.0 mV s<sup>-1</sup>. After that, the electrode was removed from the cell (which was cleaned properly and re-filled with a new fresh test solution), cleaned and polished up to the mirror finish, as described above, and then inserted in the cell for cyclic polarization measurements. Chronoamperometry (CA) technique was also applied using a new set of cleaned and polished electrodes submerged in a cleaned cell filled with a new fresh solution.

Prior to performing cyclic polarization measurements, the working electrode was allowed to stabilize at rest potential for 2 h, then swept linearly, at a sweep rate of 1.0 mV s<sup>-1</sup>, starting from a cathodic potential of -2.0 V to +8.0 V vs.SCE. The potential sweep was then reversed back with the same sweep rate to reach the start point again, thus forming one complete cycle. To conduct chronoamperometry (current vs. time) measurements, a two-step route was applied. The working electrode was first held at a starting cathodic potential of -2.0 V vs. SCE for 60 s, and then polarized towards the anodic direction at a sweep rate of 1.0 mV s<sup>-1</sup> until the required anodic potential ( $E_a$ ). Finally, the anodic current was measured versus time (5.0 min) by holding the working electrode at  $E_a$ . To ensure reproducibility, each run was repeated at least three times, where mean values of the various electrochemical parameters and their standard deviations were calculated and reported.

The XRD diffraction patterns were collected for the bulk samples using a SmartLab SE (Rigaku Americas Corporation, Oxford, MS, USA) X-ray diffractometer with Cu Kα ( $\lambda = 1.54056$  Å) operated at 40 kV and 40 mA. The scanning speed was 0.2°/min and the scanning angle ranged from 20° to 100° in  $2\theta$ . Energy dispersive X-ray spectroscopy (EDS) measurements were utilized to determine microstructural composition of investigated alloys as well as evaluate changes in chemical composition as a result of exposure to corrosive media. S-3400N SEM (Hitachi, Tokyo, Japan) was equipped with an UltraDry detector from ThermoFisher Scientific (Waltham, MA, USA). High-resolution X-ray



photoelectron spectroscopy (XPS) studies were carried out on an Escalab 250 Xi from Thermofisher Scientific (Waltham, MA, USA), equipped with Al K $\alpha$  source. Pass energy was 20 eV and the spot size diameter was 650  $\mu$ m. Charge compensation was controlled through the low-energy electron and low energy Ar<sup>+</sup> ions emission by means of a flood gun (emission current: 150  $\mu$ A, beam voltage: 2.1 V, filament current: 3.5 A). Avantage software (Thermofisher Scientific, Waltham, MA, USA) was used for deconvolution purposes.

### 3. Results and Discussion

#### 3.1. Microstructure Investigation

Based on the morphology of  $\alpha$  phase, the microstructure of titanium alloys can be classified into equiaxed, lamellar and bi-modal microstructures [24]. The microstructure of Ti-based alloys can be controlled based on their chemical composition, i.e., based on the balance between the  $\alpha$  phase stabilizing elements, such as Al, Sn and O, and the forming  $\beta$  phase elements such as V, Mo and Nb [25]. As shown in Figure 1, the microstructure of all studied titanium alloys consisted of bimodal structure of  $\alpha/\beta$  phases. The initial microstructure of Ti-Al-V and Ti-Al-Nb alloys in as-received (forged) state was represented by equiaxed grains of primary  $\alpha$  phase (dark), as well as  $\beta$ -transformed structure (light), as shown in Figure 1. The  $\beta$  phase formed in the microstructure of both alloys was globular in shape, but seemed larger in size in Ti-Al-V alloy than in Ti-Al-Nb alloy. The particle size of  $\beta$  phase in Al-Ti-V alloy was about 0.5–1.5  $\mu$ m, while its size in Ti-Al-Nb alloy was slightly lower (about 0.25–1  $\mu$ m), as depicted in Figure 1a,b.

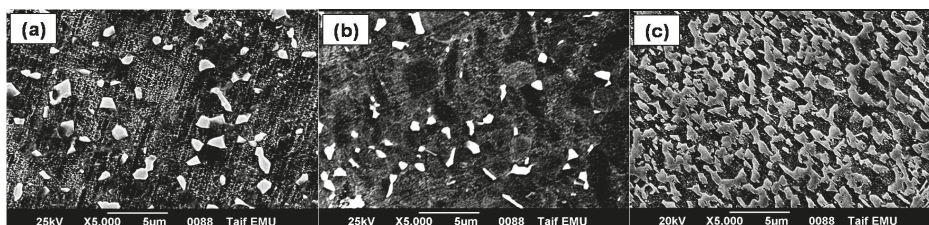


Figure 1. Microstructure of the three investigated Ti alloys: (a) Ti-Al-V; (b) Ti-Al-Nb; and (c) TC21.

Similar to Ti-Al-V and Ti-Al-Nb alloys, the microstructure of TC21 alloy (Figure 1c) contained  $\alpha$  and  $\beta$  phases, but displayed different morphologies and volume fractions. The TC21 alloy's  $\beta$  phase consisted of two shapes: an acicular-like structure (Figure 2a) and a blocky shape (Figure 2b). The thickness of the acicular  $\beta$  phase in the TC21 alloy's microstructure ranged from around 0.2 to 0.6  $\mu$ m, while the size extent of the blocky  $\beta$  phase was about 0.75–1.5  $\mu$ m. Moreover, the volume fraction of  $\beta$  phase in the microstructure of TC21 alloy was higher than that in the Ti-Al-V and Ti-Al-Nb alloys' microstructure, as depicted in Figure 1.

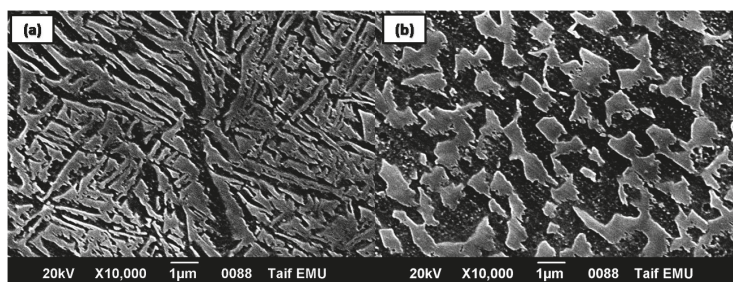


Figure 2. Morphology of  $\beta$  phase in TC21 alloy: (a) acicular-like structure; and (b) blocky shaped structure.

Table 2 illustrates the volume fraction of  $\alpha$  and  $\beta$  phases in the microstructure of the studied titanium alloys. The microstructure of pure Ti has the highest volume fraction of the  $\alpha$  phase (~100%) and the lowest volume fraction of  $\beta$  phase (~0.0%). The presence of Al ( $\alpha$ -phase stabilizer) and V ( $\beta$ -phase stabilizer) as alloying elements in the chemical composition of Ti-Al-V alloy influenced the volume fraction of  $\alpha$  and  $\beta$  phases. The values of the volume fractions of  $\alpha$  and  $\beta$  phases (Table 2) in the microstructure of Ti-Al-V alloy were 65% and 35%, respectively. Replacing V with Nb, yielding Ti-Al-Nb alloy, resulted in an obvious enhancement in the volume fraction of  $\alpha$  phase (increased to 77%) at the expense of that of the  $\beta$  phase, which decreased to 23%, as shown in Table 2. The volume fraction of both phases in the microstructure of TC21 alloy was also altered, probably due to the mutual combination of the alloying elements of that alloy (cf. Table 1). The volume fractions of  $\alpha$  and  $\beta$  phases in the microstructure of TC21 alloy recorded almost equal values: 48% for  $\alpha$  phase and 52% for  $\beta$  phase (Table 2).

**Table 2.** Volume fraction of  $\alpha$  and  $\beta$  phases in the investigated Ti based alloys.

Alloy	Volume Fraction, %		$(\alpha/\beta)$ Ratio
	$\alpha$ Phase	$\beta$ Phase	
Pure Ti	100	0	–
Ti-6Al-4V	65	35	1.86
Ti-6Al-7Nb	77	23	3.35
TC21	48	52	0.92

To further assess the influence of chemical composition on the microstructure and volume fraction of  $\alpha$  and  $\beta$  phases,  $[Al]_{eq}$  and  $[Mo]_{eq}$  were calculated, where  $[Al]_{eq}$  and  $[Mo]_{eq}$  represent the alloying elements from  $\alpha$  and  $\beta$  phases, respectively [5,26]. Table 3 illustrates the calculated values of  $[Al]_{eq}$  and  $[Mo]_{eq}$  for the tested Ti-based alloys, following Equations (1) and (2) [5,26].

$$[Al]_{eq} = [Al] + 0.33[Sn] + 0.17[Zr] + 10[O + C + 2N] \quad (1)$$

$$[Mo]_{eq} = [Mo] + 0.2[Ta] + 0.28[Nb] + 0.4[W] + 0.67[V] + 1.25[Cr] + 1.25[Ni] + 1.7[Mn] + 1.7[Co] + 2.5[Fe] \quad (2)$$

**Table 3.** and  $[Mo]_{eq}$  for the investigated alloys [26,27].

Alloy	$[Al]_{eq}$	$[Mo]_{eq}$	Ratio
Ti-6Al-4V	8.05	2.64	3.05
Ti-6Al-7Nb	8.59	2.18	3.94
TC21	8.59	5.04	1.71

As shown in Table 3, Ti-6Al-7Nb and TC21 alloys recorded the highest value (8.59) of  $[Al]_{eq}$ , while the lowest value (8.05) was measured for the Ti-6Al-4V alloy. Additionally, Ti-6Al-7Nb alloy achieved the maximum value of  $[Mo]_{eq}$ , 3.94, while TC21 alloy recorded 1.71. Table 3 also depicts the ratio  $[Al]_{eq}/[Mo]_{eq}$  for the tested alloys. Ti-6Al-7Nb alloy displayed the maximum ratio, 3.94, while a minimum ratio of 1.71 was determined for the TC21 alloy. The results shown in Table 3 agree well with those in Table 2. The calculated ( $[Al]_{eq}/[Mo]_{eq}$ ) and  $(\alpha/\beta)$  ratios were maximum in case of Ti-6Al-7Nb alloy, and minimum for the TC21 alloy.

The chemical composition of both phases in all microstructures of the investigated alloys was analyzed using the EDS unit attached to SEM. The averaged chemical composition (wt. %) for each investigated alloy is displayed in Tables 4 and 5. It was evident that the Ti, Al, Sn and Zr elements tended to more segregate to  $\alpha$  phase than to  $\beta$  phase [27]. However, V, Nb, Cr and Mo were  $\beta$  forming elements [28], meaning that higher ratios of these elements were found in  $\beta$  phase rather than in  $\alpha$  phase. The detailed EDS linescan/map analyses are discussed in the Supplementary Materials (Figures S1–S3).

**Table 4.** Chemical composition (wt %) of different phases in Ti-6Al-4V and Ti-6Al-7Nb alloys.

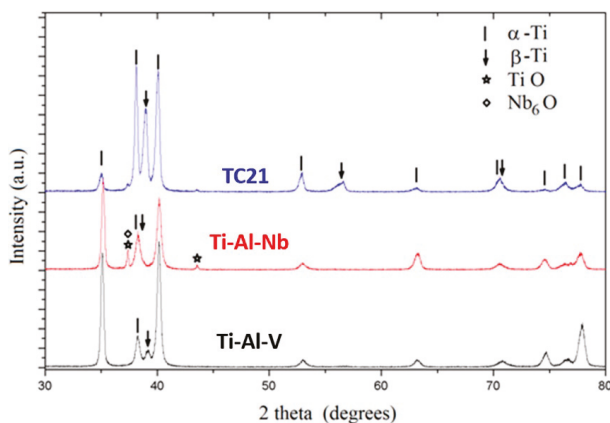
Phase	Ti-6Al-4V Alloy (wt %)			Ti-6Al-7Nb Alloy (wt %)		
	Al	V	Ti	Al	Nb	Ti
$\alpha$	5.93	3.24	90.83	6.60	7.65	85.75
$\beta$	5.57	8.04	86.39	4.88	13.79	81.33

**Table 5.** Chemical composition (at %) of different phases in TC21 alloy.

Phase	Chemical Composition, at %						
	Al	Cr	Mo	Sn	Zr	Nb	Ti
$\alpha$	6.38	1.08	1.82	2.45	1.95	1.98	84.34
$\beta$	6.21	1.71	2.62	2.24	1.11	2.39	83.72

### 3.2. X-ray Diffraction Studies

Phase identification was performed by X-ray diffraction (XRD) patterns to define the phases comprising each alloy sample. The diffraction patterns recorded for the studied alloys are compared in Figure 3. The phases were identified by matching the characteristic peaks with the Joint Committee on Powder Diffraction Standards (JCPDS) files [29]. The phases  $\alpha$ -Ti (JCPDS#00-044-1294) and  $\beta$ -Ti (JCPDS#00-044-1288) were common and dominated the composition of the three studied alloys. The Ti-Al-V and TC21 alloys were found to contain solely  $\alpha$ -Ti and  $\beta$ -Ti phases, respectively. On the other hand, Ti-Al-Nb alloy contained some Ti and Nb oxides, TiO (JCPDS#00-008-0117) and Nb<sub>6</sub>O (JCPDS#00-015-0258).

**Figure 3.** XRD diffraction patterns recorded for the Ti-6Al-4V, Ti-6Al-7Nb and TC21 samples.

An effective procedure for the simultaneous refinement of structural and microstructural parameters based on the integration of Fourier analysis for broadened peaks in the Rietveld method was first proposed by Lutterutti et al. [30] and is implemented in the Maud program [31]. Consequently, weight percent (wt.%), lattice parameters, isotropic crystallite size (D) and r.m.s. microstrain ( $\mu\epsilon$ ) were regarded as fitting parameters in the Rietveld adjustments and refined simultaneously. The structural information for all the refined phases was obtained from the Inorganic Crystal Structure Database (ICSD) [32]. The results obtained for the structural and microstructural analysis are summarized in Table 6 for all alloys. It is worth mentioning that all studied alloys were characterized with considerable degree of preferred orientation, which strongly modified the relative intensities of the Bragg reflections,

especially for  $\alpha$ -Ti and  $\beta$ -Ti phases. The MAUD program also incorporates correction for preferred orientation [33,34] in the Rietveld adjustments to obtain the best fitting parameters.

**Table 6.** The structural and microstructural parameters of the three alloys obtained by the Rietveld adjustment of the XRD patterns. Wt. % is the weight percentage of each phase, a and c are the cell parameters of the crystal lattice, D is the average crystallite-size and  $\epsilon$  is the lattice microstrain.

<b>Ti-6Al-4V</b>				
	$\alpha$ -Ti ( $P6_3/mmc$ )	$\beta$ -Ti ( $Im\bar{3}m$ )		
Wt. %	67 (5)	33 (5)		
a (Å)	2.9338 (1)	3.2353 (9)		
c (Å)	4.6780 (3)			
D (nm)	76 (3)	67 (4)		
$\epsilon$	0.00232 (1)	0.00216 (4)		
<b>Ti-6Al-7Nb</b>				
	$\alpha$ -Ti ( $P6_3/mmc$ )	$\beta$ -Ti ( $Im\bar{3}m$ )	TiO ( $Fm\bar{3}m$ )	Nb <sub>6</sub> O ( $P4_2cm$ )
Wt. %	73 (6)	20 (5)	5 (2)	2 (1)
a (Å)	2.9397 (4)	3.2437 (5)	4.1567 (1)	3.3945 (6)
c (Å)	4.6969 (3)			3.249 (3)
D (nm)	67 (2)	53 (2)	79 (12)	100 (2)
$\epsilon$	0.0028 (1)	0.024 (20)	0.0026 (1)	0.00010 (7)
<b>TC21</b>				
	$\alpha$ -Ti ( $P6_3/mmc$ )	$\beta$ -Ti ( $Im\bar{3}m$ )		
Wt. %	49 (9)	51 (9)		
a (Å)	2.9407 (7)	3.2521 (14)		
c (Å)	4.6925 (16)			
D (nm)	63 (2)	70 (3)		
$\epsilon$	0.0021 (2)	0.0035 (3)		

The calculated diffraction patterns from the Rietveld adjustment are plotted with the observed ones for the three alloys in Figure 4. The average R-values obtained for the refinements were about  $R_w$  (%) = 24–27 and  $R_b$  (%) = 15–20. The simultaneous refinements of both structural and microstructural parameters produced good matching of the calculated to observed profiles of diffracted intensities. In addition, the incorporation of the preferred orientation models enabled accounting for the variations of the peak intensities of  $\alpha$  and  $\beta$ -Ti phases.

In the Rietveld adjustment of the Ti-6Al-4V alloy, the hcp  $\alpha$ -Ti (Space group  $P6_3/mmc$ ) together with the bcc  $\beta$ -Ti (Space group  $Im\bar{3}m$ ) dominated the composition of the alloy. In the second alloy, Ti-6Al-7Nb, the formation of some TiO (Space group  $Fm\bar{3}m$ ) and Nb<sub>6</sub>O (Space group  $P4_2cm$ ) was observed and they formed larger crystallites than those formed in the Ti phases. The total weight percent of those oxide phases was less than 10% (Table 6). For the third alloy, TC21, only  $\alpha$ - and  $\beta$ -Ti phases were observed in the XRD patterns. No oxide phases were detected due to the slight oxygen content of this alloy. Nevertheless, there weresome mismatches between the wt% values obtained from the Rietveld adjustments and the corresponding wt% values determined with other techniques. This was attributed to the behavior of the preferred orientation of the  $\alpha$ -Ti phase observed for the reflection (100), which was relatively stronger for the Ti-6Al-4V and Ti-6Al-7Nb alloys than in the TC21 alloy.

As shown in Table 6, the last two alloys, Ti-6Al-7Nb and TC21, contained relatively higher portions of  $\beta$ -Ti than  $\alpha$ -Ti in contrast to the first alloy, Ti-6Al-4V, which had  $\alpha$ -Ti content higher than  $\beta$ -Ti. As known from the literature, Al is an  $\alpha$ -stabilizing while V, Nb, Mo and Fe are  $\beta$ -stabilizing elements. Nevertheless, the results indicate that Nb, Mo and Fe had stronger capabilities to stabilize  $\beta$ -Ti phase than V. These findings corroborate microstructural studies (cf. Section 3.1).

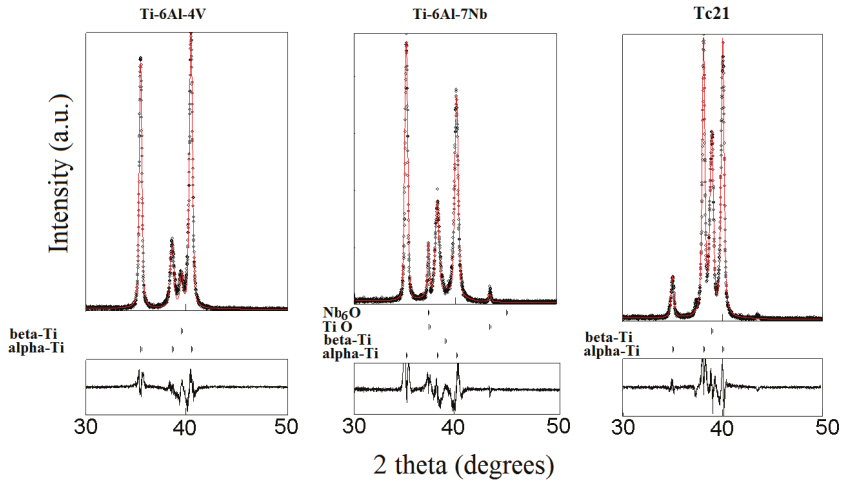


**Figure 4.** The calculated (red line) and recorded (black dots) diffraction patterns for the three alloys as obtained from the Rietveld adjustments using the MAUD program; the positions of the Bragg reflections of each phase and the difference between the calculated and observed patterns are also presented at the bottom.

### 3.3. Electrochemical Measurements

#### 3.3.1. Uniform Corrosion Studies

Figure 5 illustrates the cathodic and anodic polarization curves for the studied alloys in comparison with pure Ti, after seven days of immersion in 0.9% NaCl solution at 37 °C. As shown in Figure 5, among the studied alloys, TC21 alloy exhibited the lowest cathodic and anodic overpotentials, corresponding to enhanced corrosion rate. On the contrary, Ti-6Al-7Nb alloy displayed the highest overpotentials, close to that of Ti, for both the cathodic and anodic processes, thus referring to its highest corrosion resistance.

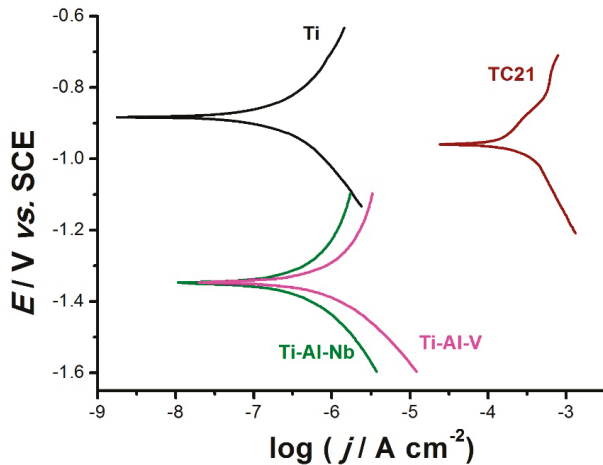


**Figure 5.** Cathodic and anodic polarization curves recorded for the three tested alloys in comparison with pure Ti, after seven days of exposure in 0.9% NaCl solution at a scan rate of 0.5 mV s<sup>-1</sup> at 37 °C.

Indeed, Tafel slopes and respective calculated uniform corrosion rates for a metal covered with a semi-conductive passive film raised strong doubts, despite the utilization of the Tafel extrapolation method to determine corrosion rates for Ti and some Ti-based alloys [35,36]. In addition, in Figure 5, the polarization curves do not display the expected log/linear Tafel behavior. This was clear in both the anodic and cathodic branches of alloys Ti-6Al-4V and Ti-6Al-7Nb and as well as in the anodic branches of Ti and TC21 alloy, which exhibited some sort of curvature over the complete applied potential range. This in turn made evaluation of Tafel slopes by Tafel extrapolation method, and hence corrosion rates, inaccurate [37–39]. There is, therefore, an uncertainty and source of error in the numerical values of Tafel slopes ( $\beta_a$  and  $\beta_c$ ), and possibly in the values of  $j_{\text{corr}}$ .

The curvature of the anodic branch might be attributed to the deposition of the corrosion products and/or passive film formation, as evidenced from XPS studies. With respect to the cathodic branch, since the solution was stationary, diffusion of the electrochemically active species was slow, and concentration polarization could act to shorten the cathodic linear Tafel region. In the extreme case, linearity might disappear altogether, with the cathodic reaction proceeding under combined activation and diffusion control at  $E_{\text{corr}}$  [37–39]. This counteracted the validity of the Tafel extrapolation method for measuring uniform corrosion rates, which was successfully applied for the charge transfer controlled processes.

EIS measurements were also conducted at the respective  $E_{\text{corr}}$  during sample's exposure in 0.9% NaCl solution at 37 °C to confirm the polarization data and to assess the kinetics of the uniform corrosion process on alloy surface. The measurements were carried day-by-day allowing for monitoring of uniform corrosion susceptibility [40–42]. Figure 6 displays the impedance plots in Bode projection, recorded for the studied alloys during the second and the last day of exposure. Pure Ti (99.99%) was also included for comparison (see Figure 6a). The impedance spectra recorded on Day 1 (after initial 120 min of conditioning) were highly scattered due to non-stationary conditions at the metal/electrolyte interface, which is a common problem in EIS measurements. This issue became negligible after a few hours of exposure. For this reason, results recorded on Days 2–7 were considered for further analysis. All the impedance plots exhibited a single time constant (capacitive loop). The overall corrosion resistance of each investigated alloy was very high; the impedance modulus  $|Z|$  linearly increased with frequency decrease, reaching over  $10^5$  at 0.1 Hz. For each studied alloy, inclination of the phase angle  $\theta$  was shifted towards lower frequencies on Day 7 of exposure, testifying to the decreased corrosion process kinetics.

An electric equivalent circuit (EEC) was proposed to analyze the impedance results. When defining the adequate EEC, one must consider whether to include the space charge layer resulting from the semi-conductive nature of titanium oxides. In his studies, Blackwood concluded that thickness of the space charge layer is considerably less than the oxide film itself in the open circuit conditions [43]. On the other hand, its dominant influence was observed under anodic polarization conditions [43–46]. The impedance measurements of titanium oxide films investigated within this manuscript were studied under open circuit conditions, thus the parallel resistance and CPE represented primarily the dielectric properties of the passive layer. Due to absence of additional time constants in the analyzed frequency range, a simple Randles circuit was proposed with constant phase element (CPE) selected instead of capacitance to account for the dispersion of the time-constant. The parallel resistance represents the sum of charge-transfer limiting effects through the metal/electrolyte interface, dominated by the passive layer resistance  $R_F$  [47]. The aforementioned time-constant dispersion originated from the presence of the charge space layer in the semi-conductive film, the surface distribution of the time-constant due to the geometric heterogeneity (pits, scratches, and porosity), and diversified surface electric properties due to adsorption processes of passive layer breakdown [48].

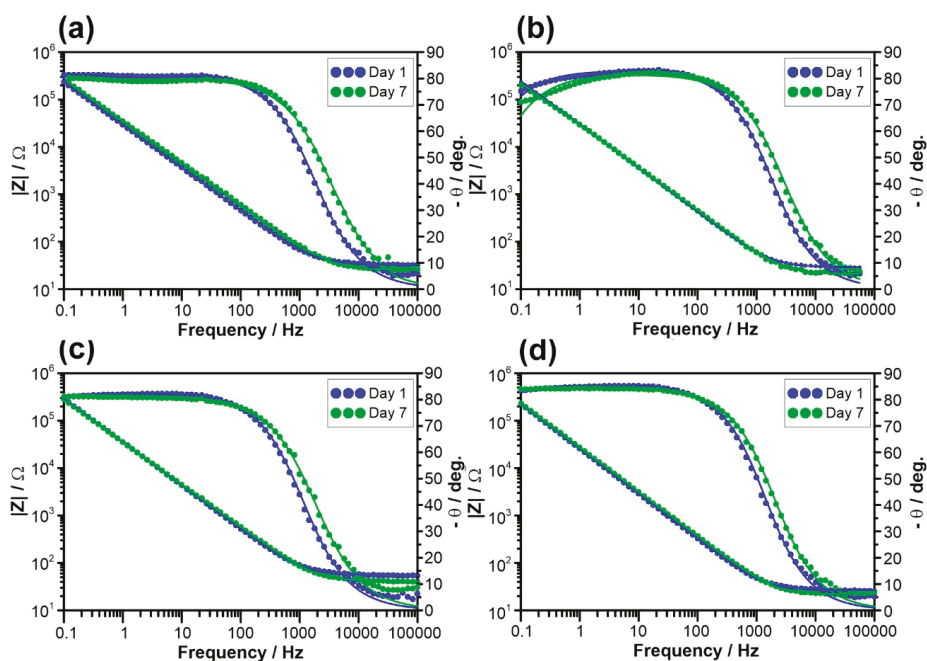


**Figure 6.** Bode impedance plots on Days 2 and 7 of exposure, recorded for: (a) pure Ti; and three tested alloys: (b) TC21; (c) Ti-6Al-4V; and (d) Ti-6Al-7Nb. Studies performed at  $E_{\text{corr}}$  in 0.9%NaCl solution at 37 °C. Points represent experimental results while the solid line was calculated based on R(QR) EEC.

The CPE impedance  $Z_{\text{CPE}} = (Q(j\omega)^n)^{-1}$  represents a capacitor with capacitance  $1/Q$  for a homogeneous surface  $n \rightarrow 1$ . Thus, it is often believed that CPE component  $n$  is the heterogeneity factor and its variation can be monitored. CPE describes quasi-capacitive behavior of the passive layer. The effective capacitance  $C_{\text{eff}}$  can be calculated based on CPE using Hirschorn's model for surface distribution of time constants [49]. The EEC can be schematically written as  $R_S(QR_F)$ , where  $R_S$  is electrolyte resistance. The aforementioned single time-constant EEC covers all the applied frequency range. The fitting quality is represented by solid lines in Figure 6a–d.

Figure 7 depicts the electric parameters obtained on the base of  $R_S(QR_F)$  EEC and their changes during the one-week exposure. The higher was the  $R_F$ , the lower was the corrosion current density, offering an easy comparison in uniform corrosion resistance of investigated alloys (see Figure 7a). Each investigated alloy was characterized with very high resistance, order of  $M\Omega$ , owing to a presence of a passive layer tightly covering the metal surface. Nevertheless, for TC21 alloy,  $R_F$  value was one order of magnitude lower and slowly but consistently decreased throughout the exposure, revealing its lower corrosion resistance and corroborating DC electrochemical studies.

The analysis of constant phase element (CPE) allowed drawing conclusions on the passive layer homogeneity. The effective capacitance  $C_{\text{eff}}$ , calculated using the surface distribution model, was similar for all investigated alloys, falling in a range between 2 and 5  $\mu\text{F}$ . The differentiation may result from differences in passive layer thickness  $d$  and to some extent from relative permittivity of alloying additives and their oxides  $\epsilon_r$  according to:  $C = \epsilon_0 \epsilon_r d/A$ , where  $\epsilon_0$  is the absolute permittivity and  $A$  is the electrochemically active surface area. A steady decrease of  $C_{\text{eff}}$  was attributed to an increase of passive layer thickness, denouncing further passivation of metal in investigated electrolytic conditions. The presence of stable corrosion pits would be visible in the form of rapid increase in  $C_{\text{eff}}$  [49,50] (likely observed in TC21 alloy on Day 4).

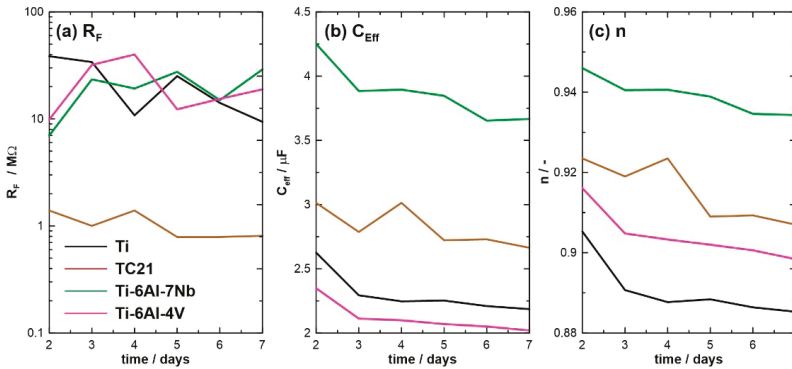


**Figure 7.** Monitoring of (a) passive layer resistance  $R_F$ , (b) effective capacitance  $C_{eff}$  and (c) CPE exponent  $n$  calculated on the base of  $R_S$  ( $QR_F$ ) EEC for each investigated alloy. The one-week exposure was carried out in 0.9% NaCl solution at 37 °C.

The initial value of CPE exponent  $n$  depends on factors such as surface phase distribution and geometric defects remaining after polishing. Its decrease throughout the exposure in corrosive electrolyte reflected the appearance of heterogeneities on analyzed sample surface, which in this case was primarily associated with initial phases of corrosion pits formation (see Figure 8c). This effect was clearly seen in SEM micrographs (see below). Notably, the value of  $n$  factor of Ti-6Al-7Nb alloy was both the highest and the least affected by exposure in corrosive media. The aforementioned observation indicated high surface homogeneity, which may be the reason behind outstanding corrosion resistance of this alloy.

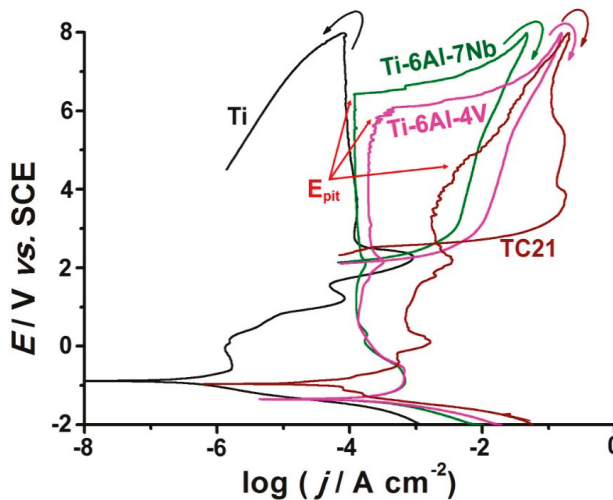


**Figure 8.** Cyclic polarization curves recorded for the studied alloys in 0.9% NaCl solutions at a scan rate of  $1.0 \text{ mV s}^{-1}$  at 37 °C.

### 3.3.2. Cyclic Polarization Measurements

Figure 8 shows typical cyclic polarization curves recorded for the studied alloys between  $-2.0 \text{ V}$  and  $+8.0 \text{ V}$  (SCE). Measurements were conducted in 0.9% NaCl solution at a scan rate of  $5.0 \text{ mV s}^{-1}$  at 37 °C.



The polarization curve of TC21 alloy exhibited active dissolution near  $E_{\text{corr}}$ , followed by an obvious enhancement in the anodic current with the applied potential due to thinning and weakening of the passive layer as a result of the aggressive attack of  $\text{Cl}^-$  anions. In addition, Ti-6Al-7Nb and Ti-6Al-4V alloys showed active dissolution near  $E_{\text{corr}}$ , but to a much lower extent than TC21, and, in addition, tended to passivate with a very low current covering a wide range of potential. These findings reflect the weaker passivity of TC21 and its higher tendency to corrode in this solution than Ti-6Al-4V and Ti-6Al-7Nb alloys. On the contrary, as expected, the anodic polarization curve of pure Ti exhibited typical passivity near  $E_{\text{corr}}$ , referring to its high corrosion resistance.

Passivity of the studied alloys persisted up to reaching pitting potential ( $E_{\text{pit}}$ ). Remarkable changes occurred within the passive region at potentials exceeding  $E_{\text{pit}}$ . These involved a sudden increase in corrosion current density and formation of a hysteresis loop on the reverse potential scan. These events were a clear sign of passivity breakdown, and initiation and propagation of pitting corrosion. Repassivation was only achieved when the reverse scan intersected the forward one within the passive region, below which the working electrode was immune to pitting [51].

A current intermission could be seen on the reverse scan of the three tested alloys. This current discontinuity was quite clear on the reverse scan of the TC21 alloy, and could be observed for Ti-6Al-7Nb and Ti-6Al-4V alloys. We previously reported similar findings during pitting corrosion studies of Zn in nitrite solutions [52]. Recently, Zakeri et al. [53] explored the transition potential and the repassivation potential of AISI type 316 stainless steel in chloride containing media devoid of and containing 0.01 M thiosulfate.

Beyond pit transition potential, the rate of anodic dissolution was diffusion-controlled [51–53]. Such a current transient relationship, when satisfied, referred to an anodic diffusion control process [53]. On reversing the potential scan, the thickness of the salt (pitting corrosion product) film diminished. This decrease in salt film thickness enhanced with back scanning until a certain potential was reached, at which the cation concentration decreased below the saturated concentration. At this stage, salt precipitation was stopped, and the remaining metal salt film dissolved, making the bottom of pits free from salt film. This in turn established an ohmic/activation control (a linear decrease of current density with potential) regime.

Ti-6Al-7Nb alloy's passivity seemed stronger and more stable than that of the Ti-6Al-4V alloy. The latter was characterized by a higher  $j_{\text{pass}}$ , which enhanced with potential until  $E_{\text{pit}}$ , which attained ~50 mV vs. SCE before that of the former. In addition, the pits existing on the surface of Ti-6Al-4V alloy were much more difficult to repassivate than those on the surface of Ti-6Al-7Nb alloy, as the hysteresis loop of the former was much larger than that of the latter.

Another important pitting corrosion controlling electrochemical parameter is the pitting corrosion resistance  $R_{\text{pit}} = |E_{\text{corr}} - E_{\text{pit}}|$ , which defines the resistance against the nucleation of new pits [38]. Referring to Figure 8, it is clear that  $R_{\text{pit}}$  increased following the order: TC21 << Ti-6Al-4V < Ti-6Al-7Nb. The resistance against growth of the pits also controlled the susceptibility toward pitting corrosion. A specific routine of the software (Autolab frequency response analyzer (FRA) coupled to an Autolab PGSTAT30 potentiostat/galvanostat with FRA2 module) (Metrohm, Herisau, Switzerland) was used to calculate the areas of the hysteresis loops, related to the charge consumed during the growth of such already formed pits. Again, the hysteresis loop of the TC21 alloy recorded the highest area (charge consumed) among the studied alloys, while the lowest value of the hysteresis loop charge consumed during was measured for Ti-6Al-7Nb alloy. Thus, the resistance against the growth of pre-existing pits was ranked as: Ti-6Al-7Nb > Ti-6Al-4V >> TC21. These findings mean that replacing V by Nb in Ti-6Al-4V alloy promoted alloy's repassivation, thus enhancing its pitting corrosion resistance.

### 3.3.3. Chronoamperometry Measurements

Chronoamperometry ( $j/t$ ) measurements were also carried out to confirm the above results and gain more information about the influence of alloyed V and Nb on the passive layer growth kinetics and breakdown. Figures 9a and 10b depict the  $j/t$  curves measured for the tested alloys at two different

$E_a$  values, far below and close to  $E_b$ . Measurements were conducted in 0.9% NaCl solution at 37 °C. The profile of the obtained curves was found to vary according to the chemical composition of the studied alloy and the position of  $E_a$  versus  $E_{pit}$ . When  $E_a$  was located far cathodic to  $E_{pit}$ , a  $j/t$  profile with two stages was obtained, as shown in Figure 9a. During the first stage, the anodic current ( $j_a$ ) declined with a rate depending upon chemical composition of the tested alloy, denoting passive layer electroformation and growth [39]. This decay in current then reached a steady-state value ( $j_{ss}$ ), an almost constant passive current related to  $j_{pass}$  (cf. Figure 8), constituting the second stage of the current. The constancy of  $j_{ss}$  originated from a balance between the rates of the passive layer growth (current builds up) and its dissolution (current decays) [54,55].

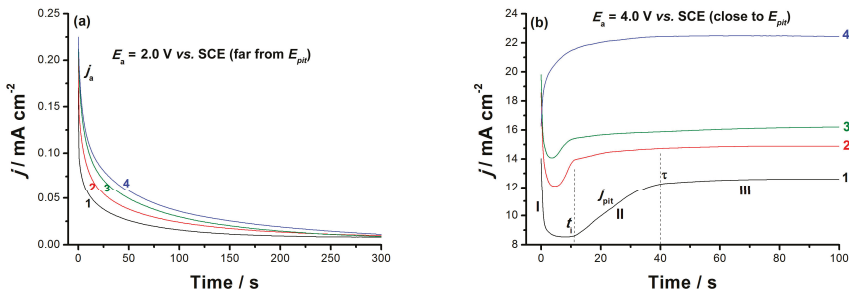


**Figure 9.** Chronoamperometry (current–time) curves recorded for the studied solder alloys in 0.9% NaCl solution at applied anodic potentials of 2.0 V (a) and 4.0 V (b) vs. SCE at 37 °C: (1) pure Ti; (2) Ti-6Al-7Nb; (3) Ti-6Al-4V; and (4) TC21.

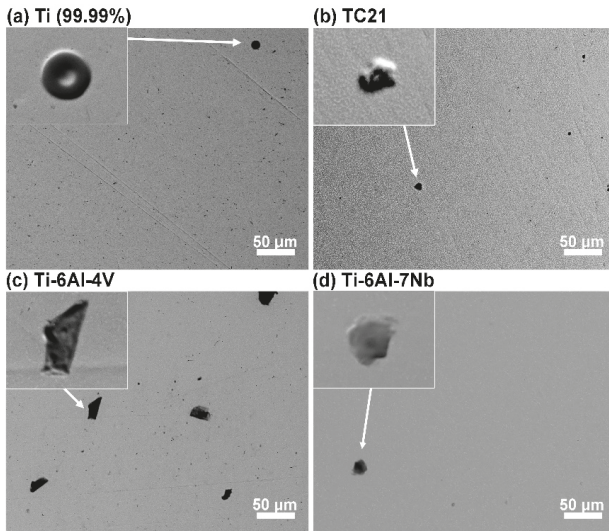


**Figure 10.** SEM micrographs taken in secondary electron mode for each investigated sample: (a) pure Ti as a reference; (b) TC21 alloy; (c) Ti-6Al-4V; and (d) Ti-6Al-7Nb at the end of one-week exposure in 0.9% NaCl at 37 °C. Magnification:  $\times 500$ . In the inset, back-scatter electron topography mode images of selected surface defects. Magnification:  $\times 2000$ .

Further, Figure 9a demonstrates that the rate of  $j_a$  decay, and consequently the rate of passive layer growth, diminished upon alloying Ti with V and Nb. These results further confirm the influence of the alloying elements V and Nb, with V being more active than Nb, which, when added to Ti,

weakened its passivity viadepassivation (destabilizing the passive oxide film through oxide film thinning/dissolution [56]). This in turn madethe passive film more susceptible to pitting.

At an  $E_a$  value very close to  $E_{\text{pit}}$  (Figure 9b), the  $j/t$  curves with three different stages (I–III) were recorded. Similar results were previously obtained in our lab [55,57]. Stage I refersto the passive layer electroformation and growth, as its current fellwith time [54,55,57]. Stage I ended at a certain time ( $t_i$ ), the incubation time, where Stage I's current reached its minimum value;  $t_i$  is defined as the time the adsorbed aggressive  $\text{Cl}^-$  anions must acquire to locally attack and subsequently remove the passive oxide film [54]. The magnitude of  $t_i$ , more specifically its reciprocal value ( $1/t_i$ ), denotes the rate of pit initiation and growth [54,55], and measures the susceptibility of the oxide film to breakdown and initiate pit formation and growth.

Stage II began at  $t_i$  and terminated at time  $\tau$ , and its current aws termed  $j_{\text{pit}}$  (pit growth current density).  $j_{\text{pit}}$  increased from the moment just after  $t_i$  and continuedto grow until  $\tau$ , suggesting that the pit formation and growth dominated over passivation during this stage. Ultimately,  $j_{\text{pit}}$  attaineda steady-state just after the time  $\tau$ , denoting the onset of Stage III, and remained almost constant until the end of the run. The constancy of Stage III's current was attributed to the hindrance of the current flow ( $j_{\text{pit}}$ ) through the pits sealed off by the pitting corrosion products formed during the events of Stage II, namely pit initiation and growth [55,57]. This hindrance in  $j_{\text{pit}}$  was balanced by a current increase due to metal dissolution, thus yielding an overall steady-state current.

Close inspection of Figure 9 reveals that  $j_{\text{pit}}$  increased and  $t_i$  shortened, thus referring to accelerated pitting attack, in presence of alloyed V. These results again support the catalytic impact of alloyed V towards pitting corrosion

### 3.4. Surface Morphology and Composition

After one-week exposure, the investigated samples were reexamined using SEM to evaluate the susceptibility to pitting corrosion. This procedure was carried out after rinsing in ethanol using ultrasonic cleaner. The results of the analysis are exhibited in Figure 10. Defects started to appear on the surface of each analyzed sample throughout the exposure. The micrographs in the inset of Figure 10 were taken using back-scatter electrons (BSE) in topography mode. This allowed bringing out the geometry of aforementioned defects. As can be seen, each analyzed defect formed a bulge above the alloy's surface, testifying to either repassivation once shallow corrosion pits formed or at an early stage of passive layer degradation. Ti-6Al-4V sample was characterized with both the highest amount and the largest defects, reaching 30  $\mu\text{m}$  in diameter. On the other hand, the surface of pure Ti and Ti-6Al-7Nb appeared the most intact. No real corrosion pits were observed on the surface of either investigated alloy at the end of exposure in 0.9% NaCl solution at 37 °C, testifying to the overall high pitting corrosion resistance.

Nevertheless, the passive layer must have weakened, hence it was possible for corrosion products to adsorb on the metal surface. EDS analysis was carried out on the defects observed on each investigated alloy to qualify their chemical constitution. The exemplary results, obtained for Ti-6Al-7Nb alloy, are summarized in Figure S4 (Supplementary Materials). The chemistry of defects observed for each investigated alloy was similar. The defects were primarily composed of carbon and oxygen, most likely forming metal carbonates typical for early pitting corrosion stages [58]. Small amount of chlorine was also found within defects. Its low amount was distorted by EDS depth of analysis ranging few microns.

The chemistry of the passive layer in each examined case was composed primarily of titanium (IV) oxides, as verified by a strong recorded  $\text{Ti}_{2p}$  peak doublet, with  $\text{Ti}_{2p_{3/2}}$  component located each time at 458.6 eV [48,59,60] (Figure 11). Furthermore, there was no sign of titanium oxides at lower oxidation states corroborating the aforementioned result (see Supplementary Materials, Figure S5). Besides the titanium, other alloying additives also tookpart in the passivation process. The strongest signal among the alloying additives was recorded for aluminum oxide  $\text{Al}_2\text{O}_3$  ( $\text{Al}_{2p_{3/2}}$  peak at 74.5 eV), ranging between 3.5 and 3.8 at.% for each sample [61,62]. The contribution of  $\text{VO}_2$  ( $\text{V}_{2p_{3/2}}$  at 516.4 eV) in Ti-Al-V and  $\text{Nb}_2\text{O}_5$  ( $\text{Nb}_{3d_{5/2}}$  at 207.1 eV) in Ti-Al-Nb alloy did not exceed 0.7 at.% [60,63,64]. The passive film

formed on the surface of TC21 alloy was naturally more complex. Besides  $\text{TiO}_2$ , it was composed of  $\text{Al}_2\text{O}_3$  (3.8 at.%),  $\text{Nb}_2\text{O}_5$  (0.3 at.%),  $\text{ZrO}_2$  (0.4 at.%,  $\text{Zr}_{3d5/2}$  at 182.4 eV),  $\text{Cr}_2\text{O}_3$  (0.8 at.%,  $\text{Cr}_{2p3/2}$  at 576.0 eV),  $\text{SnO}_2$  (0.1 at.%,  $\text{Sn}_{3d3/2}$  at 486.5 eV),  $\text{MoO}_3$  and  $\text{MoO}_2$  (0.2+0.2 at.%,  $\text{Mo}_{3d5/2}$  at 232.9 and 229.2 eV, respectively) [65–68].

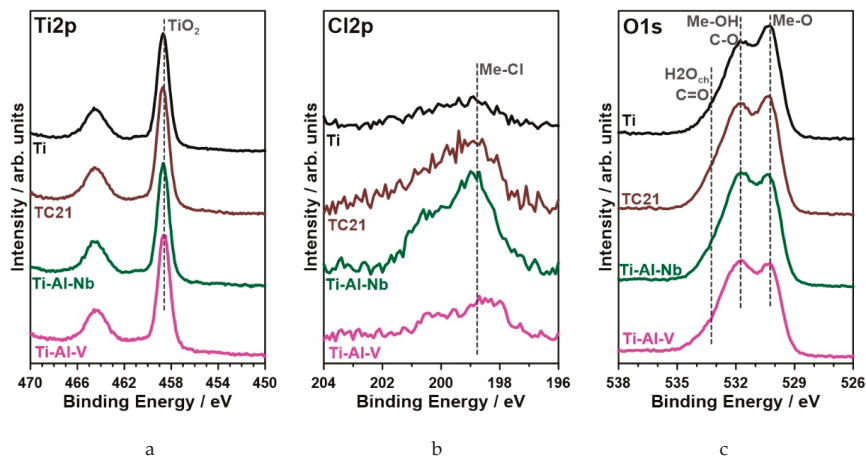


**Figure 11.** High-resolution XPS spectra recorded in (a)  $\text{Ti}_{2p}$ , (b)  $\text{Cl}_{2p}$  and (c)  $\text{O}_{1s}$  energy range for each investigated alloy after seven days of exposure to 0.9% NaCl solution at 37 °C.

The high-resolution spectra analysis carried out in the  $\text{Cl}_{2p}$  energy range confirmed the electrochemical and microscopic studies regarding chloride adsorption on the metal surface as a result of seven-day metal exposure to chloride-containing electrolyte. Full chemical analysis is summarized in Table 7. Metal chlorides were found on the surface of each investigated sample, which confirmed metal-chlorine bond formation, shown by a peak doublet:  $\text{Cl}_{2p3/2}$  at 198.9 eV [48,55,69]. Nevertheless, the amount of adsorbed chlorides was nearly 2.5 times higher for the TC21 alloy than pure titanium. The chloride concentration obtained for highly resistant Ti-6Al-7Nb alloy was nearly on par with Ti sample, and slightly smaller than in the case of Ti-6Al-4V. An interesting conclusion could be drawn based on  $\text{O}_{1s}$  peak analysis for each investigated sample. The spectra were conventionally deconvoluted into three components. Two dominant components located at 530.2 and 531.6 eV were ascribed to Me-O and Me-OH species, respectively. The second component intensity might be further influenced by the presence of C-O bonds in carbonates. Its formation may result from prolonged electrolyte exposure as well as adventitious carbon deposition due to air exposure [61,64]. The finding regarding carbonate adsorption on the metal surface was further confirmed by a third  $\text{O}_{1s}$  component at 532.8 eV, typical for C=O bonds but also chemisorbed water molecules. For clarity purposes, the analysis excluded data recorded for carbon  $\text{C}_{1s}$ , which was found in large amounts, up to 30 at.%, at binding energies corroborating adventitious carbon and carbonates. Importantly, the highest amount of the adsorbed carbonate species was found on Ti-Al-V sample surface, which is in very good agreement with SEM micrographs presented in Figure 10. The least amount of carbonate species was once more found on the surface of Ti sample.

**Table 7.** XPS deconvolution results carried out in Ti<sub>2p</sub>, Cl<sub>2p</sub> and O<sub>1s</sub> energy range after seven days of exposure to 0.9% NaCl solution at 37 °C (in at.%).

	Ti <sub>2p</sub>	Other Additives	O <sub>1s</sub>			Cl <sub>2p</sub>
	TiO <sub>2</sub>		Me-O	OH/CO	C=O/H <sub>2</sub> O	Me-Cl
BE/eV	458.6	*	530.2	531.6	532.8	198.9
Ti	21.3	–	37.5	26.2	13.1	1.9
Ti-6Al-4V	17.4	4.3	28.8	25.7	20.8	3.0
Ti-6Al-7Nb	17.1	4.4	31.1	27.0	18.2	2.2
TC21	17.2	5.8	31.2	25.1	16.1	4.6

#### 4. Conclusions

The effect of microstructure on the uniform and pitting corrosion characteristics of Ti-Al-V, and Ti-Al-Nb alloys were studied. Pure Ti and TC21 alloy were included for comparison. Measurements were conducted in 0.9% NaCl solution at 37 °C employing various electrochemical techniques, and complemented with XRD and SEM/EDS analysis. The obtained results reveal that:

1. The microstructure of the investigated alloys consisted of  $\alpha$  matrix, which was strengthened by  $\beta$  phase in all studied alloys except cp-Ti alloy.
2. The volume fraction of  $\beta$  phase in TC21 alloy was higher than in both Ti-Al-V and Ti-Al-Nb alloys. In comparison with other alloys, Ti-Al-Nb alloy had the lowest volume fraction of  $\beta$  phase.
3. Ti-Al-Nb alloy exhibited the highest corrosion resistance (lowest corrosion rate) among other alloys.
4. The addition of Nb alloying element at the expense of V in Ti-Al-V alloy decreased the volume fraction of  $\beta$  phase, which improved the corrosion resistance of Ti based alloy.
5. The polarization curve of TC21 alloy exhibited active dissolution near  $E_{\text{corr}}$ , followed by enhanced anodic current with the applied potential, thus revealing weak passivity. On the contrary, Ti-6Al-7Nb and Ti-6Al-4V alloys recorded much lower dissolution rate near  $E_{\text{corr}}$  followed by a wide potential range of stable passivity.
6. Stable passivity of Ti-6Al-7Nb and Ti-6Al-4V alloys was translated into an obvious anodic (more noble) drift in their pitting potential ( $E_{\text{pit}}$ ) versus that of the TC21 alloy.
7. Chronoamperometry measurements, conducted at a fixed anodic potential, revealed that the rate of passivity breakdown of Ti-6Al-7Nb and Ti-6Al-4V alloys was much lower than that of the TC21 alloy.
8. The XPS results reveal adsorption of chloride and carbonate species on the surface of the investigated alloys with the lowest amount recorded for cp-Ti and Ti-6Al-7Nb alloys, affecting the observed corrosion resistance.
9. Corrosion studies confirmed that the uniform and pitting corrosion rates increased following the sequence: Ti < Ti-6Al-7Nb < Ti-6Al-4V < TC21.

**Supplementary Materials:** The following are available online at <http://www.mdpi.com/1996-1944/12/8/1233/s1>. Figure S1—SEM image (a) and EDS spectrum (b) of phase in Ti-Al-V alloy; Figure S2—Line analysis of  $\beta$  phase in TiAlNb alloy; Figure S3—Microstructure of the Ti-Al-Nb alloy (a), and mapping of Ti (b), Al (c), and Nb (d) alloying elements. Figure S4—(a) SEM micrograph with marked areas for EDS analysis, (b) EDS examination at defect and at the surrounding, not corroded area. Figure S5—High-resolution Ti<sub>2p</sub> XPS spectra with the quality fit (light blue line) for each studied alloy: (a) pure Ti reference, (b) TC21, (c) Ti-6Al-4V, (d) Ti-6Al-7Nb.

**Author Contributions:** Conceptualization, M.A.A. and R.B.; resources, N.E.-B. and S.E.-H.; investigation, S.I.A. and O.A.A.A. (XRD), A.M.F. and M.M.I. (uniform corrosion), M.A.A. and G.A.M.M. (passive layer breakdown), N.E.-B., J.W. and S.E.-H. (microstructure), J.R. (XPS), and J.R. and J.W. (EIS); writing—original draft preparation, all authors; writing—review and editing, J.R., M.A.A. and R.B.; and project administration, M.A.A.

**Funding:** This study was funded by the Deanship of Scientific Research, Taif University, Saudi Arabia (Project No. 1-439-6070).

**Conflicts of Interest:** The authors declare no conflict of interest.

## References

- de Assis, S.L.; Wolyneć, S.; Costa, I. Corrosion characterization of titanium alloys by electrochemical techniques. *Electrochim. Acta* **2006**, *51*, 1815–1819. [[CrossRef](#)]
- Geetha, M.; Singh, A.K.; Asokamani, R.; Gogia, A.K. Ti based biomaterials, the ultimate choice for orthopaedic implants—A review. *Prog. Mater. Sci.* **2009**, *54*, 397–425. [[CrossRef](#)]
- Jiang, H. Enhancement of Titanium Alloy Corrosion Resistance via Anodic Oxidation Treatment. *Int. J. Electrochem. Sci.* **2018**, 3888–3896. [[CrossRef](#)]
- Moiseyev, V.N. *Titanium Alloys: Russian Aircraft and Aerospace Applications*; Advances in Metallic Alloys; Taylor & Francis: Boca Raton, FL, USA, 2006; ISBN 978-0-8493-3273-9.
- Leyens, C.; Peters, M. (Eds.) *Titanium and Titanium Alloys: Fundamentals and Applications*; Wiley-VCH: Weinheim, Germany; John Wiley: Chichester, UK, 2003; ISBN 978-3-527-30534-6.
- Lütjering, G.; Williams, J.C. *Titanium: With 51 Tables*; Springer: Berlin/Heidelberg, Germany, 2007; ISBN 978-3-540-71397-5.
- Oberwinkler, B.; Riedler, M.; Eichlseder, W. Importance of local microstructure for damage tolerant light weight design of Ti-6Al-4V forgings. *Int. J. Fatigue* **2010**, *32*, 808–814.
- Knobbe, H.; Köster, P.; Christ, H.-J.; Fritzen, C.-P.; Riedler, M. Initiation and propagation of short fatigue cracks in forged Ti6Al4V. *Procedia Eng.* **2010**, *2*, 931–940.
- Fekry, A.M.; El-Sherif, R.M. Electrochemical corrosion behavior of magnesium and titanium alloys in simulated body fluid. *Electrochim. Acta* **2009**, *54*, 7280–7285. [[CrossRef](#)]
- Whittaker, M. Titanium Alloys. *Metals* **2015**, *5*, 1437–1439. [[CrossRef](#)]
- Mountford, J.A., Jr. Titanium—Properties, Advantages and Applications Solving the Corrosion Problems in Marine Service. In Proceedings of the CORROSION, Denver, CO, USA, 7–11 April 2002.
- Al-Mayouf, A.; Al-Swayih, A.; Al-Mobarak, N.; Al-Jabab, A. Corrosion behavior of a new titanium alloy for dental implant applications in fluoride media. *Mater. Chem. Phys.* **2004**, *86*, 320–329. [[CrossRef](#)]
- García, C.; Ceré, S.; Durán, A. Bioactive coatings deposited on titanium alloys. *J. Non-Cryst. Solids* **2006**, *352*, 3488–3495.
- Sharma, A.K. Anodizing titanium for space applications. *Thin Solid Film.* **1992**, *208*, 48–54. [[CrossRef](#)]
- Barjaktarević, D.R.; Cvijović-Alagić, I.L.; Dimić, I.D.; Đokić, V.R.; Rakin, M.P. Anodization of Ti-based materials for biomedical applications: A review. *Metall. Mater. Eng.* **2016**, *22*, 129–144. [[CrossRef](#)]
- Qu, Q.; Wang, L.; Chen, Y.; Li, L.; He, Y.; Ding, Z. Corrosion Behavior of Titanium in Artificial Saliva by Lactic Acid. *Materials* **2014**, *7*, 5528–5542. [[CrossRef](#)]
- Hines, J.A.; Lutjering, G. Propagation of microcracks at stress amplitudes below the conventional fatigue limit in Ti-6Al-4V. *Fatigue Fract. Eng. Mater. Struct.* **1999**, *22*, 657–665.
- Sieniawski, J.; Ziaja, W.; Kubiak, K.; Motyk, M. Microstructure and Mechanical Properties of High Strength Two-Phase Titanium Alloys. In *Titanium Alloys—Advances in Properties Control*; Sieniawski, J., Ed.; InTech: London, UK, 2013; ISBN 978-953-51-1110-8.
- Gai, X.; Bai, Y.; Li, J.; Li, S.; Hou, W.; Hao, Y.; Zhang, X.; Yang, R.; Misra, R.D.K. Electrochemical behaviour of passive film formed on the surface of Ti-6Al-4V alloys fabricated by electron beam melting. *Corros. Sci.* **2018**, *145*, 80–89.
- Dadé, M.; Esin, V.A.; Nazé, L.; Sallot, P. Short- and long-term oxidation behaviour of an advanced Ti2AlNb alloy. *Corros. Sci.* **2019**, *148*, 379–387. [[CrossRef](#)]
- Chávez-Díaz, M.; Escudero-Rincón, M.; Arce-Estrada, E.; Cabrera-Sierra, R. Effect of the Heat-Treated Ti6Al4V Alloy on the Fibroblastic Cell Response. *Materials* **2017**, *11*, 21. [[CrossRef](#)] [[PubMed](#)]
- Hussein, M.; Kumar, M.; Drew, R.; Al-Aqeeli, N. Electrochemical Corrosion and In Vitro Bioactivity of Nano-Grained Biomedical Ti-20Nb-13Zr Alloy in a Simulated Body Fluid. *Materials* **2017**, *11*, 26. [[CrossRef](#)] [[PubMed](#)]
- Zhang, L.; Duan, Y.; Gao, R.; Yang, J.; Wei, K.; Tang, D.; Fu, T. The Effect of Potential on Surface Characteristic and Corrosion Resistance of Anodic Oxide Film Formed on Commercial Pure Titanium at the Potentiodynamic-Aging Mode. *Materials* **2019**, *12*, 370. [[CrossRef](#)] [[PubMed](#)]
- Reda, R.; Nofal, A.; Hussein, A.-H. Effect of Single and Duplex Stage Heat Treatment on the Microstructure and Mechanical Properties of Cast Ti-6Al-4V Alloy. *Metall. Microstruct. Anal.* **2013**, *2*, 388–393. [[CrossRef](#)]

25. El-Bagoury, N.; Ibrahim, K. Microstructure, Phase Transformations and Mechanical Properties of Solution Treated Bi-Modal Titanium Alloy. *Int. J. Eng. Sci. Res. Technol.* **2016**, *5*, 517–525.
26. Zhao, X.; Sun, S.; Wang, L.; Liu, Y.; He, J.; Tu, G. A New Low-Cost  $\beta$ -Type High-Strength Titanium Alloy with Lower Alloying Percentage for Spring Applications. *Mater. Trans.* **2014**, *55*, 1455–1459. [[CrossRef](#)]
27. Phukaoluan, A.; Khantachawana, A.; Dechkunakorn, S.; Anuwongnukroh, N.; Santiwong, P.; Kajornchaiyakul, J. Effect of Cu and Co Additions on Corrosion Behavior of NiTi Alloys for Orthodontic Applications. *Adv. Mater. Res.* **2011**, 378–379, 650–654. [[CrossRef](#)]
28. Lee, C.S.; Won, J.W.; Lee, Y.; Yeom, J.-T.; Lee, G.Y. High Temperature Deformation Behavior and Microstructure Evolution of Ti-4Al-4Fe-0.25Si Alloy. *Korean J. Met. Mater.* **2016**, *54*, 338–346. [[CrossRef](#)]
29. ICDD. *PDF 2, Database Sets 1-45*; The International Centre for Diffraction Data: Newtown Square, PA, USA, 1995.
30. Lutterotti, L.; Scardi, P. Simultaneous structure and size-strain refinement by the Rietveld method. *J. Appl. Crystallogr.* **1990**, *23*, 246–252. [[CrossRef](#)]
31. Lutterotti, L. Total pattern fitting for the combined size-strain-stress-texture determination in thin film diffraction. *Nucl. Instrum. Methods Phys. Res. Sect. B Beam Interact. Mater. At.* **2010**, *268*, 334–340. [[CrossRef](#)]
32. Belsky, A.; Hellenbrandl, M.; Karen, V.L.; Luksch, P. New developments in the inorganic crystal structure database (ICSD): Accessibility in support of materials research and design. *Acta Crystallogr.* **2002**, *858*, 364–369. [[CrossRef](#)]
33. Dollase, W.A. Correction of intensities for preferred orientation in powder diffractometry: Application of the March model. *J. Appl. Crystallogr.* **1986**, *19*, 267–272. [[CrossRef](#)]
34. Will, G.; Bellotto, M.; Parrish, W.; Hart, M. Crystal structures of quartz and magnesium germanate by profile analysis of synchrotron-radiation high-resolution powder data. *J. Appl. Crystallogr.* **1988**, *21*, 182–191. [[CrossRef](#)]
35. Cvijović-Alagić, I.; Cvijović, Z.; Mitrović, S.; Panić, V.; Rakin, M. Wear and corrosion behaviour of Ti-13Nb-13Zr and Ti-6Al-4V alloys in simulated physiological solution. *Corros. Sci.* **2011**, *53*, 796–808. [[CrossRef](#)]
36. Simsek, I.; Ozyurek, D. Investigation of the wear and corrosion behaviors of Ti5Al2.5Fe and Ti6Al4V alloys produced by mechanical alloying method in simulated body fluid environment. *Mater. Sci. Eng. C* **2019**, *94*, 357–363. [[CrossRef](#)] [[PubMed](#)]
37. Mansfeld, F. Tafel slopes and corrosion rates obtained in the pre-Tafel region of polarization curves. *Corros. Sci.* **2005**, *47*, 3178–3186. [[CrossRef](#)]
38. Flitt, H.J.; Schweinsberg, D.P. A guide to polarisation curve interpretation: Deconstruction of experimental curves typical of the Fe/H<sub>2</sub>O/H<sup>+</sup>/O<sub>2</sub> corrosion system. *Corros. Sci.* **2005**, *47*, 2125–2156. [[CrossRef](#)]
39. Flitt, H.J.; Schweinsberg, D.P. Evaluation of corrosion rate from polarisation curves not exhibiting a Tafel region. *Corros. Sci.* **2005**, *47*, 3034–3052. [[CrossRef](#)]
40. Krakowiak, S.; Darowicki, K.; Ślepski, P. Impedance of metastable pitting corrosion. *J. Electroanal. Chem.* **2005**, *575*, 33–38. [[CrossRef](#)]
41. Darowicki, K.; Krakowiak, S.; Ślepski, P. The time dependence of pit creation impedance spectra. *Electrochem. Commun.* **2004**, *6*, 860–866. [[CrossRef](#)]
42. Gerengi, H.; Ślepski, P.; Ozgan, E.; Kurtay, M. Investigation of corrosion behavior of 6060 and 6082 aluminum alloys under simulated acid rain conditions: Corrosion behavior of 6060 and 6082 Al alloys under acid rain. *Mater. Corros.* **2015**, *66*, 233–240. [[CrossRef](#)]
43. Blackwood, D. Influence of the space-charge region on electrochemical impedance measurements on passive oxide films on titanium. *Electrochim. Acta* **2000**, *46*, 563–569. [[CrossRef](#)]
44. Hamadou, L.; Aïnouche, L.; Kadri, A.; Yahia, S.A.A.; Benbrahim, N. Electrochemical impedance spectroscopy study of thermally grown oxides exhibiting constant phase element behaviour. *Electrochim. Acta* **2013**, *113*, 99–108. [[CrossRef](#)]
45. Gnedenkov, S.V.; Sinebryukhov, S.L. Electrochemical Impedance Spectroscopy of Oxide Layers on the Titanium Surface. *Russ. J. Electrochem.* **2005**, *41*, 858–865. [[CrossRef](#)]
46. Cámara, O.R.; Avalle, L.B.; Oliva, F.Y. Protein adsorption on titanium dioxide: Effects on double layer and semiconductor space charge region studied by EIS. *Electrochim. Acta* **2010**, *55*, 4519–4528. [[CrossRef](#)]
47. Jorcin, J.-B.; Orazem, M.E.; Pébère, N.; Tribollet, B. CPE analysis by local electrochemical impedance spectroscopy. *Electrochim. Acta* **2006**, *51*, 1473–1479. [[CrossRef](#)]

48. Alqarni, N.D.; Wysocka, J.; El-Bagoury, N.; Ryl, J.; Amin, M.A.; Boukherroub, R. Effect of cobalt addition on the corrosion behavior of near equiatomic NiTi shape memory alloy in normal saline solution: Electrochemical and XPS studies. *RSC Adv.* **2018**, *8*, 19289–19300. [[CrossRef](#)]
49. Hirschorn, B.; Orazem, M.E.; Tribollet, B.; Vivier, V.; Frateur, I.; Musiani, M. Determination of effective capacitance and film thickness from constant-phase-element parameters. *Electrochim. Acta* **2010**, *55*, 6218–6227. [[CrossRef](#)]
50. Krakowiak, S.; Darowicki, K.; Slepski, P. Impedance investigation of passive 304 stainless steel in the pit pre-initiation state. *Electrochim. Acta* **2005**, *50*, 2699–2704. [[CrossRef](#)]
51. Dong, Z.H.; Shi, W.; Guo, X.P. Initiation and repassivation of pitting corrosion of carbon steel in carbonated concrete pore solution. *Corros. Sci.* **2011**, *53*, 1322–1330. [[CrossRef](#)]
52. Amin, M.A.; Hassan, H.H.; Abd El Rehim, S.S. On the role of NO<sub>2</sub><sup>-</sup> ions in passivity breakdown of Zn in deaerated neutral sodium nitrite solutions and the effect of some inorganic inhibitors. *Electrochim. Acta* **2008**, *53*, 2600–2609. [[CrossRef](#)]
53. Zakeri, M.; Naghizadeh, M.; Nakhaie, D.; Moayed, M.H. Pit Transition Potential and Repassivation Potential of Stainless Steel in Thiosulfate Solution. *J. Electrochem. Soc.* **2016**, *163*, C275–C281. [[CrossRef](#)]
54. Amin, M.A.; Abd El-Rehim, S.S.; Aarão Reis, F.D.A.; Cole, I.S. Metastable and stable pitting events at zinc passive layer in alkaline solutions. *Ionics* **2014**, *20*, 127–136. [[CrossRef](#)]
55. Amin, M.A.; El-Bagoury, N.; Mahmoud, M.H.H.; Hessien, M.M.; Abd El-Rehim, S.S.; Wysocka, J.; Ryl, J. Catalytic impact of alloyed Al on the corrosion behavior of Co<sub>50</sub>Ni<sub>23</sub>Ga<sub>26</sub>Al<sub>1,0</sub> magnetic shape memory alloy and catalysis applications for efficient electrochemical H<sub>2</sub> generation. *Rsc Adv.* **2017**, *7*, 3635–3649. [[CrossRef](#)]
56. Amin, M.A.; Fadlallah, S.A.; Alosaimi, G.S. Activation of Titanium for Synthesis of Supported and Unsupported Metallic Nanoparticles. *J. Electrochem. Soc.* **2014**, *161*, D672–D680. [[CrossRef](#)]
57. Amin, M.A.; Abd El-Rehim, S.S.; El-Sherbini, E.E.F.; Mahmoud, S.R.; Abbas, M.N. Pitting corrosion studies on Al and Al–Zn alloys in SCN<sup>-</sup>solutions. *Electrochim. Acta* **2009**, *54*, 4288–4296. [[CrossRef](#)]
58. Scully, J.R. Localized Corrosion of Sputtered Aluminum and Al-0.5% Cu Alloy Thin Films in Aqueous HF Solution. *J. Electrochem. Soc.* **1990**, *137*, 1365. [[CrossRef](#)]
59. Pouilleau, J.; Devilliers, D.; Garrido, F.; Durand-Vidal, S.; Mahé, E. Structure and composition of passive titanium oxide films. *Mater. Sci. Eng. B* **1997**, *47*, 235–243. [[CrossRef](#)]
60. Milošev, I.; Kosec, T.; Strehblow, H.-H. XPS and EIS study of the passive film formed on orthopaedic Ti–6Al–7Nb alloy in Hank’s physiological solution. *Electrochim. Acta* **2008**, *53*, 3547–3558. [[CrossRef](#)]
61. Wysocka, J.; Cieslik, M.; Krakowiak, S.; Ryl, J. Carboxylic acids as efficient corrosion inhibitors of aluminium alloys in alkaline media. *Electrochim. Acta* **2018**, *289*, 175–192. [[CrossRef](#)]
62. Amin, M.A.; Ahmed, E.M.; Mostafa, N.Y.; Alotibi, M.M.; Darabdhara, G.; Das, M.R.; Wysocka, J.; Ryl, J.; Abd El-Rehim, S.S. Aluminum Titania Nanoparticle Composites as Nonprecious Catalysts for Efficient Electrochemical Generation of H<sub>2</sub>. *ACS Appl. Mater. Interfaces* **2016**, *8*, 23655–23667. [[CrossRef](#)]
63. Weibin, Z.; Weidong, W.; Xueming, W.; Xinlu, C.; Dawei, Y.; Changle, S.; Liping, P.; Yuying, W.; Li, B. The investigation of NbO<sub>2</sub> and Nb<sub>2</sub>O<sub>5</sub> electronic structure by XPS, UPS and first principles methods: The investigation of NbO<sub>2</sub> and Nb<sub>2</sub>O<sub>5</sub> electronic structure. *Surf. Interface Anal.* **2013**, *45*, 1206–1210. [[CrossRef](#)]
64. Kharitonov, D.S.; Sommertune, J.; Örnek, C.; Ryl, J.; Kurilo, I.I.; Claesson, P.M.; Pan, J. Corrosion inhibition of aluminium alloy AA6063-T5 by vanadates: Local surface chemical events elucidated by confocal Raman micro-spectroscopy. *Corros. Sci.* **2019**, *148*, 237–250. [[CrossRef](#)]
65. Kumar, S.; Kumar, S.; Tiwari, S.; Srivastava, S.; Srivastava, M.; Yadav, B.K.; Kumar, S.; Tran, T.T.; Dewan, A.K.; Mulchandani, A.; et al. Biofunctionalized Nanostructured Zirconia for Biomedical Application: A Smart Approach for Oral Cancer Detection. *Adv. Sci.* **2015**, *2*, 1500048. [[CrossRef](#)] [[PubMed](#)]
66. Siuzdak, K.; Szkoda, M.; Karczewski, J.; Ryl, J.; Darowicki, K.; Grochowska, K. Fabrication and Significant Photoelectrochemical Activity of Titania Nanotubes Modified with Thin Indium Tin Oxide Film. *Acta Metall. Sin. (Engl. Lett.)* **2017**, *30*, 1210–1220. [[CrossRef](#)]
67. Mandrino, D.; Godec, M.; Torkar, M.; Jenko, M. Study of oxide protective layers on stainless steel by AES, EDS and XPS. *Surf. Interface Anal.* **2008**, *40*, 285–289. [[CrossRef](#)]



68. Wang, C.; Irfan, I.; Liu, X.; Gao, Y. Role of molybdenum oxide for organic electronics: Surface analytical studies. *J. Vac. Sci. Technol. Bnanotechnol. Microelectron. Mater. Process. Meas. Phenom.* **2014**, *32*, 040801. [[CrossRef](#)]
69. Liu, J.; Alfantazi, A.; Asselin, E. Effects of Temperature and Sulfate on the Pitting Corrosion of Titanium in High-Temperature Chloride Solutions. *J. Electrochem. Soc.* **2015**, *162*, C189–C196. [[CrossRef](#)]



© 2019 by the authors. Licensee MDPI, Basel, Switzerland. This article is an open access article distributed under the terms and conditions of the Creative Commons Attribution (CC BY) license (<http://creativecommons.org/licenses/by/4.0/>).

Article

# Relationship between Phase Occurrence, Chemical Composition, and Corrosion Behavior of as-Solidified Al–Pd–Co Alloys

Marián Palcut, Libor Ďuriška, Ivona Černíčková, Sandra Brunovská, Žaneta Gerhátová, Martin Sahul, Ľubomír Čaplovič and Jozef Janovec \*

Faculty of Materials Science and Technology in Trnava, Slovak University of Technology in Bratislava, J. Bottu 25, 917 24 Trnava, Slovakia; marian.palcut@stuba.sk (M.P.); libor.duriska@stuba.sk (L.Ď.); ivona.cernickova@stuba.sk (I.Č.); brunovskas@gmail.com (S.B.); zaneta.gerhatova@stuba.sk (Ž.G.); marian.sahul@stuba.sk (M.S.); lubomir.caplovic@stuba.sk (L.Č.)

\* Correspondence: jozef.janovec@stuba.sk; Tel.: +421-918-646-072

Received: 18 April 2019; Accepted: 20 May 2019; Published: 22 May 2019

**Abstract:** The microstructure, phase constitution, and corrosion performance of as-solidified Al<sub>70</sub>Pd<sub>25</sub>Co<sub>5</sub> and Al<sub>74</sub>Pd<sub>12</sub>Co<sub>14</sub> alloys (element concentrations in at.%) have been investigated in the present work. The alloys were prepared by arc-melting of Al, Pd, and Co lumps in argon. The Al<sub>74</sub>Pd<sub>12</sub>Co<sub>14</sub> alloy was composed of structurally complex  $\epsilon_n$  phase, while the Al<sub>70</sub>Pd<sub>25</sub>Co<sub>5</sub> alloy was composed of  $\epsilon_n$  and  $\delta$  phases. The corrosion performance was studied by open circuit potential measurements and potentiodynamic polarization in aqueous NaCl solution (3.5 wt.%). Marked open circuit potential oscillations of the Al<sub>70</sub>Pd<sub>25</sub>Co<sub>5</sub> alloy have been observed, indicating individual breakdown and re-passivation events on the sample surface. A preferential corrosion attack of  $\epsilon_n$  was found, while the binary  $\delta$  phase (Al<sub>3</sub>Pd<sub>2</sub>) remained free of corrosion. A de-alloying of Al from  $\epsilon_n$  and formation of intermittent interpenetrating channel networks occurred in both alloys. The corrosion behavior of  $\epsilon_n$  is discussed in terms of its chemical composition and crystal structure. The corrosion activity of  $\epsilon_n$  could be further exploited in preparation of porous Pd–Co networks with possible catalytic activity.

**Keywords:** aluminum alloys; phase characterization; electrochemical corrosion; de-alloying

## 1. Introduction

Alloys with nominal chemical composition of approximately Al-30 at.% TM (TM stands for one or more transition metals) constitute a specific group of materials called complex metallic alloys (CMAs). These metallic materials contain, besides classical crystalline phases with simple unit cells, structurally complex intermetallic phases (SCIPs) [1]. The SCIPs are composed of giant unit cells and lack translational symmetry. Because of their complex atomic structure, the SCIPs are appealing for thin film applications, coatings, and reinforcement phases in composites [2].

The phase equilibria in the Al–Pd–Co system have been studied by Yurechko et al. [3,4], Černíčková et al. [5,6], and Ďuriška et al. [7]. The authors observed six stable ternary phases (W, Y<sub>2</sub>, U, V, F, C<sub>2</sub>) and a structurally complex  $\epsilon$ -family. Selected phases occurring in the Al–Pd–Co system are summarized in Table 1 [3,8]. Their homogeneity ranges at 790 °C are shown in the corresponding isothermal phase diagram section (Figure 1). The cluster-based orthorhombic decagonal quasicrystalline approximant of the  $\epsilon$ -family consists of five structures: two binary ( $\epsilon_6$ ,  $\epsilon_{28}$ ) and three ternary ( $\epsilon_{16}$ ,  $\epsilon_{22}$ ,  $\epsilon_{34}$ ). Since the  $\epsilon$ -family is considered to be a single phase from the thermodynamic point of view, it has been briefly denoted as  $\epsilon_n$ . Although two lattice parameters ( $a$  and  $b$ ) are identical for each structure within the family, the third lattice parameter ( $c$ ) differs for each of the structures since it is associated with

the cluster arrangement [3,9]. Contrary to Al–Pd alloys [10], Co was observed to substitute Pd in  $\epsilon_n$  in ternary Al–Pd–Co alloys. The Co solubility in  $\epsilon_n$  is up to approximately 15 at.% at 790 °C [3]. The Al–Pd–TM  $\epsilon_n$  phase is predominantly diamagnetic and has a good electrical conductivity. This phase is brittle and can be easily powdered. Furthermore, it contains Pd, a catalytically active element, which, in combination with a unique crystal structure, provides a variety of different adsorption sites. As such, the Al–Pd–Co SCIPs are interesting for catalytic applications [11].

**Table 1.** Overview of selected binary and ternary phases occurring in the Al–Pd–Co system and related binaries [3,8].

Phase	Space Group/Symmetry	Lattice Parameter			
		a (nm)	b (nm)	c (nm)	$\beta$ (°)
Al–Pd–Co system					
W	$Pmn2_1$	2.36	0.82	2.07	-
Y <sub>2</sub>	$Immm$	1.5451	1.2105	0.7590	-
U	$C121, C1m1$ or $C12/m1$	1.9024	2.9000	1.3140	117.26
V	$P121, P1m1$ or $P12/m1$	1.0068	0.3755	0.6512	102.38
F	$P2_1/a\bar{3}$	2.4397	-	-	-
C <sub>2</sub>	$Fm\bar{3}$	1.5507	-	-	-
$\epsilon_{16}$	$Anm2$	2.35	1.68	3.26	-
$\epsilon_{22}$	orthorhombic	2.35	1.68	4.49	-
$\epsilon_{34}$	orthorhombic	2.35	1.68	7.01	-
Al–Pd system					
$\epsilon_6$	$Pna2_1$	2.35	1.68	1.23	-
$\epsilon_{28}$	$C2mm$	2.35	1.68	5.70	-
Al <sub>3</sub> Pd <sub>2</sub> ( $\delta$ )	$P\bar{3}m1$	0.4227	-	0.5167	-
AlPd ( $\beta$ )	$Pm\bar{3}m$	0.3036	-	-	-
Al–Co system					
Al <sub>9</sub> Co <sub>2</sub>	$P2_1/a$	0.85565	0.6290	0.62130	94.76
O–Al <sub>13</sub> Co <sub>4</sub>	$Pmn2_1$ or $Pnmm$	0.8158	1.2347	1.4452	-
M–Al <sub>13</sub> Co <sub>4</sub>	$C2/m$	1.5173	0.81090	1.2349	107.84
Z–Al <sub>3</sub> Co	<i>monoclinic</i>	3.984	0.8148	3.223	107.97
Al <sub>5</sub> Co <sub>2</sub>	$P6_3/mmc$	0.76717	-	0.76052	-
AlCo ( $\beta$ )	$Pm\bar{3}m$	0.2854	-	-	-

The corrosion activity of Al-based SCIPs is relatively unknown. It has been found that the electrochemical properties of CMAs differ from those of aluminum metal [12]. The previous studies of Al–Cu–Fe [13,14], Al–Cr–Fe [15], and Al–Cu–Fe–Cr [16] CMAs indicated that the relative amount of alloy phases and their chemical compositions had a major influence on their electrochemical behavior. It was presented that Cr additions significantly improved the corrosion resistance of Al–Cr–Fe and Al–Cu–Fe–Cr alloys [16]. Recent studies of Al–Co CMAs [17–21] have shown that the relative amounts of the alloy's phases and electrical contact between them played an important role in their corrosion performance. The anodic dissolution of different alloy phases was found to take place by a galvanic mechanism. The electrochemical nobility of Al–Co SCIPs was found to increase with increasing Co concentration. The phase crystal structure had only a secondary influence. An exception, however, was found for the structurally complex Z–Al<sub>3</sub>Co phase. This phase was found to be more corrosion resistant compared to Al<sub>5</sub>Co<sub>2</sub> in chloride-containing environments [19]. The reason for this behavior could stem from the complex crystal structure of Z–Al<sub>3</sub>Co, formed by a complex monoclinic unit cell containing large pentagons composed of six small pentagons of monoclinic Al<sub>13</sub>Co<sub>4</sub>. The complex structure of this phase is probably stabilized by vacancies. The vacancies may influence the Co diffusivity leading to a protective layer formation on the sample surface.

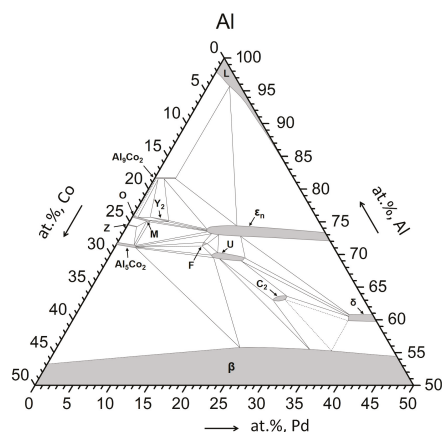


**Figure 1.** Isothermal section of the Al–Pd–Co phase diagram at 790 °C, redrawn from Reference [3].

The corrosion behavior of Al–Pd alloys in various solutions has been studied in References [22–25]. The results showed a preferential Al dissolution from  $\epsilon_n$  (~Al<sub>3</sub>Pd). The corrosion attack of the structurally complex  $\epsilon_n$  in the Al–Pd alloys led to the formation of a porous, channel-like network [22–25]. This phenomenon is known as electrochemical de-alloying [26], i.e., a corrosion-driven process during which an alloy is decomposed by selective dissolution of the most electrochemically active element (Al). This process results in the formation of nano-porous metal networks composed of noble elements. In the NaCl aqueous solution, the de-alloying of Al–Pd alloys was found to be more pronounced in as-solidified alloys compared to as-annealed samples [24]. The de-alloying of Al–TM alloys has attracted much attention in recent years as a versatile tool for creating nano-porous metal networks with high catalytic activity [25]. Nano-porous ribbons of Pd, Au, Pt, and other precious metals have been fabricated through chemical de-alloying of rapidly solidified Al-based alloys under free corrosion conditions [27].

In the present work, the corrosion performance of Al<sub>70</sub>Pd<sub>25</sub>Co<sub>5</sub> and Al<sub>74</sub>Pd<sub>12</sub>Co<sub>14</sub> alloys (element concentrations are given in at.%) have been studied by potentiodynamic polarization in 3.5 wt.% NaCl aqueous solution for the first time. The aim of this work is to investigate the effect of both phase occurrence and chemical composition on the alloy's corrosion behavior. Furthermore, the effect of Co concentration on the corrosion behavior of  $\epsilon_n$  is studied.

## 2. Materials and Methods

The alloys with nominal compositions Al<sub>70</sub>Pd<sub>25</sub>Co<sub>5</sub> and Al<sub>74</sub>Pd<sub>12</sub>Co<sub>14</sub> were prepared by repeated arc-melting of Al, Pd, and Co granules (purity of 99.95%) in argon. After melting, the alloys were rapidly solidified on a water-cooled copper mold, cast in epoxy resin, and metallographically prepared by wet grinding and polishing down to a surface roughness of 1  $\mu$ m. The as-solidified alloy's phase constitution and microstructure were studied by room temperature X-ray diffraction (XRD) and scanning electron microscopy (SEM), respectively. During XRD experiments, a Panalytical Empyrean PIXcel 3D diffractometer (Malvern Panalytical Ltd., Malvern, UK) with Bragg–Brentano geometry and Co K $\alpha$ <sub>1,2</sub> radiation was used. The measurements were conducted in the 2 $\theta$  range between 20° and 60°, with the step size 0.0131° and the counting time 98 s per step. For the microstructure observation, a JEOL JSM-7600F scanning electron microscope (JEOL, Akishima, Tokyo, Japan), equipped with an Oxford Instruments X-max 50 spectrometer (Oxford Instruments, Abingdon, UK) and operated by the INCA software (version 5.04), was employed. The microscope was operated at the acceleration voltage of 20 kV. The scanning was performed in regimes of secondary (SEI) and backscattered (BEI) electrons. Furthermore, a scanning transmission electron microscope JEOL JEM ARM200F (JEOL,

Akishima, Tokyo, Japan), operated at 200 kV and equipped with a high-angle annular dark-field detector (HAADF/STEM), was employed to obtain HAADF images. The two-dimensional (2D) projections of crystal structures were calculated in PowderCell software (version 2.4) using the data derived from References [8,28,29].

The corrosion experiments were conducted at room temperature ( $21 \pm 2$  °C) in a 500 ml glass vessel filled with an aqueous electrolyte. A three-electrode setup was used. The working electrode consisted of the polished surface of the Al–Pd–Co alloy with an exposed area of about 1 cm<sup>2</sup>. A silver–silver chloride electrode immersed in a saturated sodium chloride solution (saturated Ag/AgCl electrode) was used as a reference electrode. The counter electrode was a platinum mesh ( $2 \times 2$  cm<sup>2</sup>). The corrosion experiments were conducted in an aqueous NaCl solution (concentration 0.6 mol dm<sup>−3</sup>). The solution was prepared immediately before the experiment by dissolving 35 g of NaCl in 1 liter of de-ionized water (conductivity <20 μS). The electrolyte was not de-aerated before the experiment to simulate real environmental conditions. The progress of the reaction was controlled by a PGU 10 V-1A-IMP-S potentiostat/galvanostat from Jaisse Electronic Ltd. (Waiblingen, Germany).

The surface topography of the corroded samples was analyzed by a Zeiss LSM 700 confocal laser scanning microscope (CLSM, Zeiss, Oberkochen, Germany). The ZEN 2009 software was used for the three-dimensional topographical resolution.

### 3. Results and Discussion

#### 3.1. Microstructure and Phase Occurrence before Corrosion Testing

The microstructures of the as-solidified Al<sub>70</sub>Pd<sub>25</sub>Co<sub>5</sub> and Al<sub>74</sub>Pd<sub>12</sub>Co<sub>14</sub> alloys are illustrated in Figure 2. The XRD patterns corresponding to the above alloys are given in Figure 3a,b, respectively. The metal concentrations of microstructure constituents determined by SEM/EDX and their phase assignments are presented in Table 2.

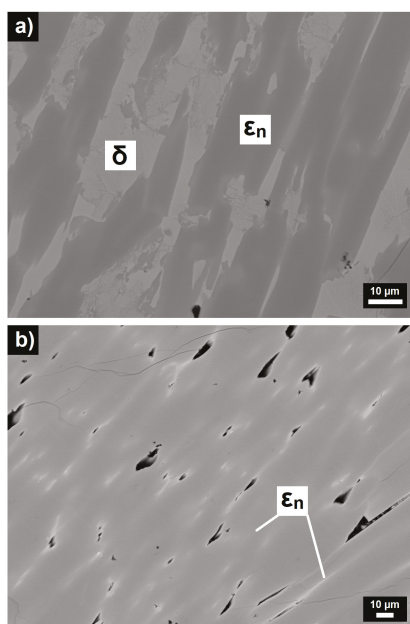


**Figure 2.** BEI/SEM images of microstructure constituents in as-solidified Al<sub>70</sub>Pd<sub>25</sub>Co<sub>5</sub> (a) and Al<sub>74</sub>Pd<sub>12</sub>Co<sub>14</sub> (b) alloys. Black areas in (b) correspond to pores. Phases assigned to particular constituents are also marked.

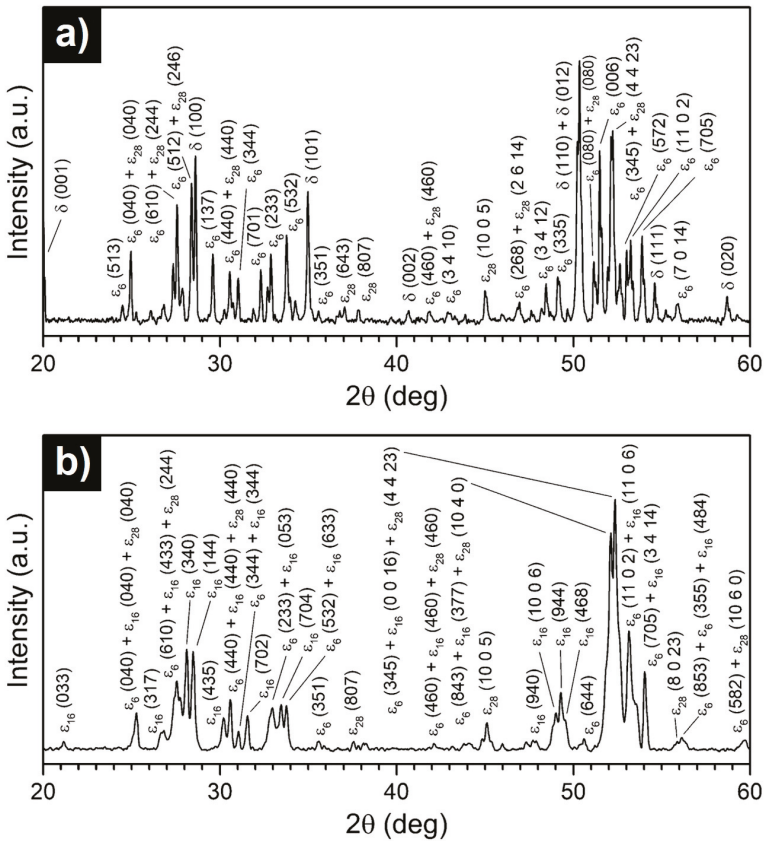


Figure 3. XRD diffraction patterns of as-solidified Al<sub>70</sub>Pd<sub>25</sub>Co<sub>5</sub> (a) and Al<sub>74</sub>Pd<sub>12</sub>Co<sub>14</sub> (b) alloys.

Table 2. Metal concentrations and phase assignments of microstructure constituents observed in as-solidified Al<sub>70</sub>Pd<sub>25</sub>Co<sub>5</sub> and Al<sub>74</sub>Pd<sub>12</sub>Co<sub>14</sub> alloys.

Alloy	Alloy Condition	Identified Phase/Structure	Element Concentration (at.%)			Volume Fraction (%)
			Al	Pd	Co	
Al <sub>70</sub> Pd <sub>25</sub> Co <sub>5</sub>	as-solidified	$\epsilon_n/\epsilon_6 + \epsilon_{28}$	72.5 ± 0.1	18.9 ± 0.3	8.6 ± 0.3	77
		$\delta$	59.8 ± 0.2	39.7 ± 0.4	0.5 ± 0.2	23
Al <sub>74</sub> Pd <sub>12</sub> Co <sub>14</sub>	as-solidified	$\epsilon_n/\epsilon_6 + \epsilon_{16} + \epsilon_{28}$	73.9 ± 1.0	12.0 ± 5.5	14.1 ± 4.6	100

The microstructure of the Al<sub>70</sub>Pd<sub>25</sub>Co<sub>5</sub> alloy consisted of two different constituents (Figure 2a). The images were acquired in a BEI regime and therefore the bright regions have a higher Pd concentration compared to the dark constituents. The metal concentrations and volume fractions of the bright-grey microstructure constituent (Table 2) indicate that it corresponds to the  $\delta$  phase (Al<sub>3</sub>Pd<sub>2</sub>). This assumption was also confirmed by X-ray diffraction (Figure 3a). The visually and chemically homogeneous dark-grey constituent was identified to be a mixture of  $\epsilon_n$  structures (Figure 3a). To index diffraction peaks of particular  $\epsilon_n$  structures, the data derived from References [8,28,29] were used.

In the XRD pattern of the Al<sub>74</sub>Pd<sub>12</sub>Co<sub>14</sub> alloy (Figure 3b), a combination of  $\epsilon_6$ ,  $\epsilon_{16}$ , and  $\epsilon_{28}$  structures was identified. In the related microstructure image, however, a chemically heterogeneous constituent has been observed (Figure 2b). The dark-grey areas had an increased Co concentration, while the bright areas showed a higher Pd concentration compared to the dark-grey areas. The atomic structure of the

as-solidified  $\text{Al}_{74}\text{Pd}_{12}\text{Co}_{14}$  alloy was observed using HAADF/STEM. Three different structural motives have been recognized in the atomic structure of this alloy ( $\varepsilon_6$ ,  $\varepsilon_{16}$ , and  $\varepsilon_{28}$ , Figure 4). For each  $\varepsilon_n$  structure, specific combinations of phason tiles are characteristic.  $\varepsilon_6$  is formed by hexagons only,  $\varepsilon_{16}$  is represented by the combination of pentagons and nonagons, while  $\varepsilon_{28}$  comprises all three types of tiles. It has been suggested that transitions between various structures of the  $\varepsilon$ -family could be associated with a small rearrangement of clusters, resulting in changes in the occurrence and/or configuration of phason tiles. The arrangement of tiles in particular  $\varepsilon_n$  structures, observed experimentally in this work, was also calculated using the data derived from References [8,28,29]. The 2D projection of the  $\varepsilon_6$ ,  $\varepsilon_{16}$ , and  $\varepsilon_{28}$  structures, presented in Figure 5, is in a good agreement with the HAADF/STEM image.

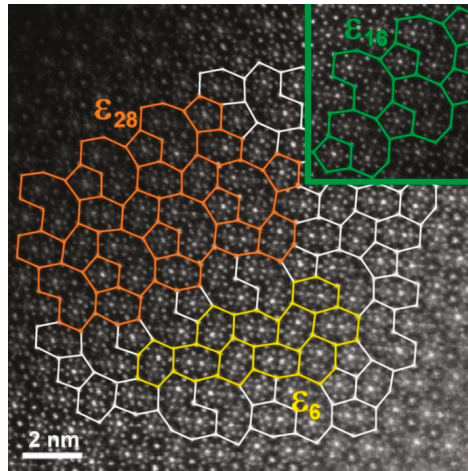


**Figure 4.** A high-angle annular dark-field (HAADF)/STEM image of the atomic structure of the as-solidified  $\text{Al}_{74}\text{Pd}_{12}\text{Co}_{14}$  alloy. Phason tiles, i.e., hexagon, pentagon, and banana-shaped nonagons, are highlighted by solid lines. Yellow, green, and orange structural motifs correspond to  $\varepsilon_6$ ,  $\varepsilon_{16}$ , and  $\varepsilon_{28}$ , respectively. For the color interpretation of this figure, the reader is referred to the web version of this article.

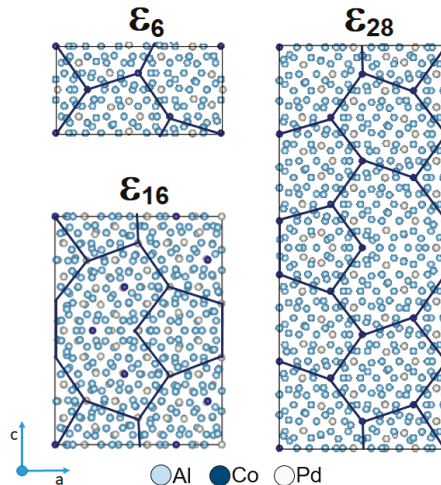


**Figure 5.** Two-dimensional projection of the crystal structure of  $\varepsilon_6$ ,  $\varepsilon_{16}$ , and  $\varepsilon_{28}$ . The phason tiling is denoted by dark-blue lines. For the color interpretation of this figure, the reader is referred to the web version of this article.

Structures of  $\epsilon_6$  and  $\epsilon_{28}$  were reported to be binary structural variants of  $\epsilon_n$ , while  $\epsilon_{16}$  has been described as a ternary  $\epsilon_n$  structure [3,10,29,30]. In the latter structure, Co atoms substitute Pd. Therefore, the dark-grey areas (Figure 2b, Table 2), enriched with Co from the Co–Pd balance point of view, could be assigned to the ternary  $\epsilon_{16}$  structure in the as-solidified  $\text{Al}_{74}\text{Pd}_{12}\text{Co}_{14}$  alloy. Similarly, the bright areas in Figure 2b could be ascribed to the mixture of  $\epsilon_6$  and  $\epsilon_{28}$  structures, which lie closer to the Al–Pd binary edge of the Al–Pd–Co ternary system. The bright areas were located preferentially around pores. The pores were formed on the grain boundaries during solidification due to shrinking. Co and Pd concentrations of  $\epsilon_n$  changed since de-mixing took place during solidification. The Pd concentration in  $\epsilon_n$  increased towards the grain boundary. Thus, the Pd-rich  $\epsilon_n$  ( $\epsilon_6 + \epsilon_{28}$ ) were located preferentially around pores. The Co-rich  $\epsilon_n$  ( $\epsilon_{16}$ ) was located in the center of the grain as this phase structure solidified from the melt. The overall chemical composition of the  $\epsilon_n$  phase in the  $\text{Al}_{74}\text{Pd}_{12}\text{Co}_{14}$  alloy is presented in Table 2. Due to the presence of  $\epsilon_{16}$ , the  $\epsilon_n$  phase in the  $\text{Al}_{74}\text{Pd}_{12}\text{Co}_{14}$  alloy had a significantly higher Co concentration compared to the  $\text{Al}_{70}\text{Pd}_{25}\text{Co}_5$  alloy where the ternary  $\epsilon_{16}$  phase has not been identified.

The distributions of particular structures within the  $\epsilon_n$  phase were previously studied in the Al–Pd and Al–Pd–Co systems; however, the exact boundaries between structures have not been determined yet. In the Al–Pd system, Yurechko et al. [10] proposed a hypothetical double-phase area ( $\epsilon_6 + \epsilon_{28}$ ) in between two single-phase areas ( $\epsilon_6$  and  $\epsilon_{28}$ ). In the partial phase diagram published by Grushko [31],  $\epsilon_6$  and  $\epsilon_{28}$  have been positioned in a common “single-phase ( $\epsilon_6 + \epsilon_{28}$ )” area consisting of two presumably separated subareas adherent to the particular structures. Earlier, the same distribution of  $\epsilon_6$  and  $\epsilon_{28}$  was studied by Balanetsky et al. [28] in the Al–Pd–Fe system at 750 °C. Moreover, the homogeneity ranges of  $\epsilon_{16}$  and  $\epsilon_{22}$  have been defined. However, the strict boundaries between particular structures have not been described. In the Al–Pd–Co system, Yurechko et al. [3] estimated the boundaries of all the structures within the  $\epsilon$ -family. Considering the results obtained using HAADF/STEM in this work and in [29], it can be assumed that the transitions between particular structures are rather open as schematically highlighted in gradient colors (green, red, yellow, and blue) in Figure 6. As follows from this figure, several  $\epsilon_n$  structures in the transient area can coexist. This situation can also be seen in the microstructure of the  $\text{Al}_{74}\text{Pd}_{12}\text{Co}_{14}$  alloy. The dark-grey areas, corresponding to the  $\epsilon_{16}$  structure, fluently transformed to the bright areas represented by the mixture of  $\epsilon_6$  and  $\epsilon_{28}$  structures (Figure 2b). The chemical composition of  $\epsilon_6$  is very close to the composition of  $\epsilon_{28}$ . Consequently, this bright-grey microstructure constituent in the  $\text{Al}_{70}\text{Pd}_{25}\text{Co}_5$  alloy (Figure 2a) can be considered to be homogeneous. Individual  $\epsilon_6$  and  $\epsilon_{28}$  structures can be recognized in the HAADF/STEM image only (Figure 4).

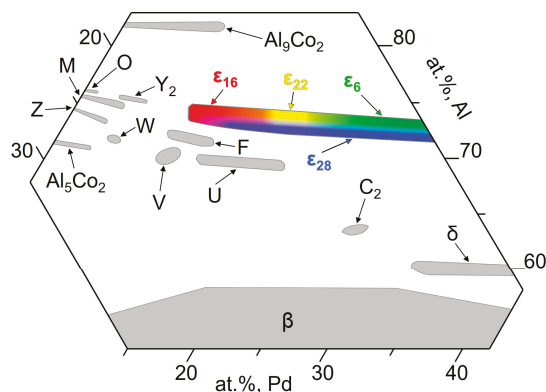


**Figure 6.** Schematic positions of binary and ternary phases in the isothermal section of a partial Al–Pd–Co diagram, redrawn from Reference [3]. For the color interpretation of this figure, the reader is referred to the web version of this article.



### 3.2. Corrosion Behavior

Immediately after the sample's immersion in aqueous NaCl, an open circuit potential (OCP) was recorded. The OCPs of the alloys are presented in Figure 7. A distinct behavior has been observed. While the OCP of the  $\text{Al}_{74}\text{Pd}_{12}\text{Co}_{14}$  alloy was relatively stable over time, irregular oscillations for the  $\text{Al}_{70}\text{Pd}_{25}\text{Co}_5$  alloy have been found. Furthermore, the OCPs of the  $\text{Al}_{70}\text{Pd}_{25}\text{Co}_5$  alloy were less negative and a difference of more than 200 mV was found compared to the  $\text{Al}_{74}\text{Pd}_{12}\text{Co}_{14}$  alloy.

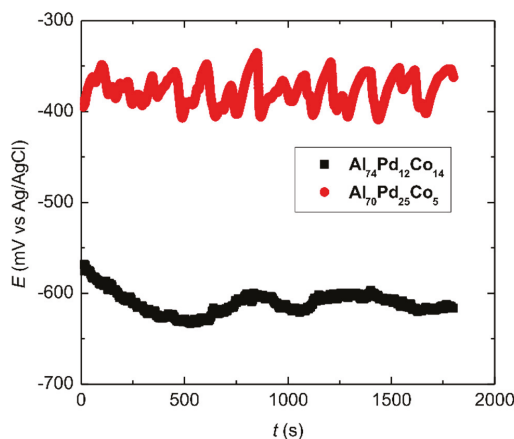


**Figure 7.** Open circuit potential of the as-solidified  $\text{Al}_{74}\text{Pd}_{12}\text{Co}_{14}$  and  $\text{Al}_{70}\text{Pd}_{25}\text{Co}_5$  alloys in 0.6 M NaCl. For the color interpretation of this figure, the reader is referred to the web version of this article.

The as-solidified  $\text{Al}_{74}\text{Pd}_{12}\text{Co}_{14}$  alloy is a single-phase alloy. The OCP of this alloy therefore corresponds to the electrochemical activity of  $\epsilon_n$ . The  $\text{Al}_{70}\text{Pd}_{25}\text{Co}_5$  alloy, on the other hand, is a double-phase alloy composed of  $\epsilon_n$  and  $\delta$  ( $\text{Al}_3\text{Pd}_2$ ). The less negative OCP of this alloy indicates a higher electrochemical potential of  $\delta$ . Because of the potential difference between  $\epsilon_n$  and  $\delta$ , local galvanic cells may have been formed on the surface of the  $\text{Al}_{70}\text{Pd}_{25}\text{Co}_5$  alloy.

Every physical contact between  $\delta$  and  $\epsilon_n$  corresponds to an elementary galvanic corrosion cell. During galvanic corrosion, there is a net current flow between the cathodic microstructure constituent ( $\delta$ ) and its adjacent matrix ( $\epsilon_n$ ). The metal ions dissolve into the solution on the anode and electrons released flow to the micro-cathodic area for the reduction process. This causes a redistribution of electrical charge between anodic ( $\epsilon_n$ ) and cathodic areas ( $\delta$ ), thereby leading to a variation of the OCP. As the OCP is measured at the tip of the Haber–Luggin capillary, it represents the overall contributions of all elementary galvanic cells on the sample surface [32]. These contributions are not correlated. A high number of elementary galvanic cells between  $\epsilon_n$  and  $\delta$  co-exist with each other in the microstructure of the  $\text{Al}_{70}\text{Pd}_{25}\text{Co}_5$  alloy (Figure 2a). Their interactions are combined and contribute to the overall corrosion behavior of this alloy.

A further insight into the peculiar corrosion behavior of the Al–Pd–Co alloys was obtained by potentiodynamic polarization. After the OCP measurement, a polarization scanning from  $-1000$  mV to  $0$  mV (Ag/AgCl) was performed using a sweeping rate of  $1 \text{ mV s}^{-1}$ . After reaching  $0$  mV (Ag/AgCl), the polarization direction was reversed and returned back to the initial potential (the direction of the polarization is indicated by open arrows in Figure 8). The resulting cyclic polarization curves are depicted in Figure 8. The forward curves are characterized by the corrosion minimum followed by an increase of the current density at potentials less negative than the corrosion potential. The current density increase was further followed either by stabilization (the  $\text{Al}_{74}\text{Pd}_{12}\text{Co}_{14}$  alloy) or even a slight decrease of the current density (the  $\text{Al}_{70}\text{Pd}_{25}\text{Co}_5$  alloy). This behavior indicates a passivation of the alloys. The transient behavior was further followed by a sudden current density increase at potentials

less negative than  $-400$  mV (Ag/AgCl), indicating a breakdown of the passive film. Upon reverse polarization, a re-passivation of the existing pits occurred. In order to compare equally polarized samples, we reversed the scanning at the fixed potential. The forward curves presented in Figure 8 have been analyzed by Tafel extrapolation [33]. The electrochemical parameters of the alloys (corrosion potential, corrosion current density, and breakdown potential) are listed in Table 3. A re-passivation potential obtained from the reverse curve is also presented. However, caution is required when comparing the individual re-passivation potentials of the alloys. The currents at the vertex were higher for the  $\text{Al}_{74}\text{Pd}_{12}\text{Co}_{14}$  alloy and this might have influenced the pit depth and local chemistry [33]. In order to obtain more comparable  $E_{rp}$  values, reversing the polarization at a constant current density would be necessary.

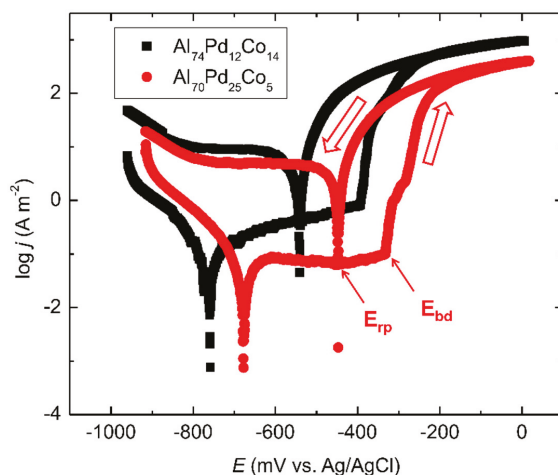


**Figure 8.** Cyclic potentiodynamic polarization curves of the as-solidified  $\text{Al}_{74}\text{Pd}_{12}\text{Co}_{14}$  and  $\text{Al}_{70}\text{Pd}_{25}\text{Co}_5$  alloys in 0.6 M NaCl. The polarization direction and positions of breakdown ( $E_{bd}$ ) and re-passivation potentials ( $E_{rp}$ ) are indicated by arrows. For the color interpretation of this figure, the reader is referred to the web version of this article.

**Table 3.** Electrochemical parameters of as-solidified  $\text{Al}_{70}\text{Pd}_{25}\text{Co}_5$  and  $\text{Al}_{74}\text{Pd}_{12}\text{Co}_{14}$  alloys. Corrosion potentials ( $E_{corr}$ ) and corrosion current densities ( $j_{corr}$ ) were obtained by Tafel extrapolation of forward curves (Figure 8).

Alloy	OCP (mV vs. Ag/AgCl)	$E_{corr}$ (mV vs. Ag/AgCl)	$j_{corr}$ ( $\text{A m}^{-2}$ )	$E_{bd}$ (mV vs. Ag/AgCl)	$E_{rp}$ (mV vs. Ag/AgCl)
$\text{Al}_{70}\text{Pd}_{25}\text{Co}_5$	$-370 \pm 35$	$-677$	0.101	$-332$	$-447$
$\text{Al}_{74}\text{Pd}_{12}\text{Co}_{14}$	$-607 \pm 9$	$-758$	0.176	$-393$	$-540$

Based on the above-presented results, a corrosion mechanism of the Al–Pd–Co alloys has been postulated. The corrosion mechanism is depicted in Figure 9. Pitting is a highly localized form of corrosion that happens in the presence of halide anions, such as  $\text{Cl}^-$  [34]. Initially, a protective alumina scale has been formed on the sample surface, which is indicated by a current density plateau observed upon sample polarization for both alloys. This plateau is observed at potentials of  $-600$  to  $-300$  mV versus Ag/AgCl for  $\text{Al}_{70}\text{Pd}_{25}\text{Co}_5$  alloy, i.e., at potentials less negative than is the corrosion potential (Figure 8). In the presence of  $\text{Cl}^-$ , however, this passive layer has been weakened. Aluminum forms unstable  $[\text{AlCl}_4]^-$  complexes that dissolve in aqueous solutions. The dissolution of the protective alumina scale in NaCl leaves a naked alloy surface susceptible to further corrosion attack (Figure 9).

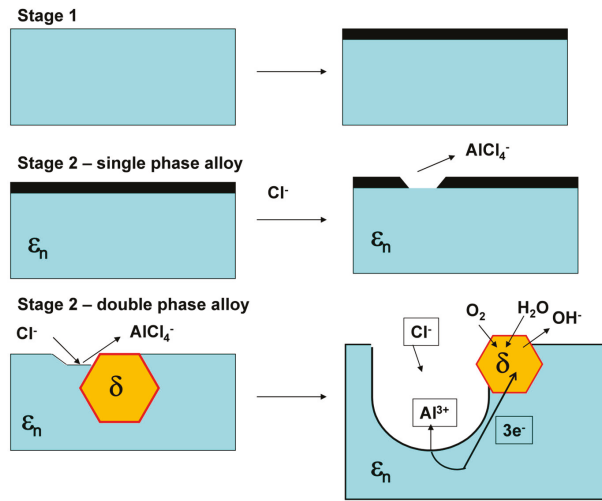
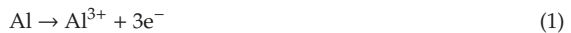
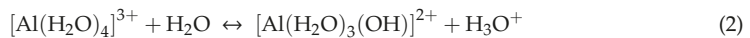


**Figure 9.** Pitting corrosion mechanism of the Al-Pd-Co alloys. For the color interpretation of this figure, the reader is referred to the web version of this article.

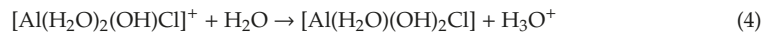
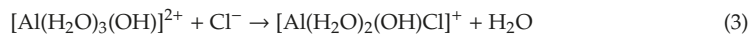
Interactions between co-existing phases in double-phase alloys may play an important role during corrosion [32,35,36]. Once the pitting potential is reached during sample polarization, the compact passivation layer becomes locally disrupted (Figure 9). As a result,  $\text{Al}^{3+}$  cations are released from the alloy into the solution in the course of the following reaction



Reaction (1) leads to positive charge enrichment within the dissolution zone [37]. As a consequence,  $\text{Cl}^-$  anions of the electrolyte rapidly migrate into the dissolution zone as presented in Figure 9. The released  $\text{Al}^{3+}$  cations become solvated by water molecules. Consequently, the hydrolysis of  $[\text{Al}(\text{H}_2\text{O})_4]^{3+}$  in aqueous environment takes place in line with the following reaction [34]



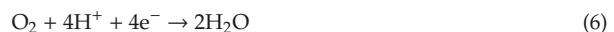
Hydroxo complexes of Al may further react with chloride and water according to the following reactions



By these reactions, hydrogen cations are released into the pit. Their accumulation yields to a local pH decrease within the dissolution zone, which is known as a self-acidifying effect [34,37]. The presence of  $\text{H}^+$  in pits further accelerates the Al dissolution. At the cathode ( $\delta$ , Figure 9), a reduction of water may take place in accordance with the following reaction



At the pit walls and possibly in their immediate vicinity, since pH is reduced due to hydrolysis reactions (2) and (4), the most likely prevailing cathodic reactions are



or



The latter reaction takes place in the case of pH having fallen to very low values. As a result, emerging bubbles of  $\text{H}_2$  evolve on the alloy surface.

The results presented in Table 3 show that the OCP of the double-phase  $\text{Al}_{70}\text{Pd}_{25}\text{Co}_5$  alloy is located between the breakdown and re-passivation potentials. This is also manifested by the OCP oscillations observed between  $-330$  mV (Ag/AgCl) and  $-400$  mV (Ag/AgCl, Figure 7), indicating periodic breakdown and re-passivation events on the sample surface. These observations indicate that this alloy was in a localized corrosion stage already upon the sample's immersion in the electrolyte, contrary to the single-phase  $\text{Al}_{74}\text{Pd}_{12}\text{Co}_{14}$  alloy. The passivation stage was found to be more pronounced in the case of the double-phase  $\text{Al}_{70}\text{Pd}_{25}\text{Co}_5$  alloy (Figure 8). This could be related to the presence of the noble  $\delta$  phase in this alloy. For the mono-phasic  $\text{Al}_{74}\text{Pd}_{12}\text{Co}_{14}$  alloy, on the other hand, a higher corrosion current density ( $j_{\text{corr}}$ ) has been found, reflecting a higher dissolution rate. Moreover, a more negative corrosion potential for this alloy has been found, indicating a higher corrosion susceptibility. The above-reported differences in the corrosion behavior of the alloys could result from their different microstructures. More information about the specific corrosion attack of different SCIPs has been therefore obtained by investigating the alloys' microstructures after electrode polarization.

The microstructures of the as-polarized alloys are documented in Figure 10. Metal concentrations of the phases after corrosion are summarized in Table 4. For both alloys, a preferential attack of  $\epsilon_n$  was found.  $\delta$  as a nobler phase in the  $\text{Al}_{70}\text{Pd}_{25}\text{Co}_5$  alloy has been retained. A de-alloying of Al from  $\epsilon_n$  as well as formation of intermittent inter-penetrating channel networks have been observed in both alloys (Figure 10). In the single-phase  $\text{Al}_{74}\text{Pd}_{12}\text{Co}_{14}$  alloy, a higher density of intermittent inter-penetrating channels and pits has been found (Figure 10). Moreover, the channels formed a cross-linked network. This behavior is similar to the Al-Pd alloys, where the pits were observed in the interconnection between two channels [24]. In the  $\text{Al}_{70}\text{Pd}_{25}\text{Co}_5$  alloy, the pits were observed to be randomly distributed in the channels (Figure 10).

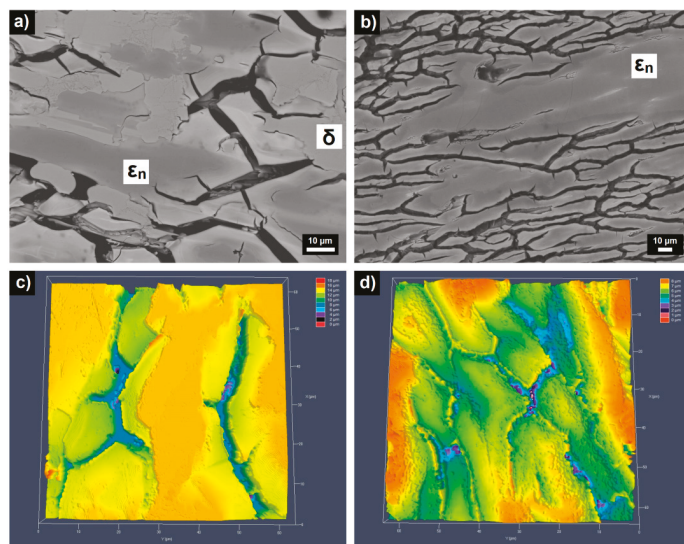


**Figure 10.** BEI/SEM images (a,b) and CLSM images (c,d) of as-polarized  $\text{Al}_{70}\text{Pd}_{25}\text{Co}_5$  (a,c) and  $\text{Al}_{74}\text{Pd}_{12}\text{Co}_{14}$  (b,d) alloys. Phases assigned to particular constituents are also marked. For the color interpretation of this figure, the reader is referred to the web version of this article.

**Table 4.** Metal concentrations and phase assignments of the as-polarized Al–Pd–Co alloys. Differences in metal concentrations between as-polarized and as-solidified alloys are also presented (compare with data in Table 2).

Alloy	Identified Phase/Structure	Element concentration (at.%)					
		Al	$\Delta(\text{Al})$	Pd	$\Delta(\text{Pd})$	Co	$\Delta(\text{Co})$
Al <sub>70</sub> Pd <sub>25</sub> Co <sub>5</sub>	$\varepsilon_n/\varepsilon_6 + \varepsilon_{28}$	69.0 ± 0.3	−3.5	22.2 ± 0.4	+ 3.3	8.8 ± 0.4	-
	$\delta$	60.0 ± 0.3	-	39.4 ± 0.3	-	0.6 ± 0.2	-
Al <sub>74</sub> Pd <sub>12</sub> Co <sub>14</sub>	$\varepsilon_n/\varepsilon_6 + \varepsilon_{16} + \varepsilon_{28}$	71.1 ± 0.9	−2.8	14.3 ± 5.3	+ 2.3	14.6 ± 4.3	-

A dissolution of Al in the Al<sub>70</sub>Pd<sub>25</sub>Co<sub>5</sub> alloy has been found (Table 4). Simultaneously, the Al concentration in  $\varepsilon_n$  decreased from 72.5 to 69.0 at.% (Table 4). In the Al<sub>74</sub>Pd<sub>12</sub>Co<sub>14</sub> alloy, a decrease of Al concentration in  $\varepsilon_n$  from 73.9 to 71.1 at.% has been found. Thus, the level of Al de-alloying was higher in the double phase Al<sub>70</sub>Pd<sub>25</sub>Co<sub>5</sub> alloy. Moreover, the pits found in this alloy were deeper compared to the Al<sub>74</sub>Pd<sub>12</sub>Co<sub>14</sub> alloy. The formation of cracks observed in the as-polarized alloys could be governed by a combination of de-alloying kinetics and the release rate of internal stresses. As the electrochemical potential is raised in a positive direction, the dissolution rate of the alloy increases (Figure 8). This electrochemical force drives the surface at the de-alloying front further away from the equilibrium [37]. The removal of Al from the alloy phases leads to microcrack initiation. The residual stress accumulated in the alloys during rapid solidification is released during de-alloying.

Corrosion potentials and corrosion current densities of the as-solidified Al–Co [17,18,20,21,38], Al–Pd [24], and Al–Pd–Co alloys are compared in Figure 11. The corrosion potentials of the Al–Co alloys show a significant dependence on the Al atomic fraction. They become more negative with increasing Al concentration. The corrosion potentials of the Al–Pd alloys, on the other hand, are relatively constant with respect to the alloy’s overall chemical composition. They are, in fact, more negative than the corrosion potentials of the remaining two groups of alloys. The corrosion currents of the Al–Pd alloys, on the other hand, are higher compared to the Al–Co and Al–Pd–Co alloys (Figure 11b). These observations suggest that the Al–Pd alloys are less corrosion-resistant compared to both the Al–Pd–Co and Al–Co alloys. The corrosion behavior of the Al–Pd–Co alloys is closer to the behavior of the Al–Co alloys. This observation is unexpected, since both alloy groups have a different chemical composition and phase constitution. Moreover,  $\varepsilon_n$ , the preferentially corroding phase in the Al–Pd–Co alloys, is not present in the Al–Co alloys. Therefore, it can be suggested that Al<sub>3</sub>Co SCIPs are nobler compared to binary  $\varepsilon_n$  (Al<sub>3</sub>Pd). This is manifested by the less negative corrosion potentials of the Al–Co alloys compared to the Al–Pd alloys with a similar Al atomic fraction (Figure 11). Furthermore, the Co substitution for Pd significantly improves the corrosion resistance of  $\varepsilon_n$ . As such, it is not the crystal structure of the phase, but its chemical composition, that plays a major role in the corrosion behavior.

To further probe this hypothesis, we have plotted the corrosion data of other ternary Al–TM systems, found in the literature, together with those of the Al–Pd–Co system. The data survey [13,39–42] is presented in Figure 12. Although the data are scattered due to large variations in alloy chemical compositions, some trends can be identified. The as-solidified Al–Cu–Pd and Al–Cu–Fe alloys have lower corrosion currents compared to the Al–Pd–Co alloys [13,39]. The addition of Pd was found to slightly decrease the corrosion current of the Al–Cu alloys in chloride solution [39]. For the Al<sub>4</sub>Cu<sub>9</sub> samples, however, not much effect from Pd has been seen [39]. The corrosion potentials of these alloys are found over a broad range of values. The scatter in  $E_{\text{corr}}$  values, however, could be caused by variations in their chemical composition. The Al–Cr–Fe alloy is also presented in Figure 12 [40]. This alloy has a more negative corrosion potential due to the absence of noble elements, such as Pd. Furthermore, it has a low corrosion current due to the presence of chromium, which forms a passive layer on the sample surface.

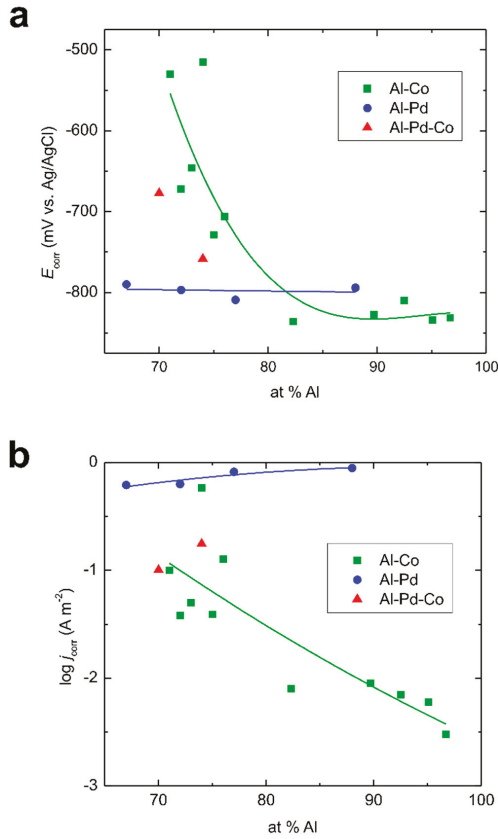


**Figure 11.** Corrosion potentials (a) and corrosion current densities (b) of as-solidified Al-Co, Al-Pd, and Al-Co-Pd alloys. Lines are a guide to the eyes only. For the color interpretation of this figure, the reader is referred to the web version of this article.

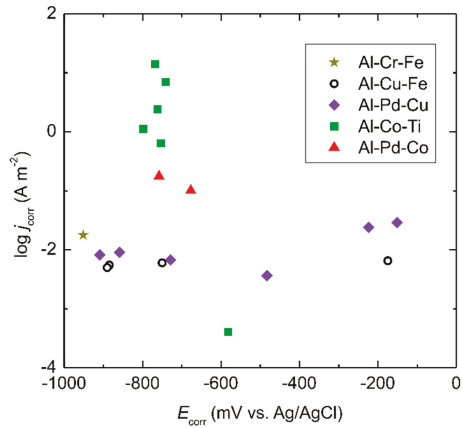


**Figure 12.** Corrosion current densities versus corrosion potentials of selected ternary Al-based complex metallic alloys (as-cast and as-annealed alloys only). For the color interpretation of this figure, the reader is referred to the web version of this article.

Interesting is the corrosion behavior of as-solidified Al–Co–Ti alloys [41]. These alloys have corrosion potentials comparable to those of the Al–Pd–Co alloys (Figure 12). The concentration of Ti in these alloys was fixed at 2 at.% and the atomic concentration of Co varied between 5 and 30 at.% (Al–xCo–2Ti alloys). As such, the materials design of these alloys had features typical of the Al–Co alloys [41,42]. In general, the corrosion currents of the Al–Co–Ti alloys are higher compared to those of the Al–Pd–Co alloys. An exception was found, however, for the Al–15Co–2Ti alloy since this alloy had a very low corrosion current. This difference is, however, attributable to the fact that the intermetallic particles present in this alloy ( $\text{Al}_9\text{Co}_2$ ,  $\text{Al}_{13}\text{Co}_4$ , and  $\text{Al}_3\text{Ti}$ ) were of different morphologies and volume fractions compared to the remainder of the alloys [41]. These observations indicate that the specific Co concentrations may greatly improve the corrosion performance of the Al–TM alloys. The  $\epsilon_n$  phase in the Al–Pd–Co alloys contains a significant amount of Co. The Co additions thus contribute to the corrosion resistance of the Al–Pd–Co alloys and this is especially obvious in the case of the double phase  $\text{Al}_{70}\text{Pd}_{25}\text{Co}_5$  alloy.

$\text{Al}_3\text{Ti}$  and  $\text{Al}_3\text{Fe}$  are noble intermetallic phases with respect to the aluminum matrix [36]. The results presented in this work show that  $\text{Al}_3\text{Co}$  is also relatively noble. These phases are nobler compared to binary  $\epsilon_n$  ( $\text{Al}_3\text{Pd}$ ). Co substitution for Pd thus significantly improves the corrosion resistance of  $\epsilon_n$ . As such, it is not the crystal structure of the phase, but its chemical composition, that plays a major role in the corrosion behavior. The electrochemical behavior of constituent phases may change over time. In a recent study, Zhu et al. studied the evolution of corrosion behavior of intermetallic phases in Al alloys over time [43]. At the early stages, the corrosion attack occurred in the form of de-alloying. However, as the time progressed, the particles became nobler as a result of Al dissolution [43]. This particle ennoblement may accelerate the galvanic dissolution of the surrounding matrix. The corrosion behavior of constituent phases may also change as a result of long-term annealing. The long-term annealing causes element redistribution and reduces stresses accumulated during rapid solidification [19]. A comparative study of as-annealed, near-equilibrium Al–Pd–Co alloys is planned and results will be reported in a future publication.

#### 4. Conclusions

In this work, the corrosion performance of as-solidified  $\text{Al}_{70}\text{Pd}_{25}\text{Co}_5$  and  $\text{Al}_{74}\text{Pd}_{12}\text{Co}_{14}$  alloys was studied by open circuit potential measurements and potentiodynamic polarization in aqueous NaCl (3.5 wt.%), following an in-depth structural characterization of the alloys. The alloys were prepared by arc-melting of Pd, Al, and Co lumps in argon. Based on the results, the following conclusions can be presented:

1. The  $\text{Al}_{74}\text{Pd}_{12}\text{Co}_{14}$  alloy was a single-phase alloy composed of  $\epsilon_n$ . In this alloy, a combination of three  $\epsilon_n$  structures was identified:  $\epsilon_6$ ,  $\epsilon_{16}$ , and  $\epsilon_{28}$ .
2. The  $\text{Al}_{70}\text{Pd}_{25}\text{Co}_5$  alloy was a double-phase alloy composed of  $\epsilon_n$  and  $\delta$  ( $\text{Al}_3\text{Pd}_2$ ). In this alloy, two  $\epsilon_n$  structures were identified:  $\epsilon_6 + \epsilon_{28}$ .
3. Marked open circuit potential oscillations of the  $\text{Al}_{70}\text{Pd}_{25}\text{Co}_5$  alloy have been observed, indicating individual breakdown and re-passivation events on the sample surface. A preferential corrosion attack of  $\epsilon_n$  was found. Binary  $\delta$  phase ( $\text{Al}_3\text{Pd}_2$ ) was less affected by corrosion.
4. De-alloying of Al from  $\epsilon_n$  and formation of intermittent inter-penetrating channel networks occurred in both alloys.
5. The corrosion attack of the  $\text{Al}_{74}\text{Pd}_{12}\text{Co}_{14}$  alloy was more significant compared to the  $\text{Al}_{70}\text{Pd}_{25}\text{Co}_5$  alloy and resulted in the formation of a de-alloyed and highly porous metallic network. The corrosion susceptibility of  $\epsilon_n$  could be further utilized in preparing porous Pd–Co alloys with possible catalytic activity.
6. The Co substitution for Pd significantly improves the corrosion resistance of  $\epsilon_n$ . As such, it is probably not the crystal structure of the phase, but its chemical composition, that plays a major role in the corrosion behavior.

7. Specific Co concentrations may greatly improve the corrosion performance of the Al–TM alloys.

**Author Contributions:** Conceptualization, M.P., L.D., I.C., and J.J.; Funding acquisition, J.J.; Investigation, M.P., L.D., I.C., S.B., Z.G., M.S., and L.C.; Methodology, M.P., L.D., and I.C.; Project administration, J.J.; Supervision, J.J.; Writing—original draft, M.P.; Writing—review & editing, M.P., L.D., and J.J.

**Funding:** This work was supported by project no. 1/0490/18 of the Grant Agency VEGA of the Slovakian Ministry of Education, Research, Science and Sport, project APVV-15-0049 of the Slovak Research and Development Agency, and project NFP313010T606 (PROGMAT) supported by European Structural Investment Funds.

**Acknowledgments:** Shinichi Watanabe (JEOL Ltd., Tokyo, Japan) is acknowledged for his assistance with the HAADF/STEM measurements. This paper is dedicated to the memory of our deceased fathers, Ján Palcut and Jozef Gerhát.

**Conflicts of Interest:** The authors declare no conflict of interest.

## References

1. Steurer, W. Twenty years of structure research on quasicrystals. Part I. Pentagonal, octagonal, decagonal and dodecagonal quasicrystals. *Z. Kristallogr.* **2004**, *219*, 391–446. [[CrossRef](#)]
2. Dubois, J.M. Properties and applications of quasicrystals and complex metallic alloys. *Chem. Soc. Rev.* **2012**, *41*, 6760–6777. [[CrossRef](#)]
3. Yurechko, M.; Grushko, B.; Velikanova, T.; Urban, K. Isothermal sections of the Al–Pd–Co alloy system for 50–100 at.% Al. *J. Alloys Compd.* **2002**, *337*, 172–181. [[CrossRef](#)]
4. Yurechko, M.; Grushko, B. A study of the Al–Pd–Co alloy system. *Mater. Sci. Eng. A* **2000**, *294–296*, 139–142. [[CrossRef](#)]
5. Černičková, I.; Ďuriška, L.; Priputen, P.; Janičkovič, D.; Janovec, J. Isothermal section of the Al–Pd–Co phase diagram at 850 °C delimited by homogeneity ranges of phases epsilon, U, and F. *J. Phase Equilib. Diffus.* **2016**, *37*, 301–307. [[CrossRef](#)]
6. Černičková, I.; Čička, R.; Švec, P.; Janičkovič, D.; Priputen, P.; Janovec, J. A study of phase equilibria in the Al–Pd–Co system at 700 °C. In *Aperiodic Crystals (Cairns)*, 1st ed.; Schmid, S., Ed.; Springer: Berlin, Germany, 2013; pp. 133–139.
7. Ďuriška, L.; Černičková, I.; Priputen, P.; Janovec, J. Partial experimental isothermal section of Al–Pd–Co phase diagram for Al-rich corner at 1020 °C. *J. Phase Equilib. Diffus.* **2019**, *40*, 45–52. [[CrossRef](#)]
8. Frigan, B.; Santana, A.; Engel, M.; Schopf, D.; Trebin, H.R.; Mihalkovič, M. Low-temperature structure of  $\xi$ -Al–Pd–Mn optimized by ab initio methods. *Phys. Rev. B* **2011**, *84*, 184203. [[CrossRef](#)]
9. Heggen, M.; Engel, M.; Balanetsky, S.; Trebin, H.; Feuerbacher, M. Structural variations in  $\epsilon$ -type Al–Pd–(Mn,Fe) complex metallic alloy phases. *Philos. Mag.* **2008**, *88*, 507–521. [[CrossRef](#)]
10. Yurechko, M.; Fattah, A.; Velikanova, T.; Grushko, B. A contribution to the Al–Pd phase diagram. *J. Alloys Compd.* **2001**, *329*, 173–181. [[CrossRef](#)]
11. Armbrüster, M.; Schlögl, R.; Grin, Y. Intermetallic compounds in heterogeneous catalysis—a quickly developing field. *Sci. Technol. Adv. Mater.* **2014**, *15*, 034803. [[CrossRef](#)]
12. Massiani, Y.; Yaazza, S.A.; Coussier, J.P.; Dubois, J.M. Electrochemical behaviour of quasicrystalline alloys in corrosive solutions. *J. Non-Cryst. Solids* **1993**, *159*, 92–100. [[CrossRef](#)]
13. Huttunen–Saarivirta, E.; Tiainen, T. Corrosion behaviour of Al–Cu–Fe alloys containing a quasicrystalline phase. *Mater. Chem. Phys.* **2004**, *85*, 383–395. [[CrossRef](#)]
14. Rüdiger, A.; Köster, U. Corrosion of Al–Cu–Fe quasicrystals and related crystalline phases. *J. Non-Cryst. Solids* **1999**, *250–252*, 898–902. [[CrossRef](#)]
15. Beni, A.; Ott, N.; Ura–Binczyk, E.; Rasinski, M.; Bauer, B.; Gille, P.; Ulrich, A.; Schmutz, P. Passivation and localised corrosion susceptibility of new Al–Cr–Fe complex metallic alloys in acidic NaCl electrolytes. *Electrochim. Acta* **2011**, *56*, 10524–10532. [[CrossRef](#)]
16. Ura–Binczyk, E.; Homazava, N.; Ulrich, A.; Hauert, R.; Lewandowska, M.; Kurzydowski, K.J.; Schmutz, P. Passivation of Al–Cr–Fe and Al–Cu–Fe–Cr complex metallic alloys in 1 M H<sub>2</sub>SO<sub>4</sub> and 1 M NaOH solutions. *Corros. Sci.* **2011**, *53*, 1825–1837. [[CrossRef](#)]
17. Palcut, M.; Priputen, P.; Kusý, M.; Janovec, J. Corrosion behaviour of Al–29at%Co alloy in aqueous NaCl. *Corros. Sci.* **2013**, *75*, 461–466. [[CrossRef](#)]



18. Palcut, M.; Priputen, P.; Šalgó, K.; Janovec, J. Phase constitution and corrosion resistance of Al-Co alloys. *Mater. Chem. Phys.* **2015**, *166*, 95–104. [[CrossRef](#)]
19. Priputen, P.; Palcut, M.; Babinec, M.; Mišík, J.; Černičková, I.; Janovec, J. Correlation between microstructure and corrosion behavior of near-equilibrium Al-Co alloys in various environments. *J. Mater. Eng. Perform.* **2017**, *26*, 3970–3976. [[CrossRef](#)]
20. Lekatou, A.; Sfikas, A.K.; Karantzalis, A.E.; Sioulas, D. Microstructure and corrosion performance of Al-32%Co alloys. *Corros. Sci.* **2012**, *63*, 193–209. [[CrossRef](#)]
21. Lekatou, A.; Sfikas, A.K.; Petsa, C.; Karantzalis, A.E. Al-Co alloys prepared by vacuum arc melting: Correlating microstructure evolution and aqueous corrosion behavior with Co content. *Metals* **2016**, *6*, 46. [[CrossRef](#)]
22. Zhang, Q.; Zhang, Z. On the electrochemical dealloying of Al-based alloys in a NaCl aqueous solution. *Phys. Chem. Chem. Phys.* **2010**, *12*, 1453–1472. [[CrossRef](#)]
23. Palcut, M.; Ďuriška, L.; Špoták, M.; Vrbovský, M.; Gerhátová, Ž.; Černičková, I.; Janovec, J. Electrochemical corrosion of Al-Pd alloys in HCl and NaOH solutions. *J. Min. Metall. Sect. B-Metall.* **2017**, *53*, 333–340. [[CrossRef](#)]
24. Ďuriška, L.; Palcut, M.; Špoták, M.; Černičková, I.; Gondek, J.; Priputen, P.; Čička, R.; Janičkovič, D.; Janovec, J. Microstructure, phase occurrence, and corrosion behavior of as-solidified and as-annealed Al-Pd alloys. *J. Mater. Eng. Perform.* **2018**, *27*, 1601–1613. [[CrossRef](#)]
25. Zhang, Z.; Wang, Y.; Qi, Z.; Zhang, W.; Qin, J.; Frenzel, J. Generalized fabrication of nanoporous metals (Au, Pd, Pt, Ag, and Cu) through chemical dealloying. *J. Phys. Chem. C* **2009**, *113*, 12629–12636. [[CrossRef](#)]
26. Erlebacher, J.; Aziz, M.J.; Karma, A.; Dimitrov, N.; Sieradzki, K. Evolution of nanoporosity in dealloying. *Nature* **2001**, *410*, 450–453. [[CrossRef](#)] [[PubMed](#)]
27. Wang, X.; Wang, W.; Qi, Z.; Zhao, Ch.; Ji, H.; Zhang, Z. High catalytic activity of ultrafine nanoporous palladium for electro-oxidation of methanol, ethanol, and formic acid. *Electrochem. Commun.* **2009**, *11*, 1896–1899. [[CrossRef](#)]
28. Balanetsky, S.; Grushko, B.; Velikanova, T.Ya.; Urban, K. An investigation of the Al-Pd-Fe phase diagram between 50 and 100 at. % Al: Phase equilibria at 750 °C. *J. Alloys Compd.* **2004**, *374*, 158–164. [[CrossRef](#)]
29. Černičková, I.; Švec, P.; Watanabe, S.; Čaplovič, L.; Mihalkovič, M.; Kolesár, V.; Priputen, P.; Bednarčík, J.; Janičkovič, D.; Janovec, J. Fine structure of phases of  $\epsilon$ -family in Al<sub>73.8</sub>Pd<sub>11.9</sub>Co<sub>14.3</sub> alloy. *J. Alloys Compd.* **2014**, *609*, 73–79. [[CrossRef](#)]
30. Yubuta, K.; Suzuki, S.; Simura, R.; Sugiyama, K. Structure of  $\epsilon_{16}$  phase in Al-Pd-Co system studied by HREM and X-ray diffraction. In *Aperiodic Crystals (Cairns)*, 1st ed.; Schmid, S., Ed.; Springer: Berlin, Germany, 2013; pp. 231–236.
31. Grushko, B. Again regarding the Al-Pd phase diagram. *J. Alloys Compd.* **2013**, *557*, 102–111. [[CrossRef](#)]
32. Cheng, Y.L.; Zhang, Z.; Cao, F.H.; Li, J.F.; Zhang, J.Q.; Wang, J.M.; Cao, C.N. Study of the potential electrochemical noise during corrosion process of aluminum alloys 2024, 7075 and pure aluminum. *Mater. Corros.* **2003**, *54*, 601–608. [[CrossRef](#)]
33. ASM International, ASM Handbook Committee. *Corrosion: Fundamentals, Testing, and Protection (ASM Handbook Vol. 13A)*, 1st ed.; ASM International: Novelt, OH, USA, 2003.
34. Szklarska-Smialowska, Z. Pitting corrosion of aluminum. *Corros. Sci.* **1999**, *41*, 1743–1767. [[CrossRef](#)]
35. Li, J.; Dang, J. A summary of corrosion properties of Al-rich solid solution and secondary phase particles in Al alloys. *Metals* **2017**, *7*, 84. [[CrossRef](#)]
36. Birbilis, N.; Buchheit, R.G. Electrochemical Characteristics of Intermetallic Phases in Aluminum Alloys: An experimental survey and discussion. *J. Electrochem. Soc.* **2005**, *152*, B140–B151. [[CrossRef](#)]
37. Zhang, Q.; Wang, X.; Qi, Z.; Wang, Y.; Zhang, Z. A benign route to fabricate nanoporous gold through electrochemical dealloying of Al–Au alloys in a neutral solution. *Electrochim. Acta* **2009**, *54*, 6190–6198. [[CrossRef](#)]
38. Lekatou, A.G.; Sfikas, A.K.; Karantzalis, A.E. The influence of the fabrication route on the microstructure and surface degradation properties of Al reinforced by Al<sub>9</sub>Co<sub>2</sub>. *Mater. Chem. Phys.* **2017**, *200*, 33–49. [[CrossRef](#)]
39. Lim, A.B.Y.; Neo, W.J.; Yauw, O.; Chylak, B.; Gan, C.L.; Chen, Z. Evaluation of the corrosion performance of Cu–Al intermetallic compounds and the effect of Pd addition. *Microelectron. Reliab.* **2016**, *56*, 155–161. [[CrossRef](#)]

40. Li, R.T.; Murugan, V.K.; Dong, Z.L.; Khor, K.A. Comparative study on the corrosion resistance of Al–Cr–Fe alloy containing quasicrystals and pure Al. *J. Mater. Sci. Technol.* **2016**, *32*, 1054–1058. [[CrossRef](#)]
41. Debili, M.Y.; Sassane, N.; Boukhris, N. Structure and corrosion behavior of Al–Co–Ti alloy system. *Anti Corros. Methods Mater.* **2017**, *64*, 443–451. [[CrossRef](#)]
42. Sassane, N.; Debili, M.Y.; Boukhris, N.E. Structural characterization of a ternary Al–Co–Ti alloy system. *J. Adv. Microsc. Res.* **2018**, *13*, 409–416. [[CrossRef](#)]
43. Zhu, Y.; Sun, K.; Frankel, G.S. Intermetallic phases in aluminum alloys and their roles in localized corrosion. *J. Electrochem. Soc.* **2018**, *165*, C807–C820. [[CrossRef](#)]



© 2019 by the authors. Licensee MDPI, Basel, Switzerland. This article is an open access article distributed under the terms and conditions of the Creative Commons Attribution (CC BY) license (<http://creativecommons.org/licenses/by/4.0/>).



Article

# Influence of Alloyed Ga on the Microstructure and Corrosion Properties of As-Cast Mg–5Sn Alloys

Jing Ren, Enyu Guo, Xuejian Wang, Huijun Kang, Zongning Chen \* and Tongmin Wang \*

Key Laboratory of Solidification Control and Digital Preparation Technology (Liaoning Province), School of Materials Science and Engineering, Dalian University of Technology, Dalian 116024, China; 18840830427@163.com (J.R.); eyguo@dlut.edu.cn (E.G.); wangxuejian0618@163.com (X.W.); kanghuijun@dlut.edu.cn (H.K.)

\* Correspondence: znchen@dlut.edu.cn (Z.C.); tmwang@dlut.edu.cn (T.W.);  
Tel.: +86-411-84709500 (Z.C.); +86-411-84706790 (T.W.)

Received: 18 September 2019; Accepted: 5 November 2019; Published: 8 November 2019

**Abstract:** In this paper, the microstructures and corrosion behaviors of as-cast Mg–5Sn– $x$ Ga alloys with varying Ga content ( $x = 0, 0.5, 1, 2, 3$  wt %) were investigated. The results indicated that Ga could not only adequately refine the grain structure of the alloys, but could also improve the corrosion resistance. The microstructures of all alloys exhibited typical dendritic morphology. No Ga-rich secondary phases were detected when 0.5 wt % Ga was added, while only the morphology of Mg<sub>2</sub>Sn phase was changed. However, when the addition rate of Ga exceeded 0.5 wt %, an Mg<sub>5</sub>Ga<sub>2</sub> intermetallic compound started to form from the interdendritic region. The volume fraction of Mg<sub>5</sub>Ga<sub>2</sub> monotonically increased with the increasing Ga addition level. Although Mg<sub>5</sub>Ga<sub>2</sub> phase was cathode phase, its pitting sensitivity was weaker than Mg<sub>2</sub>Sn. In addition, the standard potential of Ga (–0.55 V) was lower than that of Sn (–0.14 V), which relieved the driving force of the secondary phases for the micro-galvanic corrosion. An optimized composition of 3 wt % Ga was concluded based on the immersion tests and polarization measurements, which recorded the best corrosion resistance.

**Keywords:** magnesium; immersion test; polarization; microstructure; corrosion resistance

## 1. Introduction

Magnesium alloys, with their excellent properties of low density and high specific strength, have received extensive attention in automobile, aerospace, electronics, and other industries [1–4]. Among many of the binary alloy systems, the Mg–Sn phase diagram demonstrates that the Mg-rich side has a very shallow  $\alpha$ -Mg solvus curve, indicating that it is conducive to maximizing the precipitation of the thermally stable Mg<sub>2</sub>Sn particles. This infers that adding Sn potentially helps to enhance the mechanical integrity of the alloy at elevated temperatures [5–9]. On this account, the Mg–Sn-based alloy system is one of the most extensively studied alloys in recent years [6–13].

Aside from the mechanical strength, other factors that limit the application of magnesium alloys are their high chemical activity and poor corrosion resistance. It was documented, however, that alloying with some Sn results in superior corrosion resistance. Ha et al. [14] reported that Sn decreases the cathodic current density and inhibits the cathodic H<sub>2</sub> evolution. Similar effects were also observed in Mg–5Al–1Zn alloy [11] and Mg–7Al–0.2Mn alloy [12]. The reason for inhibition of H<sub>2</sub> evolution by alloying Sn was studied. Ha et al. [13] observed that the main reason for the decrease of H<sub>2</sub> evolution rate was that Sn elements were enriched on the metal surface. They further reported that Sn had a higher potential H<sub>2</sub> evolution than the Mg matrix [15,16]. Moreover, under the condition of a high cathode, Sn could form SnH<sub>4</sub> [14]. That is to say, when the matrix is corroded, the element Sn is spontaneously enriched on the matrix surface, acting as a barrier to further corrosion [13].

The addition of Ga in magnesium alloy has important research value in seawater battery and sacrificial anode [17]. In those applications, Ga enhances the mechanical performance of Mg-based alloys by solid solution and precipitation strengthening [17,18]. It was suggested that Mg–Ga, Mg–In, and Mg–Sn alloys have potential use as biomaterials [15]. Among the aforementioned three binary alloys, Mg–Ga alloys appeared to be the best candidates, considering both the mechanical properties and corrosion behaviors in 0.9 wt % NaCl solution. Marta et al. [19] pointed out that the superior corrosion resistance of Mg–Ga is mainly related to the microgalvanic corrosion between  $\alpha$ -Mg and the second phases, and the morphology and distribution of Mg<sub>5</sub>Ga<sub>2</sub> phase.

The purpose of this study is to explore the effect of Ga on the microstructure and corrosion resistance of Mg–5Sn alloy. Both potentiodynamic polarization measurements and immersion weightlessness experiments were conducted to evaluate the corrosion property of the experimental Mg–5Sn–*x*Ga alloys. By investigating the microstructures of Mg–5Sn–*x*Ga alloys with varying Ga contents, the immanent relationship between the microstructure and corresponding corrosion behavior is established, and the results are discussed.

## 2. Materials and Methods

### 2.1. Specimen Preparation

As-cast Mg–5Sn–*x*Ga (*x* = 0, 0.5, 1, 2, and 3, all in weight percentage unless otherwise specified) alloys were investigated in this work. The experimental alloys were prepared by melting pure metals in an electric resistance furnace under the protection of an atmosphere containing CO<sub>2</sub> and SF<sub>6</sub> mixture in a ratio of 99:1. Pure Mg (99.99%) ingot was cut into small pieces and put in a magnesia crucible. Once the temperature of the melt reached 973 K, pure Sn (99.99%) and Ga (99.999%) granules were added to the melt. The melt was fully stirred with a graphite impeller for 180 s before it was poured into a cylindrical steel mold preheated at 523 K. The chemical compositions of the alloys were measured by X-ray fluorescence analysis (XRF-1800, Shimadzu, Kyoto, Japan), and the results are summarized in Table 1.

**Table 1.** Chemical compositions of the experimental Mg–5Sn–*x*Ga (*x* = 0, 0.5, 1, 2, 3 wt %) alloys analyzed by XRF tests.

Nominal Composition	Element Content (wt %)		
	Sn	Ga	Mg
Mg–5Sn	5.08	-	Bal.
Mg–5Sn–0.5Ga	4.98	0.56	Bal.
Mg–5Sn–1Ga	4.81	1.12	Bal.
Mg–5Sn–2Ga	5.08	2.02	Bal.
Mg–5Sn–3Ga	4.67	2.81	Bal.

### 2.2. Microstructural Characterization

The samples for microstructural observation were cut 10 mm from the bottom of the ingot. The exposed surfaces were ground by SiC abrasive papers up to 4000 grit and then polished up to 1  $\mu$ m in a suspension of diamond pastes. The polished surfaces were etched in a mixed solution of picric and acetic acid (10 mL acetic acid, 4.2 g picric acid, 10 mL distilled water, and 70 mL ethanol). The microstructures and corrosion morphologies of the specimens were observed using an optical microscope (OM, Olympus GX51, Olympus Corp., Tokyo, Japan) and a field emission scanning electron microscope (FESEM, Zeiss supra 55, Zeiss Corp., Oberkochen, Germany), equipped with energy-dispersive X-ray spectroscopy (EDS). Phases were identified by an X-ray diffraction instrument (XRD, PANalytical Empyrean, Almelo, The Netherlands) with Cu K $\alpha$  radiation at a scanning speed of 0.142224°/s. An electron microprobe analyzer (EPMA, JXA-8530F PLUS, Tokyo, Japan) equipped with a wavelength dispersive spectrometer (WDS) was used to examine the elemental distribution of

selected phases. Grain size was measured using the OM micrographs of the alloys by the intercept method regulated in GB/T 6394-2002:

$$\tau = \frac{L}{M \times N} \quad (1)$$

where  $\tau$  is the average grain size,  $L$  is the measured mesh length,  $M$  is the magnification for observation (50 $\times$  in this work), and  $N$  is the number of intercept points on the measured mesh as indicated in Equation (1). The grain sizes were averaged with values measured from six micrographs for each alloy.

### 2.3. Corrosion Tests

The corrosion behaviors of the as-cast Mg–5Sn– $x$ Ga ( $x = 0, 0.5, 1, 2,$  and  $3$  wt %) alloys were investigated using a potentiodynamic polarization test and immersion test. All experiments were carried out at room temperature ( $298 \pm 1$  K).

For the electrochemical test, a conventional three-electrode cell was employed. The cell was composed of a working electrode (sample), a reference electrode (Ag/AgCl electrode, saturated KCl with electrode potential of 0.1981 V vs. Standard Hydrogen Electrode), and a Pt plate counter electrode. The test was carried out using a Gamry electrochemical workstation (Reference 600, Gamry Instruments Inc., Warminster, PA, USA). The samples were ground using SiC abrasive papers up to 2000 grit, and the surface of a round specimen with an area of  $1.0 \text{ cm}^2$  was exposed to 3.5 wt % NaCl solution. After reaching a steady open circuit potential (OCP), the polarization test was initiated from  $-0.3$  V versus the OCP level of the sample to  $+0.3$  V vs. OCP at a scanning rate of 1 mV/s. Three samples were tested for each alloy to ensure repeatability. The corrosion current density ( $i_{\text{corr}}$ , mA/cm $^2$ ) of the investigated alloys, which was obtained by fitting the cathodic branch of the potentiodynamic polarization curve, was converted to the average corrosion rate ( $R_i$ , mm/y) according to the following equation [20,21]:

$$R_i = 22.85 \times i_{\text{corr}} \quad (2)$$

The immersion test was performed on three parallel samples for each alloy. Samples with dimensions of 20 mm wide, 25 mm long, and 3 mm thick were mechanically ground using SiC abrasive papers up to 2000 grit. The ground samples were immersed in a 3.5 wt % NaCl solution at 298 K for 72 h. After immersion, the samples were taken out and cleaned with chromate acid (200 g/L CrO $_3$  + 10 g/L AgNO $_3$ ) to remove the corrosion products [22,23]. The obtained samples were rinsed with distilled water, cleaned in alcohol, and dried in air. The final specimens were weighed on an analytical balance (ME204E, Mettler Toledo Corp., Greifensee, Switzerland), and the corrosion rate ( $C_R$ ) for each sample was calculated by Equation (3) [24,25]:

$$C_R = \frac{K \times W}{A \times T \times D} \quad (3)$$

where  $K$  is a constant ( $8.76 \times 10^4$ ),  $W$  is the mass loss in g,  $A$  is the exposed area of the sample in cm $^2$ ,  $T$  is the exposure time in hours, and  $D$  is the density in g/cm $^3$ .

Another group of samples for observation of corrosion surface morphology, corrosion depth, and products identification were  $\Phi$  12 mm in diameter and 3 mm in thickness. These samples were prepared following the same procedure as the samples for microstructural observation mentioned in Section 2.2. Measures were taken to ensure that corrosion occurred only on the transverse surface of the cylindrical samples. After immersion in 3.5 wt % NaCl solution for 24 h, XRD was used to identify the phases in the corrosion product. The surface and cross-section morphologies of the corroded samples were observed in SEM and EPMA, respectively.

### 3. Results and Discussion

#### 3.1. Microstructure Analysis

The OM micrographs of the as-cast Mg–5Sn–*x*Ga alloys with varying Ga contents are shown in Figure 1. All the alloys present a similar typical dendritic grain structure. The solute elements could have significant effects on the growth behavior of  $\alpha$ -Mg grains and the final morphological patterns [26–29]. It was documented that Sn could form a composition undercooling zone of liquid ahead of the solid–liquid interface, leading to dendrite formation [30]. The average grain sizes were measured to be  $300.4 \pm 18.4$ ,  $227.1 \pm 19.3$ ,  $205.7 \pm 16.7$ ,  $183.3 \pm 12.7$ , and  $155.9 \pm 8.6$   $\mu\text{m}$  for the Mg–5Sn, Mg–5Sn–0.5Ga, Mg–5Sn–1Ga, Mg–5Sn–2Ga, and Mg–5Sn–3Ga alloys, respectively. The result suggests that the grain size decreased monotonically with increasing Ga content, probably due to the increasing grain growth restriction factor (*GRF*), which can be expressed by Equation (4) for a binary alloy [26]:

$$GRF = m_L C_0 (k_0 - 1) \quad (4)$$

where  $m_L$  is the slope of liquidus (assumed to be straight),  $k_0$  the equilibrium distribution coefficient, and  $C_0$  the concentration of a solute. According to the Mg–Ga phase diagram [31], in dilute binary magnesium alloys, the *GRF* value for Ga element is calculated to be 4.04, which is similar to Al and Zn element ( $GRF_{Al} = 4.32$ ,  $GRF_{Zn} = 5.31$  [26]). Composition undercooling was established by the Ga concentration gradient in the diffusion layer adjacent to the solid–liquid interface, restricting grain growth as a consequence of slow diffusion; and thus, the growth rate is limited and grain size is refined.

As for the case of the Mg–5Sn–0.5Ga alloy, the quantitative results from the WDS analysis of the areas marked by the white rectangles in Figure 1f are given in Table 2. It was found that Mg–5Sn alloy with 0.5 wt % Ga did not cause the formation of any new phases. Most of the Ga and a part of the Sn were either dissolved in the  $\alpha$ -Mg matrix or enriched at the interdendritic region (indicated by arrow *a*).

**Table 2.** The chemical compositions of the areas marked by the white rectangles in Figure 1f using the wavelength dispersive spectrometer (WDS) (in wt %).

Area	Sn	Ga	Mg
a	9.778	1.929	88.293
b	25.115	0.741	74.144
c	1.589	0.167	98.244

Dozens of studies have shown that the microstructural features, such as the grain size and the morphology of second phase, may have impacts on the corrosion resistance of magnesium alloys [32,33]. Grain refinement led to the decreased corrosion rates, possibly because of the enhanced passivity of the oxide film [34]. Because the experimental alloy with 3 wt % Ga had the finest equiaxed grains, it was most likely that the as-cast Mg–5Sn–3Ga alloy would exhibit the greatest corrosion resistance.

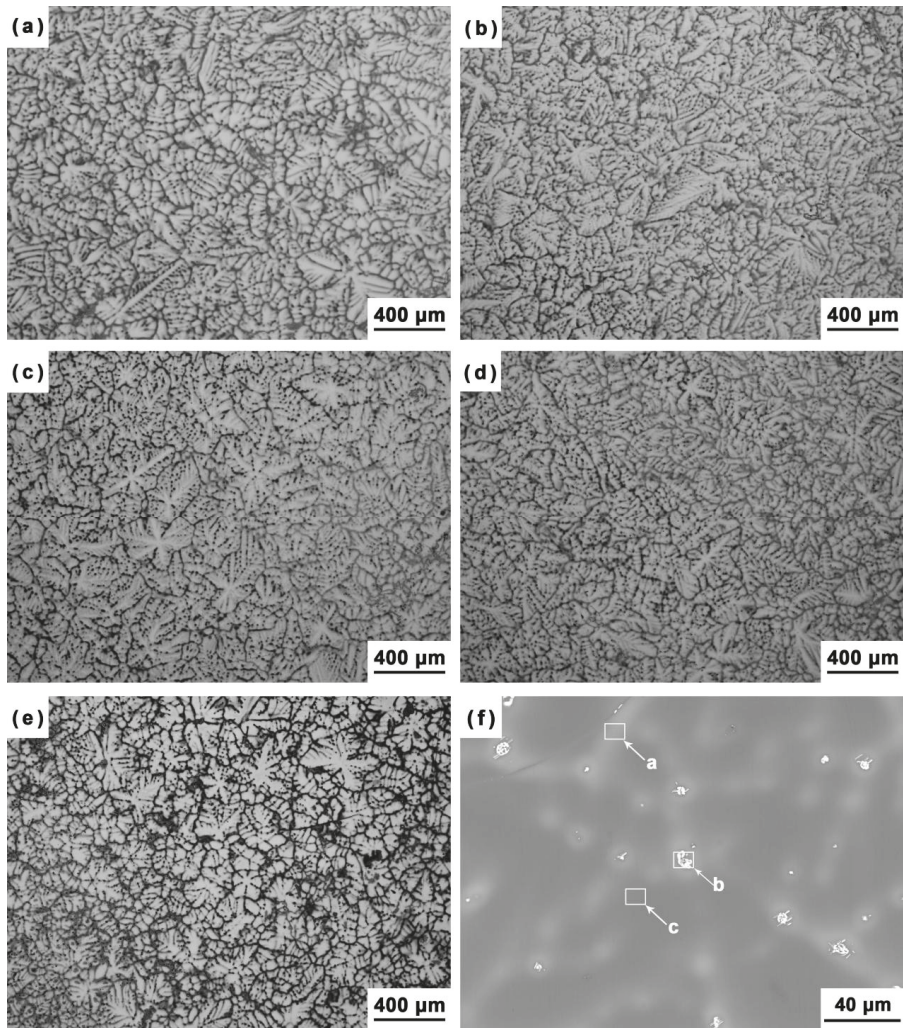


**Figure 1.** OM micrographs of the Mg–5Sn–*x*Ga alloys: (a) Mg–5Sn, (b) Mg–5Sn–0.5Ga, (c) Mg–5Sn–1Ga, (d) Mg–5Sn–2Ga, (e) Mg–5Sn–3Ga, and (f) backscattered electron (BSE) micrograph of the Mg–5Sn–0.5Ga alloy.

The backscattered electron (BSE) micrographs of the Mg–5Sn–*x*Ga alloys with varying Ga content are shown in Figure 2a–e. The OM and BSE micrographs of the alloys confirm the presence of second phases and element enrichment in the interdendritic regions. The elemental mapping results of the Ga, Mg, and Sn in the Mg–5Sn–3Ga sample using EPMA are shown in Figure 2f–i. Contrasts along the interdendritic contours demonstrate that there are two types of phases with different chemistries. According to the quantitative results measured by WDS in Table 3, the grey eutectic phase indicated by the letter *a* is Mg<sub>5</sub>Ga<sub>2</sub> intermetallic compound, and the brighter phase indicated by the letter *b* is Mg<sub>2</sub>Sn. The inserts in Figure 2a–e are zoom-in views of the two phases embedded in the interdendritic region. When 0.5 wt % Ga was added, no Ga-rich second phases were detected, according to the composition



analysis in Table 2. When the addition of Ga exceeded 0.5 wt %, Ga formed from the interdendritic region in the form of  $Mg_5Ga_2$  phase, while  $Mg_2Sn$  did so in the form of divorced eutectic phase.

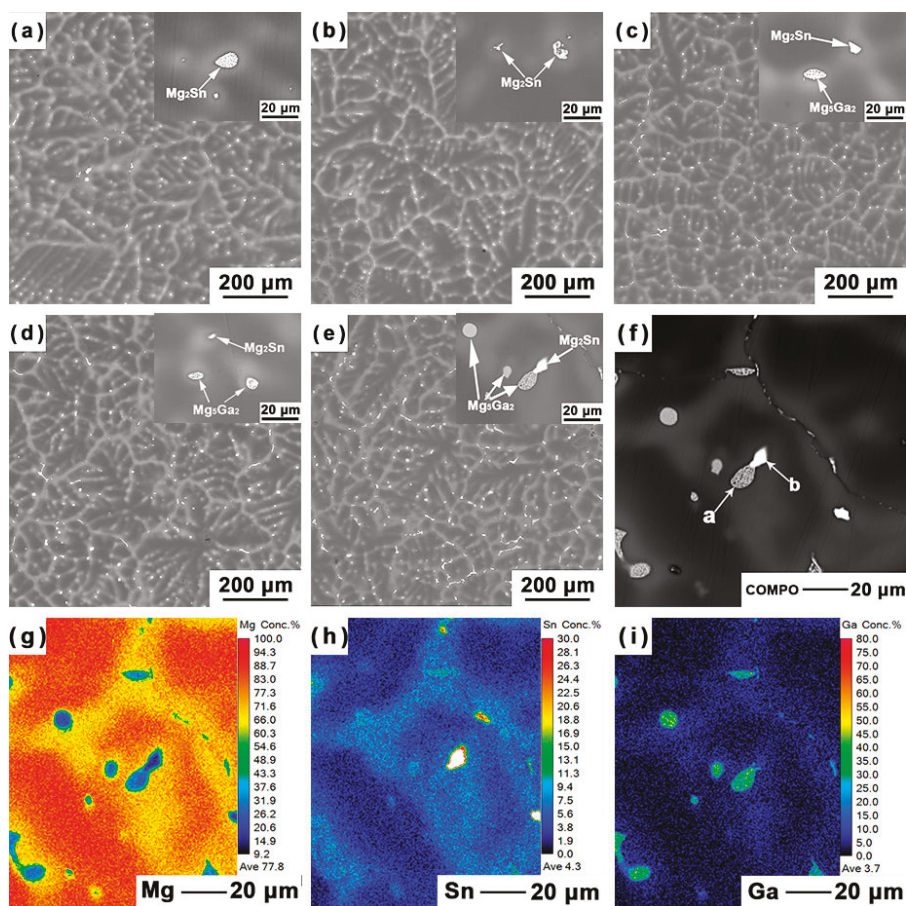


**Figure 2.** BSE micrographs of the Mg–5Sn–*x*Ga alloys: (a) Mg–5Sn, (b) Mg–5Sn–0.5Ga, (c) Mg–5Sn–1Ga, (d) Mg–5Sn–2Ga, (e) Mg–5Sn–3Ga. The inserts are zoom-in views showing the second phases. (f–i) Elemental mapping of the Mg, Sn, and Ga in the Mg–5Sn–3Ga sample using electron microprobe analyzer (EPMA).

**Table 3.** The chemical compositions of the phases measured by WDS as indicated by the arrows in Figure 2f (in at %).

Point	Sn	Ga	Mg
a	2.2	19.6	78.2
b	29.3	4.4	66.3

The XRD spectra in Figure 3a further confirmed that the Mg–5Sn alloy consisted of  $\alpha$ -Mg matrix and  $Mg_2Sn$ . When the Ga content exceeded 1 wt %, a new phase containing Ga was formed. Survey on Joint Committee on Powder Diffraction Standards indicates that the new peaks correspond to the reflections of the  $Mg_5Ga_2$  compound, which normally exists in Mg–Ga binary [15,35] and Mg–Hg–Ga ternary [18] alloys. This is consistent with the quantitative results measured by WDS in Table 3.

The increasing density of the  $Mg_5Ga_2$  peaks is expected with the increase in the Ga content of the alloys. Figure 3b shows the area fraction of the second phases in the investigated alloy calculated by ImageJ 1.47 (US NIH, Bethesda, MD, USA) [36]. It is also clear that the area fraction of  $Mg_5Ga_2$  particles increased with increasing Ga content, while the area fraction of  $Mg_2Sn$  particles decreased accordingly.

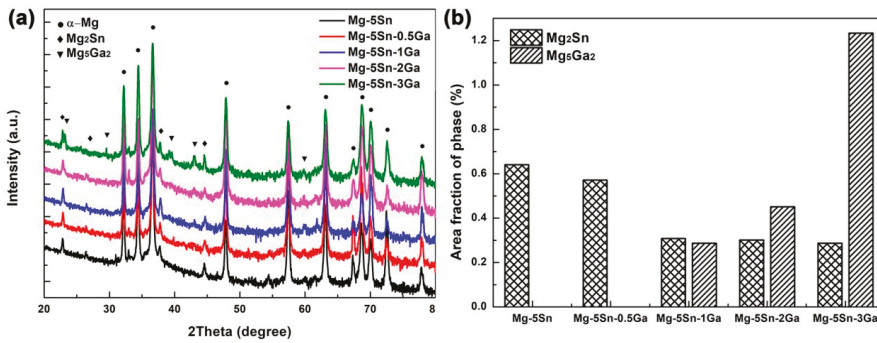


Figure 3. (a) X-ray diffraction (XRD) patterns of the Mg-5Sn-xGa alloys; (b) the area fraction of the second phases in the investigated alloy.

3.2. Polarization Tests

Figure 4 shows the potentiodynamic polarization curves of the as-cast Mg-5Sn-xGa alloys. The corrosion current density ( $i_{corr}$ ), corrosion potential ( $E_{corr}$ ), and the average corrosion rate ( $R_i$ ) obtained from the potentiodynamic polarization curves are listed in Table 4. The  $i_{corr}$  of the as-cast Mg-5Sn-xGa alloys in 3.5 wt % NaCl solution increase in the order of Mg-5Sn-3Ga, Mg-5Sn-2Ga, Mg-5Sn-0.5Ga, Mg-5Sn-1Ga, and Mg-5Sn. The lowest corrosion current density and corrosion potential are  $2.79 \times 10^{-2}$  mA/cm<sup>2</sup> and -1.684 V for Mg-5Sn-3Ga alloy, respectively.

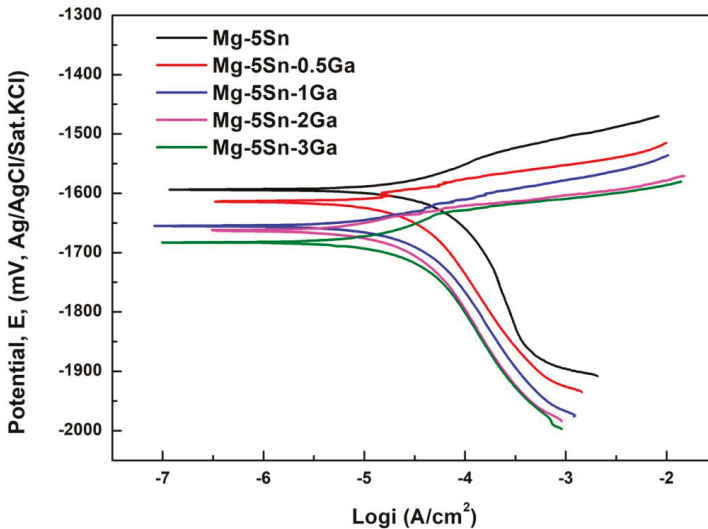
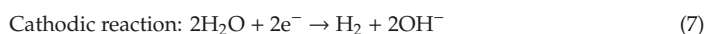
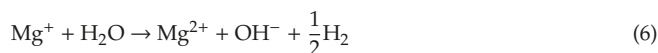
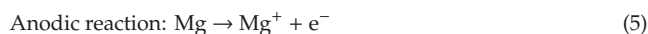


Figure 4. Polarization curves of the Mg-5Sn-xGa alloys in 3.5 wt % NaCl solution.

**Table 4.** Fitting results of polarization curves of the Mg–5Sn–xGa alloys with varying Ga content in 3.5 wt % NaCl solution.

Alloy	Mg–5Sn	Mg–5Sn–0.5Ga	Mg–5Sn–1Ga	Mg–5Sn–2Ga	Mg–5Sn–3Ga
$E_{\text{corr}}$ (V)	–1.596	–1.614	–1.658	–1.665	–1.684
$i_{\text{corr}}$ (mA/cm <sup>2</sup> )	$9.73 \times 10^{-2}$	$3.28 \times 10^{-2}$	$3.82 \times 10^{-2}$	$3.16 \times 10^{-2}$	$2.79 \times 10^{-2}$
$R_i$ (mm/y)	2.223	0.770	0.873	0.722	0.638

It is accepted that the corrosion of Mg-based alloys is generally caused by the cathodic reaction of hydrogen evolution. The anodic reaction of Mg dissolution can be described as [37,38]:



Ga is reported to have relatively high hydrogen overpotentials [15]. Alloys with Ga are thus anticipated to inhibit the cathodic reaction of Equation (6). The cathodic branches of the polarization curves show that the cathodic current density decreases with increasing Ga content, demonstrating that Ga indeed delays cathodic reaction and thus reduces corrosion rate.

Figure 5a shows the representative anode branches of the polarization curves of the Mg–5Sn–xGa alloys in 0.01 M NaCl solution. Within the whole range of anode polarization, the relation between the passive current density ( $i_{\text{passive}}$ ) of the alloys at any potential remains unchanged, so the relation between the current density of the alloys at an eigenvalue potential can be selected to describe the change of the trend of the passive current density of the alloys after adding Ga element. This method is favored by scholars in many studies. Ha et al. [39,40] used this method to study the change trend of anode passive current density at –1.7 V and cathode hydrogen evolution current density at –1.9 V of Mg–5Sn–(1–4 wt %)Zn alloy system. Similarly, Kim et al. [41] studied the polarization curve of Mg–8Sn–1Zn alloy with this method. In order to explore the role that Ga played in the anodic passive layer, Figure 5b compares the passive current density values for the alloys of different Ga contents with the alloy without Ga addition. The  $i_{\text{passive}}$  values were measured at the anodic potentials of –1.65 V. Evidently, compared with the Mg–5Sn alloy, the  $i_{\text{passive}}$  values decreased after adding Ga element, among which the Mg–5Sn–0.5Ga alloy exhibited the lowest  $i_{\text{passive}}$  value. Decreased  $i_{\text{passive}}$  indicates enhanced passive film stability. As mentioned above, Mg<sub>5</sub>Ga<sub>2</sub> phase will be formed when Ga addition exceeds 0.5 wt %, which belongs to the cathode phase and destroys the stability of passive film to some extent. Moreover, the passive film of magnesium alloy is extremely unstable and cannot protect the matrix, so the corrosion rate is mainly controlled by hydrogen evolution reaction of the cathode.

Another factor that also influences the corrosion rate is the microstructural features of an alloy [42–44]. With the increase in Ga element, the area fraction of Mg<sub>2</sub>Sn particles monotonically decreases, while the opposite trend is the case for the Mg<sub>5</sub>Ga<sub>2</sub>, as shown in Figures 2 and 3. Liu et al. [16] reported that both the hydrogen evolution rate and corrosion potential decreased with decreasing volume fraction of the Mg<sub>2</sub>Sn particles, which is consistent with the experimental results in this study.

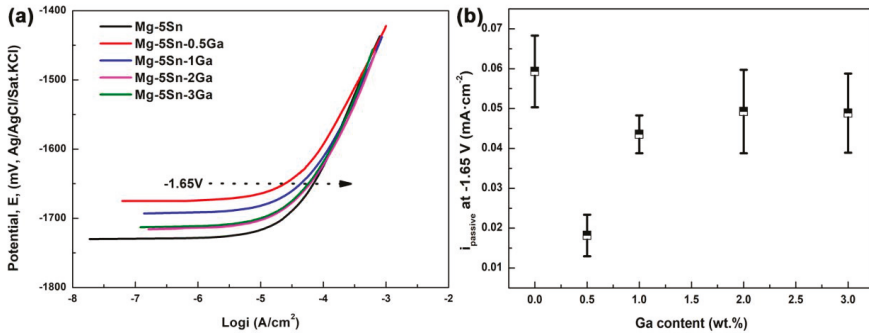


**Figure 5.** (a) The representative polarization curves of the Mg–5Sn–*x*Ga alloys in 0.01 M NaCl solution. (b) Passive current density ( $i_{\text{passive}}$ ) values measured at –1.65 V based on (a). The average and standard deviation were obtained from at least five measurements.

3.3. The Immersion Tests

Figure 6 shows the average corrosion rates of the alloys with continuously increasing Ga content calculated by Equation (2). In essence, the variation trend of the corrosion rate obtained by immersion test is in accord with the potentiodynamic polarization results. The lowest weight loss rate is  $1.15 \pm 0.1$  mm/y for the Mg–5Sn–3Ga alloy. This confirms that the addition of Ga improves the corrosion resistance of Mg–5Sn alloy.

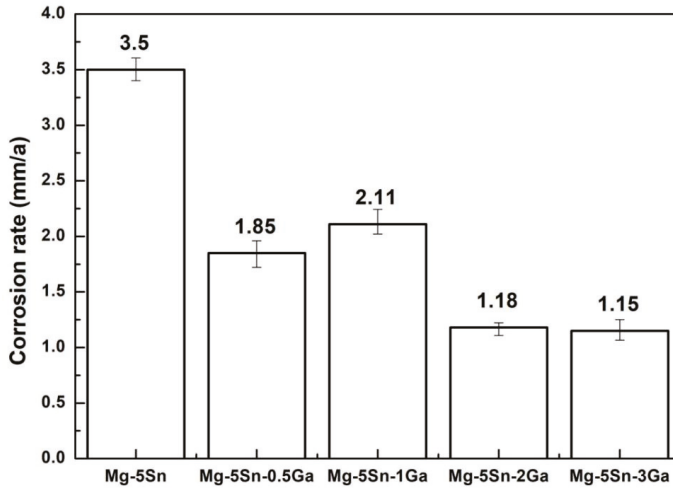


**Figure 6.** Average corrosion rate of the Mg–5Sn–*x*Ga alloys after immersion in 3.5 wt % NaCl solution for 72 h.

After immersion at 298 K for 6 h, the corrosion initiation sites were observed using SEM and EDS. Figure 7 presents the representative BSE micrographs of three alloys (Mg–5Sn, Mg–5Sn–0.5Ga, and Mg–5Sn–3Ga) and the corresponding EDS spectra of the marked areas. Figure 7a,b reveals that the Mg<sub>2</sub>Sn phase was not covered with corrosion films, and cracks were formed in the vicinity of Mg<sub>2</sub>Sn phase. Combining with the EDS analysis of points A and B (Figure 7d,e), it is inferred that corrosion began in the magnesium matrix around the Mg<sub>2</sub>Sn phase. Moreover, the adjacent distribution of the two types of phases provides the possibility for analyzing the initial corrosion location. In the Mg–5Sn–3Ga alloy (Figure 7c), the phase at point C is rich in Ga element compared with its neighboring

phase (marked by point *D*), suggesting that points *C* and *D* are  $Mg_5Ga_2$  phase and  $Mg_2Sn$  phase, respectively. Also shown in Figure 7c is that the surface film on  $Mg_2Sn$  phase was broken, while this was not the case for the film on  $Mg_5Ga_2$  phase.  $Mg_2Sn$  phase was detached from the matrix after immersion for 6 h. All the aforementioned observations indicate that  $Mg_2Sn$  phase, rather than the  $Mg_5Ga_2$  phase, provided the sites to initiate corrosion. Moreover, compared with the larger  $Mg_2Sn$  phase, eutectic  $Mg_5Ga_2$  phase is deemed to stay more firmly in the alloy matrix. Therefore, with the increase in Ga content, the increasing area fraction of  $Mg_5Ga_2$  further improved the corrosion resistance of the alloys.

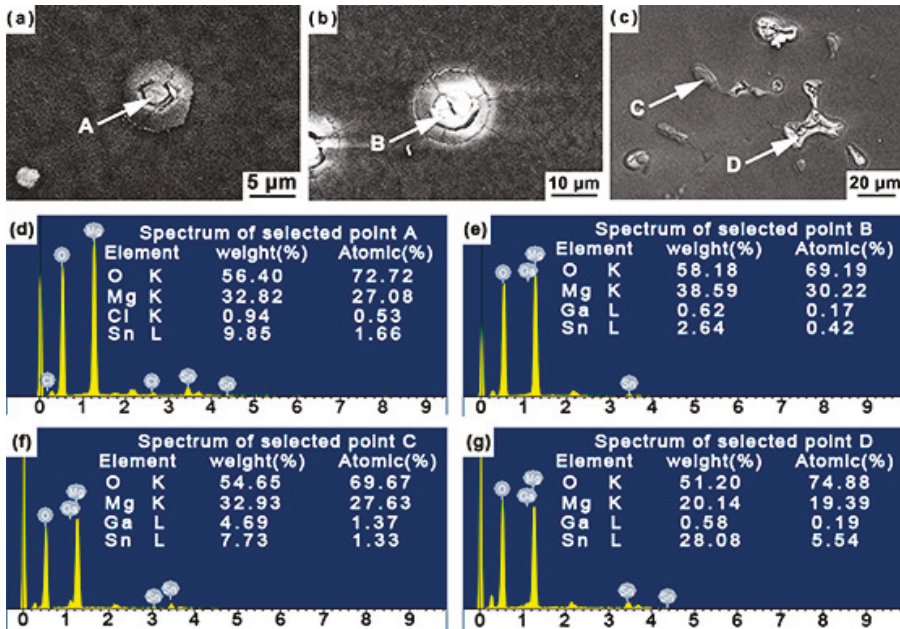


**Figure 7.** High magnification BSE micrographs showing the alloy surfaces after immersion in 3.5 wt % NaCl solution at 298 K for 6 h: (a) Mg-5Sn, (b) Mg-5Sn-0.5Ga, (c) Mg-5Sn-3Ga; (d–g) energy-dispersive X-ray spectroscopy (EDS) spectra of the points as indicated by the arrows in the BSE micrographs.

Figure 8 shows the evolution of the surface morphologies of the investigated alloys after immersing for different durations. The surfaces of the Mg-5Sn-*x*Ga alloys are covered by a mixture of dark film and bright corrosion product. A number of deep corrosion pits are observed after immersion (Figure 8a). It is noticeable that the white corrosion products increase with the decrease in Ga content.

It is noted in Figure 8 that the Mg-5Sn-0.5Ga alloy was more seriously corroded than the Mg-5Sn-1Ga alloy, while the immersion tests produced an opposite result. The reason is that in the Mg-5Sn-0.5Ga alloy, there is no Ga-rich second phase, which has a marginal effect on initiating corrosion. In addition, Sn and Ga elements are more passive than Mg (the standard potentials of Mg, Sn, and Ga are -2.36 V, -0.14 V, and -0.55 V, respectively) [45]. The dissolved Ga element was expected to increase the potential of  $\alpha$ -Mg, reducing the potential difference between  $Mg_2Sn$  and the matrix. When the Ga content exceeded 0.5 wt %,  $Mg_5Ga_2$  was formed and acted as the cathode phase to accelerate the corrosion rate.

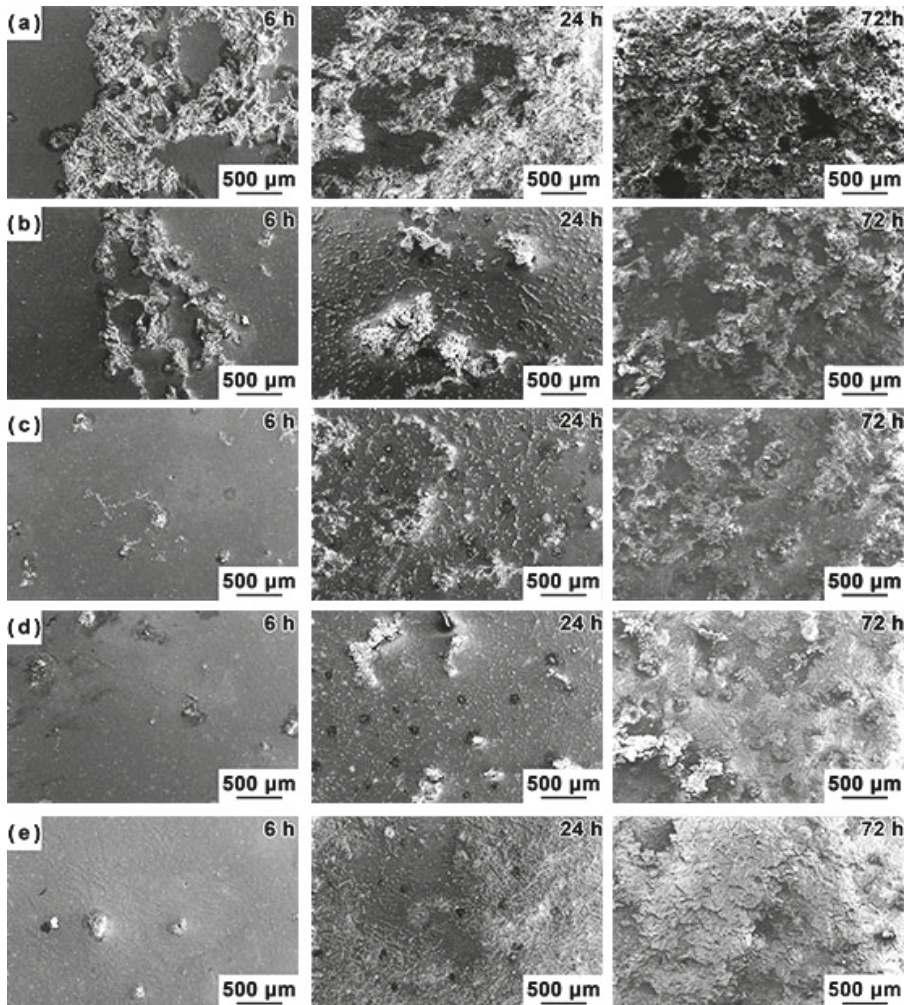


**Figure 8.** The evolution of the surface morphology of the investigated alloys after soaking for different durations in 3.5 wt % NaCl solution: (a) Mg-5Sn, (b) Mg-5Sn-0.5Ga, (c) Mg-5Sn-1Ga, (d) Mg-5Sn-2Ga, and (e) Mg-5Sn-3Ga, respectively.

Based on the above analysis, at the initial stage of corrosion, the initiation site of Mg-5Sn-0.5Ga alloy is likely to cause corrosion. However, the corrosion initiation sites of Mg-5Sn-1Ga multiply with immersion time, promoting further corrosion. Therefore, in the case of immersion test, the Mg-5Sn-0.5Ga showed superior corrosion resistance than the Mg-5Sn-1Ga alloy.

Precipitation of  $\text{Mg}(\text{OH})_2$ , as the main corrosion product on the surface, occurs when  $\text{Mg}^{2+}$  from anodic dissolution meets  $\text{OH}^-$  from water reduction [37]. The XRD patterns (Figure 9) of the investigated alloys after immersion for 24 h evidence the presence of  $\text{Mg}(\text{OH})_2$  on the surfaces, and the peak intensities of  $\text{Mg}(\text{OH})_2$  reflections decrease with increasing Ga content. This indicates that the corrosion resistance of the Mg-5Sn- $x$ Ga alloys was improved by the addition of Ga. As the addition amount of Ga was very small, the corrosion products containing Ga were not detected by XRD.

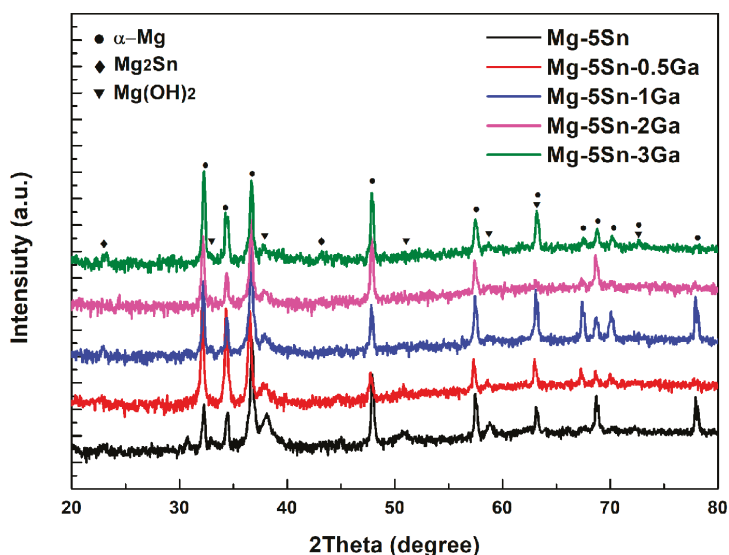


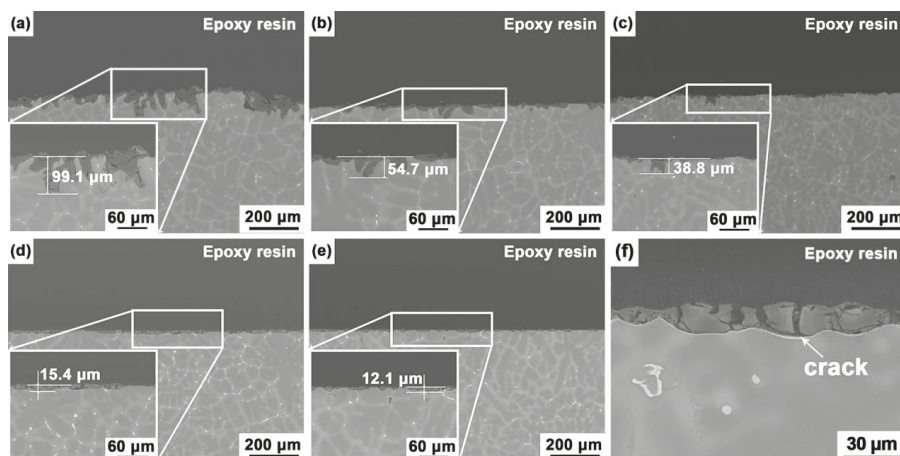
Figure 9. XRD patterns of the Mg-5Sn- $x$ Ga alloys after immersion in 3.5 wt % NaCl solution for 24 h.

Figure 10 shows the BSE micrographs of the Mg-5Sn- $x$ Ga alloys in cross-section after immersion in 3.5 wt % NaCl solution for 72 h. The samples have good uniformity. After many experiments, it was found that the corrosion depth of all three samples with the same composition showed little discrepancy. As given in Figure 10, corrosion started from the matrix near the second phases and penetrated the matrix along the area of the element-rich region. The thickness of the corrosion layer was the result of measuring the deepest corrosion in a sample. The inserts are an enlarged view of the deepest corrosion of the samples. Again, the thickness of the surface film decreases with increasing Ga content, indicating the positive effect of Ga on influencing the corrosion resistance of the alloys. Figure 10a reveals that the corrosion layer of the Mg-5Sn alloy was 99.1  $\mu\text{m}$  in thickness. The mismatch between the matrix and corrosion product would induce local mechanical stress. Such stress increases with the gradual increasing thickness of the film after immersion [46], and once it reaches a critical value, the surface film will break. The aggressive solution will penetrate the substrate surface through the broken membrane. The relatively complete surface film can protect the substrate to some extent. As a result, the pits grow along a vertical direction.

According to the immersion test, the Mg-5Sn-0.5Ga alloy is more corrosion-resistant than the Mg-5Sn-1Ga alloy. However, this is not consistent with morphologic observations made in the cross-section. The surface film of the Mg-5Sn-0.5Ga alloy (54.7  $\mu\text{m}$ ) is thicker than that of the Mg-5Sn-1Ga (38.8  $\mu\text{m}$ ) alloy. The calculated mass loss estimates the average corrosion rate in a whole immersion period, while the corrosion section reflects the local corrosion level. It is significant to see that local corrosion occurs around the second phase along the interdendritic region to the interior of the matrix in Mg-5Sn alloy (Figure 10a). The only second phase in the Mg-5Sn-0.5Ga alloy is  $\text{Mg}_2\text{Sn}$ ; hence, the two alloys should behave following the same corrosion mode. However, the oxidation state of Ga is higher than Mg in the  $\text{Mg}(\text{OH})_2$  lattice, which locally induces positive charge in the brucite lattice. Such an increase in positive charge is apt to be balanced by the interaction between Ga element and the harmful  $\text{Cl}^-$  anions, slowing down the penetration of  $\text{Cl}^-$  into the hydroxide layer [15].

To sum up, the second phases,  $\text{Mg}_2\text{Sn}$  and  $\text{Mg}_5\text{Ga}_2$ , exhibit more positive corrosion potentials than the  $\alpha$ -Mg matrix [42]. They act as the cathode, and  $\alpha$ -Mg the anode, resulting in galvanic corrosion in 3.5 wt % NaCl solution. It is worth noting that  $\text{Mg}_5\text{Ga}_2$  phase has a volta potential difference (VPD) vs. matrix around +75 mV, which will cause marginal local corrosion if the immersion time is not

long [19]. Therefore, the presence of  $Mg_5Ga_2$  phase increases the area ratio between cathode and anode, which is not conducive to the corrosion resistance, but the local corrosion sensitivity does not increase. Nevertheless, a problem with Ga addition is the uneconomic cost of metallic gallium. Therefore, higher addition levels of Ga content were not performed in this study.



**Figure 10.** Cross-section morphologies of the Mg-5Sn-xGa alloys after immersion in 3.5 wt % NaCl solution for 72 h: (a) Mg-5Sn, (b) Mg-5Sn-0.5Ga, (c) Mg-5Sn-1Ga, (d) Mg-5Sn-2Ga, (e) Mg-5Sn-3Ga; the inserts are high-magnification scanning electron microscope (SEM) micrographs of the alloys; (f) a typical SEM micrograph showing the cracks on the surface of the Mg-5Sn-3Ga alloy.

#### 4. Conclusions

The main findings of this work are:

1. The microstructures of the Mg-5Sn-xGa alloys similarly present a typical dendritic morphology, regardless of the content of Ga. Ga refines the grain structure adequately. An average grain size of  $155.9 \pm 8.6 \mu\text{m}$  was obtained for the Mg-5Sn-3Ga alloy, recording a 48.3% reduction in grain size as compared to the Mg-5Sn alloy;
2. When 0.5 wt % Ga is added to Mg-5Sn alloy, no new phase is formed. When Ga content exceeds 0.5 wt %, a new eutectic phase, identified as  $Mg_5Ga_2$ , is found in the interdendritic region. Increasing the Ga content decreases the area fraction of  $Mg_2Sn$  phase, while gradually increasing that of  $Mg_5Ga_2$  phase;
3. Immersion test in 3.5 wt % NaCl solution shows that the corrosion of the studied Mg-Sn-Ga alloys is initiated in a pitting mode, which rapidly propagates with intense  $H_2$  evolution on the surface. With the addition of 3 wt % Ga, the overall corrosion rate is decreased significantly. Despite the fact that corrosion is also initiated in a pitting mode, the number of pits is reduced, and the propagation rate is decelerated. The potentiodynamic polarization tests are basically in accordance with the immersion tests.

**Author Contributions:** Conceptualization, J.R., E.G., X.W., and Z.C.; Formal analysis, J.R.; Funding acquisition, E.G., H.K., Z.C., and T.W.; Investigation, J.R.; Methodology, X.W.; Project administration, X.W.; Resources, E.G., X.W., H.K., and T.W.; Supervision, H.K., Z.C., and T.W.; Writing—original draft, J.R.; Writing—review and editing, J.R., X.W., and Z.C.

**Funding:** This research was funded by the National Key Research and Development Program of China [grant No. 2016YFB0701203]; the National Natural Science Foundation of China [Grant Nos. 51525401, 51601028, 51774065, 51974058, 51728101, and 51690163]; and the fundamental research funds for the central universities [Nos. DUT18RC(3)042, DUT17RC(3)108].



**Conflicts of Interest:** The authors declare no conflict of interest. The funders had no role in the design of the study; in the collection, analyses, or interpretation of data; in the writing of the manuscript, or in the decision to publish the results.

## References

1. Ghali, E.; Dietzel, W.; Kainer, K. Testing of General and Localized Corrosion of Magnesium Alloys: A Critical Review. *J. Mater. Eng. Perform.* **2004**, *13*, 517–529. [[CrossRef](#)]
2. Kang, D.H.; Park, S.S.; Kim, N.J. Development of Creep Resistant Die Cast Mg–Sn–Al–Si Alloy. *Mater. Sci. Eng. A* **2005**, *413–414*, 555–560. [[CrossRef](#)]
3. Luo, A.A. Recent Magnesium Alloy Development for Elevated Temperature Applications. *Int. Mater. Rev.* **2013**, *49*, 13–30. [[CrossRef](#)]
4. Song, G.; Atrons, A. Understanding Magnesium Corrosion—A Framework for Improved Alloy Performance. *Adv. Eng. Mater.* **2003**, *5*, 837–858. [[CrossRef](#)]
5. Mendis, C.L.; Bettles, C.J.; Gibson, M.A.; Hutchinson, C.R. An Enhanced Age Hardening Response in Mg–Sn Based Alloys Containing Zn. *Mater. Sci. Eng. A* **2006**, *435–436*, 163–171. [[CrossRef](#)]
6. Cheng, W.; Zhang, Y.; Ma, S.; Arthanari, S.; Cui, Z.; Wang, H.; Wang, L. Tensile Properties and Corrosion Behavior of Extruded Low-Alloyed Mg–1Sn–1Al–1Zn Alloy: The Influence of Microstructural Characteristics. *Materials* **2018**, *11*, 1157. [[CrossRef](#)]
7. Sasaki, T.T.; Oh-ishi, K.; Ohkubo, T.; Hono, K. Enhanced Age Hardening Response by the Addition of Zn in Mg–Sn Alloys. *Scr. Mater.* **2006**, *55*, 251–254. [[CrossRef](#)]
8. Liu, H.; Chen, Y.; Tang, Y.; Wei, S.; Niu, G. The Microstructure, Tensile Properties, and Creep Behavior of as-Cast Mg–(1–10)%Sn Alloys. *J. Alloys Compd.* **2007**, *440*, 122–126. [[CrossRef](#)]
9. Huang, X.; Han, G.; Huang, W. T6 Treatment and its Effects on Corrosion Properties of an Mg–4Sn–4Zn–2Al Alloy. *Materials* **2018**, *11*, 628. [[CrossRef](#)] [[PubMed](#)]
10. Zhao, Z.; Hua, Z.; Li, D.; Wei, D.; Liu, Y.; Wang, J.; Luo, D.; Wang, H. Effect of Sn Content on the Microstructure, Mechanical Properties and Corrosion Behavior of Biodegradable Mg–X (1, 3 and 5 wt.%) Sn–1Zn–0.5Ca Alloys. *Materials* **2018**, *11*, 2378. [[CrossRef](#)] [[PubMed](#)]
11. Park, K.C.; Kim, B.H.; Kimura, H.; Park, Y.H.; Park, I.M. Microstructure and Corrosion Properties of Mg–xSn–5Al–1Zn (x = 0, 1, 5 and 9 mass%) Alloys. *Mater. Trans.* **2010**, *51*, 472–476. [[CrossRef](#)]
12. Song, G. Effect of Tin Modification on Corrosion of Am70 Magnesium Alloy. *Corros. Sci.* **2009**, *51*, 2063–2070. [[CrossRef](#)]
13. Ha, H.; Kang, J.; Yang, J.; Yim, C.D.; You, B.S. Role of Sn in Corrosion and Passive Behavior of Extruded Mg–5 wt % Sn Alloy. *Corros. Sci.* **2016**, *102*, 355–362. [[CrossRef](#)]
14. Ha, H.; Kang, J.; Kim, S.G.; Kim, B.; Park, S.S.; Yim, C.D.; You, B.S. Influences of Metallurgical Factors on the Corrosion Behaviour of Extruded Binary Mg–Sn Alloys. *Corros. Sci.* **2014**, *82*, 369–379. [[CrossRef](#)]
15. Kubásek, J.; Vojtěch, D.; Lipov, J.; Ruml, T. Structure, Mechanical Properties, Corrosion Behavior and Cytotoxicity of Biodegradable Mg–X (X = Sn, Ga, in) Alloys. *Mater. Sci. Eng. C* **2013**, *33*, 2421–2432. [[CrossRef](#)] [[PubMed](#)]
16. Liu, X.; Shan, D.; Song, Y.; Chen, R.; Han, E. Influences of the Quantity of Mg<sub>2</sub>Sn Phase on the Corrosion Behavior of Mg–7Sn Magnesium Alloy. *Electrochim. Acta* **2011**, *56*, 2582–2590. [[CrossRef](#)]
17. Feng, Y.; Wang, R.; Peng, C.; Wang, N. Influence of Mg<sub>21</sub>Ga<sub>5</sub>Hg<sub>3</sub> Compound on Electrochemical Properties of Mg–5%Hg–5%Ga Alloy. *Trans. Nonferr. Met. Soc. China* **2009**, *19*, 154–159. [[CrossRef](#)]
18. Feng, Y.; Wang, R.-c.; Peng, C.-q.; Tang, H.-p.; Liu, H.-y. Influence of Mg<sub>5</sub>Ga<sub>2</sub> Compound on Microstructures and Electrochemical Properties of Mg–5%Hg–22%Ga Alloy. *Prog. Nat. Sci.* **2011**, *21*, 73–79. [[CrossRef](#)]
19. Mohedano, M.; Blawert, C.; Yasakau, K.A.; Arrabal, R.; Matykina, E.; Mingo, B.; Scharnagl, N.; Ferreira, M.G.S.; Zheludkevich, M.L. Characterization and Corrosion Behavior of Binary Mg–Ga Alloys. *Mater. Charact.* **2017**, *128*, 85–99. [[CrossRef](#)]
20. Shi, Z.; Liu, M.; Atrons, A. Measurement of the Corrosion Rate of Magnesium Alloys Using Tafel Extrapolation. *Corros. Sci.* **2010**, *52*, 579–588. [[CrossRef](#)]
21. Cai, S.; Lei, T.; Li, N.; Feng, F. Effects of Zn On Microstructure, Mechanical Properties and Corrosion Behavior of Mg–Zn Alloys. *Mater. Sci. Eng. C* **2012**, *32*, 2570–2577. [[CrossRef](#)]

22. Gu, X.; Zheng, Y.; Zhong, S.; Xi, T.; Wang, J.; Wang, W. Corrosion of, and Cellular Responses to Mg–Zn–Ca Bulk Metallic Glasses. *Biomaterials* **2010**, *31*, 1093–1103. [[CrossRef](#)] [[PubMed](#)]
23. Ha, H.; Kang, J.; Yang, J.; Yim, C.D.; You, B.S. Limitations in the Use of the Potentiodynamic Polarisation Curves to Investigate the Effect of Zn On the Corrosion Behaviour of as-Extruded Mg–Zn Binary Alloy. *Corros. Sci.* **2013**, *75*, 426–433. [[CrossRef](#)]
24. Yang, F.; Kang, H.; Guo, E.; Li, R.; Chen, Z.; Zeng, Y.; Wang, T. The Role of Nickel in Mechanical Performance and Corrosion Behaviour of Nickel-Aluminium Bronze in 3.5 Wt.% NaCl Solution. *Corros. Sci.* **2018**, *139*, 333–345. [[CrossRef](#)]
25. Jayalakshmi, S.; Sankaranarayanan, S.; Koh, S.P.X.; Gupta, M. Effect of Ag and Cu Trace Additions on the Microstructural Evolution and Mechanical Properties of Mg–5Sn Alloy. *J. Alloys Compd.* **2013**, *565*, 56–65. [[CrossRef](#)]
26. Lee, Y.C.; Dahle, A.K.; StJohn, D.H. The Role of Solute in Grain Refinement of Magnesium. *Metall. Mater. Trans. A* **2000**, *31*, 2895–2906. [[CrossRef](#)]
27. Easton, M.; StJohn, D. Grain Refinement of Aluminum Alloys: Part II. Confirmation of, and a Mechanism for, the Solute Paradigm. *Metall. Mater. Trans. A* **1999**, *30*, 1625–1633. [[CrossRef](#)]
28. Easton, M.; StJohn, D. Grain Refinement of Aluminum Alloys: Part I. The Nucleant and Solute Paradigms—A Review of the Literature. *Metall. Mater. Trans. A* **1999**, *30*, 1613–1623. [[CrossRef](#)]
29. Fu, J.W.; Yang, Y.S. Formation of the Solidified Microstructure in Mg–Sn Binary Alloy. *J. Cryst. Growth* **2011**, *322*, 84–90. [[CrossRef](#)]
30. Liu, H.; Zhao, G.; Liu, C.; Zuo, L. Effects of Different Tempers On Precipitation Hardening of 6000 Series Aluminium Alloys. *Trans. Nonferr. Met. Soc. China* **2007**, *17*, 122–127. [[CrossRef](#)]
31. Liu, C.; Zhu, X.; Zhou, H. *Magnesium Alloy Phase Atlas*; Central South University Press: Changsha, China, 2006; p. 23.
32. Zhao, C.; Pan, F.; Zhao, S.; Pan, H.; Song, K.; Tang, A. Preparation and Characterization of as-Extruded Mg–Sn Alloys for Orthopedic Applications. *Mater. Des.* **2015**, *70*, 60–67. [[CrossRef](#)]
33. Hamu, G.B.; Eliezer, D.; Wagner, L. The Relation Between Severe Plastic Deformation Microstructure and Corrosion Behavior of Az31 Magnesium Alloy. *J. Alloys Compd.* **2009**, *468*, 222–229. [[CrossRef](#)]
34. Liao, J.; Hotta, M.; Yamamoto, N. Corrosion Behavior of Fine-Grained Az31B Magnesium Alloy. *Corros. Sci.* **2012**, *61*, 208–214. [[CrossRef](#)]
35. Liu, H.; Qi, G.; Ma, Y.; Hao, H.; Jia, F.; Ji, S.; Zhang, H.; Zhang, X. Microstructure and Mechanical Property of Mg–2.0Ga Alloys. *Mater. Sci. Eng. A* **2009**, *526*, 7–10. [[CrossRef](#)]
36. Schneider, C.A.; Rasband, W.S.; Eliceiri, K.W. NIH Image to ImageJ: 25 years of image analysis. *Nat. Methods* **2012**, *9*, 671–675. [[CrossRef](#)]
37. Zhen, Z.; Xi, T.; Zheng, Y.; Li, L.; Li, L. In Vitro Study on Mg–Sn–Mn Alloy as Biodegradable Metals. *J. Mater. Sci. Technol.* **2014**, *30*, 675–685. [[CrossRef](#)]
38. Song, G.; Unocic, K.A. The Anodic Surface Film and Hydrogen Evolution on Mg. *Corros. Sci.* **2015**, *98*, 758–765. [[CrossRef](#)]
39. Ha, H.; Kang, J.; Yim, C.D.; Yang, J.; You, B.S. Role of Hydrogen Evolution Rate in Determining the Corrosion Rate of Extruded Mg–5Sn–(1–4 Wt.%) Zn Alloys. *Corros. Sci.* **2014**, *89*, 275–285. [[CrossRef](#)]
40. Ha, H.; Kim, H.J.; Baek, S.; Kim, B.; Sohn, S.; Shin, H.; Jeong, H.Y.; Park, S.H.; Yim, C.D.; You, B.S.; et al. Improved Corrosion Resistance of Extruded Mg–8Sn–1Zn–1Al Alloy by Microalloying with Mn. *Scr. Mater.* **2015**, *109*, 38–43. [[CrossRef](#)]
41. Kim, H.J.; Kim, B.; Baek, S.; Sohn, S.; Shin, H.; Jeong, H.Y.; Yim, C.D.; You, B.S.; Ha, H.; Park, S.S. Influence of Alloyed Al On the Microstructure and Corrosion Properties of Extruded Mg–8Sn–1Zn Alloys. *Corros. Sci.* **2015**, *95*, 133–142. [[CrossRef](#)]
42. Zhao, C.; Pan, F.; Zhao, S.; Pan, H.; Song, K.; Tang, A. Microstructure, Corrosion Behavior and Cytotoxicity of Biodegradable Mg–Sn Implant Alloys Prepared by Sub-Rapid Solidification. *Mater. Sci. Eng. C* **2015**, *54*, 245–251. [[CrossRef](#)] [[PubMed](#)]
43. Rad, H.R.B.; Idris, M.H.; Kadir, M.R.A.; Farahany, S. Microstructure Analysis and Corrosion Behavior of Biodegradable Mg–Ca Implant Alloys. *Mater. Des.* **2012**, *33*, 88–97. [[CrossRef](#)]
44. Yim, C.D.; Yang, J.; Woo, S.K.; Ha, H.; You, B.S. The Effects of Microstructural Factors on the Corrosion Behaviour of Mg–5Sn–X Zn (X = 1, 3 wt%) Extrusions. *Corros. Sci.* **2015**, *90*, 597–605. [[CrossRef](#)]

45. Bratsch, S.G. Standard Electrode Potentials and Temperature Coefficients in Water at 298.15 K. *J. Phys. Chem. Ref. Data* **1989**, *18*, 1–21. [[CrossRef](#)]
46. Chen, J.; Wang, J.; Han, E.; Ke, W. In Situ Observation of Pit Initiation of Passivated Az91 Magnesium Alloy. *Corros. Sci.* **2009**, *51*, 477–484. [[CrossRef](#)]



© 2019 by the authors. Licensee MDPI, Basel, Switzerland. This article is an open access article distributed under the terms and conditions of the Creative Commons Attribution (CC BY) license (<http://creativecommons.org/licenses/by/4.0/>).

Article

# Experimental and Theoretical Studies on the Corrosion Inhibition of Carbon Steel by Two Indazole Derivatives in HCl Medium

Shenyang Xu <sup>1,2</sup>, Shengtao Zhang <sup>1,\*</sup>, Lei Guo <sup>3,\*</sup>, Li Feng <sup>1</sup> and Bochuan Tan <sup>1</sup>

<sup>1</sup> School of Chemistry and Chemical Engineering, Chongqing University, Chongqing 400044, China; 20111802011@cqu.edu.cn (S.X.); 20151802007@cqu.edu.cn (L.F.); 20161802006@cqu.edu.cn (B.T.)

<sup>2</sup> School of Chemistry and Chemical Engineering, Yibin University, Yibin 644000, China

<sup>3</sup> School of Material and Chemical Engineering, Tongren University, Tongren 554300, China

\* Correspondence: stzhang@cqu.edu.cn (S.Z.); chygl@gztrc.edu.cn (L.G.)

Received: 2 April 2019; Accepted: 23 April 2019; Published: 24 April 2019

**Abstract:** In this work, two indazole derivatives, namely 5-aminoindazole (AIA) and 5-nitroindazole (NIA), were investigated as corrosion inhibitors for carbon steel in 1 M HCl solution by experimental and density functional theory (DFT) methods. The electrochemical results indicate that the inhibition ability follows the order of AIA > NIA, which is due to the stronger electron-donating effect of  $-NH_2$  of the AIA group than the  $-NO_2$  group of NIA. Besides, the frontier orbital theory shows that the AIA exhibits higher reaction activity than NIA, and a more negative adsorption energy for AIA was also obtained, which is consistent with the analysis of the electrochemical measurements. We draw the conclusion that the electron-donating effect makes it easier for AIA to donate electrons to iron atoms to form a stronger protective layer than NIA.

**Keywords:** corrosion inhibitor; carbon steel; indazole derivatives; electrochemistry; DFT

## 1. Introduction

Carbon steels are extensively utilized as structural materials in plenty of industrial fields, especially in corrosive environments. In view of this, some protective strategies have been employed to protect steel from corrosion. The addition of corrosion inhibitors has been proved to be an easy and highly effective way to achieve this [1–3]. Organic compounds containing heteroatoms such as N, P, S or O have been used as excellent inhibitors due to their strong electron-donating ability [4–6]. Additionally, due to their high adsorption capacity, indazole derivatives have attracted the attention of several researchers [7,8]. Our previous work revealed that indazole can adsorb onto copper surfaces and exhibits a favorable inhibition efficiency for copper corrosion in a 3.0 wt.% NaCl solution [7]. Furthermore, the influence of active adsorption, which centers on the inhibition effectiveness of IA-based inhibitors, was also researched in aggressive solutions [9]. Potentially, it is important to explore the effects of functional groups of indazole-based inhibitors on inhibition effectiveness. Herein, 5-aminoindazole (AIA) and 5-nitroindazole (NIA), as shown in Figure 1, were discovered for the first time to be effective corrosion inhibitors for carbon steel in hydrochloric acid (HCl) solution.

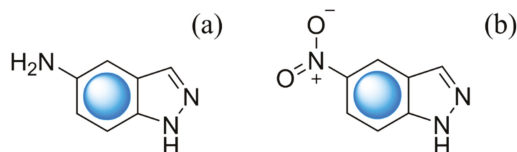


**Figure 1.** Molecular structures of indazole derivatives, (a) 5-aminoindazole; (b) 5-nitroindazole.

Specifically, this work focused on the corrosion inhibition of AIA and NIA for Q235 carbon steel in 1 M hydrochloric acid solution by using multiple techniques including electrochemical measurements, scanning electron microscopy (SEM) and DFT calculations. On account of the experimental and theoretical results, the difference of the inhibition mechanisms between AIA and NIA molecules was revealed, which would provide some reference functions to develop more efficient inhibitors for corrosion protection.

## 2. Experimental Section

### 2.1. Material and Samples Preparation

The tested inhibitors were AIA and NIA (Aladdin Company, Shanghai, China). The chemical composition of Q235 carbon steel (JIS G3101) was 0.17% C, 0.47% Mn, 0.26% Si, 0.017% S, 0.0048% P and Fe. The specimens for electrochemical measurements were sealed in ethoxyline resin with a 1 cm<sup>2</sup> area exposed as working area. Prior to experiments, all specimens were polished by emery paper from 400 to 1200 grit. Then, samples were cleaned by ethanol and distilled water and dried at room temperature. Analytical reagent grade 37.5% water-diluted HCl was used as the corrosive medium (1 M HCl).

### 2.2. Electrochemical Measurements

A three-electrode cell was used to do the electrochemical experiments, and all tests were performed in a CHI660B CHI660B electrochemical workstation (Chinstruments, Shanghai, China). Q235 carbon steel, a platinum plate of 1.5 × 1.5 cm<sup>2</sup>, and a saturated calomel electrode (SCE) with a Luggin capillary were the working electrode, counter electrode, and reference electrode, respectively. To obtain a steady open circuit potential (OCP), the electrodes were immersed into the corrosive solution for one hour before tests. The potentiodynamic polarization curves were obtained with the potential range from −250 mV to 250 mV vs. OCP at the scan rate of 0.2 mV s<sup>−1</sup>. Electrochemical impedance spectroscopy (EIS) experiments were performed in a frequency range from 10<sup>−2</sup> Hz to 10<sup>5</sup> Hz with amplitude of 5 mV at OCP (−0.45 V to −0.49 V). Z-view software was employed to fit the experimental data by an appropriate equivalent circuit.

### 2.3. Scanning Electron Microscopy

The surface morphologies of Q235 carbon steel specimens were captured with scanning electron microscopy (SEM, Joel-6490LV, Tokyo, Japan) with an accelerating voltage of 20 kV. Before SEM characterization, the samples were immersed for six hours in 1 M HCl with and without AIA or NIA inhibitor.

### 2.4. Theoretical Simulations

A Gaussian 03W program was employed for quantum chemical calculations based on DFT. The geometry optimized structures of AIA and NIA were obtained through the use of the B3LYP function with a 6-311++G(d, p) basis set. During this process, no imaginary frequency was confirmed and the structures were in their lowest-energy state. Furthermore, DFT was used to calculate the Mulliken charge, dipole moment ( $\mu$ ) and frontier molecular orbitals including the energy of the highest occupied molecular orbital ( $E_{\text{HOMO}}$ ), the energy of the lowest unoccupied molecular orbital ( $E_{\text{LUMO}}$ ) and energy gap ( $\Delta E = E_{\text{LUMO}} - E_{\text{HOMO}}$ ).

The interactions between AIA or NIA and the Fe (110) surface were modeled in a simulation box (12.4 Å × 9.9 Å × 24.1 Å) with periodic boundary conditions by the Dmol<sup>3</sup> program of Material Studio software (BIOVIA, USA). A 4-layer 5 × 5 supercell (the lower two layers were constrained) with 20 Å vacuum slab was used to simulate bulk metal. DFT calculations were treated within the generalized gradient approximation (GGA) function of Perdew–Burke–Ernzerhof (PBE) and the double numerical basis set with polarization functions on hydrogen atoms (DNP). DFT semi-core pseudopotentials (DSPPs) were used for Fe treatment. The displacement convergence, gradient, and tolerances of energy were 5 ×

$10^{-3} \text{ \AA}$ ,  $2 \times 10^{-3} \text{ Ha} \cdot \text{\AA}^{-1}$ , and  $1 \times 10^{-5} \text{ Ha}$ , respectively. The interaction energy ( $E_{\text{Fe-inhibitor}}$ ) between the Fe (110) surface and inhibitor obeyed [10–12]

$$E_{\text{Fe-inhibitor}} = E_{\text{Total}} - E_{\text{Fe}} - E_{\text{inhibitor}} \quad (1)$$

where  $E_{\text{Total}}$  is the energy of Fe(110) surface and the adsorbed inhibitor molecule,  $E_{\text{inhibitor}}$  is the energy of the isolated inhibitor molecule and  $E_{\text{Fe}}$  is the energy of the steel surface, respectively.

### 3. Results and Discussion

#### 3.1. Electrochemical Impedance Spectroscopy (EIS) Measurements

Figure 2 shows the electrochemical impedance spectra plots of AIA and NIA, respectively. In Figure 2a,c, it can be seen that the radius of the capacitive resistance arc increased with the growing concentration of inhibitors, which indicates that the protective layer was formed on the steel surface by the adsorption of AIA or NIA and that the corrosion inhibition efficiency of AIA is better than NIA. In addition, the impedance spectrum exhibits a squashed semicircle, which is caused by the formation of a protective layer on the steel surface. Figure 2b,d is Bode plots in the presence and absence of AIA and NIA, respectively. The impedance values and phase angle values increase with the growing concentration of inhibitors. In addition, a time constant can be found in the phase angle, usually due to the relaxation effect of the corrosion inhibitor molecule adsorption [2,13].

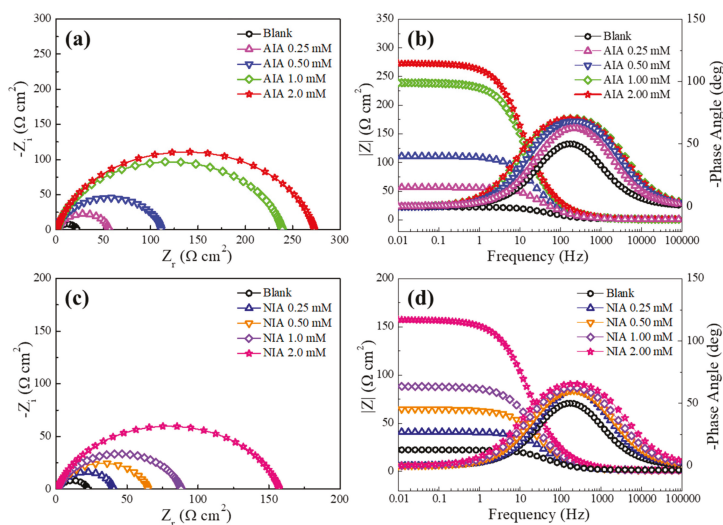


**Figure 2.** The plots of Nyquist and Bode for carbon steel in 1 M HCl with and without different concentrations of 5-aminoindazole (AIA) and 5-nitroindazole (NIA) at 298 K. AIA: (a,b); NIA: (c,d).

The equivalent circuit (Figure 3) is used to fit the impedance spectrum data, and the fitting data are shown in Table 1. In Figure 3,  $R_s$  is the solution resistance,  $R_{ct}$  is the charge transfer resistance, and CPE is a constant phase element; the impedance of the CPE is expressed as follows [14,15]:

$$Z_{\text{CPE}} = \frac{1}{Y_0(j\omega)^n} \quad (2)$$

The double-layer capacitance ( $C_{dl}$ ) can be calculated from CPE parameter values  $Y_0$  and  $n$  by the following expression [16]:

$$C_{dl} = \frac{Y_0 \omega^{n-1}}{\sin(\frac{n\pi}{2})} \tag{3}$$

where  $Y_0$  is the CPE constant,  $n$  is the phase shift, which can be explained as a degree of surface inhomogeneity,  $j$  is the imaginary unit and  $\omega$  is the angular frequency. The inhibition efficiency  $\eta_{EIS}$  can be expressed by the following equation [17–19]:

$$\eta_{EIS} = \left( \frac{R_{ct} - R_{ct}^0}{R_{ct}} \right) \times 100 \tag{4}$$

where  $R_{ct}$  and  $R_{ct,0}$  are the charge transfer resistances with and without AIA and NIA, respectively. In Table 1, we can see that as the concentration of the corrosion inhibitor increases, the value of the  $R_{ct}$  becomes larger, and the value of  $\eta_{EIS}$  also increases simultaneously. When the concentration of the inhibitor was 2 mM, the  $R_{ct}$  values of AIA and NIA are 238 and 156.2  $\Omega \text{ cm}^2$ , respectively. According to the Helmholtz model formula, the value of double layer capacitance ( $C_{dl}$ ) can be expressed as [20,21]

$$C_{dl} = \frac{\epsilon^0 \epsilon}{d} S \tag{5}$$

where  $\epsilon^0$  is the dielectric constant of air and  $\epsilon$  is the local dielectric constant.  $S$  is the surface area of the working electrode, and  $d$  is the surface film thickness. Compared with water molecules, the molecular volume of AIA and NIA is significantly larger, and their dielectric constant is smaller than that of water molecules. Therefore, with increasing concentrations of AIA or NIA, the two investigated inhibitors replace the water molecules on the surface of carbon steel continuously, and the value of  $C_{dl}$  decreases. Hence, the smaller the  $C_{dl}$ , the denser the protective film formed on the surface of the carbon steel by AIA and NIA.

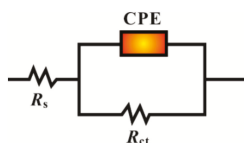


Figure 3. Electrical equivalent circuit used to fit the electrochemical impedance spectroscopy (EIS) experimental data. CPE: constant phase element.

Table 1. Impedance data for Q235 steel in 1 M HCl with various concentrations of NIA and AIA at 298 K.

Inhibitor	$C_{inh}$ (mM)	$R_s$ ( $\Omega \text{ cm}^2$ )	$R_{ct}$ ( $\Omega \text{ cm}^2$ )	CPE		$C_{dl}$ ( $\mu\text{F cm}^{-2}$ )	$\eta_{EIS}$ (%)
				$Y_0 \times 10^{-6}$ ( $\text{S s}^n \text{ cm}^{-2}$ )	$n$		
Blank	/	1.43	20.1	504.6	0.85	215.4	/
	0.25	1.26	55.3	214.5	0.85	188.8	62.1
AIA	0.50	1.11	109.9	159.6	0.88	140.4	80.9
	1.00	1.22	238.0	120.3	0.87	104.7	91.2
	2.00	1.36	271.6	113.4	0.87	98.7	92.3
	0.25	1.23	39.6	280.4	0.88	246.8	47.1
NIA	0.50	1.34	63.4	265	0.84	222.6	66.9
	1.00	1.22	86.9	247.4	0.84	207.8	75.9
	2.00	1.14	156.2	185.9	0.83	154.3	86.6

### 3.2. Potentiodynamic Polarization Measurements

Figure 4 shows the electrodynamic polarization curves of carbon steel at 298 K in 1 M HCl solutions with various concentrations of NIA and AIA. The relevant data (in Table 2) are obtained by the extrapolation method. The inhibition efficiency  $\eta_p$  is calculated by the following equation [22–24]:

$$\eta_p = \left( \frac{i_{\text{corr}}^0 - i_{\text{corr}}}{i_{\text{corr}}^0} \right) \times 100 \quad (6)$$

where  $i_{\text{corr}}^0$  and  $i_{\text{corr}}$  are the corrosion current density in 1 M HCl solutions without and with the two investigated inhibitors, respectively.

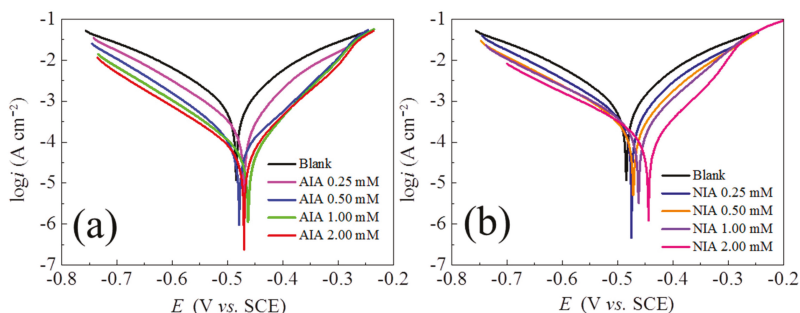


**Figure 4.** Anodic and cathodic polarization curves for carbon steel in 1 M HCl with various concentrations of (a) AIA and (b) NIA at 298 K. SCE: saturated calomel electrode.

**Table 2.** Relevant parameters for Q235 steel in 1 M HCl solution in the absence and presence of different concentrations of AIA and NIA at 298 K from polarization curves.

Inhibitor	$C_{\text{inh}}$ (mM)	$E_{\text{corr}}$ (V vs. SCE)	$\beta_c$ (mV dec <sup>-1</sup> )	$\beta_a$ (mV dec <sup>-1</sup> )	$I_{\text{corr}}$ ( $\mu\text{A cm}^{-2}$ )	$\eta_p$ (%)
Blank	/	-0.48	119.4	95.3	754.4	/
	0.25	-0.47	112.0	73.9	231.1	69.4
AIA	0.50	-0.48	70.38	78.7	72.2	90.4
	1.00	-0.47	115.3	78.7	59.8	92.1
	2.00	-0.48	81.95	82.7	34.5	95.4
NIA	0.25	-0.48	122.6	82.8	363.7	51.8
	0.50	-0.47	127.7	85.6	248.8	67.0
	1.00	-0.46	132.8	85.8	239.9	68.2
	2.00	-0.45	107.2	74.6	117.4	84.4

It can be seen in Figure 4 that, compared with the values in blank solution, the corrosion potential ( $E_{\text{corr}}$ ) and corrosion current density ( $I_{\text{corr}}$ ) of the polarization curves change obviously with the addition of the two investigated inhibitors. With the addition of AIA and NIA, the  $I_{\text{corr}}$  decreases and the  $E_{\text{corr}}$  moves in a positive direction, illustrating that the corrosion reaction is effectively controlled. Clearly, the investigated inhibitors not only reduced the corrosion of the cathode but also reduced the corrosion of the anode. In addition, the shapes of polarization curves are parallel with the increase of concentration for the two investigated inhibitors, indicating that the action mechanism is same under different concentrations of inhibitors. Generally, it is considered as a cathodic inhibitor when the potential change exceeds 85 mV, while it is a mixed inhibitor when the potential change is less than 85 mV [25,26]. From Table 2, the changed values of  $E_{\text{corr}}$  for the two inhibitors are less than 85 mV, suggesting that AIA and NIA are mixed corrosion inhibitors. The changed values of  $\beta_a$  and  $\beta_c$  also reflect the cathodic and anodic corrosion rates being retarded by the studied inhibitors. Furthermore, the inhibition efficiency ( $\eta_p$ ) is also improved with increasing concentrations of the two inhibitors, and the inhibition ability follows the order AIA > NIA, which may be due to the stronger electron-donating effect of  $-\text{NH}_2$  than the  $-\text{NO}_2$  [27,28]. The electron-donating effect of the  $-\text{NH}_2$  makes the electron cloud density of the whole AIA molecule larger than the  $-\text{NO}_2$  of NIA, which leads to AIA finding it easier to give electrons to iron atoms and having a better protective effect than NIA.



### 3.3. Morphology Analysis

To obviously display the inhibition differences between AIA and NIA inhibitors, the morphologies of untreated and treated carbon steel were studied. The obtained images are shown in Figure 5. The surface of fresh carbon steel is smooth, while large holes and cracks with a size of 10  $\mu\text{m}$  were observed after immersion in 1 M HCl (Figure 5a,b). The pitting morphology is formed due to the elimination rate of corrosion products slower than the reaction rate between  $\text{Cl}^-$  and Fe [29,30]. Besides, some small holes and cracks still appeared on the steel surface even after 2 mM NIA was added into the HCl solution (Figure 5d). However, a flat surface was achieved with the addition of 2 mM AIA (Figure 5c); meanwhile the steel surface was covered with the absorbed AIA. Hence, the AIA shows prior inhibition performance than NIA. These results are in good agreement with electrochemical measurements.

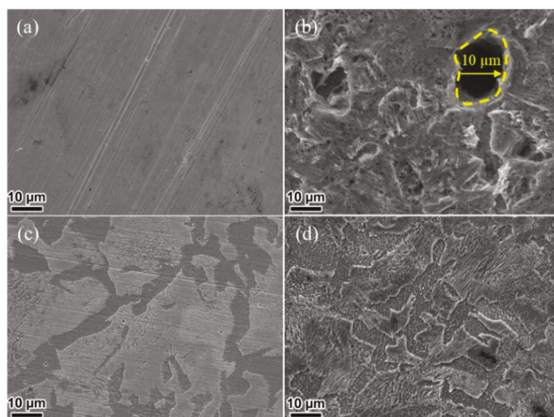


**Figure 5.** SEM images of (a) fresh carbon steel and carbon steel immersed in 1 M HCl solution (b) without and with 2 mM (c) AIA or (d) NIA.

### 3.4. Computational Study

Computational simulation is an effective way to explain reaction mechanisms. In this work, DFT calculations were used to reveal the adsorption and inhibition performances of AIA and NIA molecules. By comparison, the acidity coefficient ( $\text{p}K_{\text{a}}$ ) of both AIA and NIA displayed higher values than the pH of 1M HCl medium, proving the existence of the protonated molecule. Specifically, there are two  $\text{p}K_{\text{a}}$  (1.89 and 3.42) for AIA, indicating the existing form of  $\text{AIA-2H}^+$  in HCl solution. Instead, there is only one  $\text{p}K_{\text{a}}$  for NIA, indicating the existence of  $\text{NIA-H}^+$ . The optimized geometry structure and frontier molecular orbitals (the highest occupied molecular orbital (HOMO) and the lowest unoccupied molecular orbital (LUMO)) of  $\text{AIA-2H}^+$  and  $\text{NIA-H}^+$  are shown in Figure 6, and Table 3 shows the energy of HOMO ( $E_{\text{HOMO}}$ ) and LUMO ( $E_{\text{LUMO}}$ ). It is generally known that HOMO is related to the ability of a molecule to donate electrons, and a higher  $E_{\text{HOMO}}$  value shows a stronger electron-donating ability [31,32]. By contrast, LUMO is associated with the electron-accepting ability of a molecule, and a lower value of  $E_{\text{LUMO}}$  represents a strong electron-accepting ability [33]. As can be seen from Figure 6c,d, the LUMO of both  $\text{AIA-2H}^+$  and  $\text{NIA-H}^+$  is distributed uniformly around the whole molecule. Conversely, in comparison with  $\text{AIA-2H}^+$  (Figure 6f), the HOMO of  $\text{NIA-H}^+$  was mainly delocalized around the nitro-substituent (Figure 6e), indicating that the electron-donating ability of NIA mainly comes from the nitro-substituent. According to the frontier orbitals, both AIA and NIA tend to interact with the steel surface through the  $\pi$  bond of rings in the way of parallel adsorption configuration.

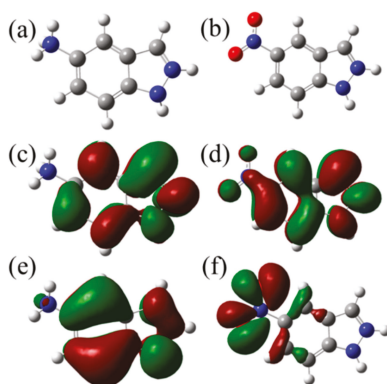


**Figure 6.** (a,b) Optimized geometric structures, (c,d) LUMO orbitals and (e,f) HOMO orbitals of AIA and NIA inhibitors.

**Table 3.** Quantum chemical parameters for AIA and NIA by using the B3LYP/6-311++G(d,p) method.

Inhibitor	$E_{\text{HOMO}}$ (eV)	$E_{\text{LUMO}}$ (eV)	$\Delta E$ (eV)	$\mu$ (Debye)	$I$ (eV)	$A$ (eV)	$\chi$ (eV)	$\gamma$ (eV)	$\Delta N$
AIA	−9.6	−6.2	3.4	5.4	9.6	6.2	7.9	1.7	−0.25
NIA	−11.7	−7.1	4.6	14.3	11.7	7.1	9.4	2.3	−0.53

In addition, the HOMO–LUMO gap ( $\Delta E$ ) is an important parameter to evaluate the stability of inhibitors, and the lower value of  $\Delta E$  indicates that the inhibitor molecule could more easily adsorb on the metal surface [34,35]. As shown in Table 3, both AIA-2H<sup>+</sup> and NIA-H<sup>+</sup> have lower values of  $\Delta E$  (3.4 eV and 4.6 eV, respectively), resulting in their strong ability to accept electrons from the d-orbital of steel as well as the high stability of the [Fe-inhibitor] complexes; namely, the AIA exhibited higher reaction activity than NIA. At the same time, the dipole–dipole ( $\mu$ ) interaction between the inhibitor and metal surface could improve the inhibition efficiency [36]. Herein, the fact that  $\mu_{\text{NIA}}$  is about three times  $\mu_{\text{AIA}}$  indicates that AIA exhibits more appropriate adsorption between the AIA and metal surface than NIA.

The ionization potential ( $I = -E_{\text{HOMO}}$ ) and electron affinity ( $A = -E_{\text{LUMO}}$ ) could be used to derive the electronegativity ( $\chi$ ) and global hardness ( $\gamma$ ). The fraction of the electron transfer ( $\Delta N$ ) between the inhibitor molecules and Fe surface is given by following equation [37–39]:

$$\Delta N = \frac{\chi_{\text{Fe}} - \chi_{\text{inh}}}{2(\gamma_{\text{Fe}} + \gamma_{\text{inh}})} \quad (7)$$

where  $\chi_{\text{Fe}}$  and  $\gamma_{\text{Fe}}$  are the absolute electronegativity and hardness of the Fe atom; and  $\chi_{\text{inh}}$  and  $\gamma_{\text{inh}}$  are the absolute electronegativity and hardness of the inhibitor molecules. A theoretical  $\chi_{\text{Fe}}$  value of bulk Fe is 7 eV/mol, whereas  $\gamma_{\text{Fe}}$  is almost zero.  $\chi_{\text{inh}}$  and  $\gamma_{\text{inh}}$  are related to  $I$  and  $A$  [40,41].

$$\chi = \frac{I + A}{2} \quad (8)$$

$$\gamma = \frac{I - A}{2} \quad (9)$$

The direction of electron transfer is manifested by positive or negative  $\Delta N$  values [42]. From Table 3, both AIA and NIA are electron acceptors. It is noteworthy that the magnitude of  $\Delta N$ 's absolute value is not connected with inhibition efficiency.

AIA-2H<sup>+</sup> and NIA-H<sup>+</sup> were placed in a simulation box parallel with or perpendicular to the Fe(110) surface. The simulation results showed that both AIA-2H<sup>+</sup> and NIA-H<sup>+</sup> tended to adsorb in

parallel on the Fe(110) surface, as shown in Figure 7. Namely, the indazole and aromatic rings were the adsorption sites, which was in agreement with previous reports. Besides, all the hydrogen atoms upturning after adsorption may be due to the hybridization between Fe and heavy atoms. The AIA molecule is possibly a more efficient inhibitor because of its more negative adsorption energy ( $-4.65$  eV) than NIA ( $-4.05$  eV). This is consistent with the analysis of the electrochemical measurements.

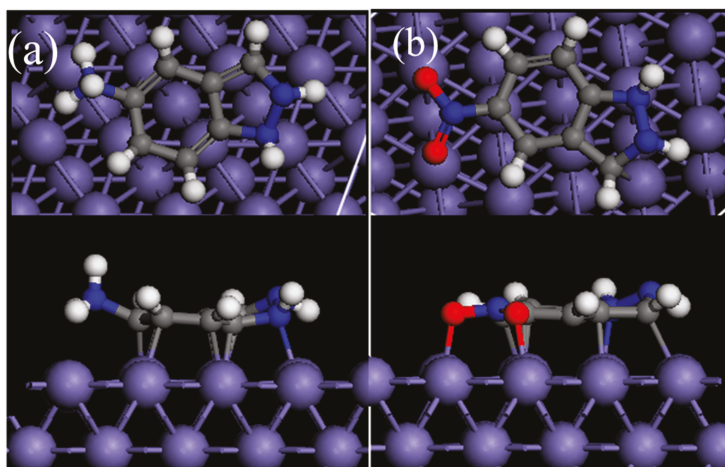


**Figure 7.** Stable adsorption configurations (side and top view) of (a) AIA-2H<sup>+</sup> and (b) NIA-H<sup>+</sup> molecules on the Fe(110) surface.

Figure 8 shows the projected density states of AIA-2H<sup>+</sup> and NIA-H<sup>+</sup> before and after adsorbing on the Fe(110) surface. By comparing these with the isolate inhibitors, the p orbitals of the adsorbed inhibitors almost disappear, revealing the strong interaction between AIA or NIA and the Fe(110) surface [43]. This is consistent with the inhibition efficiencies obtained by experiments.

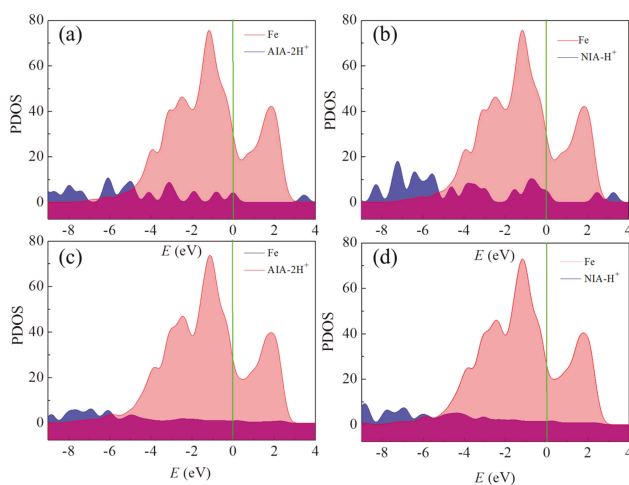


**Figure 8.** Density states projected of (a,c) AIA-2H<sup>+</sup> and (b,d) NIA-H<sup>+</sup> molecules before and after adsorbing on the Fe(110) surface.

#### 4. Conclusions

In this study, two indazole derivatives, AIA and NIA, were proved to be excellent corrosion inhibitors for carbon steel in 1 M HCl. The inhibition performance was tested by electrochemical methods. Theoretical calculations were also performed to reveal the inhibition mechanism of AIA and NIA. The detailed results are as follows:

- (1) The results of electrochemical tests indicated that AIA and NIA are efficient inhibitors for carbon steel in 1M HCl. The inhibition efficiency increased with increasing concentrations of the inhibitors, and the optimal concentration of AIA and NIA is 2 mM. By comparison, the AIA exhibits better inhibition performance than NIA.
- (2) The values of the charge transfer resistance increased in the presence of AIA and NIA in EIS tests, indicating that they can protect steel from corrosion by forming a robust protective film. Additionally, the Tafel plots illustrated that both are mixed-type inhibitors.
- (3) The results of theoretical calculations explained that the protective effect was due to the electrostatic forces between the AIA-2H<sup>+</sup> (or NIA-H<sup>+</sup>) and electronegative surface.

**Author Contributions:** S.Z. and L.G. proposed the concept and were involved in the design of the experiments. S.X. and L.F. performed the experimental work and wrote the main manuscript text. S.X. and B.T. evaluated the inhibition performance using theoretical calculations. All authors were involved in the drafting, revision and approval of the manuscript.

**Funding:** This research was supported by National Natural Science Foundation of China (21706195, 21878029), Science and Technology Program of Guizhou Province (QKHJC2016-1149), Guizhou Provincial Department of Education Fundation (QJHKYZ2016-105).

**Conflicts of Interest:** The authors declare that the research was conducted in the absence of any commercial or financial relationships that could be construed as a potential conflict of interest.

#### References

1. Feng, L.; Zhang, S.; Qiang, Y.; Xu, S.; Tan, B.; Chen, S. The synergistic corrosion inhibition study of different chain lengths ionic liquids as green inhibitors for X70 steel in acidic medium. *Mater. Chem. Phys.* **2018**, *215*, 229–241. [[CrossRef](#)]
2. Guo, L.; Zhu, S.; Li, W.; Zhang, S. Electrochemical and Quantum Chemical Assessment of 2-Aminothiazole as Inhibitor for Carbon Steel in Sulfuric Acid Solution. *Asian J. Chem.* **2015**, *27*, 2917–2923. [[CrossRef](#)]
3. Tan, B.C.; Zhang, S.T.; Liu, H.Y.; Guo, Y.W.; Qiang, Y.J.; Li, W.P.; Guo, L.; Xu, C.L.; Chen, S.J. Corrosion inhibition of X65 steel in sulfuric acid by two food flavorants 2-isobutylthiazole and 1-(1,3-Thiazol-2-yl) ethanone as the green environmental corrosion inhibitors: Combination of experimental and theoretical researches. *J. Colloid Interface Sci.* **2019**, *538*, 519–529. [[CrossRef](#)] [[PubMed](#)]
4. Tan, J.H.; Guo, L.; Lv, T.M.; Zhang, S.T. Experimental and Computational Evaluation of 3-indolebutyric Acid as a Corrosion Inhibitor for Mild Steel in Sulfuric Acid Solution. *Int. J. Electrochem. Sci.* **2015**, *10*, 823–837.
5. Zhang, S.T.; Tao, Z.H.; Liao, S.G.; Wu, F.J. Substitutional adsorption isotherms and corrosion inhibitive properties of some oxadiazol-triazole derivative in acidic solution. *Corros. Sci.* **2010**, *52*, 3126–3132. [[CrossRef](#)]
6. Zheng, X.W.; Zhang, S.T.; Li, W.P.; Yin, L.L.; He, J.H.; Wu, J.F. Investigation of 1-butyl-3-methyl-1H-benzimidazolium iodide as inhibitor for mild steel in sulfuric acid solution. *Corros. Sci.* **2014**, *80*, 383–392. [[CrossRef](#)]
7. Qiang, Y.J.; Zhang, S.T.; Xu, S.Y.; Yin, L.L. The effect of 5-nitroindazole as an inhibitor for the corrosion of copper in a 3.0% NaCl solution. *RSC Adv.* **2015**, *5*, 63866–63873. [[CrossRef](#)]
8. Qiang, Y.; Zhang, S.; Xiang, Q.; Tan, B.; Li, W.; Chen, S.; Guo, L. Halogeno-substituted indazoles against copper corrosion in industrial pickling process: A combined electrochemical, morphological and theoretical approach. *RSC Adv.* **2018**, *8*, 38860–38871. [[CrossRef](#)]
9. Qiang, Y.; Zhang, S.; Yan, S.; Zou, X.; Chen, S. Three indazole derivatives as corrosion inhibitors of copper in a neutral chloride solution. *Corros. Sci.* **2017**, *126*, 295–304. [[CrossRef](#)]
10. Kokalj, A. Formation and structure of inhibitive molecular film of imidazole on iron surface. *Corros. Sci.* **2013**, *68*, 195–203. [[CrossRef](#)]

11. Kokalj, A.; Peljhan, S. Density Functional Theory Study of ATA, BTAH, and BTAOH as Copper Corrosion Inhibitors: Adsorption onto Cu(111) from Gas Phase. *Langmuir* **2010**, *26*, 14582–14593. [[CrossRef](#)]
12. Kokalj, A.; Peljhan, S.; Koller, J. The Effect of Surface Geometry of Copper on Dehydrogenation of Benzotriazole. Part II. *J. Phys. Chem. C* **2014**, *118*, 944–954. [[CrossRef](#)]
13. Tan, B.; Zhang, S.; Qiang, Y.; Guo, L.; Feng, L.; Liao, C.; Xu, Y.; Chen, S. A combined experimental and theoretical study of the inhibition effect of three disulfide-based flavouring agents for copper corrosion in 0.5 M sulfuric acid. *J. Colloid Interface Sci.* **2018**, *526*, 268–280. [[CrossRef](#)]
14. Wang, J. The Inhibition Effect of a Novel Mannich Base on the Corrosion of A3 Mild Steel in 1.0 M Hydrochloric Acid Solution. *Int. J. Electrochem. Sci.* **2016**, *11*, 2621–2637. [[CrossRef](#)]
15. Yadav, M.; Gope, L.; Kumari, N.; Yadav, P. Corrosion inhibition performance of pyranopyrazole derivatives for mild steel in HCl solution: Gravimetric, electrochemical and DFT studies. *J. Mol. Liq.* **2016**, *216*, 78–86. [[CrossRef](#)]
16. Tao, Z.H.; Zhang, S.T.; Li, W.H.; Hou, B.R. Adsorption and Inhibitory Mechanism of 1H-1,2,4-Triazol-1-yl-methyl-2-(4-chlorophenoxy) Acetate on Corrosion of Mild Steel in Acidic Solution. *Ind. Eng. Chem. Res.* **2011**, *50*, 6082–6088. [[CrossRef](#)]
17. Zhang, J. Inhibition Effect and Adsorption Behavior of Two Imidazolium-based Ionic Liquids on X70 Steel in Sulfuric Acid Solution. *Int. J. Electrochem. Sci.* **2018**, *13*, 8645–8656. [[CrossRef](#)]
18. Ukpong, I.; Bangboye, O.; Soriyan, O. Synergistic Inhibition of Mild Steel Corrosion in Seawater and Acidic Medium by Cathodic Protection and *Monodora myristica* Using Zinc Anode. *Int. J. Corros.* **2018**, *2018*, 1–8. [[CrossRef](#)]
19. Kalaiselvi, K.; Chung, I.-M.; Kim, S.-H.; Prabakaran, M. Corrosion resistance of mild steel in sulphuric acid solution by *Coreopsis tinctoria* extract: electrochemical and surface studies. *Anti Corros. Methods Mater.* **2018**, *65*, 408–416. [[CrossRef](#)]
20. Paramasivam, S. Corrosion Inhibition of Mild Steel in Hydrochloric Acid using 4-(pyridin-2-yl)-N-p-tolylpiperazine-1-carboxamide. *Int. J. Electrochem. Sci.* **2016**, *11*, 3393–3414. [[CrossRef](#)]
21. Ma, X.; Jiang, X.; Xia, S.; Shan, M.; Li, X.; Yu, L.; Tang, Q. New corrosion inhibitor acrylamide methyl ether for mild steel in 1 M HCl. *Appl. Surf. Sci.* **2016**, *371*, 248–257. [[CrossRef](#)]
22. Tasic, Z.Z.; Mihajlovic, M.B.P.; Radovanovic, M.B.; Antonijevic, M.M. Effect of gelatine and 5-methyl-1H-benzotriazole on corrosion behaviour of copper in sulphuric acid containing Cl<sup>-</sup> ions. *J. Adhes. Sci. Technol.* **2017**, *31*, 2592–2610. [[CrossRef](#)]
23. Jiang, L.; Ma, H.; Zhang, J.; Lu, Y.; Lu, H.; Meng, X. Electro Polymerization of Polypyrrole Coatings Doped with Different Proton Acids for Corrosion Protection of 304 Stainless Steel. *MATEC Web Conf.* **2017**, *109*, 03007. [[CrossRef](#)]
24. El-Sayed Shehata, O. Effect of acetamide derivative and its Mn-complex as corrosion inhibitor for mild steel in sulphuric acid. *Egypt. J. Chem.* **2017**, *60*, 243–259. [[CrossRef](#)]
25. Loto, R.T.; Loto, C.A.; Fedotova, T. Electrochemical studies of mild steel corrosion inhibition in sulfuric acid chloride by aniline. *Res. Chem. Int.* **2014**, *40*, 1501–1516. [[CrossRef](#)]
26. Tamilarasan, R.; Sreekanth, A. Spectroscopic and DFT investigations on the corrosion inhibition behavior of tris(5-methyl-2-thioxo-1,3,4-thiadiazole) borate on high carbon steel and aluminium in HCl media. *RSC Adv.* **2013**, *3*, 23681–23691. [[CrossRef](#)]
27. Tang, Y.-M.; Yang, W.-Z.; Yin, X.-S.; Liu, Y.; Wan, R.; Wang, J.-T. Phenyl-substituted amino thiadiazoles as corrosion inhibitors for copper in 0.5 M H<sub>2</sub>SO<sub>4</sub>. *Mater. Chem. Phys.* **2009**, *116*, 479–483. [[CrossRef](#)]
28. Kovacevic, N.; Kokalj, A. DFT Study of Interaction of Azoles with Cu(111) and Al(111) Surfaces: Role of Azole Nitrogen Atoms and Dipole–Dipole Interactions. *J. Phys. Chem. C* **2011**, *115*, 24189–24197. [[CrossRef](#)]
29. Loto, R.T.; Loto, C.A. Pitting corrosion inhibition of type 304 austenitic stainless steel by 2-amino-5-ethyl-1,3,4-thiadiazole in dilute sulphuric acid. *Prot. Met. Phys. Chem. Surfaces* **2015**, *51*, 693–700. [[CrossRef](#)]
30. Bensabra, H.; Azzouz, N.; Chopart, J.P. Effect of zinc phosphating treatment on the pitting corrosion resistance of steel reinforcement. *Rev. De Metall. Cah. D Inf. Technol.* **2013**, *110*, 153–163.
31. Kokalj, A. On the HSAB based estimate of charge transfer between adsorbates and metal surfaces. *Chem. Phys.* **2012**, *393*, 1–12. [[CrossRef](#)]
32. Kokalj, A.; Peljhan, S.; Finsgar, M.; Milosev, I. What Determines the Inhibition Effectiveness of ATA, BTAH, and BTAOH Corrosion Inhibitors on Copper? *J. Am. Chem. Soc.* **2010**, *132*, 16657–16668.

33. Obot, I.B.; Obi-Egbedi, N. 2,3-Diphenylbenzoquinoxaline: A new corrosion inhibitor for mild steel in sulphuric acid. *Corros. Sci.* **2010**, *52*, 282–285. [[CrossRef](#)]
34. Umoren, S.; Obot, I.B.; Gasem, Z.; Odewunmi, N.A. Experimental and Theoretical Studies of Red Apple Fruit Extract as Green Corrosion Inhibitor for Mild Steel in HCl Solution. *J. Dispers. Sci. Technol.* **2015**, *36*, 789–802. [[CrossRef](#)]
35. Umoren, S.A.; Obot, I.B.; Madhankumar, A.; Gasem, Z.M. Effect of degree of hydrolysis of polyvinyl alcohol on the corrosion inhibition of steel: Theoretical and experimental studies. *J. Adhes. Sci. Technol.* **2015**, *29*, 271–295. [[CrossRef](#)]
36. Ren, X.L.; Xu, S.Y.; Chen, S.Y.; Chen, N.X.; Zhang, S.T. Experimental and theoretical studies of triisopropanolamine as an inhibitor for aluminum alloy in 3% NaCl solution. *RSC Adv.* **2015**, *5*, 101693–101700. [[CrossRef](#)]
37. Pearson, R.G. Hard and Soft Acids and Bases. *J. Am. Chem. Soc.* **1963**, *85*, 3533–3539. [[CrossRef](#)]
38. Pearson, R.G. Absolute electronegativity and hardness: Application to inorganic chemistry. *Inorg. Chem.* **1988**, *27*, 734–740. [[CrossRef](#)]
39. Obot, I.B.; Kaya, S.; Kaya, C.; Tuzun, B. Theoretical evaluation of triazine derivatives as steel corrosion inhibitors: DFT and Monte Carlo simulation approaches. *Res. Chem. Intermed.* **2016**, *42*, 4963–4983. [[CrossRef](#)]
40. Khadraoui, A.; Khelifa, A.; Hadjmeli, M.; Mehdaoui, R.; Hachama, K.; Tidu, A.; Azari, Z.; Obot, I.; Zarrouk, A. Extraction, characterization and anti-corrosion activity of Mentha pulegium oil: Weight loss, electrochemical, thermodynamic and surface studies. *J. Mol. Liq.* **2016**, *216*, 724–731. [[CrossRef](#)]
41. Belghiti, M.E.; Karzazi, Y.; Dafali, A.; Obot, I.B.; Ebenso, E.E.; Emran, K.M.; Bahadur, I.; Hammouti, B.; Bentiss, F. Anti-corrosive properties of 4-amino-3,5-bis(disubstituted)-1,2,4-triazole derivatives on mild steel corrosion in 2 M H<sub>3</sub>PO<sub>4</sub> solution: Experimental and theoretical studies. *J. Mol. Liq.* **2016**, *216*, 874–886. [[CrossRef](#)]
42. Obot, I.B.; Gasem, Z.M.; Umoren, S.A. Understanding the Mechanism of 2-mercaptobenzimidazole Adsorption on Fe(110), Cu(111) and Al(111) Surfaces: DFT and Molecular Dynamics Simulations Approaches. *Int. J. Electrochem. Sci.* **2014**, *9*, 2367–2378.
43. Kovacevic, N.; Milosev, I.; Kokalj, A. The roles of mercapto, benzene, and methyl groups in the corrosion inhibition of imidazoles on copper: II. Inhibitor-copper bonding. *Corros. Sci.* **2015**, *98*, 457–470.



© 2019 by the authors. Licensee MDPI, Basel, Switzerland. This article is an open access article distributed under the terms and conditions of the Creative Commons Attribution (CC BY) license (<http://creativecommons.org/licenses/by/4.0/>).



Article

# Mannich Base as Corrosion Inhibitors for N80 Steel in a CO<sub>2</sub> Saturated Solution Containing 3 wt % NaCl

Mingjin Tang <sup>1,\*</sup>, Jianbo Li <sup>1,\*</sup>, Zhida Li <sup>2</sup>, Luoping Fu <sup>1</sup>, Bo Zeng <sup>1</sup> and Jie Lv <sup>1</sup>

<sup>1</sup> School of Chemistry and Chemical Engineering, Southwest Petroleum University, Chengdu 610500, China; fuluoping@outlook.com (L.F.); zengbo\_2014@icloud.com (B.Z.); jlv6@me.com (J.L.)

<sup>2</sup> Faculty of Engineering, Computer & Mathematical Sciences, The University of Adelaide, Adelaide, SA 5005, Australia; lzd038@163.com

\* Correspondence: tangmingjin@outlook.com (M.T.); ljb0418@163.com (J.L.)

Received: 14 December 2018; Accepted: 30 January 2019; Published: 1 February 2019

**Abstract:** In this paper, a corrosion inhibitor containing nitrogen atoms and a conjugated  $\pi$  bond was synthesised, and its final product synthesised by the optimal conditions of the orthogonal test results is named multi-mannich base (MBT). The corrosion inhibition effect on the N80 steel sheet of the corrosion inhibitor was evaluated in a CO<sub>2</sub> saturated solution containing 3 wt % NaCl; the corrosion rate was 0.0446 mm/a and the corrosion inhibition rate was 90.4%. Through electrochemical and adsorption theory study, MBT is a mixed corrosion inhibitor that mainly shows cathode suppression capacity. The adsorption of MBT on the surface of the steel sheet follows the Langmuir adsorption isotherm; it can be spontaneously adsorbed on the surface of the N80 steel sheet, which has a good corrosion inhibition effect. The surface of the N80 steel sheet was microscopically characterised by atomic force microscope (AFM). It can be seen from the results that the N80 steel sheet with MBT added is significantly different from the blank control group; the surface of the steel sheet is relatively smooth, indicating that MBT forms an effective protective film on the surface of N80 steel, which inhibits the steel sheet.

**Keywords:** corrosion inhibitor; electrochemical; AFM; CO<sub>2</sub> corrosion

## 1. Introduction

To improve oil and gas recovery, CO<sub>2</sub> injection is used in the exploitation of oil, natural gas, coalbed methane and shale gas [1]. However, CO<sub>2</sub> injection is accompanied by CO<sub>2</sub> corrosion [2]. Corrosion will decrease the mining yield, resulting in oil wells failure, shutting down and even cause safety accidents, which will have a serious impact on the development of the oilfield and the economic benefits of the market [3–6]. The most common and effective way to control corrosion is to use chemical additives that reduce corrosion at very small dosages [7,8]. In recent years, various corrosion inhibitors have been successfully applied to the industry, and the corrosion has been controlled obviously and effectively [9,10].

So far, phosphorus and nitrogen-containing compounds have been widely used as corrosion inhibitors, including organic phosphorus, nitrogen-containing compounds and phosphorus-containing organic water-soluble polymers [11]. Phosphorus-containing corrosion inhibitors have excellent corrosion inhibition properties. However, they have some fatal defects; for example, phosphorus compounds are difficult to degrade in water and usually lead to eutrophication. The widespread use of this chemical may cause oxygen deficiency in the water, which leads to the death of aquatic organisms [12]. Therefore, in the last few years, the industry has not only required the effectiveness of chemical compounds but also their safety [13]. Today, chemical emissions are strictly controlled through legislation. Therefore, finding an alternative solution, namely the effective control of corrosion



by green corrosion inhibitors, is the most important research direction at the moment. Chemical products identified as “green” are based on criteria: non-toxic and degradable [14,15].

In this paper, salicylaldehyde, diethylenetriamine, formaldehyde and acetone were selected to synthesise corrosion inhibitor MBT containing nitrogen atoms with lone pairs and a conjugated  $\pi$  bond. The structure was characterised by infrared radiation spectroscopy (IR) and nuclear magnetic resonance spectroscopy ( $^1\text{H NMR}$ ). The product was evaluated for corrosion inhibition by a weight loss method. Finally, the mechanism of corrosion inhibition was studied by atomic force microscopy (AFM) and electrochemical methods.

## 2. Experiment

### 2.1. Main Experimental Materials and Instruments

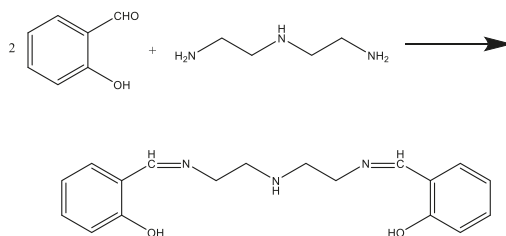
Salicylaldehyde  $\text{C}_7\text{H}_6\text{O}_2$ , diethylenetriamine  $\text{C}_4\text{H}_{13}\text{N}_3$ , ethanol  $\text{C}_2\text{H}_6\text{O}$ , acetone  $\text{C}_3\text{H}_6\text{O}$ , formaldehyde  $\text{HCHO}$ : AR, Chengdu Kelong Chemical Reagent Factory, Chengdu, China.

WQF-520 infrared spectrometer: Beijing Ruili Analytical Instrument (Group) Co. Ltd., Beijing, China; Bruker AVANCE III HD 400 nuclear magnetic resonance spectrometer: Bruker Corporation, Billerica, MA, USA; IVICMSTAT electrochemical workstation: Ivium Technologies, Eindhoven, The Netherlands; SPM-9600 atomic force microscope: Shimadzu Corporation, Kyoto, Japan.

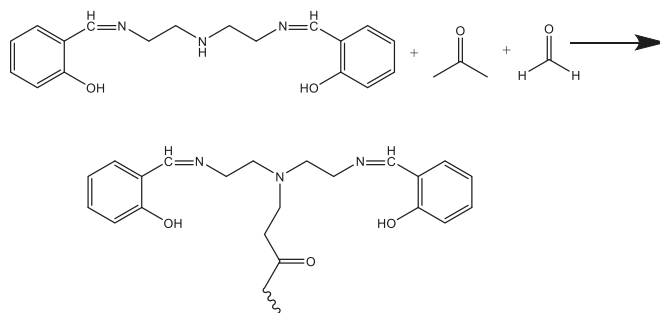
### 2.2. Synthesis of Corrosion Inhibitor

First, in a three-necked flask equipped with a condenser and a thermometer, 20 mL of ethanol was added as a solvent. When the reactant reached a certain temperature, a certain amount of salicylaldehyde and diethylenetriamine were added in a certain ratio. After a period of reaction, the reaction was terminated to give the product intermediate mannich base (MB-1).

Then, a certain amount of acetone and formaldehyde were added in order, being kept at a constant reaction temperature for a certain period, and then the reaction was terminated to obtain the target product mannich base (MB-2). The synthesis of MB-1 and MB-2 is shown in Schemes 1 and 2.



Scheme 1. The synthesis of MB-1.



Scheme 2. The synthesis of MB-2.

### 2.3. Weight Loss Measurements

A hanging N80 steel test piece (50.00 mm × 13.00 mm × 1.50 mm: length, width, height) was ground with sand paper to give a surface with a uniform metal luster [16]. To calculate the superficial area of the test piece, the carbon steel was deoiled with putty powder and then immersed in ethanol for 5 min, dried with an air blower, wrapped in filter paper, maintained in a dryer and weighed to 0.0001 g.

Then the test piece was immersed in a bottle containing 500 mL of CO<sub>2</sub> saturated solution and 3 wt % NaCl saline water with and without inhibitors at 70 °C for 72 h. According to the weight loss of each test piece and Equations (1) and (2), the rate of corrosion of the test piece and efficiency of the corrosion inhibitor at different concentrations could be calculated [4].

$$v = \frac{8.76 \times 10^4 \times \Delta m}{\rho A t}, \quad (1)$$

where  $v$ ,  $\Delta m$ ,  $\rho$ ,  $A$  and  $t$  are the corrosion rate (mm/a), weight loss (g), test sample density (g/cm<sup>3</sup>), exposed sample area (cm<sup>2</sup>) and immersion time (h), respectively. The inhibition efficiency ( $\eta$ ) of the inhibitor was calculated by Equation (2):

$$\eta(\%) = \left(1 - \frac{v}{v^0}\right) \times 100, \quad (2)$$

where  $v$  and  $v^0$  are the corrosion rates calculated from the weight loss with and without the inhibitor.

### 2.4. Electrochemical Measurements

The potentiodynamic polarisation curve method was used to measure the Tafel polarisation curve. When the self-corrosion potential ( $E_c$ ) of the system was stable, the cathode and anode scanning was from 250 mV to 300 mV. The polarisation curves of the N80 steel sheets with different concentrations of corrosion inhibitors were measured [4]. According to the relevant theory of electrochemistry, the corrosion inhibition rate ( $\eta$ ) of the corrosion process can be calculated by Equation (3) [17]:

$$\eta = \frac{i^0 - i}{i^0} \times 100, \quad (3)$$

where  $i^0$  and  $i$  are the corrosion current densities without and with the inhibitor, respectively.

The electrochemical impedance spectroscopy (EIS, Ivium Technologies, Eindhoven, The Netherlands) experiments were performed by applying a sinusoidal voltage signal of 10 mV; the frequency range was 0.01–10<sup>−5</sup> Hz; and the alternating current excitation signal amplitude was 10 mV. Impedance diagrams of the N80 steel sheets with different concentrations of corrosion inhibitors were measured. The inhibition efficiency ( $\eta$ ) was determined from the EIS data using Equation (4):

$$\eta = \frac{R_t - R_t^0}{R_t} \times 100, \quad (4)$$

where  $R_t$  and  $R_t^0$  are the charge transfer resistance in the absence and presence of inhibitors, respectively.

### 2.5. AFM Analysis

Atomic force microscopy (AFM, Shimadzu Corporation, Kyoto, Japan) was used for characterizing the surface morphology and measuring surface roughness in a CO<sub>2</sub> saturated solution containing 3 wt % NaCl without and with corrosion inhibitors. The two- and three-dimensional AFM images of steel specimens were taken in the range from 0 to 5 μm at room temperature [18].

### 3. Results and Discussion

#### 3.1. IR Characterisation Results

The IR spectrum of MB-2 is shown in Figure 1. It is demonstrated that the stretching vibration peak attributed to the carbonyl group in salicylaldehyde does not appear at  $1740\text{ cm}^{-1}$  to  $1720\text{ cm}^{-1}$ . The stretching vibration peak attributed to the  $\text{C}=\text{N}$  bond at  $1644\text{ cm}^{-1}$  indicates that the salicylaldehyde reacts with diethylenetriamine to form a compound containing  $\text{C}=\text{N}$  and the aldehyde group disappears. The absorption peak at  $3457\text{ cm}^{-1}$  and  $1270\text{ cm}^{-1}$  is attributed to the stretching vibration of the  $\text{O}-\text{H}$  bond and  $\text{C}-\text{O}$  bond of phenol; the absorption peak at  $2989\text{ cm}^{-1}$  and  $2923\text{ cm}^{-1}$  is attributed to the stretching vibration of methyl ( $\text{CH}_3$ ) and methylene ( $\text{CH}_2$ ); the bending vibration of the  $\text{N}-\text{H}$  bond belonging to the secondary amine did not occur at  $1580\text{ cm}^{-1}$  to  $1490\text{ cm}^{-1}$ , indicating that the hydrogen on the secondary amine reacted with acetone and formaldehyde, and the secondary amine disappeared into a tertiary amine; the absorption peak at  $1718\text{ cm}^{-1}$  is attributed to the stretching vibration of  $\text{C}=\text{O}$ . IR characterization results showed that the synthesized MB-2 was the target product.

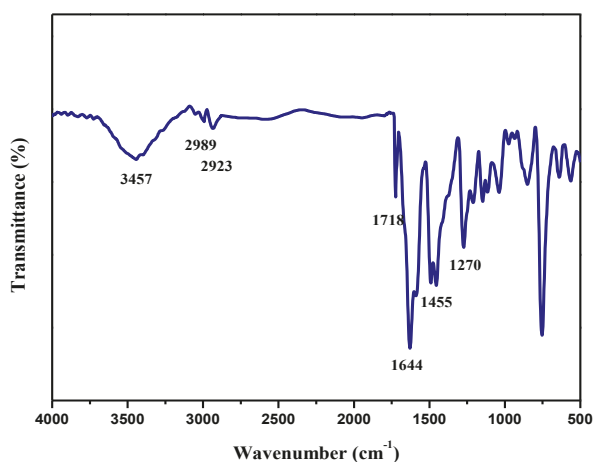


Figure 1. IR spectrum of MB-2.

#### 3.2. Optimization of MB-2 Synthesis Conditions

Through orthogonal experiments, the three-factor four-level  $L_{16}(4^3)$  orthogonal table was selected to investigate the influencing factors of MB-2 synthesis, including the ratio of reactants, reaction time and reaction temperature. Considering that both methyl groups of acetone react, the amount of acetone is fixed to adjust the ratio of MB-2 to formaldehyde. According to the product synthesised by the orthogonal experiment, when the amount was  $200\text{ mg/L}$ , the corrosion inhibition performance was evaluated in a  $\text{CO}_2$  saturated solution containing  $3\text{ wt \% NaCl}$ .

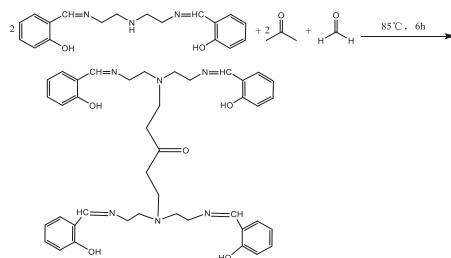
The experimental factors and levels are shown in Table 1. The results of orthogonal experiments are shown in Table 2. It can be seen from Table 2 that the optimal reaction conditions for the synthesis of MB-2 are: reaction temperature  $85\text{ }^\circ\text{C}$ ; reactant ration(MB-2):n(formaldehyde):n(acetone) = 2:2:1; and reaction time 6 h. The final product synthesised by the optimal conditions of the orthogonal test results is named MBT, and the reaction equation for the synthesis is shown in Scheme 3.

**Table 1.** Experimental factors and levels.

Level	A n(MB-2):n(HCHO):n(CH <sub>3</sub> COCH <sub>3</sub> )	B Temperature/°C	C Time (h)
1	1:1:1	70	4
2	1.5:1.5:1	75	5
3	2:2:1	80	6
4	2.5:2.5:1	85	7

**Table 2.** Orthogonal experimental results.

NO.	A	B	C	Corrosion Rate (mm/a)
1	1	1	1	0.180
2	1	2	2	0.143
3	1	3	3	0.076
4	1	4	4	0.059
5	2	1	2	0.135
6	2	2	1	0.139
7	2	3	4	0.068
8	2	4	3	0.056
9	3	1	3	0.098
10	3	2	4	0.073
11	3	3	1	0.102
12	3	4	2	0.067
13	4	1	4	0.120
14	4	2	3	0.084
15	4	3	2	0.079
16	4	4	1	0.106
I	289.2	259.8	303.2	
II	296.7	302.9	301.0	
III	341.0	338.7	307.8	
IV	308.6	334.2	322.7	
K <sub>1</sub>	0.115	0.133	0.132	
K <sub>2</sub>	0.100	0.110	0.106	
K <sub>3</sub>	0.085	0.081	0.079	
K <sub>4</sub>	0.097	0.072	0.080	
R	0.03	0.061	0.053	
Effect order			B > C > A	
Optimal level	A <sub>3</sub>	B <sub>4</sub>	C <sub>3</sub>	

**Scheme 3.** The synthesis of MBT.

### 3.3. <sup>1</sup>H NMR Analysis

The <sup>1</sup>H NMR spectrum of MBT is shown in Figure 2. It can be seen from Figure 2 that the absorption peak at chemical shift  $\delta = 12.00\sim 11.00$  is attributed to  $-\text{OH}$ ; the absorption peak at  $\delta = 8.56\sim 8.45$  is attributed to  $-\text{CH}=\text{N}$ ; the absorption peak at  $\delta = 7.36\sim 6.79$  is attributed to benzene ( $-\text{CH}$ );  $\delta = 3.68\sim 3.65$ , 3.02, the absorption peak at 2.63 is attributed to  $-\text{CH}_2$  at different positions; and the absorption peak at  $\delta = 2.5$  belongs to the solvent peak of Dimethyl sulfoxide (DMSO) and is

characterized by IR. Combined with IR characterisation, the results indicate that MBT is the target product of synthesis.

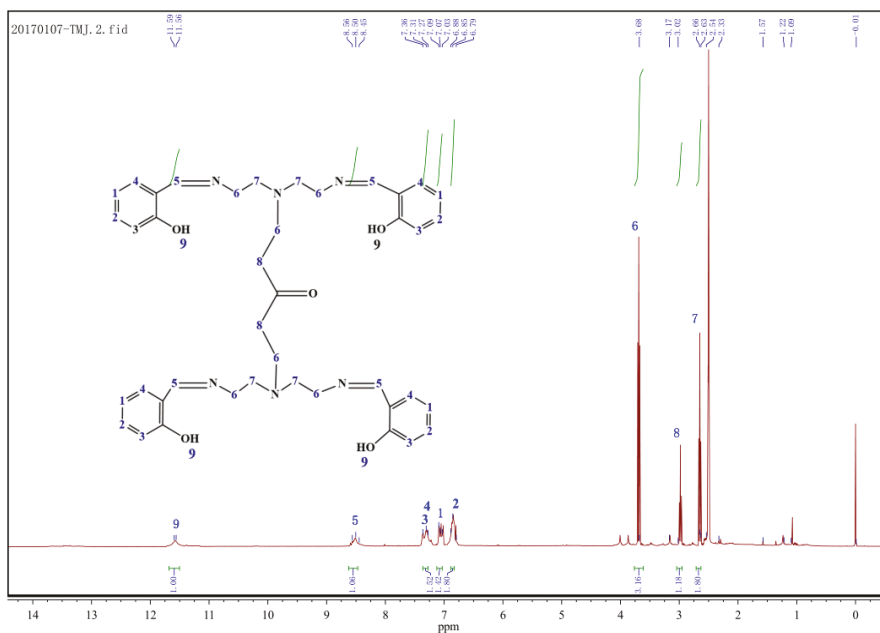


Figure 2. <sup>1</sup>H NMR spectrum of MBT.

### 3.4. Concentration Effect of MBT on Corrosion Inhibition

The corrosion inhibition performance of the corrosion inhibitor MBT was evaluated by the static weight-loss method. Test conditions: temperature 70 °C, pH = 5.6, ρ(NaCl) = 30 g/L, and constant temperature water bath 72 h. The corrosion inhibition effect of MBT on a N80 steel sheet in a CO<sub>2</sub> saturated solution containing 3 wt % NaCl was investigated under different dosages. The result is shown in Figure 3.

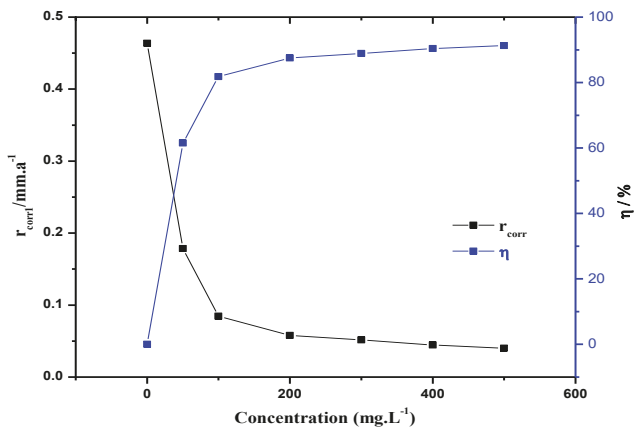


Figure 3. Effect of the dosage of MBT on the corrosion rate and corrosion inhibition rate of the N80 steel sheet.

According to Figure 3, in the case of different dosages of MBT (0, 50, 100, 200, 300, 400, 500 mg/L), when the amount of MBT was 200 mg/L, the N80 steel sheet corrosion rate was 0.0579 mm/a. The corrosion rate of the steel sheet decreases with the increase of the corrosion inhibitor concentration, indicating that MBT can form an effective protective film on the metal surface. When the amount of corrosion inhibitor is 400 mg/L, the corrosion rate is 0.0446 mm/a, and the corrosion inhibition rate can reach 90.4%.

### 3.5. Temperature Effect of MBT on Corrosion Inhibition

In order to study the corrosion inhibitor for a CO<sub>2</sub> saturated solution containing 3 wt % NaCl, the corrosion inhibition effect at different temperatures (40, 50, 60, 70, 80, 90 °C), the dosage of corrosion inhibitor in this experiment is 400 mg/L, and the evaluation time 72 h.

As shown in Figure 4, the increasing temperature increases the corrosion rate in the absence ( $r_{\text{corr}0}$ ) and appearance of MBT solution ( $r_{\text{corr}1}$ ). This is because as the temperature increases, the adsorption capacity of the corrosion inhibitor decreases, the desorption capacity increases, and the corrosion rate of the steel sheet itself increases as the temperature is higher.

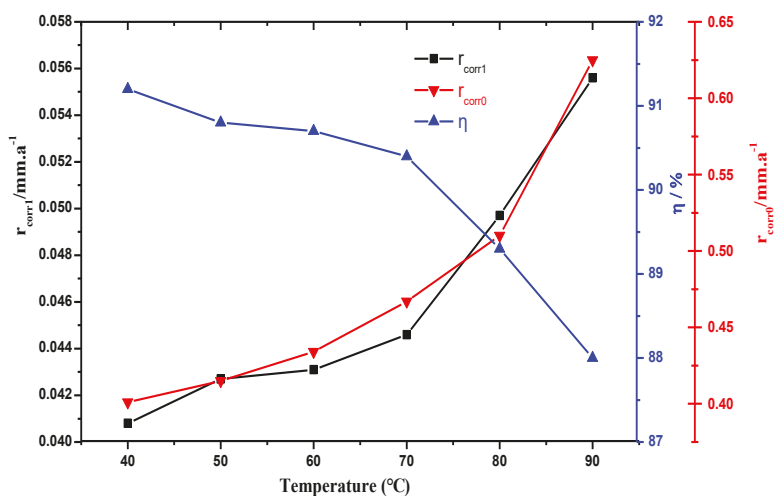


Figure 4. Evaluation of temperature on corrosion rate and corrosion inhibition rate.

### 3.6. Discussion on Corrosion Inhibition Mechanism

#### 3.6.1. Polarization Curve Data Analysis

The inhibition mechanism of MBT was studied by the Tafel polarization curve method. Different concentrations (0 mg/L, 50 mg/L, 100 mg/L, 200 mg/L, 300 mg/L) of MBT were added, and the corrosive medium was a CO<sub>2</sub> saturated solution containing 3 wt % NaCl at a temperature of 25 °C. The Tafel curve is shown in Figure 5.

It is shown in Figure 5 that when the different concentrations of MBT are added, the polarization curve moves downward as a whole, that is, the corrosion current density decreases. As the concentration of the corrosion inhibitor increases, the corrosion current density decreases. Since the corrosion current density is proportional to the corrosion rate, the concentration of the MBT increase made the corrosion rate drop, which is consistent with the results of the weight loss experiment. It can be seen from Figure 5, that after the addition of MBT, the polarization curves of the cathode and anode move in the direction of low corrosion current density, so MBT reacts to both the cathode and anode.

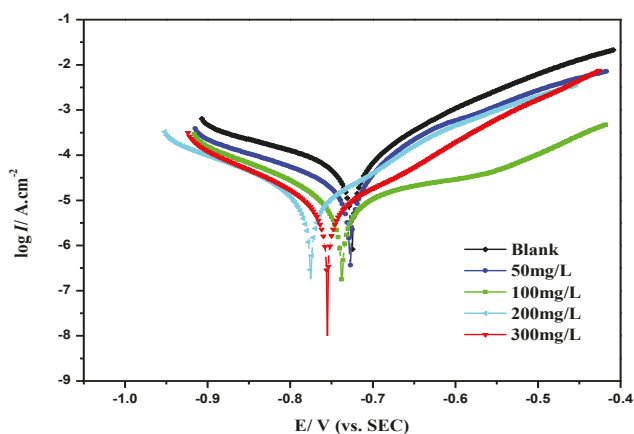


Figure 5. Tafel curve of N80 steel with different concentrations of MBT.

The corrosion potential ( $E_{corr}$ ), corrosion current density ( $I_{corr}$ ), Tafel slope ( $\beta_a$  and  $\beta_c$ ) and corrosion inhibition rate ( $\eta$ ) calculated by the equation are shown in Table 3. It can be seen in the table that the corrosion inhibitor MBT moves the self-corrosion potential of the N80 steel sheet negatively; it shows that the corrosion inhibitor blocks the cathode process, and the self-corrosion potential moves in the negative direction (fluctuating around 30 mV) [19,20], so MBT is a mixed type corrosion inhibitor mainly for suppressing the cathode.

Table 3. Electrochemical parameters of different MBT concentrations.

Inhibitor	Conc. (mg·L <sup>-1</sup> )	$E_{corr}$ (V)	$I_{corr}$ ( $\mu\text{A}\cdot\text{cm}^{-2}$ )	$B_a$ (mV·dec <sup>-1</sup> )	$B_c$ (mV·dec <sup>-1</sup> )	$\eta$ (%)
MBT	0	-0.725	60.99	10.21	5.11	-
	50	-0.727	26.10	9.86	5.98	57.2
	100	-0.737	12.62	5.59	7.58	79.3
	200	-0.775	10.06	12.06	7.23	83.5
	300	-0.755	7.99	9.74	8.07	86.9

### 3.6.2. Electrochemical Impedance Spectroscopy Data Analysis

In order to further study the corrosion inhibition mechanism of MBT on steel sheets, the impedance of the system was measured by an AC impedance method. Figure 6 is an impedance spectrum of MBT with different concentrations added.

It can be seen from Figure 6 that the Nyquist diagram of the blank sample and the added corrosion inhibitor is a set of capacitive reactance arcs with a semicircular shape; however, the impedance of the system changes significantly after adding different concentrations of MBT compared with the blank. In addition, the capacitive anti-arc increases with the increase of corrosion inhibitor concentration, and the Bode-modulus value and the phase angle Bode-phase angle increase obviously, indicating that the corrosion inhibitor can be adsorbed on the surface of the N80 steel sheet to increase the transmission resistance to corrosion of the steel sheet, thereby reducing the corrosion rate of the metal. The EIS diagram was fitted using ZSimpWin software (ZSimDemo3.30d), and the equivalent circuit was obtained as  $R(C(R(QR)))$ , as shown in Figure 7.

In Figure 7,  $R_s$  represents the solution resistance;  $R_{ct}$  represents the transfer resistance of the N80 steel sheet corrosion reaction charge;  $R_f$  and CPE represent the metal interface film resistance and constant phase element (CPE) to replace a double layer capacitance with a more accurate fit [21], the impedance of CPE was calculated following Equation (5); and  $C_{dl}$  represents the capacitance. The fitting parameters are shown in Table 4.

$$Z_{CPE} = \frac{1}{Y_0 j \omega^n}, \tag{5}$$

where  $Y_0$  is CPE constant;  $j$  is the imaginary number;  $\omega$  is the angular frequency; and  $n$  is the phase shift (which represents the deviation from ideal behavior).

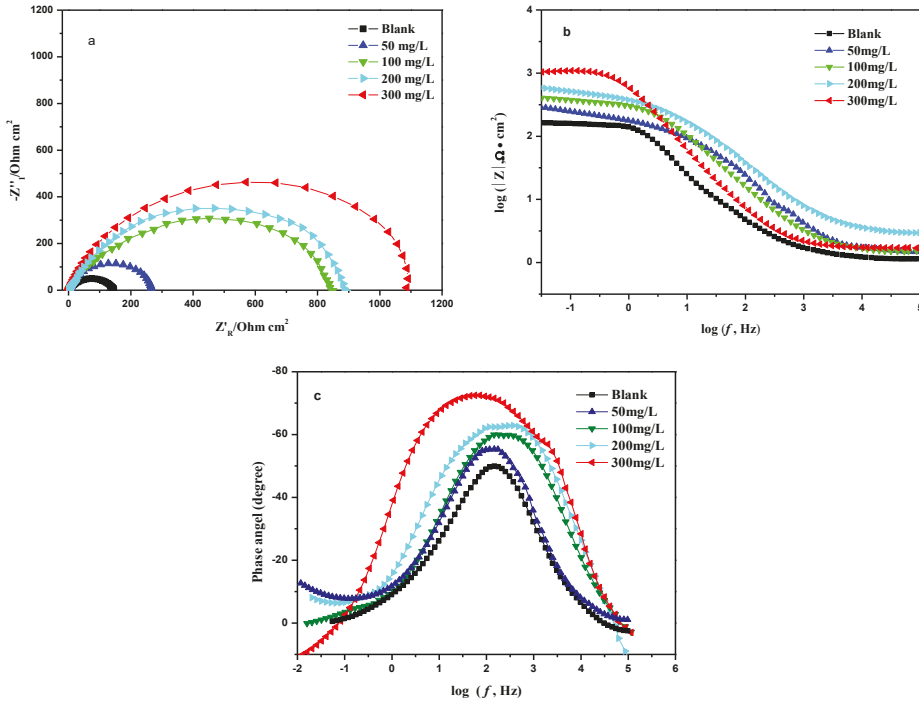


Figure 6. Nyquist (a), Bode-modulus (b) and Bode-phase angle (c) diagrams of N80 steel sheets with different concentrations of MBT.

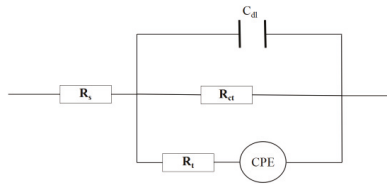


Figure 7. Fitting equivalent circuit diagram.

From the data analysis in Table 4, as the intrusion time of N80 steel increases, the charge transfer resistance  $R_{ct}$  and film resistance  $R_t$  in the different corrosion inhibitor concentration solutions increase with the concentration of the corrosion inhibitor; the compactness of  $R_t$  and MBT adsorption film formation is related to the thickness, which indirectly indicates that the MBT molecule is effectively adsorbed by the N80 steel sheet. The solution resistance  $R_s$  does not change much and is significantly smaller than the film resistance  $R_t$  and charge transfer resistance  $R_{ct}$ . Combined with the analysis of the Nyquist diagram, it is fully demonstrated that the corrosion inhibition effect is mainly absorbed by the corrosion inhibitor molecules on the metal surface, which changes the interface properties of the N80 steel surface and the electric double layer structure, thus achieving a good corrosion inhibition



effect [22]. The calculated corrosion inhibition effect is basically consistent with the results obtained by the above weight loss experiment and the polarization curve method.

**Table 4.** Electrochemical impedance spectroscopy fitting parameters of different concentrations of MBT.

Inhibitor	Conc. (mg/L)	$R_s$ $\Omega \cdot \text{cm}^2$	$C_{dl}$ $\mu\text{F} \cdot \text{cm}^{-2}$	$R_{ct}$ $\Omega \cdot \text{cm}^2$	CPE		$R_t$ ( $\Omega$ )	$\eta\%$
					$Y_0$ $\mu\text{S} \cdot \text{cm}^{-2} \cdot \text{s}^n$	n		
MBT	0	1.579	6.02	136.7	15.33	0.82	13.57	-
	50	4.507	13.96	255	8.83	0.69	23.56	46.4
	100	1.758	7.90	871.7	54.22	0.73	58.71	84.3
	200	1.571	12.13	941.2	53.71	0.67	37.77	85.5
	300	1.867	18.82	1020	10.92	0.61	42.47	86.6

### 3.7. MBT Adsorption Mode

The MBT molecule is adsorbed on the surface of the metal to form a dense adsorption film, which acts as a corrosion inhibitor, and the stronger the adsorption capacity of the molecule on the metal surface, the better the corrosion inhibition effect [23]. The adsorption of MBT molecules on the metal surface is based on the structure, spatial distribution of the groups in the MBT molecule and the surface morphology of the metal; the adsorption modes are Temkin, Langmuir, Frumkin and Freundlich.

The above four adsorption isotherms were used to fit the data obtained by the polarisation curve method and the impedance method. It was found to be in accordance with the Langmuir adsorption equation, and the Langmuir adsorption curve is shown in Figure 8.

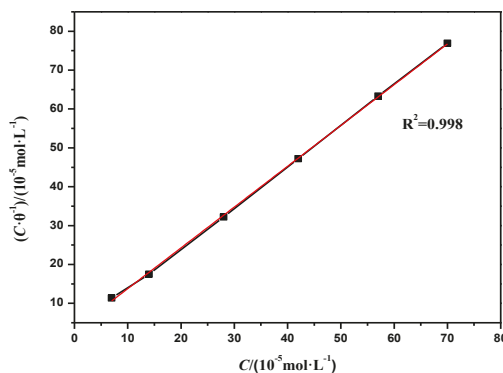


**Figure 8.** Langmuir isothermal adsorption curve of corrosion inhibitor MBT.

From Figure 8, it can be concluded that  $K_{ads} = 1.701 \times 10^4$  L/mol and  $R^2 = 0.998$ , indicating that  $C/\theta$  has a relatively good linear relationship with concentration  $C$ . The results show that at 70 °C, in a  $\text{CO}_2$  saturated solution containing 3 wt % NaCl, the adsorption of MBT on the surface of the N80 steel sheet follows the Langmuir isotherm adsorption. The formula for the adsorption free energy  $\Delta G_{ads}$  of the corrosion inhibitor MBT is as follows:

$$\Delta G_{ads} = -RT \ln(55.5K_{ads}), \quad (6)$$

Calculate  $\Delta G_{ads} = -39.25 \text{ kJ/mol} < 0$  according to the adsorption equilibrium constant  $K_{ads}$  and Equation (6), indicating that the corrosion inhibitor MBT is capable of spontaneous chemical adsorption on the N80 steel sheet, which has a good corrosion inhibition effect.

### 3.8. Corrosion Inhibition Surface Morphology Analysis

In order to study the corrosion inhibition ability of the corrosion inhibitor MBT, the surface of the N80 steel sheet was characterised by AFM. The N80 steel sheet was immersed with different concentrations of corrosion inhibitor MBT in a CO<sub>2</sub> saturated solution containing 3 wt % NaCl, and the water bath was kept at 70 °C for 72 h. The three-dimensional and planar topography of the N80 steel sheet surface is shown in Figure 9.

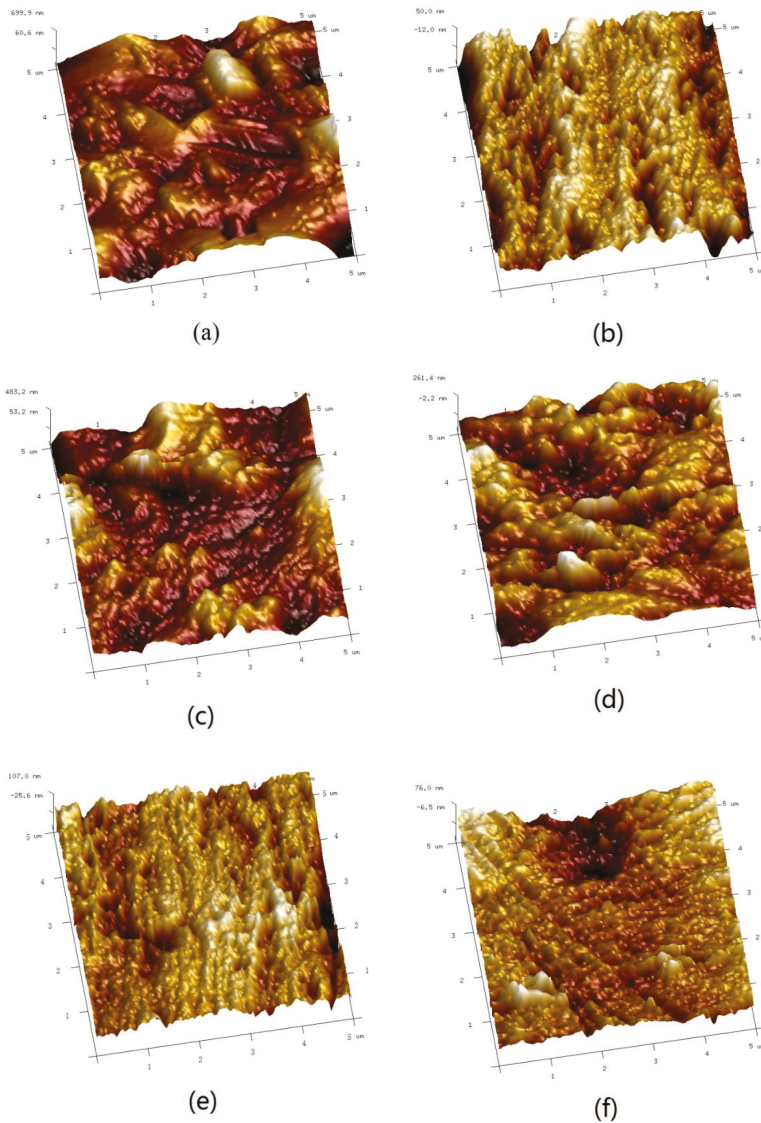


**Figure 9.** AFM three-dimensional image of N80 steel sheet: (a) blank sample; (b) initial uncorroded sample; (c–f) added 50 mg/L, 100 mg /L, 200 mg/L, 300 mg/L MBT.

Figure 9a shows the N80 steel sheet without MBT, it can be seen from the figure that the surface corrosion of the N80 steel sheet is serious and the roughness is high because the metal is strongly damaged in the etching solution; Figure 9b is the polished N80 steel sheet that has not been immersed in the etching solution, it can be seen from the figure that the surface of the steel sheet is relatively smooth and the roughness is very low. Based on Figures 9c–f and 10c–f, the N80 steel sheet added to the corrosion inhibitor MBT is significantly different from that of Figures 9a and 10a. As the concentration of the corrosion inhibitor MBT increases, the corrosion rate of the steel sheet reduces, the surface of the steel sheet is smoother and the roughness is also closer to that of Figure 9b. MBT at a concentration of 300 mg/L is exhibited in Figures 9f and 10f with sandpaper polishing marks. It shows that the surface of MBT carbon steel forms an effective protective film, which prevents the corrosion of the steel sheet.

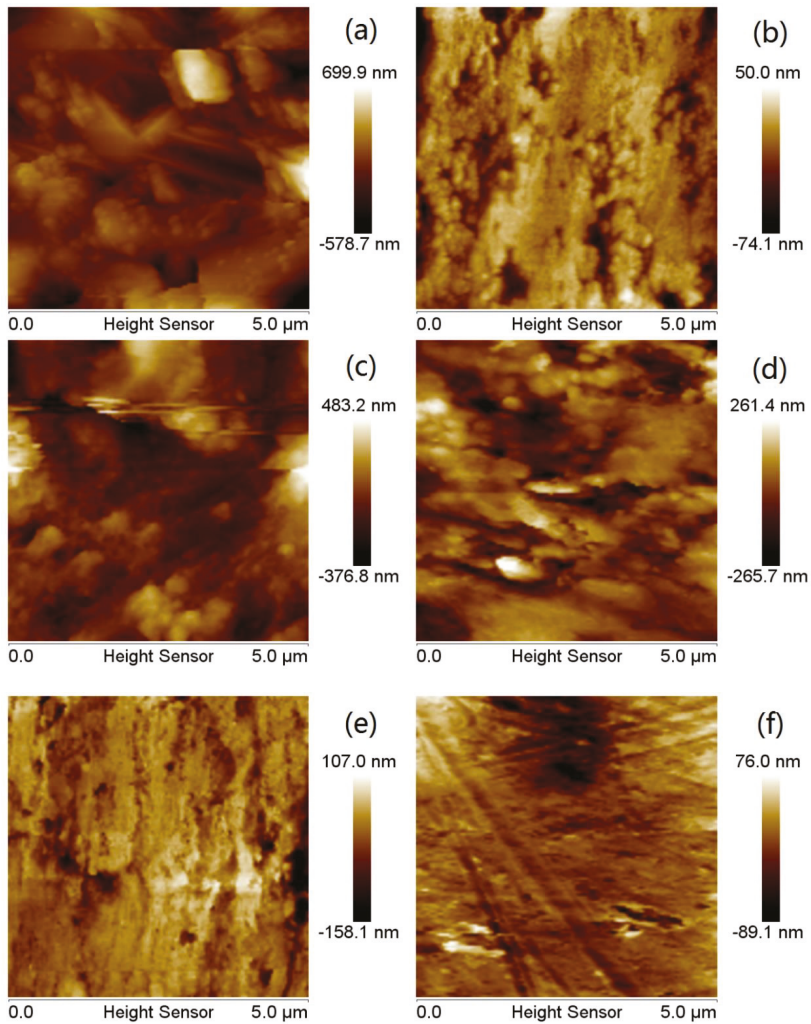


**Figure 10.** AFM plane topography of N80 steel sheet: (a) blank sample; (b) initial uncorroded sample; (c–f) is added 50 mg/L, 100 mg/L, 200 mg/L, and 300 mg/L MBT.

By analysing the data of the atomic force microscope carried by the analysis software (NanoScope Analysis v1.40), we can obtain the mean square roughness (Rq), the average roughness (Ra) and the maximum height difference (Rmax) of the surface of the N80 steel sheet, which is shown in Table 5. It can be seen from the table, that after the N80 blank is etched, the Rq is 155.0 nm, the Ra is 113.0 nm and the Rmax is 2050.0 nm, which is quite different from the Rmax of 165.0 nm which has not been etched. After adding 300 mg/L corrosion inhibitor MBT, the Rmax of the N80 steel sheet is 192.0 nm, which is very close to the maximum height difference of the unetched N80 steel sheet. Combined with Figures 9 and 10, the surface roughness of the steel sheet can be seen. The appearance of the corrosion inhibitor forms a passivation film on the surface of the N80 steel sheet, which reduces the surface roughness of the steel sheet and effectively prevents the N80 steel sheet from being eroded by corrosive media.

**Table 5.** AFM parameters after soaking in different concentrations of corrosion inhibitor MBT.

MBT (mg/L) + CM	Ra (nm)	Rq (nm)	Rmax (nm)
0 + 0	13.1	17.3	165.0
0 + CM	113.0	155.0	2050.0
50 + CM	93.0	119.0	873.0
100 + CM	58.1	73.2	597.0
200 + CM	24.4	33.2	369.0
300 + CM	15.9	21.6	192.0

Note: CM (corrosive media) refers to a CO<sub>2</sub> saturated solution containing 3 wt % NaCl.

#### 4. Conclusions

The overall aim of this study was to synthesise and assess the corrosion inhibition effect of MBT. After dosage temperature tests, the corrosion rate was 0.0446 mm/a and the corrosion inhibition rate was 90.4% while the dosage was 400 mg/L in a CO<sub>2</sub> saturated solution of 3 wt % NaCl, in a 70 °C constant temperature water bath for 72 h. As evidenced by polarisation curve analysis, MBT is a mixed type corrosion inhibitor mainly used for suppressing the cathode. The adsorption of MBT on the metal surface contributes to a dense molecular film, changing the interface properties and electric double layer structure, thus achieving a good corrosion inhibition effect. The adsorption follows the Langmuir isotherm adsorption and the calculated  $\Delta G_{\text{ads}} < 0$  indicates that the chemical adsorption of the corrosion inhibitor is spontaneous on the N80 steel sheet. AFM is applied in microscopic characterisation on the surface. Results demonstrate that the N80 steel sheet added the corrosion inhibitor MBT is different from blank the sample, showing a smooth surface, indicating that MBT contributes to the protective film with a good corrosion inhibition effect on the surface of the steel sheet.

**Author Contributions:** Conceptualization, J.L. (Jianbo Li) and M.T.; Data curation, M.T. and L.F.; Funding acquisition, J.L. (Jianbo Li); Investigation, J.L. (Jianbo Li), M.T., Z.L., L.F., B.Z. and J.L. (Jie Lv); Writing—original draft, M.T. and Z.L.; Writing—review & editing, M.T., J.L. (Jianbo Li) and Z.L.

**Funding:** This research was funded by the National Science and Technology Major Project of China, grant number 2016ZX05016-004-008 and The APC was funded by the National Science and Technology Major Project of China.

**Acknowledgments:** The authors thank the Southwest Petroleum University, Institute, Chengdu, China, for providing the research facilities needed for the above study. This work was supported by the National Science and Technology Major Project of China (No. 2016ZX05016-004-008).

**Conflicts of Interest:** The authors declare no conflict of interest.

## References

- Liu, Z.; Cheng, Y.; Wang, Y.; Wang, L.; Li, W. Experimental investigation of CO<sub>2</sub> injection into coal seam reservoir at in-situ stress conditions for enhanced coalbed methane recovery. *Fuel* **2019**, *236*, 709–716. [[CrossRef](#)]
- Franco, C.A.; Zabala, R.; Cortés, F.B. Nanotechnology applied to the enhancement of oil and gas productivity and recovery of Colombian fields. *J. Pet. Sci. Eng.* **2017**, *157*, 39–55. [[CrossRef](#)]
- Abelev, E.; Sellberg, J.; Ramanarayanan, T.A.; Bernasek, S.L. Effect of H<sub>2</sub>S on Fe corrosion in CO<sub>2</sub>-saturated brine. *J. Mater. Sci.* **2009**, *44*, 6167–6181. [[CrossRef](#)]
- Tang, M.; Li, J.; Ye, Z.; Kou, Z.; Fu, L. A Novel Eco-Friendly Scale and Corrosion Inhibitor Modified by  $\beta$ -Cyclodextrin. *Aust. J. Chem.* **2017**, *70*, 933–942. [[CrossRef](#)]
- Liu, H.; Schonberger, K.D.; Peng, C.Y.; Ferguson, J.F.; Desormeaux, E.; Meyerhofer, P.; Luckenbach, H.; Korshin, G.V. Effects of blending of desalinated and conventionally treated surface water on iron corrosion and its release from corroding surfaces and pre-existing scales. *Water Res.* **2013**, *47*, 3817–3826. [[CrossRef](#)] [[PubMed](#)]
- Molnár, V.; Fedorko, G.; Krešák, J.; Peterka, P.; Fabianová, J. The influence of corrosion on the life of steel ropes and prediction of their decommissioning. *Eng. Fail. Anal.* **2017**, *74*, 119–132. [[CrossRef](#)]
- Al-Amiery, A.A.; Kassim, F.A.; Kadhum, A.A.; Mohamad, A.B. Synthesis and characterization of a novel eco-friendly corrosion inhibition for mild steel in 1 M hydrochloric acid. *Sci. Rep.* **2016**, *6*, 19890. [[CrossRef](#)] [[PubMed](#)]
- Zhang, K.; Xu, B.; Yang, W.; Yin, X.; Liu, Y.; Chen, Y. Halogen-substituted imidazoline derivatives as corrosion inhibitors for mild steel in hydrochloric acid solution. *Corros. Sci.* **2015**, *90*, 284–295. [[CrossRef](#)]
- Pillay, C.; Lin, J. The impact of additional nitrates in mild steel corrosion in a seawater/sediment system. *Corros. Sci.* **2014**, *80*, 416–426. [[CrossRef](#)]
- Hamani, H.; Douadi, T.; Daoud, D.; Al-Noaimi, M.; Rikkouh, R.A.; Chafaa, S. 1-(4-Nitrophenyl-imino)-1-(phenylhydrazono)-propan-2-one as corrosion inhibitor for mild steel in 1 M HCl solution: Weight loss, electrochemical, thermodynamic and quantum chemical studies. *J. Electroanal. Chem.* **2017**, *801*, 425–438. [[CrossRef](#)]
- Vimalanandan, A.; Lv, L.P.; Tran, T.H.; Landfester, K.; Crespy, D.; Rohwerder, M. Redox-responsive self-healing for corrosion protection. *Adv. Mater.* **2013**, *25*, 6980–6984. [[CrossRef](#)] [[PubMed](#)]
- Li, J.; Tang, M.; Ye, Z.; Chen, L.; Zhou, Y. Scale formation and control in oil and gas fields: A review. *J. Dispers. Sci. Technol.* **2017**, *38*, 661–670. [[CrossRef](#)]
- Camargo, J.A.; Alonso, Á. Ecological and toxicological effects of inorganic nitrogen pollution in aquatic ecosystems: A global assessment. *Environ. Int.* **2006**, *32*, 831. [[CrossRef](#)] [[PubMed](#)]
- Paustovskaya, V.V. Some results of a research in the problem “inhibitors of metal corrosion. Toxicology and industrial hygiene”. *Prot. Met.* **2000**, *36*, 89–93. [[CrossRef](#)]
- Nishida, I.; Shimada, Y.; Saito, T.; Okaue, Y.; Yokoyama, T. Effect of aluminum on the deposition of silica scales in cooling water systems. *J. Colloid Interface Sci.* **2009**, *335*, 18. [[CrossRef](#)] [[PubMed](#)]
- SY/T 5273–2000, *The Oil Industry Standard of the People's Republic of China*; Petroleum Industry Press: Beijing, China, 2000.
- Zhang, H.H.; Gao, K.; Yan, L.; Pang, X. Inhibition of the corrosion of X70 and Q235 steel in CO<sub>2</sub>-saturated brine by imidazoline-based inhibitor. *J. Electroanal. Chem.* **2017**, *791*, 83–94. [[CrossRef](#)]
- Fu, L.; Yi, F.; Zeng, B.; Hu, C.; Li, J. Study of Synthesis and Corrosion Inhibition of Novel Mannich and Schiff Bases on Carbon Steel in Acid Solution. *Russ. J. Appl. Chem.* **2018**, *91*, 499–509. [[CrossRef](#)]
- Li, X.; Deng, S.; Xie, X. Inhibition effect of tetradecylpyridinium bromide on the corrosion of cold rolled steel in 7.0M H<sub>3</sub>PO<sub>4</sub>. *Arab. J. Chem.* **2014**, *84*, S3715–S3724.
- Xiang, Y.G.; Qiao, K.Q.; Cui, Y.S. Corrosion Inhibition of Eggplant Leaf Extract for Carbon Steel in Hydrochloric Acid Medium. *Corros. Prot.* **2016**, *37*, 122–127.
- Meng, Y.; Ning, W.; Xu, B.; Yang, W.; Zhang, K.; Chen, Y.; Li, L.; Liu, X.; Zheng, J.; Zhang, Y. Inhibition of mild steel corrosion in hydrochloric acid using two novel pyridine Schiff base derivatives: A comparative study of experimental and theoretical results. *RSC Adv.* **2017**, *7*, 43014–43029. [[CrossRef](#)]

22. Bentiss, F.; Lebrini, M.; Lagrenée, M. Thermodynamic characterization of metal dissolution and inhibitor adsorption processes in mild steel/2,5-bis(-thienyl)-1,3,4-thiadiazoles/hydrochloric acid system. *Corros. Sci.* **2005**, *47*, 2915–2931. [[CrossRef](#)]
23. Feng, L.; Yang, H.; Wang, F. Experimental and theoretical studies for corrosion inhibition of carbon steel by imidazoline derivative in 5% NaCl saturated Ca(OH)<sub>2</sub> solution. *Electrochim. Acta* **2011**, *58*, 427–436. [[CrossRef](#)]



© 2019 by the authors. Licensee MDPI, Basel, Switzerland. This article is an open access article distributed under the terms and conditions of the Creative Commons Attribution (CC BY) license (<http://creativecommons.org/licenses/by/4.0/>).



Article

# Corrosion Inhibition Mechanism and Efficiency Differentiation of Dihydroxybenzene Isomers Towards Aluminum Alloy 5754 in Alkaline Media

Jacek Ryl <sup>1,\*</sup>, Mateusz Brodowski <sup>1,2</sup>, Marcin Kowalski <sup>1,2</sup>, Wiktoria Lipinska <sup>1,3</sup>, Pawel Niedzialkowski <sup>4</sup> and Joanna Wysocka <sup>1</sup>

<sup>1</sup> Faculty of Chemistry, Gdansk University of Technology, Narutowicza 11/12, 80-233 Gdansk, Poland; mateusz.brodowski96@gmail.com (M.B.); m96kowalski@gmail.com (M.K.); wiktorialipinska154504@gmail.com (W.L.); joanna.wer.wysocka@gmail.com (J.W.)

<sup>2</sup> Faculty of Mechanical Engineering, Gdansk University of Technology, Narutowicza 11/12, 80-233 Gdansk, Poland

<sup>3</sup> Centre for Plasma and Laser Engineering, The Szewalski Institute of Fluid-Flow Machinery, Polish Academy of Sciences, Fiszerza 14, 80-231 Gdansk, Poland

<sup>4</sup> Faculty of Chemistry, University of Gdansk, Wita Stwosza 63, 80-308 Gdansk, Poland; pawel.niedzialkowski@ug.edu.pl

\* Correspondence: jacek.ryl@pg.edu.pl; Tel.: +48-58-347-1092

Received: 10 August 2019; Accepted: 19 September 2019; Published: 20 September 2019

**Abstract:** The selection of efficient corrosion inhibitors requires detailed knowledge regarding the interaction mechanism, which depends on the type and amount of functional groups within the inhibitor molecule. The position of functional groups between different isomers is often overlooked, but is no less important, since factors like steric hinderance may significantly affect the adsorption mechanism. In this study, we have presented how different dihydroxybenzene isomers interact with aluminum alloy 5754 surface, reducing its corrosion rate in bicarbonate buffer (pH = 11). We show that the highest inhibition efficiency among tested compounds belongs to catechol at 10 mM concentration, although the differences were moderate. Utilization of novel impedance approach to adsorption isotherm determination made it possible to confirm that while resorcinol chemisorbs on aluminum surface, catechol and quinol follows the ligand exchange model of adsorption. Unlike catechol and quinol, the protection mechanism of resorcinol is bound to interaction with insoluble aluminum corrosion products layer and was only found efficient at concentration of 100 mM (98.7%). The aforementioned studies were confirmed with Scanning Electron Microscopy and X-ray Photoelectron Spectroscopy analyses. There is a significant increase in the corrosion resistance offered by catechol at 10 mM after 24 h exposure in electrolyte: from 63 to 98%, with only negligible changes in inhibitor efficiency observed for resorcinol at the same time. However, in the case of resorcinol a change in electrolyte color was observed. We have revealed that the differentiating factor is the keto-enol tautomerism. The Nuclear Magnetic Resonance (NMR) studies of resorcinol indicate the keto form in structure in presence of NaOH, while the chemical structure of catechol does not change significantly in alkaline environment.

**Keywords:** aluminum alloy; corrosion inhibitor; alkaline environment; impedance analysis; adsorption; dihydroxybenzene

## 1. Introduction

Aluminum is the most widely spread metallic element on Earth [1], owing to its unique physico-chemical properties, such as low weight, high thermal and electrical conductivity, high linear expansion coefficient, and good corrosion resistance. It is non-magnetic, non-toxic and may be



subjected to repeated recycling [2]. Aluminum and its alloys have been used in almost all industries, in particular in mechanical engineering, the defense industry, aviation, shipbuilding, food and chemical industries, and many others. It is a strategic resource whose consumption is a measure of countries' development and industrialization level. Over the past 50 years, the world production of aluminum has been constantly increasing, with the highest leap occurring in this millennium. Limited access to bauxite ores and their gradual depletion are the main obstacles in the further development of the aluminum industry. Constantly growing demand and utilization of aluminum requires more effective methods for its recycling or protection.

Aluminum and its alloys belong to the group of passivating metals, alongside titanium, chromium and high-alloy steels. Spontaneously formed native oxide layer on the aluminum surface is built primarily of aluminum oxide  $\text{Al}_2\text{O}_3$ . The layer is thermodynamically stable in the pH range between 4 and 9, where aluminum possesses the highest corrosion resistance. On the other hand, the passive layer is not thermodynamically stable in alkaline and acidic media. In the presence of hydroxyl ions, aluminum undergoes oxidation to form  $\text{Al}(\text{OH})_4^-$ , according to the mechanism proposed by Macdonald [3]. One of the most commonly accepted aluminum corrosion mechanisms in alkaline media may be simplified to the form of equations (1–4) [4]. Other, more detailed mechanisms suggests involvement of intermediate products and/or passive layer [5–10].



The anodic dissolution is accompanied by cathodic process of water electrolysis with hydrogen generation, according to Equation (4):



The problem of aluminum corrosion in alkaline media occurs in numerous practical cases, starting from its possible application as an anode material in energy storage devices, through pre-treatment processes prior to anodization or for aesthetic purposes, up to the alkaline character of various cleaning agents used on working elements and constructions [11–14]. One of the most frequently utilized methods for lowering the corrosion rate of aluminum in these environments is the application of corrosion inhibitors.

Various organic inhibitors have been reported to be efficient corrosion inhibitors of aluminum and its alloys. Their inhibition effect depends on the molecule structure, the functional groups being electron donors or acceptors, and the number of such groups per molecule [15,16]. It is worth pointing out that the most effective inhibitors are based on molecules containing heteroatoms, such as oxygen, nitrogen, phosphorus, sulfur and aromatic rings [17,18]. Carboxylic acids in particular have been shown as highly efficient corrosion inhibitors of aluminum and its alloys in aqueous alkaline environments [19–22]. Studies carried out on maleic, malic, succinic, tartaric, citric and tricarballic acids have revealed changes in corrosion efficiency with the increased amount of  $-\text{COOH}$  groups and decreased amount of  $-\text{OH}$  groups within inhibitor molecule [20]. Similar reports involved restriction of aluminum corrosion in alkaline media by polyacrylic acids, where studies shown increase of inhibition efficiency with the increase of molecular weight of inhibitor molecule [23]. Compounds containing nitrogen and/or sulphur have also been proved to be efficient corrosion inhibitors, an example of which may be studies on 3-methyl-4-amino-5-mercapto-1,2,4-triazole (MAMT). Inhibitor molecules adsorption on protected metal surface occurs through amine and thiol functional groups [24].

Lashgari and Malek proved that phenol is a highly efficient corrosion inhibitor of aluminum [25]. Phenols are deprotonated in alkaline environments and transformed into inhibitory active forms of phenoxide and phenolate. Similar conclusions, based on theoretical studies, were later on drawn

for p-phenol derivatives, where the author confirmed that the mechanism of inhibition relies on a complicated cycle of protonation/deprotonation of inhibitor molecules in the inner area of the electrical double layer [26]. The process mentioned above leads to local neutralization of corrosive factors and their electrostatic repulsion in the vicinity of an active metal surface. Corrosion inhibition efficiency of p-phenol derivatives depends on several factors, including electron density on oxygen and hydrogen atoms in hydroxyl group, charge transfer, the energy of interaction, molecular activity, electric dipole moment and Gibbs free energy of the dissolution process.

The attention of corrosion scientists is nowadays increasingly focused on application of corrosion inhibitors of natural origin, obtained in accordance with the principles of green chemistry. Green corrosion inhibitors in the form of plant extracts are eco-friendly, non-toxic and biodegradable in neutral environments [27–35]. For example, *Phyllanthus amarus* leaf extract offers nearly 75% efficiency in 2M NaOH solution [36]. The extract contains alkaloids, cyanogenic glycosides, flavonoids, carbohydrates, sugar, proteins, triterpenoids and steroids. Functional groups –OH, –NH<sub>2</sub>, –SH, present in mentioned above compounds and  $\pi$ -bonds are most likely responsible for inhibition efficiency of *Phyllanthus amarus*. On the other hand, *Piper longum* seed extract, with 94% efficiency at concentration of 0.4 g·L<sup>-1</sup> in 1 M NaOH, contains piperine, piperlongumine, pipartine, piperlonguminine, piperundecalidinine and piperonaline [37]. The high inhibition efficiency was explained with presence of N-heteroatoms and  $\pi$ -electrons in aromatic rings. The 92% inhibition efficiency of *Gossypium hirsutum* extract in 2 M NaOH most likely originates from presence of O, N or S in amino acids such as: cysteine, lysine, methionine, phenylalanine, arginine, threonine, tyrosine, tryptophan, valine, but also polyphenolic aldehyde and tannins [32]. The authors also observed that higher concentration of active substances in present in leaves rather than seeds of *Gossypium hirsutum*.

Green corrosion inhibitors in the form of extracts from natural products are characterized by a large number of chemical compounds. In such a complex mixture of potential inhibitory compounds it is particularly important to perform phytochemical studies in order to determine the active compounds and their mechanism of interaction, which in many cases appears to be an incredibly difficult task. Therefore, in order to avoid blind-picking during selection of natural extracts containing potentially efficient inhibitor compounds one must get to know in detail the mechanism of interaction of various types of functional groups with protected metal surface as well as how it is modified by other aspects of the molecule structure. A valuable approach towards more effective determination of the active inhibitory compounds may be found in designing the extraction process. Differentiation of the type of solvents or extraction conditions leads to selective extraction of certain groups of compounds. Ryl et al. [38] showed that preparation of bee pollen extracts through extraction in different solvents results in different corrosion inhibition efficiency towards AA5754 in bicarbonate buffer at pH = 11. It has been proved that these differences are caused by varying content of carboxylic acids and phospholipids, which acted as inhibitory active substances in bee pollen extracts.

A certain group of phenol derivatives exhibits very high corrosion inhibition efficiency towards aluminum and its alloys. This group includes catechol, cresol, chlorophenol, resorcinol, nitrophenol and aminophenol [39,40]. Talati and Modi [39] suggested that –OCH<sub>3</sub>, –NH<sub>2</sub> and –CH<sub>2</sub>CHCH<sub>3</sub> functional groups lower the inhibition efficiency of phenol, while –OH, –Cl, –NO<sub>2</sub> increase it. Furthermore, they suggested three different adsorption mechanisms, namely: electrostatic forces, the formation of chelating agents with aluminum ions or covalent bond formation. The authors also observed that the inhibition efficiency decreases with the increase of electrolyte alkalinity. The synergistic interaction of resorcinol with Zn<sup>2+</sup> ions was further studied by Lakshmi et al. [40], which revealed significant increase in corrosion inhibition efficiency of aluminum. However, all the aforementioned studies were carried out using the gravimetric method, introducing significant uncertainty to the measurements. The formation of the insoluble corrosion products layer on aluminum surface hinders specific determination of weight loss of the analyzed samples.

Not only the type and the number of active functional groups but also their position in the molecule structure may have a significant influence on corrosion inhibition efficiency. The chemical structure of

isomer molecules affects modification of their physico-chemical properties such as solubility, while steric hindrance may influence both kinetics and mechanism of the adsorption process. This subject has not been given sufficient attention in the corrosion research; however, several available reports prove the importance of substituents position in the molecule [41–43]. Fouda and Elasmry [41] presented their studies on phenylthiosemicarbazide derivatives as aluminum corrosion inhibitors in 2M NaOH, with efficiency ranging between 75.0% and 98.5%, depending on the derivative. Hassan et al. [42] confirmed that the efficiency of aromatic carboxylic acids depends on the number and position of carboxylic groups and the presence of other substituents in the aromatic ring. The increasing corrosion efficiency was as follows: benzamide < benzaldehyde < acetophenone < benzoic acid < benzophenone (99.99% efficiency).

The electrochemical impedance studies on thiosemicarbazone interaction with aluminum alloys in 1 M HNO<sub>3</sub> revealed an almost 20% higher inhibition efficiency offered by para-substituted compounds in comparison to ortho-substituted ones [44]. There is no general relationship, though. The search for corrosion inhibitors of mild steel in 1 M HCl revealed that ortho-nitroaniline and ortho-methylaniline show higher corrosion inhibition efficiency in comparison with both meta- and para-substituents, but in the case of phenylenediamine, meta-substituted functional groups offered the highest efficiency [45]. A similar observation was made on aminophenol-N-salicylidene isomers' action towards zinc in 0.5 M H<sub>2</sub>SO<sub>4</sub> [46]. The goal of this work is to evaluate the influence of position of hydroxyl functional groups within dihydroxybenzene molecule on the corrosion inhibition provided by the isomer towards aluminum in alkaline electrolytes. Dihydroxybenzene isomers (catechol, quinol and resorcinol) were utilized, as presence of hydroxyl functional groups is expected to provide reasonable inhibition efficiency in studied electrolytes. In our studies we have implemented newly developed instantaneous impedance tool, i.e., Dynamic Electrochemical Impedance Spectroscopy in galvanostatic mode (g-DEIS), which is capable of accurate and time-efficient determination of the adsorption mechanism differences [19,20,38].

## 2. Materials and Methods

### 2.1. Materials

The studied material was aluminum alloy 5754, which had the following alloying additives (in wt.%): Mg 3.6, Fe 0.3, Si 0.3, Cr 0.1, Mn 0.5, Ti 0.1 and Cu 0.1. Cylindrical samples were cut from a rod and subjected to pretreatment procedure in the form of grinding and polishing, carried out on Digiprep 251 (Metkon, Bursa, Turkey) polishing machine. Samples were grinded on a waterproof abrasive papers SiC 600 and 1500, polished with diamond suspensions 6 and 1 μm and mirror-finished on 0.05 μm silica. Following polishing, samples were cleaned and degreased in acetone using ultrasonic cleaner (Polsonic, Warsaw, Poland). Samples were exposed to corrosion studies with 0.5 cm<sup>2</sup> surface area.

The primary electrolyte was the bicarbonate buffer solution. The buffer was prepared using 227 cm<sup>3</sup> 0.1 M NaOH and 500 cm<sup>3</sup> 0.05 M NaHCO<sub>3</sub>, diluted with deionized water to 1 dm<sup>3</sup> volume. The obtained buffer had pH = 11 and conductivity of 3.8 mS·cm<sup>-1</sup>. All were analytical purity Sigma Aldrich reagents (Sigma Aldrich, St. Louis, MI, USA). Three dihydroxybenzene isomers were evaluated, namely: resorcinol, catechol and quinol. Their chemical structures are presented on Figure 1. The corrosion inhibition efficiency of the aforementioned compounds was investigated at various inhibitor concentrations  $c_{inh} = 1, 10$  and 100 mM as well as with linearly changing inhibitor concentration during g-DEIS studies related to inhibitor injection into the corrosion cell.

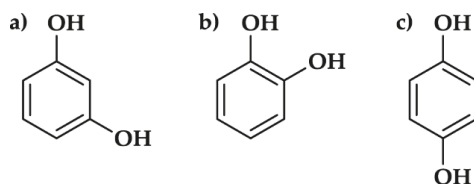


**Figure 1.** The chemical structure of dihydroxybenzene isomers: (a) resorcinol; (b) catechol; (c) quinol.

## 2.2. Electrochemical Measurements

The electrochemical impedance studies were performed in a three-electrode setup. Investigated aluminum alloy 5754 was the working electrode (WE), Ag|Ag<sub>2</sub>O was the reference electrode (RE) ( $E^\circ = +0.215$  V vs. SHE) while Pt mesh served as the counter electrode (CE). The electrolyte volume in the corrosion cell was 10 mL.

Corrosion inhibition efficiency studies were performed by means of classic Electrochemical Impedance Spectroscopy (EIS) and Dynamic Electrochemical Impedance Spectroscopy in galvanostatic mode (g-DEIS) after the initial conditioning for 15 min. EIS was carried out in potentiostatic mode, at open circuit potential (OCP) conditions. The perturbation signal for EIS measurements was applied in the frequency range between 50 kHz and 40 mHz, with 10 points per decade of frequency and amplitude of 15 mV. Multisinusoidal perturbation signal for g-DEIS studies composed of 29 superimposed elementary signal in the frequency range between 4.5 kHz and 1.0 Hz, with 8 points per decade of frequency. Sampling frequency was 128 kHz. The amplitude of perturbation signal was controlled to assure the amplitude of response signal does not exceed 15 mV. The analysis window for the Short-time Fourier Transformation was 10 s in length. A similar measurement procedure was previously applied in corrosion studies [19,20,38,47–49].

To build the adsorption isotherm, studied corrosion inhibitor was injected from the secondary cell to the corrosion cell through BQ80S microflow peristaltic pump (Lead Fluid, Baoding, China). The flow rate was set as 0.02 mL·min<sup>-1</sup>. The concentration of studied inhibitor in the secondary cell was set in a way to assure corrosion inhibitor concentration in the corrosion cell ( $c_{inh}$ ) equal to 10 mM at the end of 6000 s long experiment. The corrosion cell was thermostated at 25 °C. The electrochemical setup used during all corrosion studies is schematically presented on Figure 2.

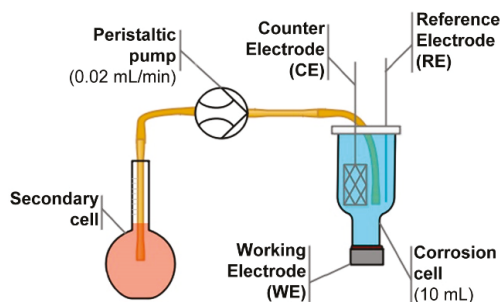


**Figure 2.** Schematic representation of the setup used during electrochemical studies.

## 2.3. Equipment

The EIS measurements were carried out using frequency-response-analysis on Gamry Reference 600+ potentiostat (Gamry Instruments, Warminster, PA, USA). The g-DEIS measurement system consisted of Autolab PGSTAT 302N (Metrohm, Herisau, Switzerland) galvanostat connected to PXI-4464 measurement card for AC signal generation and PXI-6124 card for AC/DC signal acquisition,

both operating in PXIe-1073 chassis (all from National Instruments, Austin, TX, USA). The microflow peristaltic pump used was BQ80S (Lead Fluid, Baoding, China). The thermostat was Corio CD (Julabo GmbH, Seelbach, Germany)

Microscopy analyses of AA5754 corrosion process were performed on a Scanning Electron Microscope VP-SEM S-3400 N (Hitachi, Chiyoda, Japan), equipped with a tungsten source and operating at 20 kV accelerating voltage. SEM micrographs were done in secondary electron mode.

High-resolution X-Ray Photoelectron Spectroscopy (XPS) analyses were performed on Escalab 250 Xi multispectroscopy (ThermoFisher Scientific, Waltham, MA, USA). The spectroscope is equipped in Al K $\alpha$  X-ray source with a spot diameter of 250  $\mu\text{m}$ . The measurements were carried out at 20 eV pass energy and 0.1 eV energy step size. The charge compensation was provided by means of low-energy electrons and low-energy Ar $^{+}$  ions emission from the flood gun.

Nuclear Magnetic Resonance (NMR) spectra were recorded on AVANCE III 500 MHz NanoBay spectrometer (Bruker, Billerica, MA, USA). Tetramethylsilane (TMS) was used as an internal standard in all the measurements. The 0.5 mL solution containing 80 mM dihydroxybenzene isomer in D $_2$ O was filled with NaOH. The titrated compounds ratio to NaOH was 1:1, 1:5 and 1:10.  $^1\text{H-NMR}$  and  $^{13}\text{C-NMR}$  spectra were recorded. All the measurements were performed after 24 h in 25  $^{\circ}\text{C}$  and in the same volume of solvent.

### 3. Results and Discussion

#### 3.1. Dihydroxybenzene Isomers as Corrosion Inhibitors

Electrochemical Impedance Spectroscopy (EIS) was used during the preliminary studies to assess the corrosion resistance of the investigated aluminum alloy immersed in an alkaline environment with the addition of each dihydroxybenzene isomer. The studies were carried out for three different corrosion inhibitor concentrations  $c_{\text{inh}}$ , namely: 1, 10 and 100 mM. The impedance spectra, presented in the form of Nyquist plots, are plotted in Figure 3. It can be seen by the shape of the impedance semicircles, that studied derivatives offer different level of corrosion protection; however, detailed analysis required fitting of the obtained data with electric equivalent circuit (EEC).

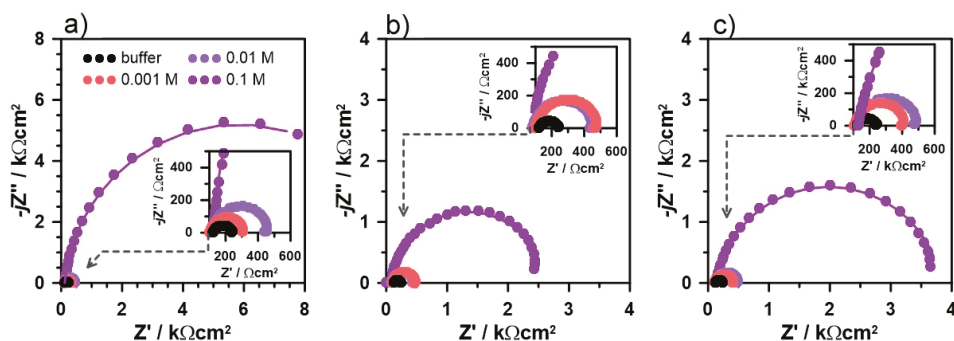


**Figure 3.** EIS impedance spectra recorded for AA5754 exposed to bicarbonate buffer (pH = 11) with the addition of the studied dihydroxybenzene isomers: (a) resorcinol; (b) catechol; (c) quinol at various concentrations in range 1–100 mM.

There is only one clear time constant present on the obtained impedance spectra, suggesting that the charge transfer through the electrode interface and through the adsorbed inhibitor layer are characterized with similar relaxation times. The authors decided to apply a simple form of Randles electric equivalent circuit (EEC) due to the prominence of one time constant on the impedance spectra in the applied frequency range. The one and only alteration was to replace the capacitance parameter with a constant phase element (CPE) in order to properly consider investigated electrode surface

heterogeneity, originating from alloy microstructure and roughness, but even more important presence of local adsorption sites of corrosion inhibitor at its low concentrations. The CPE impedance is given with Equation (5).

$$Z_{CPE} = [Q(j\omega)^\alpha]^{-1} \quad (5)$$

It should be noted that in the boundary case, if  $\alpha = 1$ , the CPE impedance responds to a capacitor of capacitance  $Q$ . Therefore, CPE exponent  $\alpha$  is often considered as the homogeneity factor, its decrease represents the increase of surface heterogeneity, while  $Q$  reflects the quasi-capacitance of the heterogeneous electrode. Furthermore, the CPE can be used to estimate the effective capacitance of studied electrode  $C_{eff}$ , with the use of Hirschorn's approximation for the surface distribution of the capacitance dispersion [50]:

$$C_{eff} = Q^{1/\alpha} \left( \frac{R_e R_{ct}}{R_e + R_{ct}} \right)^{(1-\alpha)/\alpha} \quad (6)$$

where  $R_e$  is the resistance of the electrolyte and  $R_{ct}$  is charge transfer resistance. The  $\chi^2$ -distribution of the selected EEC was in the range of  $10^{-4}$ , which is a good result, when taking into consideration EEC simplicity and system non-stationarity.

The shift in the calculated value of charge transfer resistance  $R_{ct}$  may be utilized to estimate the inhibition efficiency  $IE\%$ , using the well-known relationship (7) [19]:

$$IE\% = \left( 1 - \frac{R_{ct}^0}{R_{ct}} \right) \quad (7)$$

where  $R_{ct}^0$  denotes the measured value of charge transfer resistance in the absence of the inhibitor. The results of impedance data analysis with the R(QR) EEC are summarized in Table 1.

**Table 1.** Electric parameters of the studied systems obtained from EIS results fitted with R(QR) EEC.

$C_{inh}/mM$	Buffer		Resorcinol			Catechol			Quinol	
	-	1	10	100	1	10	100	1	10	100
$Q/\mu S s^\alpha \cdot cm^{-2}$	23.9	22	29.4	14.5	24.2	31.1	19	25.5	28	14.5
$\alpha/-$	0.94	0.94	0.92	0.94	0.91	0.89	0.9	0.93	0.93	0.96
$C_{eff}/\mu F \cdot cm^{-2}$	10.7	10	10.8	8.2	7.5	7.6	6.5	10.7	11.8	9.4
$R_{ct}/k\Omega \cdot cm^2$	0.14	0.18	0.3	10.93	0.29	0.38	3.64	0.39	0.35	2.45
$IE_{90}/\%$	-	22.2	53.3	98.7	51.7	63.2	96.2	64.1	60	94.3

Interestingly enough, the addition of resorcinol at the lowest concentration (1 mM) provided the lowest level of corrosion resistance. This feature most likely originates from the altered mechanism of molecules adsorption on the surface of aluminum alloy and was an object of further studies. On the other hand, presence of catechol and quinol offers approx. 60% efficiency already at  $c_{inh} = 1$  mM, which does not significantly improve until reaching substantially higher concentrations. This may be observed in particular through effective capacitance  $C_{eff}$  changes, which decreased by nearly 30% already at the lowest inhibitor concentrations, compared to reference buffer electrolyte. The most important factor affecting this parameter is the thickness of the adsorbed layer on aluminum surface [20].

Importantly, the highest inhibition efficiency was obtained after the addition of 100 mM of resorcinol. While the difference between  $IE\%$  at this concentration does not exceed 4%, it should be noted that it corresponds to over 3 $\times$  and nearly 5 $\times$  higher  $R_{ct}$  values of AA5754 alloy in presence of resorcinol versus catechol and quinol, respectively. The increased efficiency of resorcinol at very high inhibitor concentrations was previously revealed in gravimetric studies [51]. In our opinion, its positive interaction is directly connected to the competitive formation of the corrosion products layer,

making an additional barrier to aggressive environment. In the case of catechol and quinol, the barrier properties of the corrosion products layer are less evident, as discussed later.

### 3.2. The Adsorbed Layer Chemistry

The authors decided to focus on the core of electrochemical and physic-chemical studies on resorcinol and catechol isomers, which is due to the nearly identical response and adsorption mechanism between catechol and quinol. At the same time, there is a significant solubility difference between these two compounds in aqueous electrolytes at 25 °C, hindering possible utilization of quinol as efficient corrosion inhibitor. Quinol is sparingly soluble in water and show tendency for sedimentation over time. Its solubility in water is 5.9 g/100 g in comparison to 43 g/100 g for catechol and 110 g/100 g for resorcinol [52].

The chemistry of the adsorbed dihydroxybenzene layer and corrosion products layer on the surface of studied aluminum alloy 5754 was evaluated with the use of high-resolution XPS analysis. First, samples were pre-exposed to alkaline electrolyte with the addition of studied inhibitor at 10 or 100 mM concentration for a period of 24 h. The XPS spectra in the binding energy (BE) range of C1s, O1s, Al2p and Mg1s peaks were collected and deconvoluted using the fitting procedure described below. The results of the aforementioned deconvolution are summarized in Table 2.

**Table 2.** Surface chemical composition (in at.%) for AA5754 after 24 h exposure in bicarbonate buffer (pH = 11) with the addition of resorcinol or catechol, based on high-resolution XPS analysis.

Chemical State		BE/eV	Bicarbonate Buffer	Resorcinol		Catechol	
				10 mM	100 mM	10 mM	100 mM
Al2p <sub>3/2</sub>	Al <sub>ox1</sub>	74.8	1.5	3.2	2.3	3.4	8.0
	Al <sub>ox2</sub>	76.7	19.8	14.7	15.3	10.5	-
C1s	C-C	284.7	1.4	4.6	5.4	10.4	6.0
	C-OH	286.0	12.1	12.8	16.9	31.4	32.8
	C=O	287.6	2.3	7.6	5.1	3.9	6.1
	COOH	290.3	1.6	2.8	2.4	3.9	8.6
O1s	O <sup>2-</sup>	531.3	30.8	20.0	22.1	12.6	3.4
	CO/OH	532.6	16.4	15.2	18.5	20.2	29.2
	C=O/H <sub>2</sub> O	533.7	13.0	18.0	11.0	3.0	5.6
Mg1s	Mg <sub>ox</sub>	1303.1	1.1	1.1	1.0	0.7	0.3

Figure 4a presents the XPS spectra obtained in Al2p BE range. There is a clear shift in the peak position recorded between resorcinol-exposed and catechol-exposed aluminum samples. First, when exposed to bicarbonate buffer, but also with the addition of resorcinol, the primary peak doublet is located at higher BE values, with Al2p<sub>3/2</sub> peak at approx. 76.7 eV. This component was labeled Al<sub>ox2</sub> and ascribed to the non-stoichiometry aluminum corrosion product layer, often observed in studies of this metal in pH range 10–12 [53]. The second component (Al<sub>ox1</sub>), corresponding to native Al<sub>2</sub>O<sub>3</sub> passive film was shifted at −1.9 eV. The presence of native oxide film results from air exposure of samples. The share of non-stoichiometric oxides (Al<sub>ox2</sub>:Al<sub>ox1</sub>) is nearly 13:1 when compared to native oxides for sample exposed in bicarbonate buffer, and drops to 5:1 after addition of resorcinol, regardless the concentration. The results suggest presence of corrosion products layer, which contributes the decrease of aluminum corrosion rate in these environments.

On the other hand, the addition of catechol at c<sub>inh</sub> = 10 mM resulted in Al<sub>ox2</sub>:Al<sub>ox1</sub> share of 1:3. The significantly lower contribution from Al<sub>ox2</sub> may suggest that inhibitory action of catechol efficiently reduces formation of the corrosion products on aluminum alloy 5754 surface. This observation was confirmed for higher concentrations of catechol, where Al2p signal is composed solely of native oxide film.

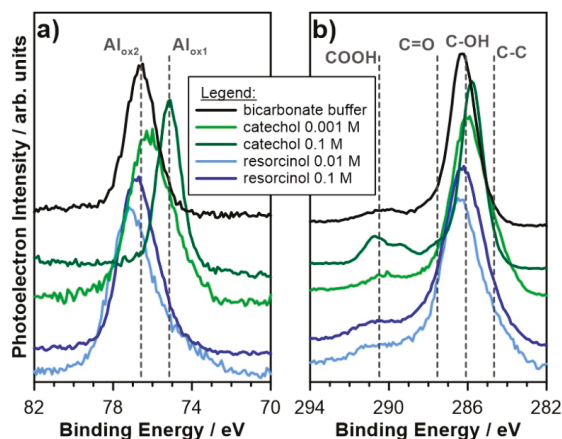


**Figure 4.** High-resolution XPS spectra recorded in (a) Al<sub>2</sub>p and (b) C1s binding energy range for aluminum alloy 5754 after 24 h exposure in bicarbonate buffer (pH = 11) and bicarbonate buffer with the addition of resorcinol or catechol at concentrations 10 and 100 mM.

When compared to bicarbonate buffer exposed sample, the C1s spectra reveal the significant presence of carbon species for both analyzed dihydroxybenzenes and at both concentrations, suggesting that inhibitor molecules indeed take part in formation of the adsorbed layer on aluminum alloy 5754 surface (Figure 4b). The chemistry of this carbon species is strongly altered, however. In the case of catechol, the amount of C-C and C-OH species, based on peaks at 284.7 and 286.0 eV, respectively, is nearly 3× compared to resorcinol at the same concentrations [54–56]. Furthermore, the C1s spectra reveal significantly higher amount of carbonyl and/or carboxyl species for catechol-containing electrolyte (at BE exceeding 287.6 eV). These results corroborate previous findings regarding possible formation of the adsorbed inhibitor layer directly on aluminum surface and negligible participation of the corrosion products layer. On the other hand, in absence of corrosion inhibitor the C1s contribution originates primarily from C-OH and C=O species, testifying the interaction of bicarbonate species with aluminum sample.

The O1s spectra deconvolution is in good accordance with previously discussed results. In the absence of dihydroxybenzene isomers, over 47 at.% of the aluminum surface consists of oxygen atoms, with peak binding energies characteristic either for aluminum metal oxides (531.3 eV) or hydroxides (531.6 eV) [19,20]. Further on, this value slowly decreases for resorcinol-containing electrolyte, still within the range of 40 at.%. However, in the presence of catechol, the amount of O<sup>2-</sup> species is significantly lower, at 10 and 100 mM. Here, the signal corresponding to peaks located at approx. 532.6 eV is still strong, but with an organic C-O interaction origin, instead. The last deconvoluted O1s component is located at binding energies exceeding 532.7 eV. Its source is adsorbed carboxyl species, but also chemisorbed water molecules [57]. The non-stoichiometric corrosion products layer reveals high hydration level, confirmed with SEM micrographs, therefore higher share of chemisorbed water on surface of bicarbonate buffer-exposed and resorcinol-exposed aluminum alloy 5754 is natural.

Finally, the amount of magnesium, the primary alloying additive, was only slightly altered between various investigated electrolytes. In each case magnesium was found in the form of hydroxides with Mg1s peak BE at 1303.1 eV, its higher contribution for resorcinol testifies the presence of magnesium oxides in the corrosion products layer, having a possible effect on the increased corrosion resistance [58].

The SEM micrographs shown in Figure 5 reveal significant difference in occurrence of the corrosion process for both studied dihydroxybenzene derivatives. The addition of resorcinol does not affect significantly surface topography when compared to reference aluminum alloy sample in buffer electrolyte (Figure 5a). The oxidation is primarily oriented around the alloy microstructure, which



can be confirmed through local dissolution of alloy matrix surrounding intermetallic particles [58–60]. These particles appear on the micrographs with bright colors. Based on own studies and the literature survey discussed, the particles are primarily composed of aluminum and alloying additives of Fe, Cr and Mn—each cathodic in nature compared to metal matrix [60,61]. Furthermore, dense network of cracks visible on Figure 5a–c testifies high hydration level of adsorbed layer and corrosion products layer on the electrode surface.

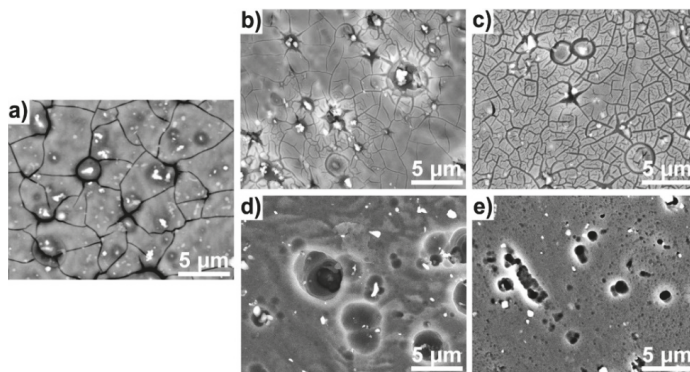


**Figure 5.** SEM micrographs of aluminum alloy 5754 surface exposed to bicarbonate buffer (pH = 11) for 24 h: (a) in absence of corrosion inhibitor; with addition of resorcinol at concentration (b) 10 mM and (c) 100 mM or with addition of catechol (d) 10 mM and (e) 100 mM.

The presence of catechol or quinol in the electrolyte consequences in localized corrosion of aluminum, which is most often restricted to anodic Mg-rich phases and areas surrounding cathodic intermetallic particles. The absence of thick corrosion product layer effects in lack of cracks, which otherwise cover metal surface. The localized corrosion is naturally more evident at lower inhibitor concentrations (see Figure 5d), where the spherical shape of caverns should be connected with local areas of hydrogen evolution in coupled cathodic reaction [53].

### 3.3. Thermodynamics of the Adsorption Process

The thermodynamics of dihydroxybenzene isomers adsorption was evaluated based on instantaneous impedance studies, carried out in galvanostatic mode (g-DEIS). The studied inhibitor is injected with linear injection rate ( $0.02 \text{ mL}\cdot\text{min}^{-1}$ ); thus, the instantaneous value of inhibitor concentration in the corrosion cell is known. Dynamic impedance measurements allow for a precise evaluation of the instantaneous values of electric parameters, where the inhibition efficiency may be estimated from  $R_{ct}$  using previously introduced Equation (7). Studies carried out in galvanostatic mode at  $i_{DC} = 0$  ensures constant measurement conditions and lack of an additional polarization component, resulting from corrosion potential changes during inhibitor injection. The approach is characterized with higher accuracy, allowing to obtain larger data set and evaluate the exact inhibitor concentration at which the linear character of the adsorption isotherm is modified due to full electrode surface coverage with inhibitor monolayer. The details of the experimental procedure are presented elsewhere [19,20].

The dynamic impedance spectra presented in the form of the Nyquist plot are shown on Figure 6a,b for resorcinol and catechol, respectively. The shape of the impedance spectra develops during corrosion inhibitor injection, where the increased impedance loop diameter testifies the increase of aluminum corrosion resistance. Fitting impedance spectra with R(QR) EEC allows for determination of dynamic changes of the electric parameters:  $R_{ct}$  and CPE within a timeframe of an analytical window length of a Short-Time Fourier Transform function, equal to 10 s in this case. The fitting procedure was carried

out using dedicated software based on Nelder-Mead algorithm and build in LabView environment. The resultant  $\chi^2$ -distribution was typically in  $10^{-4}$  range and did not exceed  $2 \times 10^{-3}$ . Determination of the instantaneous  $R_{ct}$  values allowed for calculation of momentary inhibition efficiency IE%, which is also the measure of surface coverage with inhibitor molecules  $\theta$  ( $IE\% = \theta \times 100\%$ ). According to the principles of the most commonly used Langmuir adsorption isotherm, the adsorption equilibrium constant,  $K_{ads}$ , depends on surface coverage  $\theta$ , which is given with Equation (8):

$$K_{ads}c_{inh} = \left( \frac{\theta}{1-\theta} \right) \tag{8}$$

In the linear range of Equation (8), the adsorption isotherm may serve for calculation of the adsorption Gibbs free energy  $\Delta G$ , using Equation (9):

$$\Delta G = -RT \ln(K_{ads} \times 55.5) \tag{9}$$

Importantly, Langmuir isotherm conditions are only fulfilled for concentrations below full coverage with the adsorbent monolayer. One should note, that classical approaches towards adsorption isotherm determination are based on merely few measurement points, where the non-linear behavior resulting from aforementioned situation is difficult to track. On the other hand, the quasi-capacitance parameter obtained during g-DEIS impedance measurements allows estimating the exact concentration required for monolayer formation by inhibitor molecules [20].

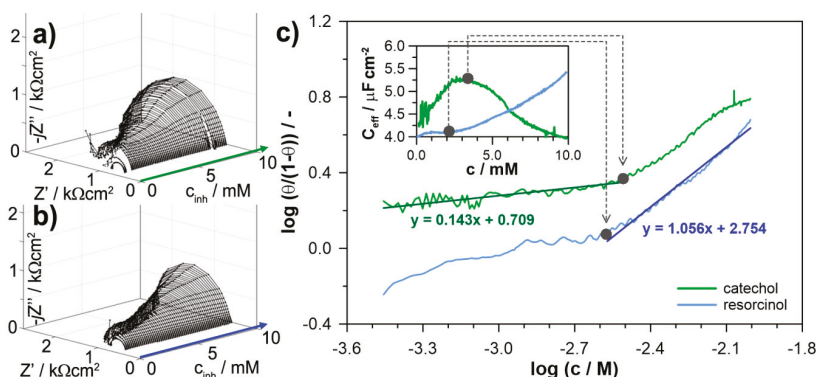


**Figure 6.** The g-DEIS impedance graphs of aluminum alloy 5754 in bicarbonate buffer (pH = 11), presented in Nyquist projection versus (a) catechol and (b) resorcinol concentration changes during its injection to corrosion cell. (c) Langmuir model of adsorption isotherms drawn based on instantaneous  $R_{ct}$  changes, in the inset the instantaneous changes of effective capacitance  $C_{eff}$ .

Figure 6c presents the adsorption isotherms obtained with g-DEIS approach and plotted according to the Langmuir model of molecules adsorption. The isotherms were drawn for resorcinol and catechol at concentrations in range 0–10 mM. It can be pointed out that both of these functions are characterized by loss of linear character and both have inflection at concentrations between 2 and 4 mM. However, the effective capacitance  $C_{eff}$  measurements plotted in the inset of Figure 6c reveals significant differences in the adsorption mechanism.

There are three primary factors affecting the value of capacitance according to Equation (10), namely, electrochemically active surface area  $A$ , permittivity  $\epsilon$ , and layer thickness  $d$ :

$$C = \frac{\epsilon_0 \epsilon A}{d} \tag{10}$$

where  $\epsilon_0$  is vacuum permittivity. Normalization of heterogeneity factor affecting quasi-capacitance  $Q$  and estimation of the effective capacitance  $C_{\text{eff}}$  allows ignoring the effect of electrode heterogeneity. Previous studies have shown that with relatively short measurement duration the key factor influencing instantaneous  $C_{\text{eff}}$  of the adsorbed layer is its thickness [20,38].

In the case of a catechol-exposed AA5754 electrode, the  $C_{\text{eff}}$  value increases until reaching its maximum at  $c_{\text{inh}} = 3.5$  mM and then decreases. Therefore, it should be assumed that the full coverage of aluminum surface with corrosion inhibitor molecules occurs at this concentration and the following  $C_{\text{eff}}$  decrease results from the increase in adsorbed layer thickness. The adsorption isotherm still remains linear afterward, but no longer following the aforementioned restriction regarding surface coverage.

The situation is essentially different in the case of resorcinol-exposed AA5754 electrodes, where according to classic EIS and XPS studies the inhibitory action is generally lower. In the whole studied concentration range, up to 10 mM the  $C_{\text{eff}}$  value effectively increases. The competitive interaction of the corrosion products layer and the resorcinol adsorption layer may have its effect on difficulties in assessing the full coverage of the adsorption layer but also influences layer permittivity. As a result, the adsorption isotherm for resorcinol was following Langmuir model of adsorption at significantly higher inhibitor concentrations than catechol. On the other hand, the estimated inhibitor efficiency at the lowest concentrations is negligible and thus hard to measure. A conclusion should be made that the applicability of the Langmuir adsorption isotherm model for catechol and resorcinol lies in different inhibitor concentration ranges.

Following Equations (8) and (9), the calculated values of Gibbs free energy  $\Delta G$  of the adsorption process are presented in Table 3. Their negative values in both cases confirm spontaneous adsorption of both studied dihydroxybenzene molecules on aluminum alloy 5754 surface. Nevertheless, the significantly different  $\Delta G$  values between resorcinol and catechol suggest an altered adsorption mechanism.

**Table 3.** The applicability range of the Langmuir adsorption model and the obtained thermodynamic parameters for resorcinol and catechol.

Isomer	Langmuir Model $c_{\text{inh}}$ Range/mM	Adsorption Equilibrium Constant $K_{\text{ads}}$	Gibbs Free Energy $\Delta G/\text{kJmol}^{-1}$
catechol	<3.5	1.39	-10.77
resorcinol	2–10	11.38	-15.98

The more negative Gibbs free energy values are typical in case of chemisorption and formation of chemical bonds between filled  $\pi$ -orbitals in the oxygen atoms and partially unoccupied  $\pi$ -orbitals in the d-block metals. This is the postulated adsorption mechanism of resorcinol. Naturally, the value of this thermodynamic parameter may be further influenced by reported presence of the nonstoichiometric corrosion products layer. On the other hand, our previous studied on carboxylic acids revealed that the less negative free Gibbs energies correspond not only to the electrostatic interaction of the physisorption process but also the ligand exchange model of adsorption, resulting in formation of coordination compounds at the metal interface [19,20]. This is the case of catechol interaction. The lower efficiency of ligand formation by resorcinol and quinol originates from the molecule geometry.

### 3.4. The Keto-Enol Tautomerism

During the long-term exposure tests, the authors observed changes in the color of the studied electrolytes over time, and resorcinol in particular (see inset of Figure 7). These changes were followed by alteration of the electrochemical characteristics over time. On the other hand, for catechol and quinol the long-term inhibition efficiency was significantly higher. The g-DEIS studies were carried out once more to track the exact change in the electrochemical behavior of aluminum alloy 5754 during 24 h exposure. The results of the impedance monitoring are presented in Figure 7.

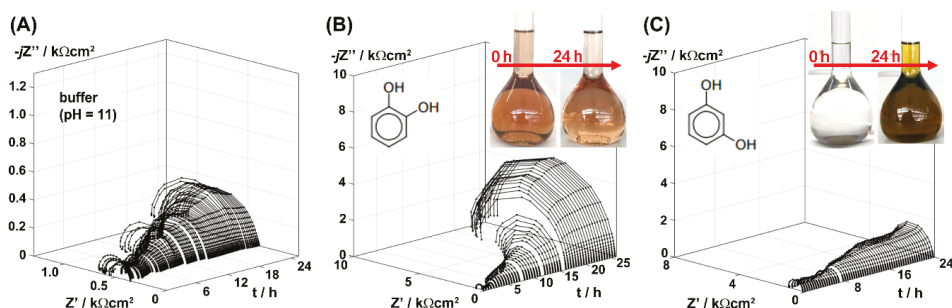


**Figure 7.** The g-DEIS impedance graphs of aluminum alloy 5754 in Nyquist projection during 24 h exposure in (A) bicarbonate buffer (pH = 11); and with the addition of (B) 10 mM catechol and (C) 10 mM resorcinol.

Analysis of the impedance data makes it possible to draw conclusions regarding the long-term behavior of AA5754 under the studied electrolytic conditions. The slight increase of the semicircle diameter over time, seen on the Nyquist projection for buffer-exposed sample, makes it possible to conclude that the corrosion product layer forming on metal surface provides partial barrier properties and decreases the corrosion rate approximately 2.5 $\times$ .

When exposed to buffer with addition of 10 mM catechol, the instantaneous charge transfer resistance is slightly higher (typically around 0.4 k $\Omega$ ) and then gradually increases over time to reach significantly improved inhibition efficiency of ~98% after 24 h exposure. On the other hand, AA5754 exposed to electrolyte containing the same amount of resorcinol shows very small increase of charge transfer resistance over duration of the long-term exposure experiment.

The long-term exposure study allows drawing two important conclusions. First, there must be an additional interaction between studied inhibitor molecules and the electrolyte or the analyzed sample, which further differentiates the electrochemical characteristics of these dihydroxybenzene isomers over time. Second, when performing inhibitor efficiency measurements one has to take into consideration possible changes of investigated system characteristics. This is possible by carrying out fast measurements with techniques that allow non-stationary process analyses (such as g-DEIS). Alternatively, one could employ a sufficiently long conditioning period, which might be different for each studied system. The latter approach, although more accessible, may cause problems in terms of meeting the conditions for many adsorption models.

The authors claim that the mechanism leading to further differentiation of adsorption by catechol and resorcinol on the aluminum alloy surface is the keto-enol tautomerism, which may occur in aqueous alkaline environments. Nuclear magnetic resonance (NMR) studies were performed in order to verify this hypothesis.

$^1\text{H-NMR}$  measurements were performed in order to determine the presence of possible keto-enol forms in resorcinol in the alkaline conditions or to determine the formation of a salt of those compounds. The studies of proton transfer by  $^1\text{H-NMR}$  titration present a useful technique to determine the keto-enol equilibria [62,63]. The  $^1\text{H-NMR}$  spectra of resorcinol dissolved in  $\text{D}_2\text{O}$  with addition of NaOH in molar ration of 1:5 and 1:10 are presented on Figure 8. The  $^1\text{H-NMR}$  spectra of resorcinol have previously been performed in  $\text{D}_2\text{O}$  [64,65], while the titration of this compound by NaOH has not been investigated.

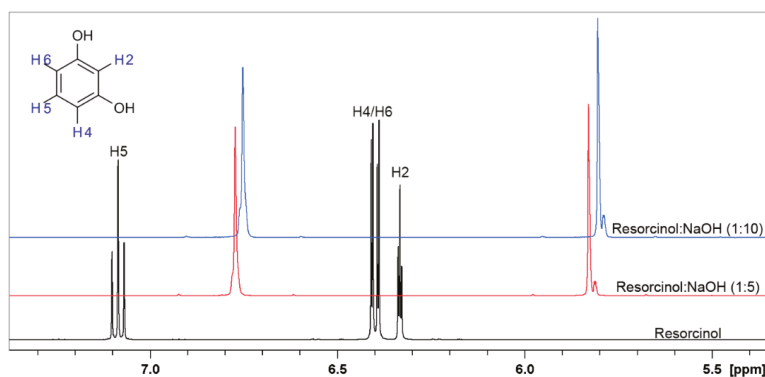


**Figure 8.**  $^1\text{H}$ -NMR spectra of resorcinol in  $\text{D}_2\text{O}$  (black line) and in the presence of NaOH in  $\text{D}_2\text{O}$  in the molar ratio 1:5 (red line) and 1:10 (blue line), respectively.

Two triplets are observed on spectra of resorcinol in  $\text{D}_2\text{O}$ , which correspond to H5 and H2, while two doublets correspond to H4 and H6. The spectra of resorcinol after the addition of NaOH in molar ratio 1:5 changed diametrically. The shape, the chemical shifts and the multiplicity are different in comparison to the first one. Two main signals shifted towards negative values are now observed. This phenomenon indicates that the protons present in the structure of resorcinol are changed, further influencing the chemical shifts and the multiplicity. The addition of molar excess of NaOH in (1:10), does not cause any additional changes in  $^1\text{H}$ -NMR spectrum shape, but the peaks are further shifted.

The determination of the new resorcinol derivative structure was possible after measuring the  $^{13}\text{C}$ -NMR spectra, shown on Figure 9. These spectra were performed in  $\text{D}_2\text{O}$  and after addition of NaOH in molar ratio 1:5 and 1:10, similar to previous experiment. It should be noticed that the peaks C4, C5, and C6 present in spectra before and after addition of NaOH do not change their position significantly. On the other hand, peaks C1 and C3, overlapping at 156.8 ppm, change their position to 167.4 ppm with the addition of NaOH, which may indicate that keto form is present in the structure of resorcinol regardless the molar ratio. Additionally, after addition of NaOH the shift of peak C2 is observed from 102.6 ppm to 106.0 ppm, this shift confirms the formation of keto form.

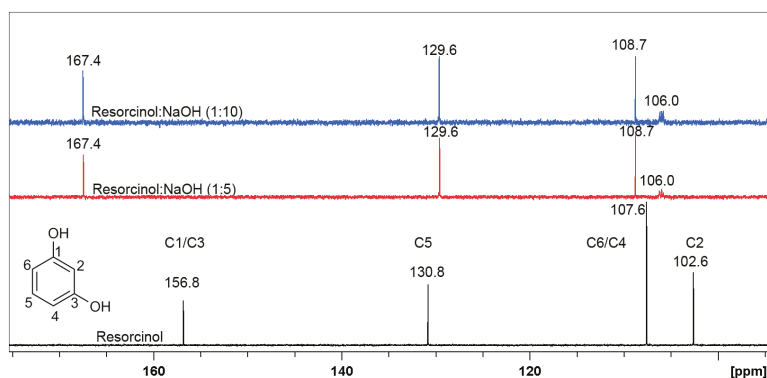


**Figure 9.**  $^{13}\text{C}$ -NMR spectra of resorcinol in  $\text{D}_2\text{O}$  (black line) and in the presence of NaOH in  $\text{D}_2\text{O}$  in molar ratio 1:5 (red line) and 1:10 (blue line), respectively.

In the next step, the  $^1\text{H}$ -NMR and  $^{13}\text{C}$ -NMR spectra were performed for catechol under the same experimental conditions. The  $^1\text{H}$ -NMR spectra of catechol have previously been performed in aqueous

solution, but under acidic pH = 2.4 [66] and in  $\text{CDCl}_3$  [67]. The shape and chemical shifts of  $^1\text{H-NMR}$  spectra illustrated on Figure 10 are very similar to those in the literature.

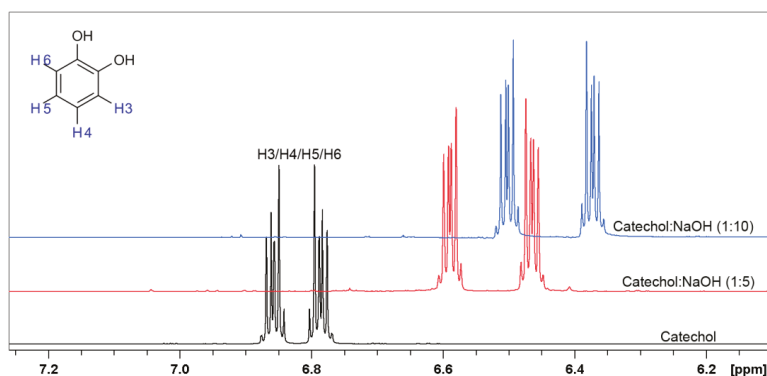


**Figure 10.**  $^1\text{H-NMR}$  spectra of catechol in  $\text{D}_2\text{O}$  (black line) and in the presence of NaOH in  $\text{D}_2\text{O}$  in molar ratio 1:5 (red line) and 1:1 (blue line), respectively.

Two multiplets are present regardless of the solution, while the addition of NaOH in ratio 1:5 and 1:10, respectively, do not cause any changes in  $^1\text{H-NMR}$  spectra shape; however, with increasing molar ratio of NaOH, the spectra are shifting towards more negative values. The above changes clearly indicate that the chemical structure of the catechol does not change significantly, while the shifts may indicate formation of sodium salts of catechol [68].

$^{13}\text{C-NMR}$  spectra were performed in order to confirm the formation of sodium salt of catechol in alkaline conditions, as shown on Figure 11. The obtained data confirm previously drawn assumptions.  $^{13}\text{C-NMR}$  spectra reveal  $^{13}\text{C}$  chemical shifts for catechol in  $\text{D}_2\text{O}$  with the presence of NaOH in molar ratio 1:5 and 1:10. The C1 and C2 atoms connected to the hydroxyl groups in catechol in investigated solutions both give signal at 143.9 ppm in absence of NaOH, but after its addition, the signal is shifted towards 152.6 ppm and 154.9 ppm for ratio 1:5 and 1:10, respectively. The shift of carbon signals directly indicates that catechol in alkaline solutions forms a salt [69]. It is worth noticing that a small change of peak position was also observed for carbon C4/C5 and C3/C6 after additions of NaOH.

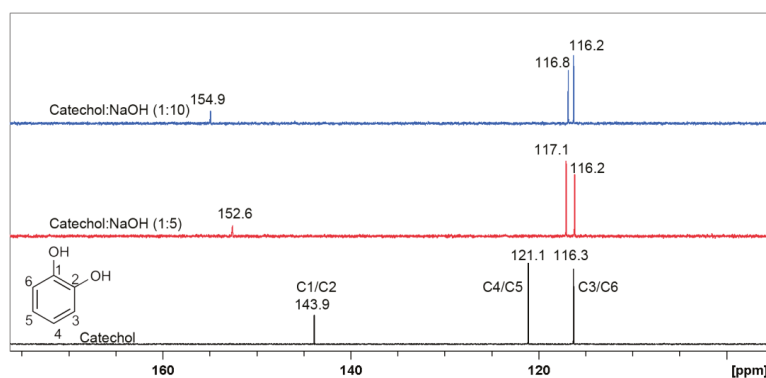


**Figure 11.**  $^{13}\text{C-NMR}$  spectra of catechol in  $\text{D}_2\text{O}$  (black line) and in the presence of NaOH in  $\text{D}_2\text{O}$  in the molar ratio 1:5 (red line) and 1:1 (blue line), respectively.

### 3.5. Dihydroxybenzene Isomers Adsorption Mechanism

The overall interaction of the studied dihydroxybenzene isomers with aluminum alloy 5754 surface may thus be explained using the scheme presented on Figure 12. Figure 12a illustrates the case of aluminum corrosion in an alkaline environment, according to the two-step mechanism discussed in the introduction section: 1) attack of  $\text{OH}^-$  ions on  $\text{Al}_2\text{O}_3$  leading to its dissolution and  $\text{Al}(\text{OH})_3$  formation, followed shortly after by 2) chemical formation of  $\text{Al}(\text{OH})_4^-$  ions. The corrosion inhibition mechanism for catechol considers formation of ligands with aluminum ions (see Figure 12b), which is hindered in the case of resorcinol. On the other hand, resorcinol depends on the formation of insoluble corrosion products layer, which to a large extent provides a barrier mechanism towards corrosive electrolyte. The molecules chemisorb on the corrosion products layer, which becomes very efficient only at high inhibitor concentrations.

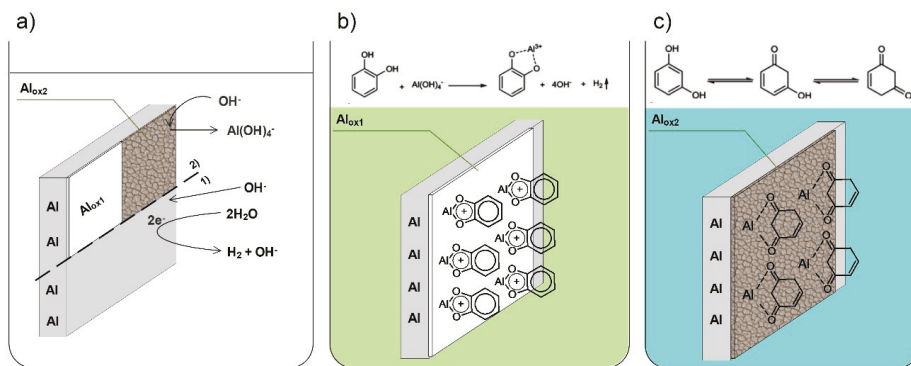


**Figure 12.** Schematic representation of aluminum corrosion mechanism in aqueous alkaline solutions: (a) in absence of corrosion inhibitor and with the addition of (b) catechol; (c) resorcinol. Phase (1) represents the  $\text{OH}^-$  attack leading to formation  $\text{Al}(\text{OH})_3$ , phase (2) describes the interaction between  $\text{OH}^-$  and  $\text{Al}(\text{OH})_3$ , leading to the formation of  $\text{Al}(\text{OH})_4^-$  and a non-stoichiometric insoluble corrosion product layer.

The lower inhibition efficiency of resorcinol at concentrations not exceeding 10 mM is connected with the keto-enol tautomerism mechanism, occurring in aqueous alkaline media and lowering the molecule influence on the corrosion protection (see Figure 12c). Due to local differences in pH in anodic and cathodic zones of electrode/electrolyte interface, the dynamics of the keto-enol tautomerism may be locally altered. The NMR spectra revealed that the process takes place in wide pH range.

## 4. Conclusions

Understanding the interaction mechanism of inhibitor molecules with the protected metal surface is of key importance in the selection of the most efficient corrosion inhibitors, the most important, in particular, in the case of green inhibitors based on natural extracts. While it is widely known how different functional groups affect the adsorption mechanism, the differences introduced by its location within the inhibitor molecule are often omitted.

In this study, we revealed how the position of hydroxyl groups affects the adsorption mechanism of dihydroxybenzene isomers and offered corrosion resistance toward aluminum alloy 5754 surface in alkaline environment. The utilization of Dynamic Electrochemical Impedance Spectroscopy in galvanostatic mode (g-DEIS) for adsorption isotherm determination made it possible to confirm different forms of dihydroxybenzene interaction. All of the studied inhibitors followed the Langmuir model of adsorption, although we have observed that its applicability lies in different inhibitor concentration ranges.

Resorcinol was found to be characterized by the chemical adsorption mechanism. Its adsorption on aluminum surface is competitive to insoluble corrosion product layer formation, as shown with SEM and XPS studies. This interaction leads to the best inhibitor efficiency at the highest investigated concentration of 100 mM, but is not as efficient at lower concentrations. On the other hand, catechol and quinol follow the ligand exchange model of adsorption. This leads to more efficient adsorption and increases corrosion protection even at lower corrosion concentrations: 1 and 10 mM. The adsorption process dominates insoluble corrosion product layer formation, the presence of which on the analyzed surface was negligible.

The next significant difference lies in the long-term behavior and corrosion protection offered by dihydroxybenzene isomers in alkaline electrolyte. We report that resorcinol molecules undergo keto-enol tautomerism in sodium hydroxide solution, while the aforementioned process was negligible in the case of quinol and catechol. The tautomerism leads to the rebuilding of the inhibitor molecule, electrolyte discoloration, but does not have significant influence on the chemical adsorption mechanism by resorcinol over longer periods of time. It is even possible that the presence of keto-enol tautomerism itself is the reason behind hindered adsorption of resorcinol and offered corrosion resistance. Keto forms were not observed in the structure of catechol and quinol molecules. At the same time, their ability to complex metal ions leads to formation of layers with higher barrier properties and increased corrosion inhibition.

**Author Contributions:** Conceptualization, J.R.; Methodology, J.R. and J.W.; Investigation, M.B., M.K., W.L. (Electrochemical Studies, SEM), J.R. (XPS) and P.N. (NMR); Resources, J.R.; Writing—Original Draft Preparation, J.R., P.N., J.W. and W.L.; Writing—Review and Editing, J.R. and J.W.; Funding Acquisition, J.R.

**Funding:** The authors acknowledge the financial support of the Polish Ministry of Science and Higher Education from the budget funds in the period 2016-2019 under Luventus Plus project IP2015 067574.

**Acknowledgments:** The authors acknowledge Pawel Slepski and Artur Zielinski from Gdansk University of Technology for development of the software dedicated to effective DEIS data collection and analysis.

**Conflicts of Interest:** The authors declare no conflict of interest.

## References

- Greenwood, N.N.; Earnshaw, A. *Chemistry of the Elements*, 2nd ed.; Butterworth-Heinemann: Oxford, UK; Boston, MA, USA, 1997; ISBN 978-0-7506-3365-9.
- Sanders, R.E. Updated by Staff Aluminum and Aluminum Alloys. In *Kirk-Othmer Encyclopedia of Chemical Technology*; John Wiley & Sons, Inc., Ed.; John Wiley & Sons, Inc.: Hoboken, NJ, USA, 2012; ISBN 978-0-471-23896-6. [[CrossRef](#)]
- Macdonald, D.D. Evaluation of Alloy Anodes for Aluminum-Air Batteries. *J. Electrochem. Soc.* **1988**, *135*, 2410. [[CrossRef](#)]
- Chu, D.; Savinell, R.F. Experimental data on aluminum dissolution in KOH electrolytes. *Electrochim. Acta* **1991**, *36*, 1631–1638. [[CrossRef](#)]
- Pyun, S.-I.; Moon, S.-M. Corrosion mechanism of pure aluminium in aqueous alkaline solution. *J. Solid State Electrochem.* **2000**, *4*, 267–272. [[CrossRef](#)]
- Moon, S.-M.; Pyun, S.-I. The corrosion of pure aluminium during cathodic polarization in aqueous solutions. *Corros. Sci.* **1997**, *39*, 399–408. [[CrossRef](#)]
- Adhikari, S.; Hebert, K.R. Factors controlling the time evolution of the corrosion potential of aluminum in alkaline solutions. *Corros. Sci.* **2008**, *50*, 1414–1421. [[CrossRef](#)]
- Adhikari, S.; Lee, J.; Hebert, K.R. Formation of Aluminum Hydride during Alkaline Dissolution of Aluminum. *J. Electrochem. Soc.* **2008**, *155*, C16. [[CrossRef](#)]
- Perrault, G.G. The Role of Hydrides in the Equilibrium of Aluminum in Aqueous Solutions. *J. Electrochem. Soc.* **1979**, *126*, 199. [[CrossRef](#)]
- Brown, O.R.; Whitley, J.S. Electrochemical behaviour of aluminium in aqueous caustic solutions. *Electrochim. Acta* **1987**, *32*, 545–556. [[CrossRef](#)]
- Li, Q.; Bjerrum, N.J. Aluminum as anode for energy storage and conversion: A review. *J. Power Sour.* **2002**, *110*, 1–10. [[CrossRef](#)]



12. Liu, Y.; Sun, Q.; Li, W.; Adair, K.R.; Li, J.; Sun, X. A comprehensive review on recent progress in aluminum–air batteries. *Gr. Energy Environ.* **2017**, *2*, 246–277. [[CrossRef](#)]
13. Yang, S. Design and analysis of aluminum/air battery system for electric vehicles. *J. Power Sour.* **2002**, *112*, 162–173. [[CrossRef](#)]
14. Zhang, X.; Yang, S.H.; Knickle, H. Novel operation and control of an electric vehicle aluminum/air battery system. *J. Power Sour.* **2004**, *128*, 331–342. [[CrossRef](#)]
15. Singh, A.; Ansari, K.; Quraishi, M.; Lgaz, H. Effect of Electron Donating Functional Groups on Corrosion Inhibition of J55 Steel in a Sweet Corrosive Environment: Experimental, Density Functional Theory, and Molecular Dynamic Simulation. *Materials* **2018**, *12*, 17. [[CrossRef](#)] [[PubMed](#)]
16. Al-Suhybani, A.A.; Sultan, Y.H.; Hamid, W.A. Corrosion of aluminium in alkaline solutions. *Mater. Werkst.* **1991**, *22*, 301–307. [[CrossRef](#)]
17. Ebenso, E.E.; Isabirye, D.A.; Eddy, N.O. Adsorption and Quantum Chemical Studies on the Inhibition Potentials of Some Thiosemicarbazides for the Corrosion of Mild Steel in Acidic Medium. *IJMS* **2010**, *11*, 2473–2498. [[CrossRef](#)] [[PubMed](#)]
18. Khanari, K.; Finšgar, M. Organic corrosion inhibitors for aluminum and its alloys in chloride and alkaline solutions: A review. *Arab. J. Chem.* **2016**, in press. [[CrossRef](#)]
19. Wysocka, J.; Krakowiak, S.; Ryl, J. Evaluation of citric acid corrosion inhibition efficiency and passivation kinetics for aluminium alloys in alkaline media by means of dynamic impedance monitoring. *Electrochim. Acta* **2017**, *258*, 1463–1475. [[CrossRef](#)]
20. Wysocka, J.; Cieslik, M.; Krakowiak, S.; Ryl, J. Carboxylic acids as efficient corrosion inhibitors of aluminium alloys in alkaline media. *Electrochim. Acta* **2018**, *289*, 175–192. [[CrossRef](#)]
21. Brito, P.S.D.; Sequeira, C.A.C. Organic Inhibitors of the Anode Self-Corrosion in Aluminum-Air Batteries. *J. Fuel Cell Sci. Technol.* **2013**, *11*, 011008. [[CrossRef](#)]
22. Müller, B. Citric acid as corrosion inhibitor for aluminium pigment. *Corros. Sci.* **2004**, *46*, 159–167. [[CrossRef](#)]
23. Amin, M.A.; El-Rehim, S.S.A.; El-Sherbini, E.E.F.; Hazzazi, O.A.; Abbas, M.N. Polyacrylic acid as a corrosion inhibitor for aluminium in weakly alkaline solutions. Part I: Weight loss, polarization, impedance EFM and EDX studies. *Corros. Sci.* **2009**, *51*, 658–667. [[CrossRef](#)]
24. Kumari, P.D.R.; Nayak, J.; Shetty, A.N. 3-Methyl-4-amino-5-mercapto-1, 2, 4-triazole as corrosion inhibitor for 6061 Al alloy in 0.5 M sodium hydroxide solution. *J. Coat. Technol. Res.* **2011**, *8*, 685–695. [[CrossRef](#)]
25. Lashgari, M.; Malek, A.M. Fundamental studies of aluminum corrosion in acidic and basic environments: Theoretical predictions and experimental observations. *Electrochim. Acta* **2010**, *55*, 5253–5257. [[CrossRef](#)]
26. Lashgari, M. Theoretical challenges in understanding the inhibition mechanism of aluminum corrosion in basic media in the presence of some p-phenol derivatives. *Electrochim. Acta* **2011**, *56*, 3322–3327. [[CrossRef](#)]
27. Al-Amiery, A.; Al-Majedy, Y.; Kadhum, A.; Mohamad, A. New Coumarin Derivative as an Eco-Friendly Inhibitor of Corrosion of Mild Steel in Acid Medium. *Molecules* **2014**, *20*, 366–383. [[CrossRef](#)] [[PubMed](#)]
28. Yang, W.; Wang, Q.; Xu, K.; Yin, Y.; Bao, H.; Li, X.; Niu, L.; Chen, S. Enhanced Corrosion Resistance of Carbon Steel in Hydrochloric Acid Solution by *Eriobotrya Japonica* Thunb. Leaf Extract: Electrochemical Study. *Materials* **2017**, *10*, 956. [[CrossRef](#)]
29. Okeniyi, J.; Loto, C.; Popoola, A. Effects of *Phyllanthus muellerianus* Leaf-Extract on Steel-Reinforcement Corrosion in 3.5% NaCl-Immersed Concrete. *Metals* **2016**, *6*, 255. [[CrossRef](#)]
30. Fares, M.M.; Maayta, A.K.; Al-Qudah, M.M. Pectin as promising green corrosion inhibitor of aluminum in hydrochloric acid solution. *Corros. Sci.* **2012**, *60*, 112–117. [[CrossRef](#)]
31. Abdel-Gaber, A.M.; Abd-El-Nabey, B.A.; Sidahmed, I.M.; El-Zayady, A.M.; Saadawy, M. Inhibitive action of some plant extracts on the corrosion of steel in acidic media. *Corros. Sci.* **2006**, *48*, 2765–2779. [[CrossRef](#)]
32. Abiola, O.K.; Otaigbe, J.O.E.; Kio, O.J. Gossipium hirsutum L. extracts as green corrosion inhibitor for aluminum in NaOH solution. *Corros. Sci.* **2009**, *51*, 1879–1881. [[CrossRef](#)]
33. Abiola, O.K.; Oforka, N.C.; Ebenso, E.E.; Nwinuka, N.M. Eco-friendly corrosion inhibitors: The inhibitive action of *Delonix Regia* extract for the corrosion of aluminium in acidic media. *Anti-Corros. Methods Mater.* **2007**, *54*, 219–224. [[CrossRef](#)]
34. Azzaoui, K.; Mejdoubi, E.; Jodeh, S.; Lamhamdi, A.; Rodriguez-Castellón, E.; Algarra, M.; Zarrouk, A.; Errich, A.; Salghi, R.; Lgaz, H. Eco friendly green inhibitor Gum Arabic (GA) for the corrosion control of mild steel in hydrochloric acid medium. *Corros. Sci.* **2017**, *129*, 70–81. [[CrossRef](#)]

35. de Souza, F.S.; Spinelli, A. Caffeic acid as a green corrosion inhibitor for mild steel. *Corros. Sci.* **2009**, *51*, 642–649. [[CrossRef](#)]
36. Abiola, O.K.; Otaigbe, J.O.E. The effects of Phyllanthus amarus extract on corrosion and kinetics of corrosion process of aluminum in alkaline solution. *Corros. Sci.* **2009**, *51*, 2790–2793. [[CrossRef](#)]
37. Singh, A.; Ahamad, I.; Quraishi, M.A. Piper longum extract as green corrosion inhibitor for aluminium in NaOH solution. *Arab. J. Chem.* **2016**, *9*, S1584–S1589. [[CrossRef](#)]
38. Ryl, J.; Wysocka, J.; Cieslik, M.; Gerengi, H.; Ossowski, T.; Krakowiak, S.; Niedzialkowski, P. Understanding the origin of high corrosion inhibition efficiency of bee products towards aluminium alloys in alkaline environments. *Electrochim. Acta* **2019**, *304*, 263–274. [[CrossRef](#)]
39. Talati, J.D.; Modi, R.M. O-Substituted Phenols as Corrosion Inhibitors for Aluminium-Copper Alloy in Sodium Hydroxide. *Br. Corros. J.* **1977**, *12*, 180–184. [[CrossRef](#)]
40. Lakshmi, D.; Rajendran, S.; Sathiabama, J. Inhibition of Corrosion of Aluminium in Aqueous Solution at pH11 by Resorcinol-Zn<sup>2+</sup> System. *Int. J. Nano Corr. Sci. Eng.* **2016**, *3*, 26–42.
41. Fouda, A.S.; Elasmay, A.A. Efficiency of some phenylthiosemicarbazide derivatives in retarding the dissolution of Al in NaOH solution. *Mon. Chem.* **1987**, *118*, 709–716. [[CrossRef](#)]
42. Hassan, S.M.; Moussa, M.N.; El-Tagoury, M.M.; Radi, A.A. Aromatic acid derivatives as corrosion inhibitors for aluminium in acidic and alkaline solutions. *Anti-Corros. Methods Mater.* **1990**, *37*, 8–11. [[CrossRef](#)]
43. Obi-Egbedi, N.O.; Obot, I.B.; El-Khaiary, M.I. Quantum chemical investigation and statistical analysis of the relationship between corrosion inhibition efficiency and molecular structure of xanthene and its derivatives on mild steel in sulphuric acid. *J. Mol. Struct.* **2011**, *1002*, 86–96. [[CrossRef](#)]
44. Khaled, K.F. Electrochemical investigation and modeling of corrosion inhibition of aluminum in molar nitric acid using some sulphur-containing amines. *Corros. Sci.* **2010**, *52*, 2905–2916. [[CrossRef](#)]
45. Ramesh Babu, B.; Holze, R. Corrosion and hydrogen permeation inhibition for mild steel in HCl by isomers of organic compounds. *Br. Corros. J.* **2000**, *35*, 204–209. [[CrossRef](#)]
46. Talati, J.D.; Desai, M.N.; Shah, N.K. Ortho-, meta-, and para-aminophenol-N-salicylidenes as corrosion inhibitors of zinc in sulfuric acid. *Anti-Corros. Meth Mater.* **2005**, *52*, 108–117. [[CrossRef](#)]
47. Ryl, J.; Darowicki, K.; Slepski, P. Evaluation of cavitation erosion–corrosion degradation of mild steel by means of dynamic impedance spectroscopy in galvanostatic mode. *Corros. Sci.* **2011**, *53*, 1873–1879. [[CrossRef](#)]
48. Gerengi, H.; Darowicki, K.; Slepski, P.; Bereket, G.; Ryl, J. Investigation effect of benzotriazole on the corrosion of brass-MM55 alloy in artificial seawater by dynamic EIS. *J. Solid State Electrochem.* **2010**, *14*, 897–902. [[CrossRef](#)]
49. Gerengi, H. The Use of Dynamic Electrochemical Impedance Spectroscopy in Corrosion Inhibitor Studies. *Prot. Met. Phys. Chem. Surf.* **2018**, *54*, 536–540. [[CrossRef](#)]
50. Hirschorn, B.; Orazem, M.E.; Tribollet, B.; Vivier, V.; Frateur, I.; Musiani, M. Determination of effective capacitance and film thickness from constant-phase-element parameters. *Electrochim. Acta* **2010**, *55*, 6218–6227. [[CrossRef](#)]
51. Talati, J.D.; Modi, R.M. Dihydroxy-benzenes as Corrosion Inhibitors for Aluminium–Copper Alloy in Sodium Hydroxide. *Br. Corros. J.* **1975**, *10*, 103–106. [[CrossRef](#)]
52. Suresh, S.; Srivastava, V.C.; Mishra, I.M. Adsorption of catechol, resorcinol, hydroquinone, and their derivatives: A review. *Int. J. Energy Environ. Eng.* **2012**, *3*, 32. [[CrossRef](#)]
53. Wysocka, J.; Krakowiak, S.; Ryl, J.; Darowicki, K. Investigation of the electrochemical behaviour of AA1050 aluminium alloy in aqueous alkaline solutions using Dynamic Electrochemical Impedance Spectroscopy. *J. Electroanal. Chem.* **2016**, *778*, 126–136. [[CrossRef](#)]
54. Djordjevic, I.; Choudhury, N.R.; Dutta, N.K.; Kumar, S. Synthesis and characterization of novel citric acid-based polyester elastomers. *Polymer* **2009**, *50*, 1682–1691. [[CrossRef](#)]
55. Amin, M.A.; Ahmed, E.M.; Mostafa, N.Y.; Alotibi, M.M.; Darabdhara, G.; Das, M.R.; Wysocka, J.; Ryl, J.; Abd El-Rehim, S.S. Aluminum Titania Nanoparticle Composites as Nonprecious Catalysts for Efficient Electrochemical Generation of H<sub>2</sub>. *ACS Appl. Mater. Interfaces* **2016**, *8*, 23655–23667. [[CrossRef](#)] [[PubMed](#)]
56. Niedzialkowski, P.; Ossowski, T.; Zięba, P.; Cirocka, A.; Rochowski, P.; Pogorzelski, S.J.; Ryl, J.; Sobaszek, M.; Bogdanowicz, R. Poly-l-lysine-modified boron-doped diamond electrodes for the amperometric detection of nucleic acid bases. *J. Electroanal. Chem.* **2015**, *756*, 84–93. [[CrossRef](#)]

57. McCafferty, E.; Wightman, J.P. Determination of the concentration of surface hydroxyl groups on metal oxide films by a quantitative XPS method. *Surf. Interface Anal.* **1998**, *26*, 549–564. [[CrossRef](#)]
58. Ryl, J.; Wysocka, J.; Jarzynka, M.; Zielinski, A.; Orlikowski, J.; Darowicki, K. Effect of native air-formed oxidation on the corrosion behavior of AA 7075 aluminum alloys. *Corros. Sci.* **2014**, *87*, 150–155. [[CrossRef](#)]
59. Wloka, J.; Bürklin, G.; Virtanen, S. Influence of second phase particles on initial electrochemical properties of AA7010-T76. *Electrochim. Acta* **2007**, *53*, 2055–2059. [[CrossRef](#)]
60. Yasakau, K.A.; Zheludkevich, M.L.; Lamaka, S.V.; Ferreira, M.G.S. Role of intermetallic phases in localized corrosion of AA5083. *Electrochim. Acta* **2007**, *52*, 7651–7659. [[CrossRef](#)]
61. Goswami, R.; Spanos, G.; Pao, P.S.; Holtz, R.L. Precipitation behavior of the  $\beta$  phase in Al-5083. *Mater. Sci. Eng. A* **2010**, *527*, 1089–1095. [[CrossRef](#)]
62. Novak, P.; Skare, D.; Sekusak, S. Substituent, temperature and solvent effects on keto-enol equilibrium in symmetrical pentane-1,3,5-triones. Nuclear magnetic resonance and theoretical studies. *Croat. Chem. Acta* **2000**, *73*, 1153–1170.
63. Billman, J.H.; Sojka, S.A.; Taylor, P.R. Investigations of keto-enol tautomerism by carbon-13 nuclear magnetic resonance spectroscopy. *J. Chem. Soc. Perkin Transaction 2* **1972**, 2034–2035. [[CrossRef](#)]
64. Gaca, K.Z.; Parkinson, J.A.; Sefcik, J. Kinetics of early stages of resorcinol-formaldehyde polymerization investigated by solution-phase nuclear magnetic resonance spectroscopy. *Polymer* **2017**, *110*, 62–73. [[CrossRef](#)]
65. Giles, R.; Kim, I.; Chao, W.E.; Moore, J.; Jung, K.W. Dual Studies on a Hydrogen-Deuterium Exchange of Resorcinol and the Subsequent Kinetic Isotope Effect. *J. Chem. Educ.* **2014**, *91*, 1220–1223. [[CrossRef](#)]
66. Lambert, F.; Ellenberger, M.; Merlin, L.; Cohen, Y. NMR study of catechol and some catecholamines. *Org. Magn. Reson.* **1975**, *7*, 266–273. [[CrossRef](#)]
67. Luisier, N.; Schenk, K.; Severin, K. A four-component organogel based on orthogonal chemical interactions. *Chem. Commun.* **2014**, *50*, 10233–10236. [[CrossRef](#)] [[PubMed](#)]
68. Kim, H.; Gao, J.; Burgess, D.J. Evaluation of solvent effects on protonation using NMR spectroscopy: Implication in salt formation. *Int. J. Pharm.* **2009**, *377*, 105–111. [[CrossRef](#)] [[PubMed](#)]
69. Pretsch, E.; Bühlmann, P.; Badertscher, M. *Structure Determination of Organic Compounds*; Springer: Berlin/Heidelberg, Germany, 2009; ISBN 978-3-540-93809-5.



© 2019 by the authors. Licensee MDPI, Basel, Switzerland. This article is an open access article distributed under the terms and conditions of the Creative Commons Attribution (CC BY) license (<http://creativecommons.org/licenses/by/4.0/>).

Article

# PDC Glass/Ceramic Coatings Applied to Differently Pretreated AISI441 Stainless Steel Substrates

Milan Parchovianský <sup>1,\*</sup>, Ivana Parchovianská <sup>1</sup>, Peter Švančárek <sup>2</sup>, Günter Motz <sup>3</sup> and Dušan Galusek <sup>1,2</sup>

<sup>1</sup> Centre for Functional and Surface Functionalised Glass, Alexander Dubček University of Trenčín, Študentská 2, 911 50 Trenčín, Slovakia; ivana.parchovianska@tnuni.sk (I.P.); dusan.galusek@tnuni.sk (D.G.)

<sup>2</sup> Joint Glass Centre of the Institute of Inorganic Chemistry Slovak Academy of Sciences, Alexander Dubček University of Trenčín and Faculty of Chemical and Food Technology Slovak University of Technology, Študentská 2, 911 50 Trenčín, Slovakia; peter.svancarek@tnuni.sk

<sup>3</sup> Ceramic Materials Engineering (CME), University of Bayreuth, D-95440 Bayreuth, Germany; guenter.motz@uni-bayreuth.de

\* Correspondence: milan.parchoviansky@tnuni.sk; Tel.: +421-944600882

Received: 16 December 2019; Accepted: 24 January 2020; Published: 31 January 2020

**Abstract:** In this work, the influence of different cleaning procedures on adhesion of composite coatings containing passive ceramic and commercial glasses was investigated. Two compositions (C2c, D2-PP) of double-layer polymer-derived ceramic (PDC) coating systems, composed from bond coat and a top coat, were developed. In order to obtain adherent coatings, stainless steel substrates were cleaned by four different cleaning procedures. The coatings were then deposited onto the steel substrate via spray coating. Pretreatment by subsequent ultrasonic cleaning in acetone, ethanol and deionised water (procedure U) was found to be the most effective, and the resultant C2c and D2-PP coatings, pyrolysed at 850 °C, indicated strong adhesion without delamination or cracks, propagating at the interface steel/bond coat. In the substrate treated by sandblasting and chemical etching, small cracks in the bond coat were observed under the same pyrolysis conditions. After oxidation tests, all coatings, except for those subjected to the U-treated substrates, showed significant cracking in the bond coat. The D2-PP coatings were denser than C2c, indicating better protection of the substrate.

**Keywords:** cleaning; bond coat; PDC coatings; fillers

## 1. Introduction

Because of the increasing costs for metals, there is an effort made to enhance the service life of steel components exposed to aggressive environment, which is commonly used in exhaust gas elements, waste incineration plants or in chemical industry. Refractory stainless steels are highly oxidation and corrosion resistant materials. As metal wear and oxidation/corrosion cause significant economic losses, the development of thermal (TB) and environmental barrier coatings (EBC) is the matter of significant importance.

Due to their extraordinary properties at high temperatures and in chemically aggressive environments, non-oxide and oxide PDC ceramic coatings are suitable for increasing the oxidation and corrosion resistance of metals [1]. Preceramic polymers offer a lot of processing advantages that are not possible with traditional ceramics [2]. For example, organosilicon polymer precursors such as polysiloxanes [3], polycarbosilanes [4], or polysilazanes [5–7], represent a class of hybrid materials which, by suitable heat treatment (pyrolysis in a controlled atmosphere), provide high purity ceramic materials with an adaptable chemical composition and a well-defined structure. These polymers are characterised by an inorganic polymer chain composed of silicon atoms and organic substituents attached to the backbone. Polysilazanes are currently used as precursors for the synthesis of Si<sub>3</sub>N<sub>4</sub> and

SiCN ceramics, mainly due to the high ceramic yield after pyrolysis (often >80 wt. %) [8]. Polysilazanes are suitable materials for the preparation of protective coatings due to their excellent oxidation and corrosion resistance, UV stability and high hardness. These polymers have excellent adhesion to a wide variety of different substrates, e.g., metal, composite, graphite and glass. The PDC route provide the application of liquid or diluted polymers by easily scalable methods, such as dip-coating [9,10], spin-coating [11], doctor-blade method [12] or spray-coating [13,14]. The choice of a particular method depends on the future use of the coating, the type and shape of the body to be coated and the deposited layer, the size of the covered area, the thickness of the coating and its desired properties.

The main disadvantage of the organosilicon polymer precursors, however, is shrinkage, often more than 50 vol. %, that occurs during the transformation from polymer to an amorphous ceramic [15]. The undesirable shrinkage of the polymer leads to crack formation and, in extreme cases, complete failure of the coating. To overcome these unwanted problems, the coatings that consist of only liquid polymer have to be loaded with beneficial components called fillers. The fillers are active [16,17] or passive, and include a large variety of materials, including YSZ [18], Si<sub>3</sub>N<sub>4</sub> [19], Al<sub>2</sub>O<sub>3</sub> [20] and NbC [21] or commercial glasses [22]. The fillers partially or completely compensate the shrinkage, close the pores and increase the coating thickness [23].

The main function of passive fillers is to decrease the bulk fraction of the polymer used, to reduce the amount of gases generated during pyrolysis and, consequently, to alleviate the overall weight loss and shrinkage, and to eliminate the presence of macro-defects by filling the void space in the material without changing its volume. The glass fillers account for densification and sealing of the system, increasing the efficiency of EBC [24]. The service temperature and softening point of the glass filler particles should be matched to increase efficiency of the coating and, in optimum case, heal any defects formed during the coating operation. In our previous work [25], composite PDC coatings with passive fillers and commercial glasses have been developed. Despite using a range of passive fillers, the bulk shrinkage of the polymer precursor has in many cases led to the preparation of porous coatings. Also, the coating often delaminated from the metal substrate, and lost its protective action as EBC.

Another factor ensuring good adhesion of PDC coatings is based on providing an appropriate surface of stainless steel substrate. A number of various pretreatment procedures, such as sandblasting or etching the substrate by different chemical agents, have been described.

In this work, the influence of pretreatment of the AISI441 steel substrate such as sandblasting, etching of the surface or combination of these methods, were investigated in order to choose the most effective type of cleaning and prevent the delamination of the bond coat from the steel substrate. The oxidation tests were performed in order to evaluate the adhesion of the bond coat at higher temperature and longer operating times.

## 2. Materials and Methods

The preparation of the PDC coating systems consisted of 3 steps: (1) synthesis of passive fillers with compositions in the Al<sub>2</sub>O<sub>3</sub>-Y<sub>2</sub>O<sub>3</sub>-ZrO<sub>2</sub> (AYZ) system by sol-gel Pechini method [26], (2) pretreatment of stainless steel by different methods and (3) preparation of double layer coatings consisting of the bond coat and top coat using a combination of a commercial polymer with passive and glass fillers.

### 2.1. Preparation of the Precursor Powder

A powder in the AYZ system with the composition (in mol. %) 61.49 Al<sub>2</sub>O<sub>3</sub>, 18.51 Y<sub>2</sub>O<sub>3</sub> and 20 ZrO<sub>2</sub> was used as a passive filler was prepared by the modified sol-gel Pechini method [27]. Y<sub>2</sub>O<sub>3</sub> (99.9%, Treibacher Industrie AG, Althofen, Austria) was converted into nitrate by dissolving powder oxide in concentrated HNO<sub>3</sub> (65% Centralchem, Bratislava, Slovakia). Al(NO<sub>3</sub>)<sub>3</sub>·9H<sub>2</sub>O (p.a., Centralchem, Bratislava, Slovakia) and ZrOCl<sub>2</sub>·8H<sub>2</sub>O (99.9%, Sigma-Aldrich Co. LLC., Darmstadt, Germany) dissolved in deionised water were then added to yttrium nitrate solution. A 1:1 molar ratio solution of C<sub>6</sub>H<sub>8</sub>O<sub>7</sub> (99.8%, Centralchem, Bratislava, Slovakia) and C<sub>2</sub>H<sub>4</sub>(OH)<sub>2</sub> (99%, Centralchem, Bratislava, Slovakia) in deionised water was then added dropwise to the mixture, which was then

refluxed under a condenser and heated in an oil bath at a temperature of 85–95 °C for 2 h. Subsequently, the solvent was evaporated under continuous stirring. The product was dried, calcined at 850 °C to a white powder and sieved through a 40 µm sieve. For better usability in relatively thin coatings, the AYZ powder was homogenised and granulated by a freeze-drying process. A flowchart of the process of preparation of AYZ powder is presented in Figure 1.

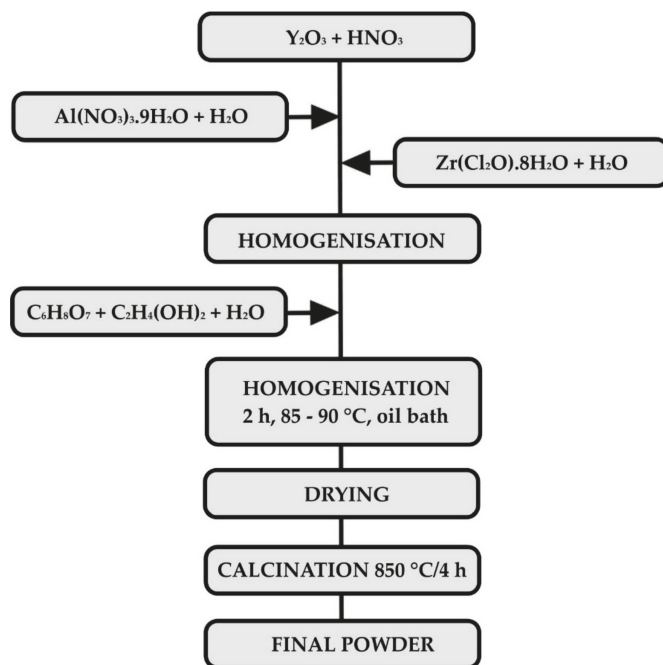


**Figure 1.** The flowchart of the processing of AYZ powder.

## 2.2. Pretreatment of the Stainless Steel

Ferritic refractory stainless steel grade AISI441, which is commonly used in exhaust gas elements, was used as the metal substrate. Prior to cleaning, the steel sheets were cut into  $1 \times 1.5 \text{ cm}^2$  plates to make the samples suitable for further characterisation and testing and to prevent damage to the coated samples by further cutting. This was followed by grinding and chamfering the edges and corners of each sample with sandpaper. To produce adhesive coatings without failure, the surface of stainless steel was treated and cleaned to achieve adhesive coatings with sufficient protective capability at temperatures up to 1000 °C. Four different cleaning procedures were applied, i.e., subsequent ultrasonic cleaning in acetone, ethanol and deionised water; sandblasting with glass beads; chemical etching with Kroll's reagent; and a combination of the last two methods. The description of cleaning procedures of the steel is summarised in Table 1.

**Table 1.** The description of cleaning procedures.

Symbol	Pretreatment of Stainless Steel
U	3-step ultrasonic vibration cleaning in acetone, ethanol and deionised water (10 min each)
S	Sandblasting with glass beads (70–110 µm), ultrasonic cleaning in deionised water
K	Chemical etching—Kroll's reagent (deionised water, HNO <sub>3</sub> , HF), 20 s
S+K	Sandblasting with glass beads + etching with Kroll's reagent

### 2.3. Preparation of the Coatings

A two-layer PDC coating, composed of a bond coat and a ceramic top coat, was applied. The bond coat was prepared from the commercial polymer Durazane 2250 (Merck KGaA, Darmstadt, Germany) by the dip-coating method (dip-coater RDC 15, Relamatic, Glattburg, Switzerland). The pyrolysis of the bond-coat was carried out in air (Nabertherm® N41/H, Nabertherm, Lilienthal, Germany) at a temperature of 450 °C for 1 hour, with heating and cooling rates of 3 K/min. The top coats were prepared from the commercial polymer—Durazane 1800 (Merck KGaA, Darmstadt, Germany), passive fillers and commercial glass. ZrO<sub>2</sub> stabilised with 8 mol. % Y<sub>2</sub>O<sub>3</sub> (8YSZ, Inframat® Advanced Materials™, Manchester, CT, USA), AYZ powder prepared by Pechini method and a commercial glass (G018-281, Schott AG, Mainz, Germany) were used as passive fillers. The basic properties of the filler materials are listed in the Table 2.

**Table 2.** Basic properties of filler materials.

Passive Fillers	d50 (µm)	ρ (g/cm <sup>3</sup> )	CTE (10 <sup>-6</sup> /K)
8YSZ	0.5	6.1	11.5
AYZ	1–10	4.6	8.6
G018-281	0.5–5	2.7	12.1

Commercially available glass was selected to form a viscous melt at the application temperature of the layers, thereby ensuring the healing of any defects and strengthening of the ceramic top layer. The combination of a liquid commercial polymer Durazane 1800 with glass frits and passive filler particles offers the possibility of designing a large range of compositions. Therefore, the composition of the top layer was designed to match the coefficient of thermal expansion (CTE) of the steel substrate and to reduce the CTE mismatch and increase the compatibility of the metal with the ceramic coating. The CTE of stainless steel was provided by the manufacturer (11.5 × 10<sup>-6</sup>/K). The CTE of the prepared coatings were estimated by the rule of mixtures using the CTE of Durazane 1800 (3.0 × 10<sup>-6</sup>/K), 8YSZ (11.5 × 10<sup>-6</sup>/K), AYZ (8.6 × 10<sup>-6</sup>/K) and glass G018-281 (12.1 × 10<sup>-6</sup>/K). Two compositions of top coat were tested, in the following text denoted as C2c and D2-PP. The prepared compositions are listed in Table 3.

**Table 3.** Compositions of the composite top coats after pyrolysis (vol. %).

Sample Name	Durazane 1800	8YSZ	AYZ	G018-281	CTE (10 <sup>-6</sup> /K)
C2c	30	35	-	35	10.1
D2-PP	25	20	20	35	9.6

In the case of the composition C2c, ZrO<sub>2</sub> stabilised with 8 mol. % Y<sub>2</sub>O<sub>3</sub> and glass frits were homogenised in a solution of di-n-butyl ether (Acros Organics BVBA, Geel, Belgium) and dispersant (DISPERBYK 2070, BYK-Chemie GmbH, Wesel, Germany). To break up the agglomerates, the suspensions were dispersed in the ultrasound and homogenised for 48 h by stirring with a magnetic stirrer. Subsequently, Durazane 1800 polymer, with 3 wt. % of dicumyl peroxide (DCP) (Sigma-Aldrich Co. LLC., Darmstadt, Germany), was added to the slurry, which was homogenised for an additional 48 hours in a plastic jar with ZrO<sub>2</sub> balls (Ø1 mm). After homogenisation, the suspension was applied to the stainless steel with a bond coat by a spray-coating technique from both sides. The suspension was deposited onto steel substrates by spray coating using a spray coater model 780S-SS (Nordson EFD, East Providence, RI, USA). The nozzle diameter of spray gun was 0.71 mm (0.028"). The final suspension was sprayed under the air pressure of 2.2 bar. The distance between the spray gun and the sample was 10 cm. In the composition D2-PP, the AYZ powder prepared by the modified Pechini sol-gel method was used as an additional passive filler. The coated samples were then pyrolysed in air

at 850 °C for 1 hour, at a heating and cooling rate of 3 °C/min. A flowchart of the coating processing is presented in Figure 2.

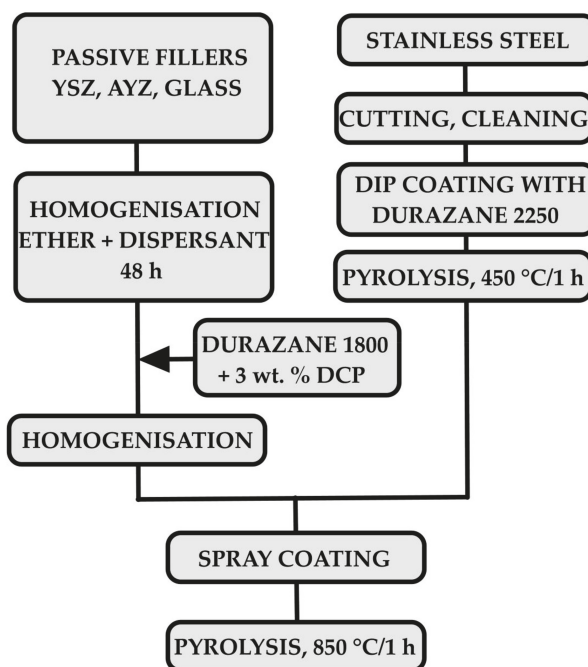


Figure 2. The flowchart of the coatings preparation process.

#### 2.4. Characterisation Methods

X-ray powder diffraction analysis was used to assign the phase composition of the prepared AYZ powder. Diffraction records were measured on an Empyrean DY1098 powder diffractometer (Panalytical, B.V., Almelo, The Netherlands) with a Cu anode and with X-ray wavelength of  $\lambda = 1.5405 \text{ \AA}$  over  $2\theta$  angles of  $10\text{--}80^\circ$ . Diffraction records were then evaluated using HighScore Plus (v. 3.0.4) using COD2019 (Crystallographic Open Database). Mean Roughness Depth (Rz) was measured using atomic force microscopy (AFM, Brooker Innova, Billerica, MA, USA). Rz was calculated by measuring the vertical distance from the highest peak to the lowest valley within five sampling lengths, then averaging these distances. The surface morphology of pretreated samples was examined by scanning electron microscopy (SEM, JEOL JSM 7600 F, JEOL, Tokyo, Japan). For detailed examination of the coating/metal interface, the cross sections were prepared via mounting in resin followed by grinding and polishing. The inspection of the coatings was then performed using an SEM equipped with an energy-dispersive X-ray spectroscopy (EDXS) detector (Oxford instruments, Abingdon, UK) and was focused on the evaluation of adhesion, homogeneity and possible failures of the coatings.

#### 2.5. Oxidation Tests

The oxidation tests were carried out in a high temperature horizontal electric tube furnace (Clasic 0213T, Clasic, Praha, Czech Republic) in flowing atmosphere of synthetic air (purity 99.5, SIAD Slovakia spol. s.r.o., Bratislava, Slovakia) at a temperature of 950 °C with a heating rate of 5 °C/min and an exposure time of 48 h. The composition of synthetic air is as follows; nitrogen (78%), oxygen (21%), argon (0.9%) and other gases (0.1%).



### 3. Results and Discussion

#### 3.1. Characterisation of the AYZ Filler

To achieve a homogenous precursor powder to be used as a filler in the prepared coating, the AYZ powder was prepared via a modified Pechini method [27]. The main advantage of this method is that the metallic ions are immobilised in a rigid polymer network, which ensures their homogeneous dispersion on the atomic scale without precipitation or phase segregation. This process allows complete control over the product stoichiometry, even for more complex oxide powders [27]. To facilitate the use of the AYZ powder in the coatings, the powder was refined by milling and freeze drying to avoid agglomeration of precursor powder and achieve the particle size below 10  $\mu\text{m}$ . SEM micrographs of the AYZ powder after freeze drying are shown in Figure 3. From the as-prepared AYZ powder consists of irregular and angular particles resulting from the crushing process, with the sizes ranging from a few to several tens of micrometres.

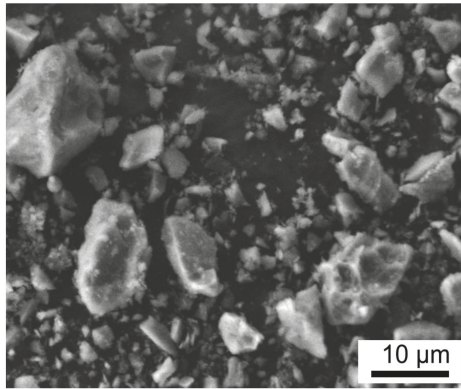


Figure 3. SEM of AYZ powder.

The XRD pattern of AYZ powder after calcination is shown in Figure 4, confirming the presence of  $t\text{-ZrO}_2$ , as well as yttrium aluminium garnet ( $\text{Y}_3\text{Al}_5\text{O}_{12}$ , YAG) as the main crystalline phases formed during calcination. Smaller amount of the mellilite  $\text{Y}_2\text{Al}_2\text{O}_6$  phase was also observed after calcination. High background in the diffraction pattern indicates the crystalline phases were embedded in an amorphous (glassy) matrix.

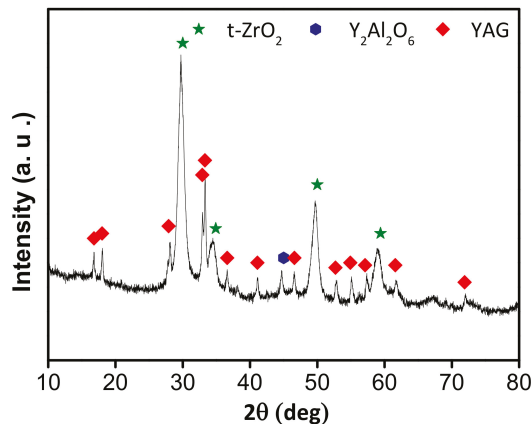
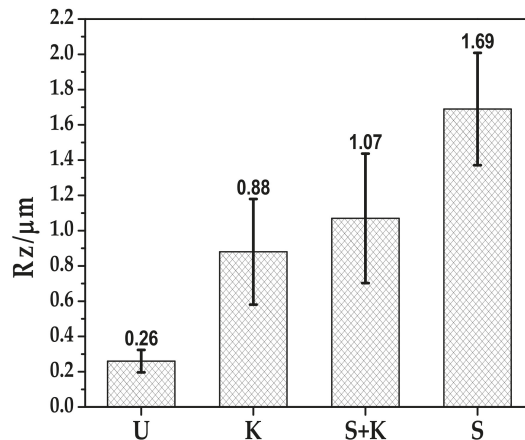


Figure 4. The X-ray powder diffraction (XRD) pattern of AYZ powder after calcination at 850  $^{\circ}\text{C}$ .

### 3.2. Treated Steel Surfaces

The metal surface quality is significant characteristic influencing the adhesion of the protective coating. In the case of double-layer PDC coatings, the weakest point is usually the interface between the bond coat and the metal substrate, due to the presence of impurities or defects on the steel surface, which often lead to delamination of the bond coat during pyrolysis or after corrosion tests. To ensure a high adhesion of the bond coat with the steel, the stainless steel substrate has to be cleaned properly to degrease its surface and remove possible contaminants. The influence of different cleaning procedures on the surface morphology was therefore examined. The Mean Roughness Depth (Rz) was determined using AFM and the surface morphology of pretreated stainless steel samples was examined by SEM. Figure 5 presents the Rz of variously pretreated stainless steel surfaces. The AFM analysis confirmed that different treatment created different sizes of roughness: there is a relation between surface topography and the type of the used cleaning procedure. The Rz was in the range of 0.26 to 1.69  $\mu\text{m}$ . A roughness similar to that observed for untreated surfaces was measured after ultrasonic cleaning, while sandblasting increased the roughness substantially. An increase of Rz was expected to result in stronger bonding at the steel-bond coat interface.



**Figure 5.** The roughness after pretreatment of stainless steel (U – ultrasonic cleaning, K – chemical etching with Kroll's reagent, S – sandblasting, S+K – sandblasting + chemical etching with Kroll's reagent).

AFM images of the stainless steel cleaned by different methods are shown in Figure 6. SEM-micrographs featuring surfaces of the stainless steel cleaned by different methods are shown in Figure 7. Chemical etching resulted in a surface with irregular topography, with slight roughening of the surface compared to ultrasonically cleaned substrates. More uniform and regular surfaces were obtained by sandblasting with glass beads, or a combination of sandblasting and chemical etching with Kroll's reagent. These treatments resulted in rough surfaces with rounded edges, with the average surface roughness 1.69  $\mu\text{m}$  for sandblasted samples. Chemical etching of sandblasted substrates slightly decreased the average surface roughness, but the sandblasting induced roughening was still significant.

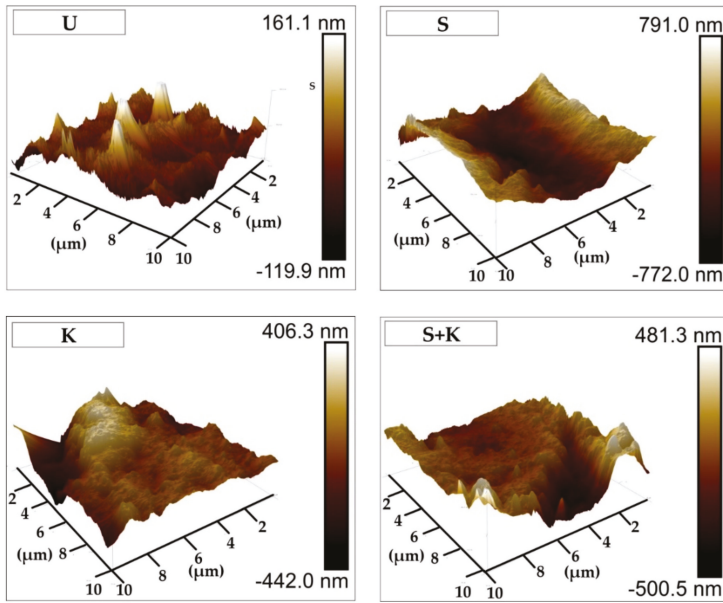


**Figure 6.** Atomic force microscopy (AFM) images representing roughness of the stainless steel surfaces treated by different cleaning procedures. The applied cleaning procedure is indicated by the abbreviation in the upper left corner of each figure (U – ultrasonic cleaning, K – chemical etching with Kroll's reagent, S – sandblasting, S+K – sandblasting + chemical etching with Kroll's reagent).

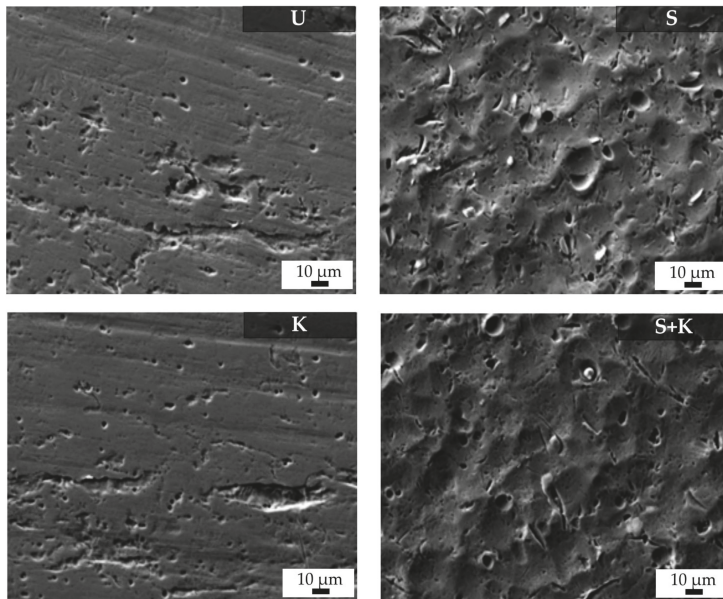


**Figure 7.** SEM micrographs of the stainless steel surfaces treated by different cleaning procedures. The applied cleaning procedure is indicated by the abbreviation in the upper right corner of each figure (U – ultrasonic cleaning, K – chemical etching with Kroll's reagent, S – sandblasting, S+K – sandblasting + chemical etching with Kroll's reagent).

### 3.3. Characterisation of the Coatings

The SEM cross-sectional micrographs of compositions C2c and D2-PP were obtained through the metal–ceramic interface to investigate the bonding between the bond coat and variously treated steel substrates (Figure 8 (C2c composition) and Figure 9 (D2-PP composition)). The weakest location in a typical double layer coating is usually the interface between the stainless steel and the bond coat, where the cracks or spallation can occur. The spallation of the bond coat is usually caused by thermal and elastic mismatch between the steel and bond coat, due to the presence of impurities at the steel surface, by changing the chemistry of the steel by chemical etching, or growth of stresses followed by the formation of thermally-grown oxides, mostly due to the weak adhesion of bond coat to steel. Irrespective of the applied surface treatment the bond coat did not delaminate from the steel surface after pyrolysis of the coatings at 850 °C, indicating its good adhesion. An undamaged bond coat approximately 1 µm thick was observed in all cases, which acts as an effective diffusion barrier to oxidation during pyrolysis. Only for the D2-PP coating deposited at the substrate etched by Kroll's reagent the bond coat peeled off from the surface. If the stainless steel was treated by sandblasting or chemical etching or their combination, a few small cracks (marked with white circles) were generated in the bond coat, perpendicular to the substrate surface. The crack formation was attributed to strong adhesion of the bond coat to the metal substrate and, at the same time, by the high volume shrinkage of the polysilazane during heat treatment. No crack formation in the bond coat was observed on samples pretreated via ultrasonic cleaning in acetone, ethanol and deionised water. Cracking could also occur due to uneven and rough sandblasted surface, with sharp edges and peaks acting as stress concentrators in the coatings [24]. The pretreatment by ultrasonic cleaning in acetone, ethanol and deionised water was found to be the most effective process, since no spallation or cracking was observed in the cross section of the bond coat after pyrolysis. Moreover, the ultrasonically cleaned steel surface was uniformly covered by the approximately 1 µm thick bond coat.

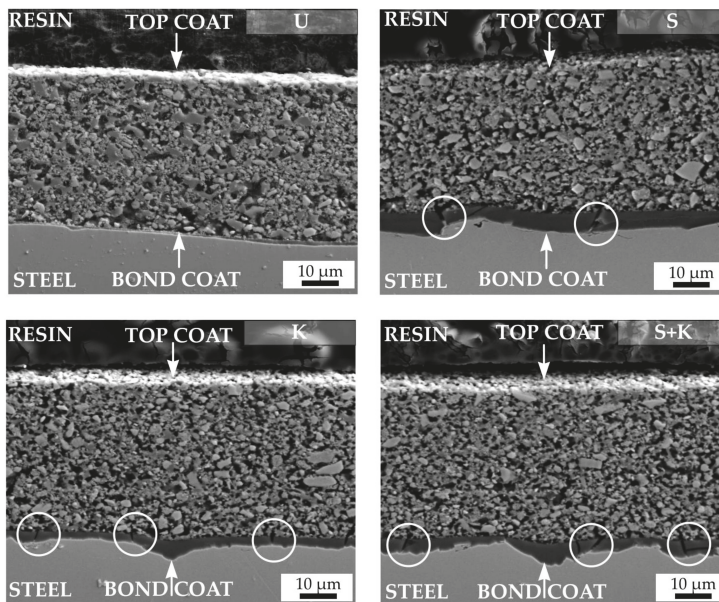


**Figure 8.** SEM cross sections of pyrolysed C2c coatings. The applied cleaning procedure is indicated by the abbreviation in the upper right corner of each figure (U – ultrasonic cleaning, K – chemical etching with Kroll's reagent, S – sandblasting, S+K – sandblasting + chemical etching with Kroll's reagent).

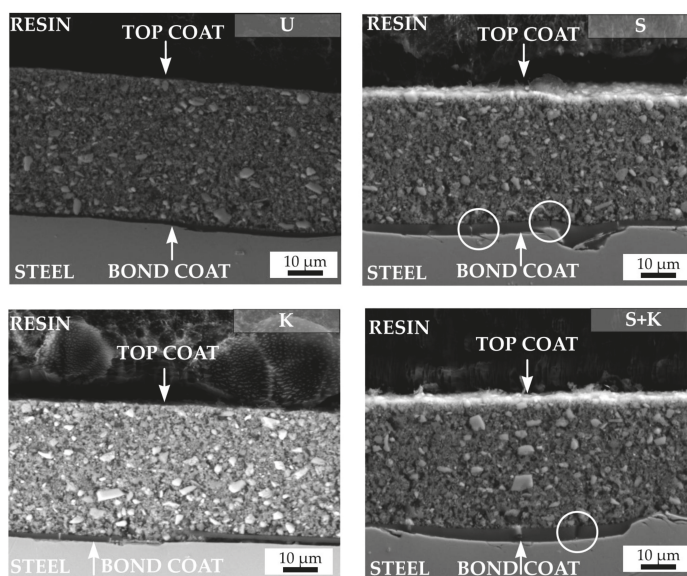
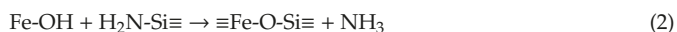
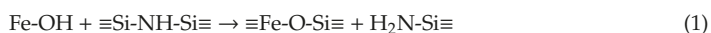


**Figure 9.** SEM cross sections of pyrolysed D2-PP coatings. The applied cleaning procedure is indicated by the abbreviation in the upper right corner of each figure (U – ultrasonic cleaning, K – chemical etching with Kroll’s reagent, S – sandblasting, S+K – sandblasting + chemical etching with Kroll’s reagent).

In addition, EDXS mapping was carried out on the cross section of D2-PP-coated steel cleaned by ultrasonic treatment in acetone, ethanol and deionised water to demonstrate the existence of an interface bond metal/base coat and base/top coat. EDXS element maps are shown in Figure 10. The bond coat contains mainly Si and O, since during pyrolysis in air the Durazane 2250 was converted to  $\text{SiO}_2$ , as confirmed by SEM/EDXS measurement. The presented element maps of Si confirm the formation of the protective bond coat at the steel surface in agreement with the literature [15]. The bond coat enhances the bonding between the steel and the top coat, and it preserves the steel from oxidation/corrosion [15,27]. On steel exposed to ambient environment, a natural oxide layer with adsorbed water is always present. Because of the reactivity of Durazane 2250 with surface-bound –OH groups, steel forms direct metal–O–Si chemical bonds with the base coat, leading to excellent adhesion [28]. The reaction of Durazane 2250 with hydroxyl groups of the substrate surface is described by the following simplified reaction equations [29]:



and a direct chemical metal–O–Si bonds between the steel and the precursor-derived coatings are formed. Therefore, the adhesive strength of the PDC coatings to the metal surface is very strong. In the case of sandblasting, we assume that it was the surface roughness of the steel that caused the coating delamination, as sandblasting should not affect the concentration of hydroxyl groups present at the steel surface. However, strong adhesion due to formation of the metal–O–Si bonds causes immobility of the coating during pyrolysis, which does not allow the coating to adjust to volume shrinkage of the steel substrate. Moreover, the sharp borders and peaks of the substrate initiate the formation of cracks perpendicular to the substrate surface. The corrosion/oxidation medium is thus able to penetrate through the cracks to the metal surface causing coating delamination. No crack formation in the bond coat was observed in samples pretreated via ultrasonic cleaning. In the case of chemical

etching, we assume that this treatment negatively influenced the adhesion of the bond coat because the concentration of hydroxyl groups on steel surface was significantly affected by etching.

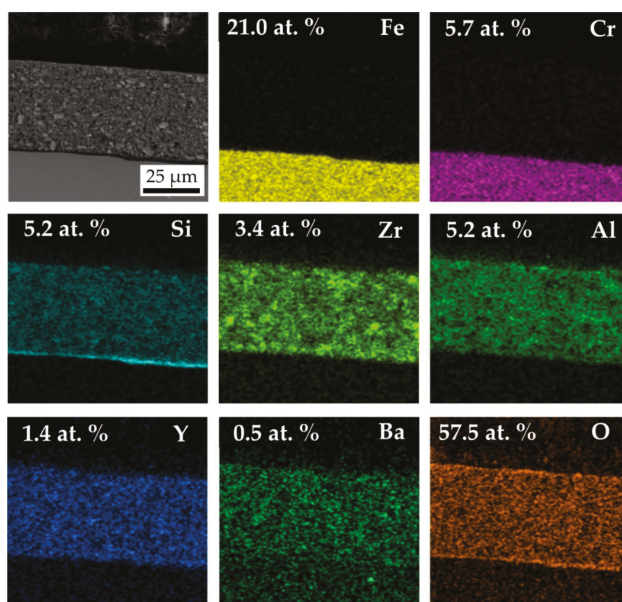


**Figure 10.** SEM/energy-dispersive X-ray spectroscopy (EDX) of D2-PP coatings documenting distribution of elements in the coating and in substrate.

The main elements of stainless steel Fe and Cr were detected below the protective bond coat. The main component of the bond was Si. The top coat consisted of Zr, Al, Y (from AYZ powder) and Ba (from commercial glass).

The top coat layers of both studied compositions—C2c (Figure 8) and D2-PP (Figure 9)—were almost dense, containing only small closed pores present predominantly at the boundaries between the filler particles and the matrix. The filler particles were well coated with the Durazane 1800 precursor, which builds up the matrix, and acts also as an adhesive between the particles. In the case of the C2c coating, all pores were almost spherical. This indicates that the closed pores could result from bubble formation due to the release of dissolved gases, as well as the expansion of insoluble gases (e.g., oxygen or air) entrapped in the initial pores. The pores could result also from the release of gases such as  $\text{NH}_3$ ,  $\text{CH}_4$ , and  $\text{H}_2$  generated during the polymer to ceramic transformation [15]. Note that pore formation cannot be completely avoided when passive fillers are used in the processing of PDC coatings, and some residual porosity usually remains in the final ceramic top coats. Existing pores provide a transportation path for gaseous products of decomposition escaping the coating. In the case of the D2-PP coating, the addition of the AYZ powder with irregular and angular particles have helped to create a rigid and articulate structure. This structure allowed outgassing of the preceramic polymer pyrolysis products from the system thereby effectively reducing the size and amount of pores. The elimination of larger pores, and thus an increased density, led to a significantly more compact coating in comparison to the C2c composition pyrolysed under the same conditions. Although the top layers were not completely dense, microstructure with residual porosity was beneficial for the thermal stability of coatings, and contributed to the mitigation of residual stresses during the heating and cooling cycles [30].

The mismatch of the CTE between the steel and the coating, together with the Young modulus, are critical factors for the resistance of coatings exposed to high temperatures [31]. By reducing the

non-conformance of the CTE and the elastic modulus, the tension in the coating is reduced, resulting in a higher stability of the coatings during thermal loading. Moreover, glasses are suitable material for sealing in PDC coatings. By decreasing both quantities (CTE mismatch and Young modulus), the stresses in the layers can be reduced, leading to better coating thermal stability during the oxidation tests. Coatings with both ceramic and glass fillers should then exhibit better thermal compatibility with the steel substrate than the coatings with active and passive fillers without glass tested in our previous work [26]. As a result, no cracks were observed in top coats, preventing penetration of oxidation agents through the coating and attack of the steel substrate.

Static oxidation tests were performed to assess the efficiency of the selected types of steel substrate cleaning. The aim of the oxidation tests was to determine whether the tested cleaning methods would ensure sufficient adhesion of the bond coat to the metal substrate not only during pyrolysis, but also at long-term operating at high temperature. The tests were performed in the atmosphere of synthetic air at 950 °C at a heating rate of 5 °C/min, with maximum duration of 48 hours. SEM cross-sections of C2c and D2-PP compositions after oxidation tests are shown in Figures 11 and 12, respectively. In all cases, except for ultrasonic cleaning, spallation of the bond coat from the surface of stainless steel was observed. Chemical etching of steel with the Kroll's solution probably caused changes in the microstructure and chemical composition of the steel, resulting in peeling of the coating. For sandblasted samples, or a combination of sandblasting and etching, detachment of the bond coat resulted from high surface roughness: as discussed above, strong adhesion of the coating on a rough surface with sharp edges resulted in formation of cracks perpendicular to the substrate. The cracks serve as a gateway for inward penetration of oxygen, which directly attacks the substrate, creating a layer of oxidation products, and eventually leading the detachment of the bond coat from the substrate. Simple cleaning by ultrasonication in acetone, ethanol and deionised water was found to be the most effective way for achieving a sufficient bonding of the bond coat to the steel substrate after oxidation tests.

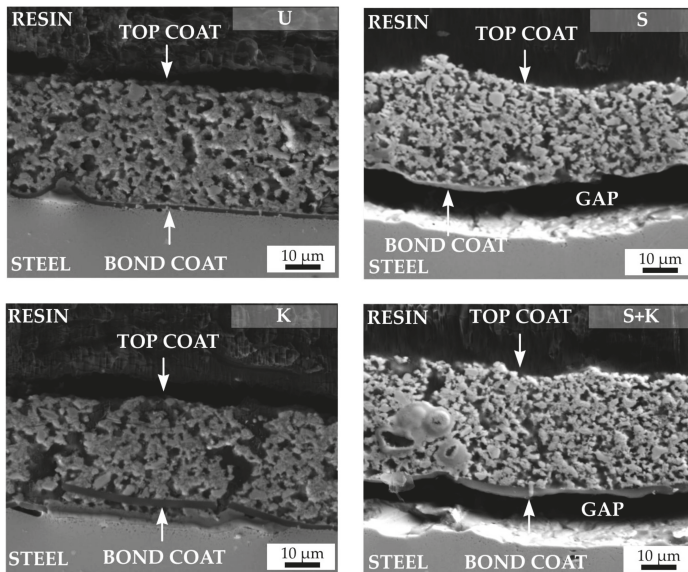


**Figure 11.** Cross sections of C2c coatings after oxidation tests. The applied cleaning procedure is indicated by the abbreviation in the upper right corner of each figure (U – ultrasonic cleaning, K – chemical etching with Kroll's reagent, S – sandblasting, S+K – sandblasting + chemical etching with Kroll's reagent).

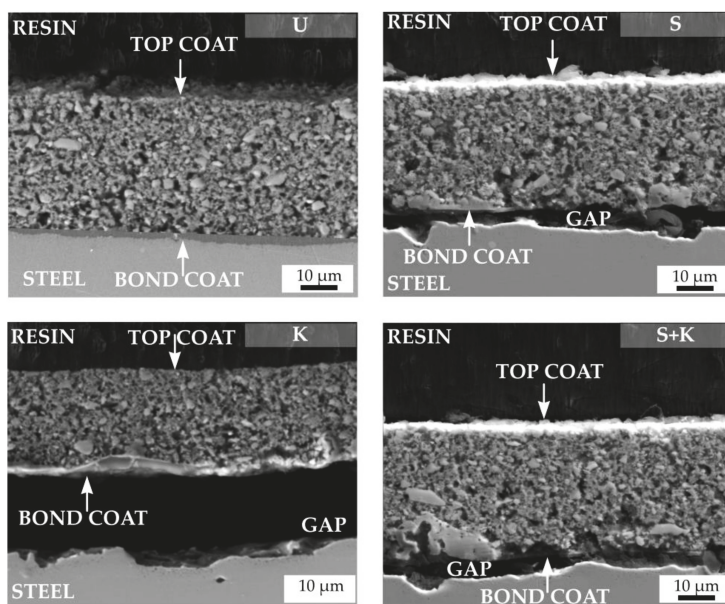


**Figure 12.** Cross sections of D2-PP coatings after oxidation tests. The applied cleaning procedure is indicated by the abbreviation in the upper right corner of each figure (U – ultrasonic cleaning, K – chemical etching with Kroll’s reagent, S – sandblasting, S+K – sandblasting + chemical etching with Kroll’s reagent).

Originally, numerous pores were observed across the whole cross-section of the as-prepared PDC glass ceramic coatings. After oxidation tests, a significant increase in the porosity of the layers accompanied by the growth of pores and a decrease of the coating thickness was observed in C2c coating. Decrease of the layer thickness was attributed to differential sintering of individual components (mainly glass fillers) by viscous flow, complemented by inadequate removal of gases entrapped in the ceramic matrix. Due to the softening of the used glass fillers, the cracks in the layers gradually heal, indicating at least partial protection of the metal substrate. After oxidation tests, the D2-PP composition exhibited a compact structure with no increase of the size and amount pores. No cracking or delamination from bond coat was observed.

#### 4. Conclusions

Suitable pretreatment of steel substrate, as well as the using a Durazane 2250 bond coat, are prerequisites for preparation of adherent composite coatings. The most effective cleaning process is a 3-step ultrasonic cleaning in acetone, ethanol and deionised water. Small cracks in the bond coat perpendicular to substrate were observed after pyrolysis in bond coats deposited at substrates treated by sandblasting and chemical etching. After oxidation tests, all coatings, except for those applied to substrates cleaned in an ultrasonic bath, delaminated or showed significant cracking of the bond coat. Combination of PDC with tailored fillers and glass systems enable the processing of dense and crack free coating system on stainless steel. Irregular and angular filler particles favour outgassing of the coating during pyrolysis, reducing the total porosity in the layer, and conferring better protection of the substrate against oxidative environment.

**Author Contributions:** M.P. performed cleaning procedures, prepared coatings and wrote the manuscript; I.P. prepared the precursor powder, performed cleaning procedures, prepared coatings and performed oxidation tests; P.S. performed the SEM and EDXS analysis; G.M. and D.G. conceived the study, supervised the project, gave



research guidelines, and finalised the manuscript. All authors have read and agreed to the published version of the manuscript.

**Funding:** Financial support of this work by the APVV 0014-15 grant and the Deutscher Akademischer Austauschdienst (DAAD) grant scheme is gratefully acknowledged. This paper was also created in the frame of the project Centre for Functional and Surface Functionalised Glass (CEGLASS), ITMS code 313011R453, operational program Research and innovation, co-funded from European Regional Development Fund.

**Acknowledgments:** The authors would like to thank Alexander Horcher and Mateus Lenz-Leite for their help to create the coating solution. The authors would also like to thank Jacob Andrew Peterson for grammar corrections in the manuscript and Branislav Hruška for AFM measurement.

**Conflicts of Interest:** The authors declare no conflicts of interest.

## References

1. Wang, K.; Günthner, M.; Motz, G.; Bordia, R.K. High performance environmental barrier coatings, Part II: Active filler loaded SiOC system for superalloys. *J. Eur. Ceram. Soc.* **2011**, *31*, 3011–3020. [[CrossRef](#)]
2. Greil, P. Polymer Derived Engineering Ceramics. *Adv. Eng. Mater.* **2000**, *2*, 339–348. [[CrossRef](#)]
3. Torrey, J.D.; Bordia, R.K. Processing of polymer-derived ceramic composite coatings on steel. *J. Am. Ceram. Soc.* **2008**, *91*, 41–45. [[CrossRef](#)]
4. Colombo, P.; Paulson, T.E.; Pantano, C.G. Synthesis of Silicon Carbide Thin Films with Polycarbosilane (PCS). *J. Am. Ceram. Soc.* **2005**, *40*, 2333–2340. [[CrossRef](#)]
5. Lukacs, A. Polysilazane precursors to advanced ceramics. *Am. Ceram. Soc. Bull.* **2007**, *86*, 9301–9306.
6. Seifert, M.; Travitzky, N.; Krenkel, W.; Motz, G. Multiphase ceramic composites derived by reaction of Nb and SiCN precursor. *J. Eur. Ceram. Soc.* **2014**, *34*, 1913–1921. [[CrossRef](#)]
7. Günthner, M.; Pscherer, M.; Kaufmann, C.; Motz, G. High emissivity coatings based on polysilazanes for flexible Cu(In,Ga)Se<sub>2</sub> thin-film solar cells. *Sol. Energy Mater. Sol. Cells* **2014**, *123*, 97–103. [[CrossRef](#)]
8. Kroke, E.; Li, Y.; Konetschny, C.; Lecomte, E.; Fasel, C.; Riedel, R. Silazane derived ceramics and related materials. *Mater. Sci. Eng. R Rep.* **2000**, *26*, 97–199. [[CrossRef](#)]
9. Lenormand, P.; Caravaca, D.; Laberty-Robert, C.; Ansart, F. Thick films of YSZ electrolytes by dip-coating process. *J. Eur. Ceram. Soc.* **2005**, *25*, 2643–2646. [[CrossRef](#)]
10. Kappa, M.; Kebianyor, A.; Scheffler, M. A two-component preceramic polymer system for structured coatings on metals. *Thin Solid Film.* **2010**, *519*, 301–305. [[CrossRef](#)]
11. Morlier, A.; Cros, S.; Garandet, J.P.; Alberola, N. Thin gas-barrier silica layers from perhydropolysilazane obtained through low temperature curings: A comparative study. *Thin Solid Film.* **2012**, *524*, 62–66. [[CrossRef](#)]
12. Barroso, G.S.; Krenkel, W.; Motz, G. Low thermal conductivity coating system for application up to 1000 °C by simple PDC processing with active and passive fillers. *J. Eur. Ceram. Soc.* **2015**, *35*, 3339–3348. [[CrossRef](#)]
13. Parchovianský, M.; Barroso, G.; Petříková, I.; Motz, G.; Galusková, D.; Galusek, D. Polymer derived glass ceramic layers for corrosion protection of metals. *Ceram. Trans.* **2016**, *256*, 187–200. [[CrossRef](#)]
14. Goerke, O.; Feike, E.; Heine, T.; Trampert, A.; Schubert, H. Ceramic coatings processed by spraying of siloxane precursors (polymer-spraying). *J. Eur. Ceram. Soc.* **2004**, *24*, 2141–2147. [[CrossRef](#)]
15. Günthner, M.; Wang, K.; Bordia, R.K.; Motz, G. Conversion behaviour and resulting mechanical properties of polysilazane-based coatings. *J. Eur. Ceram. Soc.* **2012**, *32*, 1883–1892. [[CrossRef](#)]
16. Greil, P. Active Filler Controlled Pyrolysis of Preceramic Polymers. *J. Am. Ceram. Soc.* **1995**, *78*, 835–848. [[CrossRef](#)]
17. Greil, P. Near Net Shape Manufacturing of Ceramic Components. *Cfi Ceram. Forum Int.* **1998**, *75*, 15–21. [[CrossRef](#)]
18. Petříková, I.; Parchovianský, M.; Lenz-Leite, M.; Švančárek, P.; Motz, G.; Galusek, D. Passive Filler loaded Polysilazane-Derived Glass/Ceramic coating system applied to AISI 441 stainless steel, Part 1: Processing and Characterisation. *Int. J. Appl. Ceram. Technol.* **2019**. [[CrossRef](#)]
19. Bernardo, E.; Colombo, P.; Hampshire, S. SiAlON-based ceramics from filled preceramic polymers. *J. Am. Ceram. Soc.* **2006**, *89*, 3839–3842. [[CrossRef](#)]
20. Labrousse, M.; Nanot, M.; Boch, P.; Chassagneux, E. Ex-polymer SiC coatings with Al<sub>2</sub>O<sub>3</sub> particulates as filler materials. *Ceram. Int.* **1993**, *19*, 259–267. [[CrossRef](#)]
21. Scheffler, M.; Dernovsek, O.; Schwarze, D.; Science, M.; Science, M. Polymer / filler derived NbC composite ceramics. *J. Mater. Sci.* **2003**, *8*, 4925–4931. [[CrossRef](#)]

22. Schütz, A.; Günthner, M.; Motz, G.; Greißl, O.; Glatzel, U. Characterisation of novel precursor-derived ceramic coatings with glass filler particles on steel substrates. *Surf. Coat. Technol.* **2012**, *207*, 319–327. [CrossRef]
23. Günthner, M.; Kraus, T.; Krenkel, W.; Motz, G.; Dierdorf, A.; Decker, D. Particle-Filled PHPS silazane-based coatings on steel. *Int. J. Appl. Ceram. Technol.* **2009**, *6*, 373–380. [CrossRef]
24. Günthner, M.; Schütz, A.; Glatzel, U.; Wang, K.; Bordia, R.K.; Greißl, O.; Krenkel, W.; Motz, G. High performance environmental barrier coatings, Part I: Passive filler loaded SiCN system for steel. *J. Eur. Ceram. Soc.* **2011**, *31*, 3003–3010. [CrossRef]
25. Parchovianský, M.; Petíková, I.; Barroso, G.S.; Galuskova, D.; Motz, G.; Galusek, D. Corrosion and oxidation behavior of polymer derived ceramic coatings with passive glass fillers on AISI 441. *Ceram. Silik.* **2018**, *62*, 146–157. [CrossRef]
26. Pechini, M.P. Method of Preparing Lead and Alkaline Earth Titanates and Niobates and Coating Method Using the Same to Form a Capacitor. US Patent No. 3330697, 11 July 1967.
27. Günthner, M.; Kraus, T.; Dierdorf, A.; Decker, D.; Krenkel, W.; Motz, G. Advanced coatings on the basis of Si(C)N precursors for protection of steel against oxidation. *J. Eur. Ceram. Soc.* **2009**, *29*, 2061–2068. [CrossRef]
28. Bauer, F.; Decker, U.; Dierdorf, A.; Ernst, H.; Heller, R.; Liebe, H.; Mehnert, R. Preparation of moisture curable polysilazane coatings: Part I. Elucidation of low temperature curing kinetics by FT-IR spectroscopy. *Prog. Org. Coat.* **2005**, *53*, 183–190. [CrossRef]
29. Bahloul, D.; Pereira, M.; Goursat, P.; Yive, N.S.C.K.; Corriu, R.J.; Mixte, R.I. Preparation of silicon carbonitrides from organosilicon polymer. I. Thermal decomposition of the cross-linked polysilazane. *J. Am. Ceram. Soc.* **1993**, *75*, 1156–1162. [CrossRef]
30. Padture, N.P.; Gell, M.; Jordan, E.H. Thermal barrier coatings for gas-turbine engine applications. *Science* **2002**, *296*, 280–284. [CrossRef]
31. Soliman, H.M.; Waheed, A.F. Effect of differential thermal expansion coefficient on stresses generated in coating. *J. Mater. Sci. Technol.* **1999**, *15*, 457–462.



© 2020 by the authors. Licensee MDPI, Basel, Switzerland. This article is an open access article distributed under the terms and conditions of the Creative Commons Attribution (CC BY) license (<http://creativecommons.org/licenses/by/4.0/>).



Article

# Ni/cerium Molybdenum Oxide Hydrate Microflakes Composite Coatings Electrodeposited from Choline Chloride: Ethylene Glycol Deep Eutectic Solvent

Juliusz Winiarski <sup>1,\*</sup>, Anna Niciejewska <sup>1</sup>, Jacek Ryl <sup>2</sup>, Kazimierz Darowicki <sup>2</sup>, Sylwia Baśladyńska <sup>1</sup>, Katarzyna Winiarska <sup>3</sup> and Bogdan Szczygieł <sup>1</sup>

<sup>1</sup> Faculty of Chemistry, Department of Advanced Material Technologies, Wrocław University of Science and Technology, 50-370 Wrocław, Poland; anna.niciejewska@onet.pl (A.N.); sylwia.basladynska@pwr.edu.pl (S.B.); bogdan.szczygiel@pwr.edu.pl (B.S.)

<sup>2</sup> Faculty of Chemistry, Department of Electrochemistry, Corrosion and Materials Engineering, Gdansk University of Technology, 80-233 Gdańsk, Poland; jacek.ryl@pg.edu.pl (J.R.); kazimierz.darowicki@pg.edu.pl (K.D.)

<sup>3</sup> Faculty of Chemistry; Department of Analytical Chemistry and Chemical Metallurgy, Wrocław University of Science and Technology, 50-370 Wrocław, Poland; katarzyna.winiarska@pwr.edu.pl

\* Correspondence: juliusz.winiarski@pwr.edu.pl; Tel.: +48-71-320-3193

Received: 30 January 2020; Accepted: 17 February 2020; Published: 19 February 2020

**Abstract:** Cerium molybdenum oxide hydrate microflakes are codeposited with nickel from a deep eutectic solvent-based bath. During seven days of exposure in 0.05 M NaCl solution, the corrosion resistance of composite coating (Ni/CeMoOxide) is slightly reduced, due to the existence of some microcracks caused by large microflakes. Multielemental analysis of the solution, in which coatings are exposed and the qualitative changes in the surface chemistry (XPS) show selective etching molybdenum from microflakes. The amount of various molybdenum species within the surface of coating nearly completely disappear, due to the corrosion process. Significant amounts of Ce<sup>3+</sup> compounds are removed, however the corrosion process is less selective towards the cerium, and the overall cerium chemistry remains unchanged. Initially, blank Ni coatings are covered by NiO and Ni(OH)<sub>2</sub> in an atomic ratio of 1:2. After exposure, the amount of Ni(OH)<sub>2</sub> increases in relation to NiO (ratio 1:3). For the composite coating, the atomic ratios of both forms of nickel vary from 1:0.8 to 1:1.3. Despite achieving lower corrosion resistance of the composite coating, the applied concept of using micro-flakes, whose skeleton is a system of Ce(III) species and active form are molybdate ions, may be interesting for applications in materials with potential self-healing properties.

**Keywords:** metal coatings; nickel; composite coatings; electrodeposition; XPS; polarization; electrochemical impedance spectroscopy (EIS)

## 1. Introduction

In recent years, the electrodeposition of metals from ionic liquids (ILs) has become more popular because of the many advantages, such as high solubility metals salts, high conductivity, and wide electrochemical potential windows. Ionic liquids also allow obtaining metal coatings, such as Na and Mg, which is impossible in conventional baths. ILs are non-toxic, non-flammable and can be used in a wide range of temperatures [1–4]. One of the most interesting analogues of ILs are the deep eutectic solvents (DESs). DES is a eutectic mixture of quaternary ammonium salt with hydrogen bond donor species or metal salts. DESs are relatively cheap and easy to prepare [5,6]. DES-based galvanic baths have the advantage that the metals do not passivate during deposition. DESs can be used to electrodeposition a lot of metal coatings: Ni, Cu, Zn, Cr, Sn, Co, Al, Ti, W, Ag, Mg, Se, and Pd [6]. Nickel coatings obtained from DES feature nano-crystalline morphology and lower

surface roughness than Ni-coatings from conventional aqueous Watt's baths which produce coatings with a micro-crystalline structure. Furthermore, the microhardness of Ni coatings deposited from DES is 100 HV (Vickers hardness) higher than coatings from aqueous solutions [7]. A used eutectic solvent has a significant impact on the morphology of nickel coatings (size of Ni crystallites) [8]. Moreover, from baths based on eutectic solvents it is possible to obtain Ni coatings on an aluminum substrate. Obtaining bright Ni coatings requires the use of brighteners, which differ from those used in aqueous plating baths [9,10]. The important influence on the coating's deposition from DESs is the water content in a plating bath. By changing the water content, one can control the potential for Ni deposition. Potential Ni impacts the self-limiting growth crystallite and passivation effect [11]. In addition to the above advantages, DESs liquids enable the electrodeposition of nickel alloy coatings: Zn-Ni [12], Ni-Co-Sn [13], Fe-Ni [14], Ni-Co [15], Ni-Mo [16], and nickel composite coatings. Ni-carbon nanotubes composite coatings [17,18] have much better tribological properties than pure Ni [18]. Furthermore, Ni-PTFE (poly(tetrafluoroethylene)) coatings show better wear resistance than nickel coatings and have hydrophobic properties [19]. The addition of SiC to the nickel matrix causes the increase of microhardness [20] and corrosion resistance [21]. Ni-SiO<sub>2</sub> coatings also have better microhardness and wear resistance than Ni coatings [22]. Nickel coatings with a TiO<sub>2</sub> dispersive phase show good electrocatalytic activity [23]. However, co-deposition with micro- or nano-particles of compounds of chemically active elements, e.g. cerium or molybdenum, may affect the protective properties of the composite coatings. Dong et al. prepared cerium molybdate particles with different morphologies, such as the bundle-like, flower-like, and microspheric structures [24]. The nanostructure of Ce-Mo shows excellent adsorption and catalytic properties [24]. Amino acids, for example: glycine, lysine, serine, and glutamate used at synthesis of cerium molybdate have influence on its morphology [25]. Sajad et al. proved that by using lysine in synthesis one can obtain a pure product (cerium molybdate) which is not contaminated with cerium molybdate oxides [26]. Nanocapsules are also made up of shells from cerium molybdate, while the core was a corrosion inhibitor [27,28] or hollow nanospheres have an antibacterial effect on *Escherichia coli* in the absence of light [29]. Hence their potential application in medicine or the anti-corrosion industry [29]. Patel et al. developed a method of fabrication of cerium zinc molybdate nanopigment with anticorrosive properties [30]. Cerium molybdate nanowires were also added to the coatings obtained by the sol-gel method [31]. Therefore, cerium molybdate is very popular as a corrosion inhibitor in protective coatings for aluminum alloys [32] and magnesium [33,34]. Bhanvase et al. have investigated that 5% content of cerium zinc molybdate nanocontainers, significantly increases the corrosion resistance [35].

The use of cerium molybdenum oxide, proposed in this work, is novel in electrodeposition of nickel composite coatings. Ce and Mo compounds embedded in the coating can modify its protective properties by giving it potential self-healing properties (through the selective release of cerium and molybdenum ions). Moreover, this work uses a deep eutectic solvent based on choline chloride and ethylene glycol as an excellent environment for the co-deposition of microparticles. As a result, deposition is carried out in a stable suspension bath. Microflakes of fairly large size are intentionally used to make it easier to capture the effect of their interaction with a metallic nickel matrix and the corrosive environment. Emphasis is placed on understanding qualitative and quantitative changes in surface chemical composition—X-ray photoelectron spectroscopy (XPS), caused by the presence of microflakes, on the one hand, and the exposure to a corrosive environment, on the other. The corrosion resistance of a newly obtained material is monitored in-situ by electrochemical impedance spectroscopy (EIS) and basic *dc* (direct current) polarization methods. The morphology, structure, and topography of the coatings are investigated by scanning electron microscopy (SEM), X-ray diffraction (XRD), and contact profilometry.

## 2. Materials and Methods

Cerium molybdenum oxide microflakes were synthesized at low temperature from Ce(NO<sub>3</sub>)<sub>3</sub> and Na<sub>2</sub>MoO<sub>4</sub> precursors through the precipitation method. First, the two precursors were prepared separately by the dissolution of Na<sub>2</sub>MoO<sub>4</sub>·2H<sub>2</sub>O and Ce(NO<sub>3</sub>)<sub>3</sub>·6H<sub>2</sub>O in demineralized water in the molar ratio of 2:1,

respectively. The solutions were next cooled down to 8 °C overnight in the fridge. Na<sub>2</sub>MoO<sub>4</sub> solution was instilled slowly (60 mL min<sup>-1</sup>) into Ce(NO<sub>3</sub>)<sub>3</sub> solution under continuous mechanical stirring (200 rpm), which resulted in the formation of a light yellow suspension. After 1 h mixing at 15 °C, the precipitate was filtered under the reduced pressure on a Buchner funnel. The grey-yellowish precipitate was washed several times with demineralized water and then dried in a vacuum dryer.

The plating bath for nickel electrodeposition (100 mL plating volume) was prepared by mixing choline chloride and ethylene glycol in a 1:2 molar ratio and addition of 1 mol dm<sup>-3</sup> NiCl<sub>2</sub> 6H<sub>2</sub>O at 70 °C. All these reagents were mechanically stirred until a homogeneous green liquid was obtained. Cerium molybdenum oxide microflakes were then added (2 g dm<sup>-3</sup>) and the bath was homogenized for 30 min (UP50H – Hielscher Compact Lab Homogenizer).

For the electrodeposition, copper disks (1.5 cm diameter, 0.1 cm thick) were used as cathodes. They were polished on 600–1200 grade abrasive paper. Then, the samples were degreased in an ultrasonic cleaner in methanol, acid etched (10 vol.% H<sub>2</sub>SO<sub>4</sub>), rinsed in demineralized water and again in methanol. Electroplating was carried out in a thermostatic electrolyzer consisting of two anodes (pure nickel) and a cathode placed between them. The process was carried out at a current density 6 mA cm<sup>-2</sup>, at 70 °C, for 1 h. After this time, the coatings were twice rinsed in demineralized water and methanol. At the end, the coatings were dried and stored in a vacuum desiccator until required.

Surface morphology was analyzed by Quanta 250 (FEI) scanning electron microscope equipped with an Octane Elect Plus SDD microanalyzer (operating at 25 kV, and at 10<sup>-4</sup> Pa pressure).

The crystal structure and phase composition of cerium molybdenum oxide microflakes and blank and composite nickel coatings were analyzed using powder X-ray diffraction. The XRD diffractograms were recorded on a D 5000 (Siemens) diffractometer with CuK $\alpha$  radiation ( $\lambda = 0.15409$  nm) at room temperature in the  $2\theta$  range: 10–60° for blank and composite Ni coatings, and 5–60° for cerium molybdenum oxide microflakes. Phase identification was carried out by comparing the experimental patterns with the reference patterns collected in the Powder Diffraction Files database (International Centre for Diffraction Data PDF-2 base).

The X-ray Photoelectron Spectroscopy (XPS) measurements were performed using Escalab 250Xi (Thermo Fisher Scientific, United Kingdom). Al K $\alpha$  monochromatic X-ray source with spot diameter of 250  $\mu$ m was used. The set up pass energy was 20 eV. Charge compensation was controlled through low-energy Ar<sup>+</sup> ions emission by means of a flood gun, with the final calibration made using Ni2p<sub>3/2</sub> metallic peak component at 852.6 eV. The deconvolution procedure was performed using Avantage software (Thermo Fisher Scientific, Waltham, USA).

The chemical analysis of corrosive solutions was performed by ICP-OES (Inductively Coupled Plasma-Optical Emission Spectrometry) and ICP-MS (Inductively Coupled Plasma-Mass Spectrometry) technique. The Ni concentration was determined using ICP-OES method (Vista MPX, Varian, Australia). Cu, Ce, Mo, and also Ni content was determined using ICP-MS method (XSeries2, Thermo Fisher Scientific, USA). The analyses were performed in the Chemical Laboratory of Multielemental Analysis, Wrocław University of Science and Technology, Poland, accredited by the Polish Centre for Accreditation (AB 696). The laboratory has a measurement procedure of determination of metals in water in its scope of accreditation. The procedure is based on EN-ISO 11885:2009, PN-EN ISO 17294-1:2007, and PN-EN ISO 17294-2:2006.

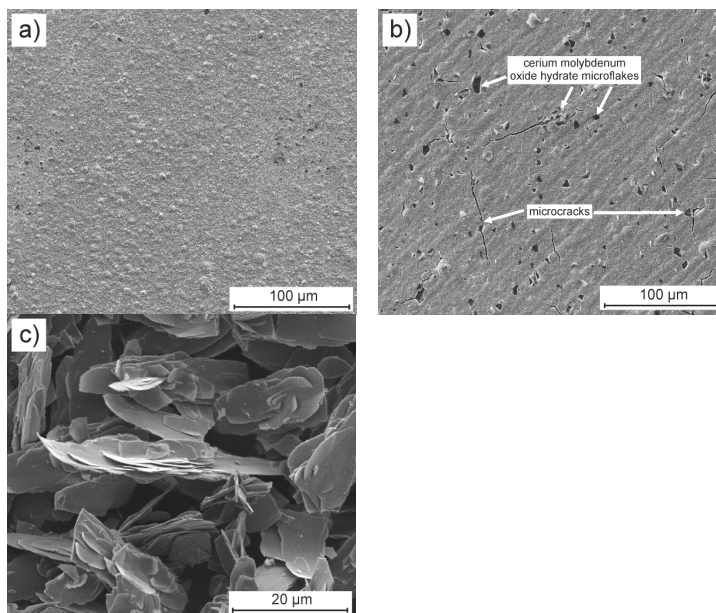
Corrosion measurements were carried out at 25 °C in 0.05 mol dm<sup>-3</sup> solution of NaCl in Autolab 400 mL corrosion cell using a Reference 1010E (Gamry, Warminster, USA) potentiostat/galvanostat/ZRA (zero resistance ammeter). The geometric area of the working electrode exposed to the solution was 1 cm<sup>2</sup>. A stainless steel rod (geometric area 5 cm<sup>2</sup>) and a saturated Ag|AgCl / 3M KCl electrode (Metrohm) mounted in a Luggin capillary were used as the counter and reference electrodes, respectively. Potentiodynamic polarization curves were recorded after 168 hours exposure starting from -0.1 V to +0.5 V vs. open circuit potential ( $E_{OC}$ ) at a scan rate of 0.166 mV s<sup>-1</sup>. The polarization resistance (LPR technique) was measured by polarization of the sample starting from -10 mV to +10 mV vs.  $E_{OC}$  at a scan rate of 1 mV s<sup>-1</sup>. Impedance spectra for electrochemical impedance spectroscopy (EIS)

were recorded at  $E_{OC}$  (potentiostatic mode) with a resolution of 10 pts/dec., in a frequency range from 100 kHz to 0.001 Hz and at a 10 mV signal amplitude. Equivalent circuit modeling, graphing, and analysis of impedance data was performed using ZView<sup>®</sup> software (Scribner Associates, version 3.5g). The deposition process was studied by cyclic voltammetry (CV) technique using Autolab RDE-2 electrode with a Pt tip (3 mm diameter) in an electrochemical vessel (20–90 mL, Metrohm) with thermostat jacket, Ag and Pt wires as the reference and counter electrodes, in the range of potentials from  $E_{OC}$  to  $-1.5$ , then  $1.5$  and ending at  $E_{OC}$  with a scan rate of  $20 \text{ mV s}^{-1}$ . Pt tip instead of Cu was chosen to avoid the influence of any copper ions on the current-potential characteristics.

### 3. Results and Discussion

#### 3.1. Morphology, Topography, and Phase Structure of Blank and Composite Ni Coatings

After electrodeposition, both blank and composite nickel coatings with a mean thickness of  $10 \mu\text{m}$  were subjected to SEM and XRD analysis. The surface of the Ni coating consisted of spheroidal particles that form randomly arranged larger agglomerates (Figure 1a). The surface of the Ni/CeMoOxide coating, like the Ni coating, consisted of spherical particles, which were noticeably smaller in this case. In addition, there were randomly embedded microflakes of CeMoOxide within the surface. Single cracks were visible, mostly spreading from the places where the microflakes are built-in (Figure 1b). Additional topographic measurements of the surface of both coatings confirmed the increase in roughness of the composite coating, expressed by the  $R_a$  parameter equaled to  $122.3 \pm 17.7 \text{ nm}$  (related to  $92.6 \pm 10.1 \text{ nm}$  for blank Ni coating). For comparison, Figure 1c shows the photomicrograph (recorded in a secondary electron - SE mode of SEM) of synthesized cerium molybdenum oxide hydrate powder. The plates are overgrown and form agglomerates with a length exceeding  $20 \mu\text{m}$ , a width below  $10 \mu\text{m}$ , and a thickness of  $100\text{--}200 \text{ nm}$  (Figure 1c).



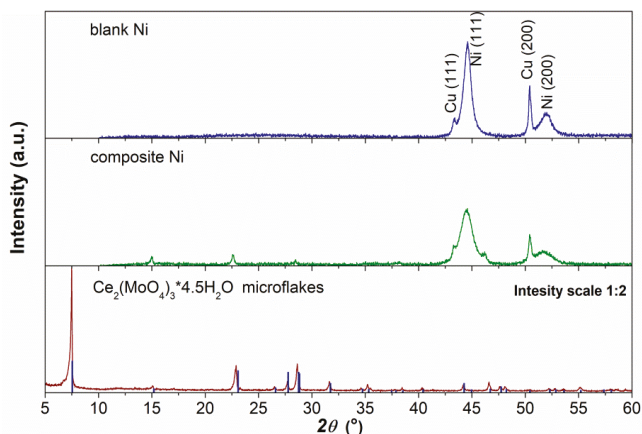
**Figure 1.** Surface morphology of (a) blank and (b) composite Ni coatings deposited on the copper substrate at a current density of  $6 \text{ mA cm}^{-2}$  at  $70 \text{ }^\circ\text{C}$  for 1 h, and (c) as-synthesized cerium molybdenum oxide hydrate microflakes for comparison. Pictures were recorded in a SE mode of SEM.

Figure 2 shows the diffractograms for of cerium molybdenum oxide microflakes and blank and composite nickel coating. The thickness of the prepared Ni coatings was sufficient to perform the XRD analysis. The dominant peaks at the diffractograms are characteristic of Ni (111) and (200) crystal planes visible at  $2\theta$  44.6° and 51.9°. The indicated reflections were well indexed to these collected in ICDD JCPDS card No. 00-004-0850 for Ni. Peaks at  $2\theta$  43.3° and 50.4° originated from the Cu substrate (JCPDS card No. 00-004-0836). The other small peaks match well with the cerium molybdenum oxide. The diffractogram recorded for as-prepared microflakes is also shown in Figure 2. All the diffraction peaks correspond to  $\text{Ce}_2(\text{MoO}_4)_3 \cdot 4.5\text{H}_2\text{O}$  phase (JCPDS card No. 00-031-0333) without the presence of other peaks from any impurities. The strong and sharp diffraction peaks indicate that the prepared cerium molybdenum oxide microflakes were well-crystallized. High-resolution diffractograms were recorded for the blank and composite Ni coatings to estimate the average crystallite size. A copper peak from the substrate overlapped the nickel peak (111), therefore, for the proper determination of FWHM (full width at half maximum) for the Ni (111) peak, a deconvolution using a pseudo-Voigt function was performed. The average crystallite size was calculated using the Scherrer Equation (1):

$$D = \frac{K \cdot \lambda}{B \cdot \cos\theta} \quad (1)$$

where D is the mean crystallite size in the direction perpendicular to the (hkl) plane of reflexes in nm, K is a Scherrer constant (0.9) [36],  $\lambda = 0.154$  nm is the X-ray wavelength used in the measurement, B was calculated from Equation (2):

$$B = \sqrt{(\beta_{FWHM}^2 - \beta_0^2)} \quad (2)$$



**Figure 2.** X-ray diffractograms for blank and composite Ni coatings deposited on the copper substrate at a current density of  $6 \text{ mA cm}^{-2}$  at  $70^\circ \text{C}$  for 1 h. A powder diffraction pattern for as-synthesized cerium molybdenum oxide hydrate is also shown at the bottom of the figure for comparison.

( $\beta_{FWHM}$  and  $\beta_0$  is the FWHM of diffraction peak at angle  $\theta$  and the corrected instrumental broadening - in radian, respectively). After deconvolution, the average crystallite size was estimated at about 10.4 nm and 6.3 nm for blank Ni and composite Ni coatings respectively. The resulting D value indicates the nano-crystalline structure of the electrodeposited nickel. It can be seen that the cerium molybdenum oxide microflakes affects the structure of the coating by co-depositing and reducing the size of the crystallites.

On the basis of the observed changes in the morphology and structure of both types of coating, it is obvious that the cerium and molybdenum compound must have modified the course of cathodic processes. Therefore, cyclic voltammetry curves were recorded under deposition conditions in both



(blank Ni and suspension) plating baths. The experiment was repeated twice to avoid accidental results. Representative CV curves are shown in Figure 3. Analyzing the course of the curves, it can be seen that the composite coating deposition can proceed probably with greater efficiency. This can be demonstrated by a much larger anodic peak within the potentials of Ni (deposit) oxidation (Figure 3). It is however not excluded that the larger area of that peak may be associated with, e.g., the oxidation of molybdenum species released at high temperature (70 °C) from the microflakes suspended in the plating bath. However, the cathode curves were not significantly different (Figure 3).

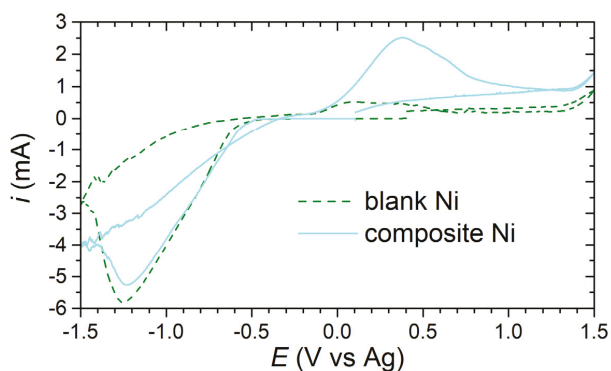


**Figure 3.** Cyclic voltammetry curves recorded in a blank Ni plating bath and suspension bath containing  $2 \text{ g dm}^{-3} \text{ Ce}_2(\text{MoO}_4)_3 \cdot 4.5\text{H}_2\text{O}$  microflakes, at 70 °C on a rotating disk electrode with Pt tip (3 mm diameter), at 600 rpm.

### 3.2. Corrosion Resistance

#### 3.2.1. *dc* Polarization

Polarization resistance ( $R_p$ ) as a function of exposure time in  $0.05 \text{ mol dm}^{-3}$  solution of NaCl for blank Ni and composite (Ni/CeMoOxide) coatings is presented in Figure 4. In the case of a blank Ni coating, a clear increase in  $R_p$  was observed. During exposure in a NaCl solution,  $R_p$  increased up to  $536.6 \text{ k}\Omega \text{ cm}^2$  after about 144 hours, then, its value decreased. The  $R_p$ -time dependency for the Ni/CeMoOxide coating was different. An increase of  $R_p$  to above  $100 \text{ k}\Omega \text{ cm}^2$  was visible within the first hours of exposure in a chloride solution. After approximately 72 hours, the  $R_p$  value decreased to approximately  $77 \text{ k}\Omega \text{ cm}^2$ , and then it showed a slight upward trend (Figure 4).

The corrosion potential ( $E_{\text{corr}}$ ) of the Ni/CeMoOxide coating increased quite rapidly in the first hours (Figure 5). After about three days it reached a constant level. The potential-time dependency for the Ni coating was different. An increase in  $E_{\text{corr}}$  towards more positive values was noticeable throughout the entire time studied. It is possible that such a direction of changes resulted from qualitative changes in the morphology of the layer of nickel oxidation products.

Finally, after 168 hours of exposure—after reaching a certain stability of the potential (at least for the composite coating), polarization curves for Ni and Ni/CeMoOxide coatings were registered. Their course is presented in Figure 6. The anodic branch of the Ni/CeMoOxide coating, compared to the anodic branch of the Ni coating, is characterized by higher corrosion current density values, which suggests more active anodic process on the surface of the former. A section with slowly a growing density of the corrosion current is visible on the anodic side in the course of Ni coating (Figure 6), which may suggest some protective/barrier action of a passive layer.

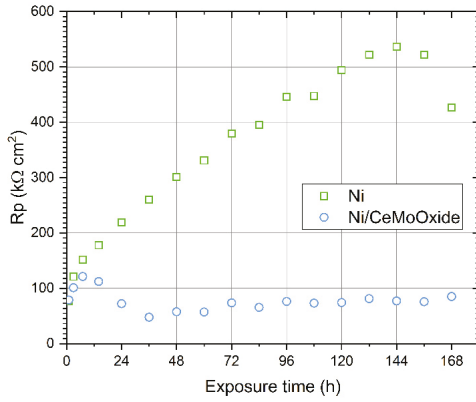


Figure 4. Polarization resistance ( $R_p$ ) recorded for blank and composite Ni coatings during 168-hour exposure in 0.05 M NaCl solution.

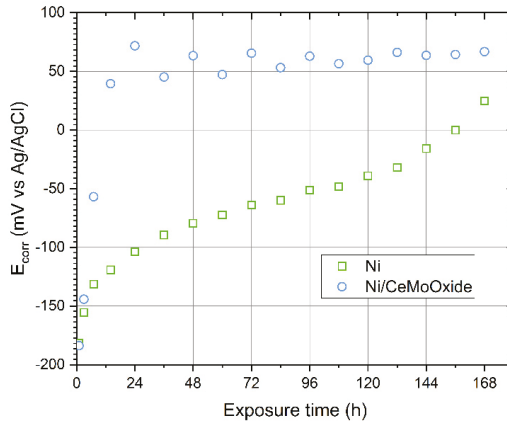


Figure 5. Corrosion potential ( $E_{corr}$ ) recorded for blank and composite Ni coatings during 168-hour exposure to 0.05 M NaCl solution.

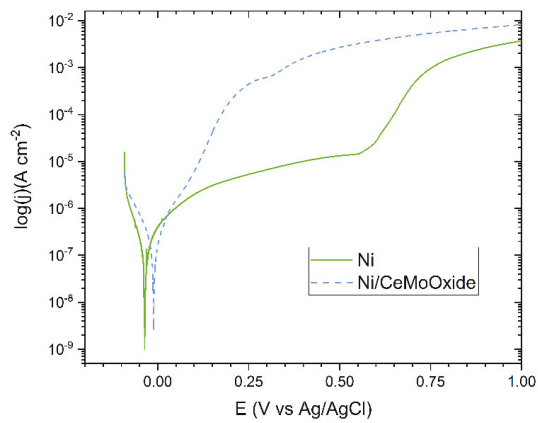
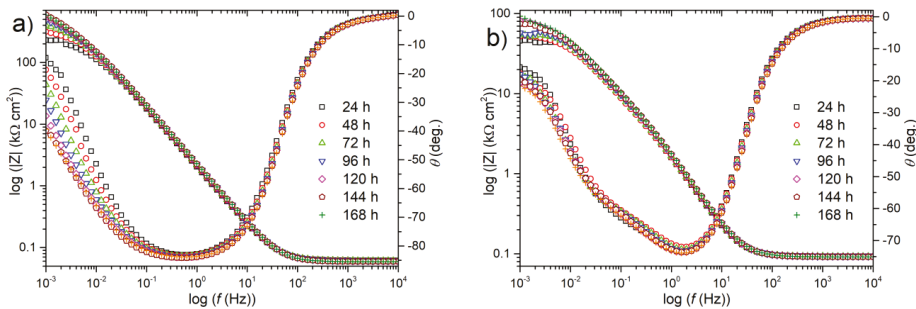


Figure 6. Potentiodynamic polarization curves recorded for blank and composite Ni coatings after 168-hour exposure to 0.05 M NaCl solution.

### 3.2.2. Electrochemical Impedance Spectroscopy

Impedance spectra of both types of coating were recorded every 24 hours during 7 days of exposure of the samples in 0.05 mol dm<sup>-3</sup> NaCl solution. They have been presented on a complex Bode plot (Figure 7) to gain better visibility of the changes of the investigated system. The first analysis of the shape of the spectra leads to the conclusion that the corrosion process of Ni coating is characteristic of “corroding coating”. The magnitude of impedance  $|Z|$  increased during exposure (Figure 7a), which may indicate increasing corrosion resistance, due to the formation of, e.g., a stable passive layer or increasing diffusion constrains (especially after 144 and 168 hours). A similar shape of impedance spectra and similar tendency (increasing) for the impedance modulus have been observed in previous work by Urcezino et al. [37] and J. Winiarski et al. [38].



**Figure 7.** Bode representation of the impedance spectra recorded for (a) blank and (b) composite Ni coatings for 168 hours exposure in 0.05 M NaCl solution.

Figure 7b presents impedance spectra for composite coating. This material behaved slightly differently, rather like “damaged coating”, due to the presence of coating discontinuities. Furthermore, not very clearly separated time constants—caused by capacitive dispersion and overlapping of time constants—were observed (Figure 7b). Therefore, for further discussion, two electric equivalent circuits (EECs) were used for the calculation of the theoretical spectra: a single time constant model for a blank Ni (Figure 8a) and a double time constant model for a composite Ni (Figure 8b).

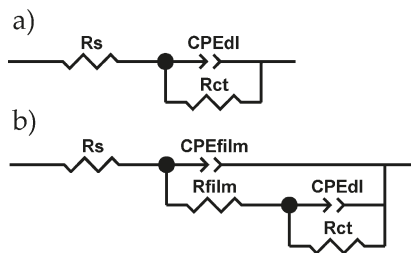


**Figure 8.** Electric equivalent circuits used for fitting the experimental spectra of (a) blank and (b) composite Ni coatings.

Both models use a constant phase element (CPE). The impedance of the CPE is defined by Equation (3), where:  $Y_0$  is a time constant parameter ( $\Omega^{-1} \text{ cm}^{-2} \text{ s}^\alpha$ ),  $\omega$  is the angular frequency of the AC signal and  $\alpha$  is the CPE exponent.

$$Z_{CPE} = Y_0^{-1} (j\omega)^{-\alpha} \tag{3}$$

The other elements used in the EECs presented in Figure 8a,b are:  $R_s$ —the resistance of NaCl solution,  $R_{ct}$ —the charge transfer resistance associated with nickel oxidation,  $Y_{0,dl}$  and  $\alpha$  corresponds

to a double layer capacitance ( $C_{dl}$ ). In the circuit for a composite coating (Figure 8b), the properties of a developed surface layer of corrosion product was modeled using  $R_{film}$  (the resistance of electrolytic solution in a porous layer) and  $C_{film}$  (the dielectric properties of this layer). Both EECs yielded a very good fit to the experimental data (parameter  $\chi_2$  in order of  $10^{-4}$ – $10^{-5}$ ) and low residual errors (0.2%–8%). However, it should be noted that the fitting was made after manually reducing the frequency range to ca. 10 kHz–0.08 Hz. This interference was intentional to avoid the influence of instability of the measured system, especially in the low frequency range, on the interpretation of the physical meaning of EECs elements and, finally, their values (collected in Tables 1 and 2).

**Table 1.** Values of electric elements calculated for EEC of blank Ni coating.

Time (h)	$R_s/\Omega\text{ cm}^2$	$CPE_{dl, Y_0}/\Omega^{-1}\text{ cm}^{-2}\text{ s}^\alpha$	$CPE_{dl, \alpha}$	$R_{ct}/\text{k}\Omega\text{ cm}^2$
24	61	$9.0 \times 10^{-5}$	0.94	214.8
48	61	$8.6 \times 10^{-5}$	0.94	299.6
72	61	$8.4 \times 10^{-5}$	0.93	394.8
96	60	$8.3 \times 10^{-5}$	0.93	478.8
120	59	$8.2 \times 10^{-5}$	0.93	552.4
144	59	$8.1 \times 10^{-5}$	0.94	604.8
168	58	$8.2 \times 10^{-5}$	0.93	580.8

**Table 2.** Values of electric elements calculated for EEC of composite Ni coating.

Time (h)	$R_s/\Omega\text{ cm}^2$	$CPE_{film, Y_0}/\Omega^{-1}\text{ cm}^{-2}\text{ s}^\alpha$	$CPE_{film, \alpha}$	$R_{film}/\text{k}\Omega\text{ cm}^2$	$CPE_{dl, Y_0}/\Omega^{-1}\text{ cm}^{-2}\text{ s}^\alpha$	$CPE_{dl, \alpha}$	$R_{ct}/\text{k}\Omega\text{ cm}^2$
24	92	$1.0 \times 10^{-4}$	0.95	5.6	$8.5 \times 10^{-5}$	0.66	74.8
48	92	$1.0 \times 10^{-4}$	0.94	5.9	$9.9 \times 10^{-5}$	0.69	59.4
72	93	$9.9 \times 10^{-5}$	0.94	7.0	$9.8 \times 10^{-5}$	0.68	77.1
96	92	$9.8 \times 10^{-5}$	0.94	7.9	$9.2 \times 10^{-5}$	0.67	81.9
120	92	$9.7 \times 10^{-5}$	0.94	8.6	$8.6 \times 10^{-5}$	0.67	84.6
144	91	$9.6 \times 10^{-5}$	0.94	8.2	$8.4 \times 10^{-5}$	0.65	92.2
168	91	$9.5 \times 10^{-5}$	0.94	8.8	$7.9 \times 10^{-5}$	0.64	102.7

For a blank Ni coating, the values of  $R_{ct}$  increased with increasing exposure time and finally exceeded  $0.5\text{ M}\Omega\text{ cm}^2$  after 7 days (Table 1). A similar tendency was observed for the  $R_p$  determined on the basis of the LPR technique, see Figure 4. This marked increase in  $R_{ct}$  was accompanied by only minor changes in CPE parameters ( $Y_0$  and  $\alpha$ ), whose values indicate the absence of significant changes in (e.g., homogeneity) of the surface at which the corrosion process occurs. In the case of a composite coating (Table 2), it was also noted that the direction of changes of a charge transfer resistance was close to the polarization resistance values obtained from the LPR method (Figure 4). Initially, for the first 48 hours, there was a drop of  $R_{ct}$  from 75 to 59  $\text{k}\Omega\text{ cm}^2$ , but after 72 hours exposure, the values of  $R_{ct}$  increased with increasing time and finally exceeded  $100\text{ k}\Omega\text{ cm}^2$  after 7 days (Table 2). For this coating the contribution of a resistance connected with the presence of a developed surface layer of corrosion products is not to be missed— $R_{film}$  values increased from 5.6 to 8.8  $\text{k}\Omega\text{ cm}^2$  over 7 days exposure (Table 2).

### 3.3. XPS Surface Analysis of Coatings

In order to better understand the role of microflakes in the corrosion process, both composite and blank Ni coatings were analyzed by X-ray photoelectron spectroscopy (XPS). The high-resolution XPS analyses were performed in the binding energy (BE) range of Ni2p, Cu2p, and O1s photopeaks, with the results presented in Figure 9. Supporting studies were also carried out in the C1s BE range.

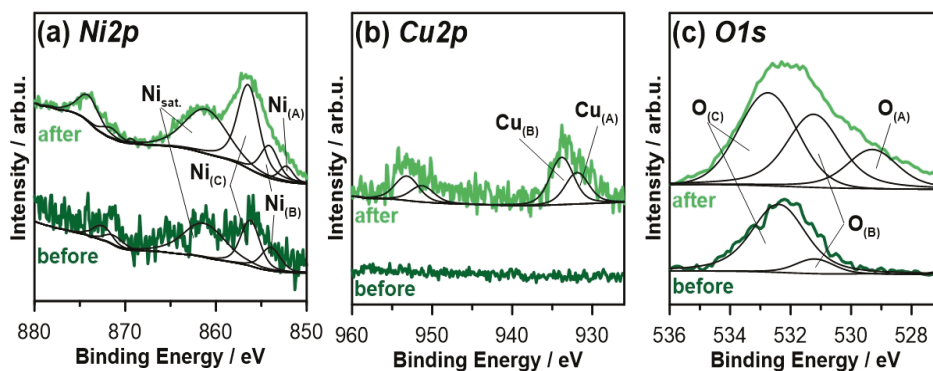


**Figure 9.** High-resolution XPS spectra recorded for blank Ni coating in (a) Ni2p, (b) Cu2p, and (c) O1s peak binding energy range, before and after the exposure to 0.05 M NaCl.

The analysis performed for the blank Ni coating prior to corrosion stability tests reveal a weak signal from nickel in the Ni2p spectra (see Figure 9a), further deconvoluted using two peak doublets Ni<sub>i(B)</sub> and Ni<sub>i(C)</sub>. The Ni2p<sub>3/2</sub> photopeaks of the aforementioned components are located at 854.0 and 856.3 eV, being highly characteristic for nickel(II) oxide NiO and nickel(II) hydroxide Ni(OH)<sub>2</sub>, respectively [38–41]. This is further confirmed by the location of the Ni satellite peak at 861.3 eV. The small signal intensity originates from substantial surface coverage with adventitious carbon layer, including oxidized carbon species. At the same time, the ion gun etching was not performed, due to significant observable changes in surface chemistry caused by the Ar<sup>+</sup> ions used for sputtering purposes. These findings are further confirmed by the O1s spectra visible at Figure 9c, where the O<sub>(B)</sub> peak was ascribed to the nickel hydroxide species, while the dominant O<sub>(C)</sub> component represents the organic carbon-oxygen bonds and carbonates formed during air exposure. The detailed analysis is summarized in Table 3.

**Table 3.** Spectral deconvolution performed for blank Ni coating.

Element		BE / eV	Blank Ni Before	Blank Ni After
Ni2p	Ni <sub>i(A)</sub>	852.4	-	1.2
	Ni <sub>i(B)</sub>	854.0	1.9	3.2
	Ni <sub>i(C)</sub>	856.3	3.7	9.7
Cu2p	Cu <sub>(A)</sub>	932.5	-	1.4
	Cu <sub>(B)</sub>	933.5	-	2.1
O1s	O <sub>(A)</sub>	529.5	-	15.6
	O <sub>(B)</sub>	530.8	12.2	30.5
	O <sub>(C)</sub>	532.4	82.2	36.7

The one weeklong exposure of the analyzed sample in 0.05 M NaCl solution resulted in partial modification of the observed sample surface chemistry. While the chemical state of Ni and O peaks appears to be unchanged, the photoelectron intensity count is significantly improved, suggesting partial removal of the carbon-based corrosion products layer. Nickel appears primarily in the form of Ni(OH)<sub>2</sub> (symbol Ni<sub>(C)</sub>), with the NiO to Ni(OH)<sub>2</sub> ratio slightly decreasing from 1:2 to 1:3. Furthermore, the third component Ni<sub>(A)</sub> emerges as a result of the exposure, its location is characteristic for metallic nickel. Again, the shape of O1s spectra corroborates the results, revealing an increased intensity of hydroxide species O<sub>(B)</sub> but also nickel oxide species O<sub>(A)</sub> at approximately 529.5 eV. The amount of adventitious carbon dropped twice.

A characteristic feature of XPS measurements carried out after blank Ni coating exposure to corrosive media is the appearance of the Cu substrate beneath the layer (see Figure 9b). Two peak

doublets could be deconvoluted on the basis of the spectra shape:  $\text{Cu}_{(A)}$  with  $\text{Cu}2p_{3/2}$  peak at 932.5 eV and  $\text{Cu}_{(B)}$  at 933.5 eV. The position of the  $\text{Cu}_{(A)}$  component is characteristic both for metallic copper as well as for  $\text{Cu}_2\text{O}$  [42], on the other hand, the  $\text{Cu}_{(B)}$  component was ascribed to  $\text{CuO}$  oxides according to previous literature findings [43–46]. The total copper contribution reached 3.5 at. %.

Similar to blank Ni coating, detailed high-resolution XPS analysis was also carried out for the composite Ni coating, where the analysis was expanded with the Ce3d and Mo3d spectral range. The results of the aforementioned analysis are presented in Figure 10 with the spectral deconvolution summarized in Table 4.

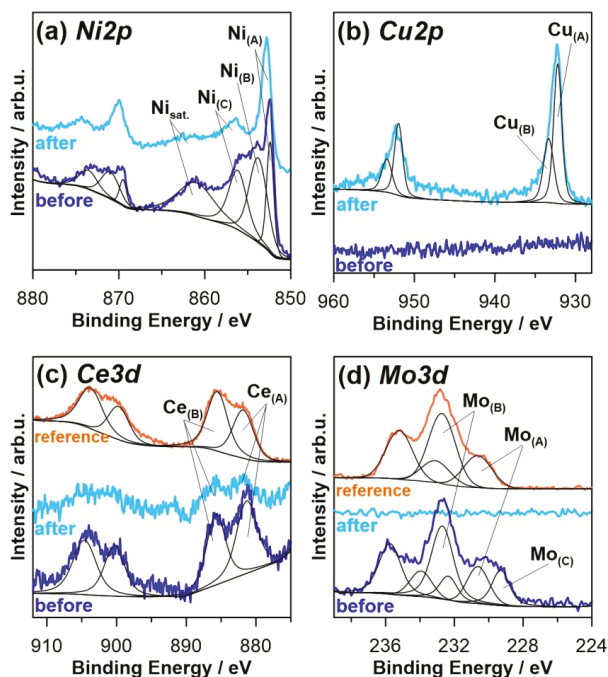


**Figure 10.** High-resolution XPS spectra recorded for composite Ni coating in (a) Ni2p, (b) Cu2p, (c) Ce3d, and (d) Mo3d peak binding energy range, before and after the exposure to 0.05 M NaCl. The chemistry of synthesized cerium molybdenum oxide hydrate powder used for electrodeposition is also shown in (c) Ce3d and (d) Mo3d spectra (“reference” spectra).

Unlike the blank Ni coating, the nickel chemistry on the surface of the composite coating prior to exposure in corrosive media is well developed, with the total Ni contribution ranging from 38 at. % compared to merely 5 at. % observed in the absence of microflake functionalization. Furthermore, the metallic Ni peak  $\text{Ni}_{(A)}$  is also well developed, proving significantly higher corrosion resistance of the protective layer under atmospheric conditions. Another difference is the strong contribution of the  $\text{Ni}_{(B)}$  component, revealing increased NiO to  $\text{Ni}(\text{OH})_2$  ratio of 1.2:1 (compared to 1:2 for blank Ni prior the exposure).

As mentioned previously, the galvanic Ni coating was modified using a cerium molybdenum oxide hydrate compound. The chemistry resulting from Ce and Mo surface modification is shown in Figure 10c,d, respectively. Comparison with the precursor compound analysis denoted as the reference confirms high spectral similarity, proving functionalization, did not introduce significant chemical changes. The cerium Ce3d spectra reveals high complexity, the deconvolution was performed using two peak doublets,  $\text{Ce}_{(A)}$  and  $\text{Ce}_{(B)}$ . Both of these were ascribed to the  $\text{Ce}^{3+}$  component on the basis of the value of peak BE (881.8 and 885.7 eV) and similar intensity, nearly at a 1:1 ratio [47–49]. It is

possible, however, that composite coating before exposure contains some  $Ce^{4+}$ , which can be inferred from the lowered position of the component at the energy 886 eV.

A similar comparison was made in the Mo3d spectral range for cerium molybdenum oxide hydrate compound and for Ni composite coating functionalized with these microflakes. Both analyses reveal the dominant presence of the component ascribed in Figure 10d as  $Mo_{(B)}$ . The peak location at 232.7 eV is a very good match with the literature BE value of  $Mo^{6+}$ , typically reported in  $MoO_3$  oxides and  $(MoO_4)_3^{2-}$  molybdates [50–52]. The second component is common for both the analyzed samples,  $Mo_{(A)}$ , is negatively shifted at approximately  $-2.1$  eV, being characteristic for the  $Mo^{5+}$  component. The  $Mo^{6+}:Mo^{5+}$  ratio of 2.8:1 remains nearly intact. Finally, the surface analysis of Ni composite coating revealed the appearance of  $Mo_{(C)}$  component at 229.5 eV bound with  $Mo^{4+}$  oxides. Its absence in cerium molybdenum oxide hydrate microflakes powder may indicate partial reduction of molybdenum during the electrodeposition process [53–55]. According to the literature, the reduction of molybdenum could take place during electrodeposition, because the shape of the voltammetric curve and currents achieved differed from those recorded in a blank Ni electrolyte (Figure 3).

The Ni chemistry on the surface of the composite Ni coating changed as a result of the exposure to the 0.05 M NaCl solution. The second analysis carried out after a one-week period revealed a double diminished Ni contribution associated primarily with the observable removal of the  $Ni_{(B)}$  component from the coating surface. It is possible that NiO got, in part, reduced to the metallic Ni in local cathodic areas and, in part, transformed to  $Ni(OH)_2$ . At the same time, the amount of molybdenum oxides within the protective coating nearly completely disappeared as a result of the corrosion process. The removal of cerium molybdenum oxide hydrate microflakes was further confirmed by significant removal of cerium species, however, it appears that the corrosion process is less selective towards it, since the spectra was still recognizable after the exposure, with nearly intact chemistry. Finally, the secondary effect of the corrosion process is the appearance of the Cu oxides,  $Cu_{(A)}$  and  $Cu_{(B)}$ . Not only the total contribution of Ni, but also Cu, is significantly increased in comparison to blank Ni coating, indicating smaller thickness of the protective layer and/or locally reduced coverage resulting from consumption of cerium/molybdenum species during the corrosion process.

**Table 4.** Spectral deconvolution performed for composite Ni coating.

Element	BE/eV	NiCeMo Before	NiCeMo After	CeMo Reference	
Ni2p	$Ni_{(A)}$	852.5	11.2	5.8	-
	$Ni_{(B)}$	853.7	14.4	3.8	-
	$Ni_{(C)}$	856.3	12.2	5.1	-
Cu2p	$Cu_{(A)}$	932.5	-	5.1	-
	$Cu_{(B)}$	933.3	-	2.9	-
Ce3d	$Ce_{(A/B)}$	881.8/885.7	6.1	2.4	11.6
Mo3d	$Mo_{(A)}$	230.6	1.2	-	5.4
	$Mo_{(B)}$	232.7	3.2	-	15.1
	$Mo_{(C)}$	229.3	1.2	-	-
O1s	$O_{(A)}$	529.5	21.8	0.3	6.0
	$O_{(B)}$	530.8	21.3	11.6	22.5
	$O_{(C)}$	532.4	7.4	63.0	39.4

### 3.4. Chemical Analysis of Corrosive Solutions

To verify the hypothesis regarding the selectivity of Ce and Mo leaching from microflakes embedded in the composite coating, an additional experiment was planned consisting of a comparative analysis of the composition of NaCl solutions both before and after the corrosion process. For this purpose, blank Ni and Ni composite coatings were immersed for 7 days in 0.05 M NaCl solutions (100 ml volume for each sample). One series of samples was just immersed and left for 7 days, a second one was immersed with an additional continuous stirring of the solution. After 7 days, all solutions were filtered and analyzed by

ICP-OES and ICP-MS. The focus was on the comparative analysis of: Ni, Cu, Ce, and Mo content, with blank 0.05 M NaCl as the reference. The results are summarized in Table 5.

**Table 5.** Concentrations of Ni, Cu, Ce, and Mo in a corrosive solution.

Element	Units	Blank (Demi Water + 0.05M NaCl)	Blank Ni	Blank Ni_m *	Composite Ni	Composite Ni_m *
Ni	µg/L	<2.0 <sup>2</sup>	2620 ± 370 <sup>1</sup>	4230 ± 590 <sup>1</sup>	2730 ± 380 <sup>1</sup>	6000 ± 840 <sup>1</sup>
Cu	µg/L	2.4 ± 0.4 <sup>2</sup>	2.1 ± 0.3 <sup>2</sup>	2.2 ± 0.3 <sup>2</sup>	29 ± 4 <sup>2</sup>	14 ± 2 <sup>2</sup>
Ce	µg/L	<0.1 <sup>2</sup>	<0.1 <sup>2</sup>	<0.1 <sup>2</sup>	0.33 ± 0.07 <sup>2</sup>	0.13 ± 0.03 <sup>2</sup>
Mo	µg/L	5.5 ± 0.8 <sup>2</sup>	5.3 ± 0.8 <sup>2</sup>	17 ± 3 <sup>2</sup>	390 ± 55 <sup>2</sup>	374 ± 52 <sup>2</sup>

<sup>1</sup> ICP-OES analysis. <sup>2</sup> ICP-MS analysis. \* Solution was mechanically stirred for 7 days exposure of the coatings.

The results presented in Table 5 clearly indicate that Ce did not go into the solution in any significant amounts (similar level before and after corrosion process). At the same time Mo content increased from ca. 5 to 370–390 µg/L. This analysis shows that molybdenum is not only leached from microflakes, but also significant amounts of Mo passed into the corrosive solution. This behavior is quite possible, because the SEM observation of composite coating after 168 hours exposure clearly indicates that some of the microflakes have probably been leached away and those that were visible have been partially dissolved, leaving something like a skeleton/frame (Figure 11a). Furthermore, XPS analysis seems to confirm that molybdenum, when released from micro-flakes, does not form a stable oxide layer on the surface of the coating. Such selective dissolution probably caused voids (well visible in Figure 11a) in the coating, which resulted in a lower corrosion resistance of this composite material.

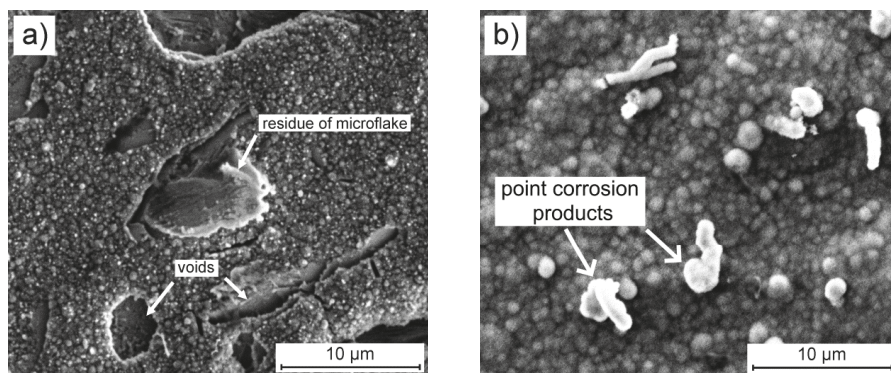


**Figure 11.** Surface morphology of (a) composite and (b) blank Ni coatings (deposited on the copper substrate at a current density of 6 mA cm<sup>-2</sup> at 70 °C for 1 h) after one-week exposure to 0.05 M NaCl solution.

The results related to Ni concentration (Table 5) very likely to confirm that Ni almost completely forms the layer of corrosion products. Only point corrosion products were visible on the surface of blank Ni coating (Figure 11b). Its (nickel) presence in the solution after corrosion at a level similar to that determined in the blank 0.05 M NaCl solution only confirms this assumption. Different behavior was observed for copper (originating from the substrate). In the case of blank Ni coating, Cu was not observed to pass into the NaCl solution, which, in the context of the results of the XPS surface analysis, only confirmed that this element is part of the relatively stable corrosion products on the surface of this coating. Only in the case of composite coating, copper was determined at the level of 14–29 µg/L, which means that this element partially passed in the form of an ion into the solution. This is even more possible because during the dissolution of the microflakes, the copper substrate was gradually exposed to chloride ions.



#### 4. Conclusions

In summary, it can be concluded that:

- (1) DES-based plating baths are an excellent environment for the electrodeposition of metal composite coatings.
- (2) The addition of cerium molybdenum oxide hydrate microflakes to a plating bath modifies the cathodic process sufficiently to obtain nanocrystalline nickel composite coatings with a smaller (6.3 nm) crystallite size than blank Ni coating (10.4 nm).
- (3) The codeposition of large CeMo oxide microflakes caused microcracks in the coating and some deterioration of the protective properties of composite coating.
- (4) Charge transfer resistance for both types of coatings increased over 7 days exposure in 0.05 M NaCl solution. However, even after this time, the  $R_{ct}$  for a blank Ni exceeded five times (581 k $\Omega$  cm<sup>2</sup>) that of a composite one (103 k $\Omega$  cm<sup>2</sup>).
- (5) On the basis of spectroscopic studies (XPS, ICP-OES and ICP-MS), it can be stated for composite Ni coating that in the course of corrosion, NiO transforms to Ni(OH)<sub>2</sub>, while molybdenum oxides nearly completely disappear from the surface of composite coating. The removal of cerium species was less than that of the molybdenum species, which suggests that the corrosion process is more selective towards Mo. The smaller thickness of the protective layer and locally reduced coverage results from the consumption of the Ce/Mo species during the corrosion process.
- (6) It would be interesting to develop the described research towards the synthesis of nanoflakes (or nanowires) of mixed cerium and molybdenum compounds. Reducing the particle size to the nano-scale would result in a composite coating with a better dispersed oxide phase. This, in turn, would improve the tightness of the metal coating.

**Author Contributions:** All authors have read and agree to the published version of the manuscript. Research concept and supervision, J.W.; methodology, J.W. (corrosion, electrochemistry, SEM, powder synthesis), J.R. (XPS), A.N. (electrodeposition, laboratory work, profilometry), K.W. (XRD), S.B. (ICP-OES and ICP-MS); writing—original draft preparation, J.W., A.N., J.R., K.W.; review, K.D., B.S.

**Funding:** This research was funded by a statutory activity subsidy from the Polish Ministry of Science and Higher Education for the Department of Advanced Material Technologies at Wrocław University of Science and Technology in 2020 year—grant number 8201003902.

**Conflicts of Interest:** The authors declare no conflict of interest.

#### References

1. Abbott, A.P.; McKenzie, K.J. Application of ionic liquids to the electrodeposition of metals. *Phys. Chem. Chem. Phys.* **2006**, *8*, 4265–4279. [[CrossRef](#)] [[PubMed](#)]
2. Abbott, A.; Frisch, G.; Ryder, K. Electroplating Using Ionic Liquids. *Annu. Rev. Mater. Res.* **2013**, *43*, 335–358. [[CrossRef](#)]
3. Simka, W.; Puszczczyk, D.; Nawrat, G. Electrodeposition of metals from non-aqueous solutions. *Electrochimica Acta* **2009**, *54*, 5307–5319. [[CrossRef](#)]
4. Liu, F.; Deng, Y.; Han, X.; Hu, W.; Zhong, C. Electrodeposition of metals and alloys from ionic liquids. *J. Alloy. Compd.* **2016**, *654*, 163–170. [[CrossRef](#)]
5. Abbott, A.; Boothby, D.; Capper, G.; Davies, D.; Rasheed, R.K. Deep Eutectic Solvents Formed between Choline Chloride and Carboxylic Acids: Versatile Alternatives to Ionic Liquids. *J. Am. Chem. Soc.* **2004**, *126*, 9142–9147. [[CrossRef](#)]
6. Smith, E.L.; Abbott, A.; Ryder, K. Deep Eutectic Solvents (DESS) and Their Applications. *Chem. Rev.* **2014**, *114*, 11060–11082. [[CrossRef](#)]
7. Abbott, A.; Ballantyne, A.; Harris, R.; Juma, J.A.; Ryder, K.; Forrest, G. A Comparative Study of Nickel Electrodeposition Using Deep Eutectic Solvents and Aqueous Solutions. *Electrochimica Acta* **2015**, *176*, 718–726. [[CrossRef](#)]

8. Wang, S.; Zou, X.; Lu, Y.; Rao, S.; Xie, X.; Pang, Z.; Lu, X.; Xu, Q.; Zhou, Z. Electrodeposition of nano-nickel in deep eutectic solvents for hydrogen evolution reaction in alkaline solution. *Int. J. Hydrogen Energy* **2018**, *43*, 15673–15686. [[CrossRef](#)]
9. Abbott, A.; El Ttaib, K.; Ryder, K.; Smith, E.L. Electrodeposition of nickel using eutectic based ionic liquids. *Trans. IMF* **2008**, *86*, 234–240. [[CrossRef](#)]
10. Abbott, A.; Ballantyne, A.; Harris, R.; Juma, J.A.; Ryder, K. Bright metal coatings from sustainable electrolytes: The effect of molecular additives on electrodeposition of nickel from a deep eutectic solvent. *Phys. Chem. Chem. Phys.* **2017**, *19*, 3219–3231. [[CrossRef](#)]
11. Cherigui, E.A.M.; Sentosun, K.; Mamme, M.H.; Lukaczynska, M.; Terryn, H.; Bals, S.; Ustarroz, J. On the Control and Effect of Water Content during the Electrodeposition of Ni Nanostructures from Deep Eutectic Solvents. *J. Phys. Chem. C* **2018**, *122*, 23129–23142. [[CrossRef](#)]
12. Fashu, S.; Gu, C.; Zhang, J.; Huang, M.-L.; Wang, X.-L.; Gu, C. Effect of EDTA and NH<sub>4</sub>Cl additives on electrodeposition of Zn–Ni films from choline chloride-based ionic liquid. *Trans. Nonferrous Met. Soc. China* **2015**, *25*, 2054–2064. [[CrossRef](#)]
13. Vijayakumar, J.; Mohan, S.; Kumar, S.A.; Suseendiran, S.; Pavithra, S. Electrodeposition of Ni–Co–Sn alloy from choline chloride-based deep eutectic solvent and characterization as cathode for hydrogen evolution in alkaline solution. *Int. J. Hydrogen Energy* **2013**, *38*, 10208–10214. [[CrossRef](#)]
14. Yanai, T.; Shiraishi, K.; Watanabe, Y.; Nakano, M.; Ohgai, T.; Suzuki, K.; Fukunaga, H. Electroplated Fe–Ni Films Prepared From Deep Eutectic Solvents. *IEEE Trans. Magn.* **2014**, *50*, 1–4. [[CrossRef](#)]
15. You, Y.; Gu, C.; Wang, X.; Tu, J. Electrodeposition of Ni–Co alloys from a deep eutectic solvent. *Surf. Coatings Technol.* **2012**, *206*, 3632–3638. [[CrossRef](#)]
16. Golgovici, F.; Pumnea, A.; Petica, A.; Manea, A.C.; Brincoveanu, O.; Enachescu, M.; Anicai, L. Ni–Mo alloy nanostructures as cathodic materials for hydrogen evolution reaction during seawater electrolysis. *Chem. Pap.* **2018**, *72*, 1889–1903. [[CrossRef](#)]
17. Martis, P.; Dilimon, V.; Delhalle, J.; Mekhalif, Z. Electro-generated nickel/carbon nanotube composites in ionic liquid. *Electrochimica Acta* **2010**, *55*, 5407–5410. [[CrossRef](#)]
18. Liu, D.; Sun, J.; Gui, Z.; Song, K.; Luo, L.; Wu, Y. Super-low friction nickel based carbon nanotube composite coating electro-deposited from eutectic solvents. *Diam. Relat. Mater.* **2017**, *74*, 229–232. [[CrossRef](#)]
19. You, Y.H.; Gu, C.D.; Wang, X.L.; Tu, J.P. Electrochemical preparation and characterization of Ni-PTFE composite coatings from a non-aqueous solution without additives. *Int. Electrochem. Sci.* **2012**, *7*, 12440–12455.
20. Li, R.; Chu, Q.; Liang, J. Electrodeposition and characterization of Ni–SiC composite coatings from deep eutectic solvent. *RSC Adv.* **2015**, *5*, 44933–44942. [[CrossRef](#)]
21. Li, R.; Hou, Y.; Liang, J. Electro-codeposition of Ni–SiO<sub>2</sub> nanocomposite coatings from deep eutectic solvent with improved corrosion resistance. *Appl. Surf. Sci.* **2016**, *367*, 449–458. [[CrossRef](#)]
22. Li, R.; Hou, Y.; Liu, B.; Wang, D.; Liang, J. Electrodeposition of homogenous Ni/SiO<sub>2</sub> nanocomposite coatings from deep eutectic solvent with in-situ synthesized SiO<sub>2</sub> nanoparticles. *Electrochimica Acta* **2016**, *222*, 1272–1280. [[CrossRef](#)]
23. Protsenko, V.; Bogdanov, D.; Korniy, S.; Kityk, A.; Baskevich, A.; Danilov, F. Application of a deep eutectic solvent to prepare nanocrystalline Ni and Ni/TiO<sub>2</sub> coatings as electrocatalysts for the hydrogen evolution reaction. *Int. J. Hydrogen Energy* **2019**, *44*, 24604–24616. [[CrossRef](#)]
24. Dong, M.; Lin, Q.; Sun, H.; Chen, D.; Zhang, T.; Wu, Q.; Li, S. Synthesis of Cerium Molybdate Hierarchical Architectures and Their Novel Photocatalytic and Adsorption Performances. *Cryst. Growth Des.* **2011**, *11*, 5002–5009. [[CrossRef](#)]
25. Xu, M.-K.; Ouyang, Z.-H.; Shen, Z. Topological evolution of cerium(III) molybdate microflake assemblies induced by amino acids. *Chin. Chem. Lett.* **2016**, *27*, 673–677. [[CrossRef](#)]
26. Ayni, S.; Sabet, M.; Salavati-Niasari, M.; Hamadani, M. Synthesis and characterization of cerium molybdate nanostructures via a simple solvothermal method and investigation of their photocatalytic activity. *J. Mater. Sci. Mater. Electron.* **2016**, *27*, 7342–7352. [[CrossRef](#)]
27. Kartsonakis, I.; Kordas, G. Synthesis and Characterization of Cerium Molybdate Nanocontainers and Their Inhibitor Complexes. *J. Am. Ceram. Soc.* **2010**, *93*, 65–73. [[CrossRef](#)]
28. Kartsonakis, I.; Balaskas, A.C.; Kordas, G.C. Influence of cerium molybdate containers on the corrosion performance of epoxy coated aluminium alloys 2024-T3. *Corros. Sci.* **2011**, *53*, 3771–3779. [[CrossRef](#)]

29. Kartsonakis, I.; Kontogiani, P.; Pappas, G.; Kordas, G. Photocatalytic action of cerium molybdate and iron-titanium oxide hollow nanospheres on Escherichia coli. *J. Nanoparticle Res.* **2013**, *15*, 1759. [[CrossRef](#)]
30. Patel, M.; Bhanvase, B.A.; Sonawane, S. Production of cerium zinc molybdate nano pigment by innovative ultrasound assisted approach. *Ultrason. Sonochemistry* **2013**, *20*, 906–913. [[CrossRef](#)]
31. Yasakau, K.; Kallip, S.; Zheludkevich, M.; Ferreira, M. Active corrosion protection of AA2024 by sol-gel coatings with cerium molybdate nanowires. *Electrochimica Acta* **2013**, *112*, 236–246. [[CrossRef](#)]
32. Yasakau, K.; Tedim, J.; Zheludkevich, M.; Drumm, R.; Shem, M.; Wittmar, M.; Veith, M.; Ferreira, M. Cerium molybdate nanowires for active corrosion protection of aluminium alloys. *Corros. Sci.* **2012**, *58*, 41–51. [[CrossRef](#)]
33. Lehr, I.; Saidman, S. Corrosion protection of AZ91D magnesium alloy by a cerium-molybdenum coating-The effect of citric acid as an additive. *J. Magnes. Alloy.* **2018**, *6*, 356–365. [[CrossRef](#)]
34. Mu, S.; Du, J.; Jiang, H.; Li, W. Composition analysis and corrosion performance of a Mo-Ce conversion coating on AZ91 magnesium alloy. *Surf. Coatings Technol.* **2014**, *254*, 364–370. [[CrossRef](#)]
35. Bhanvase, B.A.; Patel, M.; Sonawane, S. Kinetic properties of layer-by-layer assembled cerium zinc molybdate nanocontainers during corrosion inhibition. *Corros. Sci.* **2014**, *88*, 170–177. [[CrossRef](#)]
36. Langford, J.I.; Wilson, A.J.C. Scherrer after sixty years: A survey and some new results in the determination of crystallite size. *J. Appl. Crystallogr.* **1978**, *11*, 102–113. [[CrossRef](#)]
37. Urcezino, A.S.C.; Dos Santos, L.P.M.; Casciano, P.N.S.; Correia, A.N.; De Lima-Neto, P. Electrodeposition study of Ni coatings on copper from choline chloride-based deep eutectic solvents. *J. Braz. Chem. Soc.* **2017**, *28*, 1193–1203. [[CrossRef](#)]
38. Winiarski, J.; Cieřlikowska, B.; Tylus, W.; Kunicki, P.; Szczygieł, B. Corrosion of nanocrystalline nickel coatings electrodeposited from choline chloride:ethylene glycol deep eutectic solvent exposed in 0.05 M NaCl solution. *Appl. Surf. Sci.* **2019**, *470*, 331–339. [[CrossRef](#)]
39. Biesinger, M.C.; Payne, B.P.; Lau, L.W.M.; Gerson, A.; Smart, R.S.C. X-ray photoelectron spectroscopic chemical state quantification of mixed nickel metal, oxide and hydroxide systems. *Surf. Interface Anal.* **2009**, *41*, 324–332. [[CrossRef](#)]
40. Tang, Y.; Pattengale, B.; Ludwig, J.; Atifi, A.; Zinovev, A.V.; Dong, B.; Kong, Q.; Zuo, X.; Zhang, X.; Huang, J. Direct Observation of Photoinduced Charge Separation in Ruthenium Complex/Ni(OH)<sub>2</sub> Nanoparticle Hybrid. *Sci. Rep.* **2015**, *5*, 18505. [[CrossRef](#)]
41. Mansour, A.N. Characterization of NiO by XPS. *Surf. Sci. Spectra* **1994**, *3*, 231–238. [[CrossRef](#)]
42. Espinos, J.P.; Morales, J.; Barranco, A.; Caballero, A.; Holgado, J.P.; González-Elipe, A.R.; González-Elipe, A.R. Interface Effects for Cu, CuO, and Cu<sub>2</sub>O Deposited on SiO<sub>2</sub> and ZrO<sub>2</sub>. XPS Determination of the Valence State of Copper in Cu/SiO<sub>2</sub> and Cu/ZrO<sub>2</sub> Catalysts. *J. Phys. Chem. B* **2002**, *106*, 6921–6929. [[CrossRef](#)]
43. Shaikh, J.; Pawar, R.C.; Devan, R.; Ma, Y.; Salvi, P.; Kolekar, S.; Patil, P. Synthesis and characterization of Ru doped CuO thin films for supercapacitor based on Bronsted acidic ionic liquid. *Electrochimica Acta* **2011**, *56*, 2127–2134. [[CrossRef](#)]
44. Poulston, S.; Parlett, P.M.; Stone, P.; Bowker, M. Surface oxidation and reduction of CuO and Cu<sub>2</sub>O studied using XPS and XAES. *Surf. Interface Anal.* **1996**, *24*, 811–820. [[CrossRef](#)]
45. Morales, J.; Espinos, J.P.; Caballero, A.; Gonzalez-Elipe, A.R.; Mejías, J.A.; González-Elipe, A.R. XPS Study of Interface and Ligand Effects in Supported Cu<sub>2</sub>O and CuO Nanometric Particles. *J. Phys. Chem. B* **2005**, *109*, 7758–7765. [[CrossRef](#)]
46. González-Elipe, A.R.; Holgado, J.P.; Alvarez, R.; Munuera, G. Use of factor analysis and XPS to study defective nickel oxide. *J. Phys. Chem.* **1992**, *96*, 3080–3086. [[CrossRef](#)]
47. Holgado, J.P.; Alvarez, R.; Munuera, G. Study of CeO<sub>2</sub> XPS spectra by factor analysis: Reduction of CeO<sub>2</sub>. *Appl. Surf. Sci.* **2000**, *161*, 301–315. [[CrossRef](#)]
48. Al-Doghachi, F.A.J.; Rashid, U.; Taufiq-Yap, Y.H. Investigation of Ce(III) promoter effects on the tri-metallic Pt, Pd, Ni/MgO catalyst in dry-reforming of methane. *RSC Adv.* **2016**, *6*, 10372–10384. [[CrossRef](#)]
49. Beche, E.; Charvin, P.; Perarnau, D.; Abanades, S.; Flamant, G. Ce 3d XPS investigation of cerium oxides and mixed cerium oxide (Ce<sub>x</sub>Ti<sub>y</sub>O<sub>z</sub>). *Surf. Interface Anal.* **2008**, *40*, 264–267. [[CrossRef](#)]
50. Li, Z.; Gao, L.; Zheng, S. SEM, XPS, and FTIR studies of MoO<sub>3</sub> dispersion on mesoporous silicate MCM-41 by calcination. *Mater. Lett.* **2003**, *57*, 4605–4610. [[CrossRef](#)]
51. Reddy, B.M.; Chowdhury, B.; Reddy, E.P.; Fernández, A. An XPS study of dispersion and chemical state of MoO<sub>3</sub> on Al<sub>2</sub>O<sub>3</sub>-TiO<sub>2</sub> binary oxide support. *Appl. Catal. A: Gen.* **2001**, *213*, 279–288. [[CrossRef](#)]

52. Lee, Y.J.; Nichols, W.T.; Kim, D.-G.; Kim, Y.D. Chemical vapour transport synthesis and optical characterization of MoO<sub>3</sub> thin films. *J. Phys. D: Appl. Phys.* **2009**, *42*, 115419. [[CrossRef](#)]
53. Li, H.; Ye, H.; Xu, Z.; Wang, C.; Yin, J.; Zhu, H. Freestanding MoO<sub>2</sub>/Mo<sub>2</sub>C imbedded carbon fibers for Li-ion batteries. *Phys. Chem. Chem. Phys.* **2017**, *19*, 2908–2914. [[CrossRef](#)] [[PubMed](#)]
54. Kim, H.; Cook, J.; Tolbert, S.H.; Dunn, B. The Development of Pseudocapacitive Properties in Nanosized-MoO<sub>2</sub>. *J. Electrochem. Soc.* **2015**, *162*, A5083–A5090. [[CrossRef](#)]
55. Marin-Flores, O.; Scudiero, L.; Ha, S. X-ray diffraction and photoelectron spectroscopy studies of MoO<sub>2</sub> as catalyst for the partial oxidation of isooctane. *Surf. Sci.* **2009**, *603*, 2327–2332. [[CrossRef](#)]



© 2020 by the authors. Licensee MDPI, Basel, Switzerland. This article is an open access article distributed under the terms and conditions of the Creative Commons Attribution (CC BY) license (<http://creativecommons.org/licenses/by/4.0/>).



Article

# Microstructure Characterization and Corrosion Resistance of Zinc Coating Obtained on High-Strength Grade 10.9 Bolts Using a New Thermal Diffusion Process

Henryk Kania <sup>1,\*</sup> and Jacek Sipa <sup>2,\*</sup>

<sup>1</sup> Silesian University of Technology, Institute of Materials Engineering, Krasińskiego 8, 40-019 Katowice, Poland

<sup>2</sup> Remix S.A., Poznańska 36, 66-200 Świebodzin, Poland

\* Correspondence: henryk.kania@polsl.pl (H.K.); j.sipa@remiksa.pl (J.S.); Tel.: +48-68-4755400 (J.S.)

Received: 15 March 2019; Accepted: 25 April 2019; Published: 29 April 2019

**Abstract:** The article presents the results of research on the application of innovative thermal diffusion zinc coating technology with the recirculation of the reactive atmosphere to high-strength grade 10.9 bolts. The innovation of this method consists in the introduction of reactive atmosphere recirculation and the application of coating powder mix which contains zinc powder and activator. Recirculation of the reactive atmosphere ensures its uniform composition, while the presence of an activator intensifies the process of saturating steel surface with zinc, which boosts the efficiency of active agents. Coatings were created at 440 °C and a heat soaking time of 30–240 min. Coating structure (SEM) was exposed, chemical composition in microsites (EDS) was defined, and coating phase structure (XRD) was identified. The kinetics of coating growth were defined. It was found that the increment of coating thickness was controlled by square root of soaking time. Coatings obtained using innovative thermal diffusion zinc coating technology had a two-layer structure. At the substrate, a compact layer of phase  $\Gamma_1$  ( $\text{Fe}_{11}\text{Zn}_{40}$ ) was created, which was covered with a layer of phase  $\delta_1$  ( $\text{FeZn}_{10}$ ). The new method of thermal diffusion zinc coating will allow for the creation of coatings of very good corrosion resistance while maintaining strength properties of bolts defined as strength class 10.9.

**Keywords:** thermal diffusion coatings; grade 10.9 bolts; corrosion resistance

## 1. Introduction

Due to their versatility and reliability, bolted joints are among most frequent methods of joining steel structures. They demonstrate a number of advantages, which include easy and quick assembly at minimum cost of maintenance and control but also good strength at variable loads [1]. However, due to specific geometry of such joints, they are the most critical area of construction, which in numerous instances necessitates the application of high-strength bolts made of special, additionally heat-treated steel grades.

The durability of steel structures is determined by the impact of the environment whose aggressiveness speeds up corrosive wear. Therefore, adequate anti-corrosion protection of steel structures is an important factor and is decisive for safe exploitation. Steel structures are most often protected against corrosion by hot dip metallization. Zinc coatings are also used to protect bolts designed for joining structural elements [2]. However, the requirement of a proper thread match between the bolt and nut brings about the limitation of coating thickness [3]. Despite being stronger than construction steel, bolts become the weakest element of a structure in a corrosive environment.

Currently, zinc coatings on bolts are obtained by various methods. Hot dip galvanizing (HDG) is most frequently used to protect bolt surfaces [2]. Bolts are galvanized by a batch hot dip method in baskets with centrifugation [4]. Coating consists of a transient layer of intermetallic phase Fe-Zn, which is covered with an outer layer of zinc extracted from the bath [5,6]. The depth of the external layer is difficult to control, while removing an excess of zinc is not always successful at a conventional hot dip galvanizing temperature of 450 °C. Coatings obtained usually have a thickness of 45 to 65 µm. This makes it difficult to obtain a proper fit between bolts and nuts, while decreased coating thickness lowers the strength of the joint compared to other elements of the structure [7]. Much better results are achieved by high-temperature galvanizing. Galvanizing at a higher temperature allows for the effective removal of excess zinc from the surface of bolts. Coating obtained at a high temperature consists exclusively of intermetallic phase Fe-Zn. The thickness of intermetallic phase layers is more effectively controlled with process parameters. The corrosion resistance of high temperature coatings is approximately two times greater than that of conventional zinc coatings [8]. Removal of excess zinc allows one to maintain the thread fit, while increased corrosion resistance yields bolt strength comparable to other structural elements. High temperature galvanizing of bolts is effected at a temperature of ca. 560 °C [9]. In the case of high-strength quenched and tempered bolts, galvanizing at such a temperature poses a risk of compromising the high-strength properties. Furthermore, the pickling procedure in hydrochloric acid, normally applied in the procedure of surface finishing, creates a risk of hydrogen embrittlement due to hydriding in the case of high-strength bolts.

Another method of protecting bolts against corrosion is electro-galvanizing, which ensures obtaining a uniformly thick coating on a threaded surface. Due to small coating thickness (usually up to 15 µm), the corrosion resistance of the bolts, which is significant at the beginning of exploitation, decreases fairly quickly, which considerably shortens the life of the entire structure. The application of galvanized coatings does not require heating of treated elements during the process, which minimizes the risk of high-strength bolts losing their strength after quenching and tempering. However, this method leads to extensive contamination of the natural environment as well as possible hydrogen embrittlement in high-strength steel [10].

Much better results are achieved when zinc coatings on bolts are obtained by sherardizing. The sherardizing process is run in closed rotary retorts in which bolts are placed together with zinc powder and zinc oxide [11]. The retort is soaked at a temperature of 380–450 °C, which allows for the creation of a layer of intermetallic phase Fe-Zn on the bolts [12–14]. The protective layer created by sherardizing, similar to the one obtained through high-temperature galvanizing, consists exclusively of intermetallic phase Fe-Zn, which permits the control of case depth and ensures high corrosion resistance. Meanwhile, due to a much lower processing temperature, the high-strength bolts retain their strength properties [13]. It is usually enough to have the surfaces cleaned mechanically before sherardizing in order to prevent hydrogen embrittlement. The major drawback of sherardizing is its relatively long processing time. In order to obtain coatings of the required depth of 15–30 µm, 6 to 12 h will be needed, to be further extended if the process temperature is lowered.

## **2. Innovative Thermal Diffusion Zinc Coating Technology with Reactive Atmosphere Recirculation**

The technology of thermal diffusion zinc coating with recirculation of reactive atmosphere is a new technology in zinc coating. The process is run in a closed retort, which is loaded with products to be coated together with powder mixture. The rotating motion of the retort ensures continuous contact of powder mix with the surfaces of processed products. The powder mix is composed of zinc powder, ZnO as a filler, and NH<sub>4</sub>Cl as an activator. In the course of heating the powder mix in the retort, gaseous reaction products are created that move towards the surfaces to be coated. On steel substrate adsorption of zinc atoms created from the gaseous mixture as a result of reduction, dissociation, or exchange occurs.

Forming of thermal diffusion coating results from the chemical reaction of vapor deposition [15–17]. Previous studies have shown that  $\text{NH}_4\text{Cl}$  decomposes according to the following reaction [16]:



Zn powder reacts with HCl vapors to form  $\text{ZnCl}_2$  by the reaction:



$\text{ZnCl}_2$  is reduced by hydrogen to Zn as a result of heating process [16]. During heating, active zinc atoms can also be formed according to Equation [18], as follows:



The concentration of active Zn atoms in the powder mixture is higher than on the steel surface. The concentration gradient causes internal diffusion of zinc, which in a gaseous form deposits on the steel surface [18].

Active zinc atoms easily diffuse into the steel substrate along existing vacancies, leading to distortion of the crystallographic structure of the steel substrate. The iron atoms on the surface of the substrate can be activated by the following reactions [18]:



Crystal lattice distortion accelerates the diffusion of active Fe atoms outside [18]. During heating, there is a two-way diffusion between Zn and Fe, causing the formation of Fe-Zn intermetallic phases [17].

The process, besides rotary movement of the retort, is aided by an innovative solution that consists of forced circulation of reactive atmosphere along the retort cylinder [19]. This ensures a better and more uniform contact of product surface with powder mix, both on external and internal surfaces as well as on surfaces of intricate shape. Introduction of atmosphere recirculation along the retort cylinder permits uniformity of reactive atmosphere within the entire volume of the retort, which leads to uniform temperature in the working space, lower consumption of powder mix, and more effective use thereof in comparison to typical sherardizing [19]. Due to recirculation and better use of active agents, it is possible to create the layers of intermetallic phase Fe-Zn [20] on low-carbon steel at a much shorter time compared to conventional sherardizing technology. At the same time, the coatings obtained through this method demonstrate higher corrosion resistance than the hot dip coatings [21]. The new technology constitutes an alternative to traditional process of sherardizing, in which an activator is not used and mixture motion in the atmosphere is determined solely by the rotating movement of the retort.

### 3. Materials and Methods

Coatings for research were created on a prototype plant equipped with a furnace with a rotary working chamber of capacity 100 kg and forced recirculation of reactive atmosphere. The workload consisted of M10 bolts and threaded bars of strength grade 10.9 made of quenched and tempered 1.7225 steel (42CrMo4). The powder mix was composed of zinc powder with an addition of 15% of zinc oxide ZnO as a filler and 3% of  $\text{NH}_4\text{Cl}$  as an activator. All that was soaked at the temperature of 440 °C and times of 30, 60, 120, and 240 min. Before filling the working chamber of the furnace, the ingredients of powder mix were dried at the temperature of 120 °C for 12 h in order to reduce moisture content to approx. 1%. The activator was added to the mixture right before processing due to its high hygroscopicity. Before processing, bolt surfaces were cleaned mechanically using sandblasting process to prevent the risk of hydrogen embrittlement.



In order to establish the structure of the thus-produced coatings, metallographic tests were performed with a light microscope. The microstructure and chemical composition in micro-areas of coatings were analyzed with a Hitachi S-3400 N (Tokyo, Japan) scanning microscope equipped with a X-ray energy dispersion spectroscopy.

Phase analysis by X-ray diffraction was performed with a JEOL JDX-7S X-ray (Tokyo, Japan) diffractometer using a copper anode lamp ( $\lambda_{CuK\alpha} = 1.54178 \text{ \AA}$ ) powered with 20 mA current at 40 kV, and with a graphite monochromator. Recording was performed with a stepwise approach of  $0.05^\circ$  step and counting time of 3 s in the range of  $10$  to  $90^\circ 2\theta$ . Phases were identified with the help of the ICDD (Newtown Square, PA, USA) PDF-4+ database. Diffractometric tests were performed on skew-ground sample surfaces so that phase structure could be displayed in the entire cross-section of the coating.

Testing of resistance to the impact of neutral salt spray was performed in accordance with the standard EN ISO 9227 in a salt chamber CORROTHERM Model 610 by Erichsen. (Hemer, Germany) Testing was conducted in a 5% spray of sodium chloride in distilled water at the temperature of  $35^\circ\text{C}$ . In order to determine mass changes, gravimetric analyses were performed in the course of testing following 48, 96, 164, 240, 480, 720, and 1000 h of the exposure of samples in the chamber. Corrosion tests were carried out on grade 10.9 screws with thermal diffusion zinc coating obtained at  $440^\circ\text{C}$  and heating time of 12 min.

Tensile strength testing was performed on a tensile strength testing machine Inspekt Table 100 by Hegewald und Peschke MPT GmbH (Nossen, Germany) with maximal load 100 kN.

## 4. Results and Discussion

### 4.1. Surface and Cross-Sections Appearance

External appearance of zinc coatings obtained on a grade 10.9 bolt with the new technology of thermal diffusion zinc coating with reaction of reactive atmosphere is presented in Figure 1. The coatings obtained do not show any discontinuity, while their surface looks matt grey. No traces of powder mix were found on the thread surface after zinc coating (Figure 1a). Additionally, in a cross-section the coating shows no discontinuity and densely covers the bolt surface both on the head (Figure 1b) and on the tip of thread (Figure 1c) as well as in the groove (Figure 1d). The grey and matt appearance of the coating and its cross-sectional morphology are a proof of intermetallic Fe-Zn phases in its structure. The appearance of cracks located mainly in the upper part of the coating can be observed in the coating structure, which may indicate the brittleness of the coating. The occurrence of transverse cracks is characteristic of the intermetallic phases of the Fe-Zn phases.

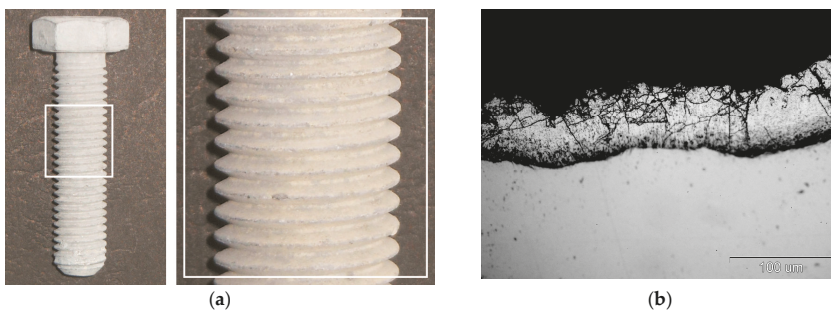
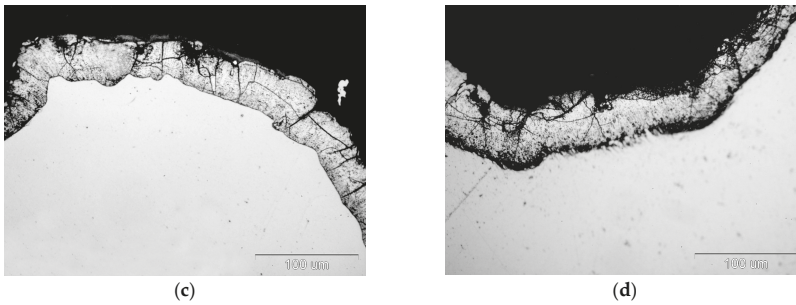


Figure 1. Cont.



**Figure 1.** Appearance of surface (a) and cross-section of coating on bolt head (b), thread tip (c), and thread groove (d) of grade 10.9 bolt.

4.2. Growth Kinetics

Growth kinetics of coatings obtained on high strength grade 10.9 bolts at the temperature of 440 °C and soaking time from 30 to 240 min is presented in Figure 2. Coating thickness increases with the increase of soaking time. However, the increment of coating thickness becomes slower and slower. After 120 min, a coating of average thickness of 50.61 µm was obtained. During further soaking, the increment was over 2 x slower with thickness of 72.62 µm obtained after the time of 240 min (Figure 2a).

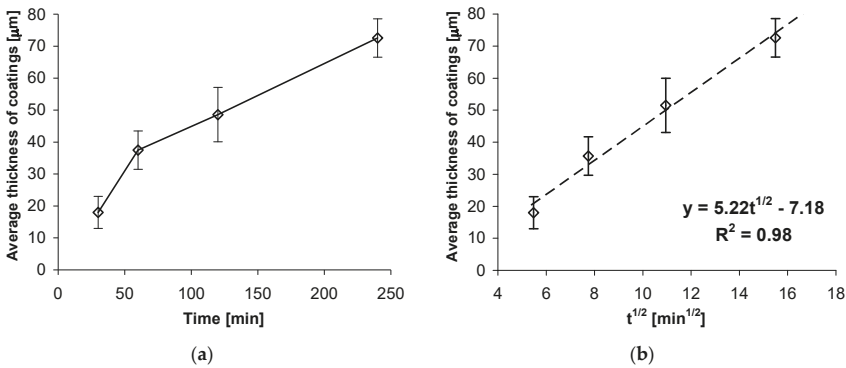


**Figure 2.** Growth kinetics (a) and plot of coating thickness as a function of  $t^{1/2}$  (b).

The impact of temperature soaking time on coating thickness is shown in more detail as the dependence of thickness in the square root function of soaking time  $t^{1/2}$ . For the experimentally defined dependence of coating thickness from soaking time, there is a nearly linear correlation of coating thickness against square root of soaking time  $t^{1/2}$ . The determined trend function and high value of correlation factor  $R^2 = 0.98$  confirm the linear nature of coating thickness increment. Thus, the growth kinetics for a coating may be described by the following equation:

$$y \text{ (thickness)} = 5.22 \times t^{1/2} - 7.18, \tag{4}$$

The presence of a factor equaling  $t^{1/2}$  in the equation describing growth kinetics means that the coating increase is a process controlled by diffusion. Since those coatings are created as a result of zinc diffusion into the substrate, it may be concluded that the kinetics of that phenomenon are controlled by square root of time, which appears to be in compliance with literature data [22]. The equation also shows that the growth of the coating begins after the time that is necessary to reach the temperature allowing the diffusion of ingredients.

#### 4.3. Microstructure (SEM) and Microanalysis (EDS)

The microstructure of a coating obtained at a temperature of 440 °C and time of 120 min is presented in Figure 3. Percentage contents of analysed elements are shown in Table 1. The coating is composed of two layers: outer layer defined as site A and a layer adjoining the substrate marked as site B. In the outer layer (Figure 3b), the presence of 7.2 wt % Fe and 92.8 wt % Zn was found in outer zone (point 1, Table 1) and 11.4 wt % Fe and 88.6 wt % Zn in the zone bordering on the underlying layer (point 2, Table 1). Chemical composition of outer layer is comprised within intermetallic phase  $\delta_1$  ( $\text{FeZn}_{10}$ ) [23]. Change of concentration of components on the cross-section of that phase is typical of phase  $\delta_1$  and may be an evidence of its varied morphology: phases  $\delta_{1P}$  of palisade structure in the upper zone and phase  $\delta_{1k}$  of compact structure in the substrate zone [5]. Chemical composition of the underlying layer (Figure 3c) is more homogenous. In the outer layer, there is 19.7 wt % Fe and 80.3 wt % Zn (point 3, Table 1), whereas the substrate layer contains 21.2 wt % Fe and 78.8 wt % Zn (point 4, Table 1). Chemical composition in the underlying layer corresponds to stability range for phase  $\Gamma_1$  ( $\text{Fe}_{11}\text{Zn}_{40}$ ) [6].

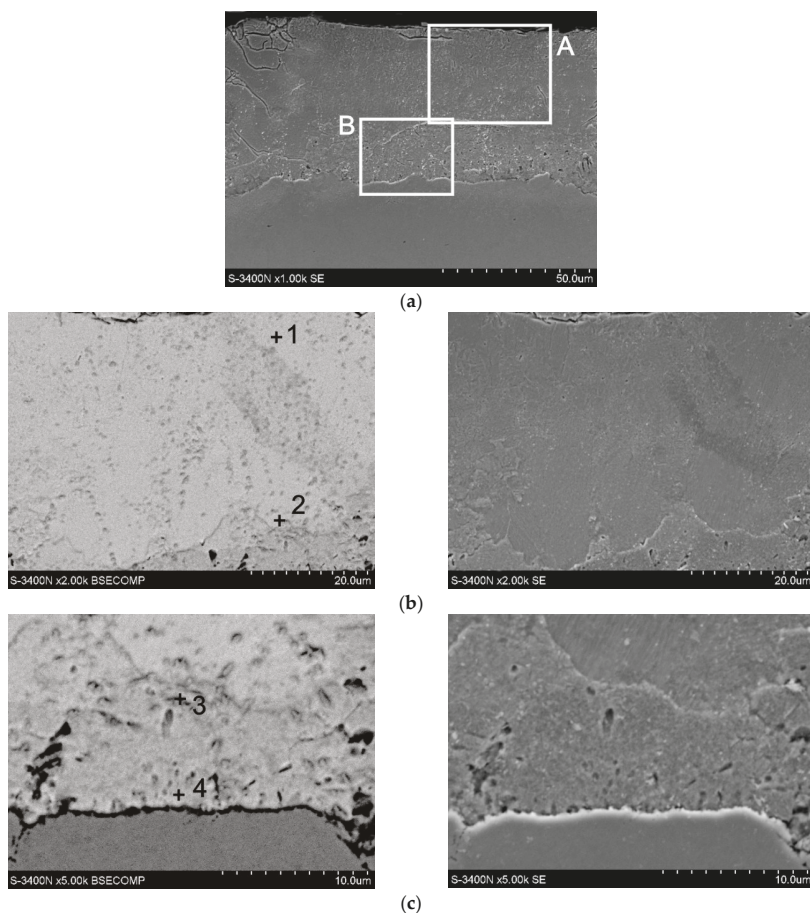


**Figure 3.** Microstructure (SEM) of coating obtained on high-strength grade 10.9 bolts via thermal diffusion method with reactive atmosphere recirculation: cross-section of the coating with selected areas (a), microstructure of the coating in area A (b), microstructure of the coating in area B (c).

**Table 1.** Chemical composition at selected micro-areas of coating obtained on high-strength grade 10.9 bolts (measurement points acc. to Figure 3).

Measurement Point	Content of Elements			
	Fe-K		Zn-K	
	wt %	at. %	wt %	at. %
point 1	7.2%	8.3%	92.8%	91.7%
point 2	11.4%	13.1%	88.6%	86.9%
point 3	19.7%	22.3%	80.3%	77.7%
point 4	21.2%	24.0%	78.8%	76.0%

4.4. X-ray Phase Analysis (XRD)

XRD analysis performed on the surface of a skew-ground coating (Figure 4) demonstrates phase  $\delta_1$  ( $FeZn_{10}$ ) and phase  $\Gamma_1$  ( $Fe_{11}Zn_{40}$ ). Considering chemical composition in the coating microsites (Table 1), it may be claimed that the outer layer of the coating is phase  $\delta_1$ , whereas the layer adjacent to the substrate is phase  $\Gamma_1$ . The research did not confirm any presence of other phase Fe-Zn, although these are stable in the conditions the coating is created. According to phase equilibrium system, phases  $\Gamma$  ( $Fe_3Zn_{10}$ ) and  $\zeta$  ( $FeZn_{13}$ ) are also stable [24]. Configuration of all stable phases ( $\Gamma$ ,  $\Gamma_1$ , and  $\delta_1$  i  $\zeta$ ) occurs in the diffusion layer of coatings obtained by HDG method at the temperature of 450 °C [6]. However, the mechanism of producing a hot dip galvanizing coating is more complex than that, and the transition layer is created as a result of simultaneous processes of diffusive growth, solutioning in liquid zinc, and recrystallization [24].

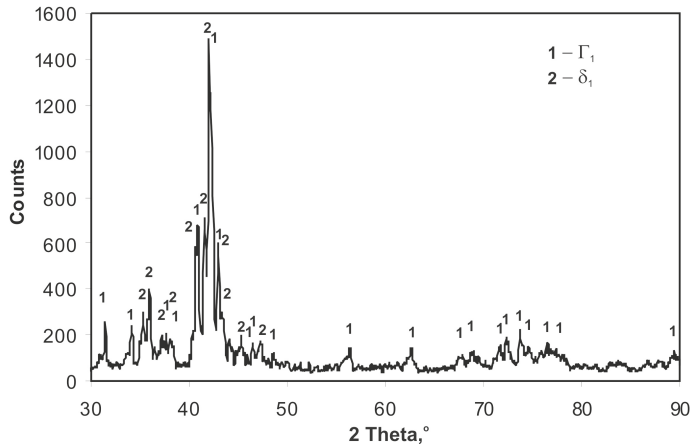


**Figure 4.** Diffractogram of the surface of skew-ground coating obtained on high-strength grade 10.9 bolts through thermal diffusion method with reactive atmosphere recirculation.

For technologies using powder mixtures as zinc carrier, the available literature does not allow an unambiguous determination of coating phase structure. In conventional sherardizing, a coating is created that is composed of a compact layer of phase  $\delta_1$  (marked as  $FeZn_7$ ) and a non-homogenous outer layer of phase  $\zeta$  ( $FeZn_{13}$ ) [14]. However, Konstantinov [25] claims that the coating is built of phases  $\Gamma$  and  $\delta_1$ . Liu [26] obtained a similar structure, making his coatings with a pack cementation method in a powder mix with an addition of activator on 1.7225 (42CrMo4) steel. On the other hand, Wortelen [27] claims that the coating obtained through sherardizing in powder mix with an activator is composed of phases  $\Gamma$ ,  $\Gamma_1$ ,  $\delta_1$ , and  $\zeta$ . It must be pointed out that characteristic spectra for phases  $\Gamma$  and  $\zeta$  coincide largely with the spectra of phases  $\Gamma_1$  and  $\delta_1$ ; therefore, XRD examination does not

allow for unambiguous exclusion of the presence of phases  $\Gamma$  and  $\zeta$ . However, no other structural components were determined in the microstructure of the tested coating, whose chemical composition might correspond to the range of homogeneity of phases  $\Gamma$  and  $\zeta$ . This was also confirmed in the research conducted by Chaliampalias [15,28], who obtained a coating composed of phases  $\Gamma_1$  and  $\delta_1$  in the pack cementation process.

#### 4.5. Corrosion Resistance

The surface appearance of grade 10.9 bolts with thermal diffusion after corrosion testing in neutral salt spray is presented in Figure 5. During exposure in a salt chamber, the thermal diffusion coating becomes covered with products of white rust. After 1000 h of exposure in the salt chamber, local rusty discolouring becomes visible on the surface (Figure 5a). White rust products accumulate in thread grooves and expose the thread tips, where the intensity of corrosion is clearly higher. Upon completion of corrosion test, no distinctive permeation of coating into substrate was visible, which was confirmed by structural research on a cross-section of coating (Figure 5b). After testing, a non-uniform depletion of coating thickness was manifested on the cross-section; however, the coating did not yet lose its continuity. The presence of rusty discolourations on the surface of zinc coatings is characteristic of corrosion of intermetallic phase Fe-Zn. Such a phenomenon is observed during exposure of HDG coatings to an environment that contains chlorides [8].

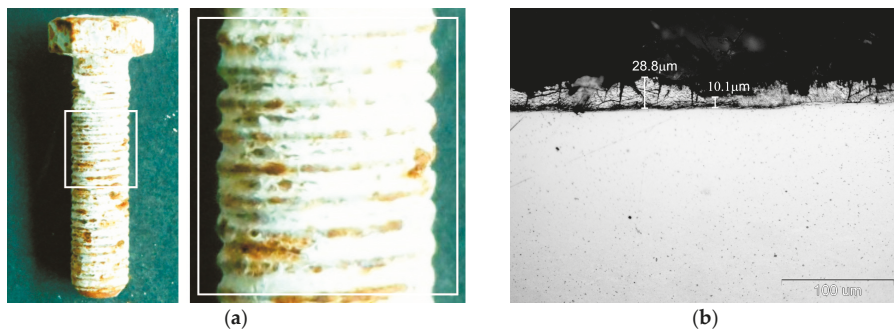


**Figure 5.** The appearance (a) and structure (b) of the thermal diffusion zinc coating after corrosion tests in a salt chamber.

Dependence of mass changes in tested coatings from the time of exposure in the salt chamber is presented in Figure 6a. It may be concluded that during exposure to neutral salt spray, the tested coatings are characterized by increment of mass, which is an evidence of accumulation of corrosion products on their surfaces. Changes of bolt mass, and at the same time corrosive wear of thermal diffusion coating, follow a linear relationship. The trend function, determined in the course of experimental research, and the high correlation factor  $R^2 = 0.97$  (Figure 6a) constitute proper linear match with data and confirm the linear character of the wear of thermal diffusion coating.

The linear character of coating wear is also evidenced by coating loss in its cross-section. Average coating thickness changes after 480, 720, and 1000 h of exposure in a salt chamber are presented in Figure 6b. Assuming average initial thickness of  $51.52 \pm 8.48 \mu\text{m}$ , they decreased to  $18.03 \pm 5.53 \mu\text{m}$  after a 1000 h corrosion test. The trend function, determined through measurements of average thickness of coating and good match of correlation factor  $R^2 = 0.96$ , confirm the linear character of corrosive wear of coating in its cross-section. Extrapolation of trend line allows an estimation that the total loss of thermal diffusion coating on a bolt's surface and at the same loss of protective properties will happen after approx. 1540 h of exposure in the salt chamber. In comparison to conventional hot dip galvanizing zinc coatings, the durability of the thermal diffusion coating tested in a corrosion test in a salt chamber [22] results in an approx. 2–3-fold increase in the durability time to penetration

of the substrate surface (steel). While carrying out the corrosion test in a salt-spray chamber (acc. EN ISO 9227) traditional hot dip galvanizing coating of comparable thickness (average thickness  $50.8 \pm 6.42 \mu\text{m}$ ), distinctive permeation of coating into substrate was visible after 480 h of exposure in neutral salt-spray environment [21]. For conventional hot dip zinc coating, much more severe corrosion losses can be observed in the initial stage of corrosion process when the outer layer of zinc is subject to corrosion. When this layer is worn out, the corrosion process proceeds more slowly in the Fe-Zn intermetallic layers [8]. Thermal diffusion zinc coating does not show increased corrosion intensity in the initial stage of corrosion process due to the lack of an outer zinc layer. The corrosion process proceeds only in the Fe-Zn intermetallic layers, whose thickness is higher in comparison with conventional hot dip coatings. The average thickness loss of the coating was used to estimate coating durability. Locally, in areas of lower thickness, the coating may be broken through to the base material. Due to the very good protection properties of the coating and the significant share of areas with a higher coating thickness, the protection of the steel in the initial stages of coating penetration will still be preserved.

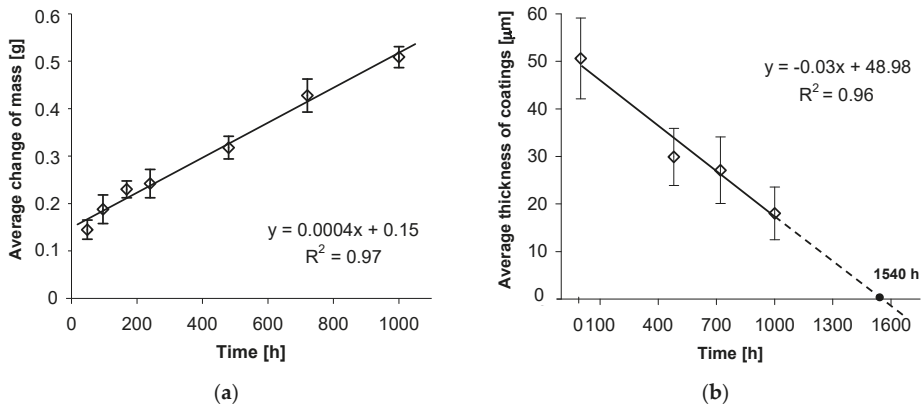


**Figure 6.** Average change of mass in tested bolts grade 10.9 (a) and average change of thermal diffusion coating thickness (b) during exposure in salt spray chamber.

#### 4.6. Tensile Test

A diagram of a static tension test on threaded bar grade 10.9 without coating and with thermal diffusion coating is presented in Figure 7. The values of tensile strength limit  $R_m$  and conventional yield limit  $R_{p0.2}$  for three tests on each bar are presented in Table 2. The tensile strength of grade 10.9 threaded bar decreased slightly after creation of thermal diffusion coating. The average tensile strength limit was  $R_m = 1024 \text{ MPa}$  for the uncoated bar and  $R_m = 1007 \text{ MPa}$  for the thermal diffusion coated one, respectively. The process of creating a coating by the new method of thermal diffusion zinc coating did not compromise the tensile strength below the required limit. However, the ratio of conventional yield limit to tensile strength had a similar value of 0.94–0.95 both for the uncoated bar and the thermal diffusion coated one. Tensile strength of the threaded bar coated with the new method of thermal diffusion zinc coating with recirculation of reactive atmosphere fulfilled the tensile strength requirement for grade 10.9.

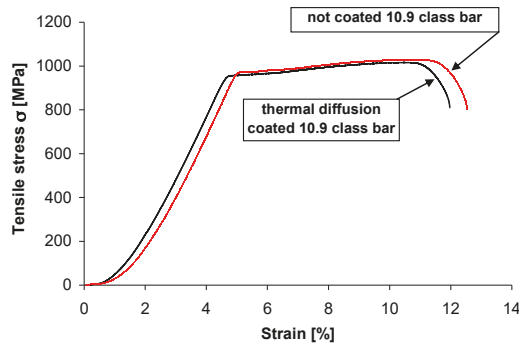


Figure 7. Tensile stress-displacement relationship curve of coated and uncoated 10.9 grade threaded bar.

Table 2. Results of tensile strength test of coated and uncoated 10.9 grade threaded bar.

Type of Threaded Bar	Sample Number	$R_m$ [MPa]	$R_{p0,2}$ [MPa]	$R_{p0,2}/R_m$ [MPa]
not coated 10.9 grade bar	test 1	1031.73	980.87	0.95
	test 2	1016.93	955.24	0.94
	test 3	1023.36	968.32	0.95
thermal diffusion coated 10.9 grade bar	test 1	1004.01	946.00	0.94
	test 2	1001.11	936.56	0.94
	test 3	1018.41	962.87	0.95

In these tests, threaded bars M10 in strength grade 10.9 made of 42CrMo4 steel (1.7225) after quenching and tempering process were used. The total length of the sample was 220 mm, gauge length 160 mm. Special high nuts were screwed on the ends of the bar, and then the sample was placed in the holders of the testing machine and stretched until it was broken.

## 5. Conclusions

The innovative technology of thermal diffusion zinc coating with recirculation of reactive atmosphere provides effective anti-corrosion protection for high-strength grade 10.9 bolts while retaining their strength properties. The application of reactive atmosphere recirculation ensured homogenization of its composition and a better contact of product surface with powder mix, which permitted one to obtain continuous coatings of a compact structure in a shorter time compared to the conventional sherardizing method.

The research conducted allows for the following conclusions to be made:

1. The new method of thermal diffusion zinc coating with recirculation of reactive atmosphere permits one to obtain coatings 50–72  $\mu\text{m}$  thick in soaking time of 120–240 min at a temperature of 440  $^{\circ}\text{C}$  upon grade 10.9 bolts;
2. The coatings obtained on grade 10.9 bolts feature a two-layer structure. Directly on the substrate, a compact layer of intermetallic phase  $\Gamma_1$  ( $\text{Fe}_{11}\text{Zn}_{40}$ ) is created, which is covered with a layer of intermetallic phase  $\delta_1$  ( $\text{FeZn}_{10}$ );
3. The coatings obtained in this way feature very good corrosion resistance. It is estimated that corrosion strength of 50  $\mu\text{m}$  thermal diffusion coatings on grade 10.9 bolts in neutral salt spray amounts to approx. 1500 h;
4. Thermal diffusion zinc coating parameters permit retaining the strength properties for bolts defined by strength grade 10.9.

**Author Contributions:** Conceptualization, H.K., J.S., Experimental research, J.S., Methodology, H.K., Research of structure and corrosion resistance, H.K., Tensile test, J.S., Data curation, H.K., Visualization, H.K. Analysis of results H.K., Project administration, J.S.; Funding acquisition, J.S.

**Funding:** The research on thermal diffusion zinc coating was conducted within the R&D project “Innovative Technology of Thermal Diffusion Zinc Coating of Key Structural Elements with Application of Reactive Atmosphere Recirculation” (project no. POIG.01.04.00-08-383/13) co-financed by European Union within Operating Programme Innovative Economy from the means of European Regional Development Fund.

**Conflicts of Interest:** The authors declare no conflict of interest. The funders had no role in the design of the study; in the collection, analyses, or interpretation of data; in the writing of the manuscript; or in the decision to publish the results.

## References

1. Lokaj, A.; Klajmonova, K. Comparison of behaviour of laterally loaded round and squared timber bolted joints. *Frattura Integr. Strutt.* **2017**, *11*, 56–61. [CrossRef]
2. Votava, J. Anticorrosion protection of strength bolts. *Acta Univ. Agric. Silv. Mendel. Brun.* **2012**, *1*, 181–188. [CrossRef]
3. Bickford, J.H. *Introduction to the Design and Behavior of Bolted Joints*; CRC Press Taylor & Francis Group LLC: Boca Raton, FL, USA, 2008.
4. Hot Dip Galvanized Fasteners. Advantages of and Design Considerations for Hot-Dip Galvanized Fasteners. Copyright © by American Galvanizers Association. 2009. Available online: [https://galvanizeit.org/uploads/publications/Galvanized\\_Steel\\_Fasteners.pdf](https://galvanizeit.org/uploads/publications/Galvanized_Steel_Fasteners.pdf) (accessed on 23 January 2019).
5. Kania, H.; Liberski, P. Synergistic influence of Al, Ni, Bi and Sn addition to a zinc bath upon growth kinetics and the structure of coatings. *IOP Conf. Ser. Mater. Sci. Eng.* **2012**, *35*, 012004. [CrossRef]
6. Wolczyński, W.; Guzik, E.; Janczak-Rusch, J.; Kopyciński, D.; Golczewski, J.; Hyuck, M.L.; Kloch, J. Morphological characteristics of multi-layer/substrate systems. *Mater. Charact.* **2006**, *56*, 274–280. [CrossRef]
7. Townsend, H.E.; Gorman, C.D.; Fischer, R.J. Atmospheric corrosion performance of hot-dip galvanized bolts for fastening weathering steel guiderail. *Mater. Perform.* **1999**, *38*, 66–70.
8. Liberski, P.; Podolski, P.; Kania, H.; Gierek, A.; Mendala, J. Corrosion resistance of zinc coatings obtained in high-temperature baths. *Mater. Sci.* **2003**, *39*, 652–657. [CrossRef]
9. *High Temperature Galvanizing*, 1st ed.; International Lead Zinc Research Organization, Inc.: New York, NY, USA, 1980; pp. 35–36.
10. Kwiatkowski, L. Cynk i ochrona przed korozją. *Ochr. Koroz.* **2004**, *10*, 256–257.
11. Porter, F. *Zinc Handbook: Properties Processing and Use in Design*; Marcel Dekker: New York, NY, USA, 1991.
12. Chatterjee, B. Sherardizing. *Met. Finish.* **2004**, *102*, 40–46. [CrossRef]
13. Smith, C.A. Sherardizing: Part 2. In *Anti-Corros. Method*; M. MCB UP Ltd.: Bingley, UK, 1980; Volume 27, pp. 6–7. [CrossRef]
14. Jiang, J.H.; Ma, A.B.; Fan, X.D.; Gong, M.Z.; Zhang, L.Y. Sherardizing and Characteristic of Zinc Protective Coating on High-Strength Steel Bridge Cable Wires. *Adv. Mat. Res.* **2010**, *97*, 1368–1372.
15. Chaliampalias, D.; Pistofidis, N.; Vourlias, G. Effect of temperature and zinc concentration on zinc coatings deposited with pack cementation. *Surf. Eng.* **2008**, *24*, 259–263. [CrossRef]
16. Pistofidis, N.; Vourlias, G.; Chaliampalias, D.; Chrysafis, K.; Stergioudis, G.; Polychroniadis, E.K. On the mechanism of formation of zinc pack coatings. *J. Alloys Compd.* **2006**, *407*, 221–225. [CrossRef]
17. Shen, T.-H.; Tsai, C.-Y.; Lin, C.-S. Growth behavior and properties of Zn–Al pack cementation coatings on carbon steels. *Surf. Coat. Tech.* **2016**, *306*, 455–461. [CrossRef]
18. Yu, S.; Liu, L. Zn-Fe and Zn-Fe-Y Cementation Coatings for Enhancing Corrosion Resistance of Steel. *Int. J. Electrochem. Sci.* **2017**, *12*, 4782–4794.
19. Kania, H.; Sipa, J. Thermal diffusion zinc coating technology with reactive atmosphere recirculation. Part 1: General description of technology and structure of coatings. *Ochr. Koroz.* **2018**, *11*, 338–345.
20. Kania, H.; Sipa, J. Zinc coating deposition with new thermal diffusion process on low carbon steel substrates. *Hutn. Wiad. Hutn.* **2019**, *1*, 2–8.
21. Kania, H.; Sipa, J.; Skupińska, A. Thermal diffusion zinc coating technology with reactive atmosphere recirculation. Part 2: Corrosion resistance of coatings. *Ochr. Koroz.* **2018**, *12*, 375–382.
22. Marder, A.R. The metallurgy of zinc-coated steel. *Prog. Mater. Sci.* **2000**, *45*, 191–271. [CrossRef]



23. Kubaschewski, O. *Iron Binary Phase Diagrams*; Springer-Verlag: Berlin, Germany, 1982.
24. Tatarek, A.; Saternus, M. Badanie zjawisk rozpuszczania dyfuzyjnego stali reaktywnych w kąpeli cynkowej z dodatkiem bizmutu. *Ochr. Koroz.* **2018**, *7*, 186–190.
25. Konstantinov, V.M.; Bulochyik, I.A. Some aspects of sherardizing implementation during anticorrosion protection of heat-treated metal parts. *IOP Conf. Ser. Mater. Sci. Eng.* **2015**, *71*, 012063. [[CrossRef](#)]
26. Liu, L.; Yu, S. A comparative study on Zn and Zn-Y coatings on 42CrMo steel by pack cementation process. *Int. J. Electrochem. Sci.* **2017**, *12*, 9575–9587. [[CrossRef](#)]
27. Wortelen, D.; Frieling, R.; Bracht, H.; Graf, W.; Natrup, F. Impact of zinc halide addition on the growth of zinc-rich layers generated by sherardizing. *Surf. Coat. Tech.* **2015**, *263*, 66–77. [[CrossRef](#)]
28. Chaliampalias, D.; Papazoglou, M.; Tsipas, S.; Pavlidou, E.; Skolianos, S.; Stergioudis, G.; Vourlias, G. The effect of Al and Cr additions on pack cementation zinc coatings. *Appl. Surf. Sci.* **2010**, *256*, 3618–3623. [[CrossRef](#)]



© 2019 by the authors. Licensee MDPI, Basel, Switzerland. This article is an open access article distributed under the terms and conditions of the Creative Commons Attribution (CC BY) license (<http://creativecommons.org/licenses/by/4.0/>).

Article

# High-Temperature Oxidation of Heavy Boron-Doped Diamond Electrodes: Microstructural and Electrochemical Performance Modification

Jacek Ryl <sup>1,\*</sup>, Mateusz Cieslik <sup>1</sup>, Artur Zielinski <sup>1</sup>, Mateusz Ficek <sup>2</sup>, Bartłomiej Dec <sup>2</sup>, Kazimierz Darowicki <sup>1</sup> and Robert Bogdanowicz <sup>2</sup>

<sup>1</sup> Department of Electrochemistry, Corrosion and Materials Engineering, Faculty of Chemistry, Gdansk University of Technology, Narutowicza 11/12, 80-233 Gdansk, Poland; matciesl2@student.pg.edu.pl (M.C.); artzieli@pg.edu.pl (A.Z.); kazdarow@pg.edu.pl (K.D.)

<sup>2</sup> Department of Metrology and Optoelectronics, Faculty of Electronics, Telecommunication and Informatics, Gdansk University of Technology, Narutowicza 11/12, 80-233 Gdansk, Poland; matficek@pg.edu.pl (M.F.); bartlomiej.dec@pg.edu.pl (B.D.); robbogda@pg.edu.pl (R.B.)

\* Correspondence: jacek.ryl@pg.edu.pl; Tel.: +48-58-347-1092

Received: 28 January 2020; Accepted: 19 February 2020; Published: 21 February 2020

**Abstract:** In this work, we reveal in detail the effects of high-temperature treatment in air at 600 °C on the microstructure as well as the physico-chemical and electrochemical properties of boron-doped diamond (BDD) electrodes. The thermal treatment of freshly grown BDD electrodes was applied, resulting in permanent structural modifications of surface depending on the exposure time. High temperature affects material corrosion, inducing crystal defects. The oxidized BDD surfaces were studied by means of cyclic voltammetry (CV) and scanning electrochemical microscopy (SECM), revealing a significant decrease in the electrode activity and local heterogeneity of areas owing to various standard rate constants. This effect was correlated with a resultant increase of surface resistance heterogeneity by scanning spreading resistance microscopy (SSRM). The X-ray photoelectron spectroscopy (XPS) confirmed the rate and heterogeneity of the oxidation process, revealing hydroxyl species to be dominant on the electrode surface. Morphological tests using scanning electron microscopy (SEM) and atomic force microscopy (AFM) revealed that prolonged durations of high-temperature treatment lead not only to surface oxidation but also to irreversible structural defects in the form of etch pits. Our results show that even subsequent electrode rehydrogenation in plasma is not sufficient to reverse this surface oxidation in terms of electrochemical and physico-chemical properties, and the nature of high-temperature corrosion of BDD electrodes should be considered irreversible.

**Keywords:** boron-doped diamond; high-temperature treatment; surface oxidation; microstructure defects; electrochemical activity

## 1. Introduction

Boron-doped diamond (BDD) surfaces are widely studied due to their unique electrochemical and physico-chemical properties [1]. While the most often reported applications are for sensing [2], energy storage [3], or water treatment [4], BDD does play an important role in high-temperature environments [5]. The electrically conductive nanocrystalline boron-doped diamond (BDD) layers can be applied as a protective coating of Si photoelectrodes in sun-driven photoelectrochemical cells in aqueous electrolyte solutions [6]. Furthermore, wastewater treatment with advanced oxidation processes at BDD usually strongly depends on the potentials and current densities. It has been shown that a larger current promotes stability for urea removal at high potentials [7], which could also induce

the thermal issues and electrode surface defects [8]. Moreover, the relatively high thermal conductivity coefficient ( $\sim 700$  W/mK) of BDD allows for its use as a heat spreader, replacing the commonly used metal spreaders such as copper, copper/refractory, or copper laminate in high power RF/microwave devices resulting in higher isolation of the ground plane at below 1.5 GHz [9,10].

BDD thin films are found to be particularly attractive as electrodes for electrolysis and electroanalytical applications due to their outstanding properties, which are significantly different from those of other conventional electrodes (e.g., glassy carbon or platinum electrodes [11]). In addition to the innate properties of diamond, such as high thermal conductivity, high hardness, and chemical inertness, the attractive features of conductive BDD include a wide electrochemical potential window in aqueous and non-aqueous media, very low capacitance, and extreme electrochemical stability [12]. BDDs are said to possess higher oxidation resistance at elevated temperatures in comparison to pure diamond [13], which is due to the formation of a  $B_2O_3$  surface layer. Wang and Swain [14] reported a Pt/diamond composite electrode that exhibited superb morphological and microstructural stability during vigorous electrolysis in acidic media at a temperature of around 170 °C and current density around 0.1 A/cm<sup>2</sup>. In addition, BDD layers can operate at high temperatures in electronics, an example being diamond-based Schottky barrier diodes for high-power devices [15,16].

High-temperature treatment is also one of the reported routes to modify and oxidize the surface termination of BDD electrodes [17–19]. Other approaches include oxidation under electrochemical polarization [20,21], chemical agents [22,23], ozone [24], plasma and/or UV treatment [25,26], but also natural aging in air [27–29]. The surface termination type significantly differentiates the electric and physico-chemical properties of boron-doped diamond electrodes. Hydrogen termination (HT-BDD) leads to hydrophobic and non-polar behavior, as well as high surface electrical conductivity and low electric transfer resistance [22,25]. The presence of hydroxyl or carbonyl surface bonds and oxidized BDD termination (OT-BDD) results in hydrophilicity and much lower surface electrical conductivity [30,31]. On the other hand, the electrochemical potential window for OT-BDD electrodes is reported to be wider than in the case of hydrogen-terminated ones [31,32]. Importantly, Zielinski et al. [29] reported that oxidation homogeneity of polycrystalline electrodes as well as oxidation rate in general highly depend on the above-mentioned modification route and confirmed that various treatment procedures produce different surface terminating species (C–OH, C–O–C, C=O, C–OOH, etc.), which may have a significant influence on tailoring desired functionalization procedures and BDD electrode characteristics.

Among the multitude of reported oxidation routes, high-temperature oxidation is characterized by a few unique features [29]. First of all, it appears to be the most heterogeneous at low durations, which was claimed to be related to the diverged propensity of differently oriented BDD crystal planes towards surface oxidation. Furthermore, according to studies where X-ray photoelectron spectroscopy (XPS) was performed, high-temperature oxidation tends to produce a significantly larger amount of surface hydroxyl species than any other reported approach. Their high polarity in comparison to other surface species results in very small reported contact angles during drop shape analysis tests. Next to electrochemical anodization, high-temperature treatment is one of the most often used pretreatment methods to clean the impurities on as-prepared BDD electrodes after the chemical vapor deposition (CVD) process [19,33].

High-temperature oxidation may also lead to changes in surface morphology as well as the altered  $sp^2/sp^3$ -carbon ratio [34,35]. The surface structure of BDD electrodes exposed to elevated temperatures in an oxygen-containing atmosphere was presented by Jiang et al. [17], who noticed that during such a treatment the amorphous carbon phase converts to the diamond phase and that the diamond grain increases with the decrease of grain boundaries. In addition, the short high-temperature treatments (30 min) led to the arrangement of grain boundaries on the electrode surface, which had a positive effect on their conductivity. An interesting consequence of the high-temperature oxidation is the enhancement of the peak ratio between the diamond peak and the graphitic peak, showing a decreasing amount of  $sp^2$ -carbon after the process, resulting in an increased carrier concentration [36,37]. However, prolonged high-temperature oxidation led to disordered grain boundaries and significantly

deteriorated conductivity of the BDD electrode. High-temperature treatment may also lead to a diffusion of silicon substrate through the columnar structure of the diamond film and corrosion [33].

In light of the above presented discussion, the aim of this work was to present the effect of high-temperature treatment in air at 600 °C on the utility properties of boron-doped diamond electrodes, in particular for electrochemical applications. To the best of our knowledge, there are no dedicated studies on BDD electroactivity and stability of the properties when subjected to prolonged high-temperature exposure, the homogeneity and the rate of high-temperature corrosion of BDD, and its reversibility.

## 2. Materials and Methods

BDD films were synthesized in a microwave plasma-assisted chemical vapor deposition system (SEKI Technotron AX5400S, Tokyo, Japan). The substrates were seeded by sonication in nanodiamond suspension for 30 min following the standard procedure [38]. The chamber stage was maintained at 700 °C during the deposition process and the growth time was 6 h. The boron level expressed as [B]/[C] ratio in the gas phase was 10,000 ppm (boron dopant concentrations  $2 \times 10^{21}$  atoms  $\text{cm}^{-3}$ ) [39]. A more detailed description of the thin film synthesis can be found elsewhere [40,41]. Then, the electrode surface was cleaned and hydrogenated. First, metallic impurities were dissolved in hot aqua regia ( $\text{HNO}_3:\text{HCl}/1:3$ ), followed by the removal of organic impurities by hot “piranha” solution ( $\text{H}_2\text{O}_2:\text{H}_2\text{SO}_4/1:3$ ) at 90 °C. Microwave hydrogen plasma treatment was performed using 1000 W microwave power and 300 sccm of hydrogen gas flow for 10 min.

The high-temperature treatment was carried out in an MRT-20 furnace (Czylok, Jastrzebie-Zdroj, Poland). The BDD electrodes were treated at 600 °C for 3, 10, 30, or 90 min in air. Afterward, the samples were removed from the furnace and cooled in air. A similar procedure was carried out in other studies [29,30,33]. After the electrochemical and physico-chemical examination, the hydrogenation procedure described earlier was carried out for high-temperature-treated BDD samples in order to determine surface oxidation reversibility.

Electrochemical measurements were carried out in a three-electrode cell. The working electrode was Si/BDD, with Ag/AgCl used as a reference electrode and platinum mesh as a counter electrode. All reagents were analytical purity (Sigma-Aldrich, Saint Louis, MO, USA). The exposed BDD sample area was 0.25  $\text{cm}^2$ . Cyclic voltammetry (CV) studies were carried out in the polarization range between  $-0.9$  V and 1.1 V vs. Ag/AgCl, at different scan rates between 5 and 800 mV/s. The electrolyte used was 0.5M  $\text{Na}_2\text{SO}_4$  with 2.5 mM  $\text{K}_3[\text{Fe}(\text{CN})_6]$  and 2.5 mM  $\text{K}_4[\text{Fe}(\text{CN})_6]$ . Scanning electrochemical microscopy (SECM) studies were performed using a three-step motor system (Sensolytics, Bochum, Germany) with 1  $\mu\text{m}$  resolution in each direction, coupled to an Autolab 302 N potentiostat equipped with bipotentiostat module (Metrohm, Herisau, Switzerland). The commercially available ultramicroelectrodes (UMEs) made of platinum wire sealed in glass were used, with a platinum disc diameter of 5  $\mu\text{m}$ . Each probe was polished and rinsed with acetone prior to the study. The electrolytic solution was composed of 2.5 mM  $\text{K}_4[\text{Fe}(\text{CN})_6]$  and 0.5M  $\text{Na}_2\text{SO}_4$ , purged with argon prior to BDD sample examination. The potential applied to the UMEs and the BDD sample was +0.4 and 0.0 vs. Ag/AgCl, respectively. In such a setup, the oxidation of redox species occurs at the UME tip. The SECM maps were recorded with a scanning speed of 5  $\mu\text{m}/\text{s}$  and 1  $\mu\text{m}$  steps in the x-y plane. A similar experimental approach was previously applied by authors [40].

Topographic and electrical microscopic measurements were made using an NTegra Prima device by NT-MDT (Moscow, Russia) in contact mode. CTD-NCHR-10 probes from Nanosensors (Neuchatel, Switzerland) were used with the following catalog parameters:  $L \times W \times T$  lever dimensions:  $125 \times 29 \times 4$   $\mu\text{m}$ . Lever spring constant was equal to 71 N/m. The contact force determined from the approach curve was 8  $\mu\text{N}$ . The tip radius of the curvature was in the 100–200 nm range according to manufacturer data. Conductivity measurements were made in the scanning spreading resistance mode using a constant voltage of 20 mV. Scanning electron microscopy (SEM) micrographs were taken with an S-3400

N microscope (Hitachi, Tokyo, Japan), with 20 kV accelerating voltage and operating in secondary electron mode.

High-resolution X-ray photoelectron spectroscopy (XPS) analyses were carried out in C1s binding energy range using an Escalab 250Xi multispectroscop (ThermoFisher Scientific, Waltham, MA, USA). The spectroscop was equipped with a monochromatic Al K $\alpha$  energy source. The applied X-ray spot diameter was 650  $\mu$ m and the pass energy through the hemisphere analyzer was 10 eV. Prior to operation, the spectroscop was calibrated on Cu and Au single crystals. Charge compensation was controlled through low-energy electron and Ar<sup>+</sup> ion flow by means of a flood gun. Spectral deconvolution was performed with Avantage software (v5.973, ThermoFisher Scientific, Waltham, MA, USA) provided by the spectroscop manufacturer.

### 3. Results and Discussion

The heavy boron-doped diamond electrodes were subjected to electrochemical and physico-chemical examination in order to evaluate the effect of oxidation under high temperature on the charge transfer kinetics. Afterward, the oxidation and corrosion reversibility was evaluated and determined.

#### 3.1. Electron Transfer through High-Temperature-Treated BDD Interface

Figure 1 shows the results of the cyclic voltammetry studies, which were carried out on BDD electrodes before and after high-temperature oxidation in air at 600 °C. The redox couple used within this study, [Fe(CN<sub>6</sub>)]<sup>3-/4-</sup>, is characterized by an inner-sphere electron transfer (ISET) mechanism, which is said to be more dependent on the electrode homogeneity and applied modification procedures, thus offering a more sensitive approach to track subtle changes of charge transfer kinetics [42]. Figure 1a reveals [Fe(CN<sub>6</sub>)]<sup>3-/4-</sup> oxidation/reduction kinetics for each sample, observed at a 50 mV/s scan rate. High-temperature oxidation leads to hindered charge transfer kinetics, demonstrated by the decrease in peak current *i*<sub>A</sub> and *i*<sub>C</sub> when comparing to the as-prepared BDDs, a feature observed even at the shortest treatment duration. The peak current decreased nearly by a factor of 2 after merely 3 min of sample exposure to high temperature, and by a factor of 4 after 10 min. Detailed analysis is presented in Table 1.

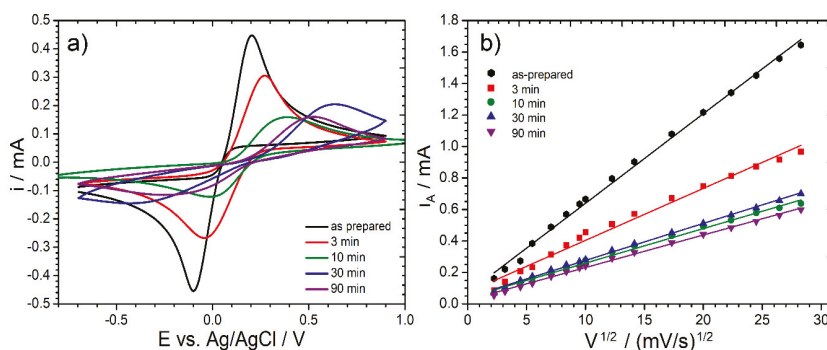


**Figure 1.** Cyclic voltammetry (CV) studies for boron-doped diamond (BDD) electrodes after high-temperature oxidation at 600 °C. (a) CV scans recorded at 50 mV/s for different oxidation durations; (b) CV anodic peak current vs. scan rate square root function for each studied electrode. Electrolytic solution: 0.5 M Na<sub>2</sub>SO<sub>4</sub> with 2.5 mM K<sub>3</sub>[Fe(CN)<sub>6</sub>] and 2.5 mM K<sub>4</sub>[Fe(CN)<sub>6</sub>].

**Table 1.** Electrochemical properties (anodic peak current  $i_A$ , anodic-to-cathodic peak current ratio  $i_A/i_C$ , peak separation  $\Delta E$ ) based on CV studies (at 50 mV/s scan rate) of BDD samples after various high-temperature treatment durations.

Parameter	Untreated	High-Temperature Treatment			
		3 min	10 min	30 min	90 min
$i_A$ /mA	0.44	0.29	0.16	0.20	0.16
$i_A/i_C$ /-	0.97	1.14	1.33	1.45	1.43
$\Delta E$ /V	0.35	0.31	0.39	1.04	0.72
$k_0$ /cm/s	$3.58 \times 10^{-3}$	$1.96 \times 10^{-3}$	$1.94 \times 10^{-3}$	$1.78 \times 10^{-3}$	$1.91 \times 10^{-3}$

It should also be noted that the modification of BDD surface termination type translates into a significant peak separation  $\Delta E$  increase, the parameter which is inseparably connected with reversibility of the corrosion process. In the case of a single electron transfer reaction, the fully reversible processes should have  $\Delta E$  equal to 59 mV [43]. The as-prepared BDD sample is characterized by  $\Delta E$  value of approximately 350 mV. The value is quite high taking into consideration other reported heavy boron-doped electrodes, which is due to the lack of any other electrode pretreatment procedures [41,44]. Nevertheless, the  $\Delta E$  increase resulting from the applied high-temperature treatment should be explained by the move further away from the diffusion-controlled mechanism, due to the slowing down of the charge transfer kinetics. Prolonged high-temperature treatment is also characterized by the increased anodic and cathodic peak asymmetry, indicating a change in process kinetics, a feature typical for irreversible processes.

The discussed irreversibility of the studied redox process, as well as the decrease in electrode kinetics, are a testimony for surface modification from HT- to OT-BDD as a result of high-temperature treatment. The above-mentioned behavior results in BDD electrode corrosion, causing variability in electrode behavior and worsening its efficiency in electroanalytical studies.

The CV anodic peak vs. the scan rate square root function in the wide scan rate range is illustrated in Figure 1b. These plots show a strong linear trend, with local deviations explained by the heterogeneous nature of the polycrystalline electrodes [45]. To determine the standard reaction rate constant  $k^0$ , a numerically determined current function is used, depending on peak separation. The standard rate constant was calculated with the approach proposed by Velasco [46] to estimate completely irreversible processes. The following equation was used:

$$k^0 = 2.415 \exp\left(-0.02 \frac{F}{RT}\right) D^{\frac{1}{2}} (E_p - E_{p/2})^{-\frac{1}{2}} v^{\frac{1}{2}} \quad (1)$$

where  $E_p$  and  $E_{p/2}$  are the potentials of the CV peak and half-peak, respectively, and  $v$  refers to the rate of change of potential; the diffusion coefficient was assumed as  $D = 6.67 \times 10^{-6} \text{ cm}^2/\text{s}$  [47].

Figure 2 reveals the effect of high-temperature treatment on the local distribution of charge transfer kinetics during  $[\text{Fe}(\text{CN})_6]^{4-}$  oxidation, assessed with scanning electrochemical microscopy (SECM). The relative current values strongly depend on the distance between the SECM tip and the electrode and vary from sample to sample. The current value is less important than its local changes due to electrode charge transfer heterogeneity. A normalization procedure was applied for the Z-axis of these graphs in order to show local discrepancies in the oxidation currents. The procedure based on a negative shift of the tip current displayed on each map to the position where the lowest recorded value equaled zero. A similar procedure was successfully applied in previous studies on heterogeneous charge transfer through the BDD electrode [40].

The obtained SECM micrographs clearly illustrate that the surface distribution of the oxidation currents is significantly increasing already after a short 10 min high-temperature treatment (Figure 2b) as compared to the as-prepared BDD electrode (Figure 2a). The heterogeneous electron transfer results from an altered propensity towards surface oxidation by BDD grain of various crystallographic

orientations. A similar observation was previously reported for various methods of BDD surface treatment, in particular through electrochemical anodic polarization [40]. Importantly, increasing the high-temperature treatment length does not significantly increase surface homogeneity. Large tip current discrepancies are still observed after 90 min of oxidation (Figure 2c). At the same time, the as-prepared BDD electrode reveals positive feedback on the approach curve, suggesting low charge transfer resistance at the electrode interface [48]. The longer the high-temperature treatment, the higher was the negative feedback observed, whereas the sample oxidized for 10 min was characterized with large discrepancies of the approach curve shapes, depending on tip landing location. These results corroborate the decrease of the electron transfer kinetics with high-temperature treatment duration and the heterogeneous nature of the oxidation process.

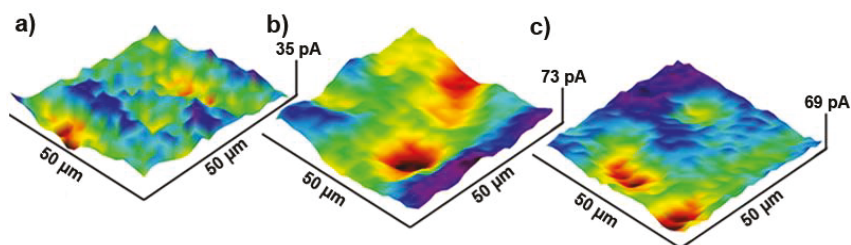


**Figure 2.** Typical scanning electrochemical microscopy (SECM) maps revealing charge transfer heterogeneity at heavy-doped BDD electrode interface after (a) 10 min, (b) 30 min, and (c) 90 min of high-temperature oxidation at 600 °C in air. Electrolyte: 0.5 M Na<sub>2</sub>SO<sub>4</sub> + 2.5 mM K<sub>4</sub>[Fe(CN)<sub>6</sub>].

### 3.2. High-Temperature Oxidation Influence on BDD Physico-Chemical Properties

The effect of high-temperature oxidation and corrosion on the microstructure of boron-doped diamond electrodes is shown on the SEM micrographs in Figure 3. The first 10 min of exposure to 600 °C do not lead to significant changes in grain structure; however, after this period the material undergoes gradual degradation.

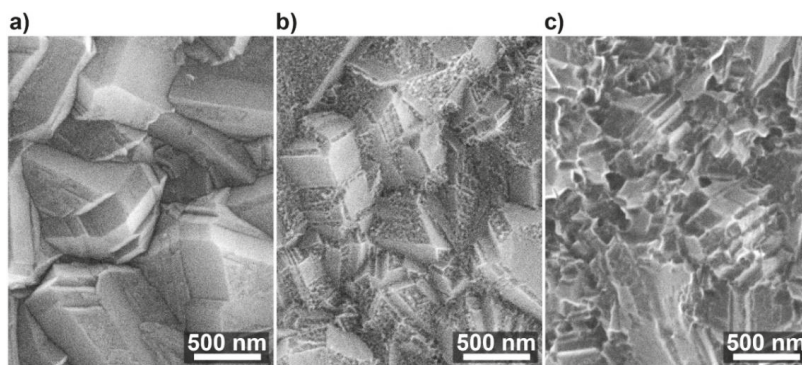


**Figure 3.** Typical scanning electron microscopy (SEM) micrographs of heavy-doped BDD surface after (a) 10 min, (b) 30 min, and (c) 90 min of high-temperature oxidation at 600 °C in air.

After 30 min of high-temperature oxidation, small and shallow etch pits start to appear throughout the diamond surface (Figure 3b), yet the grain structure is still recognizable. It is said that diamond can react with O<sub>2</sub> and water vapor contained within the atmosphere, to create surface etch pits [37]. Treatment in the oxygen-containing environment leads to high BDD surface etching and corrosion in the relatively short periods and a large surface area with respect to the geometric electrode area [49].

Furthermore, it is evident that certain crystallographic planes on the diamond surface are more prone to surface etching. Ohashi et al. [50] reported steam-activated high-temperature treatment in 600–900 °C to be an efficient nanotexturing tool for diamond surfaces. Notably, it was observed that, in the case of heavy-doped BDD films, the (111) facets are more prone to etching [19]. This observation lies in compliance with the fact that (111) facets have the dominant presence in the texture of studied BDD electrodes [51,52]. Other studies revealed that the propensity towards the modification of BDD surface termination is also dependent on crystallographic orientation [40,51].

Extended exposure at elevated temperature leads to advanced electrode decay, where the grain structure of the polycrystalline electrode almost completely fades away after 90 min of high-temperature oxidation (Figure 3c). Overall, the combined effect of surface area enhancement as well as previously reported [36,37] increased charge carrier concentration within the diamond structure may possibly result in an improved electrochemical response by BDD electrodes.

The detailed topography studies were carried out using atomic force microscopy (AFM) in contact mode. Next, scanning spreading resistance microscopy (SSRM), an AFM technique derivative, allows obtaining maps of local distribution of surface resistance, originating from changes in BDD termination type due to high-temperature treatment. The topographic images (Figure 4) were acquired simultaneously with surface conductivity maps (Figure 5).

The sequence of three-dimensional images of the surface shown in Figure 4 allows observing the evolution of surface morphology consistent with that obtained by scanning electron microscopy (refer to Figure 3). The first clearly represented pyramidal crystallites change into fractured, irregularly shaped structures with high-temperature treatment duration, clearly visible in the red-marked areas. It should be noted that this form of surface development affects the modification of the conductivity distribution through the geometric factor of the contact surface between the surface and various parts of the surface of the AFM pyramid tip [29]. Furthermore, possible surface development increases might contribute to the increase of the electrochemically active surface area.

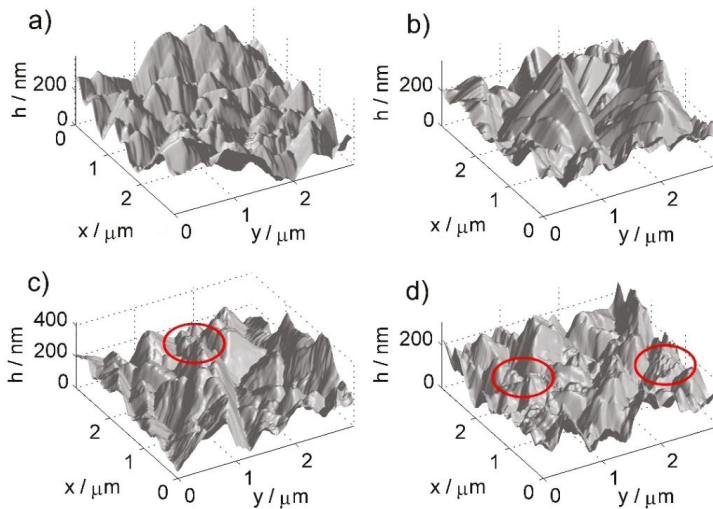


**Figure 4.** The atomic force microscopy (AFM) topography maps for exemplary BDD samples subjected to high-temperature treatment for different durations: (a) reference, untreated sample; (b) 10 min; (c) 30 min; (d) 60 min.



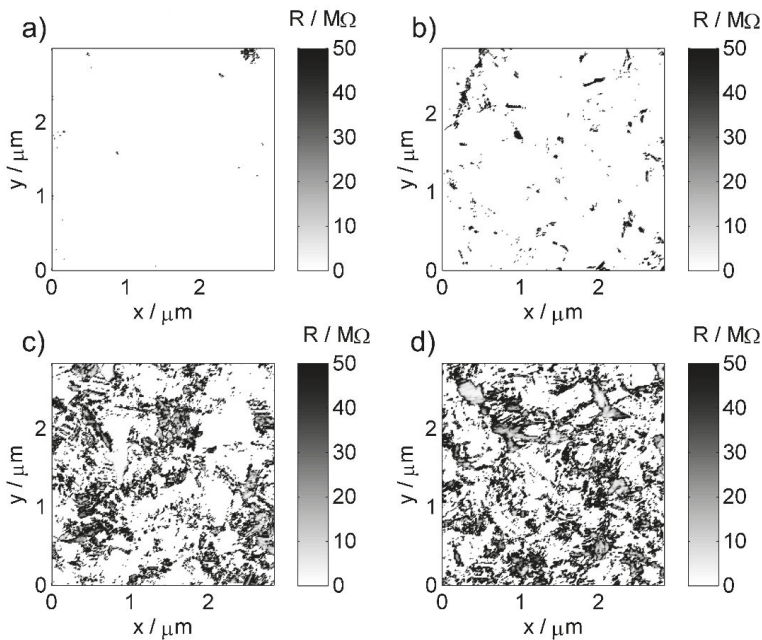


**Figure 5.** Typical spreading resistance (SSRM) maps for BDD samples subjected to different durations of high-temperature treatment in air at 600 °C: (a) reference untreated sample; (b) 10 min; (c) 30 min; (d) 90 min.

For the statistical description of the sample topography, the average roughness parameter was used, defined as:

$$S_a = \frac{1}{MN} \sum_{k=0}^{M-1} \sum_{l=0}^{N-1} |z(x_k, y_l) - \mu| \tag{2}$$

where  $M = N = 256$  are the length and width of the analyzed image in pixels and  $\mu$  is the average height, defined as:

$$\mu = \frac{1}{MN} \sum_{k=0}^{M-1} \sum_{l=0}^{N-1} z(x_k, y_l) \tag{3}$$

The above statistical parameters were determined for areas of  $3 \times 3 \mu\text{m}$ , the scan was repeated 4 times for each sample in different places, and the average roughness contained in Table 2 is the average value from each set of topographic scans.

**Table 2.** Statistical parameters: average roughness  $S_a$  and mean surface resistance  $R$  of studied BDD samples, based on AFM and scanning spreading resistance microscopy (SSRM) analyses.

Parameter	Untreated	High-Temperature Treatment			
		3 min	10 min	30 min	90 min
Mean $S_a/\text{nm}$	55.1374	55.860	51.4811	54.4982	36.3451
Mean $R_s/\Omega$	0.1505	0.7993	1.6417	13.0889	16.1148

The value defined in Equation (2) as  $S_a$  determines the local height deviations from the average value for a given area. Maxima can be associated with the presence of high crystallites; however, their degradation, which progresses over the course of the heat treatment process, causes their degradation

and additionally the formation of fragments of relatively small sizes, contributing to the reduction of maxima.

Figure 5 reveals the results of surface conductance analysis in accordance with the previously presented assumptions. The SSRM technique makes it possible to create a map of the quantity defined as the spreading resistance [53], characterizing the local changes in nanocontact conductivity between the probe tip and the sample surface. A simplified, commonly used formula [54]:

$$R_s = \frac{1}{4\sigma a} \quad (4)$$

where  $a$  is the radius of curvature of the probe tip and  $\sigma$  is the specific conductivity of the sample material, indicates the need for a trade-off between spatial resolution and probe durability, related to the thickness of the conductive layer and the radius of curvature  $a$ . The probes used in this report have a significantly increased radius of curvature for typical topographic ones (10 nm); however, they provide sufficient resolution to visualize changes in conductivity structure.

There is a visible decrease in the surface resistance average value, as well as a significant change in the mutual relationship between areas with relatively high and low electrical conductivity. For samples subjected to longer exposure, a bimodal character of conductivity can be seen with a gradual increase in the share of low conductivity areas. The observable changes present a good representation of the transition from HT- to OT-BDD under the oxidation agent [29]. Furthermore, it may be observed that high-temperature treatment leads to significant heterogeneity in surface oxidation, where the areas of altered spreading resistance are corresponding to different grain areas of the polycrystalline electrode. This observation may suggest that a varied crystallographic orientation is affecting the oxidation propensity, thus translating to locally variable electrochemical activity, as demonstrated by SECM studies.

It should be noted that the recorded heterogeneity in conductive regions can only be treated as a rough estimate of the variable electrochemical activity due to the difference in the conditions on the nanocontact in the atmosphere of air and in an electrolytic environment. Nevertheless, changes in the spreading resistance should to some extent correlate with changes in the charge transfer resistance on the surface of BDD and additionally reflect the trend of its changes together with the variability of heat treatment conditions. In this sense, the above discussed heterogeneity may correspond to the Compton model of partially blocked electrodes [55,56].

The high-resolution XPS spectra of BDD electrodes after different durations of high-temperature treatment are presented in Figure 6. These data were recorded in C1s peak binding energy range. The spectra were then deconvoluted according to the fitting model presented below and the results of the analysis summarized in Table 3.

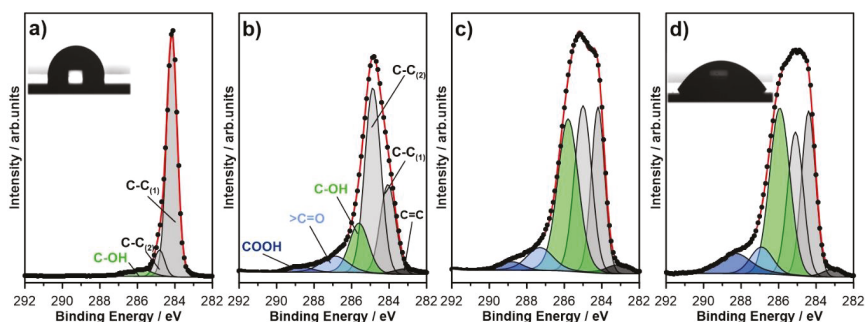


**Figure 6.** High-resolution X-ray photoelectron spectroscopy (XPS) spectra recorded in C1s binding energy range with applied spectral deconvolution. Spectra recorded for BDD samples: (a) as-prepared and after high-temperature treatment in air at 600 °C: (b) 3 min; (c) 10 min; (d) 30 min.

**Table 3.** Chemical composition (in %) of various carbon chemical states on the surface of untreated BDD electrodes and after high-temperature treatment in air at 600 °C, based on high-resolution XPS analysis.

Chemical State	BE/eV	Untreated	High-Temperature Treatment				
			3 min	10 min	30 min	90 min	
C1s	C-C sp <sup>2</sup>	283.2	2.1	2.4	2.9	1.8	1.5
	C-C <sub>(1)</sub>	284.2	83.5	23.1	23.7	24.4	25.3
	C-C <sub>(2)</sub>	284.9	8.7	49.2	30.3	23.9	20.8
	C-OH	285.6	4.8	15.8	31.6	35.6	36.8
	>C=O	287.0	0.6	7.4	6.6	6.4	6.5
	COOH	288.7	0.3	2.1	4.9	7.9	9.1

The C1s spectra recorded for the as-prepared BDD electrode, not subjected to high-temperature oxidation, reveals relatively simple surface chemistry. The registered spectra may be deconvoluted using three separate components. The primary peak, denoted as C-C<sub>(1)</sub> and located at approximately 284.2 eV, lies in the energy range characteristic for sp<sup>3</sup>-carbon CH species on the hydrogen-terminated diamond surface and sp<sup>3</sup>-carbon within the BDD bulk. The exact location of this peak depends on crystallographic texture rather than boron dopant concentration [57,58]. Thus, the peak position is in good agreement with previous studies on heavy boron-doped diamond substrates [20,29,59]. The second notable component, C-C<sub>(2)</sub>, is usually attributed to non-hydrogenated carbon atoms on the BDD surface but also adsorbed polyhydride carbon (CH<sub>x</sub>) species [20,60]. The position of this component is typically shifted by +0.7 eV vs. C-C<sub>(1)</sub>, which is also in this case.

The oxidation of BDD surface termination, occurring as a result of high-temperature treatment in air, results in the substitution of hydrogenated terminal bonds with oxygen-containing species: hydroxyl C-OH (peak at 285.6 eV), but also carbonyl >C=O (at 287.0 eV) and carboxyl COOH (at 288.7 eV) groups [41,57,61]. The XPS analyses confirmed that hydroxyl species are the dominant ones on the surface of high-temperature-treated BDD electrode, unlike other types of surface oxidation treatments (electrochemical, oxygen plasma, ozone treatment, etc.) [29]. The HT- to OT-BDD transition is bound to the increase in surface hydrophobicity, as illustrated by the drop shape analyses in the inset of Figure 6a,d.

The total share of oxidized BDD surface area, OT-BDD, counted as a sum of the above-mentioned components is naturally increasing with the duration of sample exposure to the high temperature. The share of OT-BDD surface for the untreated samples was 5.7% and gradually increased up to 43.1% after 10 min of exposure. Prolonged treatment leads to further surface oxidation, but the total OT-BDD share tends to the plateau with only 52.4% oxidized surface after 90 min of treatment. This effect is partially bound to the fact that the XPS analysis is partially obtained from ~5 nm volume beneath the electrode surface. However, similar studies on BDD electrodes, but oxidized by electrochemical or oxygen plasma treatment, have led to significant diminishing of C-C<sub>(1)</sub> peak, down to 12%–14% [29]. Retaining around 25% of HT-BDD surface even after 90 min of high temperature is well represented and imaged on the SSRM micrographs (see Figure 5), which reveals a significant heterogeneity of oxidized areas on the BDD electrode surface. Following the electric BDD spatial heterogeneity is the electrochemical behavior, determining the conditions of the charge transfer mechanism by a partially blocked electrode.

It was also observed that prolonged high-temperature treatment durations have led to the disappearance of the spectral component, located at approximately 283.2 eV, and originating from surface sp<sup>2</sup>-carbon, which is well explained by a previously mentioned theory that such an exposure results in disordered grain boundaries and significantly deteriorated BDD conductivity.

The above discussed effect of high-temperature treatment in air at 600 °C on BDD surface chemistry is schematically presented in Figure 7. The initially hydrogen-terminated surface of the polycrystalline BDD electrode undergoes surface oxidation over very short durations, even after a few minutes of exposure to the oxidation agent. This effect is heterogeneous in nature and hypothetically limited to

specific crystallographic planes, based on previous studies [29,51,62]. The authors did not investigate the exact planes of high-temperature interaction within this study. The prolonged treatment leads to the appearance of etch pits on the diamond surface. This effect is said to increase the electroactive surface area; however, it was not confirmed since the OT-BDD surface is characterized by lower values of the standard reaction rate constant. Most importantly, the appearance of the etch pits is heterogeneous and depends on the crystallographic orientation, which is similar to surface oxygen termination. According to the literature survey, the etch pits are primarily initiated at (111) facets [19], which, on the other hand, are the least prone to surface oxidation [63].

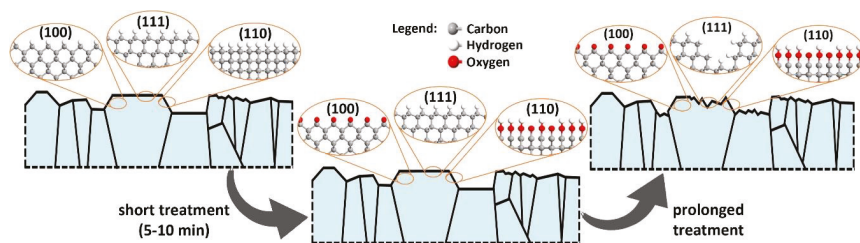


**Figure 7.** Schematic visualization of the oxidation process under high-temperature treatment in air at 600 °C.

### 3.3. Reversibility of the High-Temperature BDD Surface Oxidation

A few available routes for surface rehydrogenation have been reported in the literature, where hydrogen plasma treatment is claimed to be the most efficient [64]. Despite growing awareness and interest in this topic, some studies reveal issues with the reversibility of oxidized BDD electrodes [31]. Various surface physico-chemical properties (such as surface chemistry or contact angle) are often reported to be on par with those observed for BDD electrodes prior to their oxidation; however, electrochemical and electric parameters seem to be a subject of irreversible change. The above-mentioned characterization is most often discussed in the case of electrochemically oxidized BDDs. We decided to evaluate the reversibility of the oxidation process under study since both the mechanism of oxidation and the resultant surface chemistry are claimed to be different in the case of high-temperature treatment than any other oxidation route.

Figure 8a reveals the CV scans at 50 mV/s for high-temperature oxidized (at various durations) and then plasma rehydrogenated BDDs, compared to the as-prepared BDD electrode. Our studies show that neither of the investigated electrodes is characterized by improved peak current values. On the other hand, a significant improvement is visible when compared to oxidized BDD electrode kinetics. It appears that very short high-temperature treatments might lead to a certain improvement in electrochemical characteristics, that is, the peak separation  $\Delta E$  is significantly improved and closer to the theoretical value of diffusion-controlled electrode processes, with high peak symmetry and peak currents equal to nearly 90% of its original value. This feature might be explained by the removal of  $sp^2$ -carbon species adsorbed on the BDD electrode surface after the CVD process, demonstrating a successful electrode cleaning. The longer the high-temperature treatment duration, the lower the value of both anodic and cathodic peak currents and the more irreversible the character of the oxidation process. This effect is naturally connected with the degradation of the BDD grain structure. While the deterioration of the electrode kinetics is progressive, an interesting feature may be observed for the sample after 90 min oxidation and rehydrogenation, which is characterized by the most narrowly observed  $\Delta E$  value. Following the previously defined partially blocked electrode mechanism, it may be concluded that deep etching of BDD grains (refer to Figure 3c) leads to homogenization of the electrode surface and unification of the diffusion fields at the electrode interface, a conclusion supported by SSRM studies. The detailed analysis is summarized in Table 4.

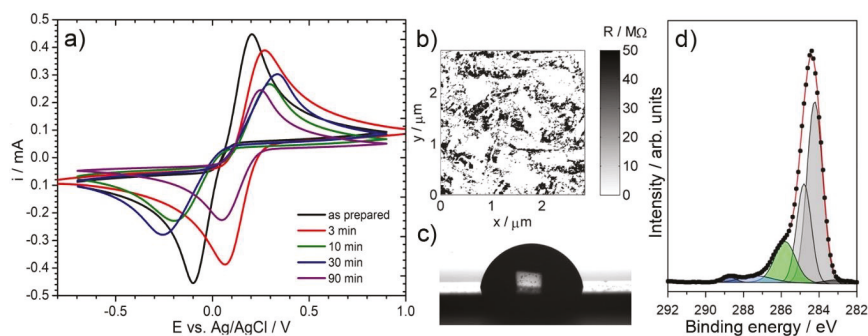


**Figure 8.** The effect of BDD surface rehydrogenation in plasma: (a) CV studies after various durations of oxidation. A scan rate of 50 mV/s. Electrolytic solution: 0.5 M  $\text{Na}_2\text{SO}_4$  with 2.5 mM  $\text{K}_3[\text{Fe}(\text{CN})_6]$  and 2.5 mM  $\text{K}_4[\text{Fe}(\text{CN})_6]$ ; (b–d) exemplary results for electrodes after 30 min oxidation followed by rehydrogenation: (b) SSRM map, (c) contact angle analysis, and (d) high-resolution XPS C1s spectrum.

**Table 4.** Electrochemical properties (anodic peak current  $i_A$ , anodic-to-cathodic peak current ratio  $i_A/i_C$ , peak separation  $\Delta E$ ) based on CV studies (at 50 mV/s scan rate) of BDD samples after various high-temperature treatment durations, followed by sample rehydrogenation in plasma.

Parameter	Untreated	High-Temperature Treated and Rehydrogenated			
		3 min	10 min	30 min	90 min
$i_A/\text{mA}$	0.44	0.39	0.26	0.29	0.24
$i_A/i_C$	0.97	1.00	1.19	0.88	1.06
$\Delta E/\text{V}$	0.35	0.22	0.50	0.55	0.20

A similar observation is revealed by SSRM maps, shown in Figure 8b for BDD electrodes after 30 min of high-temperature treatment and rehydrogenation. While the hydrogen plasma is increasing the surface conductance, the  $R_s$  is far off from its original value (10.416 M $\Omega$ ) and the local distribution of electric properties on the BDD surface remains heterogeneous. This is an important observation, confirming that not only the electrochemical but also the electric parameter characteristics have been modified. However, the rehydrogenation process undoubtedly does have a positive effect on BDD surface chemistry, demonstrated by the XPS analysis (Figure 8d). The hydrogenation process led to a significant reduction in the OT-BDD share (from 49.9% to 20.6%) and, in particular, in the number of surface hydroxyl groups (from 35.6% to 15.7%), which decreased more than twice for prolonged oxidized samples. The reappearance of the hydrogen-terminated surface resulted in the increase of surface hydrophobicity, observed with the drop shape analysis (Figure 8c). However, the process is not fully reversible, thus leading to a conclusion regarding the corrosive nature of the high-temperature treatment, in particular at prolonged oxidation durations.

#### 4. Conclusions

In summary, we performed a detailed study of the influence of high temperature on the oxidation processes for heavy boron-doped diamond electrodes. Electrode surface was investigated by both electrochemical and physico-chemical techniques to reveal its charge transfer kinetics and oxidation behavior.

High-temperature oxidation leads to:

- ✓ hindered charge transfer kinetics, demonstrated by the decrease in peak current on CV scans when comparing to the as-prepared BDDs, a feature observed even at the shortest treatment duration;
- ✓ the modification of BDD microstructure and the appearance of small and shallow etch pits throughout the diamond surface, damaging diamond structure at prolonged treatments;

- ✓ the disappearance of the spectral component, located at approximately 283.2 eV, and originating from surface sp<sup>2</sup>-carbon in XPS;
- ✓ the bimodal character of BDD conductivity observed by SRRM with a gradual increase in the share of low conductivity areas, dependent on the BDD crystallographic structure.

The change in the electrode's surface electric properties by local surface oxidation is reflected in a more heterogeneous distribution of the diffusion field, observed by SECM. The longer the high-temperature exposure duration, the lower the value of both anodic and cathodic peak currents and the more irreversible is the character of the oxidation process, which is mainly attributed to the corrosion of BDD grain structure and the deterioration of electrochemical activity.

**Author Contributions:** Conceptualization, J.R. and A.Z.; Methodology, J.R. and A.Z.; Investigation, J.R. (XPS, SEM, electrochemical studies), M.C. (electrochemical studies), M.F. and B.D. (BDD synthesis and structural studies), and A.Z. (AFM and SSRM); supervision, J.R.; writing—original draft preparation, all authors; writing—review and editing, J.R., R.B., and A.Z.; funding acquisition: J.R., K.D., and R.B. All authors have read and agreed to the published version of the manuscript.

**Funding:** This research was funded by the National Science Centre, grant SONATA number 2015/17/D/ST5/02571, and by the National Centre for Science and Development, grant Techmatstrateg number 347324. The DS funds from the Faculty of Chemistry and the Faculty of Electronics, Telecommunication, and Informatics are also acknowledged.

**Acknowledgments:** The authors acknowledge Lukasz Burczyk for performing the SECM measurements.

**Conflicts of Interest:** The authors declare no conflict of interest.

## References

1. Sussmann, E.S. *CVD Diamond for Electronic Devices and Sensors*; John Wiley & Sons: New York, NY, USA, 2009; ISBN 978-0-470-74039-2.
2. Muzyka, K.; Sun, J.; Fereja, T.H.; Lan, Y.; Zhang, W.; Xu, G. Boron-doped diamond: Current progress and challenges in view of electroanalytical applications. *Anal. Methods* **2019**, *11*, 397–414. [[CrossRef](#)]
3. Yu, S.; Yang, N.; Jiang, X.; Zhang, W.; Liu, S. Conductive Diamond for Electrochemical Energy Applications. In *Nanocarbon Electrochemistry*; Yang, N., Zhao, G., Foord, J., Eds.; John Wiley & Sons: New York, NY, USA, 2020; pp. 171–199. ISBN 978-1-119-46823-3.
4. Nidheesh, P.V.; Divyapriya, G.; Oturan, N.; Trellu, C.; Oturan, M.A. Environmental Applications of Boron-Doped Diamond Electrodes: 1. Applications in Water and Wastewater Treatment. *ChemElectroChem* **2019**, *6*, 2124–2142. [[CrossRef](#)]
5. Yang, N. (Ed.) *Novel Aspects of Diamond: From Growth to Applications*; Springer International Publishing: Cham, Switzerland, 2019; Volume 121, ISBN 978-3-030-12468-7.
6. Ashcheulov, P.; Taylor, A.; Mortet, V.; Poruba, A.; Le Formal, F.; Krýsová, H.; Klementová, M.; Hubík, P.; Kopeček, J.; Lorinčík, J.; et al. Nanocrystalline Boron-Doped Diamond as a Corrosion-Resistant Anode for Water Oxidation via Si Photoelectrodes. *ACS Appl. Mater. Interfaces* **2018**, *10*, 29552–29564. [[CrossRef](#)]
7. Schranck, A.; Doudrick, K. Effect of reactor configuration on the kinetics and nitrogen byproduct selectivity of urea electrolysis using a boron doped diamond electrode. *Water Res.* **2020**, *168*, 115130. [[CrossRef](#)] [[PubMed](#)]
8. Mei, R.; Zhu, C.; Wei, Q.; Ma, L.; Li, W.; Zhou, B.; Deng, Z.; Tong, Z.; Ouyang, G.; Jiang, C. The Dependence of Oxidation Parameters and Dyes' Molecular Structures on Microstructure of Boron-Doped Diamond in Electrochemical Oxidation Process of Dye Wastewater. *J. Electrochem. Soc.* **2018**, *165*, H324–H332. [[CrossRef](#)]
9. Zhang, Y.; Teo, K.H.; Palacios, T. Beyond Thermal Management: Incorporating p-Diamond Back-Barriers and Cap Layers Into AlGaN/GaN HEMTs. *IEEE Trans. Electron. Devices* **2016**, *63*, 2340–2345. [[CrossRef](#)]
10. Williams, G.; Calvo, J.A.; Fails, F.; Dodson, J.; Obeloer, T.; Twitchen, D.J. Thermal Conductivity of Electrically Conductive Highly Boron Doped Diamond and its Applications at High Frequencies. In Proceedings of the 2018 17th IEEE Intersociety Conference on Thermal and Thermomechanical Phenomena in Electronic Systems (ITherm), San Diego, CA, USA, 29 May–1 June 2018; pp. 235–239.
11. Panizza, M.; Cerisola, G. Application of diamond electrodes to electrochemical processes. *Electrochim. Acta* **2005**, *51*, 191–199. [[CrossRef](#)]

12. Luong, J.H.T.; Male, K.B.; Glennon, J.D. Boron-doped diamond electrode: Synthesis, characterization, functionalization and analytical applications. *Analyst* **2009**, *134*, 1965. [\[CrossRef\]](#)
13. Herrmann, M.; Matthey, B.; Gestrich, T. Boron-doped diamond with improved oxidation resistance. *Diam. Relat. Mater.* **2019**, *92*, 47–52. [\[CrossRef\]](#)
14. Wang, J.; Swain, G.M. Dimensionally Stable Pt/Diamond Composite Electrodes in Concentrated H<sub>3</sub>PO<sub>4</sub> at High Temperature. *Electrochem. Solid State Lett.* **2002**, *5*, E4. [\[CrossRef\]](#)
15. Umezawa, H.; Nagase, M.; Kato, Y.; Shikata, S. High temperature application of diamond power device. *Diam. Relat. Mater.* **2012**, *24*, 201–205. [\[CrossRef\]](#)
16. Ueda, K.; Kawamoto, K.; Soumiya, T.; Asano, H. High-temperature characteristics of Ag and Ni/diamond Schottky diodes. *Diam. Relat. Mater.* **2013**, *38*, 41–44. [\[CrossRef\]](#)
17. Jiang, M.; Yu, H.; Li, X.; Lu, S.; Hu, X. Thermal oxidation induced high electrochemical activity of boron-doped nanocrystalline diamond electrodes. *Electrochim. Acta* **2017**, *258*, 61–70. [\[CrossRef\]](#)
18. Pehrsson, P.E.; Mercer, T.W.; Chaney, J.A. Thermal oxidation of the hydrogenated diamond (100) surface. *Surf. Sci.* **2002**, *497*, 13–28. [\[CrossRef\]](#)
19. Zhang, J.; Nakai, T.; Uno, M.; Nishiki, Y.; Sugimoto, W. Effect of the boron content on the steam activation of boron-doped diamond electrodes. *Carbon* **2013**, *65*, 206–213. [\[CrossRef\]](#)
20. Ryl, J.; Burczyk, L.; Bogdanowicz, R.; Sobaszek, M.; Darowicki, K. Study on surface termination of boron-doped diamond electrodes under anodic polarization in H<sub>2</sub>SO<sub>4</sub> by means of dynamic impedance technique. *Carbon* **2016**, *96*, 1093–1105. [\[CrossRef\]](#)
21. Martínez-Huitle, C.A.; Ferro, S.; Reyna, S.; Cerro-López, M.; De Battisti, A.; Quiroz, M.A. Electrochemical oxidation of oxalic acid in the presence of halides at boron doped diamond electrode. *J. Braz. Chem. Soc.* **2008**, *19*, 150–156. [\[CrossRef\]](#)
22. Hayashi, K.; Yamanaka, S.; Watanabe, H.; Sekiguchi, T.; Okushi, H.; Kajimura, K. Investigation of the effect of hydrogen on electrical and optical properties in chemical vapor deposited on homoepitaxial diamond films. *J. Appl. Phys.* **1997**, *81*, 744–753. [\[CrossRef\]](#)
23. Grot, S.A.; Gildenblat, G.S.; Hatfield, C.W.; Wronski, C.R.; Badzian, A.R.; Badzian, T.; Messier, R. The effect of surface treatment on the electrical properties of metal contacts to boron-doped homoepitaxial diamond film. *IEEE Electron. Dev. Lett.* **1990**, *11*, 100–102. [\[CrossRef\]](#)
24. Švorc, L.; Rievaj, M.; Bustin, D. Green electrochemical sensor for environmental monitoring of pesticides: Determination of atrazine in river waters using a boron-doped diamond electrode. *Sens. Actuators B Chem.* **2013**, *181*, 294–300. [\[CrossRef\]](#)
25. Yagi, I.; Notsu, H.; Kondo, T.; Tryk, D.A.; Fujishima, A. Electrochemical selectivity for redox systems at oxygen-terminated diamond electrodes. *J. Electroanal. Chem.* **1999**, *473*, 173–178. [\[CrossRef\]](#)
26. Boukherroub, R.; Wallart, X.; Szunerits, S.; Marcus, B.; Bouvier, P.; Mermoux, M. Photochemical oxidation of hydrogenated boron-doped diamond surfaces. *Electrochem. Commun.* **2005**, *7*, 937–940. [\[CrossRef\]](#)
27. Geisler, M.; Hugel, T. Aging of Hydrogenated and Oxidized Diamond. *Adv. Mater.* **2010**, *22*, 398–402. [\[CrossRef\]](#)
28. Vanhove, E.; de Sanoit, J.; Arnault, J.C.; Saada, S.; Mer, C.; Mailley, P.; Bergonzo, P.; Nesladek, M. Stability of H-terminated BDD electrodes: An insight into the influence of the surface preparation. *Phys. Status Solidi* **2007**, *204*, 2931–2939. [\[CrossRef\]](#)
29. Zielinski, A.; Cieslik, M.; Sobaszek, M.; Bogdanowicz, R.; Darowicki, K.; Ryl, J. Multifrequency nanoscale impedance microscopy (m-NIM): A novel approach towards detection of selective and subtle modifications on the surface of polycrystalline boron-doped diamond electrodes. *Ultramicroscopy* **2019**, *199*, 34–45. [\[CrossRef\]](#)
30. Ghodbane, S.; Haensel, T.; Coffinier, Y.; Szunerits, S.; Steinmüller-Nethl, D.; Boukherroub, R.; Ahmed, S.I.-U.; Schaefer, J.A. HREELS Investigation of the Surfaces of Nanocrystalline Diamond Films Oxidized by Different Processes. *Langmuir* **2010**, *26*, 18798–18805. [\[CrossRef\]](#)
31. Girard, H.; Simon, N.; Ballutaud, D.; Herlem, M.; Etcheberry, A. Effect of anodic and cathodic treatments on the charge transfer of boron doped diamond electrodes. *Diam. Relat. Mater.* **2007**, *16*, 316–325. [\[CrossRef\]](#)
32. Ryl, J.; Bogdanowicz, R.; Slepski, P.; Sobaszek, M.; Darowicki, K. Dynamic Electrochemical Impedance Spectroscopy (DEIS) as a Tool for Analyzing Surface Oxidation Processes on Boron-Doped Diamond Electrodes. *J. Electrochem. Soc.* **2014**, *161*, H359–H364. [\[CrossRef\]](#)
33. Ferro, S.; Dal Colle, M.; De Battisti, A. Chemical surface characterization of electrochemically and thermally oxidized boron-doped diamond film electrodes. *Carbon* **2005**, *43*, 1191–1203. [\[CrossRef\]](#)

34. Shpilman, Z.; Gouzman, I.; Minton, T.K.; Shen, L.; Stacey, A.; Orwa, J.; Praver, S.; Cowie, B.C.C.; Hoffman, A. A near edge X-ray absorption fine structure study of oxidized single crystal and polycrystalline diamond surfaces. *Diam. Relat. Mater.* **2014**, *45*, 20–27. [[CrossRef](#)]
35. Zolotukhin, A.; Kopylov, P.G.; Ismagilov, R.R.; Obratsov, A.N. Thermal oxidation of CVD diamond. *Diam. Relat. Mater.* **2010**, *19*, 1007–1011. [[CrossRef](#)]
36. Show, Y.; Witek, M.A.; Sonthalia, P.; Swain, G.M. Characterization and Electrochemical Responsiveness of Boron-Doped Nanocrystalline Diamond Thin-Film Electrodes. *Chem. Mater.* **2003**, *15*, 879–888. [[CrossRef](#)]
37. Szunerits, S.; Boukherroub, R.; Downard, A.; Zhu, J.-J. (Eds.) Nanocarbon chemistry and interfaces. In *Nanocarbons for Electroanalysis*, 1st ed.; John Wiley & Sons: Hoboken, NJ, USA, 2017; ISBN 978-1-119-24395-3.
38. Ficek, M.; Bogdanowicz, R.; Ryl, J. Nanocrystalline CVD Diamond Coatings on Fused Silica Optical Fibres: Optical Properties Study. *Acta Phys. Pol. A* **2015**, *127*, 868–873. [[CrossRef](#)]
39. Zielinski, A.; Bogdanowicz, R.; Ryl, J.; Burczyk, L.; Darowicki, K. Local impedance imaging of boron-doped polycrystalline diamond thin films. *Appl. Phys. Lett.* **2014**, *105*, 131908. [[CrossRef](#)]
40. Ryl, J.; Burczyk, L.; Zielinski, A.; Ficek, M.; Franczak, A.; Bogdanowicz, R.; Darowicki, K. Heterogeneous oxidation of highly boron-doped diamond electrodes and its influence on the surface distribution of electrochemical activity. *Electrochim. Acta* **2019**, *297*, 1018–1027. [[CrossRef](#)]
41. Bogdanowicz, R.; Sawczak, M.; Niedzialkowski, P.; Zieba, P.; Finke, B.; Ryl, J.; Karczewski, J.; Ossowski, T. Novel Functionalization of Boron-Doped Diamond by Microwave Pulsed-Plasma Polymerized Allylamine Film. *J. Phys. Chem. C* **2014**, *118*, 8014–8025. [[CrossRef](#)]
42. Richard, W. Kinetic Study of Redox Probes on Glassy Carbon Electrode Functionalized by 4-nitrobenzene Diazonium. *Int. J. Electrochem. Sci.* **2019**, 453–469. [[CrossRef](#)]
43. Bard, A.J.; Faulkner, L.R. *Electrochemical Methods: Fundamentals and Applications*, 2nd ed.; Wiley: New York, NY, USA, 2001; ISBN 978-0-471-04372-0.
44. Bogdanowicz, R.; Sawczak, M.; Niedzialkowski, P.; Zieba, P.; Finke, B.; Ryl, J.; Ossowski, T. Direct amination of boron-doped diamond by plasma polymerized allylamine film: Direct amination of boron-doped diamond. *Phys. Status Solidi* **2014**, *211*, 2319–2327. [[CrossRef](#)]
45. Actis, P.; Denoyelle, A.; Boukherroub, R.; Szunerits, S. Influence of the surface termination on the electrochemical properties of boron-doped diamond (BDD) interfaces. *Electrochem. Commun.* **2008**, *10*, 402–406. [[CrossRef](#)]
46. Velasco, J.G. Determination of standard rate constants for electrochemical irreversible processes from linear sweep voltammograms. *Electroanalysis* **1997**, *9*, 880–882. [[CrossRef](#)]
47. Konopka, S.J.; McDuffie, B. Diffusion coefficients of ferri- and ferrocyanide ions in aqueous media, using twin-electrode thin-layer electrochemistry. *Anal. Chem.* **1970**, *42*, 1741–1746. [[CrossRef](#)]
48. Holt, K.B.; Bard, A.J.; Show, Y.; Swain, G.M. Scanning Electrochemical Microscopy and Conductive Probe Atomic Force Microscopy Studies of Hydrogen-Terminated Boron-Doped Diamond Electrodes with Different Doping Levels. *J. Phys. Chem. B* **2004**, *108*, 15117–15127. [[CrossRef](#)]
49. Kondo, T.; Kodama, Y.; Ikezoe, S.; Yajima, K.; Aikawa, T.; Yuasa, M. Porous boron-doped diamond electrodes fabricated via two-step thermal treatment. *Carbon* **2014**, *77*, 783–789. [[CrossRef](#)]
50. Ohashi, T.; Zhang, J.; Takasu, Y.; Sugimoto, W. Steam activation of boron doped diamond electrodes. *Electrochim. Acta* **2011**, *56*, 5599–5604. [[CrossRef](#)]
51. Ryl, J.; Zielinski, A.; Bogdanowicz, R.; Darowicki, K. Heterogeneous distribution of surface electrochemical activity in polycrystalline highly boron-doped diamond electrodes under deep anodic polarization. *Electrochem. Commun.* **2017**, *83*, 41–45. [[CrossRef](#)]
52. Siuzdak, K.; Bogdanowicz, R.; Sawczak, M.; Sobaszek, M. Enhanced capacitance of composite TiO<sub>2</sub> nanotube/boron-doped diamond electrodes studied by impedance spectroscopy. *Nanoscale* **2015**, *7*, 551–558. [[CrossRef](#)]
53. Denhoff, M.W. An accurate calculation of spreading resistance. *J. Phys. D Appl. Phys.* **2006**, *39*, 1761–1765. [[CrossRef](#)]
54. Dickens, L.E. Spreading Resistance as a Function of Frequency. *IEEE Trans. Microw. Theory Technol.* **1967**, *15*, 101–109. [[CrossRef](#)]
55. Chevallier, F.G.; Fietkau, N.; del Campo, J.; Mas, R.; Muñoz, F.X.; Jiang, L.; Jones, T.G.J.; Compton, R.G. Experimental cyclic voltammetry at partially blocked electrodes: Elevated cylindrical blocks. *J. Electroanal. Chem.* **2006**, *596*, 25–32. [[CrossRef](#)]
56. Davies, T.J.; Banks, C.E.; Compton, R.G. Voltammetry at spatially heterogeneous electrodes. *J. Solid State Electrochem.* **2005**, *9*, 797–808. [[CrossRef](#)]



57. Ivandini, T.A.; Watanabe, T.; Matsui, T.; Ootani, Y.; Iizuka, S.; Toyoshima, R.; Kodama, H.; Kondoh, H.; Tateyama, Y.; Einaga, Y. Influence of Surface Orientation on Electrochemical Properties of Boron-Doped Diamond. *J. Phys. Chem. C* **2019**, *123*, 5336–5344. [[CrossRef](#)]
58. Ghodbane, S.; Ballutaud, D.; Deneuille, A.; Baron, C. Influence of boron concentration on the XPS spectra of the (100) surface of homoepitaxial boron-doped diamond films. *Phys. State Solid* **2006**, *203*, 3147–3151. [[CrossRef](#)]
59. Ballutaud, D.; Simon, N.; Girard, H.; Rzepka, E.; Bouchet-Fabre, B. Photoelectron spectroscopy of hydrogen at the polycrystalline diamond surface. *Diam. Relat. Mater.* **2006**, *15*, 716–719. [[CrossRef](#)]
60. Girard, H.A.; Simon, N.; Ballutaud, D.; Etcheberry, A. Correlation between flat-band potential position and oxygenated termination nature on boron-doped diamond electrodes. *Comptes Rendus Chim.* **2008**, *11*, 1010–1015. [[CrossRef](#)]
61. Catalan, F.C.I.; Hayazawa, N.; Yokota, Y.; Wong, R.A.; Watanabe, T.; Einaga, Y.; Kim, Y. Facet-Dependent Temporal and Spatial Changes in Boron-Doped Diamond Film Electrodes due to Anodic Corrosion. *J. Phys. Chem. C* **2017**, *121*, 26742–26750. [[CrossRef](#)]
62. Pleskov, Y.V.; Evstefeeva, Y.E.; Krotova, M.D.; Varnin, V.P.; Teremetskaya, I.G. Synthetic semiconductor diamond electrodes: Electrochemical behaviour of homoepitaxial boron-doped films orientated as (111), (110), and (100) faces. *J. Electroanal. Chem.* **2006**, *595*, 168–174. [[CrossRef](#)]
63. Wolfer, M.; Biener, J.; El-dasher, B.S.; Biener, M.M.; Hamza, A.V.; Kriele, A.; Wild, C. Crystallographic anisotropy of growth and etch rates of CVD diamond. *Diam. Relat. Mater.* **2009**, *18*, 713–717. [[CrossRef](#)]
64. zevedo, A.F.; Braga, N.A.; Souza, F.A.; Matsushima, J.T.; Baldan, M.R.; Ferreira, N.G. The effect of surface treatment on oxidation of oxalic acid at nanocrystalline diamond films. *Diam. Relat. Mater.* **2010**, *19*, 462–465. [[CrossRef](#)]



© 2020 by the authors. Licensee MDPI, Basel, Switzerland. This article is an open access article distributed under the terms and conditions of the Creative Commons Attribution (CC BY) license (<http://creativecommons.org/licenses/by/4.0/>).

MDPI  
St. Alban-Anlage 66  
4052 Basel  
Switzerland  
Tel. +41 61 683 77 34  
Fax +41 61 302 89 18  
[www.mdpi.com](http://www.mdpi.com)

*Materials* Editorial Office  
E-mail: [materials@mdpi.com](mailto:materials@mdpi.com)  
[www.mdpi.com/journal/materials](http://www.mdpi.com/journal/materials)





MDPI  
St. Alban-Anlage 66  
4052 Basel  
Switzerland

Tel: +41 61 683 77 34  
Fax: +41 61 302 89 18

[www.mdpi.com](http://www.mdpi.com)



ISBN 978-3-03936-177-9